frontiers | Research Topics

Physico-mechanical properties and treatment technology of hazardous geomaterials, volume II

Edited by
Xianze Cui, Bing Bai and Wenbin Fei

Published in
Frontiers in Materials

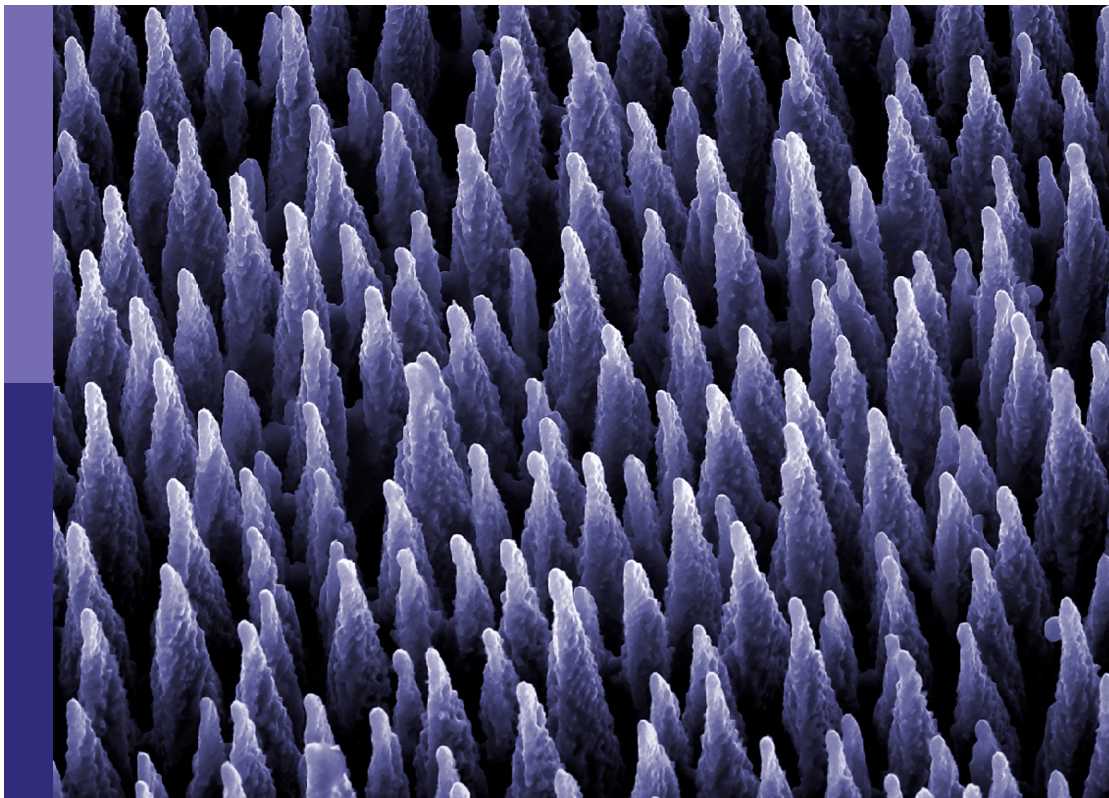

ISSN 1664-8714
ISBN 978-2-8325-4159-3
DOI 10.3389/978-2-8325-4159-3

About Frontiers

Frontiers is more than just an open access publisher of scholarly articles: it is a pioneering approach to the world of academia, radically improving the way scholarly research is managed. The grand vision of Frontiers is a world where all people have an equal opportunity to seek, share and generate knowledge. Frontiers provides immediate and permanent online open access to all its publications, but this alone is not enough to realize our grand goals.

Frontiers journal series

The Frontiers journal series is a multi-tier and interdisciplinary set of open-access, online journals, promising a paradigm shift from the current review, selection and dissemination processes in academic publishing. All Frontiers journals are driven by researchers for researchers; therefore, they constitute a service to the scholarly community. At the same time, the *Frontiers journal series* operates on a revolutionary invention, the tiered publishing system, initially addressing specific communities of scholars, and gradually climbing up to broader public understanding, thus serving the interests of the lay society, too.

Dedication to quality

Each Frontiers article is a landmark of the highest quality, thanks to genuinely collaborative interactions between authors and review editors, who include some of the world's best academicians. Research must be certified by peers before entering a stream of knowledge that may eventually reach the public - and shape society; therefore, Frontiers only applies the most rigorous and unbiased reviews. Frontiers revolutionizes research publishing by freely delivering the most outstanding research, evaluated with no bias from both the academic and social point of view. By applying the most advanced information technologies, Frontiers is catapulting scholarly publishing into a new generation.

What are Frontiers Research Topics?

Frontiers Research Topics are very popular trademarks of the *Frontiers journals series*: they are collections of at least ten articles, all centered on a particular subject. With their unique mix of varied contributions from Original Research to Review Articles, Frontiers Research Topics unify the most influential researchers, the latest key findings and historical advances in a hot research area.

Find out more on how to host your own Frontiers Research Topic or contribute to one as an author by contacting the Frontiers editorial office: frontiersin.org/about/contact

Physico-mechanical properties and treatment technology of hazardous geomaterials, volume II

Topic editors

Xianze Cui — China Three Gorges University, China
Bing Bai — Beijing Jiaotong University, China
Wenbin Fei — The University of Melbourne, Australia

Citation

Cui, X., Bai, B., Fei, W., eds. (2023). *Physico-mechanical properties and treatment technology of hazardous geomaterials, volume II*. Lausanne: Frontiers Media SA. doi: 10.3389/978-2-8325-4159-3

Table of contents

frontiers | Frontiers in Materials

TYPE Editorial
PUBLISHED 05 December 2023
DOI 10.3389/fmats.2023.1334484

OPEN ACCESS

EDITED AND REVIEWED BY
John L. Provis,
Paul Scherrer Institut (PSI), Switzerland

*CORRESPONDENCE
Bing Bai,
bbai@bjtu.edu.cn

RECEIVED 07 November 2023
ACCEPTED 15 November 2023
PUBLISHED 05 December 2023

CITATION
Bai B, Cui X and Fei W (2023), Editorial: Physico-mechanical properties and treatment technology of hazardous geomaterials–volume II.
Front. Mater. 10:1334484.
doi: 10.3389/fmats.2023.1334484

Editorial: Physico-mechanical properties and treatment technology of hazardous geomaterials–volume II

Bing Bai[1]*, Xianze Cui[2] and Wenbin Fei[3]

[1]School of Civil Engineering, Beijing Jiaotong University, Beijing, China, [2]College of Hydraulic & Environmental Engineering, China Three Gorges University, Yichang, China, [3]Department of Infrastructure Engineering, The University of Melbourne, Parkville, VIC, Australia

KEYWORDS

geomaterial, mechanical property, disaster soil, theory model, reinforcement technology

Editorial on the Research Topic
Physico-mechanical properties and treatment technology of hazardous geomaterials-volume II

Introduction

New geomaterials and technologies are emerging in every branch of geotechnical engineering, such as soil improvement, underground excavation, tunnel waterproofing, coal engineering, and high-speed railway subgrade measures. These complex projects include the research and treatment of hazardous geomaterials, industrial waste utilization, geopolymer materials, geo-environments and other newly developed materials. The advancement of new materials has promoted the development of geotechnical engineering and its close intersection with other disciplines. In recent years, many scholars have achieved good research results, but the understanding of these new materials and methods is not very clear.

The Research Topic aims to consolidate original research and review articles on recent developments in hazardous geomaterials, synthetic materials and disaster soil reinforcements. A total of sixteen articles are presented in this Research Topic, including theoretical methods, laboratory experiments, numerical simulations and field tests. The Editorial includes the following information.

- Physico-mechanical properties of hazardous geomaterials
- Disaster soils and reinforcement technology
- New materials and special applications

Physico-mechanical properties of hazardous geomaterials

The physico-mechanical properties of hazardous geomaterials under complex environmental conditions have attracted substantial attention from researchers. Yan et al. introduced an elastic

damage element by considering time-dependent damage and verified the unloading creep characteristics of a stiff flint limestone by a large number of triaxial compression grade-unloading creep tests. Huang et al. modified a power function model to explain the creep strain characteristics of coarse- and fine-grained soils and proposed two creep subsidence prediction algorithms considering stress history based on Bjerrum's reclassification of consolidation, which was verified in practical engineering by two widely used subsidence prediction algorithms.

Wang et al. carried out multilevel cyclic loading mechanical tests on flawed marble samples with different fissure angles, and the test results showed that rock strength, fatigue lifetime, peak strain and dissipated energy increase with increasing fissure angle and that the rates of increase become sharp at high cyclic levels. Guo et al. reported the effects of particle size distribution on the shear properties of sand through four types of sand samples with different particle size distributions, and the research results can aid in the understanding of the changes in particle contact, internal stress, and particle sliding during the shear failure of sand.

Zhang et al. investigated the disaster mechanism influenced by freeze–thaw cycling and hanging wall mining in an open pit iron mine by a 3-dimensional intelligent recognition technology (i.e., a laser scanning method) and numerical simulation, which can effectively reveal the stress, displacement, plasticity zone, and maximum shear strain patterns in detail. Chen et al. delved into explored the mechanical behaviors of mixed soils across various particle contents and sizes using direct shear testing and dissected the distinctive mechanical responses by examining the interplay of particle contact interfaces and adsorption energy through a multiscale energy approach. The experimental research of Deng et al. revealed that the cohesion of saturated reinforced soil exhibited a significant decrease relative to unsaturated reinforced soil, with matrix suction serving as a critical consideration for reinforced structural design, and the results obtained using postshear moisture content were closer to the measured values than those using initial moisture content.

Disaster soils and reinforcement technology

The disposal and reinforcement technology of disaster soils is an important Research Topic in the field of geo-environmental engineering. Yang et al. established a constitutive relationship of a cable body on the basis of the coupling of corrosion force with statistical damage mechanics, derived the relationship between the degree of corrosion of the cable body and the holding prestress using the load transfer method, and verified the rationality of highway slopes during the operation period by actual measurements. Han et al. investigated the influence of the flocculant dosage on the drainage behavior and experimentally showed that the coefficient of secondary consolidation is very significant in slurries modified by the flocculation-enhanced surcharge (vacuum) preloading method. Yang et al. conducted model experiments to reveal the changes in water level outside the pit caused by precipitation, which provided a research basis for the reasonable control and prevention of surface settlement and for the adverse deformation of diaphragm walls in narrow spaces under subsequent seepage conditions in the surrounding area.

By taking the homogeneous slope model as an example, Li et al. analyzed the influences of the location and depth of a single fracture on slope stability and of slope top fractures on the slope seepage field and slope stability with and without rainfall. To make a new type of vertically loaded double-plate anchor, Xing et al. investigated the influences of parameters on the ultimate penetration depth in soft clay and showed that increasing the length of the bottom fluke could increase the ultimate penetration depth when the included angles were the same in clay with zero strength and in clay with uniform strength at the seabed. Feng et al. determined the bearing capacity of a prestressed high-intensity concrete pipe pile (a cement–soil mixing pile) by applying a slow-speed maintenance load, discovering that the characteristic value of the bearing capacity could reach 2,300 kN; this research provided design references for similar site foundation projects.

New materials and special applications

New geomaterials are emerging in many complicated and special geotechnical engineering applications. Dong et al. proposed a prefabricated underground utility tunnel featuring a composite shell system as a new system; the study showed that the composite shell top plate specimen had good collaborative performance, and the researchers proposed an accurate bearing capacity formula. Zhao et al. used a silane coupling agent to modify polyvinyl alcohol (PVA) fibers and discussed the mechanism influencing the modification of the admixture by experimentation and molecular dynamics simulation; macroscopic mechanical experiments showed that the bending resistance of PVA fiber concrete significantly improved after PVA fiber modification.

Li et al. addressed the issue of large solid waste output and surface subsidence and focused on the large filling working face of a typical mine; the scholars employed a combination of theoretical analysis, numerical simulation, and field practice to analyze the limit caving and cycle pressure characteristics of the working face.

Although the submission for this Research Topic has been closed, more in-depth research in the field of hazardous geomaterials and geotechnical environment is being conducted to address these challenges. All of the selected contributions help discover innovative methods and advanced technologies in this field. We would like to thank all editors, reviewers and authors for their crucial contributions.

Author contributions

BB: Conceptualization, Writing–original draft. XC: Writing–original draft. WF: Conceptualization, Writing–review and editing.

Funding

The author(s) declare that no financial support was received for the research, authorship, and/or publication of this article.

Conflict of interest

The authors declare that the research was conducted in the absence of any commercial or financial relationships that could be construed as a potential conflict of interest.

Publisher's note

frontiers | Frontiers in Materials

TYPE Original Research
PUBLISHED 31 March 2023
DOI 10.3389/fmats.2023.1177733

OPEN ACCESS

EDITED BY
Bing Bai,
Beijing Jiaotong University, China

REVIEWED BY
Jinping Li,
Wuhan University, China
Qin Weimin,
Institute of Rock and Soil Mechanics (CAS), China

*CORRESPONDENCE
Shifu Qin,
qinshifu33@163.com

SPECIALTY SECTION
This article was submitted to Structural Materials, a section of the journal Frontiers in Materials

RECEIVED 02 March 2023
ACCEPTED 24 March 2023
PUBLISHED 31 March 2023

CITATION
Yan Q, Qin S, Sang X, Luo Z and Liang M (2023), Research on creep characteristics of loading and unloading of hard Flint limestone.
Front. Mater. 10:1177733.
doi: 10.3389/fmats.2023.1177733

Research on creep characteristics of loading and unloading of hard Flint limestone

Qiao Yan[1,2], Shifu Qin[1,3]*, Xuefeng Sang[2], Zuosen Luo[1,3] and Minghao Liang[4]

[1]Key Laboratory of Geological Hazards on Three Gorges Reservoir Area, Ministry of Education, China Three Gorges University, Yichang, China, [2]College of Hydraulic and Environment, China Three Gorges University, Yichang, China, [3]College of Civil Engineering and Architecture, China Three Gorges University, Yichang, China, [4]China Three Gorges Corporation River Basin Complex Administration Center, Yichang, China

The hard Flint limestone of Shuibuya hydropower station underground construction cavern is utilized as a research object to investigate the creep problem caused by excavation of rock masses such as caverns. In order to perform a triaxial compression grade-unloading creep test, the actual adjustment path of stress during excavation of underground cavern surrounding rock is used. Limestone under different confistiff pressures is then evaluated. Based on the Nishihara model, the elastic damage element considering time-dependent damage is introduced, and the unloading creep constitutive model of stiff Flint limestone is established and verified by experiments. The results show: 1) Deformation and creep strain appear at all stress levels. 2) As the unloading amount increased from 2 to 4 MPa, the quasi-destructive stresses of the samples were smaller from 83 to 79 MPa, indicating that the unloading amount affected the final creep damage strength of the rock samples. In other words, the higher the unloading amount, the lower the ultimate creep failure strength. 3) When entering the accelerated creep stage, the axial and lateral creep strains of the sample increase non-linearly, and the rupture duration of the sample is very short. Therefore, the creep deformation and creep rate characteristics of this stage should be paid attention to in practical engineering. 4) Different from the loading stress path, the failure mode of the Flint limestone rock sample is different. When the unloading amount is 2 and 4 MPa, the creep failure mode of the Flint limestone rock sample is shear failure, showing a significant oblique section crack. 5) The non-linear creep model curve of aging damage and the fitting effect of the unloading creep test curve are acceptable. The rationality of the established non-linear creep model is illustrated.

KEYWORDS

unloading, non-linear, creep model, time-dependent damage, Flint limestone

1 Introduction

According to many engineering practices, surrounding rock at the early stage of construction will not show damage or instability immediately, but with the passage of time, rock mass engineering develops the long-term load creep phenomenon, resulting in rock mass engineering damage (Li, 1999; Sun, 1999; Peng et al., 2020). Therefore, it is necessary to study the creep characteristics of actual engineering rock mass to ensure the safety and stability of its long-term operation.

The rock creep mechanics test is the main method for studying the creep characteristics of rock under long-term loads. Because soft rock has significant creep characteristics, the creep characteristics of soft rock have been studied in the past (Fan et al., 2010; Li and Yang, 2018; Liu et al., 2020). At the same time, creep tests under more loading stress paths were carried out, and more rock creep results were obtained (Park et al., 2017; Li et al., 2019). Despite this, few studies have been conducted on creep under unloading stress. The excavation of rock mass for engineering structures such as caverns causes the stress of surrounding rocks to be redistributed. This results in some rock being in an unloading stress state. For practical engineering purposes, it is necessary to study the creep properties of rock under unloading paths. Underground caverns, tunnels and tunnels are often excavated in layers, and the size of the excavation unload affects the stability of the rockwork. Therefore, it is necessary to study the effect of unloading amount on rock creep under the unloading stress path (Li, 2000; Li et al., 2007).

According to Zhu (2009), the green sandstone in the diversion tunnel of Jinping II hydropower station was used as a research object. Indoor rheological tests were conducted under constant axial pressure and gradual unloading of confining pressure to determine the rotational and lateral deformation characteristics. Huang et al. (2016) carried out triaxial unloading creep tests of sandy mudstone under continuous axial pressure and step-by-step unloading confining pressure, and studied the horizontal, lateral and volumetric creep laws of soft rock and the characteristics of the deviatoric stress-strain relationship during the unloading process. A grading unloading rheological test was conducted under axial pressure unloading confining pressure and constant axial pressure unloading confining pressure by Deng et al. (2016). Sun et al. (2021) and Wang et al. (2018) proposed an improved Nishihara model reflecting non-linear creep characteristics. They analyzed the results of sandstone creep tests to describe accelerated creep behavior. Sun et al. (2015) established a non-constant Nishihara model by considering the relationship between creep flexibility and stress level and time, and non-constant Nishihara coefficients of the traditional Nishihara model were non-constant.

The influence of different unloading amounts on rock creep characteristics was less considered in the past unloading creep test because the research object was less stiff. To ensure the safety of reservoir dams in water-conservancy projects, hard-rock foundations with a rough texture are often chosen for the dam foundation. It is generally believed that hard rock is not prone to creep. But, under high stress conditions, hard rock with a dense texture will also show the creep deformation phenomenon (Wang et al., 2016; Wu et al., 2016). Under long-term loads, the creep of these hard rocks has brought significant potential safety hazards to the safe operation of hydropower stations (Li et al., 2009). It is necessary to carry out creep test research on such dense rocks to explore the creep characteristics and creep deformation mechanism of rocks.

In view of this, this paper uses the RLW-2000 triaxial creep test system to take the soft Flint limestone from the underground construction cavern of Shuibuya hydropower station as the test object, and carries out the triaxial unloading confining pressure creep test reflecting the time-dependent deformation characteristics of limestone after excavation. The creep deformation and failure law of rock under different unloading conditions is obtained. The unloading creep characteristics of surrounding rock are revealed, and the unloading creep deformation constitutive model is established.

FIGURE 1
Rock sampling site.

2 Engineering background

Shuibuya hydropower station is located in Badong County, Hubei Province, China, the project began construction in 2000, completed in 2008, the project's main buildings are dams, underground plants, emptying holes and spillways, etc., (Yang, 2010). The underground powerhouse and underground cavern of Shuibuya hydropower station are located on the right bank of the dam site, and the lithology in the stratum is complex. The stratum contains not only soft rock strata but also hard rock strata (Zhang et al., 2003).

Despite the underground cavern of Shuibuya hydropower station being stable at the beginning of its construction, monitoring data of the underground cavern of Shuibuya hydropower station shows that the top of the local cavern has deformed, fallen, and cracked (Chen et al., 2010; Jin, 2013). It not only damages the lines and equipment in the cavern of the hydropower station, but also seriously compromises its safety and stability. According to Dong et al. (2019), rock creep is the principal factor affecting the deformation of underground cavern chambers caused by rock excavation, unloading and stability monitoring. According to the theoretical analysis of this research result, it is known that rock creep is the main cause of the deformation of the underground cavern in Shuibuya hydropower station. However, experiments are needed to verify.

In order to clarify the root cause of underground cavern failure, it is necessary to carry out relevant rock tests for the phenomenon of local cavern failure. Due to severe deformation and failure on the top of the partially underground caverns of Shuibuya hydropower station and the strata below, which is Permian Qixia Formation, the rock of this formation is primarily composed of Flint limestone. Therefore, in order to ensure the safe operation of the hydropower station and take preventive measures, it is urgent to study the creep characteristics of Flint limestone and explore its failure mode, so as to evaluate the stability of underground caverns and put forward reasonable countermeasures, so as to provide scientific decision-making reference for the safe operation of underground caverns. Which is not only of great significance to the stability of Shuibuya hydropower station underground caverns, but also of significant significance to ensure the safe operation of Shuibuya hydropower station.

FIGURE 2
Complete rock and prepared standard rock specimens.

TABLE 1 Loading and unloading creep test scheme of Flint limestone.

Sample	Axial compression/MPa	Confining pressure/MPa	Creep test under different unloading amounts
XR-1	90	15	Unloading amount of 2 MPa, grading unloading to failure
XR-2			Unloading amount of 4 MPa, grading unloading to failure

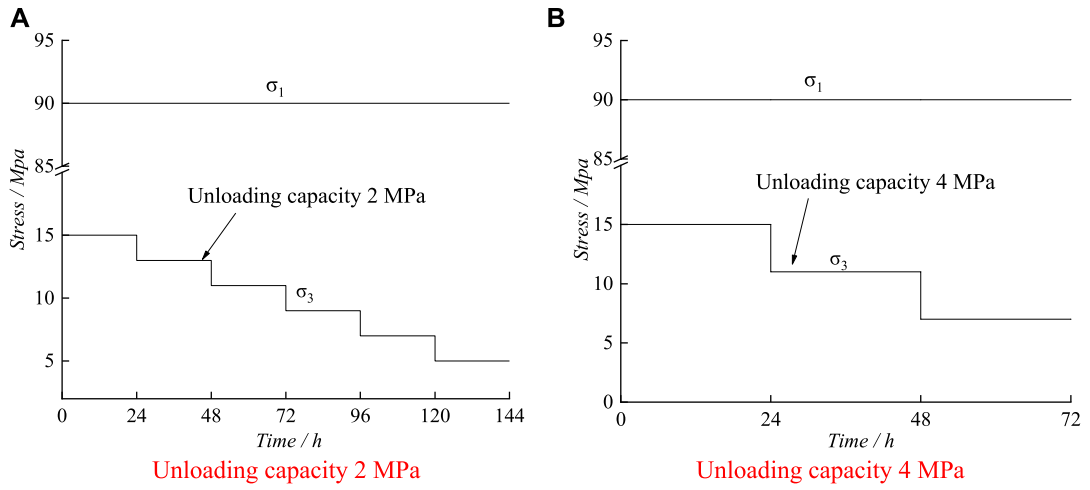

FIGURE 3
Stress path diagram of stepped unloading. **(A)** Unloduading capacity 2 MPa **(B)** Unloading capacity 4 MPa.

3 Test scheme

3.1 Sample preparation

The relevant design, construction, and monitoring data of the Shuibuya hydropower station underground construction cavern group are collected, and the existing engineering investigation reports and research reports are examined and analyzed. According to the area with obvious deformation and failure signs on site, the representative tunnel section is selected as the key research area. The rock sample collection site is shown in Figure 1. Samples were taken on site to obtain complete rock samples. After drilling, cutting and grinding, a cylindrical standard sample with a diameter of 50 mm and a height of 100 mm was obtained. Acoustic wave detection is used to eliminate the discrete nature of rock samples by eliminating samples with abnormal wave velocity. In addition, rock samples with similar wave velocity are selected. Some test rock samples are shown in Figure 2.

FIGURE 4
RLW-2000 Microcomputer controlled triaxial creep testing machine.

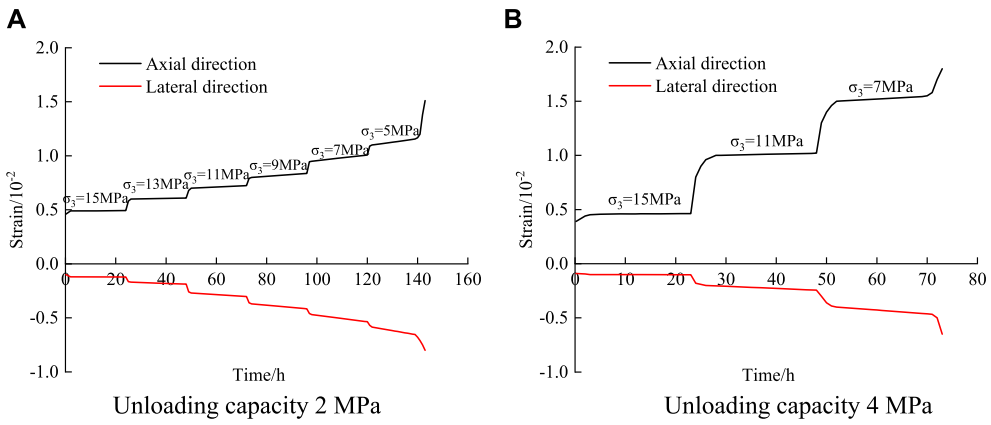

FIGURE 5
Triaxial unloading creep test curves of Flint limestone under different unloading amounts. **(A)** Unloading capacity 2 MPa **(B)** Unloading capacity 4 MPa.

3.2 Test scheme design

When undertaking underground cavern engineering, foundation engineering is not only in the state of axial loading, but is also in the state of lateral unloading. In order to study the creep characteristics of underground cavern rock under unloading stress state, this paper designs the creep test of Flint limestone under unloading condition. The experimental scheme for creep properties of Flint limestone is shown in Table 1. This experiment simulates the unloading of underground cavern excavations with constant and reduced loads.

The procedure for testing the creep properties of Flint limestone graded unloading is as follows: under the stress path of constant axial pressure and unloading confining pressure, the initial confining pressure is set to 15 MPa, and the axial pressure is loaded to 90 MPa (the triaxial compressive strength under the same circumferential pressure is 127.61 Mpa, and the axial pressure is about 70% of its value), and the confining pressure is unloaded with different unloading amounts, each stage is unloaded foru 24 h.

In the grading and unloading stress path, the axial pressure is constant, while the confining force is constant until failure, as shown in the stress path diagram Figure 3.

The test instrument used in the creep characteristic test is the RLW-2000 triaxial creep test system, as shown in Figure 4. The three-axis pressure chamber of this test system adopts a self-balancing pressure chamber, so that the pressure on the rock in all directions is the same when the rock is not under axial pressure, and in addition, there is no additional force on the axial pressure when the axial pressure is added, so the axial and radial deformation

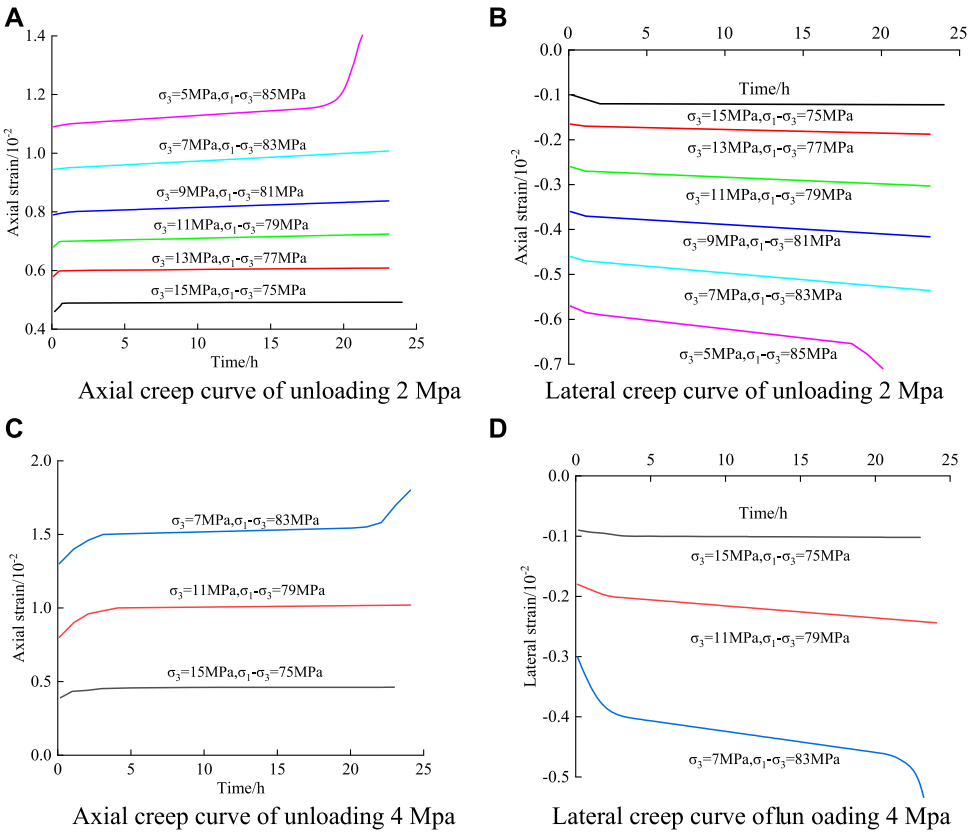

FIGURE 6
Triaxial unloading creep curve clusters of Flint limestone under different unloading amounts. **(A)** Axial creep curve of unloading 2 Mpa **(B)** Lateral creep curve of unloading 2 Mpa. **(C)** Axial creep curve of unloading 4 Mpa **(D)** Lateral creep curve of unloading 4 Mpa.

TABLE 2 Unloading creep characteristic indexes of Flint limestone under different unloading amounts.

Unloading degree/MPa	Confining pressure/MPa	Deviatoric stress/MPa	Axial direction		Lateral direction	
			Instantaneous strain/%	Creep strain/%	Instantaneous strain/%	Creep strain/%
2	15	75	0.49	0.0021	0.12	0.002
	13	77	0.1079	0.0088	0.0479	0.0176
	11	79	0.0912	0.0242	0.0824	0.033
	9	81	0.0758	0.0374	0.067	0.0462
	7	83	0.1126	0.0572	0.0538	0.066
	5	85	0.0928	0.0544	0.054	0.064
4	15	75	0.454	0.0018	0.1	0.002
	11	79	0.05384	0.02	0.098	0.044
	7	83	0.48	0.0375	0.156	0.0525

can be measured directly, which is especially suitable for long time creep test. The maximum load of this equipment is 2000 kn, measuring range 2%–100%, axial pressure measuring range 0–100 Mpa, measuring accuracy ±2%, displacement measuring range 0–50 mm, measuring accuracy ±0.5%, continuous working time more than 1,000 h.

4 Test results and analysis

4.1 Creep deformation law

Under the graded unloading creep stress path, the initial confining pressure is 15 MPa. The graded unloading creep test

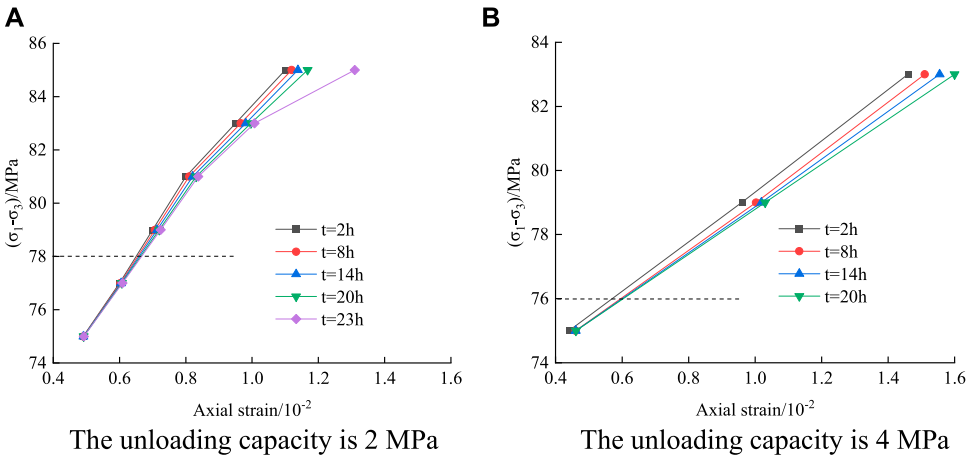

FIGURE 7
Creep isochronous curve clusters under different unloading amounts. **(A)** The unloading capacity is 2 MPa **(B)** The unloading capacity is 4 MPa.

with an unloading amount of 2 and 4 MPa is carried out. Each stage is unloaded for 24 h. Test results with unloading amounts of 2 and 4 MPa are used to analyze the creep deformation law of Flint limestone under unloading stress conditions. The creep curve of Flint limestone is shown in Figure 5.

The value above the creep curve in the figure indicates the size of the confining pressure at this stage. The longitudinal strain is positive in compressive strain and negative in tensile strain.

The specimen under constant confining pressure has experienced both decay creep and steady creep at all levels as shown in Figure 5. It transits from steady creep to non-linear accelerated creep until the specimen is destroyed at the rupture confining pressure level. This is consistent with the curve characteristics of creep under step loading.

The creep characteristic curve obtained by the graded unloading creep test is not convenient for the analysis of the creep characteristics of rock masses. It is necessary to process the results of the test. Chen's loading treatment method (Liu, 1994) is a rock creep curve processing method proposed by Professor Chen Zongji. Compared with other creep curve processing methods, Chen's loading treatment method has the advantages of being applicable to both linear creep and non-linear creep. Therefore, this paper uses Chen's unloading treatment method to process the data of the graded unloading creep test. It transforms the whole curve into creep curves under various loads, as shown in Figure 6.

Data statistics of instantaneous deformation and creep deformation of Flint limestone specimens under unloading amounts of 2 and 4 MPa were collected. These data were used to investigate the characteristics of creep deformation of Flint limestone under unloading paths. The unloading creep characteristics of Flint limestone under different unloading amounts are shown in Table 2.

From Figures 5, 6 and Table 2, the unloading creep deformation characteristics of Flint limestone are as follows:

1) Instability and strain appear at all levels of stress. The total strain of the sample increases with the gradual unloading of confining pressure. Under the condition of constant confining pressure at all levels, the lateral creep deformation of the sample is more significant than its axial creep deformation. This indicates that the lateral deformation of the sample is more significant than the vertical deformation, and the lateral expansion effect is obvious. This is different from the deformation law of creep under step loading. According to the test curve shown in Figure 5A, for the test curve with an initial confining pressure of 15 MPa, the axial creep strain and lateral creep strain under the first-stage steady state are 0.21×10^{-4} and 0.2×10^{-4}, respectively. When unloading to 13 MPa, the axial creep strain and lateral creep strain are 0.88×10^{-4} and 1.76×10^{-4}, respectively, which are 3.19 and 7.8 respectively compared with the previous level. The other levels also show the same law. Based on the above analysis, it can be seen that with the gradual reduction of pressure, lateral deformation develops rapidly. Additionally, lateral deformation is more sensitive to unloading. The reason is that during the test, with the gradual unloading of confining pressure, when the confining pressure is unloaded to the lowest level of confining pressure, the horizontal constraint on the sample is small, while the bias is large, and the sample is prone to lateral expansion failure.
2) Comparing the steady-state creep curves of samples under different unloading levels, the slope of the linear steady-state creep curve of the sample is close to 0 under the first and second confining pressure levels (15 MPa, 13 MPa) under the confining pressure unloading amount of 2 MPa, and the first confining pressure level (15 MPa) under the confining pressure unloading amount of 4 MPa. With the gradual unloading of confining pressure, when the confining pressure is unloaded to 11 MPa under the two test conditions, the steady-state creep curve of the sample develops from a nearly horizontal trend to a certain inclination angle. At this time, the axial steady-state creep rates are $0.01 \times 10^{-3}\ h^{-1}$ and $0.0083 \times 10^{-3}\ h^{-1}$, both of which are greater than 0. The reason is that the stress level gradually increases and exceeds the crack initiation strength of the sample, which leads to a certain plastic deformation of the sample. After the axial stress reaches a high level, a large number of cracks

TABLE 3 Long-term strength of Flint limestone under unloading stress path.

Test scheme	Unloading degree/MPa	Long-term strength/MPa	Creep rupture strength/MPa
Decrementation	2	78	85
	4	76	83

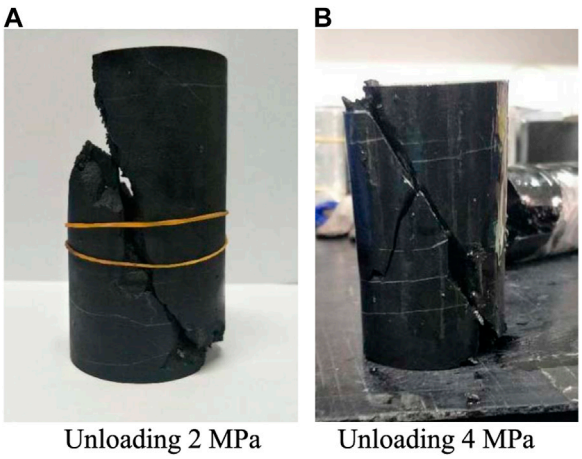

FIGURE 8
The creep failure modes of graded unloading under different unloading amounts. **(A)** Unloading 2 MPa **(B)** Unloading 4 MPa.

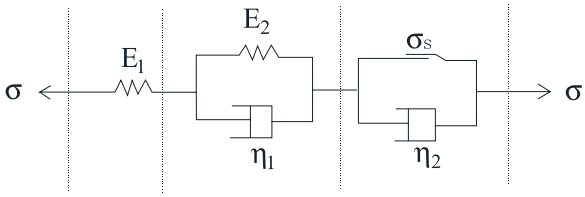

FIGURE 9
Nishihara model.

are generated within the rock sample, which expand rapidly, and the creep rate increases. The sample enters the accelerated creep stage after the steady-state creep stage, and the sample deforms rapidly until a macroscopic failure surface forms to reach the failure state. The creep failure of the specimen occurs at the last stress level, indicating that creep failure will occur when the deviatoric stress exceeds the reciprocal second-order stress level. Therefore, the reciprocal second-order stress level is determined as the quasi-failure stress of the rock specimen, and the quasi-failure stress σ_f is the maximum stress level when the specimen does not undergo creep failure. In this test, the quasi-failure stress σ_f of the limestone specimens under the confining pressure of unloading of 2 and 4 MPa is 83 and 79 MPa respectively. With the increase of the unloading amount, the quasi-failure stress σ_f of the specimens gradually decreases, indicating that the unloading amount affects the final creep failure strength of the rock specimens.

3) The total duration of creep failure of samples under confining pressure unloading of 2 and 4 MPa is different, which is 143.1 and 73.7 h respectively, and the start-up time of accelerated creep under different conditions is significantly different. It can be seen from Figure 5A that under the rupture stress level of confining pressure of 5 MPa and deviatoric stress of 83 MPa, the whole creep process lasted 23.7 h, the decay creep stage lasted 4.3 h, accounting for about 18.1% of the total time, the steady creep stage lasted 17.2 h, accounting for about 72.6% of the total time, and the non-linear rapid creep stage lasted 2.2 h, accounting for about 9.3% of the total time. Similarly, the creep time under the fracture stress level in Figure 5B is analyzed, and it is found that the change rule is basically the same as the above. The attenuation creep stage and non-linear accelerated creep stage lasted relatively short, while the steady creep stage lasted relatively long, but the deformation was small. When entering the accelerated creep stage, the axial and lateral creep strains of the sample increase non-linearly, and the rupture duration of the sample is very short. Therefore, the creep deformation and creep rate characteristics of this stage should be paid attention to in practical engineering.

4.2 Determination of long-term strength

In consideration of the time effect, the creep test data of rock are sorted. In this paper, the long-term strength index of Flint limestone is obtained by the isochronous curve method. On the basis of determining the long-term strength of Flint limestone, the relationship between long-term strength and instantaneous failure strength of Flint limestone is explored.

With the step unloading stress path, as shown in Figure 7, the isochronous curve method is used to obtain the isochronous curve clusters of Flint limestone under different unloading amounts. These amounts are under the unloading limits of 2 and 4 MPa.

Isochronous curves initially have a parabolic shape, then move towards a horizontal direction as shown in Figure 7. It can be seen from Table 3 that compared with the instantaneous strength of Flint limestone, the long-term strength of Flint limestone under long-term load is significantly lower than its creep failure strength.

4.3 Creep failure mode analysis

Under different stress paths, the creep failure forms for limestone are distinct. In order to further study the creep failure characteristics of Flint limestone, this paper lists photos of creep failure forms of Flint limestone under different stress states. Under the constant unloading stress path of axial compression, when the

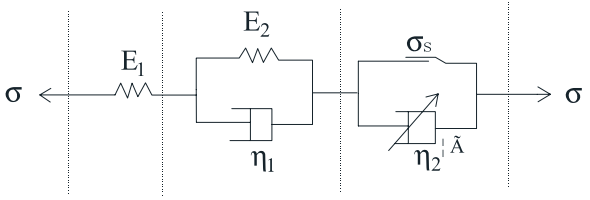

FIGURE 10
Non-linear creep damage model considering time-dependent damage.

unloading amount is 2 and 4 MPa, the failure form of Flint limestone is shown in Figure 8.

Based on Figure 8, it can be seen that the Flint limestone rock sample shows a different failure mode than the loading stress path. When the unloading amount is 2 and 4 MPa, the creep failure mode of the Flint limestone rock sample is shear failure. This is because the crack shows a significant oblique section crack, and the crack penetrates the upper and lower surfaces of the rock sample. When the unloading amount is 4 MPa, multiple cracks appear in the Flint limestone rock sample, and the crushing characteristics are severe, indicating a significant expansion phenomenon.

5 Study on unloading creep model and parameter identification of Flint limestone

5.1 Unloading creep constitutive model of Flint limestone

A study of the unloading creep curve characteristics of Flint limestone found that the instantaneous strain, attenuation creep, and uniform creep stages could be well described by the Nishihara model, while the non-linear accelerated creep stage could not be adequately explained by its viscoplastic element. Bai et al. (2021), Bai et al. (2023) obtained the generalized effective stress principle by varying the internal variable parameters to achieve a model that automatically takes into account the effects of stress paths, and the established model can accurately capture the loading path effects. Therefore, it is necessary to modify the Nishihara model to describe the curve of the non-linear accelerated creep stage of Flint limestone.

5.1.1 Western model

The traditional Nishihara model is shown in Figure 9, which is composed of elastomer, viscoelastic body and viscoplastic body. In the diagram, E_1 and E_2 are the elastic modulus of elastomer and viscoelastic body respectively, η_1 and η_2 are the viscosity coefficient of viscoelastic body and viscoplastic body respectively, and σ_s is the long-term strength of rock. The creep constitutive equation of Flint limestone in one-dimensional state can be divided into two different cases based on the rock's stress state.

(1) When $\sigma < \sigma_s$, only part I and II in the model are involved in the rheology. Nishihara's model degenerates into the generalized Kelvin model, which can describe attenuation creep, and the rock is in a stable state.

$$\frac{\eta_1}{E_1+E_2}\dot{\sigma}+\sigma=\frac{E_1\eta_1}{E_1+E_2}\dot{\varepsilon}+\frac{E_1\eta_2}{E_1+E_2}\varepsilon \tag{1}$$

The corresponding creep constitutive model is obtained as follows:

$$\varepsilon(t)=\frac{\sigma}{E_1}+\frac{\sigma}{E_2}\left(1-e^{\frac{E_2}{\eta_1}t}\right) \tag{2}$$

(2) When $\sigma \geq \sigma_s$, the I, II and III parts of the model are all involved in the response. At this time, the model can fully reflect the viscoelastic-plastic rheological properties of the rock. According to the combination relationship of the components, the constitutive equation of the model is derived as follows:

$$\ddot{\sigma}+\left(\frac{E_1}{\eta_1}+\frac{E_2}{\eta_1}+\frac{E_2}{\eta_2}\right)\dot{\sigma}+\frac{E_1E_2}{\eta_1\eta_2}(\sigma-\sigma_s)=E_2\ddot{\sigma}+\frac{E_1E_2}{\eta_1}\dot{\sigma} \tag{3}$$

The corresponding creep constitutive model is further derived as follows:

$$\varepsilon(t)=\frac{\sigma}{E_1}+\frac{\sigma}{E_2}\left(1-e^{\frac{-E_2}{\eta_1}t}\right)+\frac{\sigma-\sigma_s}{\eta_2}t \tag{4}$$

Therefore, the creep equation of the Nishihara model is:

$$\varepsilon(t)=\begin{cases}\dfrac{\sigma}{E_1}+\dfrac{\sigma}{E_2}\left(1-e^{\frac{E_2}{\eta_1}t}\right) & (\sigma<\sigma_s)\\ \dfrac{\sigma}{E_1}+\dfrac{\sigma}{E_2}\left(1-e^{\frac{E_2}{\eta_1}t}\right)+\dfrac{\sigma-\sigma_s}{\eta_2}t & (\sigma\geq\sigma_s)\end{cases} \tag{5}$$

5.1.2 Establishment of non-linear creep model of Flint limestone

Any real number γ, Riemann-Liouville fractional order function can be expressed as

$$\frac{d^{-\gamma}f(t)}{dt^{-\gamma}}=\frac{1}{\Gamma(\gamma)}\int_0^t(t-\xi)^{\gamma-1}f(\xi)d\xi \tag{6}$$

Where γ is the derivative order, ξ is the variable, f (t) is a function of t, and Γ(γ) is the Gamma function.

The fractional-order Abel viscous pot does not take into account the damage degradation of the material, and the intrinsic model is only applicable to the case where the external load is less than the yield stress, i.e., when creep does not enter the accelerated phase. The intrinsic relationship (Liu, 2019) for the Abel viscous pot is

$$\sigma(t)=\eta^{\gamma}\frac{d^{\gamma}\varepsilon(t)}{dt^{\gamma}}\quad(0\leq\gamma\leq1) \tag{7}$$

where ηγ is the viscosity coefficient.

Keeping the stress σ constant and applying the Riemann-Liouville type fractional order calculus theory to solve Eq. 7, we can obtain the Abel viscous pot instanton equation.

$$\varepsilon(t)=\frac{\sigma}{\eta^{\gamma}}\frac{t^{\gamma}}{\Gamma(1+\gamma)}\quad(0\leq\gamma\leq1) \tag{8}$$

During the non-linear accelerated creep phase, the creep parameters of the rock are time-dependent, requiring the introduction of damage variables to describe the degradation of the viscosity coefficient ηγ of the Abel viscous pot.

$$\eta^{\gamma}=\eta^{\gamma}(D)=\eta^{\gamma}(1-D) \tag{9}$$

10.3389/fmats.2023.1177733

TABLE 4 Parameter identification of a non-linear creep model with aging damage.

Unloading degree/MPa	Confining pressure/MPa	Deviatoric stress/MPa	E_1/GPa	E_2/GPa	$\eta_1/\times10^3$ GPa·h	$\eta_2^\gamma/\times10^3$ GPa·h	γ	α	R^2
2	15	75	32.78	63.58	4.29	—	—	—	0.961
	13	77	28.47	84.63	3.51	—	—	—	0.978
	11	79	25.16	101.68	0.53	6.43	1	2.385	0.991
	9	81	20.85	123.73	0.41	7.35	1	3.532	0.993
	7	83	17.54	149.78	0.38	8.27	1	4.668	0.996
	5	85	13.23	183.83	0.27	8.79	0.985	5.973	0.997
4	15	75	32.78	63.58	2.34	—	—	—	0.969
	11	79	26.32	102.37	0.58	6.831	1	2.573	0.993
	7	83	16.37	148.76	0.37	8.532	1	4.813	0.996

where D is the damage variable, $0 \le D \le 1$.

The damage variable is assumed to accumulate as a negative exponential function over time (Wu et al., 2020).

$$D = 1 - e^{-\alpha t} \tag{10}$$

Where α is the time effect coefficient.

Substituting Eqs 9, 10 into Eq. 7 yields the intrinsic structure relationship for Abel's viscous pot.

$$\sigma(t) = \eta^\gamma e^{-\alpha t} \frac{d^\gamma \varepsilon(t)}{dt^\gamma} \quad (0 \le \gamma \le 1) \tag{11}$$

Keeping the stress σ constant, applying the Riemann-Liouville type fractional order calculus theory to solve Eq. 11, we get

$$\varepsilon(t) = \frac{\sigma}{\eta^\gamma} t^\gamma \sum_{k=0}^{\infty} \frac{(\alpha t)^k}{\Gamma(1 + k = \gamma)} \tag{12}$$

Based on the Nishihara model, the viscous element of the viscoplastic body is replaced by the variable coefficient Abel viscous pot. A non-linear creep damage model considering age damage is established as shown in Figure 10.

In the one-dimensional stress state, the total strain ε is,

$$\varepsilon = \varepsilon_e + \varepsilon_{ve} + \varepsilon_{vp} \tag{13}$$

where the stress-strain relationship for the elastic Hooke body, viscoelastic body is,

$$\varepsilon_e = \frac{\sigma}{E_1} \tag{14}$$

$$\varepsilon_{ve} = \frac{\sigma}{E_2}\left(1 - e^{\frac{E_2}{\eta_2}t}\right) \tag{15}$$

For viscoplastic strains in viscoplastic bodies, there are 2 cases depending on the magnitude of the stress σ and the long-term strength σ_s.

(1) When $\sigma < \sigma_s$, the friction slider does not start and the viscoplastic strain is 0, i.e., $\varepsilon_{vp} = 0$.
(2) When $\sigma \ge \sigma_s$, the friction slider is activated and the intrinsic relationship of the viscoplastic body can be determined.

$$\sigma = \eta_2^\gamma e^{-at} \frac{d^\gamma \varepsilon_{vp}(t)}{dt^\gamma} + \sigma_s \tag{16}$$

$$\frac{d^\gamma \varepsilon_{vp}(t)}{dt^\gamma} = \frac{\sigma - \sigma_s}{\eta_2^\gamma} e^{at} \tag{17}$$

where η_2^γ is the viscosity coefficient of Abel's viscous pot.

The non-constant fractional order viscoplastic strain can be obtained by Laplace transform and Laplace inverse transform as,

$$\varepsilon_{vp} = \frac{\sigma - \sigma_s}{\eta_2^\gamma} t^\gamma \sum_{k=0}^{\infty} \frac{(at)^k}{\Gamma(1 + k + \gamma)} \tag{18}$$

Considering the strain of model 3 individuals together, the intrinsic equation of the non-linear creep damage model can be expressed as,

$$\varepsilon(t) = \begin{cases} \dfrac{\sigma}{E_1} + \dfrac{\sigma}{E_2}\left(1 - e^{\frac{E_2}{\eta_1}t}\right) & (\sigma < \sigma_s) \\ \dfrac{\sigma}{E_1} + \dfrac{\sigma}{E_2}\left(1 - e^{\frac{E_2}{\eta_1}t}\right) + & \\ \dfrac{\sigma - \sigma_s}{\eta_2^\gamma} t^\gamma \sum_{k=0}^{\infty} \dfrac{(at)^k}{\Gamma(1 + k + \gamma)} & (\sigma \ge \sigma_s) \end{cases} \tag{19}$$

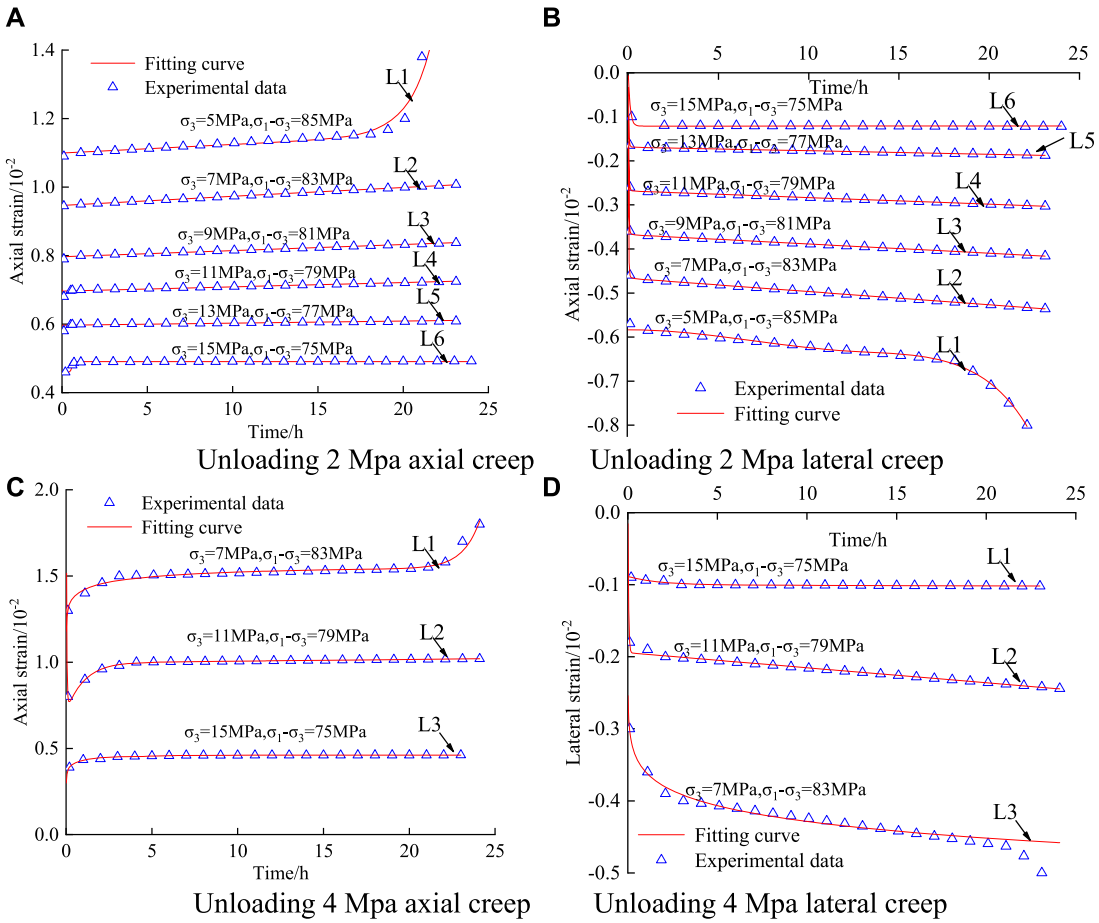

FIGURE 11
Creep curve and model curve fitting results. **(A)** Unloading 2 Mpa axial creep **(B)** Unloading 2 Mpa lateral creep. **(C)** Unloading 4 Mpa axial creep **(D)** Unloading 4 Mpa lateral creep.

5.2 Identification and validation of parameters of a non-linear creep model considering aging damage

The results of the identification of the parameters of the non-linear creep model considering aging damage are shown in Table 4.

As can be seen in Table 4, the fitted R^2 values are all larger than 0.961. This is because the non-linear Nishihara creep model considering the damage variables can better reflect the creep characteristics of Flint limestone. The relationship between the creep parameters and the ambient pressure is complicated, but the general rule is: when the unloading amount is certain, the smaller the surrounding pressure is, the smaller the instantaneous elastic modulus E_1 and viscosity coefficient η have a tendency to decrease, and the trend is more obvious when the unloading amount increases. It shows that the decrease in the surrounding pressure will not only reduce the instantaneous elastic modulus of the rock, but also intensify the plastic flow characteristics of the rock and enhance the viscous flow characteristics.

In order to verify the proposed non-linear creep damage model considering aging damage, the curves simulated by the non-linear creep model incorporating decay damage and the data curves from the indoor tests were fitted for comparison, and the results are shown in Figure 11, which show that the two fits are better and illustrate the reasonableness of the revised non-linear creep model considering aging damage.

6 Conclusion

(1) The specimens have been subjected to decay creep and steady creep stages under all levels of constant confining pressure, and have transitioned from steady creep to non-linear accelerated creep until failure under rupture confining pressure.
(2) With the increase of the unloading amount, the quasi-failure stress of the sample gradually increases, indicating that the unloading amount affects the final creep failure strength of the rock sample, that is, the greater the unloading amount, the lower the final creep failure strength.
(3) In the accelerated creep stage, the axial and lateral creep strains of the specimen increase non-linearly, and the rupture duration of the specimen is very short. Therefore, the creep deformation

and creep rate characteristics of this stage should be paid attention to in practical engineering.

(4) When the unloading amount is 2 and 4 MPa, the creep failure mode of the Flint limestone rock sample is shear failure, showing a significant oblique section crack. When the unloading amount is 2 and 4 MPa, the creep failure mode of the Flint limestone rock sample is different from the failure mode caused by the loading stress path.

(5) Based on damage mechanics theory, a non-linear creep damage model considering time-dependent damage is established. Unloading creep models are identified based on creep test results. It provides a theoretical basis for geotechnical engineering design when the creep model curve and the test curve agree well.

Data availability statement

The original contributions presented in the study are included in the article/supplementary material, further inquiries can be directed to the corresponding author.

Author contributions

All authors listed have made a substantial, direct, and intellectual contribution to the work and approved it for publication.

Funding

This work was supported by Key Laboratory of Geological Hazards on Three Gorges Reservoir Area (China Three Gorges University), Ministry of Education (2017KDZ12); Natural Science Foundation of Hubei Provincial (2021CFB191); Natural Science Research Project of Yichang City (A21-3-005); Research Fund for Excellent Dissertation of China Three Gorges University (2022BSPY).

Conflict of interest

Author ML was employed by China Three Gorges Corporation.

The remaining authors declare that the research was conducted in the absence of any commercial or financial relationships that could be construed as a potential conflict of interest.

Publisher's note

References

Bai, B., Zhou, R., Cai, G., Hu, W., and Yang, G. (2021). Coupled thermo-hydro-mechanical mechanism in view of the soil particle rearrangement of granular thermodynamics. *Comput. Geotech.* 137, 104272. doi:10.1016/j.compgeo.2021.104272

Bai, B., Zhou, R., Yang, G., Zou, W., and Yuan, W. (2023). The constitutive behavior and dissociation effect of hydrate-bearing sediment within a granular thermodynamic framework. *Ocean. Eng.* 268, 113408. doi:10.1016/j.oceaneng.2022.113408

Chen, Y. F., Zhou, C. B., Mao, X. Y., and Hu, R. (2010). Numerical simulation and assessment of seepage control effects on surrounding rocks of underground powerhouse in Shuibuya hydropower project. *Chin. J. Rock Mech. Eng.* 29 (2), 308–318.

Deng, H. F., Zhou, M. L., Li, J. L., Hu, Y. Y., Xiao, Z. Y., and Wang, Y. (2016). Experimental research on unloading triaxial rheological mechanical properties of sandy mudstone. *Rock Soil Mech.* 37 (2), 315–322. doi:10.16285/j.rsm.2016.02.002

Dong, Z. H., Ding, X. L., Huang, S. L., Wu, A. Q., Chen, S. H., and Zhou, Z. (2019). Analysis of ageing-stress characteristics and long-term bearing risk of anchor cable for a large cavern in high geo-stress area. *Rock Soil Mech.* 40 (1), 351–362. doi:10.16285/j.rsm.2018.0508

Fan, Q. Y., Yang, K. Q., and Wang, W. M. (2010). Study of creep mechanism of argillaceous soft rocks. *J. Rock Mech. Eng.* 29 (8), 1555–1561.

Huang, X., Liu, Q. S., Kang, Y. S., and Pang, Y. C. (2016). Triaxial unloading creep experimental study of sandy mudstone. *Chin. J. Rock Mech. Eng.* 35 (1), 2653–2662. doi:10.13722/j.cnki.jrme.2014.1528

Jin, B. O. (2013). *Stability evaluation of surrounding rock and analysis of groundwater leakage in underground caverns of shuibuya hydropower station*. Yichang, China: China Three Gorges University.

Li, C., Bažant, Z. P., Xie, H., and Rahimi-Aghdam, S. (2019). Anisotropic microplane constitutive model for coupling creep and damage in layered geomaterials such as gas or oil shale. *Int. J. Rock Mech. Min. Sci.* 124, 104074. doi:10.1016/j.ijrmms.2019.104074

Li, J. L. (2000). A test study on tension-shear rheological of rock. *Chin. J. Geotech. Eng.* 22 (3), 299–303.

Li, J. L. (1999). *Theory and application of unloading rock masses*. Beijing, China: China Architecture and Building Press.

Li, J., and Wang, L. H. (2007). Research on unloading nonlinear mechanical characteristics of jointed rock masses. *Chin. J. Rock Mech. Eng.* (10), 1968–1975.

Li, T. Z., and Yang, X. L. (2018). Reliability analysis of tunnel face in broken soft rocks using improved response surface method. *Int. J. Geomech.* 18 (5), 04018021. doi:10.1061/(asce)gm.1943-5622.0001129

Li, Z. K., Zhou, Z., Tang, X. F., Liao, C. G., Hou, D. Q., Xing, X. L., et al. (2009). Stability analysis and considerations of underground powerhouse caverns group of Jinping I hydropower station. *Chin. J. Rock Mech. Eng.* 28 (11), 2167–2175.

Liu, D. (2019). *The fractional derivative constitutive model and micro-mechanisms of salt rock during creep*. Beijing, China: China University of Mining and Technology.

Liu, X. (1994). *Introduction to rock rheology*. Beijing, China: Geology Press.

Liu, Z., Zhou, C., Li, B., Zhang, L., and Liang, Y. (2020). Effects of grain dissolution–diffusion sliding and hydro-mechanical interaction on the creep deformation of soft rocks. *Acta Geotech.* 15 (5), 1219–1229. doi:10.1007/s11440-019-00823-9

Park, K. H., Jung, Y. H., and Chung, C. K. (2017). Evolution of stiffness anisotropy during creep of engineered silty sand in South Korea. *KSCE Jj. Civ. Eng.* 21 (6), 2168–2176. doi:10.1007/s12205-016-1105-1

Peng, Y., Wu, L., Peng, H., Hao, Y., and An, Y. (2020). Theoretical and experimental study on rock resistance coefficient of soft rock tunnel considering creep effect. *Arab. J. Sci. Eng.* 45 (5), 4333–4342. doi:10.1007/s13369-020-04452-3

Sun, J. (1999). *Rheology of geomaterials and its engineering application*. Beijing, China: China Architecture and Building Press.

Sun, K., Chen, Z. L., Chen, J., and Xu, X. Y. (2015). A modified creep constitutive equation for frozen soil based on Nishihara model. *Rock Soil Mech.* 36 (S1), 142–146. doi:10.16285/j.rsm.2015.S1.024

Sun, X. M., Miao, C. Y., Jiang, M., Zhang, Y., Yang, L., and Guo, B. (2021). Experimental and theoretical study on creep behaviors of sandstone with different moisture contents based on modified Nishihara model. *Chin. J. Rock. Mech. Eng.* 40 (12), 2411–2420. doi:10.13722/j.cnki.jrme.2021.0302

Wang, H., Chen, W. Z., Wang, Q. B., and Zheng, P. Q. (2016). Rheological properties of surrounding rock in deep hard rock tunnels and its reasonable support form. *J. Cent. South Univ.* 23 (4), 898–905. doi:10.1007/s11771-016-3137-6

Wang, X., Huang, Q., Lian, B., Liu, N., and Zhang, J. (2018). Modified Nishihara rheological model considering the effect of thermal-mechanical coupling and its experimental verification. *Adv. Mater. Sci. Eng.* 2018, 1–9. doi:10.1155/2018/4947561

Wu, C., Chen, Q., Basack, S., Xu, R., and Shi, Z. (2016). Biaxial creep test study on the influence of structural anisotropy on rheological behavior of hard rock. *J. Mater. Civ. Eng.* 28 (10), 04016104. doi:10.1061/(asce)mt.1943-5533.0001571

Wu, F., Zhang, H., Zou, Q., Li, C., Chen, J., and Gao, R. (2020). Viscoelastic-plastic damage creep model for salt rock based on fractional derivative theory. *Mech. Mater.* 150, 103600. doi:10.1016/j.mechmat.2020.103600

Yang, Q. G. (2010). *Dam construction technology of shuibuya concrete face rockfill dam*. Beijing, China: China Water Resources and Hydropower Press.

Zhang, L., Ding, X. L., and Fu, J. (2003). Numerical analysis of excavation for underground powerhouse in Shuibuya Project. *J. Yangtze River Sci. Res. Inst.* 20 (3), 42–46.

Zhu, J. B. (2009). *Study on unloading mechanics and its rheological properties of rock under high stress*. Beijing, China: Graduate School of Chinese Academy of Sciences.

frontiers | Frontiers in Materials

TYPE Original Research
PUBLISHED 13 April 2023
DOI 10.3389/fmats.2023.1166551

OPEN ACCESS

EDITED BY
Bing Bai,
Beijing Jiaotong University, China

REVIEWED BY
Hongtao Fu,
Wenzhou University, China
Jianwen Ding,
Southeast University, China

*CORRESPONDENCE
Rongjun Zhang,
ce_zhangrj@hust.edu.cn

SPECIALTY SECTION
This article was submitted to Structural Materials, a section of the journal Frontiers in Materials

RECEIVED 15 February 2023
ACCEPTED 27 March 2023
PUBLISHED 13 April 2023

CITATION
Han C, Fan Z, Zhang R, Cheng J, Sun K and Peng Q (2023), Consolidation characteristics of high-water-content slurries improved by flocculation-enhanced surcharge (vacuum) preloading method.
Front. Mater. 10:1166551.
doi: 10.3389/fmats.2023.1166551

Consolidation characteristics of high-water-content slurries improved by flocculation-enhanced surcharge (vacuum) preloading method

Chao Han[1], Zhou Fan[1], Rongjun Zhang[2]*, Jinkang Cheng[2], Ke Sun[1] and Qian Peng[1]

[1]Construction Company, State Grid Jiangsu Electric Power Co., Ltd, Nanjing, China, [2]Huazhong University of Science and Technology, Wuhan, China

The high volume and unfavorable properties of high-water-content slurries make their treatment difficult and costly. Improving the slurries through prefabricated drains combined with surcharge or vacuum preloading represents an environmental and economic means of reusing these slurries as subsoil. As conventional methods are inefficient in dealing with low-permeability slurries, flocculation is often applied. In this study, the influence of the flocculant dosage on the drainage behavior is observed, and the secondary consolidation of the slurries is examined through laboratory tests. Flocculation is found to accelerate the consolidation process, although the flocculant dosage has an optimal value when combined with the surcharge preloading method. The coefficient of secondary consolidation is more significant in slurries improved by the flocculation-enhanced surcharge (vacuum) preloading method than in the case without flocculation. The use of flocculation must be carefully controlled.

KEYWORDS

flocculation, slurries, secondary consolidation, preloading method, drainage

1 Introduction

The maintenance of navigation channels and the expansion of storage capacity produce massive amounts of slurry that are dredged from rivers, lakes, seas, and reservoirs (Kang et al., 2016). The dredged slurries have several unfavorable properties, including a high water content, low bearing capacity, and low permeability, which make their management difficult (Liu et al., 2022). Traditional methods, such as stacking in the storage yard and transporting to the outside environment, do not enable any reuse of the slurries and may cause environmental problems.

The use of dredged slurries as filling and reclamation materials is a popular post-treatment application (Kang et al., 2016). Obviously, the slurries cannot be reused directly because of their unfavorable properties, so prefabricated drains combined with surcharge and vacuum preloading methods are often applied to improve the strength of the slurries (Walker and Indraratna, 2006; Indraratna et al., 2011). The mechanism of the surcharge (vacuum) preloading method increases the hydraulic gradient, which accelerates the water flow (Pu et al., 2020). However, due to the low permeability and high fine-particle content, the drainage path can easily become blocked, which reduces the efficiency of the preloading

method. Consolidation takes time and the does not produce any real improvement in quality, especially when the soil layer is thick.

To improve the efficiency of the surcharge (vacuum) preloading method, flocculation can be introduced to the slurry treatment process (Wang et al., 2017; Wu et al., 2022). Flocculants change the physicochemical actions between the soil particles and gather the fine particles to form flocs, which change the inner structure of the soil layer (Kang et al., 2019). After changing the clay fabric and particle levels, the consolidation properties, including compressibility and permeability, are modified accordingly (Xu et al., 2021). The influence of the dosage and type of flocculant on the sedimentation behavior of slurries has been studied for several years. For example, Zhao et al. (2016) conducted experiments using lime as a flocculant in the vacuum preloading method. They found that flocculation reduces the loss of vacuum pressure and increases the water drainage efficiency. Wang et al. (2019) applied anionic polyacrylamide (APAM) and $FeCl_3$ to treat dredged slurries, and reported that the composite flocculants not only increased the size of soil particles, but also stabilized the heavy metals. Lei et al. (2019) found that APAM-enhanced vacuum preloading accelerates the dissipation of pore water pressure, while Liu et al. (2020) conducted settling-column tests to optimize the dosage of flocculants. Although there has been some work on the effects of flocculation, the settlement process of APAM-enhanced preloading methods has seldom been investigated.

Previous work has usually focused on the principal consolidation. However, the secondary consolidation characteristics are also essential, having a significant effect on the safety of the ground. Studies on the secondary consolidation of slurries have been carried out by Yin et al. (2003), who proposed a rheological model based on numerous consolidation and triaxial tests, and Lei et al. (2013, 2016), who compared the secondary consolidation of two slurries and found that the secondary consolidation coefficient increased with the initial loading and decreased with subsequent loading. Slurries treated by the vacuum preloading method have a smaller secondary consolidation coefficient; additionally, the secondary consolidation coefficient increases with the water content. The abovementioned studies are based on normal soft soil. The influence of flocculation on secondary consolidation requires further study.

This paper describes the results of a series of model tests using the organic flocculant APAM to enhance the surcharge (vacuum) preloading method. Different dosages of APAM are applied to slurry samples, and the influence of the dosage on the effect of the enhancement method is examined. The time-dependent height of the slurries is recorded and analyzed to observe the promotion of water drainage. After improvement, the secondary consolidation behavior is evaluated through oedometer tests.

2 Sample preparation and laboratory tests

2.1 Test materials

The soils used in the tests were collected from a dredged slurry dumping site in Wenzhou, China. The basic properties of the soil are summarized in Table 1. The distribution of soil particle sizes is shown in Figure 1.

Previous work has shown that the organic flocculant AN926SH produces a good flocculation effect (Wu et al., 2017). Thus, this is chosen as the flocculant in the tests.

2.2 Test apparatus

The apparatus for the surcharge preloading tests is shown in Figure 2. The device measures 25 cm in length, 25 cm in width, and 60 cm in height. A scale sticker with an accuracy of 1 mm is placed on the surface of the box to allow the settlement of the soil to be measured. The bracket shown in Figure 2 consists of three metal sheets. Holes are punched in the bottom sheet and wrapped by five-sheet geotextiles to form the uniform permeable upper surface on the soil. The upper two metal sheets hold weights to form the surcharge preloading. The chamber separates into two parts (upper and bottom) so that the consolidated soil can be rapidly removed. The apparatus used for the vacuum preloading method is shown in Figure 3. Each test chamber measures 70 cm in length, 10 cm in width, and 40 cm in height. The tubes are connected to the vacuum pump and prefabricated vertical drains are laid in the bottom of the box, offering a path along which the vacuum pressure is expected to spread and allowing pore water to flow out.

2.3 Experimental procedure

Two different tests were conducted to test the influence of flocculation on promoting the water drainage of the soil and on the secondary consolidation behavior.

2.3.1 Surcharge (vacuum) preloading improvement

Surcharge preloading and vacuum preloading tests were conducted according to the following steps. First, anAN926SH solution with a mass ratio of 1:1000 was prepared by routine methods. Vaseline was applied to the inner wall of the test chamber to reduce the friction between the loading plate and the wall. The water contents of the specimens were arranged according to Table 2. After slurry samples with the target water contents had been prepared, they were mixed with the flocculant solution until large flocs were formed and supernatant appeared. The slurries and flocculants were then poured into the surcharge test chamber. The loading bracket and 11 pieces of 5.5 kg weight were then placed on the mixture to form the surcharge preloading. During slurry consolidation under preloading, the height of the soil layer was recorded. When the height had become stable, the drained pore water was drawn out, and the wet density and water content of the settled soil were measured.

The chamber shown in Figure 3 was used in the vacuum preloading tests. Prefabricated horizontal drains were laid on the bottom of the chamber and connected to the vacuum pump. After pouring the slurry/flocculant mixture into the chamber, membranes were placed on top of the chamber to seal it. The vacuum pressure offered by the pump was fixed to −50 kPa throughout the improvement process. According to pretesting, the water content of the slurries would have reduced to approximately 60% once the

TABLE 1 Basic properties of the collected soil.

Natural water content (%)	Specific gravity of soil particles	Wet density (g/cm^3)	Dry density (g/cm^3)	Void ratio	Liquid limit (%)	Plastic limit (%)	Clay content (%)	Silt content (%)	Sand content (%)
93	2.66	1.560	0.828	2.25	81	34	54	44	2

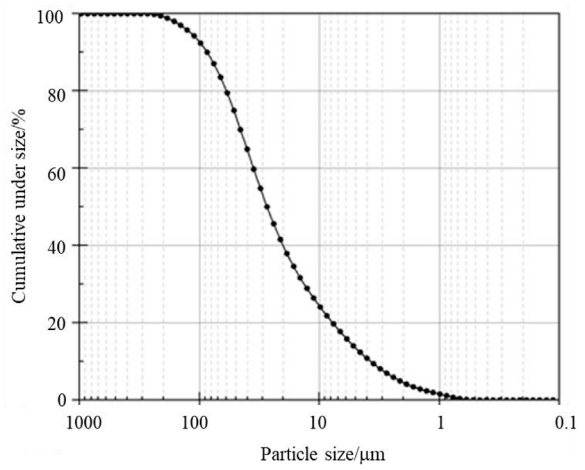

FIGURE 1
Particle size distribution.

height of the soil reached 7 cm, at which time the vacuum pump would be closed. Details of the vacuum preloading test are presented in Table 3.

2.3.2 Consolidation test

The samples obtained in another series of surcharge preloading and vacuum preloading tests in Section 2.3.1 were then subjected to consolidation tests. Figure 4 shows the apparatus and samples for the test. The chamber for preparing samples treated by surcharge preloading is similar to that shown in Figure 5A, but it consists of two parts. The upper part of the chamber can be taken off after finishing the surcharge preloading. Then the samples were collected from the two red line height in the sublayer once the improvement stopped by cut rings to make the samples for the consolidation tests. In this series of surcharge preloading tests, 18 pieces of 5.5 kg weight were applied on the sand layer by the metal bracket. A triple low-pressure oedometer, as shown in Figure 4, was used to measure the coefficient of secondary consolidation. Loading was applied according to the standard method at 12.5 kPa, 25 kPa, 50 kPa, 100 kPa, 200 kPa, and 300 kPa in turn.

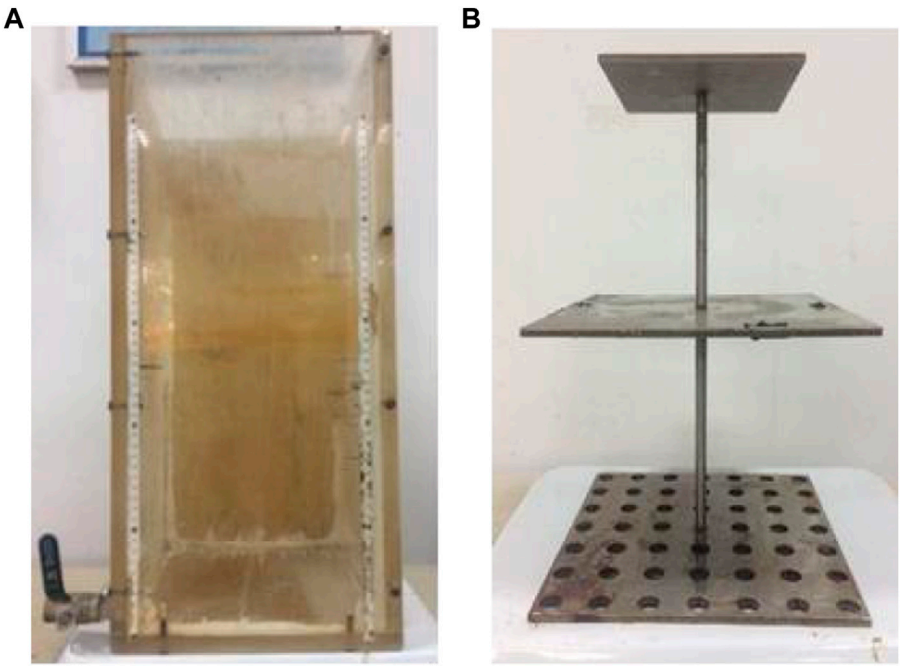

FIGURE 2
Apparatus for the surcharge preloading test **(A)** the chamber; **(B)** the loading bracket.

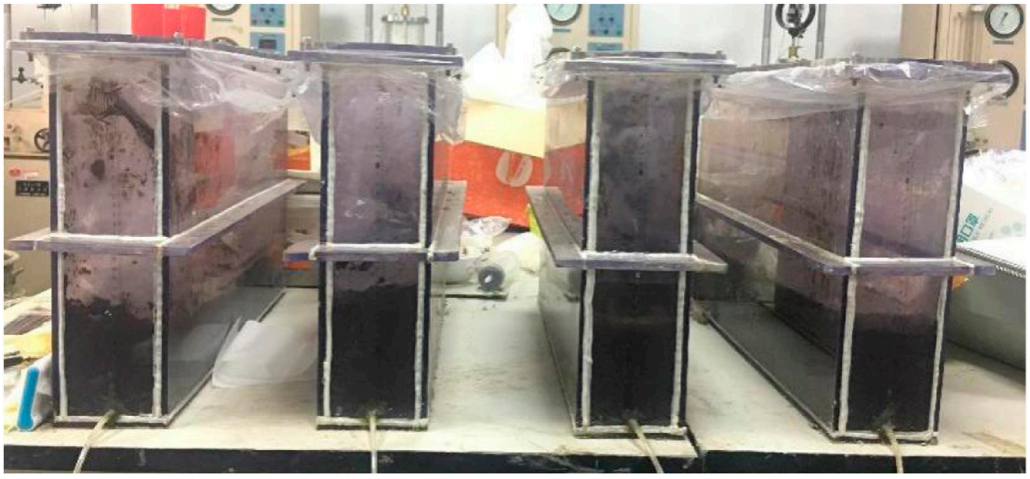

FIGURE 3
Device for vacuum preloading test.

TABLE 2 Parameters of samples in surcharge preloading test.

Group	No.	Mass of dry soil/g	Mass of slurry/g	Water content of slurry (%)	Mass of flocculant solution/g	Equivalent initial water content (%)
A	1	5,000	20000	300	——	300
	2		16650	233	3353.4	
	3		15650	213	4354.4	
	4		14500	190	5505.5	
B	1	5,000	17500	250	——	250
	2		13150	163	4354.4	

TABLE 3 Plan of vacuum preloading test.

Group	No.	Mass of dry soil/g	Mass of slurries/g	Water content of slurries/%	Mass of flocculation solution/g	Equivalent initial water content/%
C	1	6,000	27000	350	——	350
	2		21780	263	5,225.2	
D	1		30000	400	——	400
	2		24780	313	5,225.2	

3 Test results and analysis

3.1 Effect of flocculation on pore water drainage

Figure 6 shows the settlement of slurries with the parameters listed in Table 2. A1 represents the case in which no flocculant was added to the slurry. It is evident that, with the same water content, the addition of APAM leads to a greater degree of settlement. Moreover, the water drainage for cases with flocculation finishes within 40 h, while the consolidation is still ongoing in case A1. The speed of settlement in cases A2, A3, and A4 is much faster than that in case A1 in the early stage, indicating that flocculation significantly improves the consolidation coefficient and the permeability coefficient of the soil. Considering the flocculation mechanism, the formation of large flocs increases the void ratio and improves the drainage path of pore water, which further increases the permeability of the slurries.

Comparison of the ultimate height indicates that flocculation also influences the final improvement effect. The eventual settlement in case A4 is smaller than in cases A2 and A3, indicating that the improvement effect of flocculation is not always positively correlated with the dosage.

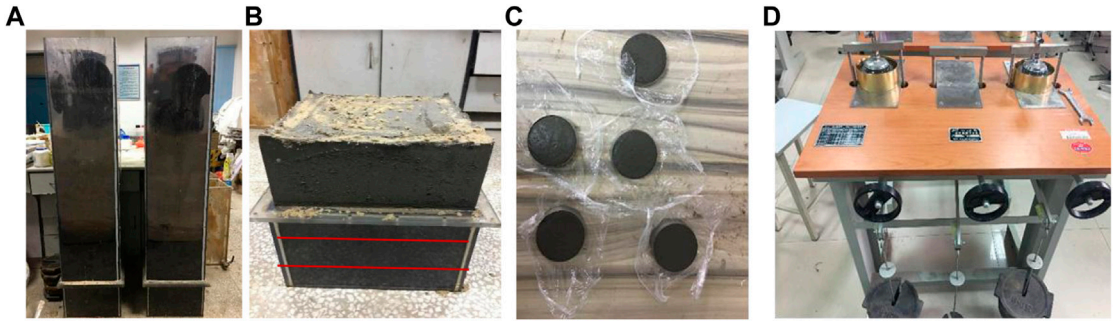

FIGURE 4
Samples and apparatus for consolidation tests: **(A)** chamber; **(B)** sampling position; **(C)** samples for consolidation; **(D)** triple oedometer.

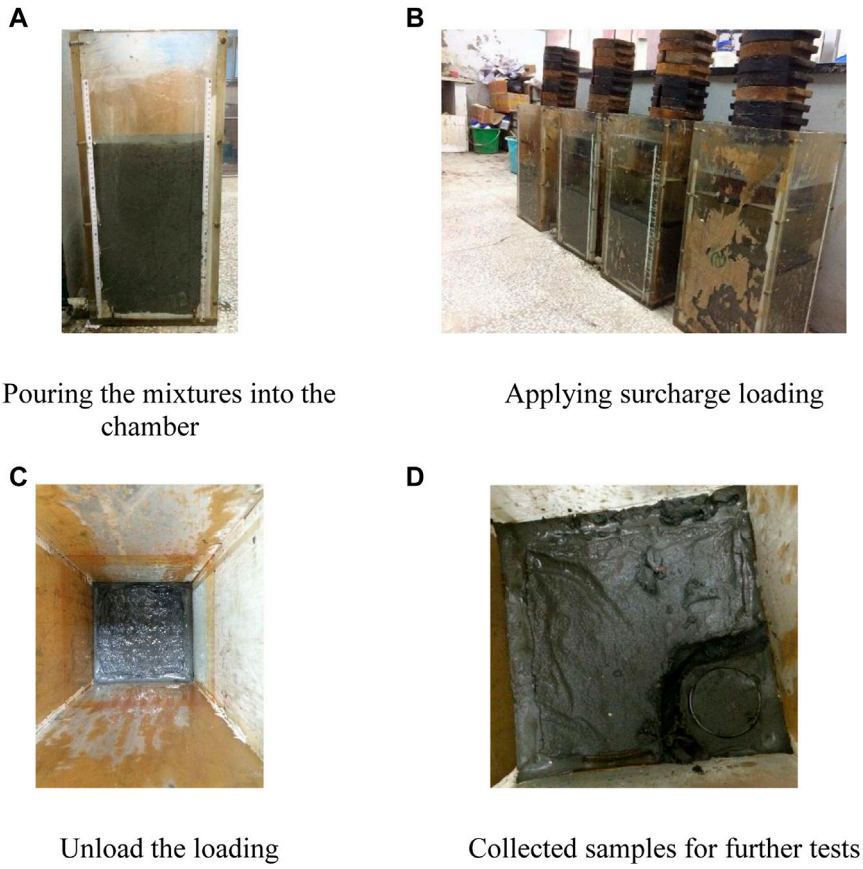

FIGURE 5
Experimental procedure for surcharge preloading tests: **(A)** pouring the mixtures into the chamber; **(B)** applying surcharge loading; **(C)** unload the loading; **(D)** collected samples for further tests.

In a specific range, the effect increases with increasing dosage because flocculation increases the permeability of the soil. However, when too much flocculant is used, the drainage effect decreases because the flocculant is combined with too much water, which makes drainage more difficult. An overdose of flocculant wraps the soil particles, preventing the inner water from flowing out.

Figure 7 shows the height variation in case B, where the equivalent water content is lower than in case A. Comparing the results in Figures 6, 7, the speed of settlement, as well as the ultimate settlement, exhibits little difference between cases A and B when no flocculant is used. For the cases with flocculant, an equivalent water content of 300% produces a larger degree of settlement and higher

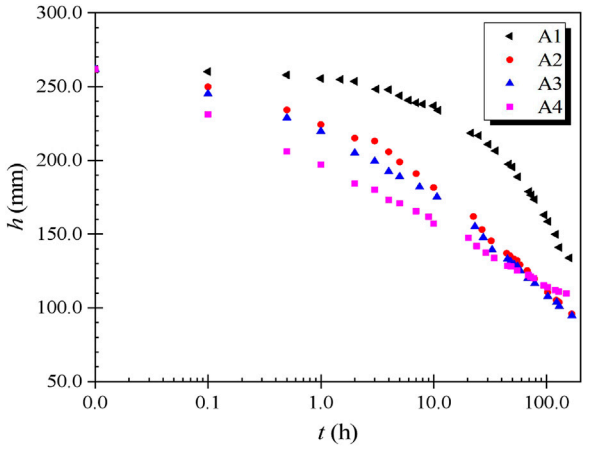

FIGURE 6
Variation of slurry height in case A of surcharge preloading tests.

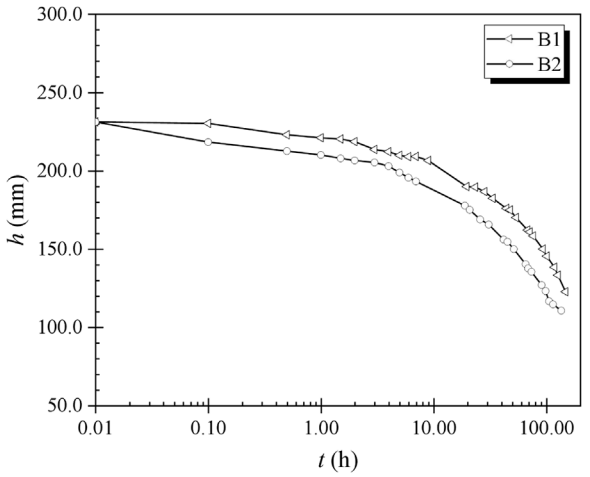

FIGURE 7
Variation of slurry height in case B of surcharge preloading tests.

consolidation speed because of the greater void ratio. Moreover, the effect of flocculation is more evident with a higher water content when surcharge preloading is applied. Figure 8 illustrates the settlement of slurries under vacuum preloading combined with flocculation. As stated in Table 3, cases A and C have no flocculant added. The settlement in cases with flocculation is greater than in cases without flocculation. Different from the performance in the surcharge preloading method, the height initially decreases more slowly in slurries with flocculant than in those without flocculant, but the opposite is eventually the case. As stated when describing the test apparatus, the bottom of the surcharge preloading test is impermeable, so the water drains out through the upper surface. Considering the self-weighted settlement, soil in the lower stratum is denser and has lower permeability. In contrast, the upper part of the slurry samples has large voids and high permeability. Flocculation increases the void ratio of the upper

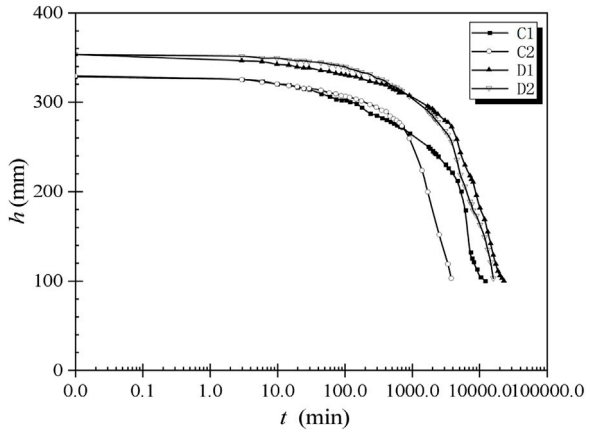

FIGURE 8
Variation of height in vacuum preloading tests.

TABLE 4 Parameters after surcharge preloading improvement.

No.	A1	A2	A3	A4	B1	B2
Water content/%	75.7%	69.2%	68.7%	69.6%	69.5%	63.6%
Wet density/g cm^{-3}	1.573	1.608	1.621	1.596	1.584	1.605

slurry, so the initial settlement is higher. In the case of vacuum preloading, the permeable boundary is at the bottom. Under the flocculation effect, the lower stratum is thicker and denser than in the case without flocculation because the self-weight consolidation proceeds faster in the case with flocculation. Hence, the permeability is lower than in the case without flocculation. This causes a smaller initial height reduction in the case with flocculation. With time, clogging gradually occurs in the cases without flocculation, which makes the permeability lower than in cases with flocculation. Thus, the settlement develops slower thereafter.

Comparing the results with different equivalent water contents, Figure 8 indicates that the finish times for cases C and D are almost the same. In contrast, cases A and B have significantly different finish times, indicating that the flocculation effect influences samples with relatively low water contents more than those with extremely high water contents when vacuum preloading is applied. This investigation seems contrary to the results obtained with samples improved by surcharge preloading, but this is not necessarily the case. Because a water content of 300% is considered high, the smaller difference for a water content of 400% is more likely to be the result of an insufficient flocculant dosage. Cases without flocculation show different consolidation speeds because the clogging around the drain is more severe at higher water contents.

The results presented in Table 4 indicate that the slurry water content and wet density improve after surcharge preloading. Flocculation enhanced preloading method reduces the water content of the soil more than in cases without flocculation. Compared with the results of 250% water content, the case with higher initial water content

TABLE 5 Parameters of consolidation test samples before surcharge preloading.

Group (No.)	Mass of dry soil/g	Initial water content (%)	Flocculant solution concentration (%)	Equivalent initial water content (%)
E	24000	300	0	387
F	24000	300	0.087	387

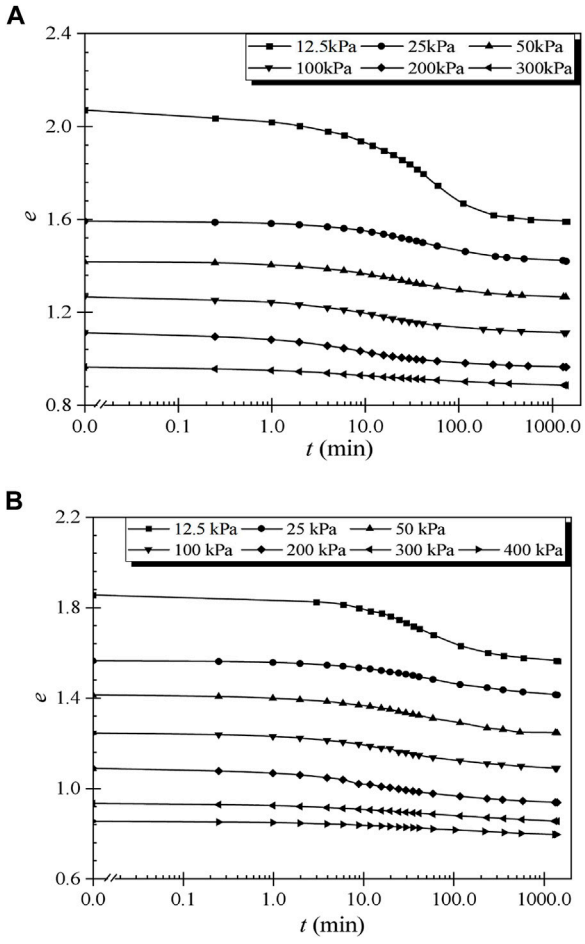

FIGURE 9
Variation of void ratio with time for samples after surcharge preloading: **(A)** case E; **(B)** case F.

improved more. Cases with flocculation have a higher wet density, which corresponds to a lower water content.

3.2 Effect of flocculation on the secondary consolidation behavior of slurries

As the treated slurries are expected to be used in infrastructure construction, knowledge of the long-term performance is essential. Thus, the secondary consolidation behavior is now studied in detail. Secondary consolidation refers to the deformation of the soil layer and the variation of the void changes over the long term, which significantly influence the reuse of dredged fills. According to previous work, the secondary consolidation behavior is related to the loading in the principal consolidation stage. Hence, different loading values were applied to samples improved by the vacuum preloading method and the surcharge preloading method. The parameters of the samples improved by surcharge loading are listed in Table 5. In group E, additional water was added with the same volume as the flocculation solution in group F.

The evolution of the void ratio for representative cases following surcharge preloading and vacuum preloading is shown in Figures 9, 10. According to Yin et al. (2003), the *e*-log*t* curve can be divided into primary consolidation stage and secondary consolidation stage. The secondary consolidation part of each curve is almost linear, and the gradient reflects the coefficient of secondary consolidation. In both cases with surcharge preloading, the curves seem more stable when larger preloading is applied. In contrast, the gradient for the cases under vacuum preloading initially increases with the loading and decreases afterward, which is similar to the results obtained by Lei et al. (2016). Comparing the results in cases E and F, it is evident that the gradients in case F are larger. To clarify this, the coefficients of secondary consolidation are calculated.

Using the conventional method of Yin et al. (2003), the coefficients of secondary consolidation were obtained (see Figure 11). The coefficient of secondary consolidation is larger when flocculation plays a role, and is typically 1.five to two times that of cases without flocculation. Figure 12 shows the coefficient of secondary consolidation for samples improved by the vacuum preloading method. Similar to the results shown in Figure 11, the cases with flocculation have larger coefficients in general. Moreover, the coefficient varies significantly with the loading when flocculation is applied. Comparing the results shown in Figure 12, a higher initial water content produces a larger coefficient of secondary consolidation after vacuum preloading combined with flocculation, indicating that flocculation has a greater effect on increasing the secondary consolidation coefficient when the initial water content is higher.

Considering the flocculation mechanism, there are two reasons for the increase in the secondary consolidation coefficient. First, the flocculant APAM consists of long polymer chains with molecular weights of 4–20 million, which form a reticular structure combined with the soil particles. Because the reticular structure is nonuniform, the settlement cannot stabilize over the test duration. Second, the formation of flocs changes the pore structure in the soil. The bone formed by the flocs have high elasticity, so the degree of consolidation in the secondary consolidation stage is large.

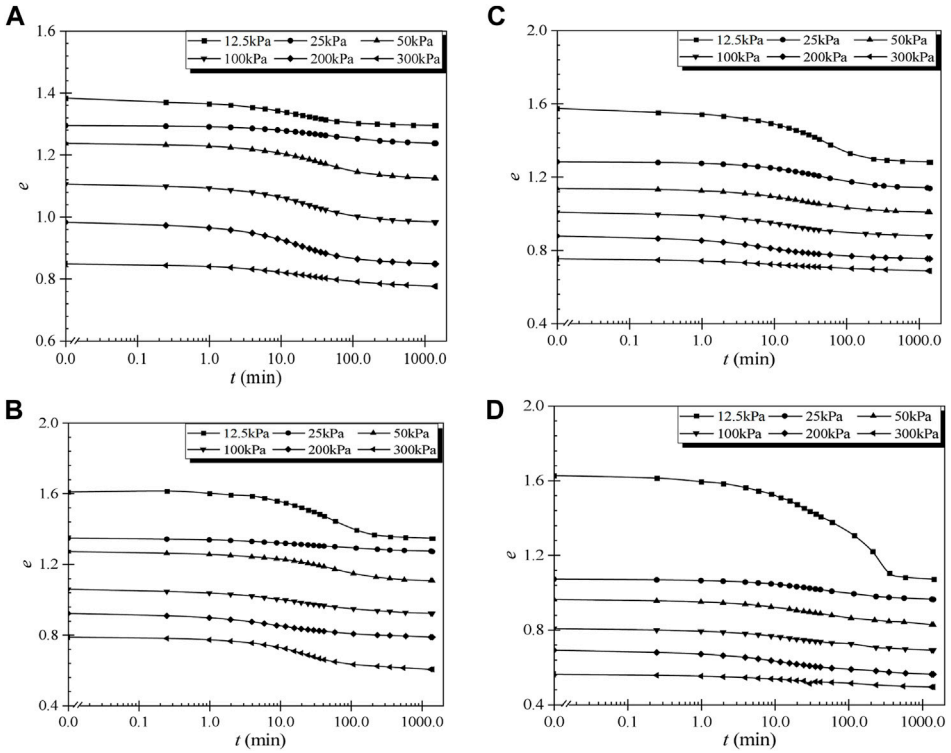

FIGURE 10
Variation of void ratio with time for samples after vacuum preloading improvement: **(A)** case C1; **(B)** case C2; **(C)** case D1; **(D)** case D2.

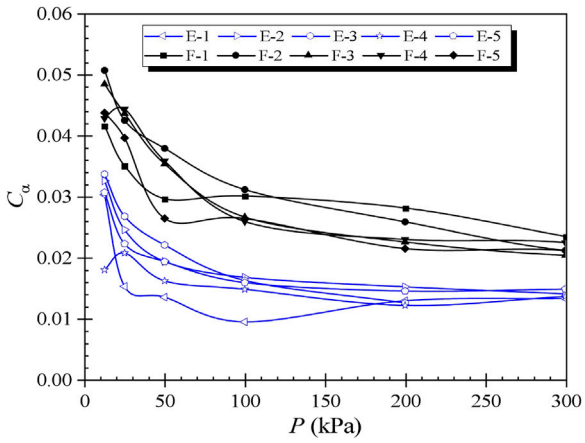

FIGURE 11
Coefficient of secondary consolidation under different loading values.

4 Discussion

The analysis in the previous section indicates that the usage of APAM has significant advantages in improving the consolidation speed and ultimate consolidation effects, especially when the soil has a high initial water content. Flocculation increases the permeability of slurries with several fine particles in the case of both surcharge preloading and vacuum preloading. The use of flocculants prevents clogging in the slurries using the vacuum preloading method, which significantly increases the efficiency of this improvement method. However, as shown by the secondary consolidation behavior, the coefficient of secondary consolidation is enhanced following flocculation, which may cause greater post-construction settlement. Therefore, the amount of flocculant should be chosen considering the multi-effects.

For example, as stated in the results of surcharge preloading tests, settlements increase before flocculant amount reaching the optimized value but decrease after then with the increase of flocculant's amount. Therefore, considering the influence of flocculation on both settlement and secondary consolidation, the amount of the flocculant is better to be lower than the optimized value. As shown in Figure 6, the variation of the flocculant amount changes the settlement little for the two test amounts. In that case, the effect of secondary consolidation is the determining factor.

In practice, pre-tests are suggested to be conducted before applying the proper amount of flocculants in engineering practice because the optimized value of flocculant amount is affected by the properties of the slurries. Based on the test results of this work, both primary consolidation performance and secondary consolidation performance should be considered. In a word, when using APAM in soil improvement, the dosage must be determined carefully.

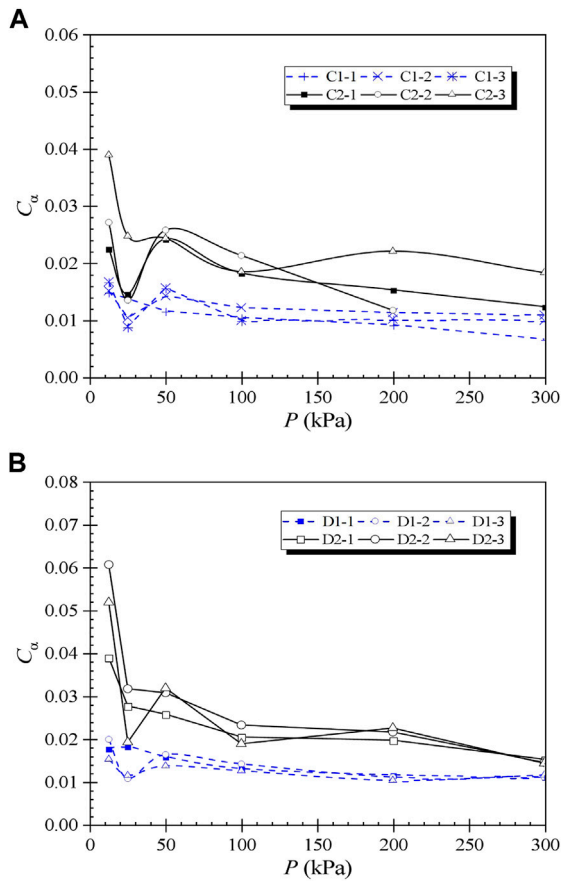

FIGURE 12
Coefficient of secondary consolidation of samples improved by vacuum preloading method: **(A)** Case C; **(B)** Case D.

5 Conclusion

This manuscript has described the performance of slurries improved by two flocculant-enhanced methods, especially the influence of flocculation on water drainage and secondary consolidation. This study has mainly been conducted through laboratory experiments. By analyzing the test results, the following conclusions can be drawn.

- The application of flocculant improves the permeability coefficient. Furthermore, it improves the speed of settlement and the ultimate value of settlement.
- There is an optimized flocculant dosage from the perspective of water drainage. When the dosage of APAM is lower than the optimal value, an increase in the dosage will improve the efficiency of the surcharge preloading method. However, the efficiency decreases when the dosage exceeds the optimal value.
- In both the surcharge preloading and vacuum preloading processes, the influence of a sufficient dosage of flocculant is more significant when the initial water content is higher.
- The consolidation tests show that the application of APAM increases the secondary consolidation coefficient, which would cause larger post-construction settlement. Therefore, the dosage of APAM needs to be determined carefully prior to its application.

Data availability statement

The original contributions presented in the study are included in the article/supplementary material further inquiries can be directed to the corresponding author.

Author contributions

Data collection, JC; Formal analysis, ZF; Funding acquisition, CH and KS; Investigation, JC; Methodology, JC; Project administration, CH and RZ; Resources, CH and RZ; Writing—original draft, JC, CH and QP.

Funding

This work is funded by the Science and Technology Project of State Grid Jiangsu Electric Power Co., Ltd. (Grant No. J2020070).

Conflict of interest

Author CH, ZF, KS, and QP were employed by the company State Grid Jiangsu Electric Power Co., Ltd.

The remaining authors declare that the research was conducted in the absence of any commercial or financial relationships that could be construed as a potential conflict of interest.

Publisher's note

All claims expressed in this article are solely those of the authors and do not necessarily represent those of their affiliated organizations, or those of the publisher, the editors and the reviewers. Any product that may be evaluated in this article, or claim that may be made by its manufacturer, is not guaranteed or endorsed by the publisher.

References

Indraratna, B., Rujikiatkamjorn, C., Ameratunga, J., and Boyle, P. (2011). Performance and prediction of vacuum combined surcharge consolidation at Port of Brisbane. *J. Geotech. Geoenviron. Eng.* 137 (11), 1009–1018. doi:10.1061/(asce)gt.1943-5606.0000519

Kang, G., Tsuchida, T., and Athapaththu, A. M. R. G. (2016). Engineering behavior of cement-treated marine dredged clay during early and later stages of curing. *Eng. Geol.* 209, 163–174. doi:10.1016/j.enggeo.2016.05.008

Kang, X., Bate, B., Chen, R. P., Yang, W., and Wang, F. (2019). Physicochemical and mechanical properties of polymer-amended kaolinite and fly ash–kaolinite mixtures. *J. Mat. Civ. Eng.* 31 (6), 04019064. doi:10.1061/(asce)mt.1943-5533.0002705

Lei, H., Wang, X., Chen, L., Huang, M., and Han, J. (2016). Compression characteristics of ultra-soft clays subjected to simulated staged preloading. *KSCE J. Civ. Eng.* 20 (2), 718–728. doi:10.1007/s12205-015-0343-y

Lei, H., Xu, Y., Li, X., Jiang, M., and Liu, L. (2019). Effect of polyacrylamide on improvement of dredger fill with vacuum preloading method. *J. Mat. Civ. Eng.* 31 (9), 04019193. doi:10.1061/(asce)mt.1943-5533.0002860

Lei, H. Y., Chen, L., Ding, X. D., Zheng, G., and Kang, J. W. (2013). Properties of secondary consolidation of two types of dredger fill sites. *Chin. J. Geotech. Eng.* 33 (S1), 90–96.

Liu, F., Wu, W., Fu, H., Wang, J., Hai, J., Cai, Y., et al. (2020). Application of flocculation combined with vacuum preloading to reduce river-dredged sludge. *Mar. Georesour. Geotechnol.* 38 (2), 164–173. doi:10.1080/1064119x.2018.1564092

Liu, S., Sun, H., Geng, X., Cai, Y., Shi, L., Deng, Y., et al. (2022). Consolidation considering increasing soil column radius for dredged slurries improved by vacuum preloading method. *Geotext. Geomembr.* 50 (3), 535–544. doi:10.1016/j.geotexmem.2022.01.002

Pu, H., Yang, P., Lu, M., Zhou, Y., and Chen, J. N. (2020). Piecewise-linear large-strain model for radial consolidation with non-Darcian flow and general constitutive relationships. *Comput. Geotech.* 118, 103327. doi:10.1016/j.compgeo.2019.103327

Walker, R., and Indraratna, B. (2006). Vertical drain consolidation with parabolic distribution of permeability in smear zone. *J. Geotech. Geoenviron. Eng.* 132 (7), 937–941. doi:10.1061/(asce)1090-0241(2006)132:7(937)

Wang, J., Huang, G., Fu, H., Cai, Y., Hu, X., Lou, X., et al. (2019). Vacuum preloading combined with multiple-flocculant treatment for dredged fill improvement. *Eng. Geol.* 259, 105194. doi:10.1016/j.enggeo.2019.105194

Wang, J., Ni, J., Cai, Y., Fu, H., and Wang, P. (2017). Combination of vacuum preloading and lime treatment for improvement of dredged fill. *Eng. Geol.* 227, 149–158. doi:10.1016/j.enggeo.2017.02.013

Wu, Y., Tran, Q. C., Zhang, X., Lu, Y., Xu, J., and Zhang, H. (2022). Experimental investigation on the treatment of different typical marine dredged sludges by flocculant and vacuum preloading. *Arab. J. Geosci.* 15 (7), 642–715. doi:10.1007/s12517-022-09839-0

Wu, Y., Zhou, Z., Wang, D., Lu, Y., Wang, J., Lin, F., et al. (2017). Experimental study of Ningbo waste slurry treatment by vacuum preloading with flocculants. *J. Dalian Univ. Technol.* 57 (02), 157–163.

Xu, G. Z., Qiu, C. C., Song, M. M., Cao, Y. P., and Yin, J. (2021). Flocculant effects on fluidity and strength behavior of cemented dredged clay with high water content. *Mar. Georesour. Geotechnol.* 39 (8), 951–961. doi:10.1080/1064119x.2020.1786198

Yin, Z. Z., Zhang, H. B., Zhu, J. G., and Li, G. W. (2003). Secondary consolidation of soft soils. *Chin. J. Geotech. Eng.-Chin. Ed.-* 25 (5), 521–526.

Zhao, S., Zeng, F. J., Wang, J., Fu, H., and Wang, Y. (2016). Experimental study of flocculation combined with vacuum preloading to reinforce silt foundation. *Chin. J. Rock Mech. Eng.* 35 (6), 1291–1296.

frontiers | Frontiers in Materials

TYPE Original Research
PUBLISHED 15 May 2023
DOI 10.3389/fmats.2023.1204264

OPEN ACCESS

EDITED BY
Xianze Cui,
China Three Gorges University, China

REVIEWED BY
Bo Zhang,
Guizhou Minzu University, China
Xiaoshan Shi,
China Coal Research Institute, China

*CORRESPONDENCE
Yu Wang,
wyzhou@ustb.edu.cn

RECEIVED 12 April 2023
ACCEPTED 05 May 2023
PUBLISHED 15 May 2023

CITATION
Wang D, Luo Z, Xia H, Gao S, Li P, Li J and Wang Y (2023), Fatigue failure and energy evolution of double-stepped fissures contained marble subjected to multilevel cyclic loads: a lab-scale testing.
Front. Mater. 10:1204264.
doi: 10.3389/fmats.2023.1204264

Fatigue failure and energy evolution of double-stepped fissures contained marble subjected to multilevel cyclic loads: a lab-scale testing

Di Wang[1], Zhixiong Luo[1], Hongbo Xia[1], Shangqing Gao[1], Peiliang Li[1], Juzhou Li[2] and Yu Wang[2]*

[1]Information Institute of the Ministry of Emergency Management of the PRC, Beijing, China, [2]Beijing Key Laboratory of Urban Underground Space Engineering, Department of Civil Engineering, School of Civil and Resource Engineering, University of Science and Technology Beijing, Beijing, China

The instability of rock mass induced by the deterioration and failure of rock bridge is often encountered in hard rock engineering. Under engineering disturbance, a steep and gentle stepped sliding surface is prone to forming along the rock bridges between the intermittent rock joints, which directly controls the rock mass instability modes. In order to reveal the influence of fissure angle on the fatigue deterioration and energy evolution mechanism of stepped double-flawed hard rock, the multilevel cyclic loading mechanical test were carried out on flawed marble samples with fissure angle of 10°, 30°, 50°, and 70° angles. The testing shows that rock strength, fatigue lifetime, peak strain and dissipated energy increase with increasing fissure angle and the increase rate of them becomes sharply in the high cyclic level. In addition, the increase of dissipated energy accelerates with the increase of cyclic loading level, and shows a sudden increase trend in the last cyclic loading stage. When the joint fissure angle is 10°, the dissipated energy is the smallest and the dissipated energy is the largest at 70°. Moreover, a damage evolution model based on dissipated energy is established to describe the characteristics of damage accumulation. The model is in good agreement with the experimental data and reflects the nonlinear characteristics of damage accumulation.

KEYWORDS

rock bridge, fatigue loading, fracture evolution, energy dissipation, damage evolution model

1 Introduction

Rock is the basic material for building large rock projects such as mines, tunnels, slopes, water conservancy and underground spaces (Cerfontaine and Collin, 2018). The interior of the rock contains abundant fractures, pores and other micro defects. These randomly distributed microdefects accumulate, expand and penetrate under dynamic loads such as impact, earthquake, engineering blasting and vehicle loading (Erarslan and Williams, 2012; Yin et al., 2018; Orozco et al., 2019). These actions may then lead to damage and fracture of the rock, which in turn induces many catastrophic accidents in rock engineering. Especially in the hard rock projects, such as the Jiama Copper Polymetallic Mine in Tibet and Baiyunebo Iron Ore Mine, China, the rock bridge is likely to be communicated under

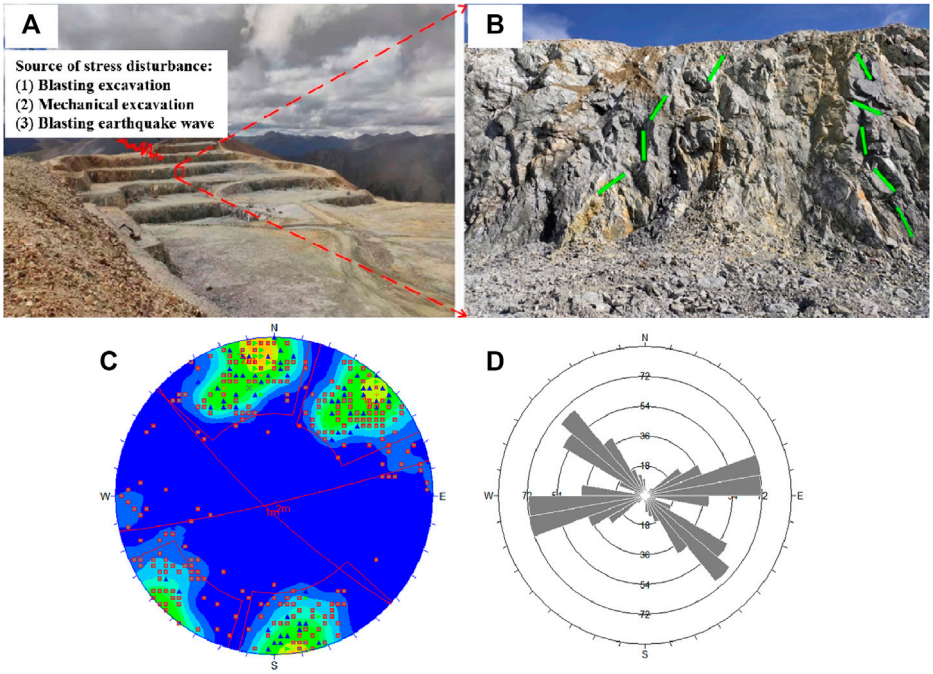

FIGURE 1
Description of the slope rock mass structure of the jiama copper polymetallic mine in tibet **(A)** Schematic diagram of stress disturbance; **(B)** Stepped rock bridge structure; **(C)** Result of stereographic projection; [**(D)** Rose diagram of dominant joints in rock mass].

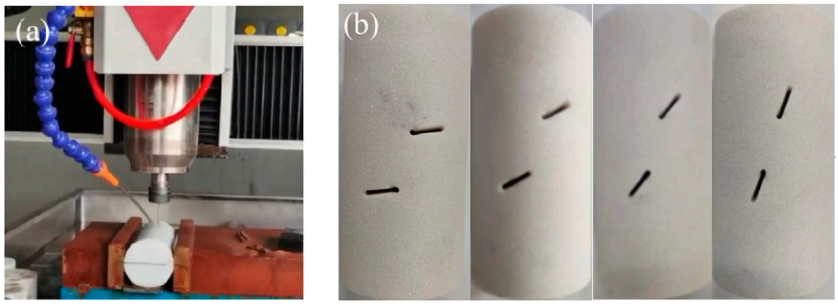

FIGURE 2
Preparation of marble specimens with two pre-existing flaws **(A)** Working diagram of rock engraving machine; [**(B)** Marble specimens with double stepped fissures].

engineering disturbances such as unloading, excavation and blasting. It is very easy to form a stepped slip surface, resulting in the deterioration and failure of the rock bridge, thus causing the slope destabilization and huge catastrophic losses. Therefore, it is of great importance to investigate the fracture and energy evolution characteristics of stepped marble under multi-stage fatigue loading, in order to maintain the long-term stability of rock engineering.

Nowadays, many scholars in the field of rock mechanics have conducted a lot of researches on the fatigue mechanical properties of rocks under cyclic loading, and have obtained a large number of research results (Ray et al., 1999; Momeni et al., 2015; Erarslan, 2021; Faradonbeh et al., 2021). In terms of rock deformation law under cyclic loading, Zhao et al. (2014) studied the fatigue characteristics of limestone under cyclic loading at different frequencies by using the MT S810 dynamic testing machine. The results clarified that the linear relationship between the fatigue life of limestone and the loading frequency satisfied the double logarithmic coordinate system, and the fatigue life increased with the increase of loading frequency. Afterwards, they proposed a fatigue life calculation model based on the average strain increment. By studying the fatigue mechanical properties of rock materials, Xiao et al. (2011) pointed out that the higher the upper limit stress, the higher the

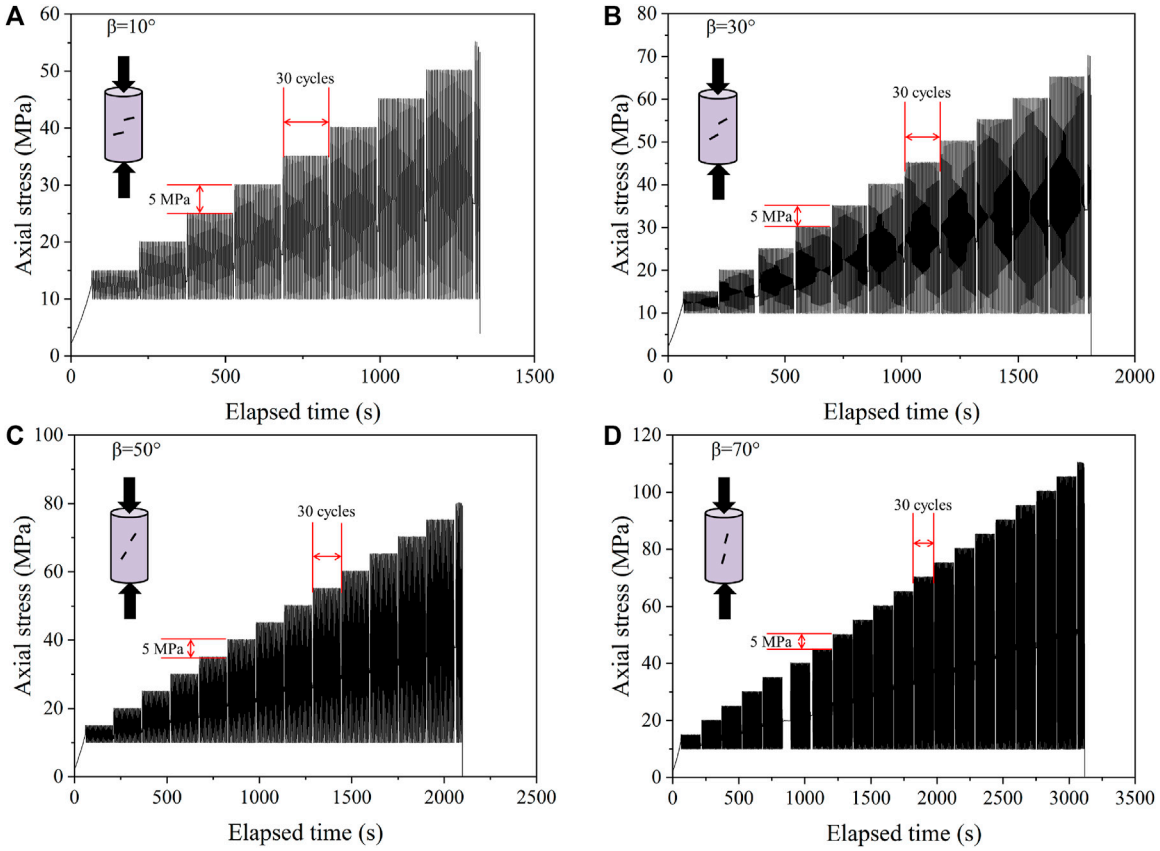

FIGURE 3
Loading paths of marble specimens with different fissure angles [**(A–D)** Rock specimens with fissure angles of 10°, 30°, 50°, and 70°, respectively].

stress amplitude, the higher the loading frequency, the shorter the fatigue life of the rock, etc. However, the essence of rock damage is driven by energy conversion (Wang and Zheng, 2015; Peng et al., 2019), and the fracture mechanism is influenced by many factors. The commonly used mechanical indicators are hard to describe the damage evolution and fracture process of rocks. Therefore, employing energy analysis to describe the damage evolution during rock deformation is effective to reveal the damage mechanism under cyclic fatigue loading (Erarslan and Williams, 2012; Wang et al., 2020; Bai et al., 2021; Shirani Faradonbeh et al., 2021; Zhou et al., 2021; Bai et al., 2022; 2023; Wang et al., 2023a; Wang et al., 2023b; Wang et al., 2023c; Wang et al., 2023d). Xie et al. (2005, 2008) pointed out that energy dissipation caused rock damage and led to structural deterioration and loss of strength. At the same time, energy release was intrinsically responsible for triggering the sudden destruction of the rock as a whole. Finally, the overall connection between rock strength and energy dissipation and release was established. Zhang et al. (2014) carried out conventional triaxial tests on marble, limestone and sandstone to study the characteristics of energy nonlinear evolution of rock deformation process. It was shown that most of the external work was converted into elastic strain energy stored inside the rock specimens before failure, and the dissipated energy increased little, and the dissipated energy increased rapidly after the yielding point, and the elastic energy increased slowly. Wang et al. (2020) investigated the anisotropic fracture and energy dissipation characteristics of interbedded marble under multistage cyclic loading, they found that the dissipated energy was impacted by the interbed angle. Li et al. (2017) analyzed and developed a theoretical model between axial strain and number of cycles under cyclic loading and unloading conditions by conducting uniaxial graded cyclic loading and unloading tests on two sets of sandstone specimens, and derived an evolution equation for damage variables to evaluate the degree of rock damage. Wang et al. (2023a) performed triaxial alternative cyclic loading and unloading confining pressure tests to investigate the influence of prior damage and rock macro-meso failure characteristics, and they found that the energy-driven failure evolution of rock is strongly impacted by the previous damage degree.

Although plenty of studies have been achieved on rock damage evolution investigations, there are fewer studies on the fracture and energy evolution characteristics of rock double-stepped fissure contained rock. As a result, a series of multilevel fatigue loading tests were carried out in this work to reveal the fracture and energy evolution characteristics of pre-flawed rock samples. This study is focusing on the effects of fissure angle on rock peak strain, fatigue strength, and dissipated energy evolution pattern. The results are of great significance for revealing the mechanical properties of double stepped fissure contained rock mass under fatigue disturbance.

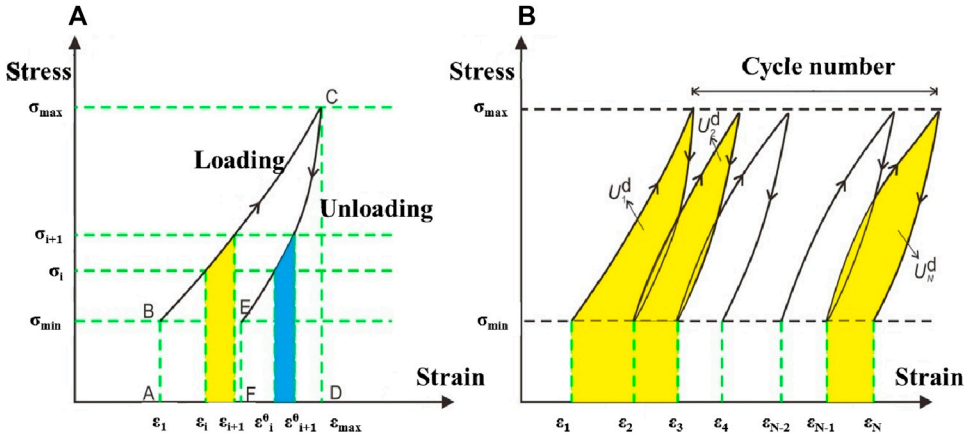

FIGURE 4
Calculation of strain energy density, adopted from Wang et al. (2021) [**(A)**: Schematic diagram of strain energy calculation: **(B)** N cycles cumulative dissipated strain energy].

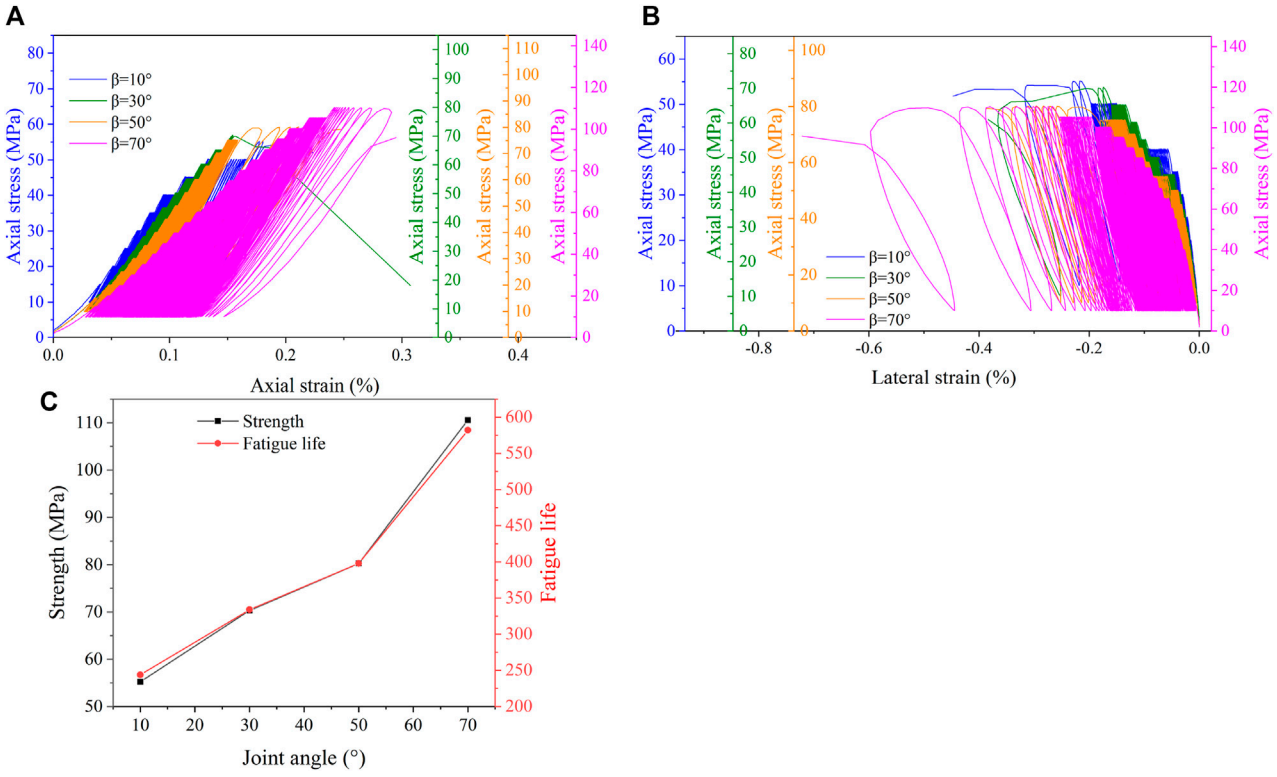

FIGURE 5
Stress-strain curves, strength and fatigue life curves ofmarble specimens with different fissure angles [**(A)** Axial strain; **(B)** Lateral strain; **(C)** Changes of strength and fatigue life of marble specimens with different fissure angles].

2 Testing methods

2.1 Rock specimen preparation

The tested rock material was obtained from an open pit slope located at the Jiama Copper Polymetallic Mine in Tibet, China, as shown in Figures 1A, B. The stepped fissures can be clearly observed and the information of rock structure is obtained by using 3D laser detection technology in Figures 1C, D. According to the method recommended by ISRM (Ulusay, 2015), the rock mass obtained from the open pit slope was prepared into a cylinder with a diameter (D) of 50 mm and a height (H) of

TABLE 1 Mechanical parameters of marble specimens with different fissure angles under fatigue loads.

Specimen	Height × Diameter	Peak strength	Peak axial strain	Peak lateral strain	Peak volumetric strain	Number of loading stages	Number of cycles
ID	(mm × mm)	(MPa)	(%)	(%)	(%)		
M10-1	99.56 × 49.21	55.21	0.1249	−0.2965	−0.4681	9	244
M10-2	99.23 × 49.17	56.46	0.1267	−0.3011	−0.4755	9	248
M30-1	99.11 × 49.02	70.32	0.1888	−0.3358	−0.4828	12	334
M30-2	98.89 × 49.58	71.25	0.1895	−0.3392	−0.4889	11	304
M50-1	99.12 × 49.06	80.24	0.2685	−0.3878	−0.5071	14	398
M50-2	98.69 × 49.51	79.68	0.2621	−0.3813	−0.5005	15	426
M70-1	99.85 × 48.89	110.55	0.3834	−0.5973	−0.8112	20	582
M70-2	99.45 × 49.13	111.56	0.3866	−0.6024	−0.8182	21	649

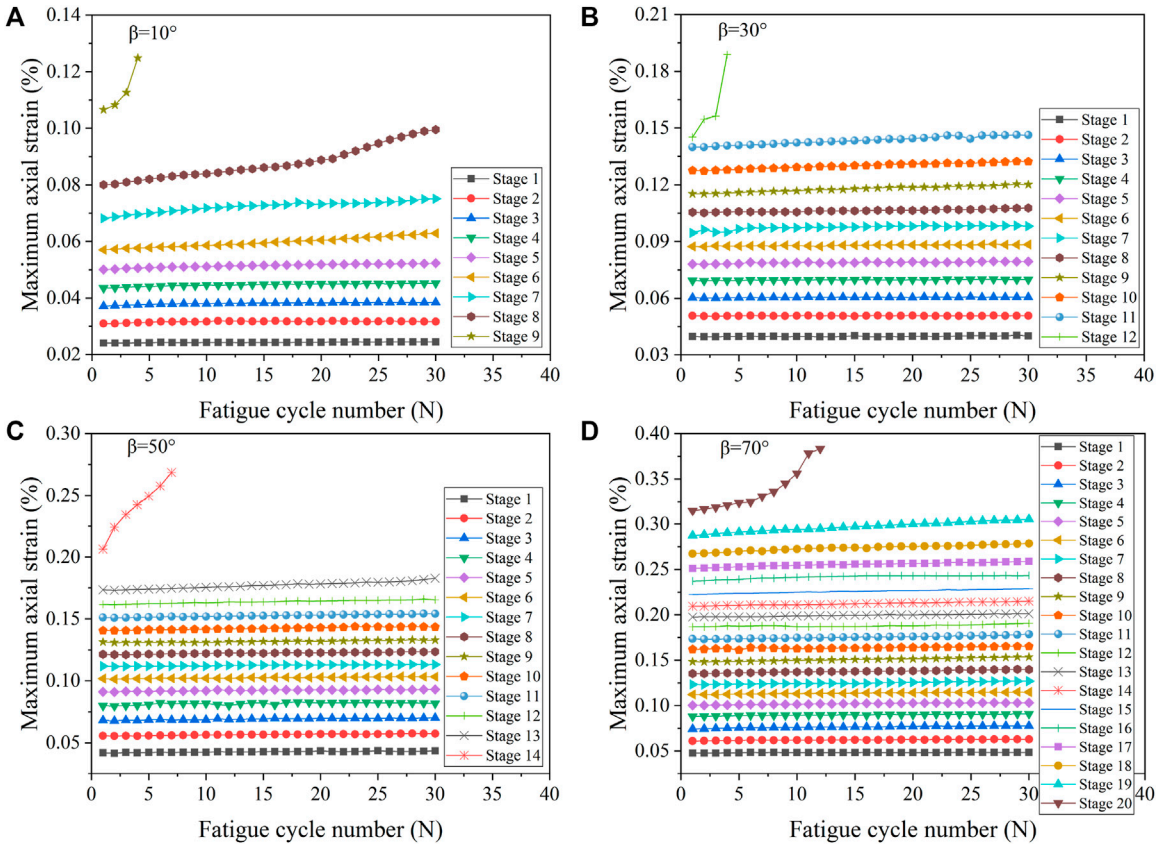

FIGURE 6
Variation diagram of axial strain of marble specimens with different fissure angles during fatigue strain [**(A–D)** Rock specimens with fissure angles of 10°, 30°, 50°, and 70°, respectively].

100 mm. Both ends of the specimens were polished to ensure that the non-uniformity error is less than 0.05 mm and the parallelism is less than 0.1 mm. Two parallel fissures were prefabricated on the specimens using a precision carving machine as shown in Figure 2A. The angle between the fissure and the horizontal plane was set to be 10°, 30°, 50°, and 70°, respectively. For all the prepared rock specimens, the angle and length of the rock bridge between the two fissures were the same. Typical marble specimens with different fissure angle used in this work are shown in Figure 2B.

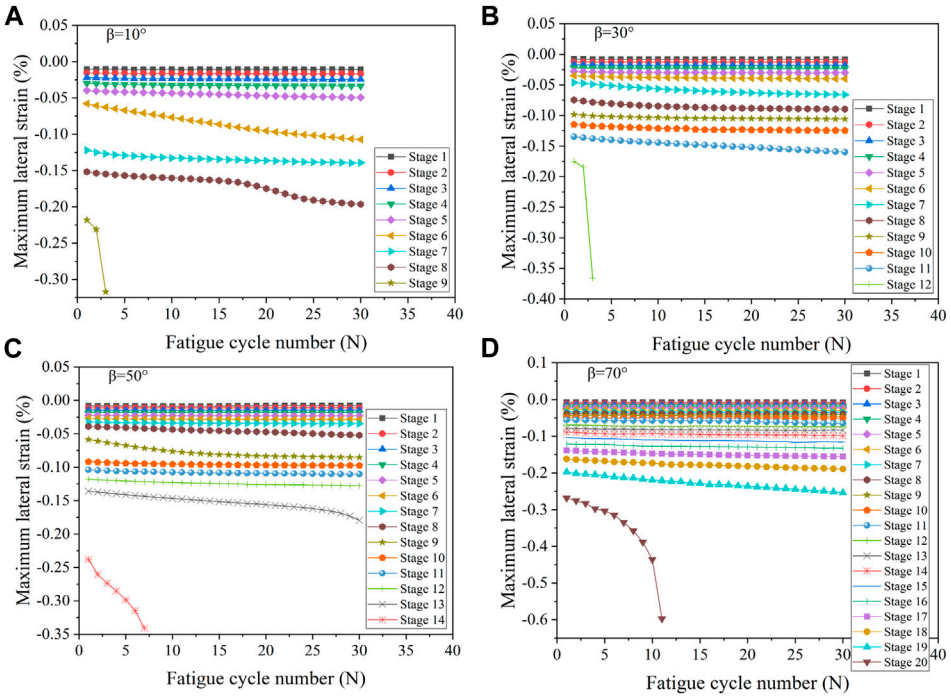

FIGURE 7
Radial strain curves of marble specimens with different fissure angles during fatigue strain [**(A–D)** Rock specimens with fissure angles of 10°, 30°, 50°, and 70°, respectively].

2.2 Testing scheme

All mechanical tests were conducted in an electro-hydraulic servo-controlled rock testing system RDST 1000, which can apply the dynamic loading frequencies in the range of 0–10 Hz. During rock deformation, the axial strain and lateral strain were continuously measure using grating sensors installed at the longitudinal and circumferential of rock specimens. The information of axial stress, axial strain, and lateral strain were recorded by computer at the same loading sampling frequency. The following gives the detailed experimental procedures.

(1) Static loading stage: Loading to 15 MPa using a constant loading rate which the loading rate was 0.06 mm/min (1.0×10^{-5} s^{-1}).
(2) Fatigue loading stage: Based on the field monitoring data of blasting and tramcar loads, the testing was conducted using a cyclic load applied at a dynamic frequency of 0.2 Hz. During the cyclic loading process, the stress amplitude increases by 5 MPa for each cyclic loading phase and is controlled by the sine wave stress cyclic loading. During each dynamic cyclic loading stage, 30 cycles were applied to the specimens. Stress cycling was performed using this multi-stage approach until the specimen were finally damaged. The loading paths are shown in Figure 3.

According to the loading path, it can be found that different flaw angles greatly affect the duration of the test. The test duration increases significantly with the increase of the fissure angles. The fatigue strength of the rocks with fissure angles of 10°, 30°, 50°, and 70° are 55.21 MPa, 70.32 MPa, 80.24 MPa, and 110.55 MPa, respectively. The rock specimens are subjected to different stages of fatigue loading until destruction, going through 9, 12, 14, and 20 loading stages, respectively. The total number of loading cycles for the four sets of specimens varied due to the different fissure angles, which are 244, 334, 398, and 582, respectively. The number of cyclic loading increases with the increase of the fissure angles, indicating that the fissure angles have a significant effect on the strength and strain of the rock.

2.3 Energy conversion during rock failure

According to the energy dissipation and release theory proposed by Xie et al. (2011), the process of compressive deformation and damage of rocks contains energy input, accumulation of releasable elastic strain energy, and continuous energy dissipated and release. The whole process is very complex. Assuming that in an energy-independent closed environment, the rock unit is subjected to external work to produce damage strain, and according to the law of conservation of energy and transformation, the following relationship exists between each strain energy:

$$E_n = E_{n_e} + E_{n_d} \quad (1)$$

Where: E_n is the total energy; E_{n_e} is the elastic energy; E_{n_d} is the dissipated energy used for rock damage as well as irreversible strain to drive crack initiation, extension and coalescence.

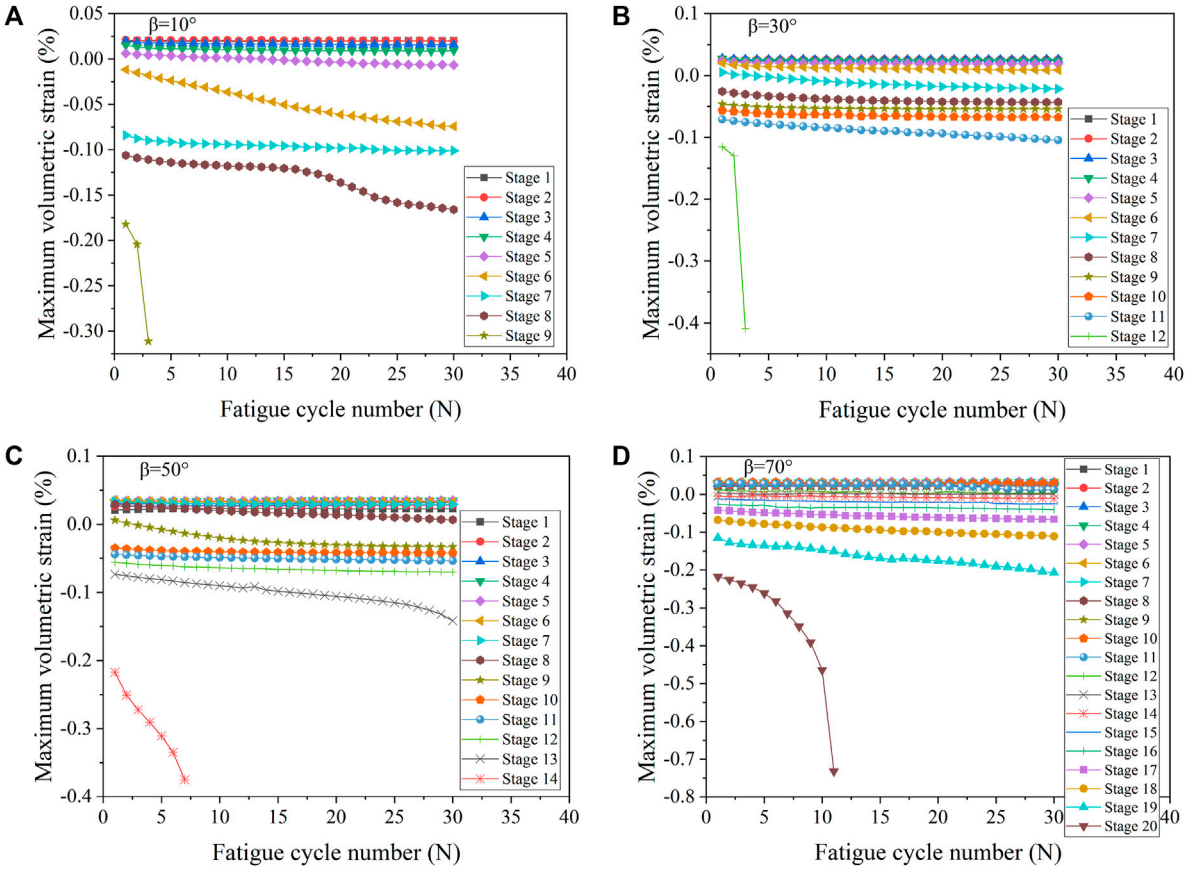

FIGURE 8
Volumetric strain curves of marble specimens with different fissure angles during fatigue strain [**(A–D)** Rock specimens withfissure angles of 10°, 30°, 50°, and 70°, respectively].

According to the studies of Solecki and Conant (2003), Formula 1 can be converted in terms of energy density, as shown in Formula 2:

$$\int U dV = \int U_e dV + \int U_d dV \tag{2}$$

Where: V is the volume of the rock, U is the total strain energy density, U_e is the elastic energy density, U_d is the dissipated energy density.

The total energy, elastic energy, and dissipated energy are calculated as follows:

$$U = \int_{\varepsilon_1}^{\varepsilon_{max}} \sigma d\varepsilon = \sum_{i=1}^{n} \frac{1}{2}(\sigma_i + \sigma_{i+1})(\varepsilon_{i+1} - \varepsilon_i) \tag{3}$$

$$U_e = \int_{\varepsilon_1}^{\varepsilon_{max}} \sigma d\varepsilon = \sum_{i=1}^{n} \frac{1}{2}(\sigma_i + \sigma_{i+1})(\varepsilon_{i+1}^{e} - \varepsilon_i^{e}) \tag{4}$$

$$U_d = U - U_e = \int_{\varepsilon_1}^{\varepsilon_{max}} \sigma d\varepsilon - \int_{\varepsilon_2}^{\varepsilon_{max}} \sigma d\varepsilon \tag{5}$$

The calculation process of total energy (U), elastic energy (U_e) and dissipated energy (U_d) are shown in Figure 4A. The area of the ABCD region under the loading curve represents the total energy (Wang et al., 2021). The area of the EFDC region under the unloading curve represents the elastic energy released during the unloading process. The dissipated energy is the difference between the total energy and the elastic energy area.

In cyclic loading tests, the study of fatigue damage variables for accumulative damage evolution is essential for the prediction of fatigue instability. The damage variables can be defined in terms of different physical-mechanical parameters such as elastic modulus, acoustic emission, density, damping, dissipated energy, etc. Xiao et al. (2010) used six common definition methods to obtain damage variables, revealing the advantages and disadvantages of these methods. In this work, the dissipated energy is used to define the fatigue damage variable, as shown in Formula (6):

$$D_{FL} = \sum_{i=1}^{N_i} U_i^d \Big/ \sum_{i=1}^{N_f} U_i^d \tag{6}$$

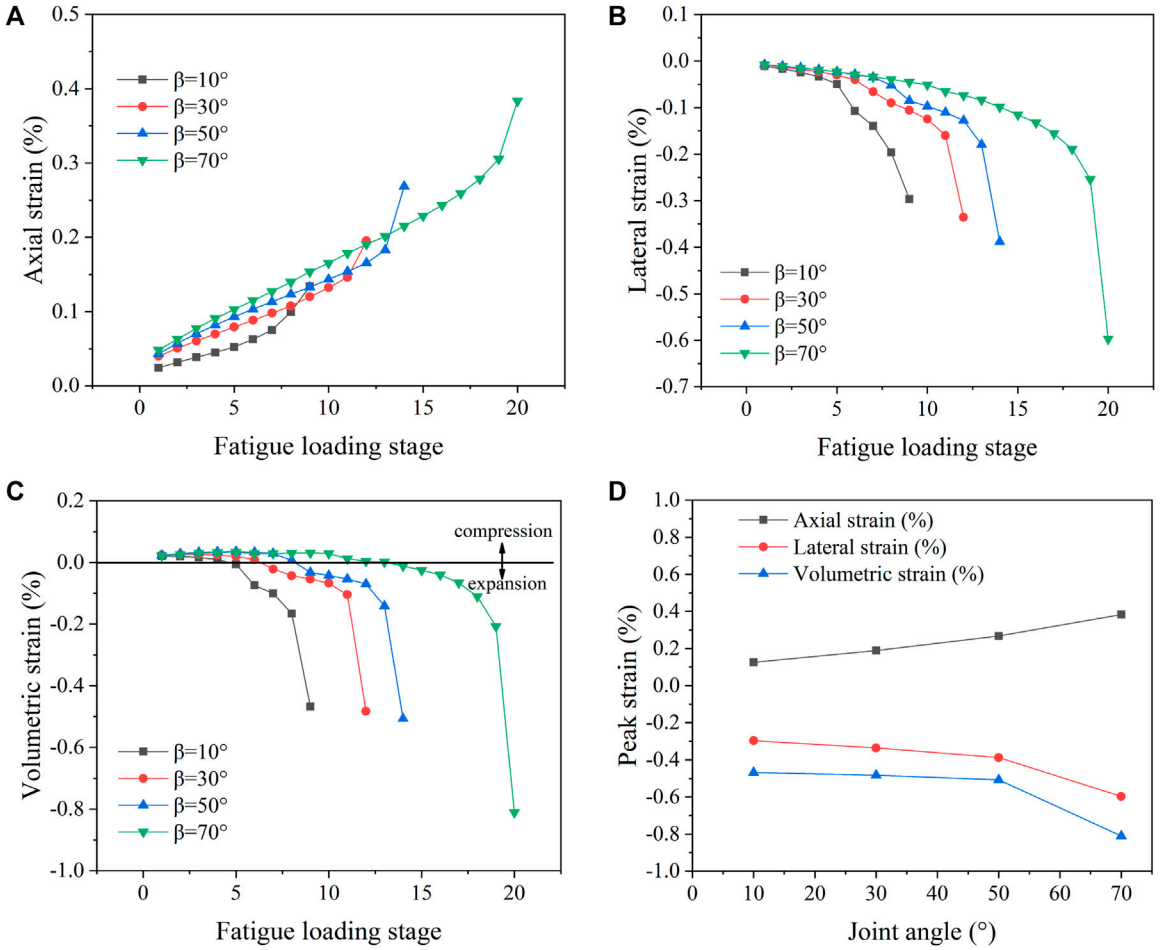

FIGURE 9
Relationship between strain and fatigue loading stage and variation trend of peak strain [**(A–C)** Relationship between axial, lateral and volumetric and fatigueloading stage; **(D)** Variation trend of peak strain of marble specimens under different fissure angles].

Where: D_{FL} is the damage variable caused by fatigue loading, N_i is the stage number, N_f is the number of stages in the failure of the rock, U_i^d is the dissipated energy of the i-th stage.

3 Results and discussions

3.1 Typical stress strain responses

For multi-stage fatigue loading tests on rock specimens with different fissure angles, the axial and lateral stress and strain curves can be obtained as shown in Figures 5A, B. It can be found that as the test time increases, the loading curve and unloading curve no longer coincide due to the plastic deformation of the specimen's interior, thus forming a hysteresis loop. The form of the hysteresis loop varies with the loading time, and for each fatigue loading stage before specimen damage, the hysteresis loop exhibits a change from sparse to dense. The sparse morphology of the hysteresis curve is due to the increase in stress amplitude, which causes a large plastic strain. Subsequently the formed cracks are gradually closed, resulting in the hysteresis curve becoming dense. Compared with the hysteresis curves of the previous fatigue loading stage, the final stage of fatigue loading shows violent crack development, a significant increase in dissipated energy, and a significant increase in deformation of the specimen during the compressive yielding stage. Therefore, the hysteresis curve in this stage becomes increasingly sparse until the specimen failure.

In order to study the effect of different fissure angles on marble specimens, the effect of different fissure angles on the strength and fatigue life of marble specimens are analyzed, as shown in Figure 5C. It can be visualized from the Figure 5C that the strength as well as the lifetime of the marble specimens increases gradually with the increase of the fissure angles under the fatigue loading condition.

In order to describe more intuitively the effect of fissure angles on the marble specimens fatigue responses, the loading path (Figure 3) and the stress strain curves (Figure 5) are combined to obtain the damage characteristics of the marble specimens under fatigue loading conditions, detailed mechanical parameters as shown in Table 1.

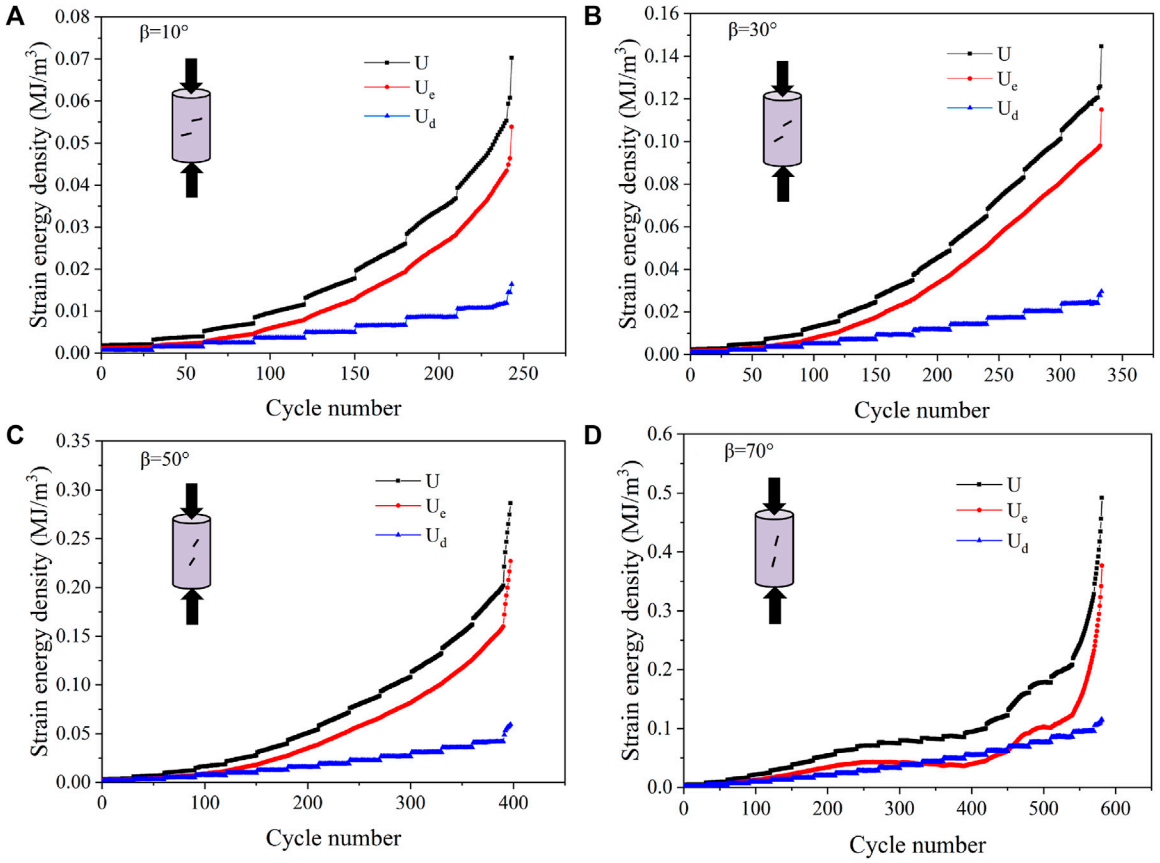

FIGURE 10
Variation of total strain energy, elastic energy and dissipated energy of marble specimens with the cycle number [**(A–D)**Rocks pecimens with fissure angles of 10°, 30°, 50°, and 70°, respectively].

3.2 Specimen deformation characteristics

The form of the hysteresis loops at each fatigue loading stage reflects the changes in the internal microstructure of the rock, which is closely related to the crack extension behavior. Afterwards, the relationship curves of the maximum axial strain with the number of fatigue cycles for marble specimens with different fissure angles are plotted, as shown in Figure 6. It can be observed that the axial strain increases with the increase in the number of cycles and exhibits a significantly different trend at the beginning of cyclic loading than at the middle and the end. At the beginning of each loading stage, the strain increases rapidly and then tends to become stable until the last cyclic loading stage. At the same time, the sudden increase in stress amplitude also leads to larger axial deformation, and the accumulative plastic strain increases continuously with the cyclic loading stage, and the axial strain increases sharply at the last fatigue loading stage until the specimens are damaged.

In order to further analyze the relationship between lateral strain and fissure angle during the whole fatigue loading process, the relationship curves between the lateral strain and the number of fatigue cycles during the fatigue loading process of the marble specimens with different fissure angles are plotted as shown in Figure 7. It can be found that the lateral strain increases significantly faster at the end of cyclic loading relative to the earlier loading stages, and the radial strain increases suddenly at the last loading level until the damage of the rock. Meanwhile, in order to be able to better describe the effect of axial and lateral strains on the volume change of the specimen, the volumetric strain is calculated from the axial and lateral strains. The volumetric strain reflects the volume change of the rock during deformation and is also a good indicator to reveal the fracture behavior of the rock. The relationship curves between the volumetric strain and the number of fatigue cycles are shown in Figure 8. Combining Figures 7, 8, it can be found that the trends of lateral strain and volumetric strain are very similar, which indicates that the lateral strain of the rock has a greater effect on the fatigue damage of the rock.

The relationship curves between axial, lateral and volumetric strains and fatigue loading stages can be more intuitive to see that with the increasing loading stages, the axial, lateral and volumetric strains gradually become larger, and in the final stage of fatigue loading, they all increase sharply. In addition, the peak axial strain, peak lateral strain and peak volumetric strain of the marble specimens with different fissure angles under fatigue loading conditions are obtained as shown in Figure 9D. It can be found that each peak strain gradually increases with the increasing angle of the joint. Meanwhile, with the increase of cyclic loading stage, the volumetric strain changes from positive to negative, as shown in Figure 9C. The phenomenon indicates that the rock specimens

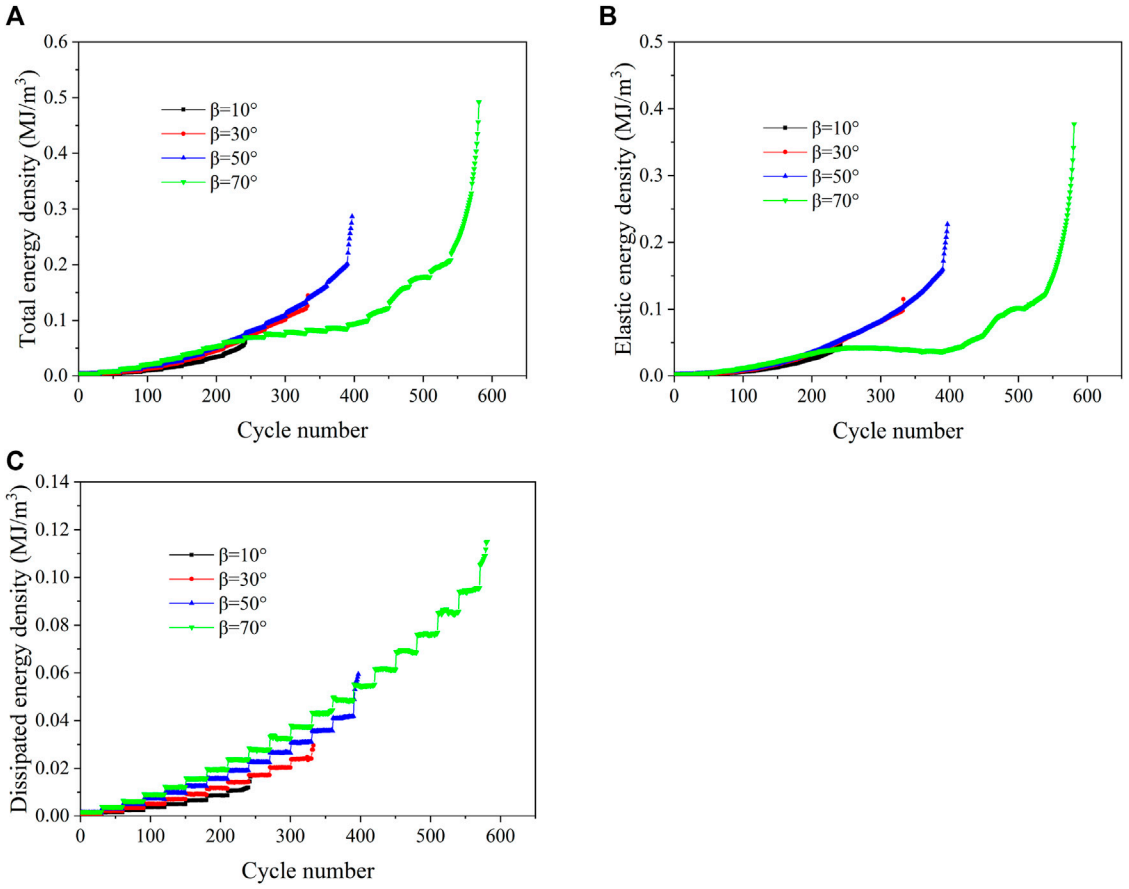

FIGURE 11
Relationship between the strain energy and fatigue loading stage [**(A–C)** Respectively the relationship between total strain energy, elastic energy and dissipated energy and the number of cycles].

underwent a process of compression followed by expansion. The results also further illustrate that the degree of damage as well as the damage form of different marble specimens of fissure angles under fatigue loading conditions are different.

3.3 Energy evolution characteristics

The relationship between the total input energy, elastic energy, dissipated energy and the number of cycles is plotted using Eqs 3–5, as shown in Figures 10A–D. The results show that the overall trend of the energy curves is similar under the effect of static loading. During the initial cyclic loading stage, the total input energy is almost entirely converted into elastic energy and stored in the interior of the rock. At this time, the damage of the rock is smaller, so the dissipated energy is also smaller, the total energy curve and the elastic energy curve basically overlap, and the dissipated energy is almost zero.

As the number of fatigue cycles increases, damage occurs inside the rock, the accumulation of damage gradually increases, and part of the input energy is consumed to produce cracks, so the elastic energy curve no longer coincides with the total energy curve. As the number of fatigue cycles gradually increases, the dissipated energy also begins to increase, and the growth rate accelerates. It can be found that the increase of dissipated energy within the same cyclic loading stage is not obvious. When the stress amplitude increases, the dissipated energy increases suddenly. In the final fatigue loading stage, the dissipated energy increases faster and faster until the rock is damaged (Figure 10). The results show that fatigue loading causes further damage to the marble specimens, but the damage accumulation is not severe, while the increasing stress amplitude accelerates the damage deterioration of the rock. Meanwhile, the overall increasing trend in dissipated energy prior to damage of the marble specimens accelerates, indicating a continued increase in the energy required to drive crack expansion and a gradual increase in the degree of rock damage.

In order to investigate the effects of different fissure angles on the damage extension and the corresponding energy release and dissipation of marble specimens under fatigue loading conditions, the evolution process between the total energy, elastic energy, dissipated energy and the number of cycles of marble specimens with different angles of joint is analyzed and obtained as shown in Figures 11A–C. It can be visualized from the figure that the input energy is converted into elastic energy and dissipated energy, and the proportion of dissipated energy increases with the increase of cyclic loading stage. During the fatigue deformation of the marble

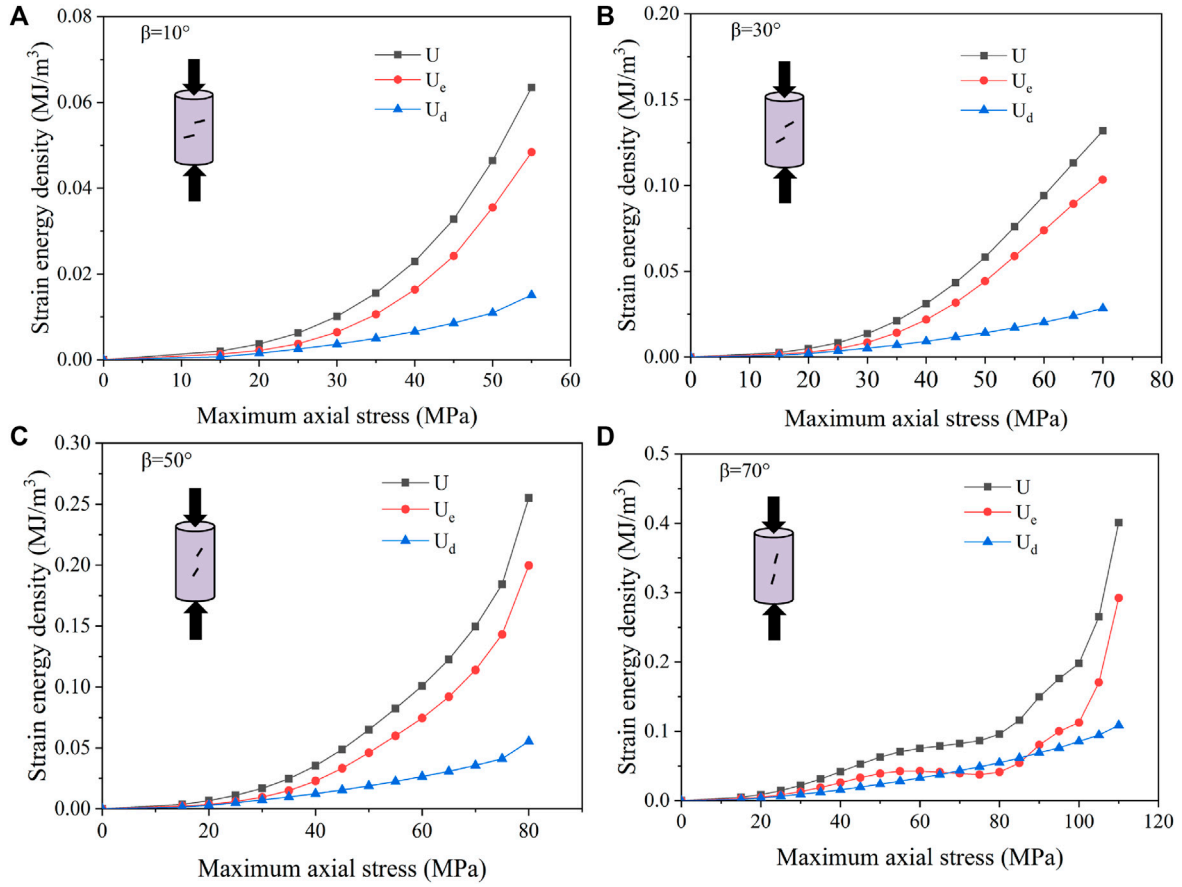

FIGURE 12
Relationship between strain energy density and the maximum axial stress [**(A–D)** Rock specimens with fissure angle of 10°, 30°, 50°, and 70°, respectively].

TABLE 2 Fitting results of strain energy and maximum axial stress of marble specimens with different fissure angles.

Specimen number	Fissure angle (°)	Strain energy (MJ/m^3)	Fitting equation	Correlation coefficient (R^2)
M-0-1	0	U	$U = 2.476E\text{-}7 \times \sigma^{3.1053}$	0.999
		U_e	$U_e = 6.942E\text{-}8 \times \sigma^{3.3574}$	0.994
		U_d	$U_d = 9.369E\text{-}7 \times \sigma^{2.407}$	0.994
M-30–1	30	U	$U = 2.690E\text{-}6 \times \sigma^{2.548}$	0.998
		U_e	$U_e = 1.093E\text{-}6 \times \sigma^{2.706}$	0.996
		U_d	$U_d = 5.133E\text{-}6 \times \sigma^{2.027}$	0.999
M-50–1	50	U	$U = 6.206E\text{-}7 \times \sigma^{2.934}$	0.990
		U_e	$U_e = 1.427E\text{-}6 \times \sigma^{3.215}$	0.992
		U_d	$U_d = 4.170E\text{-}8 \times \sigma^{2.146}$	0.986
M-70–1	70	U	$U = 6.689E\text{-}8 \times \sigma^{3.278}$	0.906
		U_e	$U_e = 4.014E\text{-}13 \times \sigma^{5.782}$	0.877
		U_d	$U_d = 1.120E\text{-}5 \times \sigma^{1.944}$	0.998

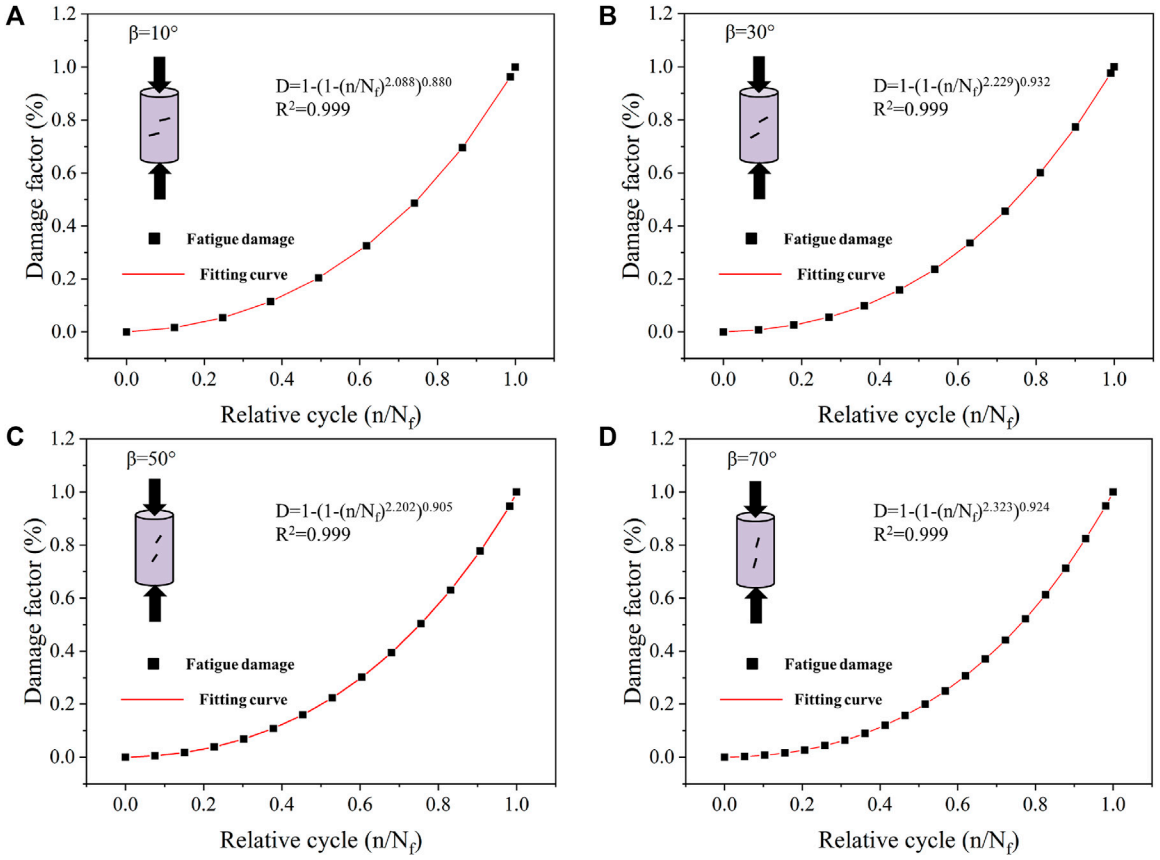

FIGURE 13
Damage evolution modeling of the marble specimens under multiple level cyclic loading [**(A–D)** Rock specimens with fissure angles of 10°, 30°, 50°, and 70°, respectively].

specimens, most of the energy is released from the elastic energy, and the accumulation of damage caused by fatigue loading is increasing, which in turn leads to an increase in dissipated energy. The dissipated energy increases slowly at the initial stage of fatigue loading, but increases rapidly near the failure of the specimen, and increases sharply at the last fatigue loading stage until the specimen is damaged. The sharp increase of dissipated energy indicates the unstable propagation and coalescence mode of the crack. The dissipated energy is maximum for a fissure angle of 70° and minimum for a fissure angle of 10°. The dissipated energy for different fissure angles are 0.016 MJ/m^3, 0.030 MJ/m^3, 0.059 MJ/m^3 and 0.115 MJ/m^3, respectively.

The energy curves exhibit a stepped growth mode, and the energy increment is larger when the stress amplitude increases abruptly. The results indicate that the number of cycles of fatigue loading and the fatigue loading stage greatly affect the dissipation and release characteristics of rock energy. The relationship between the total energy, elastic energy, dissipated energy and maximum axial stress of the rock specimens are shown in Figures 12A–D. The curve fitting method is adopted to reveal the relationship between strain energy density and the upper limit of stress amplitude. The fitting results show that during each fatigue loading, the total energy, elastic energy and dissipated energy of four groups of marble specimens with different fissure angles increase with the increase of the upper limit of axial stress, and the increasing rate is gradually accelerated. In addition, a significant non-linear increasing trend is observed, and the data satisfies a power function with high correlation. The fitting results are listed in Table 2.

After investigation, it is found that there is a non-linear damage accumulation law in rocks under multi-stage fatigue cyclic loading conditions, and the previous models are not suitable for describing the damage evolution characteristics of rocks under this loading path (Figure 13). As rock damage and fracture is energy-driven, in my opinion, the energy index is better than other parameters to express damage propagation. In addition, the energy parameter contains rock stress and strain information, it is the comprehensive reflection of rock failure. According to Formula 6, a new dissipated energy-based damage accumulation model is proposed to describe the damage process of rocks by using dissipated energy to calculate the damage variables (Wang Y et al., 2020) which is shown in Formula 7.

$$D = 1 - \left(1 - \left(n/N_f\right)^a\right)^b \tag{7}$$

Where: D is the damage variable caused by dissipative energy, when n is 0, D is 0, when n is N_f, D is 1; N is the number of total cycles; N_f is the fatigue lifetime; a and b are the material related parameters.

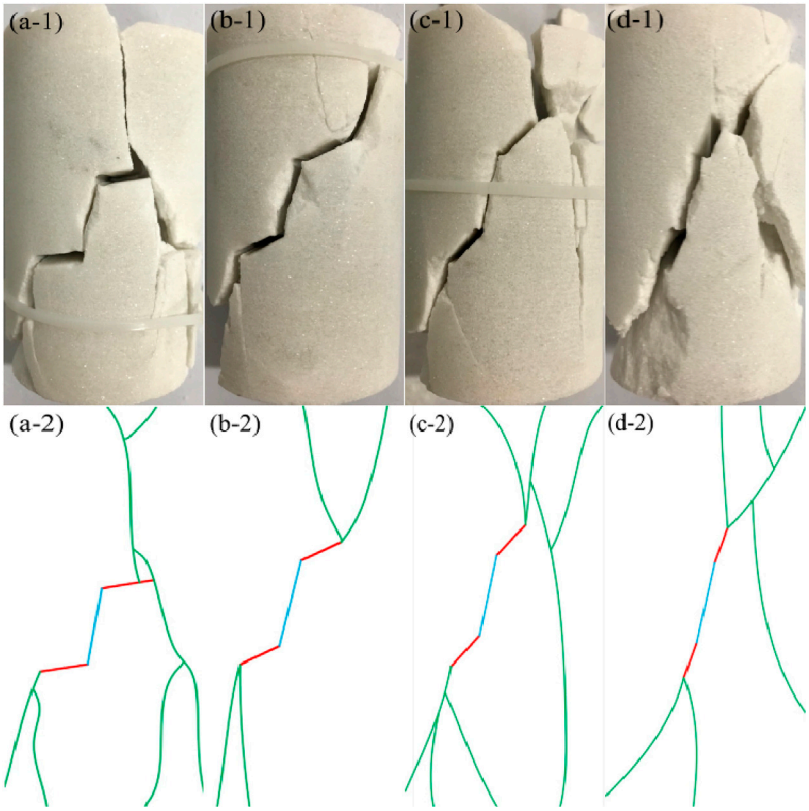

FIGURE 14
Typical failure modes of rock specimens with different fissure angles [**(A–D)** Rock specimens with fissure angle of 10°, 30°, 50°, and 70°, respectively].

According to the fitting results and the value of R^2, it can be seen that the accumulative damage curves show a trend of slow increasing and then fast increasing, and have obvious non-linear characteristics as well as high correlation.

3.4 Failure morphology analysis

Since rock crack initiation and fracture evolution are essentially energy-driven, and the different joint angle may lead to different capacities for energy storing and releasing in stepped marble, which causes differences in the damage forms and fracture morphology of the specimens. The macroscopic fracture forms of the typical marble specimens after destruction are shown in Figure 14. It can be clearly observed that the joints play a dominant and controlling role in the crack expansion path of the whole specimen. The crack extension paths of the four groups of typical marble specimens have similarities. The crack extensions of the specimens at the time of damage all start from the end of the fracture, and the development direction of the rock bridge is consistent with that of the joint. All of them develop through along the rock bridge starting fracture and are similar to the wing crack, and the crack extension direction gradually approaches 90° and gradually converges to the maximum principal stress direction. When the angles of the joint vary, there are also some differences. From Figure 14, it can be found that the cracks gradually transition from tension failure to shear failure as the angles of the joint increases. When β is 10°, in the longitudinal, the specimen shows vertical splitting cracks with some secondary cracks. When β is 30°, 50°, and 70° respectively, the upper and lower main crack tips are obviously controlled by the maximum principal stress. The angle between the main crack and the maximum principal stress is basically the same, showing a symmetric development trend. The expansion path of "X" conjugate crack is formed by the expansion from the tip of the joints.

4 Conclusion

Multilevel cyclic loading tests were carried out on marble specimens with double-stepped fissures with angle of 10°, 30°, 50°, and 70°, respectively. The dynamic fracture and energy evolution properties of rocks are studied experimentally. The main conclusions are summarized as follows.

(1) The peak strain, strength, lifetime, and dissipated energy of the rock are all influenced by the fissure angle. With the increase of the fissure angle, the increasing rate of those mechanical parameters becomes dramatically at high fatigue loading level. The formation of the hysteresis loop further reveals the plastic deformation characteristics. It is found that rock volumetric strain increases slowly during the first few cyclic stages and increases sharply near to fatigue failure.
(2) The total input energy, elastic energy and dissipated energy all increase with the increase of the fissure angle. Meanwhile, the

proportion of dissipated energy using to drive crack propagation increases rapidly with increasing cycles, indicating a coalescence pattern of crack network.

(3) An obvious nonlinear damage accumulation law for rock subjected to multilevel cyclic loading was revealed. A model of rock damage evolution is developed based on dissipated energy, which can fit well with testing data and can be used to describe the nonlinear damage accumulation.

Data availability statement

The original contributions presented in the study are included in the article/supplementary material, further inquiries can be directed to the corresponding author.

Author contributions

DW and ZL: Experiments, data analysis; HX and SG: Methodology, conceptualization; PL and JL: Visualization, data curation, resources; YW: Supervision, funding acquisition, project administration. All authors contributed to the article and approved the submitted version.

Funding

This study was supported by the National Natural Science Foundation of China (52174069), Beijing Natural Science Foundation (8202033) and the Fundamental Research Funds for the Central Universities (FRF-TP-20-004A2).

Conflict of interest

The authors declare that the research was conducted in the absence of any commercial or financial relationships that could be construed as a potential conflict of interest.

Publisher's note

All claims expressed in this article are solely those of the authors and do not necessarily represent those of their affiliated organizations, or those of the publisher, the editors and the reviewers. Any product that may be evaluated in this article, or claim that may be made by its manufacturer, is not guaranteed or endorsed by the publisher.

References

Bai, B., Bai, F., Li, X., Nie, Q., Jia, X., and Wu, H. (2022). The remediation efficiency of heavy metal pollutants in water by industrial red mud particle waste. *Environ. Technol. Innovation* 28, 102944. doi:10.1016/j.eti.2022.102944

Bai, B., Zhou, R., Cai, G., Hu, W., and Yang, G. (2021). Coupled thermo-hydro-mechanical mechanism in view of the soil particle rearrangement of granular thermodynamics. *Comput. Geotechnics* 137, 104272. doi:10.1016/j.compgeo.2021.104272

Bai, B., Zhou, R., Yang, G., Zou, W., and Yuan, W. (2023). The constitutive behavior and dissociation effect of hydrate-bearing sediment within a granular thermodynamic framework. *Ocean. Eng.* 268, 113408. doi:10.1016/j.oceaneng.2022.113408

Cerfontaine, B., and Collin, F. (2018). Cyclic and fatigue behaviour of rock materials: Review, interpretation and research perspectives. *Rock Mech. Rock Eng.* 51 (2), 391–414. doi:10.1007/s00603-017-1337-5

Erarslan, N. (2021). Experimental and numerical investigation of plastic fatigue strain localization in brittle materials: An application of cyclic loading and fatigue on mechanical tunnel boring technologies. *Int. J. Fatigue* 152, 106442. doi:10.1016/j.ijfatigue.2021.106442

Erarslan, N., and Williams, D. J. (2012). The damage mechanism of rock fatigue and its relationship to the fracture toughness of rocks. *Int. J. Rock Mech. Min. Sci.* 56, 15–26. doi:10.1016/j.ijrmms.2012.07.015

Faradonbeh, R. S., Taheri, A., and Karakus, M. (2021). Failure behaviour of a sandstone subjected to the systematic cyclic loading: Insights from the double-criteria damage-controlled test method. *Rock Mech. Rock Eng.* 54, 1–21.

Li, X. M., Liu, C. Y., and Speng, S. (2017). Fatigue deformation characteristics and damage model of sandstone subjected to uniaxial step cyclic loading. *J. China Univ. Min. Technol.* 46 (1), 8–17.

Momeni, A., Karakus, M., Khanlari, G. R., and Heidari, M. (2015). Effects of cyclic loading on the mechanical properties of a granite. *Int. J. Rock Mech. Min. Sci.* 77, 89–96. doi:10.1016/j.ijrmms.2015.03.029

Orozco, L. F., Delenne, J. Y., Sornay, P., and Radjai, F. (2019). Discrete-element model for dynamic fracture of a single particle. *Int. J. Solids Struct.* 166, 47–56. doi:10.1016/j.ijsolstr.2019.01.033

Peng, K., Wang, Y. Q., Zou, Q. L., Liu, Z. P., and Mou, J. H. (2019). Effect of crack angles on energy characteristics of sandstones under a complex stress path. *Eng. Fract. Mech.* 218, 106577. doi:10.1016/j.engfracmech.2019.106577

Ray, S. K., Sarkar, M., and Singh, T. N. (1999). Effect of cyclic loading and strain rate on the mechanical behaviour of sandstone. *Int. J. Rock Mech. Min. Sci.* 36 (4), 543–549. doi:10.1016/s0148-9062(99)00016-9

Shirani Faradonbeh, R., Taheri, A., and Karakus, M. (2021). Post-peak behaviour of rocks under cyclic loading using a double-criteria damage-controlled test method. *Bull. Eng. Geol. Environ.* 80, 1713–1727. doi:10.1007/s10064-020-02035-y

Solecki, R., and Conant, R. J. (2003). *Advanced mechanics of materials*. London: Oxford University Press.

R. Ulusay (Editor) (2015). *The ISRM suggested methods for rock characterization, testing and monitoring*, 2007–2014.

Wang, C., He, B., Hou, X., Li, J., and Liu, L. (2020). Stress–energy mechanism for rock failure evolution based on damage mechanics in hard rock. *Rock Mech. Rock Eng.* 53, 1021–1037. doi:10.1007/s00603-019-01953-y

Wang, Y., Tang, P. F., Han, J. Q., and Li, P. (2023d). Influence of dynamic disturbed frequency on rock failure characteristics under triaxial cyclic and multistage unloading confining pressure loads. *Fatigue Fract. Eng. Mater Struct.* 46, 1527–1544. doi:10.1111/ffe.13946

Wang, Y., Yan, M. Q., and Song, W. B. (2023c). The effect of cyclic stress amplitude on macro-meso failure of rock under triaxial confining pressure unloading. *Fatigue & Fract. Eng. Mater. Struct.* 31 (12), 3008–3025. doi:10.1111/ffe.13993

Wang, Y., Cao, Z., Li, P., and Yi, X. (2023b). On the fracture and energy characteristics of granite containing circular cavity under variable frequency-amplitude fatigue loads. *Theor. Appl. Fract. Mech.* 125, 103872. doi:10.1016/j.tafmec.2023.103872

Wang, Y. F., and Zheng, X. J. (2015). Energy evolution mechanism in deformation and destruction process of grit stone. *J. Henan Polytech. Univ.* 34 (1), 30–34.

Wang, Y., Han, J., Ren, J., and Li, C. (2021). Anisotropic fracture and energy dissipation characteristics of interbedded marble subjected to multilevel uniaxial compressive cyclic loading. *Fatigue & Fract. Eng. Mater. Struct.* 44 (2), 366–382. doi:10.1111/ffe.13365

Wang, Y., Tang, P., Han, J., and Li, P. (2023a). Energy-driven fracture and instability of deeply buried rock under triaxial alternative fatigue loads and multistage unloading conditions: Prior fatigue damage effect. *Int. J. Fatigue* 168, 107410. doi:10.1016/j.ijfatigue.2022.107410

Xiao, J. Q., Feng, X. T., Ding, D. X., and Jiang, F. L. (2011). Investigation and modeling on fatigue damage evolution of rock as a function of logarithmic cycle. *Int. J. Numer. Anal. Methods Geomechanics* 35 (10), 1127–1140. doi:10.1002/nag.946

Xiao, J. Q., Ding, D. X., Jiang, F. L., and Xu, G. (2010). Fatigue damage variable and evolution of rock subjected to cyclic loading. *Int. J. Rock Mech. Min. Sci.* 47 (3), 461–468. doi:10.1016/j.ijrmms.2009.11.003

Xie, H. P., Ju, Y., and Li, L. Y. (2008). Energy mechanism of deformation and failure of rock masses. *Chin. J. Rock Mech. Eng.* 27 (9), 12.

Xie, H. P., Li, L. Y., Ju, Y., Peng, R. D., and Yang, Y. M. (2011). Energy analysis for damage and catastrophic failure of rocks. *Sci. China Technol. Sci.* 54 (1), 199–209. doi:10.1007/s11431-011-4639-y

Xie, H. P., Ju, Y., and Li, L. Y. (2005). Criteria for strength and structural failure of rocks based on energy dissipation and energy release principles. *Chin. J. Rock Mech. Eng.* 24 (17), 3003–3010.

Yin, P., Ma, H. C., Liu, X. W., Bi, J., Zhou, X. P., and Berto, F. (2018). Numerical study on the dynamic fracture behavior of 3D heterogeneous rocks using general particle dynamics. *Theor. Appl. Fract. Mech.* 96, 90–104. doi:10.1016/j.tafmec.2018.04.005

Zhang, L. M., Gao, S., and Wang, Z. Q. (2014). Rock elastic strain energy and dissipated strain energy evolution characteristics under conventional triaxial compression. *J. China Coal Soc.* 39 (7), 1238–1242.

Zhao, K., Qiao, C. S., and Luo, F. R. (2014). Experimental study of fatigue characteristics of limestone samples subjected to uniaxial cycle loading with different frequencies. *Chin. J. Rock Mech. Eng.* 33, 3466–3475.

Zhou, Y., Zhao, D., Li, B., Wang, H., Tang, Q., and Zhang, Z. (2021). Fatigue damage mechanism and deformation behaviour of granite under ultrahigh-frequency cyclic loading conditions. *Rock Mech. Rock Eng.* 54 (9), 4723–4739. doi:10.1007/s00603-021-02524-w

frontiers | Frontiers in Materials

TYPE Original Research
PUBLISHED 09 June 2023
DOI 10.3389/fmats.2023.1193527

OPEN ACCESS

EDITED BY
Bing Bai,
Beijing Jiaotong University, China

REVIEWED BY
Yang Gaosheng,
Shanxi Agricultural University, China
Chen Peipei,
Beijing University of Civil Engineering and Architecture, China

*CORRESPONDENCE
Hongru Li,
lhrbj@xaut.edu.cn

RECEIVED 25 March 2023
ACCEPTED 24 May 2023
PUBLISHED 09 June 2023

CITATION
Li H, Yang M and Dang T (2023), Influence of the fracture on the seepage stability of loess slopes.
Front. Mater. 10:1193527.
doi: 10.3389/fmats.2023.1193527

Influence of the fracture on the seepage stability of loess slopes

Hongru Li[1,2]*, Min Yang[1,2] and Tong Dang[1,2]

[1]Institute of Geotechnical Engineering, Xi'an University of Technology, Xi'an, China, [2]Loess Soil Mechanics and Engineering Key Laboratory of Shaanxi Province, Xi'an, China

The development of fractures in loess slopes often has a great influence on the stability of slopes. In this paper, taking the homogeneous slope model as an example, fractures with different distances and depths from the slope top angle are provided at the top of the slope. Firstly, the influence of single fracture location and depth on slope stability is analyzed, and after the most unfavorable location and depth of the fractures are determined, the influence of the slope top fractures on the slope seepage field and slope stability under the conditions with and without rainfall is studied secondly. The results show that with the increase of the distance from the fracture to the top angle of the slope, the safety coefficient of the slope shows the change law of decreasing first and then increasing. The critical fracture depth corresponding to the fractures at different locations is different, and when the critical fracture depth is exceeded, the slope safety factor tends to be stable. At the end of the rainfall moment through 1-1 section to analyze, it is found that at this time the pore water pressure and volume water content of the soil at the bottom of the fracture at different depths are greater than those of the upper soil, and the shallow fracture has less influence on the seepage field of the slope, and through 2-2 section it is found that the pore water pressure and volume water content in the soil far from the fracture are greater than those of the soil near the location of the fracture. When 288 h after the end of rainfall, the pore water pressure and volumetric water content of the soil around the fracture in section 2-2 were greater than those far from the fracture location. With the passage of time, the pore water pressure at the location of the fracture gradually dissipated and the corresponding volumetric water content gradually decreased, indicating that the fracture had an obvious influence on the characteristics of the seepage field in the soil at different times of rainfall. Under the condition of no rainfall, there exists a critical depth of fractures affecting slope safety stability, while under the condition of rainfall, the slope safety coefficient continuously decreases with the increase of fracture depth, and there is no critical fracture depth. The research results promote the understanding of the safety and stability of loess fracture slopes and provide a reference for slope management.

KEYWORDS

loess, fracture, rainfall, seepage field, safety factor

1 Introduction

Landslides are one of the most common geological hazards in loess areas. The occurrence of landslides often causes significant property losses (Wang et al., 1996; Zhang et al., 2011). The main reason is that the tensile stress of the slope exceeds its tensile strength, resulting in tension cracks at the trailing edge of the slope. The cracks intersect and cut structural plane of the loess, which weakens the overall stability of the slope. The loess soil of the slope will further deteriorate and accelerate the formation of landslides under precipitation infiltration,

wind erosion, earthquake and human factors (Wang et al., 2018; Sun et al., 2019; Wu et al., 2019; Yan et al., 2019; Zhang et al., 2019).

Slope stability analysis methods are usually divided into three types categories: limit analysis method, limit equilibrium method and numerical analysis method (Chen et al., 2002). Spencer (1967) introduced tension fractures and derived the formulae of fracture depth to analyze the effect of unit weight, cohesion and internal friction angle on the fracture depth. Michalowski (2012) and Utili (2013) proposed a stability analysis method for slopes with fractures based on limit analysis theory to analyze the effect of fracture depth as well as fracture location on slope stability. Zhu et al. (2022) analyzed the influence of constraint width, slope grade, internal friction angle and fracture depth on the critical height of three-dimensional vertical fracture loess slope. He et al. (2021) studied the effect of slope top dip angle on the stability of fractured slopes, and analyzed it using a logarithmic spiral rotating mechanism of plane strain of plane strain. Yan et al. (2022) studied the variation of slope stability under three working conditions, such as seepage of fracture water from the trailing edge to the foot of the slope, drainage at the foot of slope and elevation of the watered point on the slope. Zhou et al. (2021) established the sliding model of single fracture and multi-fracture and the ultimate limit state of slope, deduced the formula for calculating the limit depth of vertical fracture at the top of loess inclined slope, and explored the variation of fracture depth with different influencing factors. The formula was verified according to the limit analysis upper bound method and practical engineering examples.

The seepage and stability of fractured soil slope under rainfall are also the research hotspots of scholars. The research methods are mainly numerical simulation and laboratory test. Scholars (Zeng et al., 2020; Zhang et al., 2020; Zhou et al., 2020) divided slopes containing fractures into soil zone and fracture zone and assigned different material properties to them respectively. They analyzed the rainfall infiltration characteristics of fracture slopes in conditions of accumulated water and influence of the depth of fracture depth, inclination angle and location on the seepage characteristics of slope. Gao et al. (2021) established the relationship between slope material parameters as a function of fracture rate, and studied the influence of rainfall conditions, the development degree of fractures and the types of the vegetation root system on the stability of red clay slope by finite element method. It showed that fracture development can easily lead to shallow damage of red clay slope and significantly reduce slope stability. Yao et al. (2001) analyzed the stability of expansive soil slope considering fractures and rainfall infiltration, and compared the stability of expansive soil slope between considering fractures and without considering fractures through engineering examples. Cao et al. (2022) carried out model experiment on the fracture evolution, rainfall infiltration and scour of red clay slopes to reveal the fracture evolution law of red clay slopes and analyze the influence of the fracture development and rainfall intensity on the seepage characteristics and scour pattern of red clay slopes. Chen et al. (2019) discussed the seepage mechanism of fissured soil, established a two-dimensional saturated-unsaturated seepage analytical model of fissured soil based on the one-dimensional analytical solution, and derived the explicit analytical solution of the two-dimensional seepage control equation by Fourier integral variation. Zeng et al. (2022) carried out indoor model tests of red clay slopes with different parameters in the overbreak zone under rainfall by fluorescence tracer method and digital image processing techniques to analyze the variation of moist sharp, transient saturated zone and volumetric water content of red clay slope. Liu et al. (2017) studied the infiltration law of slope under the combined action of fracture anisotropy and different rainfall intensities. He (2018) studied the effect of fracture content variation on the seepage field of slopes with the increase of rainfall holding time, and also considered the variation of fracture network volume to explore its effect on the safety factor. Wang et al. (2020) and Qian et al. (2020) investigated the influence of different shapes of fractures on the seepage field of the slope by physical simulation experiment. Therefore, little literature is available on the seepage stability of slopes with fractures.

Taking the homogeneous slope model as an example, this paper calculates the influence of a single fracture on the slope stability at different locations and depths from the slope top. After determining the most unfavorable location and depth of fractures, the influence of fractures at the top of the slope on the seepage field and stability of the slope is further analyzed with and without rainfall.

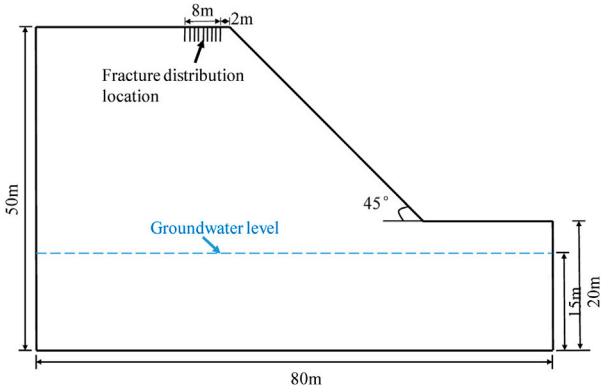

FIGURE 1
The schematic diagram of slope calculation model.

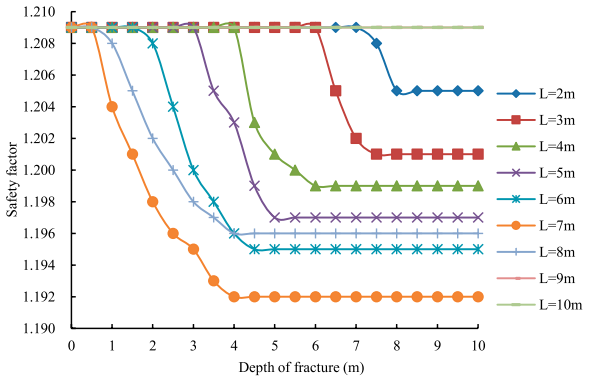

FIGURE 2
The effect of crack propagation depth on slope stability.

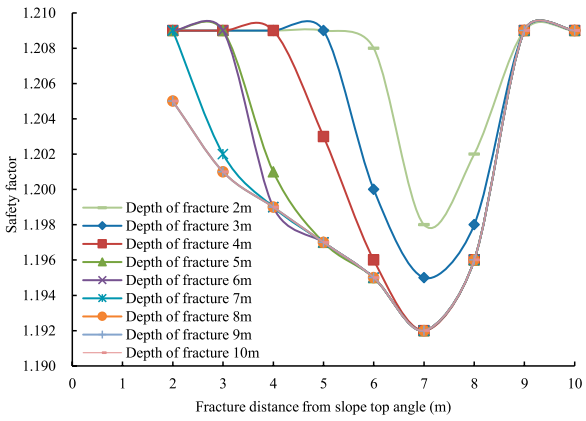

FIGURE 3
Effect of fracture location on slope stability.

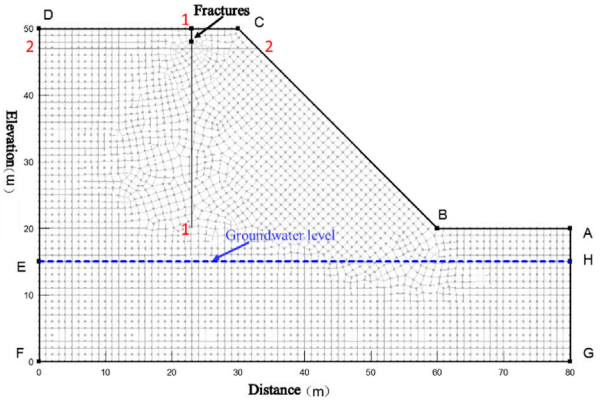

FIGURE 4
Computational model and grid division.

2 Influence of fracture location and depth on slope stability

The influence of a single fracture on the stability of the slope at different positions and depths of the slope top is calculated. The ideal homogeneous slope calculation model with slope angle of 45° is adopted. Fracture are located at the top of the slope, which with a distance from the top of the slope top angle are 2 m, 3 m, 4 m, 5 m, 6 m, 7 m, 8 m, 9 m, 10 m respectively, and the depth of the fracture continues to expand from 0 m to 10 m. The groundwater level is located at a depth of 35 m below the slope top. The natural density of the soil is 16.5 kN/m^3, the cohesion is 30 kPa, and the internal friction angle is 25°. The computational model of the slope is shown in Figure 1.

The effect of fracture extension depth on slope stability is shown in Figure 2, where L is the distance from the fracture locations to the slope top angle. Figure 2 shows that the safety factor of the slope decreases obviously with the increase of the spacing within the range of 7 m from the fracture locations to the slope top angle, the reduction magnitude of safety factor increases gradually with the expansion of the fracture depth. When the fracture is 7 m away from the slope top angle and the fracture depth expands to about 4 m, the safety factor of the slope tends to a minimum value, and the curve change tends to be flat. The crack depth at this time is called the critical crack depth. The fracture depth in this case is defined as the critical fracture depth. When the fracture depth is greater than 8 m, the fracture at different locations has little influence on the slope safety factor. The closer the distance between the fracture and the slope top angle, the deeper the fracture depth when the slope safety factor reaches a stable value. The reason for these phenomena is that when the shallow fracture is close to the top of the loess slope, the failure mode of the slope is in the form of sliding damage through the arc at the top of the slope. When the sliding surface is far away from the bottom of fracture, fracture has little effect on slope stability. When the fracture depth at the top of the slope extends deeper, the sliding surface of the slope develops from the initial arc-shaped sliding surface to the combined sliding surface through crack. In this case, the position of the sliding surface intersects with the fracture, which changes the stress of the slope and seriously affects the stability of the whole slope. As the crack depth continues to expand, the intersection of the circular slip surface and the fracture continues to move downward, and the safety factor of slope also shows a decreasing trend. When the fracture at the top of the slope continues to expand to a certain depth and the intersection of the circular slip surface and the bottom of the crack reaches the critical value, the safety factor of the slope reaches the minimum value, after which the safety coefficient tends to stabilize. The slope safety factor remains unchanged at first with the deepening of the fracture depth, then decreases rapidly and finally tends to be gentle.

Figure 3 shows that with the increase of the distance from the fracture to the slope top angle, the influence of the fracture on the slope stability gradually increases and the reduction rate of safety factor gradually increases. When it reaches 7 m, the fracture has the greatest influence on the slope stability and the safety factor is the smallest. When it is greater than 7 m and less than 9 m, the influence of the fracture on the slope stability decreases rapidly. When it is greater than 9 m, fracture have little effect on slope stability. Therefore, the critical fracture depth has a critical location at the top of the slope. Attention should be paid to the treatment of fractures in this area in the process of slope management.

3 Influence of slope top fractures on seepage field and slope stability under rainfall

3.1 Numerical calculation model

A slope model with a fissure at the top of the slope is established. It is assumed that there is a fissure at 7 m from the slope top angle, the length of the model bottom is 80 m, the slope toe is 45°, the height is 50 m, and the distance from the bottom of the model is 15 m. In order to analyze the influence of pore water pressure and volume water content of soil on slope stability in the process of rainwater seepage, two observation sections are set in the model. Section 1-1 passes through the fracture, which is consistent with the extension direction of the fracture. Section 2-2 is located at the bottom of the fracture at 1 m, which is perpendicular to the

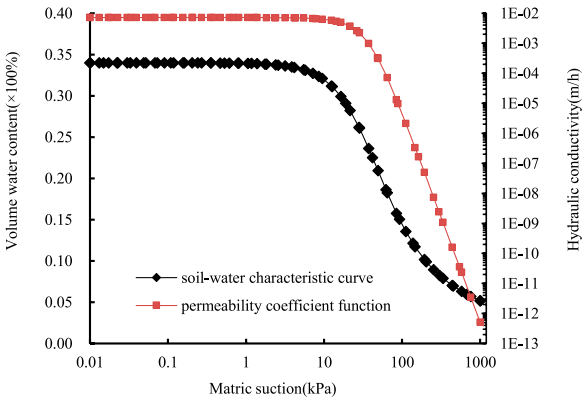

FIGURE 5
Soil water characteristic curve and osmotic coefficient function of slope soil.

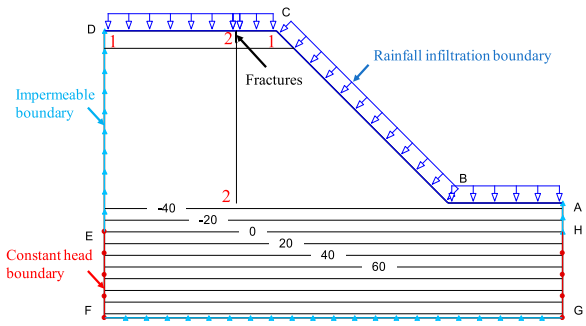

FIGURE 6
The boundary condition of the model and the initial pore water pressure.

extension direction of the fracture. Volumetric water content and pore water pressure of each section obtained by numerical calculation of this model. The finite element mesh is divided into 12,953 nodes and 12,826 elements. The specific model and mesh division are shown in Figure 4.

3.2 Calculation parameters and their boundary condition settings

In this paper, the mechanical parameters of loess are obtained by consulting a large number of literatures. According to the characteristics of loess material, the soil-water characteristic curve of slope is obtained by V-G model. The permeability coefficient function of unsaturated loess is obtained by soil-water characteristic curve and saturated permeability coefficient.

Because there are fractures, there is no strength parameter. Therefore, when calculating the transient seepage field, the equivalent permeability coefficient method is used for the fractures. The permeability coefficient of the fracture is large relative to the surrounding soil, and adopts the saturated permeability coefficient. The natural gravity of soil is 16.5 kN/m^3, the effective cohesion is 30 kPa, the effective internal friction angle is 25°, the saturated permeability coefficient is 2×10^{-6} m/s. The natural gravity, the effective cohesion and the effective internal friction angle of fracture are all 0, and the saturated permeability coefficient is 0.78 m/s. The soil-water characteristic curve of unsaturated soil is shown in Figure 5.

The strength parameters of soil materials, soil-water characteristic curves and permeability coefficient functions provided above should also be used for calculations under other working conditions.

Boundary conditions: for the following part of the water table on both sides of the model set the head boundary, the position of the fixed head is at the water table line, and the part above the water table line is set as the zero-flow boundary. The surface of the slope is set as the free infiltration boundary, and the flow boundary is taken, and the bottom of the model is set as the impermeable boundary. The rainfall intensity is 2 mm/h. It is considered that the rainfall is all infiltrated into the slope, and no surface runoff is formed on the slope surface. The rainfall time is 72 h, and the duration after rain is 288 h.

Initial conditions: when calculating the transient seepage field of the slope, the water content of the slope soil in its natural state and the distribution of pore water pressure within the slope soil should be obtained first and used as the initial conditions to calculate the subsequent conditions of the seepage field at different moments.

The boundary conditions of the model set the rainfall infiltration boundary as AB, BC, CD. In the process of rainfall, there will be a catchment inflow at the fracture location, so the infiltration flow relative to other infiltration boundaries should be added at the fracture width position. The impervious boundary is DE, FG, AH, and the constant head boundary is EF and GH. The groundwater level and the constant head height are the same. The initial conditions and boundary conditions of the model are shown in Figure 6.

3.3 Influence of the depth of slope top fracture on the seepage field of slopes under rainfall

Before the instability failure of soil slope, there will be some tension cracks at the top of the slope. These cracks make the isolated soil column formed inside the slope, which is equivalent to the unconfined condition (Li et al., 2006). The fracture will provide a potential sliding surface for the slope failure to increase the sliding surface of the slope.

Fracture provide infiltration channels for rainwater and enhance the infiltration capacity of water under rainfall. On the one hand, the infiltration rainwater into the soil increases the weight of the soil itself. On the other hand, the fracture is filled with water, and the downward infiltration of water under gravity will soften the potential sliding surface of the slope. In addition, it will produce hydrostatic pressure on the structural plane, which will lead to the decrease of stability of slope, short the creep time of slope body and increase the possibility of slope failure.

Therefore, it is necessary to study the influence of fractures on slope seepage field under rainfall when analyzing the influence of fractures on slope stability. In this paper, the equivalent model with rainfall intensity of 3 mm/h is used. The rainfall time is 72 h and the post-rain time is 288 h. The fracture depth at the position of 7 m

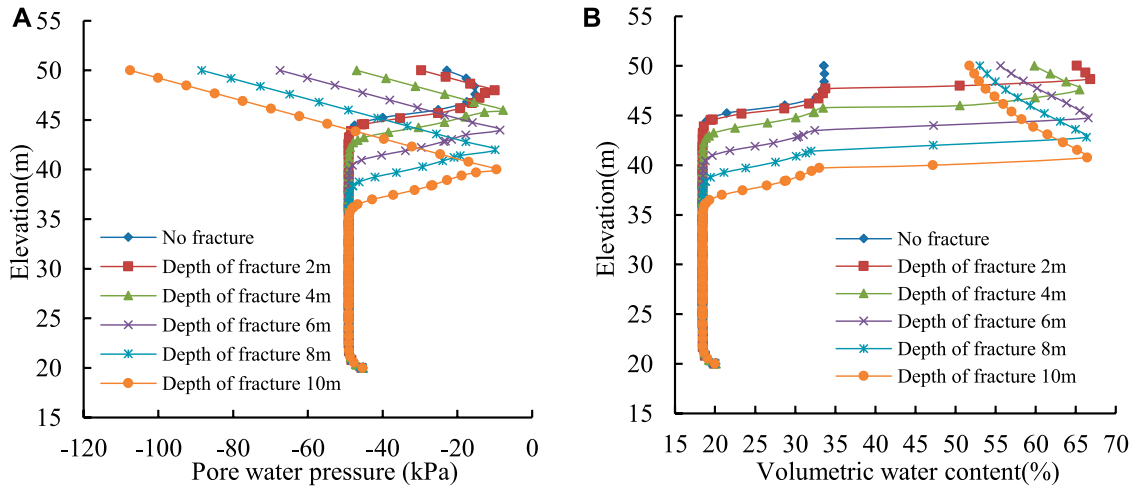

FIGURE 7
(A) The variation curve of pore water pressure. **(B)** The variation curve of and volume water content.

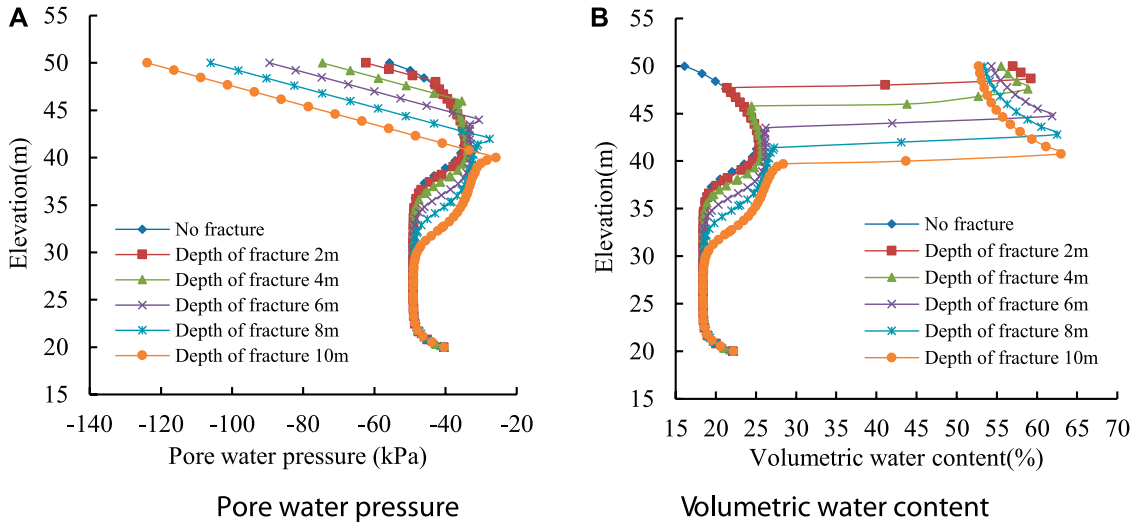

FIGURE 8
The variation curve of pore water pressure and volume water content at 288 h 1-1 section after the end of rainfall at different depths **(A)** Pore water pressure **(B)** Volumetric water content.

from the slope top angle is 0 m, 2 m, 4 m, 6 m, 8 m, and 10 m respectively. The seepage field of the slope is calculated by SEEP/W software, and then the calculated results are imported into SLOPE/W software for slope stability analysis.

Figures 7, 8 show that when the rainfall ends, as the crack depth continues to expand, the water stored in the fracture gradually increases, and the corresponding pore water pressure and volumetric water content gradually increase. The pore water pressure and volumetric water content at the bottom of the fracture reach the maximum under gravity, which is much larger than the pore water pressure and volumetric water content of the upper soil. When the fracture depth is shallow and the depth is 2 m, the pore water pressure on the 1-1 section is almost the same as that without fracture, indicating that the shallow fracture has little effect on the seepage field of the slope. When the rainfall ended 288 h, the water molecules had enough time to move from the fracture with high saturation to the surrounding with low saturation. The pore water pressure in the fracture gradually dissipates, and the water content at the bottom of the fracture also decreases.

Figures 9, 10 show that the fracture in the soil provide a channel for the diffusion of rainwater, and the water inside the fracture diffuses from high saturation to low saturation through the bottom and side of the fissures during rainfall. In the process of water diffusion, the pore water pressure and volumetric water content of the soil around the fracture are larger than those of the soil away from the fracture due to the loss of hydraulic gradient. When the rainfall ends, the wetting front depth of rainwater infiltration is greater than the depth of the fracture, resulting in the pore water pressure and volumetric water content in the soil far from the

10.3389/fmats.2023.1193527

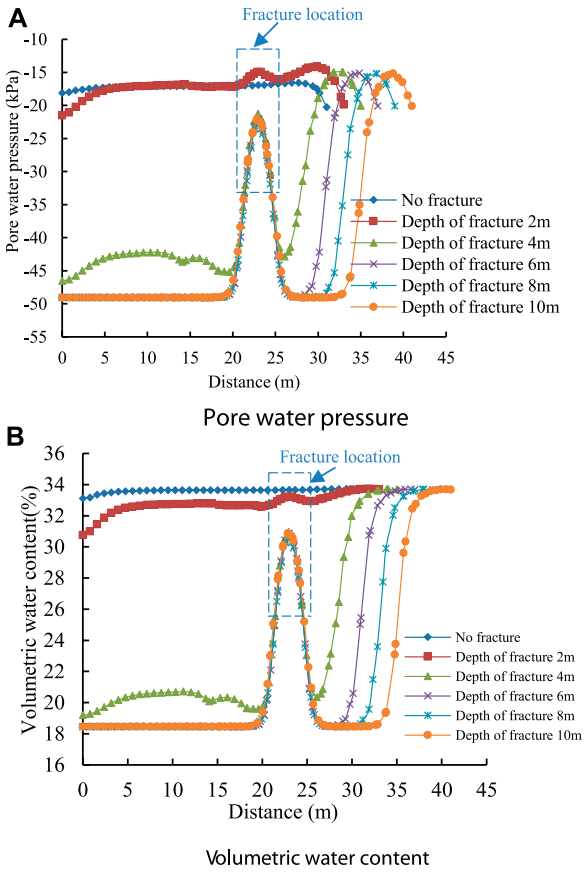

FIGURE 9
The variation curve of pore water pressure and volume moisture content of 2-2 sections at the end of rainfall were observed in different depths **(A)** Pore water pressure **(B)** Volumetric water content.

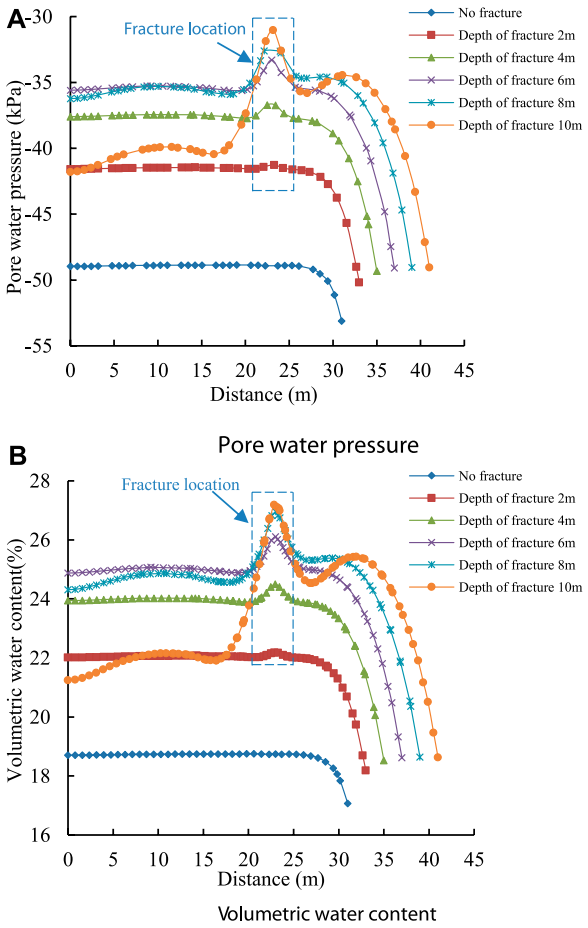

FIGURE 10
Variation curves of pore water pressure and volumetric water content of 2-2 fracture surface at different depths at 288 h after rainfall **(A)** Pore water pressure **(B)**Volumetric water content.

fracture is greater than the soil near the fracture. When the rainfall ends 288 h, the pore water pressure and volumetric water content of the soil around the fracture are greater than those far away from the fracture. Because the soil lacks the supply of rainwater, and the water diffuses around under the action of gravity, the pore water pressure in a certain depth of the slope surface continues to dissipate, and the corresponding volumetric water content also continues to decline. Because the lack of rainwater supply in the soil and the continuous diffusion of water under gravity, the pore water pressure in a certain depth of the slope is continuously dissipated, and the corresponding volumetric water content is also decreasing.

3.4 Influence of the depth of slope top fractures on slope stability under rainfall

By analyzing the seepage field of the slope with fracture, the safety factor of the slope is further analyzed in the case of fracture affecting the seepage field. In this paper, the seepage results calculated by SEEP/W are imported into SLOPE/W software. The influence of fracture depth change on slope stability under rainfall is analyzed by M-P method.

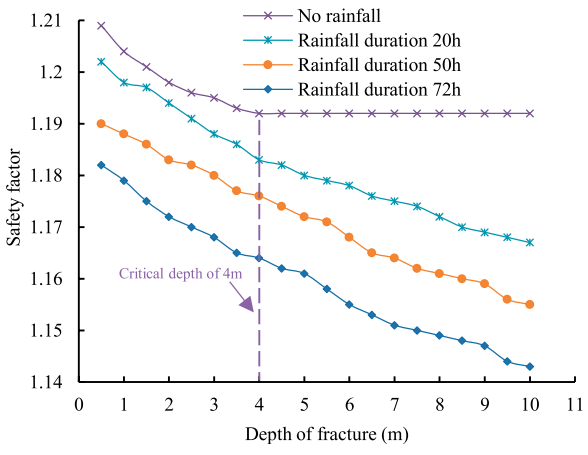

FIGURE 11
The influence of fracture depth on slope safety coefficient under different rainfall duration.

Figure 11 shows that in the absence of rainfall, the decrease of safety factor is small and tends to be a stable value when the fracture depth exceeds 4 m. Under rainfall, the safety factor of slope is decreases obviously and the magnitude of decline varies greatly. As the time of rain increases, the safety factor decreases more, the critical depth disappears, and the deeper the crack depth, the smaller the slope safety factor.

4 Conclusion

By establishing a two-dimensional calculation model, the influence of different locations and depths of fracture at the top of the slope on slope stability was studied. The distribution of pore water pressure and volumetric water content of the slope under rainfall is obtained. The influence of fracture depth on slope stability under rainfall is explored. The conclusions are as follows.

(1) With the increase of the distance from the fracture to the slope top angle, the safety factor of the slope decreases first and then increases. The critical fracture depth has a critical position at the slope top. When the fracture is 7 m away from the slope top angle and the fracture propagation depth exceeds 4 m, the slope safety factor is the smallest.
(2) With the increase of fracture depth, the safety factor of slope decreases rapidly at first and then tends to be stable. There is a critical crack depth, and the critical crack depth corresponding to different positions is different. Beyond the critical crack depth, the safety factor of slope tends to be stable.
(3) At the end of rainfall, with the increase of fracture depth, the pore water pressure and volumetric water content of the soil at the bottom of the fracture of 1-1 section are greater than those of the upper soil, and the shallow fracture has little effect on the seepage field of the slope. Since the damp-surface depth of rainwater infiltration is greater than the depth of the fissure, the pore water pressure and volumetric water content in the soil far from the fracture in 2-2 section are greater than those in the soil near the fracture.
(4) At 288 h after the end of rainfall, the pore water pressure and volumetric water content of the soil around the fracture of 2-2 section are greater than those of the soil far away from the fracture. Due to the lack of water supply in the fracture, the water is continuously diffused around under gravity. Finally, the pore water pressure of the soil at the location of the fracture gradually dissipates, and the corresponding volumetric water content gradually decreases. Due to the lack of water recharge in the fracture, the water spreads around under gravity, and finally the pore water pressure of the soil at the location of the fracture gradually dissipates, and the corresponding volumetric water content gradually decreases.
(5) When there is no rainfall, with the increase of fracture depth, the safety factor of slope decreases slightly, and the existence of critical fracture depth makes the safety factor of slope tend to a stable value. Under rainfall, the safety factor of slope decreases continuously with the increase of fracture depth, and the critical fracture depth disappears, which is less than the safety factor of slope stability under the condition of no rainfall (Wang, et al., 2021).

Data availability statement

The original contributions presented in the study are included in the article/Supplementary Material, further inquiries can be directed to the corresponding author.

Author contributions

HL provided overall guidance on the article and wrote this paper. MY and TD modified the article language. All authors contributed to the article and approved the submitted version.

Funding

This work was supported by the Loess Soil Mechanics and Engineering Key Laboratory of Shaanxi Province Foundation (13JS073) and Natural Science Foundation of Shaanxi Province (2017JM5059).

Conflict of interest

The authors declare that the research was conducted in the absence of any commercial or financial relationships that could be construed as a potential conflict of interest.

Publisher's note

References

Cao, S., Fu, H., Gao, Q., Guangtao, Z., and Zeng, L. (2022). Seepage characteristics and erosion patterns of fractured red clay slope under rainfall. *China J. Highw. Transp.* 35 (05), 33–43.

Chen, Z., Ren, H., and Ring, Y. (2019). Two-dimensional analytical analysis of coupling deformation and seepage coupling of fractured unsaturated soil. *Geol. Hazards Environ. Preserv.* 30 (04), 29–35.

Chen, Z. (2002). Limit analysis for the classic problems of soil mechanics. *Chin. J. Geotechnical Eng.* 24 (1), 1–11.

Gao, Q. F., Zeng, L., and Shi, Z. N. (2021). Effects of desiccation cracks and vegetation on the shallow stability of a red clay cut slope under rainfall infiltration. *Comput. Geotechnics* 140, 104436. doi:10.1016/j.compgeo.2021.104436

He, Y., Yu, J., Yuan, R., and Fang, Y. (2021). Stability analysis of soil fracture slope considering slope top inclination. *China J. Highw. Transp.* 34 (05), 45–54.

Li, R., Yu, Y., and Guangxin, L. I. (2006). Application of strength reduction finite element method in slope stability analysis of unsaturated soil. *Water Resour. Hydropower Eng.* 36 (3), 42–45.

Liu, D., He, Z., Zhou, K., Li, T., and Zeng, L. (2017). Influence of fracture anisotropy on slope seepage under rainfall conditions. *Min. Metallurgical Eng.* 37 (04), 14–18.

Lu, H. E. (2018). *Analysis of seepage field and stability of fractured soil slope under rainfall conditions*. Zhejiang, China: Zhejiang University.

Michalowski, R. L. (2012). "Cracks in slopes: Limit analysis approach to stability assessment," in Proceedings of the GeoCongress 2012: State of the Art and Practice in Geotechnical Engineering, Oakland, California, March, 2012, 442–450.

Qian, Z., Tu, G., Zhao, S., and Li, M. (2020). Differential effects of X and Y shaped fractures on rainfall infiltration of accumulation. *Hydroelectr. Power* 46 (08), 92–98.

Spencer, E. (1967). A method of analysis of the stability of embankments assuming parallel inter-slice forces. *Geotechnique* 17 (1), 11–26. doi:10.1680/geot.1967.17.1.11

Sun, P., Wang, G., Li, R., Zhang, Z., Huo, X., Li, Z., et al. (2019). Field test of loess slope under rainfall condition. *J. Eng. Geol.* 27 (2), 466–476.

Utili, S. (2013). Investigation by limit analysis on the stability of slopes with cracks. *Geotechnique* 63 (2), 140–154. doi:10.1680/geot.11.p.068

Wang, Q., Tu, G., Zhao, S., and Qiu, X. (2020). Effects of Y-shaped and primary and secondary plume fractures on rainfall infiltration of accumulations. *Yangtze River* 51 (11), 179–184.

Wang, G., and Liao, X. (1996). Study on land-slide disaster and its prevention and control of China railway. *Chin. J. Geol. Hazard Control* 1, 6–9.

Wang, L., Pu, X., Wu, Z., Xu, S., and Liu, K. (2018). Shaking table test study on dynamic response of loess slope under the coupling effect of earthquake and rainfall. *J. Geotechnical Eng.* 40 (7), 1287–1293.

Wang, L., Liu, F., and Zhang, Z. (2021). Research on characteristics of unsaturated soil water characteristic curve. *Adhesion* 46 (05), 147–150.

Wu, Z., Chen, Y., Wang, Q., Zhao, D., and Zhang, D. (2019). Mechanism analysis of yongguangcun landslide caused by the 6.6 earthquake in zhangxian county, minxian county. *J. Geotechnical Eng.* 41 (2), 165–168.

Yan, G., Yin, Y., Huang, B., Zhang, Z., and Dai, Z. (2019). Genesis mechanism and deformation characteristics of jinjiling landslide in the three gorges. Reservoir area. *Rock Soil Mech.* 40 (S1), 329–340.

Yan, J., Huo, Z., Li, H., Zhou, Y., and Liu, Y. (2022). Study on seepage sliding analysis and stability of near-horizontal slope under fracture water. *J. Min. Saf. Eng.* 39 (03), 607–614.

Yao, H., Zheng, S., and Chen, S. (2001). Analysis on the slope stability of expansive soils considering cracks and infiltration of rain. *Chin. J. Geotechnical Eng.* 23 (5), 606–609.

Zeng, L., Xiao, L., Zhang, J., and Gao, Q. (2020). Effect of the characteristics of surface cracks on the transient saturated zones in colluvial soil slopes during rainfall. *Bull. Eng. Geol. Environ.* 79 (2), 699–709. doi:10.1007/s10064-019-01584-1

Zeng, L., Chen, J., Liu, J., Gao, Q., Yuan, Y., and Kuang, B. (2022). Study on seepage characteristics of fracture-bearing red clay slope based on fluorescence tracer method. *China J. Highw. Transp.* 36, 1–13. doi:10.19721/j.cnki.1001-7372.2023.03.010

Zhang, J., Zhu, D., and Zhang, S. H. (2020). Shallow slope stability evolution during rainwater infiltration considering soil cracking state. *Comput. Geotechnics* 117, 103285. doi:10.1016/j.compgeo.2019.103285

Zhang, M., and Li, T. (2011). Study on the inducing factors and forming mechanism of loess land-slides. *J. Eng. Geol.* 19 (4), 530–540.

Zhang, S., Pei, X., Huang, R., Zhang, X., Chang, Z., and Zhang, Z. (2019). Model test on rainfall infiltration characteristics and deformation failure mode of loess fill slope. *China J. Highw. Transp.* 32 (9), 32–41.

Zhou, Z., Zhang, J., Ning, F., Luo, Y., and Wang, J. (2020). Temporal and spatial characteristics of moisture migration and instability mechanism of cracked soil slope under rainfall infiltration. *J. Traffic Transp. Eng.* 20 (4), 107–119. doi:10.19818/j.cnki.1671-1637.2020.04.008

Zhou, Z., Zhu, L., and Chen, L. (2021). Calculation method of vertical fracture depth of loess slope at inclined slope. *China J. Highw. Transp.* 34 (05), 37–44.

Zhu, X., Shao, S., Shen, X., Shao, S., and Liu, X. (2022). Three-dimensional stability limit analysis of fractured loess slope. *Rock Soil Mech.* 43 (10), 2735–2743+2756.

frontiers | Frontiers in Materials

TYPE Original Research
PUBLISHED 15 June 2023
DOI 10.3389/fmats.2023.1192557

OPEN ACCESS

EDITED BY
Xianze Cui,
China Three Gorges University, China

REVIEWED BY
Wenlin Feng,
Harbin Institute of Technology, China
Mi Yang,
Tianjin University, China

*CORRESPONDENCE
Song Chen,
chennsongg@163.com
Ying Yuan,
yuanyingson@hgu.edu.cn

RECEIVED 23 March 2023
ACCEPTED 30 May 2023
PUBLISHED 15 June 2023

CITATION
Yang Q, Chen S and Yuan Y (2023), Experimental study on the variation rule of water level outside the pit caused by dewatering in the pit and the rule of reinjection outside the pit.
Front. Mater. 10:1192557.
doi: 10.3389/fmats.2023.1192557

Experimental study on the variation rule of water level outside the pit caused by dewatering in the pit and the rule of reinjection outside the pit

Qingyuan Yang[1], Song Chen[2,3]* and Ying Yuan[3]*

[1]School of Architecture and Engineering, Guangzhou Panyu Polytechnic, Guangzhou, China, [2]Hebei Key Laboratory of Optoelectronic Information and Geo-detection Technology, Hebei GEO University, Shijiazhuang, China, [3]College of Urban Geology and Engineering, Hebei GEO University, Shijiazhuang, China

Studying the surface settlement caused by foundation pit dewatering has certain practical significance for engineering construction. When the aquifer in the foundation pit is located within a large burial depth range, the impermeable wall does not completely separate the water layer, resulting in water inside and outside the foundation pit communicating around the bottom of the impermeable wall. Taking the foundation pit project of a subway station in Shenzhen as the background, model experiments were conducted to reveal the changes in water level outside the pit caused by precipitation under different conditions inside the pit. (1) Considering the influence of surrounding seepage, the precipitation curve outside the pit presents a concave and then convex form, which is different from the Dupuit theory precipitation curve. (2) For large foundation pit dewatering in layered soil, the downward trend of the dewatering curve outside the foundation pit decreases with the increase of soil depth. (3) Compared to vertical reinjection in close proximity to dense buildings, inclined reinjection has a smaller impact on the side adjacent to the retaining wall, while it is far away from the retaining wall, with a larger impact range. The full well deep reinjection well with an angle of 20° from the vertical direction has the largest reinjection range and the best reinjection effect. It provides a research basis for reasonable control and prevention of surface settlement and adverse deformation of diaphragm walls in narrow spaces under subsequent surrounding seepage conditions.

KEYWORDS

dewatering of foundation pit, model test, precipitation curve, reinjection form, experimental study

1 Introduction

At present, scholars, both domestically and internationally, have conducted extensive research on foundation pit dewatering based on the Dupuit theory, which assumes that the water flow in the dewatering well during the dewatering process is horizontal. Infiltration of water in rock and soil is a complex migration process (Bai et al., 2021).

Meinzer (1928) paid attention to and studied the unstable movement of groundwater and the water storage properties of confined aquifers. Li et al. (2020) evaluated the surface settlement near the drawdown well using statistical analysis and numerical simulation, as well as a layered

TABLE 1 Physical and mechanical parameters of similar strata.

Similar stratum	Density/g/cm^3	Internal friction angle/°	Cohesion/kPa	Permeability coefficient/m/d	Void ratio
Silty clays	1.93	19	0.46	0.015	0.92
Conglomerate clayey soils	1.78	18	0.62	0.07	0.98
Completely decomposed granites	1.83	22	0.56	0.15	0.91
Strongly weathered granites	1.88	25	0.49	0.43	0.83

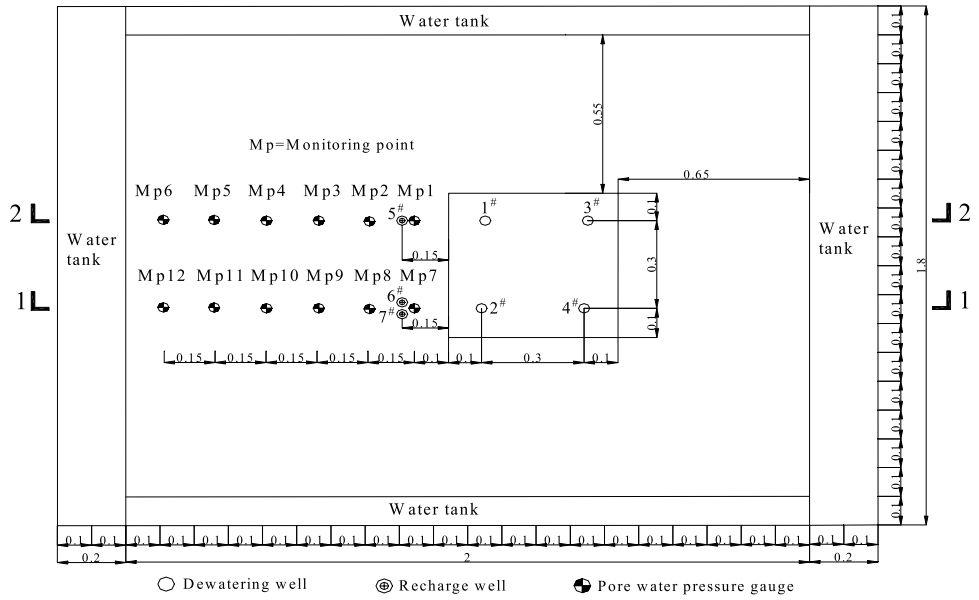

FIGURE 1
Layout diagram of the test.

summation method based on the principle of effective stress. The evaluation values were too high, and it was recommended to use coefficients for correction. Xu et al. (2014, 2019) studied the effects of the depth of the well filter screen and the cutoff depth of the water stop curtain on precipitation-induced deformation in aquifers through indoor experiments and numerical simulation. Zeng et al. (2019) investigated the mechanism of support lateral displacement caused by pre-precipitation through engineering measurement and numerical simulation. Wu et al. (2020) studied the characteristics and influencing factors of settlement outside the foundation pit caused by leakage of the water-stop curtain during foundation pit dewatering through numerical simulation. Zhang et al. (2018) found through field measurement and analysis of four foundation pit projects in Singapore that when the water level outside the pit decreases during precipitation, the deformation of the support structure is small and the settlement outside the pit is large. Roy and Robinson (2009) studied the surface settlement of soft soil sites caused by bedrock drainage. Huang et al. (2009) proposed an evaluation method for ground settlement caused by foundation pit dewatering in specific areas. Wang et al. (2009) proposed a calculation method for precipitation-induced settlement of deep foundation pits in subway stations. Yuan and Zhang (2013) proposed an estimation method for ground settlement caused by precipitation under the constraint of lateral friction. Wu and Zhu (2016) proposed a calculation method for ground settlement caused by foundation pit dewatering considering the influence of unsaturated soil in the drainage zone.

When the aquifer where the foundation pit is located is deeply buried, the aquifer is not completely isolated by the diaphragm wall. The water inside and outside the foundation pit flows around the bottom of the diaphragm wall, meaning that the water flow will move horizontally and vertically. Therefore, it is speculated that there will be some differences between the dewatering law of the foundation pit and the aforementioned research results under the influence of the surrounding seepage. Many studies have been conducted on the technology and theory of groundwater recharge outside the foundation pit to control the water level outside the pit and ground settlement (Yu and Gong, 2001; Wang et al., 2012; Zheng et al., 2014; Gambolati and Teatini, 2015; Huang et al., 2015; Zhang et al., 2017), which are all based on vertical recharge. When the foundation pit site is close to dense buildings, only a single row of recharge wells can be arranged between the foundation pit and the building, which cannot meet the requirements for the water level recharge range.

Taking the foundation pit project of a subway station in Shenzhen as an example and using model test methods to study and explore the changes in water level outside the pit caused by precipitation in the pit

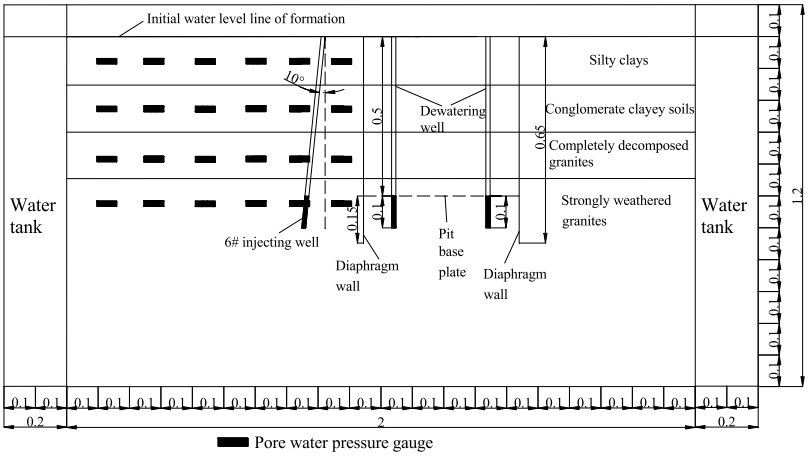

FIGURE 2
1–1 profile of the test.

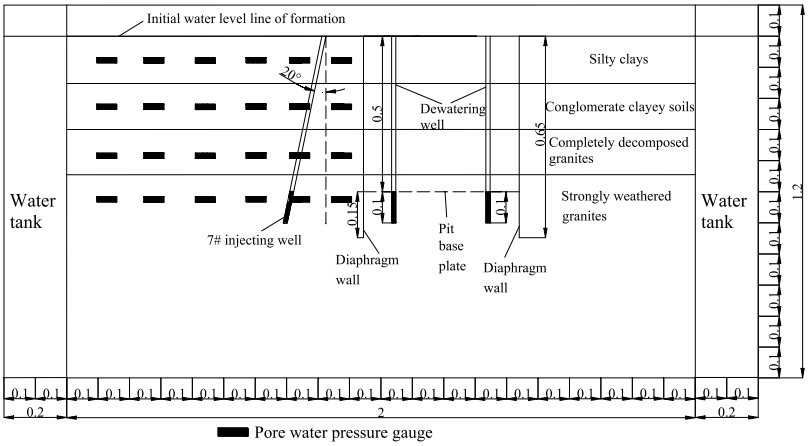

FIGURE 3
1–1 profile of the test.

under different conditions under the influence of surrounding leakage, this paper compares and analyzes the vertical recharge and the inclined recharge with an angle of 10° and 20° from the vertical direction and proposes a recharge strategy suitable for small and narrow spaces. It provides a research basis for reasonable control and prevention of surface settlement and adverse deformation of diaphragm walls in narrow spaces under subsequent surrounding seepage conditions.

2 Design of model tests

The geometric similarity constant, the gravitational acceleration similarity constant, and the density similarity constant are determined as C_l = 1/50, C_ρ = 1, and Cg = 1, respectively. Other relevant similarity constants of this test can be obtained by the traditional dimensional analysis method.

2.1 The practical engineering cases

The length, width, and buried depth of the subway station foundation pit are 365 m, 25 m, and 32 m, respectively. Two dewatering wells are arranged every 15 m along the long side of the foundation pit, and the distance between the dewatering wells along the width of the foundation pit is also 15 m. Considering the limitations of the test site, the two rows of dewatering wells in the middle of the foundation pit were selected for the test.

2.2 Design of formation material

The model test in this paper selected 40 orders of refined quartz sand with 150 and 300 orders of quartz sand powder to, respectively,

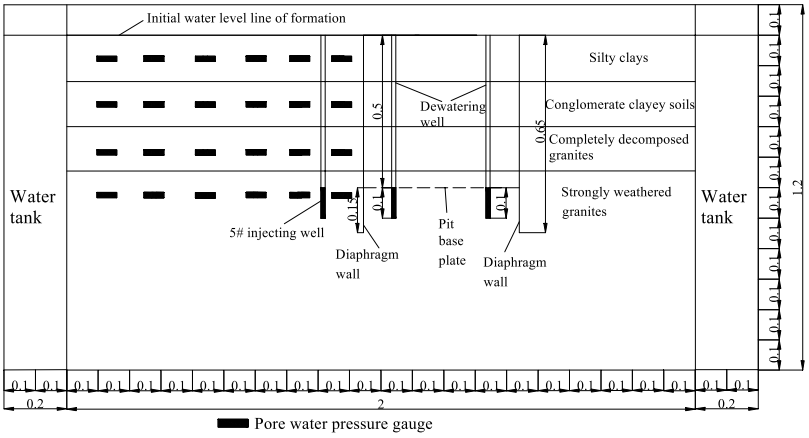

FIGURE 4
2–2 profile of the test.

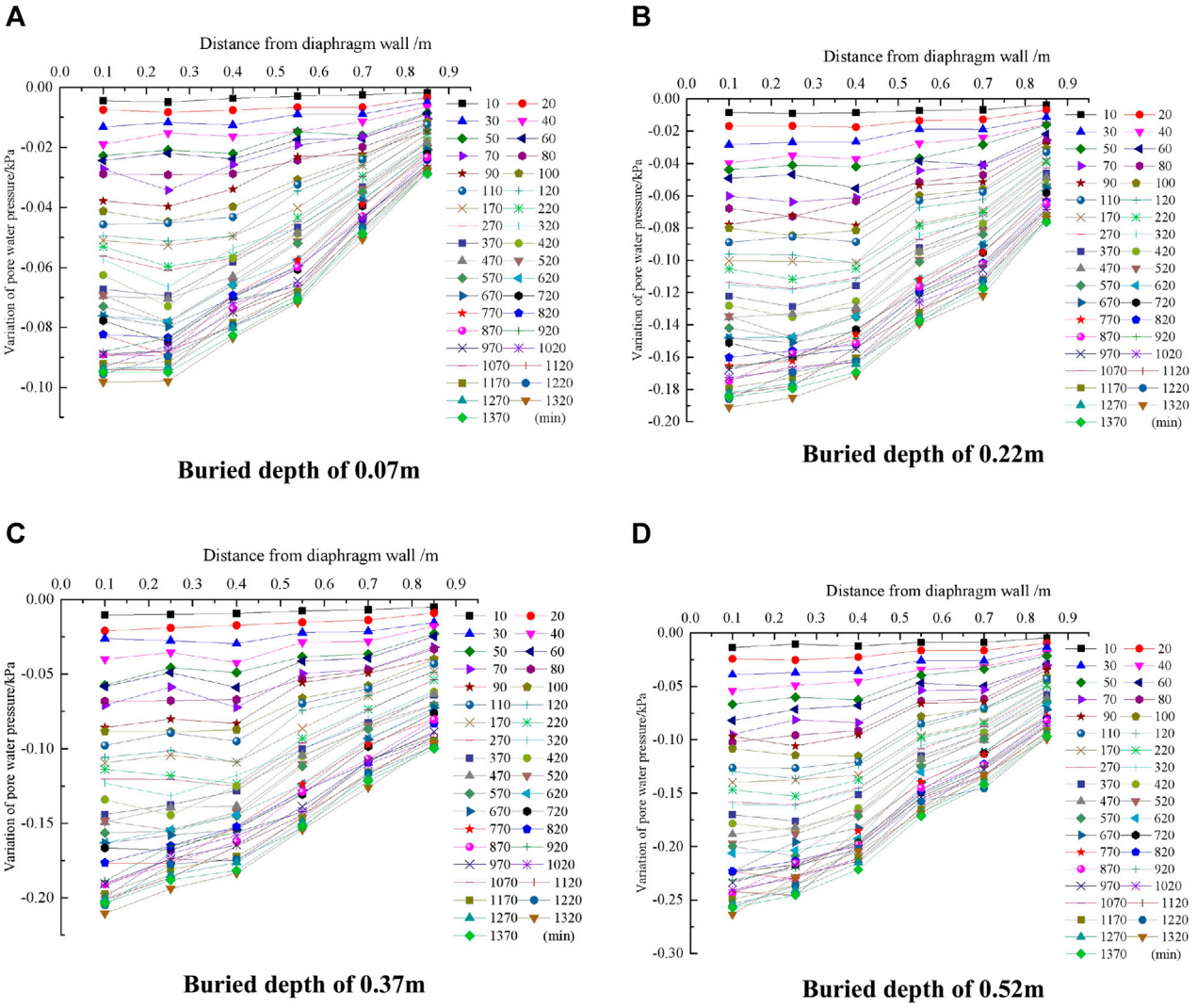

FIGURE 5
Time-history curves of pore water pressure in different depths.

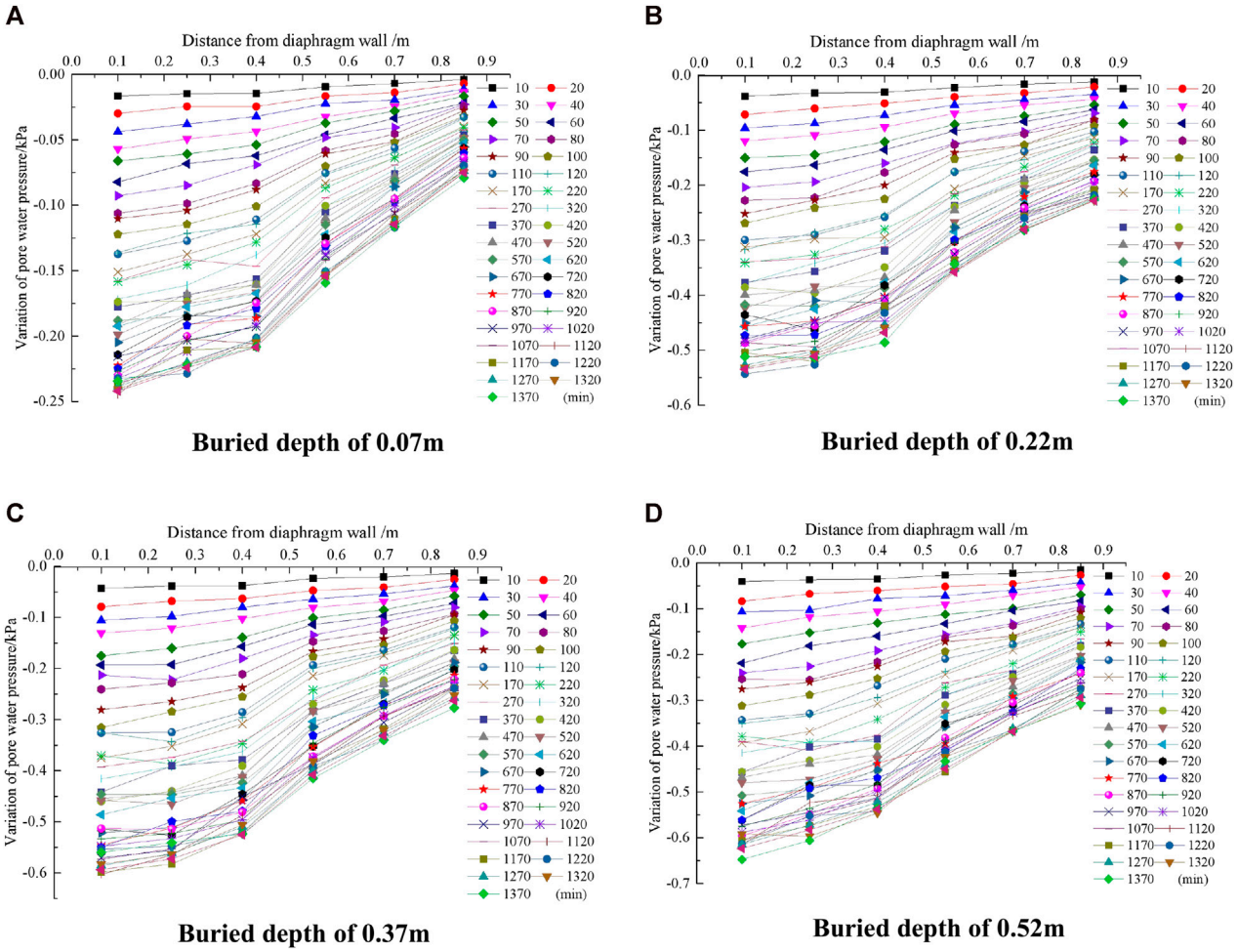

FIGURE 6
Time-history curves of pore water pressure in different depths.

make the mass matching and obtained the matching result meeting the similar proportion, as shown in Table 1.

2.3 Design of similar material of diaphragm wall

Based on the separation similarity design theory, upon the test, the PMMA material was selected as the material similar in structure to the underground continuous wall, and the PMMA sheet model of 11 mm thickness was obtained through calculation according to the similarity equivalence principle of flexural stiffness. A partly station foundation pit structure was considered for the test.

2.4 Design of the test model box

The multi-functional PMMA testing apparatus was applied as the test model tank, with main test dimensions of 2 m (length) × 1.8 m (width) × 1.2 m (height). Around the model tank, the water tank was separated from the main testing apparatus by a clapboard with small holes, which can meet water replenishment requirement upon the test for the main part.

2.5 Design of the test pumping system

The precipitation and observation well tubes are made of PVC spool with an outer diameter of 20 mm. The whole pumping system consists of a suction pump, suction pipe, pump output control valve, and pumping filter screen.

2.6 Preparation before the precipitation test

For every 10 cm of layer material laid, the layer should be immediately compacted. By injecting water from the top of the water tank into the test water tank, the soil layer is saturated from the bottom to top. As certain settlement deformation may occur after saturation inside the soil layer, it is required to continue filling the soil to the required height. Only after 1–2 times of saturation and filling processes, the continued filling and installation of instruments

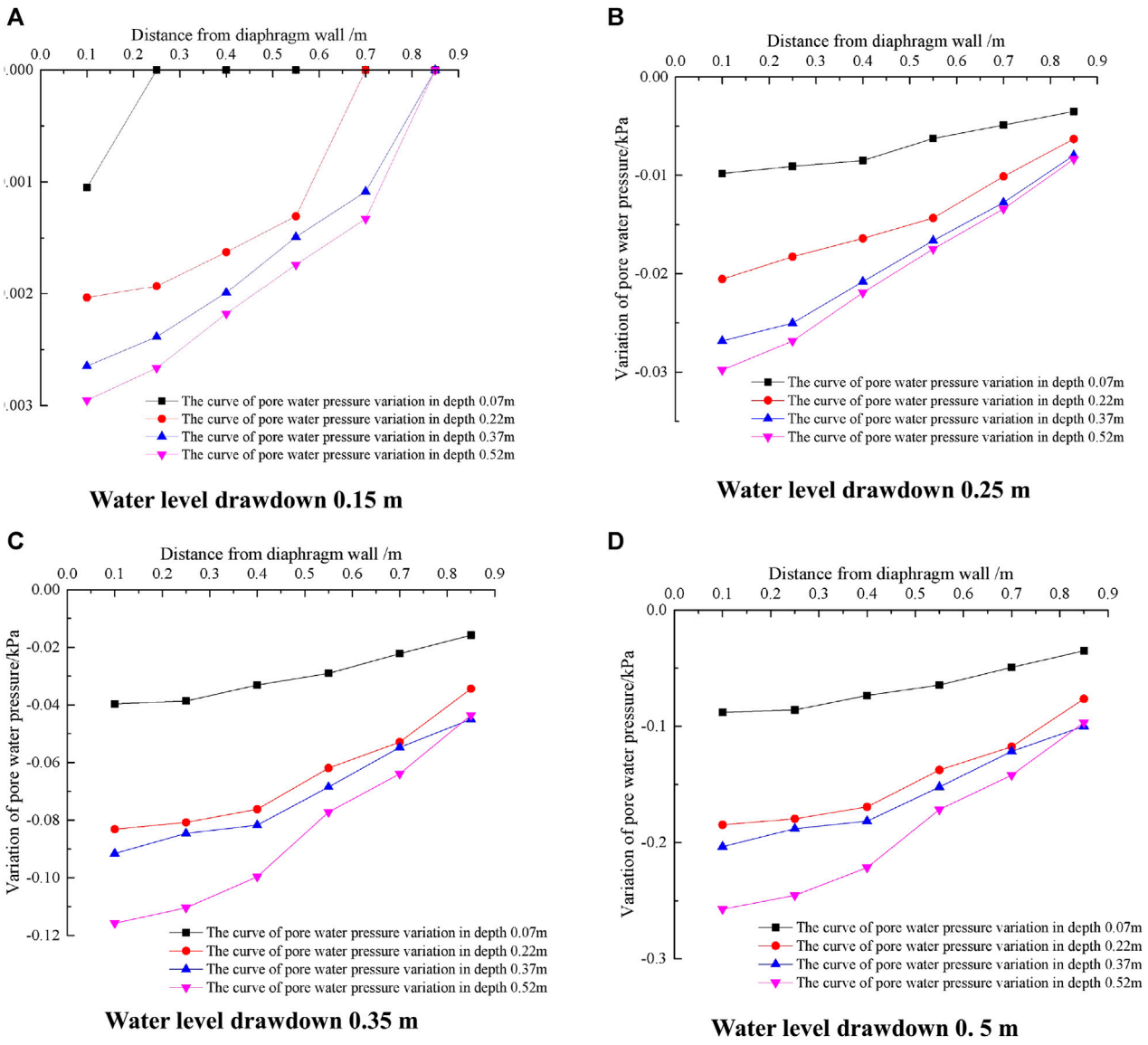

FIGURE 7
Variation curves of pore water pressure in each soil layer of different drawdown.

and soil can be monitored, until filling to the height of 1.1 m as required by the test. Upon solidification of the soil layer in the test tank, the water tanks and main tank around shall maintain the water level at a height of 1.1 m. As the formation solidifies under the weight force, when the reading change of the displacement meter at the settlement observation point on the soil layer surface is less than 0.001 mm/d, it shows that the soil layer solidification was basically accomplished. At the time, the model test had achieved the initial status prior to the construction and meets the precipitation test condition.

The layout plan and section of the foundation pit dewatering model test are shown in Figures 1–4. At 0.1 m, 0.25 m, 0.4 m, 0.55 m, 0.7 m, and 0.85 m away from the exterior of the diaphragm wall, measurement points 1–6 are set in the direction of the line connecting 1# and 3#, and measurement points 7 to 12 are set in the direction of the line connecting 2# and 4#. At measurement points 1 to 6 and measurement points 7 to 12, a single pore water pressure gauge is arranged along the depth direction of the model box at the burial depth of 0.07 m, 0.22 m, 0.37 m, and 0.52 m, mainly to monitor the variation of pore water pressure at different distances from the exterior of the foundation pit and the diaphragm wall.

The foundation pit of the subway hub is relatively close to the surrounding buildings, and the foundation of the buildings is mostly pile foundations with a relatively significant burial depth. Therefore, when conducting an inclined recharge, the inclination angle should not be too large, and generally the included angle with the vertical direction should not exceed 20°. Otherwise, the existing building foundation will be affected by the construction of the dewatering well, and may even be damaged. The dewatering well is set in the middle of the building and the foundation pit connecting wall, and in the test, it is set at a distance of 0.15 m from the connecting wall.

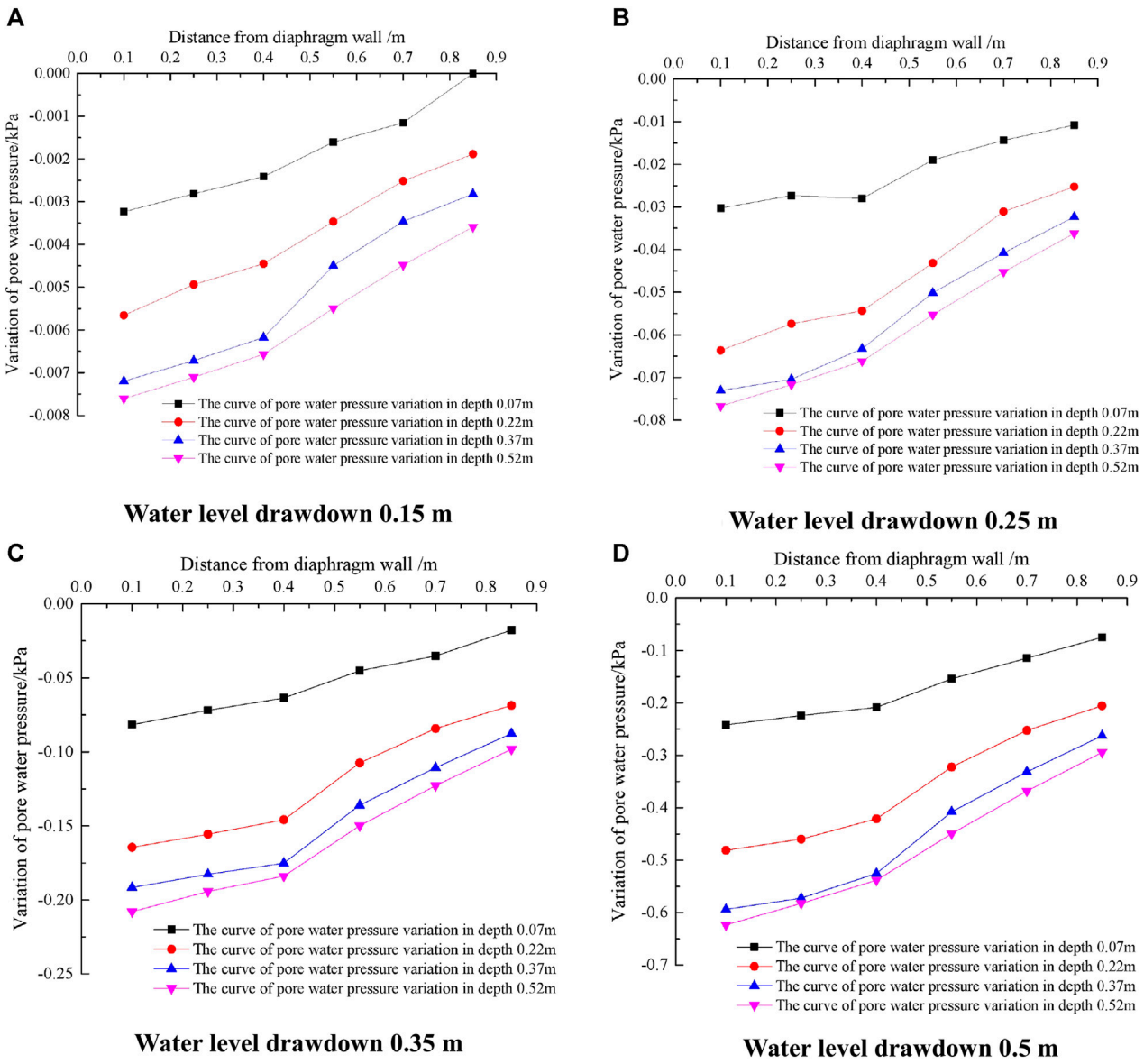

FIGURE 8
Variation curves of pore water pressure in each soil layer of different drawdown.

As shown in Figures 2, 4, wells 5 #, 6 #, and 7 # are vertical recharge wells and inclined recharge wells with an angle of 10° and 20° from the vertical direction. Precipitation and reinjection shall be conducted simultaneously, and the reinjection amount shall be taken as 1/2 of the pumping amount.

3 Experimental study on water level change outside the pit caused by precipitation in the pit

Test condition 1: Dewatering of single well in the foundation pit with large drop depth (with a drop depth of 0.5 m).

Test condition 2: Dewatering of double wells in the foundation pit with large drop depth (with a drop depth of 0.5 m).

Test condition 3: Dewatering in single well in the foundation pit by layers (with a drop depth of 0.15 m, 0.25 m, 0.35 m, and 0.5 m).

Test condition 4: Dewatering in double wells in the foundation pit by layers (with a drop depth of 0.15 m, 0.25 m, 0.35 m, and 0.5 m).

3.1 Analysis of test results in condition 1

After decreasing to the specified depth and stabilizing the precipitation, the pore water pressure monitoring data for different burial depths at measurement points 1 to 6 are collated and analyzed to obtain the time-history change curve of pore water pressure for different burial depths outside the foundation pit, as shown in Figure 5.

From Figure 5, it can be seen that within the depth range of the underground continuous wall, as the soil depth increases, the variation

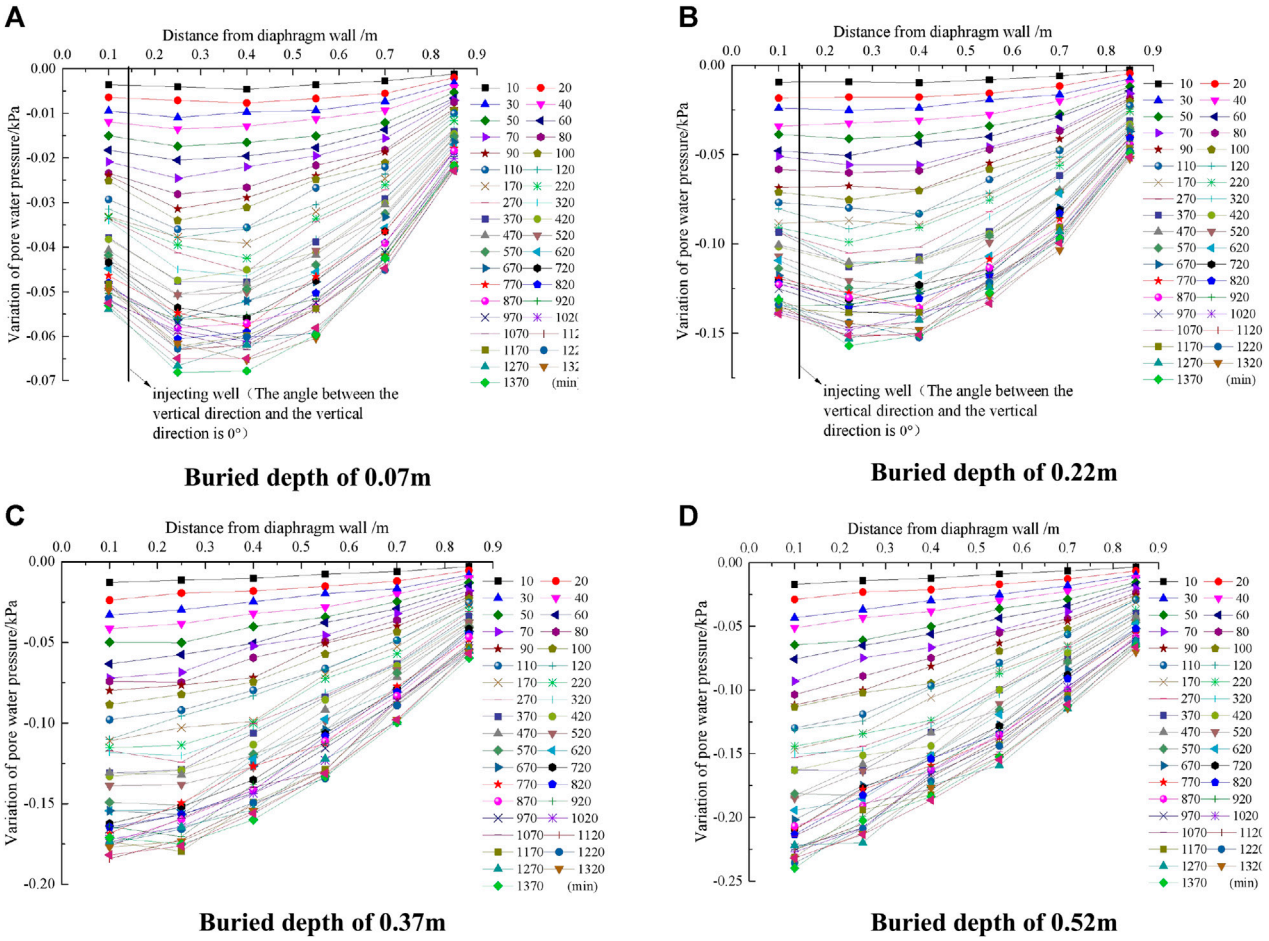

FIGURE 9
Time-history curves of pore water pressure in different depths.

value of pore water pressure outside the foundation pit increases, and the variation value of pore water pressure at the bottom of the underground continuous wall is the largest. This is due to the influence of seepage around the bottom of the diaphragm wall, which generates horizontal and vertical water flow, leading to an increase in the depth of incomplete well precipitation and an increase in the degree of precipitation impact at the bottom of the diaphragm wall. The precipitation curve outside the diaphragm wall has a similar form to that of the homogeneous formation, both of which are "concave first and then convex upward." Within the depth range of the diaphragm wall, as the depth of the soil layer increases, the concave amplitude of the precipitation curve outside the foundation pit decreases, and the concave amplitude of the precipitation curve at the bottom of the diaphragm wall is the smallest. It indicates that under the influence of infiltration, the study of precipitation outside the pit does not follow the Dupuit precipitation curve.

3.2 Analysis of test results in condition 2

After decreasing to the specified depth and stabilizing the precipitation, the pore water pressure monitoring data for different burial depths at measurement points 1 to 6 are collated and analyzed to obtain the time-history change curve of pore water pressure for different burial depths outside the foundation pit, as shown in Figure 6.

From Figure 6, it can be seen that the variation pattern of pore water pressure outside the pit caused by double-well precipitation and single-well precipitation is similar, within the depth range of the anti-seepage wall, as the soil layer depth increases, the variation value of pore water pressure outside the pit increases, and the variation value of pore water pressure at the bottom of the diaphragm wall is the largest. The form of the precipitation curve outside the diaphragm wall is also "first concave and then slightly convex." Within the depth range of the diaphragm wall, as the depth of the soil layer increases, the concave amplitude of the precipitation curve outside the foundation pit decreases, and the concave amplitude of the precipitation curve at the bottom of the diaphragm wall is the smallest.

After stable precipitation, the variation value of precipitation outside the foundation pit caused by double-well precipitation with different burial depths is 2–3 times greater than the variation value of pore water pressure outside the foundation pit caused by single-well precipitation. It can be seen that the variation of water level outside the

foundation pit caused by double-well precipitation cannot be simply considered the superposition of two single-well precipitation, but will produce a superposition increase effect. Therefore, when multiple-well precipitation is used, the influence of the superposition increase effect should be considered.

3.3 Analysis of test results in condition 3

After decreasing to the specified depth and stabilizing the precipitation, the pore water pressure monitoring data for different depths at measurement points 1–6 are collated and analyzed to obtain the pore water pressure change curve for different depths after stabilizing the precipitation outside the foundation pit, as shown in Figure 7.

From Figure 7, it can be seen that as the water level decreases, the variation values of pore water pressure in various soil layers outside the underground continuous wall gradually increase. Among them, the variation value of pore water pressure in strongly weathered granite similar strata is the largest, with a drawdown of 0.15 m, and the maximum variation value of pore water pressure is 0.003 kPa. The ratio to the maximum variation value of pore water pressure in this stratum with large drawdown is 0.012, with a drawdown of 0.25 m, and the maximum variation value of pore water pressure is 0.033 kPa. The ratio to the maximum variation value of pore water pressure in the deep drawdown of this formation is 0.115, the drawdown is 0.35 m, the maximum variation value of pore water pressure is 0.12 kPa, and the ratio to the maximum variation value of pore water pressure in the deep drawdown of this formation is 0.46. It can be seen that within the burial depth range of the diaphragm wall, the variation amplitude of pore water pressure increases with the increase in the burial depth.

3.4 Analysis of test results in condition 4

After decreasing to the specified depth and stabilizing the precipitation, the pore water pressure monitoring data for different depths at measurement points 1 to 6 were collated and analyzed, and the variation curve of pore water pressure for different depths outside the foundation pit after stabilizing the precipitation was obtained, as shown in Figure 8.

From Figure 8, it can be seen that as the depth decreases, the variation range of pore water pressure in various soil layers outside the anti-seepage wall gradually increases. Among them, the pore water pressure in strongly weathered granite formations changes the most, with a depth decrease of 0.15 m and a maximum change of 0.007 kPa. The ratio to the maximum variation of pore water pressure in this stratum with a large drawdown is 0.011, with a drawdown of 0.25 m and a maximum variation of 0.075 kPa. The ratio to the maximum variation value of pore water pressure in the deep drawdown of this formation is 0.121, the drawdown is 0.35 m, the maximum variation value of pore water pressure is 0.22 kPa, and the ratio to the maximum variation value of pore water pressure in the deep drawdown of this formation is 0.35. It can be seen that the variation law of the water level outside the pit caused by dual-well layered precipitation is similar to that caused by single-well layered precipitation. Within the burial depth range of the diaphragm wall, the variation range of pore water pressure increases with the increase in the burial depth.

For typical strata in Shenzhen, when the first layer of precipitation is conducted, the variation range of pore water pressure is relatively small. Starting from the second layer of precipitation, the variation range of pore water pressure gradually increases, and the changes in the surrounding environment caused by the changes in pore water pressure also increase. Therefore, starting from the second layer of precipitation, monitoring and analysis of changes in pore water pressure should be strengthened.

4 Experimental study on water level change and deformation caused by dewatering in the foundation pit and reinjection outside the foundation pit

Test condition 1: Dewatering at a large depth within the foundation pit (with a drop depth of 0.5 m) and reinjection at a depth of 1/2 well outside the foundation pit.

Test condition 2: Dewatering at a large depth within the pit (with a drop depth of 0.5 m) and deep reinjection of the entire well outside the foundation pit.

Test condition 3: Dewatering at a large depth within the pit (with a drop depth of 0.5 m) and inclined recharge with an angle of 10° from the vertical direction outside the foundation pit.

Test condition 4: Dewatering at a large depth within the pit (with a drop depth of 0.5 m) and inclined recharge with an angle of 20° from the vertical direction outside the foundation pit.

Test condition 5: Dewatering shall be conducted in layers within the foundation pit (with a drop depth of 0.15 m, 0.25 m, 0.35 m, and 0.5 m), while reinjection shall be conducted at 1/2 well depth outside the foundation pit.

Test condition 6: Dewatering shall be conducted in layers within the foundation pit (with a drop depth of 0.15 m, 0.25 m, 0.35 m, and 0.5 m), while the entire well depth outside the foundation pit shall be reinjected.

Test condition 7: Dewatering shall be conducted in layers within the foundation pit (with a drop depth of 0.15 m, 0.25 m, 0.35 m, and 0.5 m), and the angle between the outside of the foundation pit and the vertical direction was 10° inclined for reinjection.

Test condition 8: Dewatering shall be conducted in layers within the foundation pit (with a drop depth of 0.15 m, 0.25 m, 0.35 m, and 0.5 m), and the angle between the outside of the foundation pit and the vertical direction was 20° inclined for reinjection.

4.1 Analysis of test results in condition 1

After decreasing to the specified depth and stabilizing the dewatering and reinjection processes, the pore water pressure monitoring data for different burial depths at measurement points 1–6 were collated and analyzed, and the time-history variation curve of pore water pressure for different burial depths outside the foundation pit was obtained, as shown in Figure 9.

From Figure 9, it can be seen that during the reinjection process at 1/2 well depth, the variation of pore water pressure in the soil layer within the reinjection depth is significantly affected by reinjection. Within the reinjection depth, when the precipitation reinjection is stable, the negative variation value of pore water pressure gradually

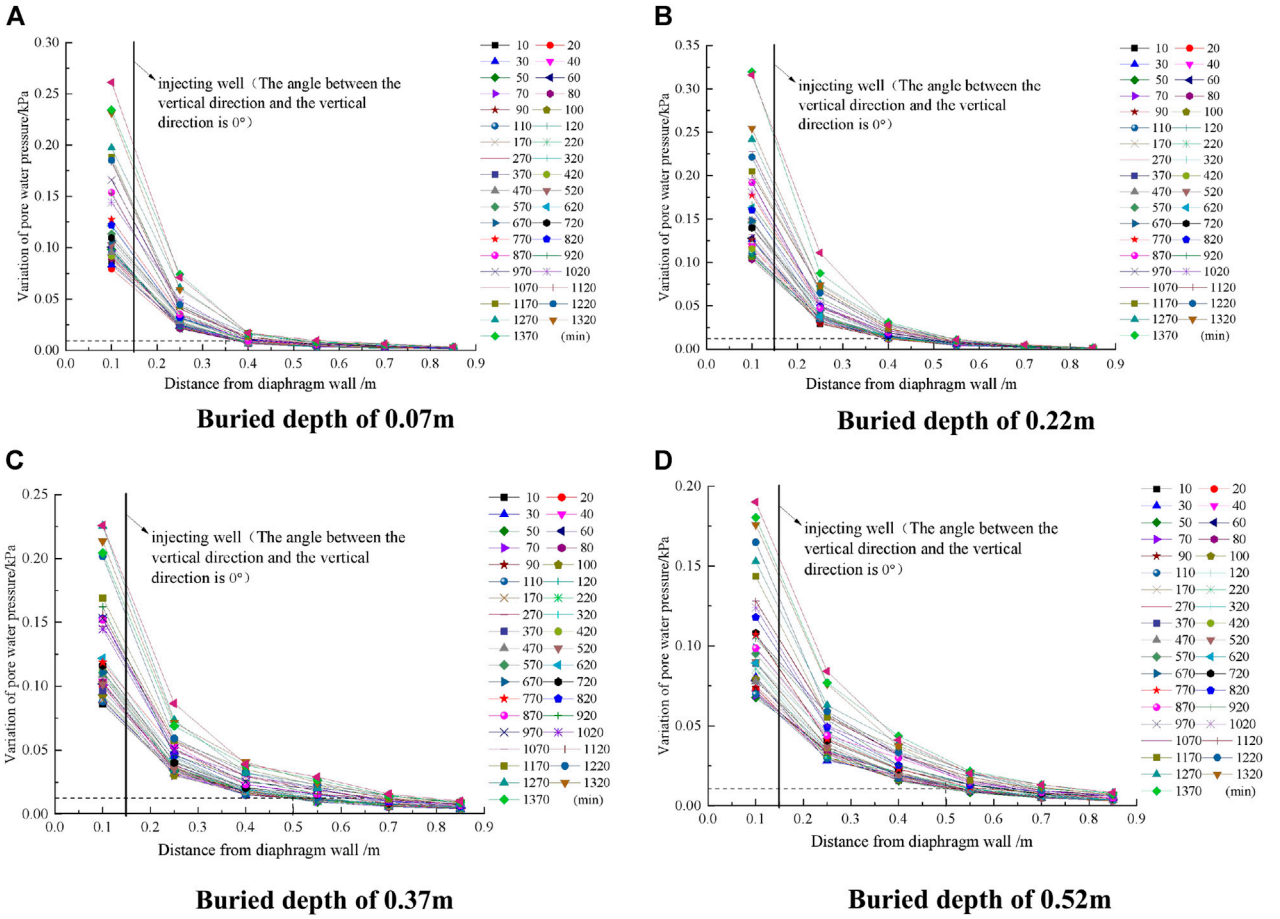

FIGURE 10
Time-history curves of pore water pressure in different depths.

decreases toward the ground wall side of the reinjection well, and when the precipitation reinjection is stable, the maximum negative variation value is 0.13 kPa. When the precipitation reinjection is stable, the negative variation value of pore water pressure gradually decreases away from the ground wall side. When the precipitation recharge is stable, the maximum negative change occurs in the stratum with a burial depth of 0.22 m, which is 0.16 kPa, which is only reduced by 0.03 kPa compared to no recharge. The variation value of pore water pressure in the outer layer at the depth of reinjection is basically the same as that without reinjection. During the process of reinjection, the length of the reinjection well plays a crucial role in the depth of soil layer reinjection. If the length of the reinjection well is insufficient, that is, the depth of the reinjection well is less than the depth of the precipitation well, it will not be able to effectively carry out soil layer reinjection, and the improvement effect on surface settlement caused by groundwater recharge and precipitation is insufficient.

4.2 Analysis of test results in condition 2

After decreasing to the specified depth and stabilizing the dewatering and reinjection processes, the pore water pressure monitoring data for different burial depths at measurement points 1 to 6 were collated and analyzed, and the time-history variation curve of pore water pressure for different burial depths outside the foundation pit was obtained, as shown in Figure 10.

From Figure 10, it can be seen that when the vertical full well is reinjected at a significant depth, the impact on the reinjection of different burial depths within the reinjection depth range is significant. On the side of the reinjection well adjacent to the diaphragm wall, the positive change value of pore water pressure gradually increases toward the diaphragm wall. When the precipitation reinjection is stable, the maximum positive change values of the strata with different burial depths are 0.08 kPa, 0.1 kPa, 0.07 kPa, and 0.06 kPa, respectively. On the side away from the diaphragm wall, the positive change value of pore water pressure in different burial depths gradually decreases. When precipitation recharge is stable, the maximum positive change values in different buried depths are 0.025 kPa, 0.025 kPa, 0.03 kPa, and 0.04 kPa. When the positive change value of pore water pressure is less than 0.0125 kPa after the stabilization of precipitation reinjection, the water level of the soil layer is less affected by reinjection. It can be considered that the horizontal distance between the reinjection well and the corresponding formation position with the positive change value of pore water pressure of

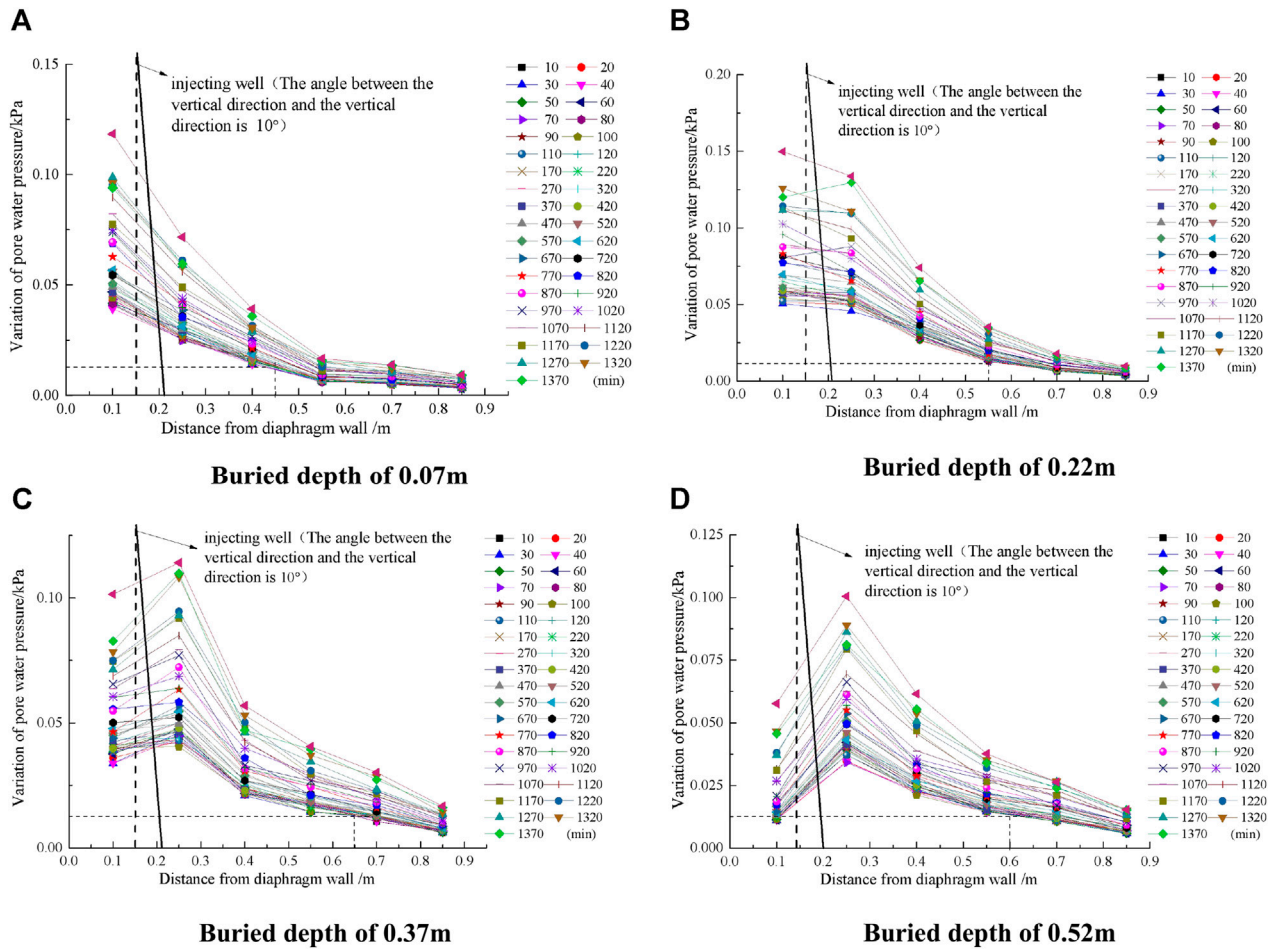

FIGURE 11
Time-history curves of pore water pressure in different depths.

0.0125 kPa is the main influence range of reinjection, and the average main influence range of reinjection for different burial depths of soil layers on the side away from the diaphragm wall is 0.3 m.

When the length of the recharge well is the same as the length of the precipitation well, it can provide certain recharge to groundwater and have a certain improvement effect on surface subsidence caused by precipitation. At the same time, vertical recharge can cause a significant increase in groundwater level in the area adjacent to the diaphragm wall, resulting in significant recharge effects. However, it can also cause significant uplift and deformation of the soil on the side adjacent to the diaphragm wall. For the side far from the ground wall, the range of recharge is small, and the increase in groundwater level caused by recharge is limited.

4.3 Analysis of test results in condition 3

After decreasing to the specified depth and stabilizing the dewatering and reinjection processes, the pore water pressure monitoring data for different burial depths at measurement points 7 to 12 were collated and analyzed, and the time-history variation curve of pore water pressure for different burial depths outside the foundation pit was obtained, as shown in Figure 11.

From Figure 11, it can be seen that when reinjection is carried out at a full well depth at an angle of 10° to the vertical direction, the impact of reinjection on different burial depths within the reinjection depth range is significant. On the side of the reinjection well adjacent to the diaphragm wall, the positive change value of pore water pressure gradually decreases toward the diaphragm wall. When precipitation reinjection is stable, the maximum positive change values of the strata with different burial depths are 0.025 kPa, 0.05 kPa, 0.04 kPa, and 0.03 kPa, respectively. On the side away from the diaphragm wall, except for the positive change value of pore water pressure in the strata with a burial depth of 0.07 m, the positive change value of pore water pressure in other strata first increases and then gradually decreases. When the precipitation recharge is stable, the maximum positive change values for the strata with different burial depths are 0.025 kPa, 0.05 kPa, 0.04 kPa, and 0.03 kPa. When the positive change value of pore water pressure after stabilization of precipitation recharge is less than 0.0125 kPa, the water level of the soil layer is less affected by recharge. It can be considered that the horizontal distance between the recharge well and the corresponding formation position with the

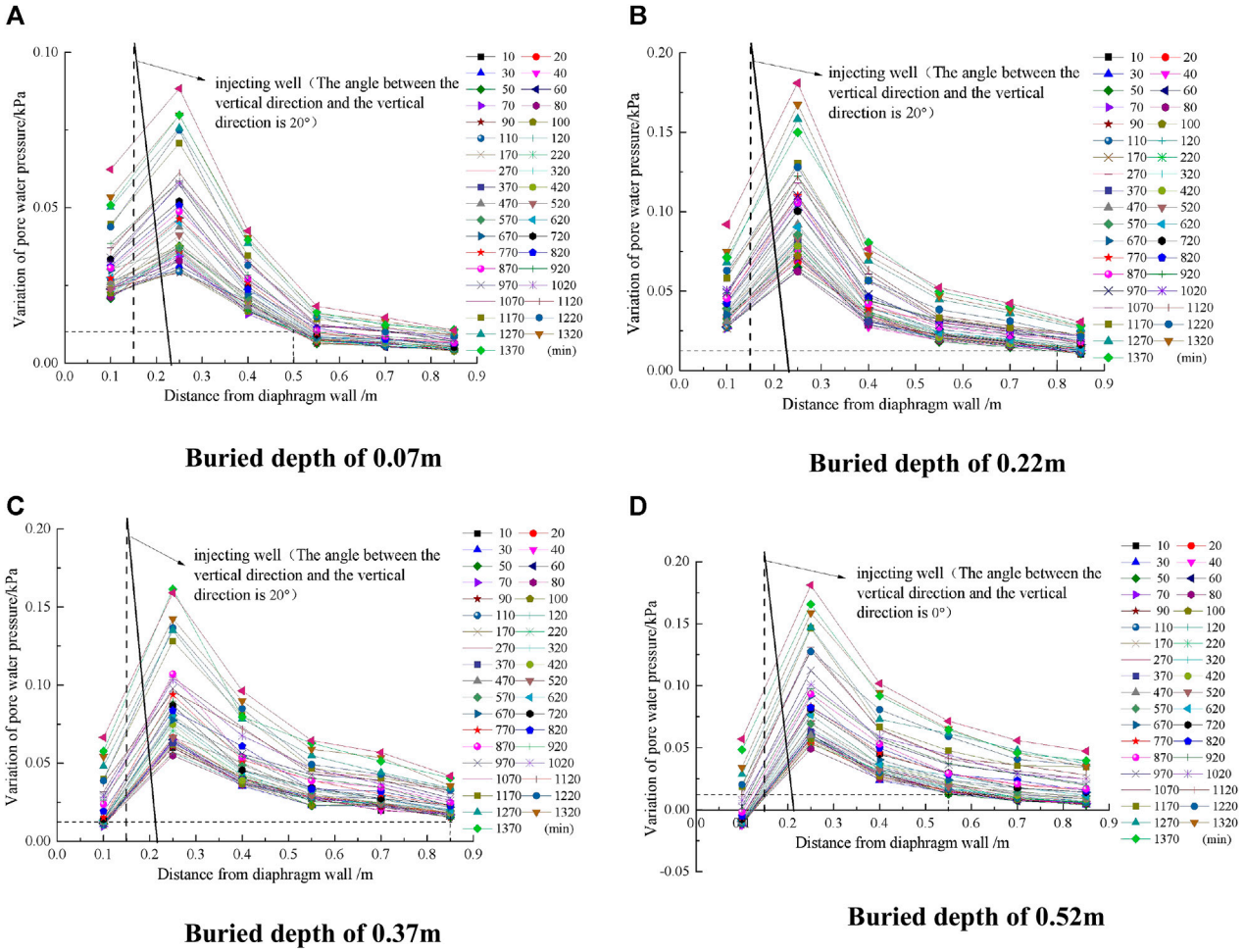

FIGURE 12
Time-history curves of pore water pressure in different depths.

positive change value of pore water pressure of 0.0125 kPa is the main influence range of recharge, and the average influence range of different burial depths of the soil layer far from the diaphragm wall is 0.4 m.

4.4 Analysis of test results in condition 4

After decreasing to the specified depth and stabilizing the dewatering and reinjection processes, the pore water pressure monitoring data for different burial depths at measurement points 7–12 were collated and analyzed, and the time-history variation curve of pore water pressure for different burial depths outside the foundation pit was obtained, as shown in Figure 12.

From Figure 12, it can be seen that when reinjection is carried out at a full well depth at an angle of 20° to the vertical direction, the impact of reinjection on different burial depths within the reinjection depth range is significant. On the side of the reinjection well adjacent to the diaphragm wall, the positive change value of pore water pressure gradually decreases toward the diaphragm wall. When precipitation reinjection is stable, the maximum positive change values of the strata with different burial depths are 0.02 kPa, 0.025 kPa, 0.012 kPa, and 0 kPa. On the side away from the diaphragm wall, the positive variation values of pore water pressure in different burial depths first increase and then gradually decrease. When the precipitation recharge is stable, the maximum positive variation values in different burial depths are 0.03 kPa, 0.07 kPa, 0.06 kPa, and 0.05 kPa. When the positive variation value of pore water pressure is less than 0.0125 kPa after the stabilization of precipitation and reinjection, the water level of the soil layer is less affected by reinjection. It can be considered that the horizontal distance between the reinjection well and the corresponding formation position with the positive variation value of pore water pressure of 0.0125 kPa is the main impact range of reinjection, and the average impact range of reinjection for different burial depths of soil layers on the side away from the diaphragm wall is 0.5 m.

4.5 Analysis of test results in condition 5

After decreasing to the specified depth and stabilizing the dewatering and reinjection processes, it is necessary to collate

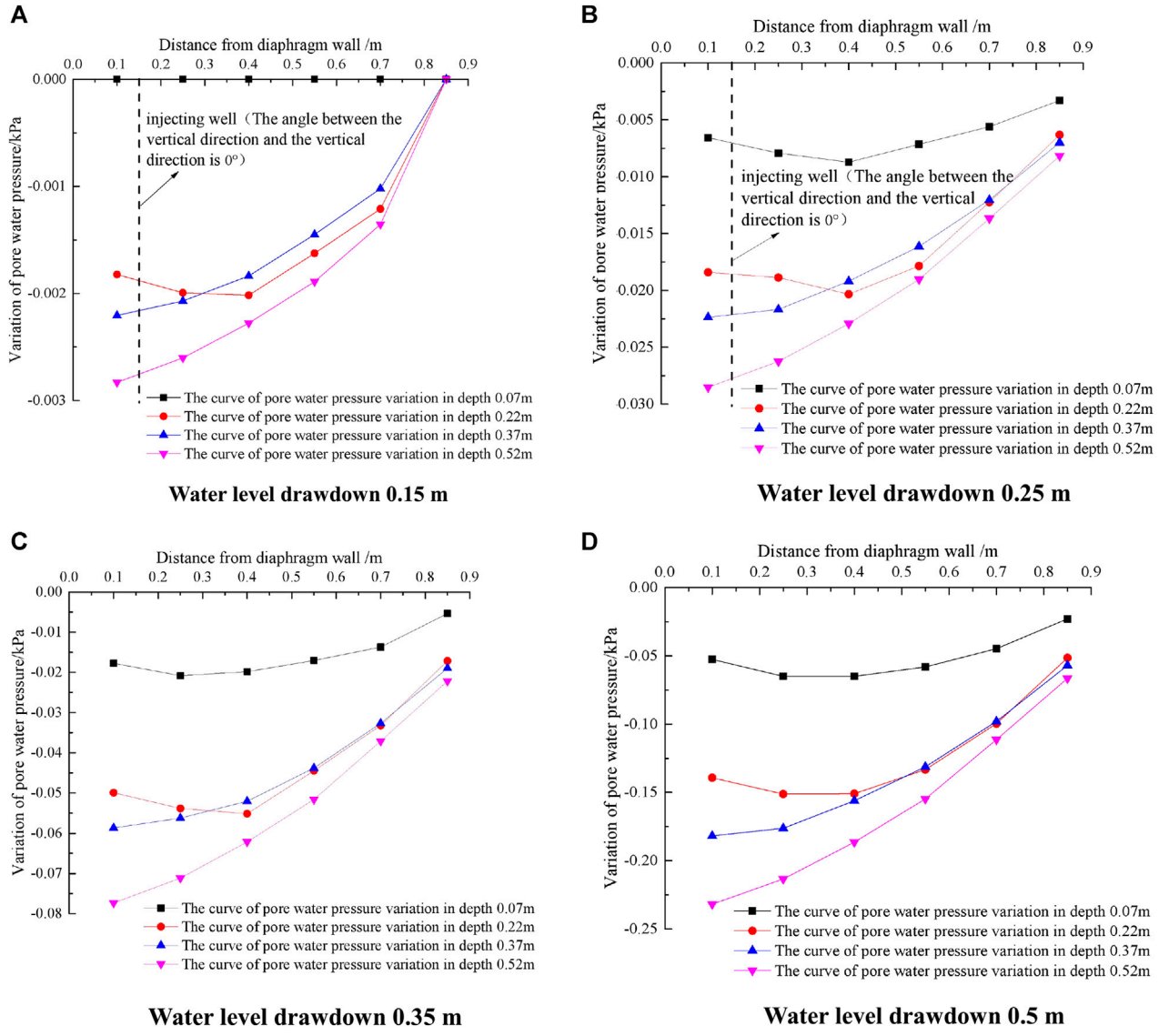

FIGURE 13
Variation curves of pore water pressure in each soil layer of different drawdown.

and analyze the monitoring data of pore water pressure at different depths of measurement points 1–6 and obtain the time-history change curve of pore water pressure at different depths outside the foundation pit, as shown in Figure 13.

From Figure 13, it can be seen that during the reinjection process at 1/2 well depth, when the water level does not decrease beyond the reinjection depth, the reinjection has a significant impact on the changes in pore water pressure in the soil layer. The negative change in pore water pressure gradually decreases toward the diaphragm wall side of the reinjection well, while the negative change in pore water pressure gradually decreases away from the diaphragm wall side. When the drawdown exceeds the reinjection depth, the pore water pressure changes in silty clay similar formations and gravelly clay similar formations located within the reinjection depth are less affected by reinjection, and the pore water pressure changes in completely weathered granite similar strata and strongly weathered granite similar strata located outside the reinjection depth are basically the same as those without reinjection.

4.6 Analysis of test results in condition 6

After decreasing to the specified depth and stabilizing the dewatering and reinjection processes, the pore water pressure monitoring data for different depths at measurement points 1 to 6 were collated and analyzed, and the time-history variation curve of pore water pressure for different depths outside the foundation pit was obtained, as shown in Figure 14.

From Figure 14, it can be seen that when the vertical full well depth layered dehydration and reinjection are stable, the positive change value of pore water pressure at different burial depths increases with the increase in the dehydration and reinjection

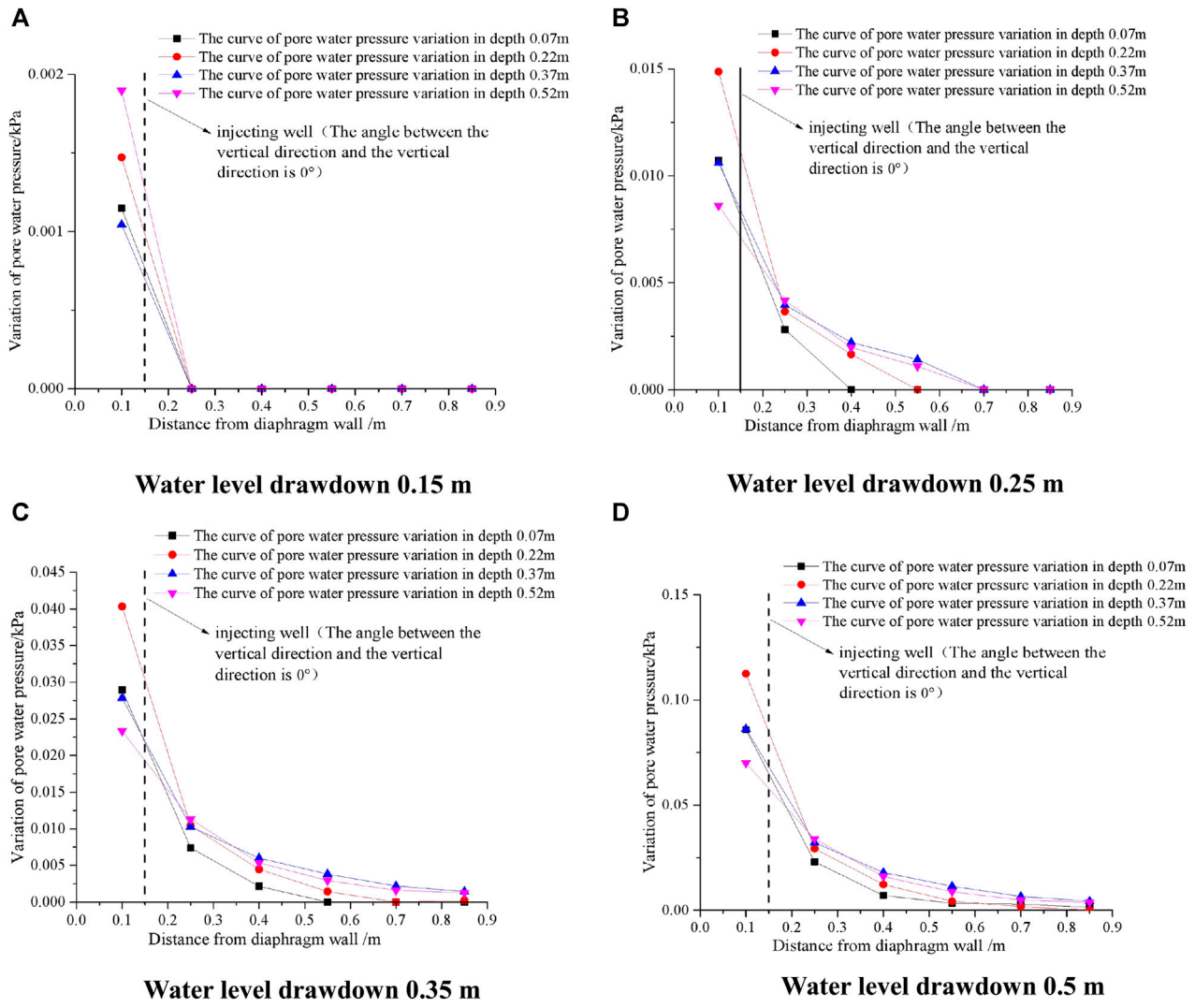

FIGURE 14
Variation curves of pore water pressure in each soil layer of different drawdown.

depth. When the dewatering and reinjection depth is 0.5 m, the positive change value of pore water pressure in different burial depths reaches the maximum. The positive change value of pore water pressure gradually decreases toward the diaphragm wall side of the reinjection well. The maximum positive change values for different precipitation reinjection depths are 0.002 kPa, 0.015 kPa, 0.04 kPa, and 0.11 kPa, respectively. On the side away from the diaphragm wall, the positive change value of pore water pressure gradually decreases toward the direction away from the diaphragm wall, and the maximum positive change values for different precipitation reinjection depths are 0 kPa, 0.004 kPa, 0.012 kPa, and 0.025 kPa.

When the positive change value of pore water pressure after the stabilization of the precipitation recharge is 0 kPa, the formation water level is less affected by recharge. It can be considered that the horizontal distance between the recharge well and the corresponding formation position with the positive change value of pore water pressure of 0 kPa is the main influence range of recharge, and the influence range of soil recharge at different precipitation recharge depths on the side away from the diaphragm wall is 0.1 m, 0.25 m, 0.4 m, and 0.4 m.

4.7 Analysis of test results in condition 7

After decreasing to the specified depth and stabilizing the dewatering and reinjection processes, the pore water pressure monitoring data for different drawdowns at measurement points 7–12 were collated and analyzed, and the variation curve of pore water pressure for different drawdowns outside the foundation pit after stabilizing the dewatering process was obtained, as shown in Figure 15.

From Figure 15, it can be seen that the layered dehydration and reinjection of the full well depth are stable at an angle of 10° to the vertical direction, and the positive changes in pore water pressure at different burial depths increase with the increase in the dehydration

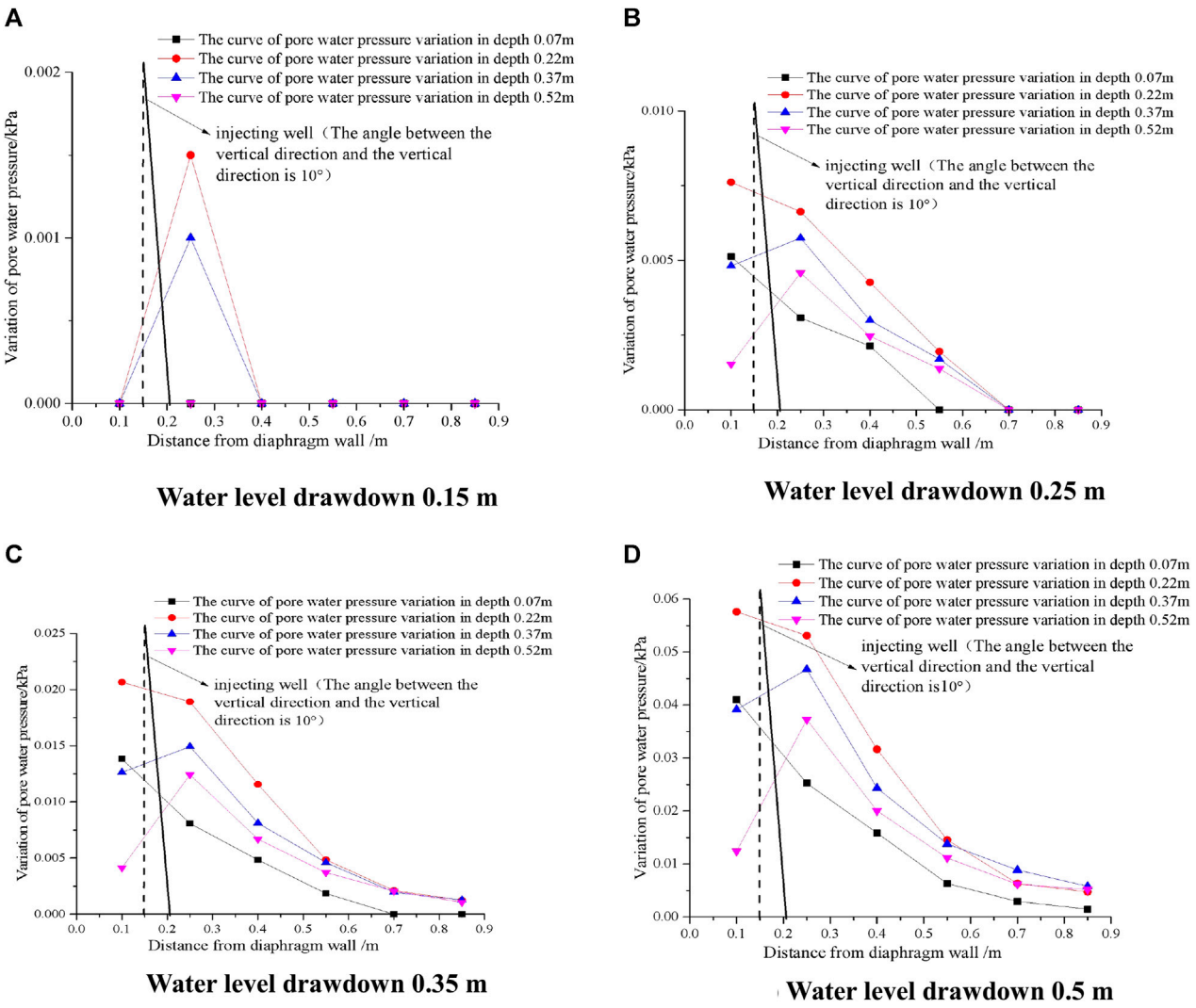

FIGURE 15
Variation curves of pore water pressure in each soil layer of different drawdown.

and reinjection depth. When the dewatering and reinjection depths are 0.5 m, the positive variation value of pore water pressure in different burial depths reaches the maximum. The positive change value of pore water pressure gradually decreases toward the diaphragm wall when the reinjection well is close to the diaphragm wall. The maximum positive change values for different precipitation reinjection depths are 0 kPa, 0.005 kPa, 0.02 kPa, and 0.06 kPa. The positive change value of pore water pressure gradually decreases toward the direction away from the diaphragm wall when the reinjection well is away from the diaphragm wall. The maximum positive change values for different precipitation reinjection depths are 0.001 kPa, 0.004 kPa, 0.02 kPa, and 0.055 kPa.

When the positive change value of pore water pressure after the stabilization of precipitation recharge is 0 kPa, the formation water level is less affected by recharge. It can be considered that the horizontal distance between the recharge well and the corresponding formation position with the positive change value of pore water pressure of 0 kPa is the main influence range of recharge. The influence ranges of soil recharge at different precipitation recharge depths on the side away from the diaphragm wall are 0.25 m, 0.4 m, 0.55 m, and 0.65 m.

4.8 Analysis of test results in condition 8

After decreasing to the specified depth and stabilizing the dewatering and reinjection processes, the pore water pressure monitoring data for different burial depths at measurement points 7–12 were collated and analyzed, and the pore water pressure change curve for different burial depths outside the foundation pit after stabilizing the dewatering process was obtained, as shown in Figure 16.

From Figure 16, it can be seen that when the vertical angle is 20°, the positive change value of pore water pressure in different burial depths of soil layers increases with the increase in the precipitation

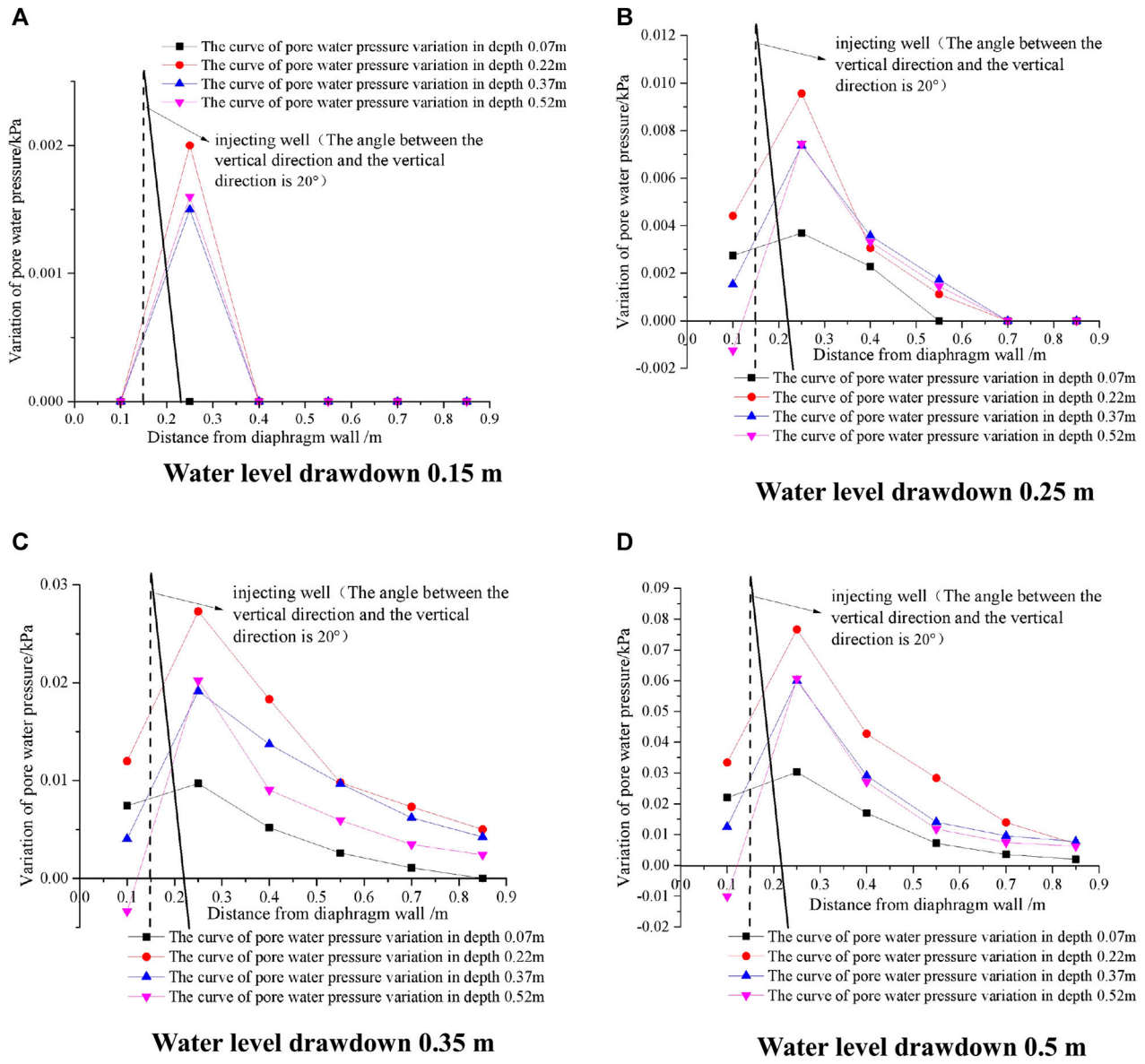

FIGURE 16
Variation curves of pore water pressure in each soil layer of different drawdown.

and reinjection depth. When the depth of precipitation and reinjection is 0.5 m, the positive variation value of pore water pressure in the soil layers with different burial depths reaches the maximum. The positive change value of pore water pressure gradually decreases toward the diaphragm wall when the reinjection well is close to the diaphragm wall. The maximum positive change values for different precipitation reinjection depths are 0 kPa, 0.004 kPa, 0.01 kPa, and 0.03 kPa. The positive change value of pore water pressure gradually decreases toward the direction away from the diaphragm wall when the reinjection well is away from the diaphragm wall. The maximum positive change values for different precipitation reinjection depths are 0.002 kPa, 0.01 kPa, 0.03 kPa, and 0.08 kPa.

When the positive change value of pore water pressure after stabilization of precipitation recharge is 0 kPa, the formation water level is less affected by recharge. It can be considered that the horizontal distance between the recharge well and the corresponding formation position with the positive change value of pore water pressure of 0 kPa is the main influence range of recharge. The influence ranges of soil recharge at different precipitation recharge depths on the side away from the diaphragm wall are 0.24 m, 0.4 m, 0.7 m, and 0.7 m.

5 Conclusion

Based on the model experiment of foundation pit dewatering in the phreatic layer, the focus was on studying the changes in water level outside the foundation pit and surface settlement caused by dewatering inside the phreatic layer foundation pit. The following conclusions are drawn:

(1) By studying the incomplete precipitation inside the foundation pit within the depth range of the underground continuous wall, the variation curve of the outer water level of the foundation pit is "concave first and then convex," which is different from the Dupuit theory precipitation curve form.
(2) For the case of a large amount of precipitation in a layered soil foundation pit, as the depth of the soil layer increases, the curve of downward depression of precipitation outside the foundation pit is smaller, and the curve of the downward depression of the precipitation at the bottom of the retaining wall is the smallest. For layered dewatering of foundation pits, with the increase in precipitation, the variation value of pore water pressure in the soil layer outside the underground continuous wall gradually increases.
(3) Compared with vertical reinjection adjacent to dense buildings, inclined reinjection has a smaller impact on the side near the retaining wall and a greater impact on the side away from the retaining wall. Among them, the full well deep reinjection well with an angle of 20° from the vertical direction has the largest reinjection range and the best reinjection effect.

Data availability statement

The original contributions presented in the study are included in the article/Supplementary Material; further inquiries can be directed to the corresponding authors.

Author contributions

There are some authors in this manuscript and each one has contributed properly. The mathematical model has been proposed and all the numerical computations and their graphs have been carried out by QY, the final review and amendments in the manuscript have been carried out by SC, and YY has performed corresponding work on revising and polishing the paper. All authors contributed to the article and approved the submitted version.

Funding

This study is supported by the National Science Fund (52272341) and Guangzhou Panyu Polytechnic project (XJ2023000601) and funded by the Science and Technology Project of Hebei Education Department (QN2023060), the National Pre-research Funds of Hebei GEO University in 2023 (KY202305), and the Technology Innovation Team Project of Hebei GEO University (KJCXTD-2021-08).

Conflict of interest

The authors declare that the research was conducted in the absence of any commercial or financial relationships that could be construed as a potential conflict of interest.

Publisher's note

All claims expressed in this article are solely those of the authors and do not necessarily represent those of their affiliated organizations, or those of the publisher, the editors, and the reviewers. Any product that may be evaluated in this article, or claim that may be made by its manufacturer, is not guaranteed or endorsed by the publisher.

References

Bai, B., Jiang, S. C., Liu, L. L., Li, X., and Wu, H. Y. (2021). The transport of silica powders and lead ions under unsteady flow and variable injection concentrations. *Powder Technol.* 387, 22–30. doi:10.1016/j.powtec.2021.04.014

Gambolati, G., and Teatini, P. (2015). Geomechanics of subsurface water withdrawal and injection. *Water Resour. Res.* 51 (6), 3922–3955. doi:10.1002/2014wr016841

Huang, Y. H., Lu, Y. J., Zhou, Y., and Zhao, J. T. (2009). A method for estimating land subsidence induced by groundwater extraction and its application to site evaluation of Yizhuang light railway in Beijing. *ROCK SOIL Mech.* 30 (8), 2457–2462.

Huang, Y., Yang, Y., and Li, J. (2015). Numerical simulation of artificial groundwater recharge for controlling land subsidence. *KSCE J. Civ. Eng.* 19, 418–426. doi:10.1007/s12205-015-0505-y

Li, M. G., Chen, J. J., Xia, X. H., Zhang, Y. Q., and Wang, D. F. (2020). Statistical and hydro-mechanical coupling analyses on groundwater drawdown and soil deformation caused by dewatering in a multi-aquifer-aquitard system. *J. Hydrology* 589, 125365. doi:10.1016/j.jhydrol.2020.125365

Meinzer, O. E. (1928). Compressibility and elasticity of artesian aquifers. *Econ. Geol.* 23 (3), 263–291. doi:10.2113/gsecongeo.23.3.263

Roy, D., and Robinson, K. E. (2009). Surface settlements at a soft soil site due to bedrock dewatering. *Eng. Geol.* 107 (3-4), 109–117. doi:10.1016/j.enggeo.2009.05.006

Wang, J., Wu, Y., Zhang, X., Liu, Y., Yang, T., and Feng, B. (2012). Field experiments and numerical simulations of confined aquifer response to multi-cycle recharge–recovery process through a well. *J. Hydrology* 464, 328–343. doi:10.1016/j.jhydrol.2012.07.018

Wang, J. X., Wu, L. G., Zhu, Y. F., Tang, Y., Yang, P., and Lou, R. (2009). Mechanism of dewatering-induced ground subsidence in deep subway station pit and calculation method. *Chin. J. Rock Mech. Eng.* 28 (5), 1010–1019.

Wu, Y. Q., and Zhu, Y. P. (2016). Calculation of settlement considering unsaturated soil influence on the dewatering of foundation pits. *Eng. Mech.* 33 (3), 179–187.

Wu, Y. X., Shen, S. L., Lyu, H. M., and Zhou, A. (2020). Analyses of leakage effect of waterproof curtain during excavation dewatering. *J. Hydrology* 583, 124582. doi:10.1016/j.jhydrol.2020.124582

Xu, Y. S., Shen, S. L., Ma, L., Sun, W. J., and Yin, Z. Y. (2014). Evaluation of the blocking effect of retaining walls on groundwater seepage in aquifers with different insertion depths. *Eng. Geol.* 183, 254–264. doi:10.1016/j.enggeo.2014.08.023

Xu, Y. S., Yan, X. X., Shen, S. L., and Zhou, A. N. (2019). Experimental investigation on the blocking of groundwater seepage from a waterproof curtain during pumped dewatering in an excavation. *Hydrogeology J.* 27 (7), 2659–2672. doi:10.1007/s10040-019-01992-3

Yu, J. L., and Gong, X. N. (2001). Study on the design and the application of the groundwater recharge system in excavation. *J. Build. Struct.* 22 (5), 70–74.

Yuan, H., and Zhang, Q. (2013). Estimation method for surface subsidence induced by dewatering under the constraint of lateral friction. *J. Shanghai Jiaot. Univ.* 47 (08), 1328.

Zeng, C. F., Zheng, G., Zhou, X. F., Xue, X. L., and Zhou, H. Z. (2019). Behaviours of wall and soil during pre-excavation dewatering under different foundation pit widths. *Comput. Geotechnics* 115, 103169. doi:10.1016/j.compgeo.2019.103169

Zhang, W. G., Goh, A. T. C., Goh, K. H., Chew, O. Y. S., Zhou, D., and Zhang, R. (2018). Performance of braced excavation in residual soil with groundwater drawdown. *Undergr. Space* 3 (2), 150–165. doi:10.1016/j.undsp.2018.03.002

Zhang, Y. Q., Li, M. G., Wang, J. H., Chen, J. J., and Zhu, Y. F. (2017). Field tests of pumping-recharge technology for deep confined aquifers and its application to a deep excavation. *Eng. Geol.* 228, 249–259. doi:10.1016/j.enggeo.2017.08.019

Zheng, G., Zeng, C. F., Diao, Y., and Xue, X. L. (2014). Test and numerical research on wall deflections induced by pre-excavation dewatering. *Comput. Geotechnics* 62, 244–256. doi:10.1016/j.compgeo.2014.08.005

frontiers | Frontiers in Materials

TYPE Original Research
PUBLISHED 19 June 2023
DOI 10.3389/fmats.2023.1225258

OPEN ACCESS

EDITED BY
Xianze Cui,
China Three Gorges University, China

REVIEWED BY
Yuqi Wu,
China University of Petroleum, China
Yukun Zhanh,
Shandong, China

*CORRESPONDENCE
Guoqi Xing,
xgq1105@163.com

RECEIVED 19 May 2023
ACCEPTED 02 June 2023
PUBLISHED 19 June 2023

CITATION
Xing G, Cao Y, Zhang B, Li J and Zhang X (2023), Influence of parameters on the ultimate penetration depth of a double-plate vertically loaded anchor in soft clay. *Front. Mater.* 10:1225258. doi: 10.3389/fmats.2023.1225258

Influence of parameters on the ultimate penetration depth of a double-plate vertically loaded anchor in soft clay

Guoqi Xing[1]*, Yupeng Cao[1], Baoliang Zhang[2], Jian Li[2] and Xiaotong Zhang[1]

[1]School of Civil and Architectural Engineering, Weifang University, Weifang, Shandong, China, [2]School of Civil and Architectural Engineering, Liaocheng University, Liaocheng, Shandong, China

To make a new type of double-plate vertically loaded anchor (DPVLA) penetrate into clay deeper, the influence of parameters on the ultimate penetration depth of DPVLAs in soft clay should be investigated. The expression of the ultimate penetration depth applicable to DPVLAs in clay was determined in terms of the formula of the ultimate penetration depth of anchors with a wedge-shaped section. Based on the drag penetration tests, the movement direction of the bottom fluke of DPVLAs with different lengths of the bottom fluke and different included angles was obtained. By the finite-element method, the upper bound solutions of bearing capacity factors of DPVLAs with different included angles and different lengths of the bottom flukes were also obtained, which correspond to the maximum penetration depth induced by the initial orientation of the anchor. According to the determined expression of the ultimate penetration depth of DPVLAs, the ultimate penetration depth of DPVLAs with different included angles and different lengths of the bottom fluke in clay can be calculated. The results showed that increasing the length of the bottom fluke can increase the ultimate penetration depth when the included angles were the same for DPVLAs not only in the clay with zero strength at the seabed but also in the clay with uniform strength. However, when the length of the bottom fluke is the same, increasing the included angle of DPVLAs in clay can significantly reduce the ultimate penetration depth.

KEYWORDS

ultimate penetration depth, double-plate vertically loaded anchor, included angle, length of a bottom fluke, soft clay

1 Introduction

Vertically loaded anchors (VLAs) are widely employed in the mooring system for deep waters platforms due to the high pullout capacity and low installation cost of VLAs (Aubeny, and Murff, 2005; Aubeny and Chi, 2010). In addition, VLAs can simultaneously withstand horizontal and vertical loads compared with the conventional drag embedment anchors which only withstand the horizontal load (Yang et al., 2010). When VLAs are penetrated into the specified position in the seabed, then the anchor line can be reconfigured to be normal to the fluke, which induces a higher pullout capacity than the conventional drag embedment anchors (Tian et al., 2015). To enhance the pullout capacity of VLAs, the area of the anchor plate of VLAs should be increased. However, the larger area of the anchor plate cannot be conveniently penetrated into the seabed (Liu et al., 2010b). Therefore, it is not feasible to only

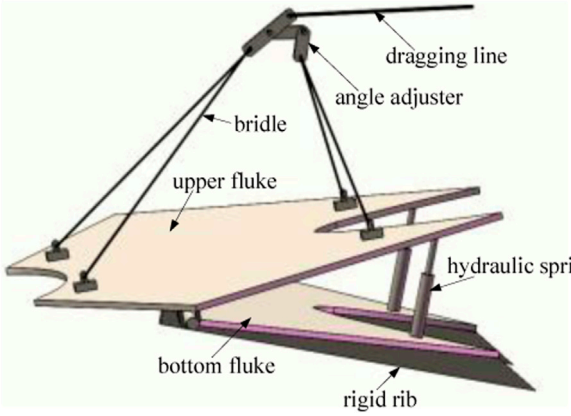

FIGURE 1
Double-plate vertically loaded anchors (Xing et al.,2020).

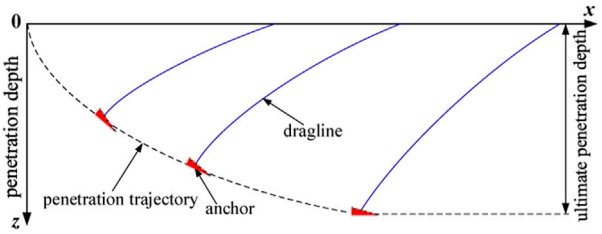

FIGURE 2
Penetration trajectory of the anchor in soil.

increase the area of the anchor plate to increase the pullout capacity of VLAs. To effectively increase the pullout capacity of anchors, a new type of anchor was put forward by the authors, as illustrated in Figure 1 (Xing et al., 2020). Furthermore, experiments have been carried out to find that the ultimate loading capacity of double-plate VLAs (DPVLAs) in the sand is greater than that of VLAs by about 30.0% (Xing et al., 2021). In addition, it is also found that the ultimate loading capacity increases with the increase in included angle. However, when the included angle of the DPVLA is greater than 30°, it cannot conveniently penetrate into the soil in model tests (Xing et al., 2021). In the follow-up studies, the authors improve the dragging penetration method, which can make the included angle greater than 30° in the penetration tests. The improved dragging penetration method will be introduced in the following section.

The ultimate loading capacity of anchors is related to the ultimate penetration depth as shown in Figure 2, and the deeper the anchor penetrates, the higher the ultimate loading capacity (O'Neill et al., 1997). Therefore, the ultimate penetration depth is an important parameter for anchors, and some researchers have investigated it (Neubecker and Randolph, 1995; Neubecker and Randolph, 1996; Ruinen and Degenkamp, 2002; Miedema et al., 2007; Liu et al., 2010a).

Currently, empirical design charts are widely used to evaluate the ultimate penetration depth of anchors in clay and sand (NCEL, 1987; Vryhof Anchors, 2005). However, the empirical design charts do not take into account the properties of the soil, anchor, and dragline, and they cannot ensure the accuracy of prediction of the ultimate penetration depth of anchors.

Ruinen and Degenkamp (2002) and Miedema et al. (2007) employed numerical calculation methods to reveal some parameters influencing the ultimate penetration depth. However, the results showed that the differences in the prediction results of the ultimate penetration depth were substantial because numerical procedures used by the predictors were different (Murff et al., 2005). The studies indicate that numerical calculation methods are not credible in predicting the ultimate penetration depth.

For the soft clay with the strength represented by $S_u = S_{u0} + kz$, where z is the penetration depth below the seabed and S_{u0} is the shear strength of clay at the surface of the seabed, the following empirical expression was derived to estimate the ultimate penetration depth (Ruinen and Degenkamp, 2001; Vryhof Anchors, 2005):

$$Z_{UED} = 1.5k^{0.6}d^{-0.7}A^{0.3}(\tan\theta_s)^{1.7}, \quad (1)$$

where Z_{UED} represents the ultimate penetration depth; k is the gradient of undrained shear strength of clay with depth; d is the diameter of embedded draglines; A is the fluke area of the anchor; and θ_s is the angle of the shank to the top surface of the fluke of an anchor. It is also illustrated that Eq. 1 does not consider soil conditions, the type of the anchor, the type and size of the anchor forerunner, the fluke angle of the anchor, and the uplift angle at the surface of the seabed. Therefore, Eq. 1 is not widely applied up to now.

For the soft clay with the strength represented by $S_u = S_0(\frac{z}{z_0})^{\xi}$, where s_0 is the shear strength of the clay at the reference depth z_0 and ξ represents the exponent, Neubecker and Randolph (1995) and Neubecker and Randolph (1996) derived the expression of the ultimate penetration depth of anchor as follows:

$$Z_{UED} = \frac{(\xi+1)fA_p\theta_w}{2b.\cos\theta_w}\left(\theta_w + \frac{2}{\eta_w}\right), \quad (2)$$

where f is the form factor of the anchor; b is the effective width of the embedded dragline; θ_w is the drag angle to the fluke at the shackle of the weightless anchor; A_p is the projected anchor area; and η_w is the efficiency factor, which can be expressed as $\eta_w = T_w/W$, where W is the submerged weight of the anchor and T_w is the drag force at the shackle of the weightless anchor. Therefore, if the abovementioned parameters are known, the ultimate penetration depth of anchors can be calculated with Eq. 2. However, Eq. 2 does not apply the most common strength profile because the expression of the strength of the clay is only suitable for the soil with strength $S_u = S_0(\frac{z}{z_0})^{\xi}$. In addition, the form factor of the anchor, f, cannot be exactly obtained (O'Neill et al., 1997; O'Neill and Randolph, 2001).

By analyzing the equilibrium forces acting on the anchor and embedded dragline, and the interaction between them at the ultimate penetration depth, Liu et al. (2010a) derived the concise expressions of the ultimate penetration depth of VLAs in soft clay as follows:

$$z_{UED} = \Delta z - \frac{s_{u0}}{k} + m + \sqrt{\left(\frac{s_{u0}}{k}\right) + m^2 + 2m\Delta z}, \quad (3)$$

where $m=(m_1A_b + m_2A_s)/(2b)$ $m_1 = N_{cf}(\theta_a\text{-}\theta_m)^2/[N_{cl}\cos(\theta_a\text{-}\theta_m)]$ $m_2 = \alpha_f(\theta_a\text{-}\theta_m)^2/[N_{cl}\cos(\theta_a\text{-}\theta_m)]$, in which Δz is the distance from

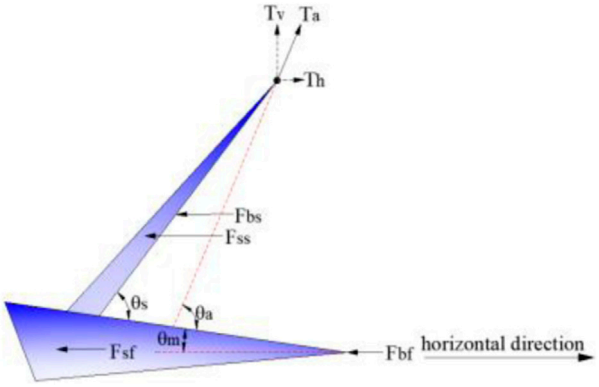

FIGURE 3
Diagram of resistant force acting on the anchor in the horizontal direction at the ultimate penetration depth (Liu et l.,2010a).

the shackle to the plane of the anchor fluke; A_b is the total projected area of the anchor at the ultimate penetration depth onto the plane perpendicular to the horizontal, including the shank and fluke; and A_s is the total shear area of the anchor at the ultimate penetration depth along the horizontal, including the shank and fluke. N_{cf} and N_{cl} are the bearing capacity factors of the anchor and dragline in clay, respectively; θ_a and θ_m are the drag angle to the top surface of the fluke and the angle of the top surface of the fluke to the movement direction at the ultimate penetration depth, respectively; and α_f represents the adhesion factor of the anchor. In addition, Eq. 3 was examined by other prediction formulas, and the credibility of the expression of the ultimate penetration depth of anchors in clay has been verified.

For the new type of anchor-DPVLA, it is very necessary to reveal the ultimate penetration depth and the influence of parameters on the ultimate penetration depth of DPVLAs. In this paper, the expression of the ultimate penetration depth applicable to DPVLAs in clay was determined and two parameters, such as the included angle and the length of bottom fluke, relating to the ultimate penetration depth of DPVLAs were obtained through laboratory model test and finite-element analysis. Moreover, the influence of the included angle and the length of the bottom fluke of DPVLAs was investigated based on the determined expression of the ultimate penetration depth.

2 Ultimate penetration depth applicable to DPVLA in clay

2.1 Improved penetration method for DPVLA in soil

When the anchor is dragged into the position of the ultimate penetration depth, the resistant force acting on the anchor is shown in Figure 3, where T_a represents the drag force at the shackle; T_v and T_h are the vertical and horizontal components of T_a, respectively; F_{bs} and F_{bf} are the end bearings on the shank and fluke in the horizontal, respectively; F_{ss} and F_{sf} are shear forces on the shank and fluke in the horizontal, respectively; and θ_m represents the angle of the top surface of the fluke to the horizontal. Based on the abovementioned forces acting on the anchor and embedded dragline in Figure 3, Liu et al. (2010a) derived the expression of the ultimate penetration depth of the anchor in soft clay as Eq. 3.

To make the included angle of DPVLAs greater than 30° and make it conveniently penetrate the soil, an improved penetration method was put forward, as illustrated in Figure 4. As shown in Figure 4A, the installation method in the first stage is the same as the conventional anchors. In the first stage of installation, the soil is filled in the space between the upper and bottom flukes, as illustrated in Figure 5, and the shape of DPVLAs in the ultimate penetration depth is similar to that of anchors with a wedge-shaped section in Figure 3. Therefore, the improved penetration method of DPVLAs also contributes to the penetration of anchors. In the second stage of installation, when the anchor is dragged to the ultimate penetration depth, then the DPVLA moves in the opposite direction of movement, as shown in Figure 4B, which can induce the increase of the included angle of DPVLAs, i.e., improve the ultimate pullout capacity of DPVLAs (Xing et al., 2021). Therefore, the modified penetration method not only contributes to the penetration of DPVLAs in soil but also improves the ultimate pullout capacity of DPVLAs.

2.2 Ultimate penetration depth applicable to DPVLAs in clay

The resistant forces acting on the DPVLA in Figure 5A are almost the same as those in Figure 3 except that the shear forces acting on the upper and bottom flukes of the DPVLA in the horizontal, F_{sfu} and F_{sfb}, in Figure 5A. Since the shape and the resistant forces of DPVLAs are almost the same as that of anchors with a wedge-shaped section in the improved penetration method, Eq. 3 can be considered to be also applicable to the DPVLA at the ultimate penetration depth. However, the effective shear area of DPVLAs, A_s, is different from that of VLAs in Eq. 3, which can be expressed as the sum of the effective shear area of the upper and bottom flukes, i.e., $A_s = A_{su} + A_{sb}$.

Since DPVLAs is a new type of anchor, the bearing capacity factors of the DPVLA in clay are also different from those of the conventional dragging anchor. Therefore, the bearing capacity factor, N_{cf}, applicable to VLAs in Eq. 3, should be replaced by the bearing capacity factors of DPVLAs in clay, N_{cd}. In the following section, the bearing capacity factors of the DPVLA in clay will be discussed. For the lack of knowledge of the bearing capacity factor, Liu et al.(2010a) adopted $N_{cf} = N_{cl}$ in Eq. 3. In this section, the bearing capacity factors of DPVLAs and dragline, N_{cd} and N_{cl}, are also not distinguished, i.e., $N_{cd} = N_{cl}$. Therefore, the expressions of m_1 and m_2 in Eq. 3 can be revised as follows:

$$m_1 = N_{cd}(\theta_a - \theta_m)^2 \Big/ [N_{cd}\cos(\theta_a - \theta_m)], \quad (4)$$

$$m_2 = \alpha_f(\theta_a - \theta_m)^2 \Big/ [N_{cd}\cos(\theta_a - \theta_m)]. \quad (5)$$

When $\eta = \frac{s_{uo}}{kb}$ is defined, Eq. 3 can be further represented as follows:

$$z_{UED} = \Delta z - \eta b + m + \sqrt{(\eta b) + m^2 + 2m\Delta z}. \quad (6)$$

In this paper, we only discuss two special cases of clay; the first, $s_{uo} = 0$ or $\eta = 0$, and Eq. 6 can be further simplified as follows:

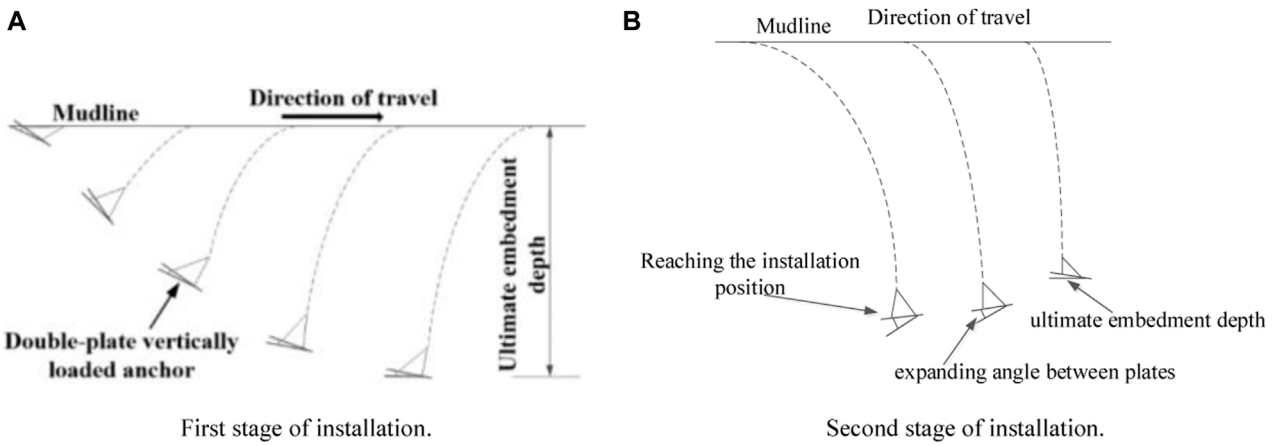

FIGURE 4
Installation method for DPVLAs in the seabed. **(A)** First stage of installation. **(B)** Second stage of installation.

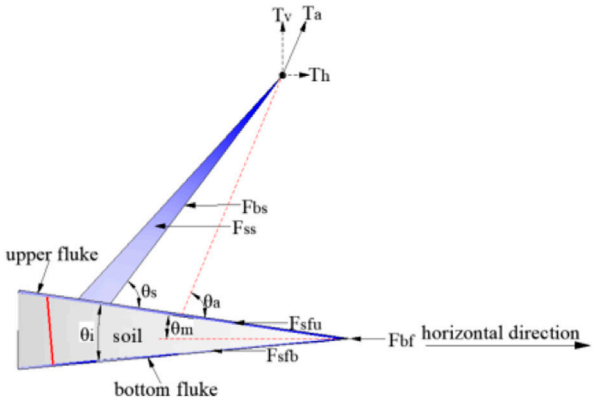

FIGURE 5
Improved penetration method for DPVLAs.

$$z_{UED} = \Delta z + m + \sqrt{m^2 + 2m\Delta z}, \quad (7)$$

and the second, the strength of clay is uniform; in this case, $k = 0$ or $\eta = \infty$, and Eq. 6 can be simplified as follows:

$$Z_{UED} = \Delta z + m. \quad (8)$$

2.3 Movement directions of the bottom fluke of DPVLA models

It is shown in Eq. 6 that the movement direction, θ_m, of the bottom fluke of DPVLAs at the ultimate penetration depth is an important parameter; therefore, it should be determined. For the VLA with a wedge-shaped section, Liu et al. (2010a) carried out experiments to investigate the possible movement directions of the fluke at the ultimate penetration depth and found that the accurate direction of movement of the fluke was difficult to obtain. In this section, through the laboratory model tests, the movement direction of the bottom fluke of DPVLAs with different lengths of the bottom fluke and different included angles in clay at the ultimate penetration depth was determined.

2.3.1 Anchor model

To investigate the influence of the length of the bottom fluke of DPVLAs on the movement directions of the bottom fluke at the ultimate penetration depth, the length of the bottom fluke of DPVLA models was set to 80 mm, 100 mm, and 120 mm, respectively. In addition, the width of the bottom fluke of DPVLA models was all set to 120 mm. For the dimensions of the upper bottom of DPVLA models, they were all set such that the length and width of the upper fluke were all 120 mm. Moreover, the thickness of the fluke was set to 2.0 mm.

To investigate the influence of the included angle of DPVLAs on the movement directions of bottom fluke at the ultimate penetration depth, the included angle (angle between the upper and bottom fluke) of DPVLA models was set 10°, 20°, and 30°, respectively. The magnitude of the included angle was controlled by a bolt as shown in Figure 6. One end of the bolt was connected to the bottom fluke, which can rotate about the bottom fluke; the other end of the bolt passed through the upper fluke, and the screw nut was on the end of the bolt, which can adjust the length of the bolt.

2.3.2 Model experimental system

Figures 7A–C show the drag penetration test system for the DPVLAs, which includes an experimental flume, drag system, measurement system, and data acquisition system.

In the drag penetration test system, water and fine sand were filled in the experimental flume to simulate the seabed environment. In the drag penetration test, DPVLA models penetrated the simulated seabed environment by the dragging force, then gradually increasing to reach the maximum penetration depth in the experimental flume, as illustrated in Figure 7A. Since the height of fine sand should exceed 5.0B (where B represents the length of anchor fluke, i.e., 120 mm) (Ruinen and Degenkamp, 2001), and the

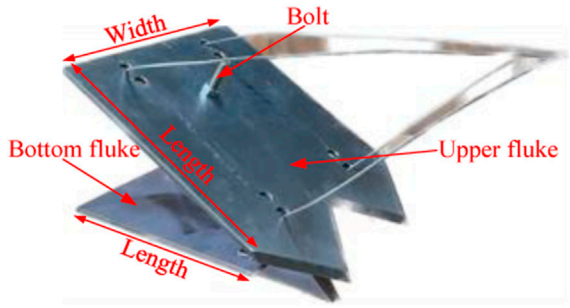

FIGURE 6
DPVLA model used in tests.

height of water above the fine sand surface did not exceed 500 mm, the height of the experimental flume in the drag penetration test system was set to 1,200 mm. To avoid side effects, the width of the experimental flume should be sufficiently wide (i.e., greater than 6.0*B*) (Liu et al., 2010b) so that the side walls of the experimental flume cannot influence the penetration of DPVLA models; therefore, the width of the experimental flume was set to 1,000 mm. To ensure that the DPVLA model could reach the ultimate penetration depth, the length of the experimental flume should be sufficiently long. Murff et al. (2005) considered that the length of the experimental flume should exceed 30.0*B*; therefore, it was set to 4,000 mm in the drag penetration test system.

In addition, to control the water level and drain, four drain valves were installed at the bottom of the experimental flume. Moreover, gravels with the particle size range of 15–20 mm were scattered uniformly to the bottom of the flume with about 6.0 cm thickness, and it can ensure that the water level uniformly dropped during drainage by opening the valves.

The drag system was used to exert the dragging force by using an electric motor, and the dragging force was applied to the DPVLA models through a steel wire, as illustrated in Figure 7A. The electric motor can control the dragging speed of the DPVLA models, and the dragging speed of the DPVLA models was set to 20 mm/s in the drag penetration test.

2.3.3 Sand used in tests

To make the water quickly drain from the model experimental system, natural fine sand was used in the drag penetration test of DPVLA models. The particle size distribution curve of fine sand used in tests is shown in Figure 8, and it indicates that the sand is poorly graded and relatively uniform, which is suitable for the consistent testing condition in the drag penetration test system. For the granular materials, Bai et al. (2017) and Bai et al. (2021) investigated the physical–chemical interaction between particles and

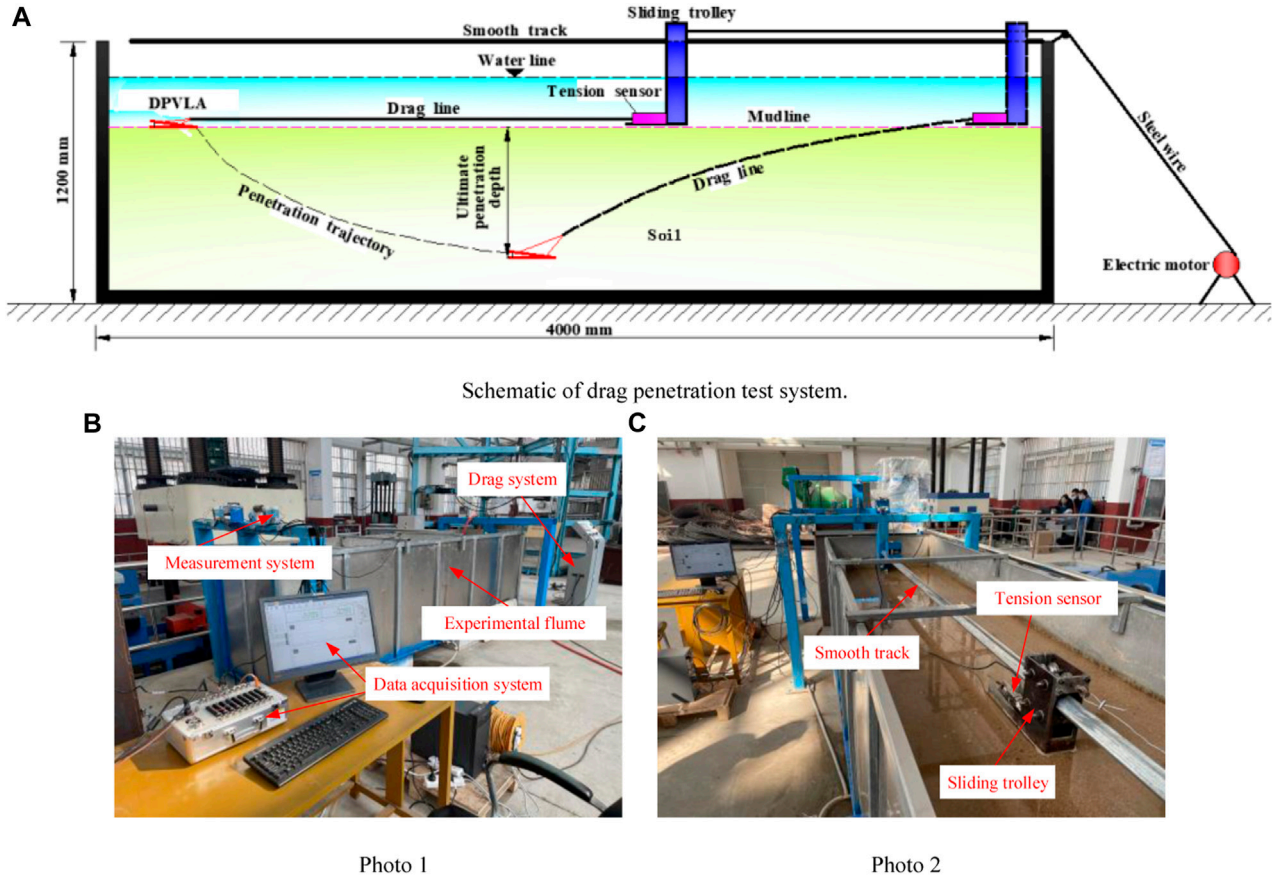

FIGURE 7
Setup of the drag penetration test system. **(A)** Schematic of the drag penetration test system. **(B)** Photo 1. **(C)** Photo 2.

TABLE 1 Physical parameters of fine sand used in the finite-element model.

e_{min} –	e_{max} –	e_0 –	D_{50} mm	C_u –	C_c–	γ_d kN/m^3	γ' kN/m^3	G_s–
0.59	0.91	0.65	0.1008	1.8	0.994	19.5	10.6	2.68

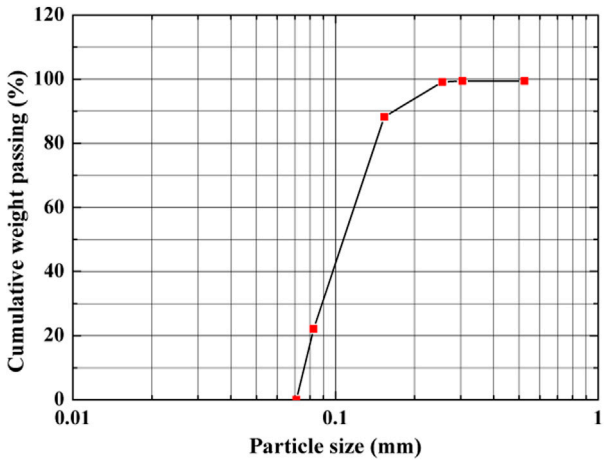

FIGURE 8
Particle size distribution curve.

the phenomenon of particle reorganization. The physical properties of fine sand were obtained in terms of standard tests and listed in Table 1.

2.3.4 Testing procedure

In the drag penetration test, the initial orientations of the bottom fluke of DPVLA models with different lengths of the bottom fluke and different included angles were all set to 0°; i.e., the bottom fluke of DPVLA models were placed horizontally on the simulated surface of the seabed. To ensure the repeatability of experiments, maintaining the relative density of fine sand in the same state is crucial. Therefore, before each test, the fine sand in the experimental flume was loosened to a depth of approximately 3.0 times the length of the anchor fluke to obtain the same stress level. Then, the DPVLA model was placed on the surface of the fine sand and water was poured into the experimental flume until its level was 200 mm higher than the surface of fine sand. Finally, the drain valve was opened until the water level was 100 mm above the surface of the fine sand. The penetration test of DPVLA models should be terminated if the dragging force was maintained constant.

2.3.5 Test results

The test results showed that when the ultimate penetration depths of the DPVLA model with different lengths of the bottom fluke and different included angles were reached, the movement directions of the bottom fluke of DPVLA models were all almost parallel to the surface of fine sand, as illustrated in Figure 9; i.e., θ_m is equal to θ_i. The results also show that the length of the bottom fluke and the included angle of DPVLA models have little influence on the movement directions of the bottom fluke at the ultimate penetration depth.

2.4 Bearing capacity factors for DPVLAs in clay

The bearing capacity factor, N_{cd}, in Eq. 6 is also an important parameter of DPVLAs, which influences the ultimate penetration depth of DPVLAs in clay. However, the bearing capacity factor, N_{cd}, in Eq. 6 is different from that of VLAs. Therefore, it is necessary to investigate the bearing capacity factor of DPVLAs with different lengths of the bottom fluke and different included angles in clay.

For the bearing capacity factor, N_{cf}, of the VLA in clay in Eq. 3, it can be obtained through the following expression (Det Norshke Veritas, 2002):

$$F_u = N_{cf}.A.S_u, \tag{9}$$

where F_u is the ultimate pullout capacity of anchors; A is the bearing area of the fluke of anchors; and s_u is the undrained shear strength of clay located in the place where the anchor is embedded.

Equation 9 also can be applied to the DPVLA. However, the area of the fluke of DPVLAs is different from that of the VLA. As illustrated in Figure 10, the effective bearing area of the fluke of DPVLAs, A_d, can be expressed as follows:

$$A_d = A_u + A_b.\cos\theta_i, \tag{10}$$

where A_u and A_b are the area of the upper and bottom fluke of DPVLAs in clay, respectively, and θ_i is the included angle of DPVLAs. When determining the bearing capacity factor of the DPVLA in clay, the effective bearing area of fluke, A, in Eq. 9 should be replaced by A_d.

However, Eq. 3 does not take into account the effects of the initial orientation of the anchor, which also affects the ultimate penetration depth of the anchor (Liu et al., 2010b). It is known that if the anchor fluke is initially set on the seabed at a shallow angle to the horizontal, the anchor will not reach its full embedment depth. However, the ultimate penetration depth is related to the ultimate pullout capacity of anchors. To obtain the maximum ultimate pullout capacity of DPVLAs, the ultimate penetration depth should also be the maximum. Therefore, to obtain the maximum ultimate pullout capacity, the upper bound solution of the ultimate pullout capacity of the DPVLA in clay should be considered. In addition, the finite-element method is utilized in this section to obtain the upper bound solution of the ultimate pullout capacity of the DPVLA in clay.

2.4.1 Three-dimensional finite-element model

Figure 11 represents the three-dimensional finite-element model along with meshes for the upper bound solution. The ZSOIL.PC software was used in the finite-element analysis, and eight-node continuum brick elements for both clay and DPVLAs were used in the three-dimensional finite-element model. In the plane strain condition, to avoid the boundary effects, the computational region of soil in length and width directions should be within

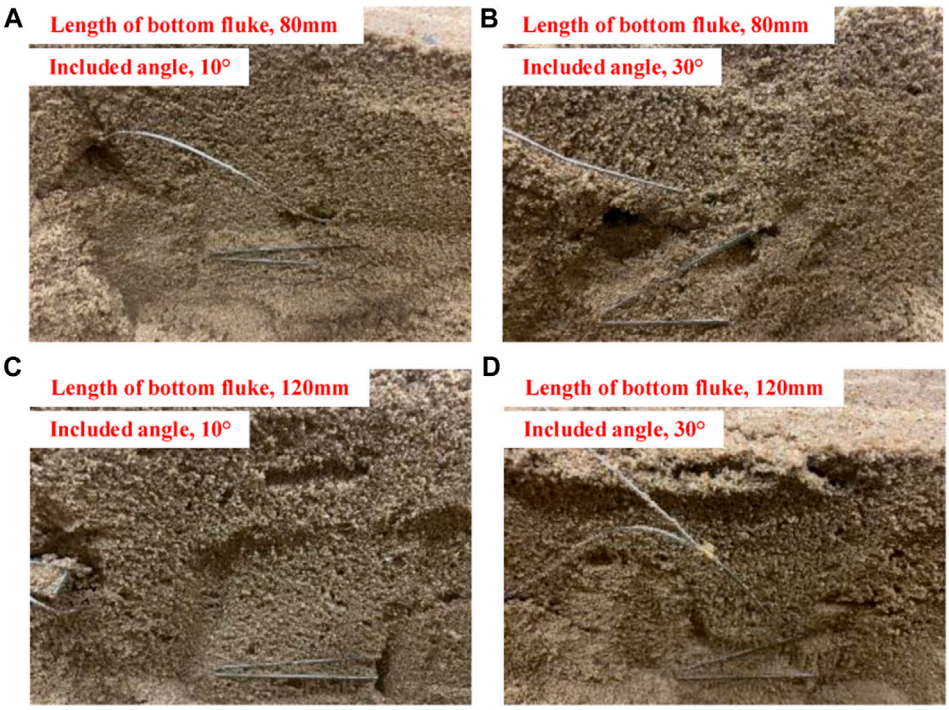

FIGURE 9
State of DPVLA at the ultimate penetration depth. **(A)** Photo 1; **(B)** Photo 2; **(C)** Photo 3; **(D)** Photo 4

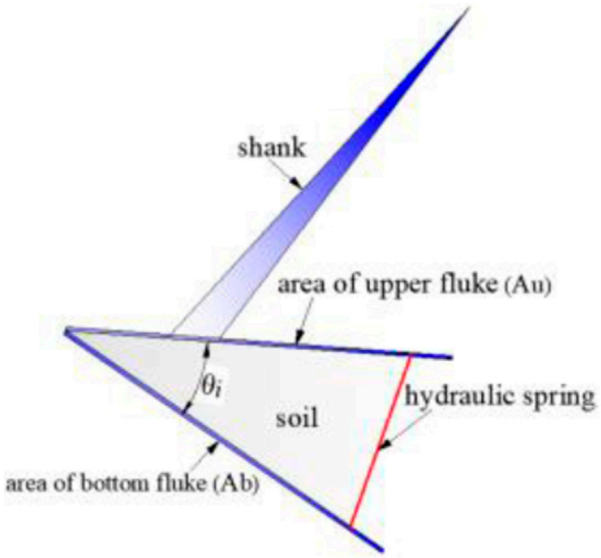

FIGURE 10
Scheme of DPVLA at the state of mooring.

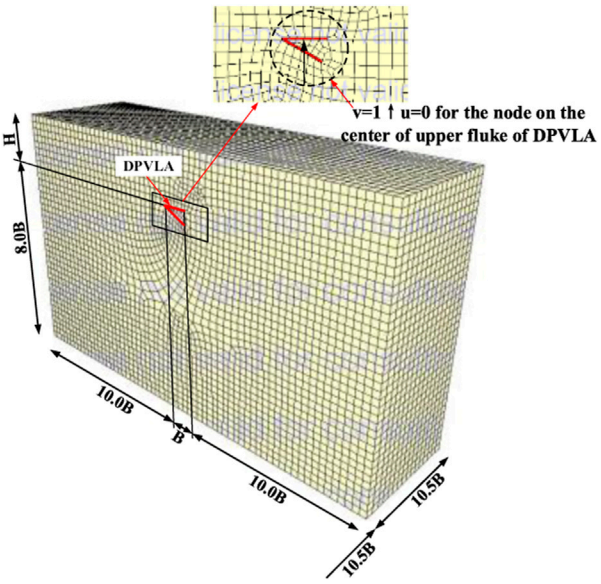

FIGURE 11
Three-dimensional finite-element model for the upper bound solution.

about 16.0*B* and the computational region of soil in depth direction was not less than 5.0*B*, where *B* was the length of the fluke of anchors (Merrifield et al., 2001). To eliminate far-away boundary in the three-dimensional finite-element model, the computational region of soil in length and width directions were all set to 21.0*B*, and the computational region of soil in the depth direction was set to 8.0*B*, where *B* was the length of the upper fluke of the DPVLA, as indicated in Figure 11. Displacements in the *x*, *y*, and *z* directions at the bottom boundary were all fully fixed and

horizontal displacements at the lateral boundaries were only constrained. Moreover, for the displacements at the top boundary, they were all not constrained, which simulated the surface of the seabed.

In the upper bound analysis of the three-dimensional finite-element model, the DPVLA was assumed to be rigid and it cannot move horizontally ($u = 0$); through prescribing a unit vertical velocity to the nodes on the center of the upper fluke of DPVLAs (as illustrated in Figure 11), the upper bound solution of the ultimate loading capacity of DPVLAs can be obtained. Furthermore, based on Eq. 9, the bearing capacity factors of DPVLAs can be calculated.

2.4.2 Constitutive model and parameters

The ideal elastic–plastic constitutive relationship obeying Von Mises' yield criterion is often used to model the clay (Qiao and Ou, 2012), with untrained shear strength as $S_u = 1.41H$, where H is the embedded depth below the seabed, as illustrated in Figure 10. The deformation modulus, E, of clay was assumed to be $E = 1000S_u$, and the Poisson's ratio of clay can be taken as $\nu = 0.49$. For the DPVLA model, it was assumed to be rigid, and the linear elastic constitutive model was used to simulate it. The modulus of elasticity and Poisson's ratio of DPVLAs were assumed to be $E = 2.06$ GPa and $\nu = 0.3$, respectively. In addition, the submerged unit weights of the clay and anchor were 6.3 and 77.0 kN/m^3, respectively.

To validate the credibility of the three-dimensional finite-element model, the results obtained from the finite-element method should be compared with the test results. Ruinen (2004) carried out field tests to obtain the ultimate pullout capacity of 2,741.1 kN of VLAs. In the field tests, the embedded depth of the VLA was $H = 18.0$ m and the dimensions of the VLA was 3000.0 mm in length, 3000.0 mm in width, and 200.0 mm in thickness. In addition, the parameters of clay and VLA in field tests were the same as those assumed previously. Based on the three-dimensional finite-element model established previously and the parameters of clay and VLA, the curve of load *vs.* displacement for the VLA can be obtained, as illustrated in Figure 12. As can be seen from Figure 12, the ultimate pullout capacity of the VLA was 2,705.0 kN. Comparing the result from the three-dimensional finite-element method with the test results, the error of the ultimate loading capacity of VLAs was only 1.3%, indicating that the three-dimensional finite-element model and the parameters used in the model are all credible. Furthermore, based on Eq. 9, the bearing capacity factor of the VLA can be calculated as $N_{cf} = \frac{F_u}{A.S_u} = \frac{2705}{9.0 \times 25.38} = 11.84$, which is very close to $N_{cf} = 11.87$ proposed by O'Neill *et al.* (2003).

2.4.3 Bearing capacity factors of DPVLAs

The results from the work of Cheng et al. (2019) indicate that the ultimate pullout capacity of full-scale VLAs is higher than that of reduced-scale VLAs due to the higher overburden pressure of full-scale VLAs compared to reduced-scale VLAs. In this section, the full-scale DPVLA is utilized to obtain the ultimate pullout capacity.

In the three-dimensional finite-element model, the dimensions of the DPVLA were that the length, width, and thickness of the upper fluke of the DPVLA were 3000.0, 3000.0, and 200.0 mm, respectively, which were the same as those of the VLA as mentioned in Section 4.2. The width and thickness of the bottom fluke was the same as that of the upper fluke. To investigate the influence of the included angle and the length of the bottom fluke on the bearing capacity factors of DPVLAs, the included angles were set at 10°, 20°, 30°, 40°, 50°, 60°, 70°, and 80°, respectively, and the lengths of the bottom fluke were set 2000, 2500, and 3000 mm, respectively.

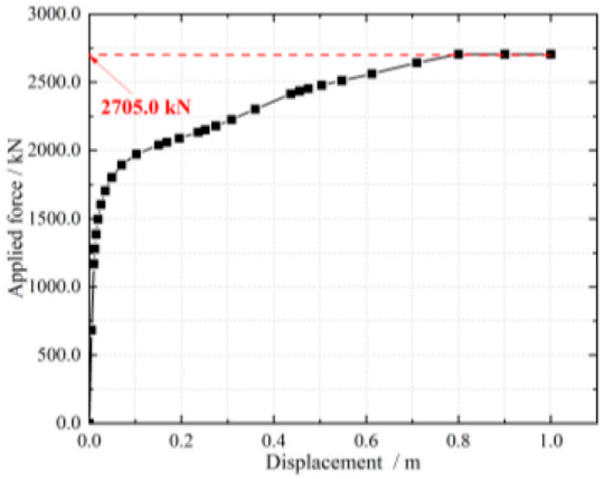

FIGURE 12
Load *vs.* displacement for VLAs in clay.

For the VLA, the critical embedded depth is about 3.0–4.5 times the length of the fluke in clay (Ruinen and Degenkamp, 2001; Det Norshke Veritas, 2002). When the embedded depth of VLAs is 18.0 m (i.e., 6.0 times the length of the fluke), it is the deeply embedded anchor and the ultimate pullout capacity of VLAs cannot increase with further increasing the penetration depth. In this section, the deeply embedded DPVLA in the three-dimensional finite-element model should also be ensured. To obtain the deeply embedded DPVLA, the embedded depths of DPVLAs were set at 18.0, 19.0, and 20.0 m, respectively. In addition, the included angle of the DPVLA was assumed to be 50°. The change of the normalized ultimate pullout capacity with embedded depth is shown in Figure 13. As illustrated in Figure 13, when the embedded depth of the DPVLA was 18.0 m, further increasing the embedded depth cannot significantly increase the ultimate loading capacity, which indicated that the DPVLA was a deeply embedded anchor at the embedded depth of 18.0 m. In the following analysis, the embedded depth of the DPVLA was all set to 18.0 m, i.e., 6B, where B represents the length of DPVLAs.

Based on the upper bound solution of the ultimate loading capacity obtained from the finite-element method, the bearing capacity factors of DPVLAs with different included angles and different lengths of the bottom fluke can be calculated with Eqs 9, 10. Figure 14 shows the influence of the included angle and the length of the bottom fluke on the bearing capacity factors. As illustrated in Figure 14, the trend of the influence of included angle on the bearing capacity factor of DPVLAs with different lengths of the bottom fluke was the same. It all showed that the bearing capacity factors of DPVLAs increased with the increase in the included angle. However, the bearing capacity factors of DPVLAs increased with the decrease in the length of the bottom fluke when the included angles were the same. In addition, with the included angle becoming larger, such as 80°, the length of the bottom fluke of DPVLAs has a minor influence on the bearing capacity factor.

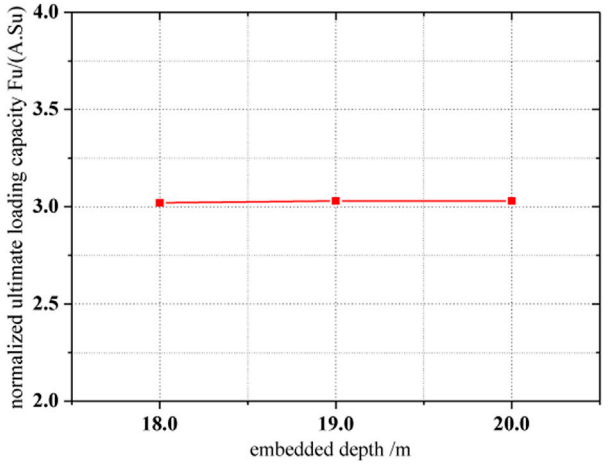

FIGURE 13
Variation of normalized ultimate loading capacity with embedded depth.

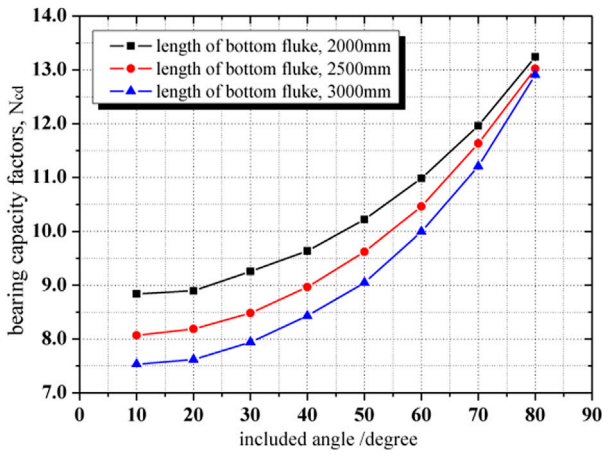

FIGURE 14
Influence of the included angle and length of the bottom fluke on the bearing capacity factor of DPVLA.

3 Parametric study

Based on Eq. 3, Liu et al. (2010a) investigated the influence of some parameters, such as the shape and dimensions of the fluke, size of the dragline, soil properties, and bearing capacity factors, on the ultimate penetration depth of VLAs in clay. In this section, based on Eqs 7, 8, the influence of the included angle and the length of the bottom fluke of DPVLAs on the ultimate penetration depth was investigated.

DPVLA models used in the parametric study were anchors with soft shanks, and the dimensions of the upper fluke of the DPVLA model were assumed to be 3000 (length) × 3000 (width)× 200 mm (thickness). Three sizes of the bottom fluke were assumed, i.e., 3000 mm × 3000 mm × 200 mm, 2500 mm × 3000 mm × 200 mm, and 2000 mm × 3000 mm × 200 mm. The distance from the shackle to the gravity center of the upper fluke, l_0, for the DPVLA model was assumed to be 3600 mm. The distance from the shackle to the plane of the upper fluke of DPVLAs, Δz, can be approximately calculated with $\Delta z = l_0 \sin\theta_a$. For the adhesion factor, α_f, in Eq. 3, Det Norshke Veritas (2000) and Det Norshke Veritas (2002) suggested that the value of α_f was between 0.2 and 0.6, and the value of α_f in Eq. 5 was assumed to be 0.5. In addition, based on the results from drag penetration tests, the movement direction of the bottom fluke at the ultimate penetration depth, θ_m, was equal to the included angle, θ_i.

Three hypothetical cases and parameters used in the parametric study for DPVLAs are listed in Table 2, where L_b denotes the length of the bottom fluke of DPVLAs. The bearing capacity factors, N_{cd}, of DPVLAs with different lengths of the bottom fluke and different included angles in Table 2 are from Figure 14. Using Eqs 3–8, variations of the ultimate penetration depth with the included angle, θ_i, and the length of the bottom fluke of DPVLAs, L_b, were obtained and presented in Figures 15, 16, respectively.

3.1 Influence of the length of the bottom fluke on the ultimate penetration depth of DPVLA

As can be seen from Figure 15A, when the strength of clay at the surface of the seabed was s_{uo} = 0, i.e., η = 0, increasing the length of the bottom fluke all increased the ultimate penetration depth of DPVLAs at included angles 10°, 30°, and 50°, respectively. The ultimate penetration depth increased by about 14.3, 13.7, and 7.1% from the length of the bottom fluke 2000 mm–3000 mm when the included angles are 10°, 30°, and 50°, respectively. It was also shown that when the included angle was 10°, increasing the length of the bottom fluke can significantly increase the ultimate penetration depth of DPVLAs. However, the larger included angle, such as 50°, did not contribute to penetrating into the soil even after increasing the length of the bottom fluke of DPVLAs.

When the strength of clay was uniform, the results were as shown in Figure 15B. As can be seen from Figure 15B, the trend of influence of the length of the bottom fluke on the ultimate penetration depth of DPVLAs was similar to that in Figure 15A. However, the ultimate penetration depths of DPVLAs in soft clay with s_{uo} = 0 were greater than those of DPVLAs in soft clay with uniform strength when the included angle and the length of the bottom fluke were the same for DPVLAs.

3.2 Influence of the included angle on the ultimate penetration depth of DPVLAs

When the strength of the clay at the surface of the seabed was s_{uo} = 0, the change of the ultimate penetration depth of DPVLAs with included angles was as shown in Figure 16A. As illustrated in Figure 16A, increasing the included angle decreased the ultimate penetration depth of DPVLAs at the length of the bottom fluke 2000, 2500, and 3000 mm, respectively. The ultimate penetration depth decreased by about 77.1, 77.9, and 78.5% from the included angle 10°

TABLE 2 Parameters for hypothetical cases in clay.

Case	θ_s(°)	θ_a(°)	b(m)	N_{cd}	α_f	s_{uo}(kPa)	θ_m	θ_i(degree)	L_b(mm)	k(kPa/m)	η
DPVLA1	45	30	0.005	8.68	0.5	0	10	10	2000	1.41	0
				9.25			30	30			
				10.25			50	50			
				8.68		20	10	10		0	∞
				9.25			30	30			
				10.25			50	50			
DPVLA2	45	30	0.005	7.95	0.5	0	10	10	2500	1.41	0
				8.51			30	30			
				9.65			50	50			
				7.95		20	10	10		0	∞
				8.51			30	30			
				9.65			50	50			
DPVLA3	45	30	0.005	7.53	0.5	0	10	10	3000	1.41	0
				7.94			30	30			
				9.07			50	50			
				7.53		20	10	10		0	∞
				7.94			30	30			
				9.07			50	50			

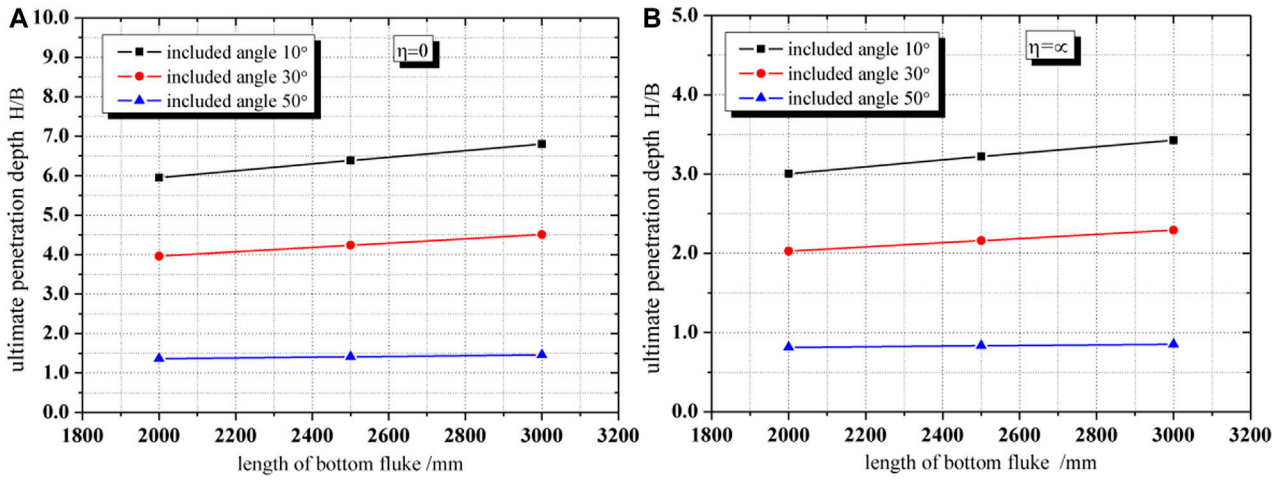

FIGURE 15
Influence of length of the bottom fluke on the ultimate penetration depth for two cases. **(A)** η=0; **(B)** η=∞.

to 50° when the length of the bottom fluke was 2000, 2500, and 3000 mm, respectively. Figure 16A also indicated that when the included angle was larger, such as 50°, the change in the length of the bottom fluke of DPVLAs had little influence on the ultimate penetration depth, which also indicated that the included angle should be less than 50° in the process of penetrating into the soil for DPVLAs.

When the strength of clay is uniform, i.e., η = ∞, the trend of influence of the included angle on the ultimate penetration depth of DPVLAs was also the same as that in Figure 16A. In addition, Figure 16B also indicates that the ultimate penetration depths of DPVLAs in soft clay with s_{uo} = 0 were greater than those of DPVLAs in soft clay with uniform strength when the included angle and the length of the bottom fluke were the same.

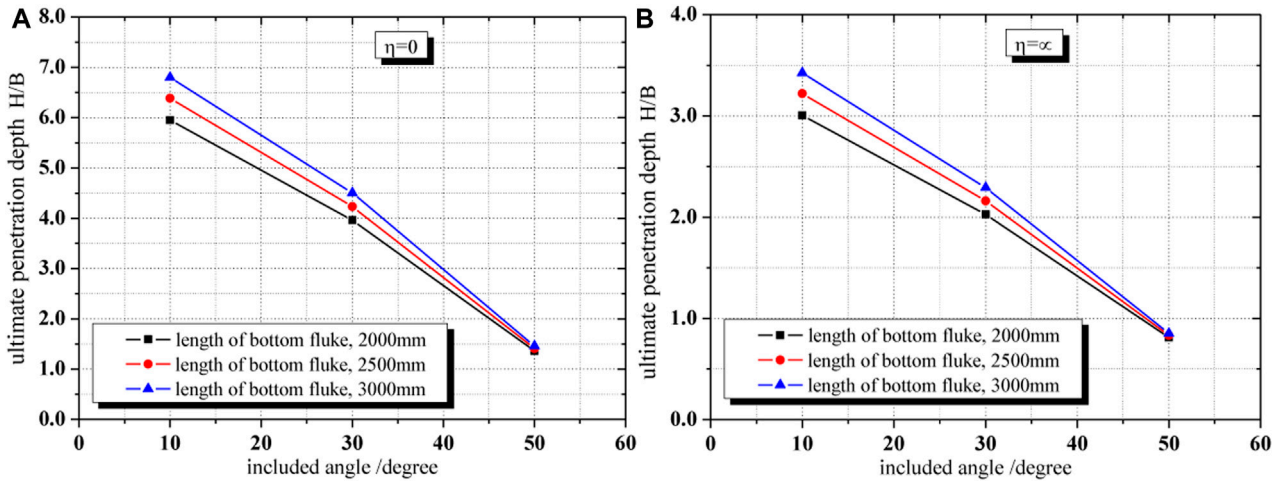

FIGURE 16
Influence of included angle on the ultimate penetration depth for two cases. **(A)** η=0; **(B)** η=∞.

4 Conclusion

The ultimate penetration depth of DPVLAs relates to the ultimate loading capacity. In this paper, based on the formula of the ultimate penetration depth of VLAs in clay proposed by Liu et al.(2010a), which was also applicable to DPVLAs in theory, the influence of the parameters on the ultimate penetration depth of DPVLAs in clay was investigated. In addition, two important parameters, θ_m and N_{cd}, in the expression of the ultimate penetration depth of DPVLAs in clay were first investigated in this paper, which contributed to obtaining the ultimate penetration depth of DPVLAs.

Through the drag penetration tests, the movement directions of the bottom fluke of DPVLAs with different lengths of the bottom fluke and different included angles were obtained. The results showed that the movement directions of the bottom fluke of DPVLA models were all parallel to the surface of fine sand, i.e., θ_m were equal to θ_i.

The bearing capacity factor, N_{cd}, of DPVLAs in clay is different from that of VLA, which is influenced by the length of the bottom fluke and included angle. To consider the influence of the initial orientation of DPVLAs on the ultimate penetration depth, the upper bound solutions of the ultimate pullout capacity were utilized to obtain the bearing capacity factor of DPVLAs with different included angles and different lengths of the bottom fluke in clay, which corresponded with the maximum penetration depth induced by the initial orientation of the anchor. The results showed that when the lengths of the bottom fluke of DPVLAs were the same, increasing the included angle can significantly increase the bearing capacity factors of DPVLAs. When the included angles were the same, increasing the length of the bottom fluke of DPVLAs can decrease the bearing capacity factors.

Based on the expression of the ultimate penetration depth of DPVLAs and two important parameters, θ_m and N_{cd}, the influence of the included angle and the length of the bottom fluke on the ultimate penetration depth of DPVLAs was obtained. The results showed that increasing the length of the bottom fluke of DPVLAs can increase the ultimate penetration depth when the included angles were the same not only for the clay with zero strength at the seabed but also for the clay with uniform strength. When the lengths of the bottom fluke of DPVLAs were the same, increasing the included angle can decrease the ultimate penetration depth. However, when the included angle was larger, such as 50°, the ultimate penetration depth increases little, even when increasing the length of the bottom fluke of DPVLAs compared with the smaller included angle, such as 10° and 30°.

Data availability statement

The original contributions presented in the study are included in the article/Supplementary Material. Further inquiries can be directed to the corresponding author.

Author contributions

GX: methodology, formal analysis, and writing. YC: conceptualization, methodology, investigation, and writing—review and editing. BZ: conceptualization and methodology. JL: investigation. XZ: investigation. All authors contributed to the article and approved the submitted version.

Funding

This work was financially supported by the National Natural Science Foundation of China (Grant No. 52178347) and the Natural Science Foundation of Shandong Province (Grant Nos. ZR2021ME068 and ZR2022ME165). The authors are also grateful to the undergraduates, such as Kai Jia, Junjie Yi, Shaoshuai Cui, Xurao Wang, and Jiansong Song, for their generous assistance with this work.

Conflict of interest

The authors declare that the research was conducted in the absence of any commercial or financial relationships that could be construed as a potential conflict of interest.

Publisher's note

References

Aubeny, C. P., and Chi, C. (2010). Mechanics of drag embedment anchors in a soft seabed. *J. Geotechnical Geoenvironmental Eng.* 136 (1), 57–68. doi:10.1061/(asce)gt.1943-5606.0000198

Aubeny, C. P., and Murff, J. D. (2005). *Suction caissons and vertical loaded anchors: Design analysis method*. Texas, USA: Final Report, Department of Civil Engineering, Texas A&M University.

Bai, B., Long, F., Rao, D. Y., and Xu, T. (2017). The effect of temperature on the seepage transport of suspended particles in a porous medium. *Hydrol. Process.* 31 (2), 382–393. doi:10.1002/hyp.11034

Bai, B., Zhou, R., Cai, G. Q., Hu, W., and Yang, G. C. (2021). Coupled thermo-hydro-mechanical mechanism in view of the soil particle rearrangement of granular thermodynamics. *Comput. Geotechnics* 137 (8), 104272. doi:10.1016/j.compgeo.2021.104272

Cheng, X. L., Li, Y. F., Wang, P. G., Liu, Z. X., and Zhou, Y. D. (2019). Model tests and finite element analysis for vertically loaded anchors subjected to cyclic loads in soft clays. *Comput. Geotechnics* 119, 103317. doi:10.1016/j.compgeo.2019.103317:

Det Norshke Veritas (DNV) (2000). "Design and installation of fluke anchors in clay," in *Recommended practice RP-e301dnv RP-e301*. Norwegian: Det Norske Veritas.

Det Norshke Veritas (DNV) (2002). *RP-E302 Design and installation of drag-in plate anchors in clay*. Norwegian: Det Norske Veritas.

Liu, H. X., Liu, Y., Yang, H. T., Zhang, W., Liu, C. L., and Zhang, W. (2010a). Analytical study on the ultimate embedment depth of drag anchors. *Ocean. Eng.* 37, 1292–1306. doi:10.1016/j.oceaneng.2010.06.007

Liu, H. X., Zhang, W., Zhang, X. W., Liu, C. L., and Liu, C. (2010b). Experimental investigation on the penetration mechanism and kinematic behavior of drag anchors. *Appl. Ocean Res.* 32 (4), 434–442. doi:10.1016/j.apor.2010.09.004

Merrifield, R. S., Sloan, S. W., and Yu, H. S. (2001). Stability of plate anchors in undrained clay. *Geotechnique* 51 (2), 141–153. doi:10.1680/geot.51.2.141.40290

Miedema, S. A., Lagers, G. H. G., and Kerkvliet, J. (2007). *An overview of drag embedded anchor holding capacity for dredging and offshore applications*. Orlando, FL: WODCON.

Murff, J. D., Randolph, M. F., Elkhatib, S. H., Kolk, J. R., Ruinen, M., Strom, P. J., et al. (2005). Vertically loaded plate anchors for deepwater applications. *Front. Offshore Geotechnics*. doi:10.1201/noe0415390637.ch2

Naval Civil Engineering Laboratory (NCEL) (1987). "Drag embedment anchors for navy moorings,". Techdata Sheet 83–08 R (Port Hueneme, CA: Naval Civil Engineering Laboratory NCEL.

Neubecker, S. R., and Randolph, M. F. (1995). Profile and frictional capacity of embedded anchor chains. *J. Geotechnical Eng. Div.* 121 (11), 797–803. doi:10.1061/(asce)0733-9410(1995)121:11(797)

Neubecker, S. R., and Randolph, M. F. (1996). The performance of drag anchor and chain systems in cohesive soil. *Mar. Georesouces Geotechnol.* 14, 77–96. doi:10.1080/10641199609388305

O'Neill, M. P., Bransby, M. F., and Randolph, M. F. (2003). Drag anchor fluke–soil interaction in clays. *Can. Geotechnical J.* 40, 78–94. doi:10.1139/t02-096

O'Neill, M. P., and Randolph, M. F. (2001). Modelling drag anchors in a drum centrifuge. *Int. J. Phys. Model. Geotechnics* 2, 29–41. doi:10.1680/ijpmg.2001.010203

O'Neill, M. P., Randolph, M. F., and Neubecker, S. R. (1997). "A novel procedure for testing model drag anchors," in Proceedings of the Seventh International Offshore and Polar Engineering Conference, Honolulu, USA, May 25-30, 1997.

Qiao, D. S., and Ou, J. P. (2012). Analysis on ultimate pullout bearing capacity of drag embedment anchor under cyclic loading. *J. Harbin Inst. Technol.* 44 (12), 112–117. doi:10.1007/s11783-011-0280-z

Ruinen, R. M., and Degenkamp, G. (2001). "Anchor selection and installation for shallow and deepwater mooring systems," in Proceedings of the 11th International Offshore and Polar Engineering Conference, Stavanger, Norway, June 17-22, 2001.

Ruinen, R. M., and Degenkamp, G. (2002). "Prediction of the holding capacity and trajectory of drag embedment anchors," in Proceedings of the 34th Annual Offshore Technology Conference, OTC 14305, Houston, USA, May 6-9, 2002.

Ruinen, R. (2004). "Penetration analysis of drag embedment anchors in soft clays," in Proceedings of the 14th International Offshore and Polar Engineering Conference ISOPE, Toulon, France, May 23-28, 2004, 531–537.

Tian, Y., Randolph, M. F., and Cassidy, M. J. (2015). Analytical solution for ultimate embedment depth and potential holding capacity of plate anchors. *Géotechnique* 65 (6), 517–530. doi:10.1680/geot.14.p.228

Vryhof Anchors (2005). *Anchor manual*. Netherlands: Krimpen ad Yssel.

Xing, G. Q., Xuan, W., and Zhang, B. (2020). *Towed embedded double-layer flat plate bearing anchor*. State Intellectual Property Office of the P.R. China. ZL201910259959.x.

Xing, G. Q., Zhang, L. J., Xuan, W., Ma, J. H., Ye, X. C., Guo, S. W., et al. (2021). Capacity of double-plate vertically loaded anchor in saturated marine fine sand. *Mar. Georesources Geotechnol.* 40, 1302–1315. doi:10.1080/1064119X.2021.1991062

Yang, M., Murff, J. D., and Aubeny, C. P. (2010). Undrained capacity of plate anchors under general loading. *J. Geotechnical Geoenvironmental Eng.* 136 (10), 1383–1393. doi:10.1061/(ASCE)GT.1943-5606.0000343

frontiers | Frontiers in Materials

TYPE Original Research
PUBLISHED 29 June 2023
DOI 10.3389/fmats.2023.1219765

OPEN ACCESS

EDITED BY
Bing Bai,
Beijing Jiaotong University, China

REVIEWED BY
Wenyuan Ren,
Northwest A&F University, China
Yu Wang,
University of Science and Technology Beijing, China

*CORRESPONDENCE
Yalin Nan,
nan.yalin@dky53.com
Mingjiang Tao,
taomj@wpi.edu

RECEIVED 09 May 2023
ACCEPTED 19 June 2023
PUBLISHED 29 June 2023

CITATION
Guo H, Wang S, Guo C, Yang K, Guo R, Fu J, Nan Y and Tao M (2023), Effect of grain size distribution on the shear properties of sand.
Front. Mater. 10:1219765.
doi: 10.3389/fmats.2023.1219765

Effect of grain size distribution on the shear properties of sand

Hong Guo[1,2], Shaofei Wang[1,2], Chen Guo[1,2], Kuibin Yang[1,2], Rui Guo[1,2], Jiangtao Fu[1,2], Yalin Nan[3,4]* and Mingjiang Tao[5]*

[1]School of Civil Engineering and Architecture, Shaanxi University of Technology, Hanzhong, China, [2]Research Center of Geotechnical Environment and Geological Hazards Control in Qinling-Daba Mountains, Shaanxi University of Technology, Hanzhong, China, [3]China Electronic Research Institute of Engineering Investigations and Design, Xi'an, China, [4]Shaanxi Provincial Soil Engineering Technology Research Center, Xi'an, China, [5]Department of Civil and Environmental Engineering, Worcester Polytechnic Institute, Worcester, MA, United States

In this study, we investigated the effect of particle size distribution on the shear properties of sand. Direct shear tests were conducted using four types of sand samples with different particle size distributions obtained from standard sand produced by Xiamen ISO Co. Ltd. The results show that the influence of particle size distribution on the internal friction angle was significant. Typically, the internal friction angle increases with increasing the coefficient of non-uniformity (Cu) and decreasing the curvature coefficient (Cc). The discrete element results show that the initial particle size distribution significantly affects the porosity, coordination number, and particle slide fraction. In addition, the grey relation analysis revealed that the sliding fraction and coordination number have the greatest correlation with the internal friction angle. The research results of this study help to understand the changes in particle contact, internal stress, and particle sliding during the shear failure process of sand.

KEYWORDS

sand, particle size distribution, shear properties, discrete element method, internal friction angle

1 Introduction

Sandy soil, as a porous material (Bai et al., 2017) is widely used in practical geotechnical engineering, such as rockfill dams, sandy soil foundations, slopes, etc. (Sato et al., 2022; Kamalzadeh and Pender, 2023; Pei et al., 2023). Researches showed that sand's physical and mechanical properties are closely related to its particle size (BELKHATIR et al., 2011; Murat and Eyubham, 2020; Li et al., 2022; Wang et al., 2022), or rearrangement (Bai Bing Zhou et al., 2021), even reinforced sand is no exception (Liu et al., 2022). It is difficult for conventional geotechnical tests to understand the deeper mechanism of the shear deformation of sand. Therefore, discrete element numerical analysis has been widely increasing in the mechanical property analysis of sand (Ibrahim and Meguid, 2023; Li et al., 2023; Xie et al., 2023). The discrete element can easily consider the effect of sand particle gradation. Kong and Jiefeng, 2013) studied the shear characteristics of Qingdao sea sand. They observed that sand with better gradation shows higher shear strength, larger local coordination number, and weaker dilatancy. Liu Yingjing Wang Jianhua Yin Zhenyu, 2015) established the correspondence between the particle gradation index non-uniformity coefficient (Cu) and the critical state parameters of granular materials. They introduced the critical state mechanical characteristics related to particle size into the constitutive model of sand. Li (2013) observed that the larger the content of coarse particles, the greater the internal friction, which was also reported by Vangla and Latha (2015). Belkhatir et al. (2012)

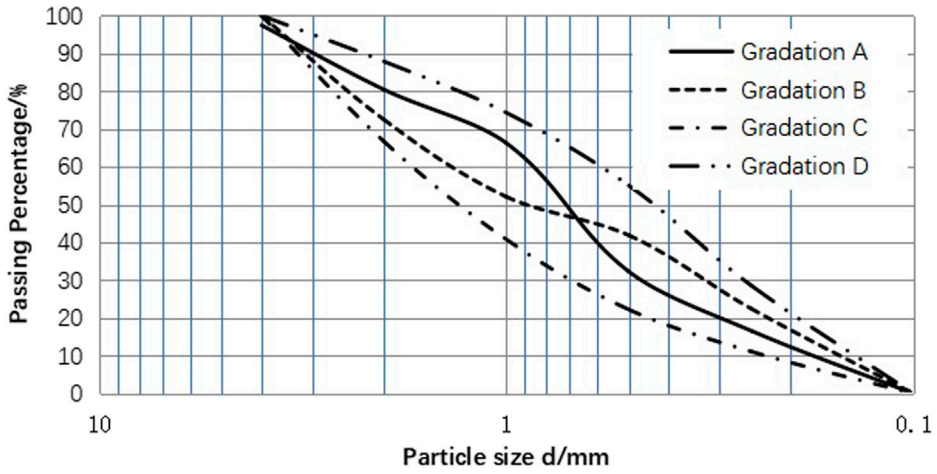

FIGURE 1
Particle size distributions of 4 types of sands.

analyzed the influence of effective particle size d_{10}, average particle size d_{50}, and non-uniformity coefficient Cu on the shear peak of sand, and found that the shear peak of sand increases with d_{10} and d_{50}, decreases with Cu. Bayat and Bayat (2013) observed that under constant d_{50}, the shear strength increases with Cu. For discontinuously graded sand, decreasing d_{50} can increase its shear strength. Havaee et al. (2015) studied sandy soil in central Iran as a research object equation and established the prediction of the internal friction angle and cohesion of the soil with the content of each component (clay, silt, sand, gravel, etc.) as a variable. Sezer (2013) proposed an internal friction angle fitting equation that considers the regularity of particles, fractal dimension, curvature coefficients (Cc), d_{10}, and relative density. However, there are currently no literature reports on how Cc and Cu jointly affect the shear strength of sand. In addition, the relationship between the mesoscopic indexes, such as porosity, coordination number and contact slip of sand in the shear process, and the shear process needs further study.

Further research is still needed in the following two aspects: one is establishing a quantitative relationship between the particle gradation parameters, such as non-uniformity and curvature coefficient, and the shear strength of the sand is rarely reported in the literature; another is investigating the effect of the combining porosity, coordination number, and particle contact slip on the shear strength of sand.

Based on this, the standard sand (hereinafter referred to as standard sand) produced by Xiamen Aisou Company was used as the primary raw material. Sand samples of different grades were prepared. Laboratory shear tests were conducted to obtain the particle size parameters and their influence on the internal friction angle. Due to the indoor direct shear test limitations, analyzing the microscopic changes of sand samples during the shearing process was quite difficult. Therefore, this paper applied the particle flow analysis software PFC2D to prepare discrete element numerical samples with the same gradation as the laboratory test. The mechanical properties of the particle-level paired sands were further explained by the changes in microscopic indicators such as porosity, coordination number, and sliding fraction.

TABLE 1 Cc and Cu values of 4 types of sands.

	d_{10}/mm	d_{30}/mm	d_{60}/mm	Cc	Cu	φ
A	0.176	0.473	0.865	1.47	4.91	34.41
B	0.152	0.324	1.353	0.51	8.90	36.76
C	0.228	0.705	1.686	1.29	7.39	38.27
D	0.138	0.260	0.584	0.84	4.23	35.87

2 Direct shear test

Standard sand was used as the raw material, and its relative density was 2.66. The sand was sieved through standard sieves (round hole) of 4, 2, 1, 0.75, 0.5, 0.25, and 0.1 mm, and sand samples of different grades were configured. In this test, the sand sample has a total of four gradations, namely A, B, C, and D. The particle gradation curve is shown in Figure 1. The Cc and Cu values of different graded sand samples were calculated based on d_{10}, d_{30}, and d_{60}, as shown in Table 1. The direct shear test was conducted using a direct shear instrument by Nanjing Soil Instrument Factory. The sand was dried and packed in a 6.18 cm diameter and 2 cm height shear box. The initial state was considered medium sand, and the initial void ratio e_0 was controlled to 0.64. Each graded sample was divided into three groups of parallel samples. Each group of four samples was loaded with 100, 200, 300, and 400 kPa vertical pressure. It should be noted that initial void ratio is achieved by controlling the total volume and mass of dry sand samples, and the shear rate is 1 mm per minute.

Each group of sand samples was tested in parallel three times, and the shear stress under each level of vertical pressure was finally obtained. The average value was denoted as the basic value of the histogram, and the standard deviation as the error line, as shown in

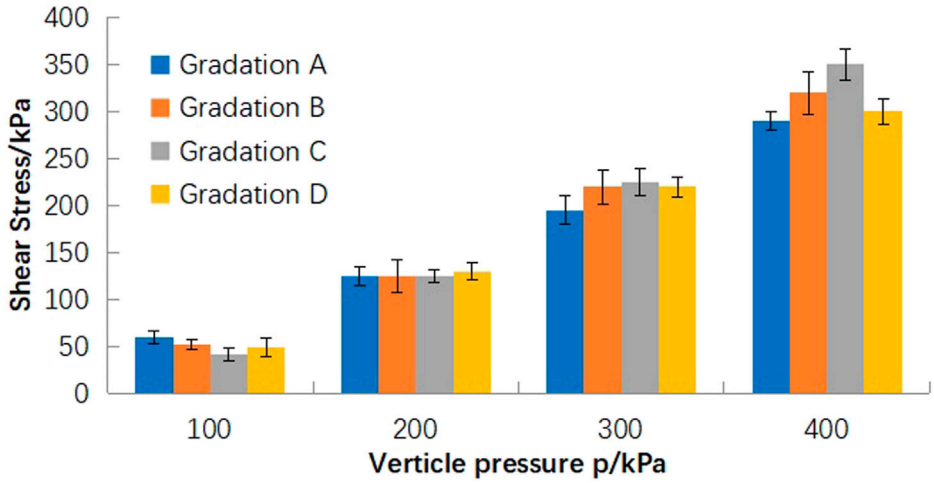

FIGURE 2
Vertical pressure-shear stress histogram of 4 graded sand samples.

Figure 2. The slopes of the histograms of each group were fitted to 0.685, 0.747, 0.789, and 0.723, and the arc tangent values were calculated. The internal friction angles of the four groups of sand samples were 34.41°, 36.76°, 38.27°, and 35.87°.

Based on Table 1, it is easy to observe that from the curvature coefficient (Cc) and non-uniformity coefficient (Cu), the engineering evaluation of gradation C is good, and its internal friction angle is relatively the largest. This indicates the importance of particle grading in practical engineering. The internal friction angle of gradation B is also relatively large due to its large non-uniformity coefficient (Cu). Although its curvature coefficient (Cc) indicates that it is not a well graded soil. This indicates that, compared to the curvature coefficient (Cc), the non-uniformity coefficient (Cu) is the main factor affecting the internal friction angle. This has been verified in the gradation A soil samples, as although the curvature coefficient (Cc) of gradation A soil is between 1 and 3, the internal friction angle is small due to the small non-uniformity coefficient (Cu). In addition, comparing gradation A and D, it can be observed that the internal friction angle decreases with the increase of curvature coefficient.

3 DEM simulation analysis

Direct shear test, as a method to study the macro shear characteristics of soil, has some limitations. For example, it fails to understand the action mechanism from a meso-level. Therefore, it is imperative to investigate the contact change and internal stress of sand particles of different grades in the shearing process. The discrete element method (numerical direct shear test) is the better way to achieve this goal.

3.1 Numerical experiment

(a) 2D numerical packing fraction

Two-dimensional particles (discs) were used to simulate three-dimensional particles (spheres). The particle porosity (n) and the degree of compaction varied with the dimensions of the same particle system. Therefore, referring to the ideas of soil mechanics, the concept of relative density was used to link the relative density in three dimensions ($3d$) with the relative density in two dimensions ($2d$). According to the concept of relative density, there are:

$$D = \frac{e_{max}^{(j)} - e^{(j)}}{e_{max}^{(j)} - e_{min}^{(j)}}, j = 2d, 3d, \tag{1}$$

where e is the void ratio ($e = \frac{n}{1-n}$), the subscripts max and min represent the maximum and minimum void ratios; D is the relative density.

The relationship between packing fraction $P^{(j)}$ (the ratio of the particles' volume to the total volume) and void ratio $e^{(j)}$ can be expressed as:

$$e^{(j)} = \frac{1 - P^{(j)}}{P^{(j)}}, j = 2d, 3d. \tag{2}$$

Therefore, we get

$$P^{(j)} = \frac{P_{min}^{(j)}}{1 - D\left(1 - \frac{P_{min}^{(j)}}{P_{max}^{(j)}}\right)}, \tag{3}$$

where $P_{max}^{(j)} = \begin{cases} 0.9069, j = 2d \\ 0.7405, j = 3d \end{cases}$ and $P_{min}^{(j)} = \begin{cases} 0.7854, j = 2d \\ 0.5236, j = 3d \end{cases}$ represent the packing fraction of the densest and the sparsest arrangement of equal-diameter particles, respectively.

Substituting the value of the initial void ratio ($e_0 = 0.64$) into Eq. 2 can determine the relative density, and then using Eq. 4 to calculate the packing fraction in two dimensions. The packing fraction is the control parameter (Initial packing fraction) of the two-dimensional discrete element model.

TABLE 2 Microscopic parameters of numerical samples.

Density/g·cm^{-3}	Stiffness/kN·m^{-1}	Coefficient of friction	Initial packing fraction
2.66	10000	0.65	0.84

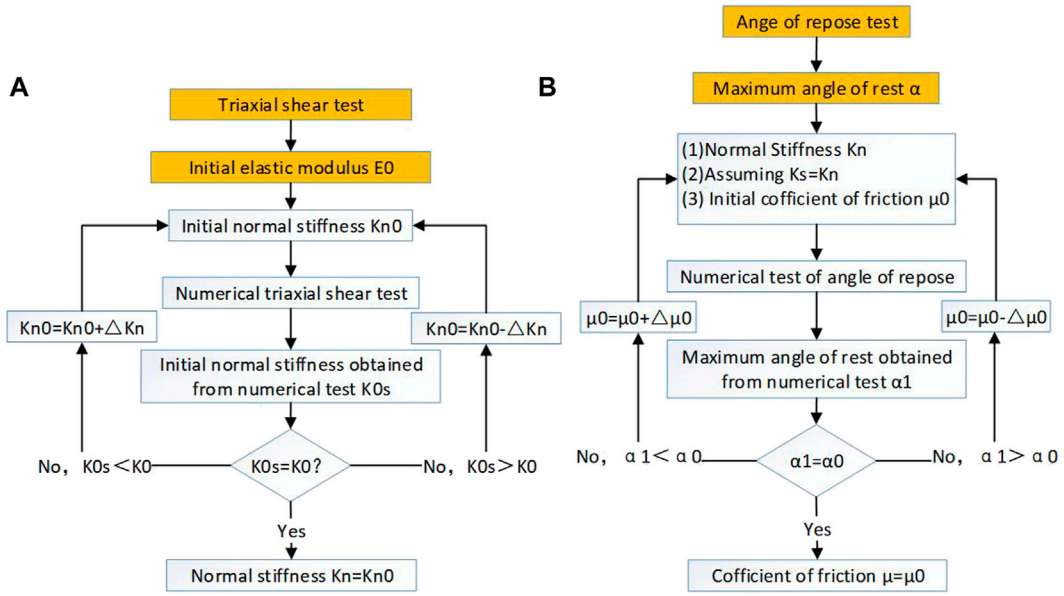

FIGURE 3
Process for obtaining stiffness and friction coefficient in discrete element simulation: **(A)** stiffness; **(B)** coefficient of friction.

(b) Discrete Element Modeling

The DEM simulation applied a linear elastic contact model to establish a two-dimensional shear test model. The sample size was consistent with the indoor shear sample, with 2 cm high and 6.18 cm wide. The sample used the layering method of Jiang et al. (2003). The dimensions as those of the indoor shear test were maintained, and the effect of sample size was overlooked for the time being (Omar and Sadrekarimi, 2014; Park and Jeong, 2015). Consistent with the indoor test, the lateral compression test and angle of repose test were used to calibrate the sand particles' stiffness and friction coefficient. The microscopic parameters of the simulated sand particles are shown in Table 2. The shear box stiffness was selected as ten times the sand's stiffness as 100,000 kN m^{-1}; irrespective of the shear box roughness, its friction coefficient was 0. Notably, the particle size in the discrete element simulation was set according to the gradation of the actual particles. The system's local damping uses the default value of 0.7, and the normal and tangential stiffness of the sand particles use the same value. The Cc and Cu values were also consistent with the laboratory test values. The method for obtaining important microscopic parameters is shown in the Figure 3. As shown in Figures 3A–D are discrete element model diagrams under the four particle gradations of A, B, C, and D, respectively. Three measuring circles, 1, 2, and 3, were set on each gradation of the numerical samples to capture the variation of the mesoporosity, coordination number, local shear stress, and particle slip of the numerical samples (Figure 4). The radius of the measuring circles was 5 mm, and the centers were 1, 3, and 5 cm from the left side of the shear box. Fish language programming was used to simulate the process of direct cutting. The lower part of the cutting box was fixed. When the vertical pressure was applied and stabilized, the upper part of the cutting box was moved to the left at a constant speed, and the cutting rate was controlled to 1 mm/min. The shear failure criterion was used at the peak value of the shear displacement of 6 mm.

Figure 5A is the force chain diagram of gradation A under a steady vertical compressive stress. Figure 5B is the force chain diagram of gradation A immediately after the shear stress peaks. The black line in the figure is the force chain, and its width is proportional to the magnitude of the force. The higher the density of the force chain, the more particles in that area come into contact with each other. The force chain diagrams of the other samples in these two cases are similar to those of the gradation C and, therefore, not listed here individually. Before shearing, the entire specimen reaches equilibrium under the action of vertical compressive stress (the figure uses 100 kPa vertical compressive stress as an example). The main force chain after shear failure is distributed from the upper right corner to the lower left corner of the shear box. The force chain distribution at the upper part of the shear box is left sparse and right dense. Thus, it explains that in

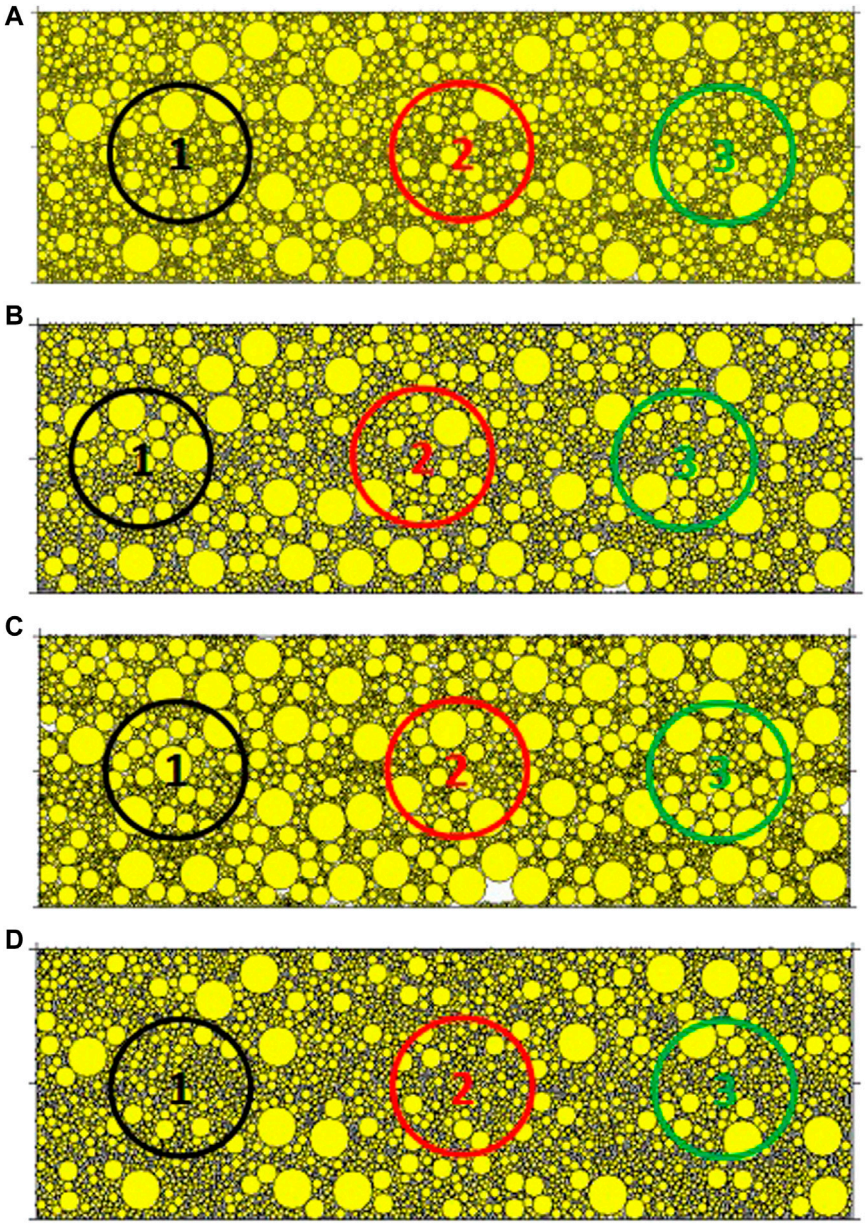

FIGURE 4
Discrete model of 4 types of sands: **(A)** Gradation A; **(B)** Gradation B; **(C)** Gradation C; **(D)** Gradation D.

actual shear tests, the shear "lift" phenomenon of the top cover of the cutting box near the shearing force is essentially the dilatancy effect of sand particles.

3.2 Coordination number

The particles produce local dilatancy or shrinkage during shearing in the macroscopic view. The dilatancy and shrinkage of particles vary with different initial packing fractions and particle gradations. This study focused on analyzing the meso-particle contact situation of different grading particles and ignored the different initial packing fractions for the time being. Therefore, this section explores the change law of the coordination number under different particle gradations.

The coordination number is a parameter characterizing the closeness of the particle contact in a certain range. For one particle, the coordination number refers to the number of other particles in contact with the particle. For particles in a region, the coordination number is the ratio of the total number of particles with particles in a specific range to the total number of particles. Its expression is shown in Eq. 4:

$$C_n = \frac{\sum_{N_b} N_c^{(b)}}{N_b}, \tag{4}$$

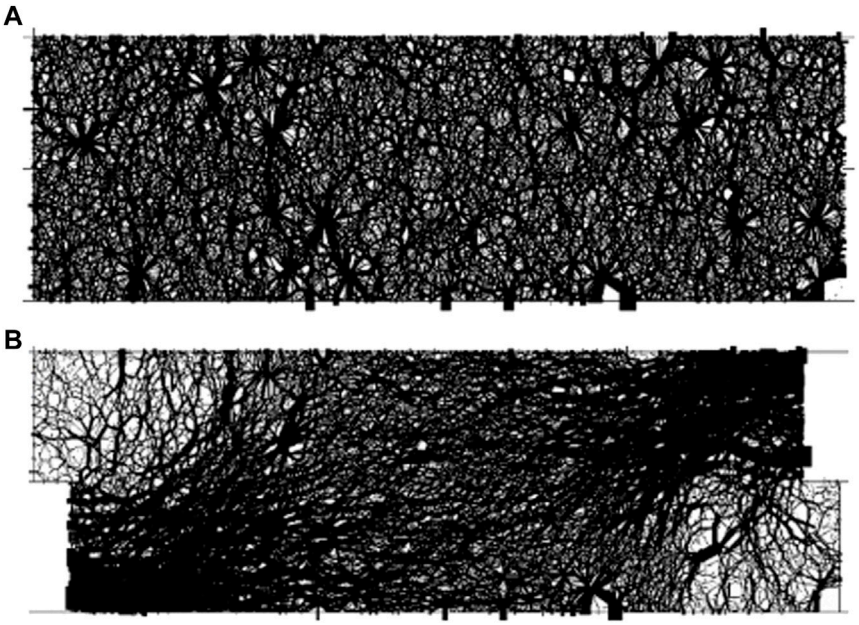

FIGURE 5
Force chain distribution before and after shearing: **(A)** Force chain diagram before shearing; **(B)** Force chain diagram after shearing.

where N_b is the number of particles in the circle, and $N_c{}^{(b)}$ the number of contacts with particle b.

Figure 6 shows the variation in the coordination number of the particles in the three measurement circles with shear displacement. The effect of the gradation coordination number is pronounced. Gradation D exhibited the highest content of fine particles in the three measurement circles because it had the largest content of fine particles and relatively close contact with large particles. Although the fine particle content of gradation A in Figure 6A is smaller than that of gradation D, its coordination number reaches the maximum in the later stage, which indicates that the samples with good gradation were in closer contact with each other in the late stage of shear. The coordination numbers in Figures 6B, C increased and decreased, respectively, which is consistent with the nature of the porosity changes analyzed earlier. Figure 6D shows the coordination law of different positions during gradation A (the situation of gradation B, C, and D is similar to that of gradation A). When the shear displacement is small, the coordination numbers in circle 1 and circle 2 gradually increase, indicating that the particles at the middle and right ends of the shear box more closely mesh with each other during the shearing process. However, with the continuous increase of the shear displacement, the coordination number at the right end decreased, and the corresponding coordination number at the middle continuously increased, indicating that the shear "pushes" the middle particles to continue to bite. The coordination number of particles at the left end of the shear box kept decreasing, indicating that its bite was weakened and its fluidity was enhanced.

The coordination number in Figure 6 is averaged over the entire shear displacement, and the results are shown in Table 3. For different positions, the average coordination number of gradation C was the lowest, and the average coordination number of gradation B was the second lowest. In measurement circle 1, the average coordination number of gradation A was the highest, and the average coordination number of gradation D was the second highest. The above rule seems to be the opposite of the internal friction angle rule, except for measurements 2 and 3, where the gradations A and D are slightly different.

3.3 Variation of local shear stress

The shear stress at different shear positions (inside the measurement circle) is obtained by Eq. 5:

$$\bar{\sigma}_{ij} = \frac{1}{V}\sum_{Np}\bar{\sigma}_{ij}^{(p)}V^{(p)}, \tag{5}$$

where $\bar{\sigma}_{ij}$ is the stress tensor of the aggregate of all particles in the measurement circle, $\bar{\sigma}_{ij}^{(p)}$ is the stress tensor of the force on the single particle, $V^{(p)}$ and V the volume of the single particle and the measurement circle (area in two dimensions), Np is the particle number within the measurement circle.

Figure 7 shows the typical relationship between local shear stress *vs.* shear displacement. The shear stress near the shear direction (green line in the figure), the shear stress far from the shear direction (black line in the figure), and the shear stress in the middle part of the sample (red line in the figure) reaching the peak particle grading vary. For example, in gradation A, the order of peak shear stress is measurement circle 1> measurement circle 3> measurement circle 2. Also, the initial slope of the local shear stress curve of measurement circle 2 is significantly lower. The overall trend of other gradation situations is identical to that of gradation A and is not repeated in this section. Thus, while shearing, the shear box boundary significantly constrained the local shear stress (measurement circles 1 and 3 are on the left and right

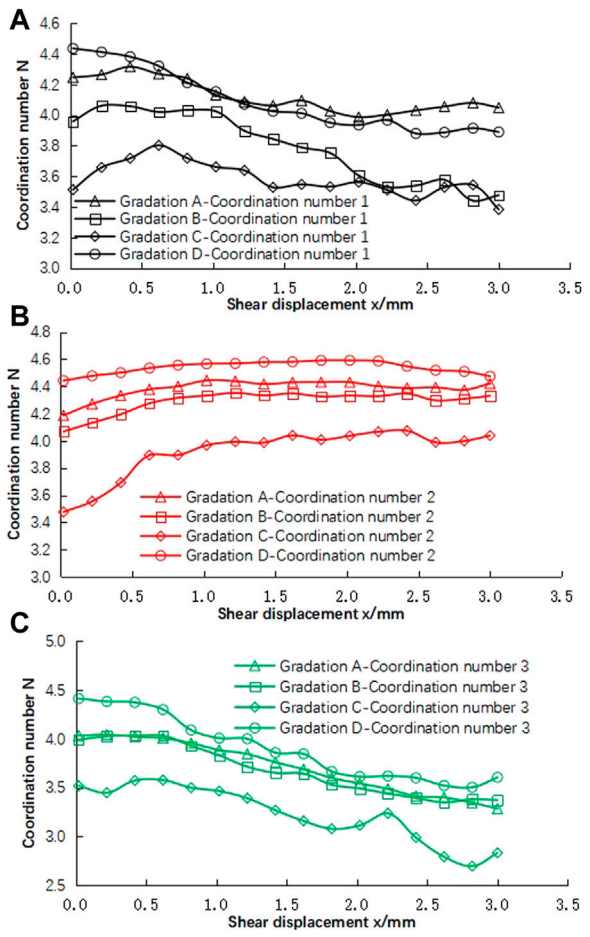

FIGURE 6
Relation curve of coordination number *vs.* shear displacement: **(A)** relations of shear displacement *vs.* coordination number of measure circle 1; **(B)** relations of shear displacement *vs.* coordination number of measure circle 2; **(C)** relations of shear displacement *vs.* coordination number of measure circle 3.

TABLE 3 Coordination number of different gradations at different positions.

Measurement circle No.	1	2	3	Average
Gradation A	4.12	4.38	3.71	4.07
Gradation B	3.79	4.29	3.67	3.92
Gradation C	3.58	3.92	3.23	3.58
Gradation D	4.09	4.54	3.90	4.18

boundaries, respectively). Further, the peak value of measurement circle 1 is the largest because the upper shear box is pushed from right to left, and the particles near the left border squeeze slightly.

3.4 Sliding fraction

In the discrete element simulation, the particle sliding fraction is measured by the ratio of the contacts that cause slippage to the total number of contacts. Table 4 summarizes the average particle sliding fraction over the whole shear displacement at different positions (measurement circles) under different gradations. Generally, the sliding fraction of gradation C is the largest, and that of gradation A is the smallest. This behavior is nearly the same as the law of influence of the internal friction angle of the gradation.

3.5 Grey relation analysis

This section used the grey relation theory (Zhao et al., 2023) to analyze the correlation between the four factors of uniformity coefficient—Curvature coefficient, coordination number, sliding fraction, and the angle of internal friction. The relevant parameters are listed in Table 5 and are represented as a matrix in Eq. 6. It should be noted that the coordination number and sliding fraction are the average values in the shearing process.

$$\left(X_1^{'}, X_2^{'}, X_3^{'}, X_4^{'}\right) = \begin{pmatrix} x_1^{'}(0) & x_2^{'}(0) & x_3^{'}(0) & x_4^{'}(0) \\ x_1^{'}(1) & x_2^{'}(1) & x_3^{'}(1) & x_4^{'}(1) \\ x_1^{'}(2) & x_2^{'}(2) & x_3^{'}(2) & x_4^{'}(2) \\ x_1^{'}(3) & x_2^{'}(3) & x_3^{'}(3) & x_4^{'}(3) \\ x_1^{'}(4) & x_2^{'}(4) & x_3^{'}(4) & x_3^{'}(4) \end{pmatrix}. \quad (6)$$

Defining the first column in the matrix as the reference data column, we get

$$\begin{aligned} X_0^{'} &= \left(x_0^{'}(0), x_0^{'}(1), x_0^{'}(2), x_0^{'}(3), x_0^{'}(4)\right) \\ &= \left(x_1^{'}(0), x_1^{'}(1), x_1^{'}(2), x_1^{'}(3), x_1^{'}(4)\right). \end{aligned}$$

Then all values in the table, including the friction angle, were normalized using $x_i(k) = \frac{x_i^{'}(k)}{x_i^{'}(1)}, i = 1, 2, 3, 4, k = 0, 1, 2, 3, 4.$

$$(X_1, X_2, X_3, X_4) = \begin{pmatrix} x_1(0) & x_1(0) & x_3(0) & x_4(0) \\ x_1(1) & x_2(1) & x_3(1) & x_4(1) \\ x_1(2) & x_2(2) & x_3(2) & x_4(2) \\ x_1(3) & x_2(3) & x_3(3) & x_4(3) \\ x_1(4) & x_2(4) & x_3(4) & x_4(4) \end{pmatrix}. \quad (7)$$

The resolution coefficient ρ was set to 0.5, and the relation coefficient was calculated using Eq. 8.

$$\zeta_i(k) = \frac{\min\limits_i \min\limits_k |x_0(k) - x_i(k)| + \rho \max\limits_i \max\limits_k |x_0(k) - x_i(k)|}{|x_0(k) - x_i(k)| + \rho \max\limits_i \max\limits_k |x_0(k) - x_i(k)|}, \quad i = 1, 2, 3, 4, k = 0, 1, 2, 3, 4. \quad (8)$$

By considering the average of the relation coefficient in the entire gradation range, we get the following:

$$\zeta(1) = 0.60, \zeta(2) = 0.62, \zeta(3) = 0.84, \zeta(4) = 0.95.$$

This indicates that the correlation between sliding fraction and internal friction angle is strongest, and it is not that sliding fraction affects the internal friction angle. The larger the internal friction angle, the more fully the particles engage, and the more obvious the sliding phenomenon of particles during shear failure. The correlation between coordination number and internal friction angle can also be explained in this way. Due to the fact that the non-uniformity and curvature coefficients of samples with different gradations remain unchanged throughout the shear

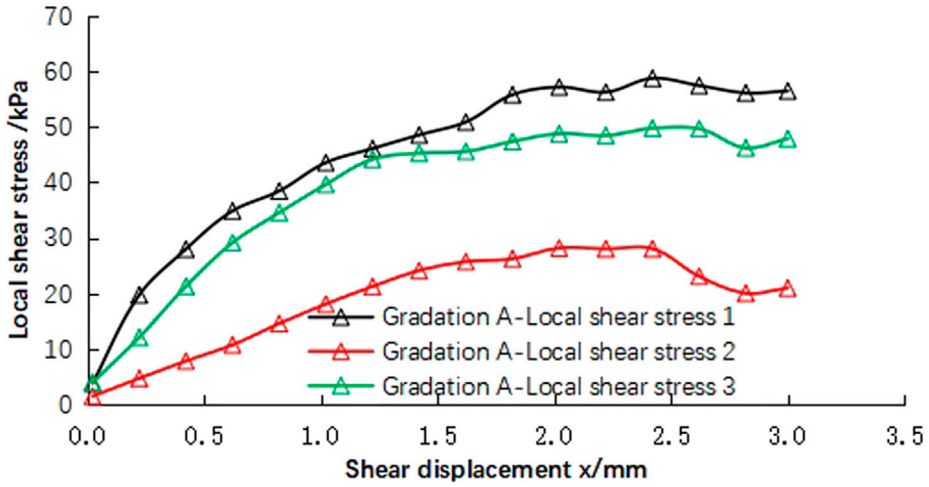

FIGURE 7
Relationship between local shear stress *vs.* shear displacement (Gradation A).

TABLE 4 Particle slide fraction of different gradations at different positions (%).

Measure circle No.	1	2	3	average
Gradation A	1.92	0.79	2.34	1.68
Gradation B	1.97	0.81	2.47	1.75
Gradation C	2.01	0.86	2.49	1.79
Gradation D	1.89	0.90	2.45	1.75

TABLE 5 Particle slide fraction of different gradations at different positions (%).

Gradation	A	B	C	D
Friction angle	34.41	36.76	38.27	35.87
Curvature coefficient	1.47	0.51	1.29	0.84
Non-uniformity coefficient	4.91	8.9	7.39	4.23
Coordination number	4.07	3.92	3.58	4.18
Sliding fraction	1.68	1.75	1.79	1.75

test, it can be seen from $\zeta(1) = 0.60$ and $\zeta(2) = 0.62$ that the non-uniformity coefficient has a greater impact on the internal friction angle. This is consistent with the previous analysis (Section 2). The above numerical simulation results suggest that the particles' sliding fraction is closely related to the sand shape because the particles' shape affects the rotation and sliding between each other. Further study will be conducted in terms of the particle size effect.

4 Conclusion and discussion

The research of this paper can be summarized as the following conclusions:

(1) The indoor direct shear test results and grey correlation analysis both indicate that the non-uniformity coefficient and curvature coefficient of sand particles have a significant impact on the internal friction angle, but the non-uniformity coefficient has a relatively large impact. Specifically, the larger the non-uniformity coefficient, the larger the internal friction angle, the larger the curvature coefficient, and the smaller the internal friction angle.

(2) The results of force chain analysis explain the stress concentration and dilatancy in the sand direct shear test from the meso perspective. Through the change of Coordination number, local stress, and sliding fraction with the shear process, the internal mechanism of shear failure can be more deeply understood from the microscopic perspective. For example, the contact between particles, the stress inside the particle cluster, and the sliding of particles can all be clearly presented through discrete element simulation. This is of great significance for studying the shear failure process of particulate matter.

Due to the relatively small number of graded samples, there may be limitations in the applicability of the relationship between curvature coefficient, non-uniformity coefficient, and internal friction angle of sand. In addition, this article did not consider the influence of confining pressure through simple direct shear tests.

The particles of sand are relatively large, and the influence of sand particle shape was not considered in the discrete element simulation modeling in this article, which may lead to inconsistency with the actual situation. For example, different particle shapes may exhibit different occlusions and rotations when subjected to shear forces.

Based on the two limitations mentioned above, the next step of work will continue in the following areas: increasing the number of samples, using triaxial shear tests instead of direct shear tests, and establishing a discrete element numerical model that can consider particle shape.

Data availability statement

The original contributions presented in the study are included in the article/supplementary material, further inquiries can be directed to the corresponding authors.

Author contributions

For research articles with several authors, a short paragraph specifying their individual contributions must be provided. The following statements should be used: "conceptualization, HG and MT; methodology, HG; software, KY; validation, CG; formal analysis, SY; resources, HG; data curation, RG; writing—Original draft preparation, HG and JF; writing—Review and editing, HG, CG, SW, and YN". All authors contributed to the article and approved the submitted version.

Funding

This research was funded by Shaanxi Province Key R&D Program, grant number 2023-YBSF-324; Research Project of China Electronic Research Institute of Engineering Investigations and Design, grant number 2020-DKY-W02.

Acknowledgments

I express my gratitude to all those who have helped me during the writing of this paper. Especially, I gratefully acknowledge the financial support of Shaanxi Province, and the Research Project of the China Electronic Research Institute of Engineering Investigations and Design.

Conflict of interest

The authors declare that the research was conducted in the absence of any commercial or financial relationships that could be construed as a potential conflict of interest.

Publisher's note

All claims expressed in this article are solely those of the authors and do not necessarily represent those of their affiliated organizations, or those of the publisher, the editors and the reviewers. Any product that may be evaluated in this article, or claim that may be made by its manufacturer, is not guaranteed or endorsed by the publisher.

References

Bai, B., Long, F., Rao, D., and Xu, T. (2017). The effect of temperature on the seepage transport of suspended particles in a porous medium. *Hydrol. Process.* 31 (2), 382–393. doi:10.1002/hyp.11034

Bai, B., Zhou, R., Cai, G., Hu, W., and Yang, G. (2021). Coupled thermo-hydro-mechanical mechanism in view of the soil particle rearrangement of granular thermodynamics. *Comput. Geotechnics* 137 (8), 104272. doi:10.1016/j.compgeo.2021.104272

Bayat, E., and Bayat, M. (2013). Effect of grading characteristics on the undrained shear strength of sand: Review with new evidences. *Arabian J. Geosciences 2013 6* 6 (11), 4409–4418. doi:10.1007/s12517-012-0670-y

Belkhatir, M., Arab, A., Della, N., et al. (2012). Experimental study of undrained shear strength of silty sand: Effect of fines and gradation. *Geotechnical Geol. Eng.* 30 (5), 1103–1118. doi:10.1007/s10706-012-9526-1

Belkhatir, M., Arab, A., and Schanz, T. (2011). Laboratory study on the liquefaction resistance of sand-silt mixtures: Effect of grading characteristics. *Granul. Mater* 13 (5), 599–609. doi:10.1007/s10035-011-0269-0

Havaee, S., Mosaddeghi, M. R., and Ayoubi, S. (2015). *In situ* surface shear strength as affected by soil characteristics and land use in calcareous soils of central Iran. *Geoderma* 237-238, 137–148. doi:10.1016/j.geoderma.2014.08.016

Ibrahim, A., and Meguid, M. A. (2023). CFD-DEM simulation of sand erosion into defective gravity pipes under constant groundwater table. *Tunn. Undergr. space Technol.* 131, 1–17. doi:10.1016/j.tust.2022.104823

Jiang, M., Konrad, J. M., and Leroueil, S. (2003). An efficient technique for generating homogeneous specimens for DEM studies. *Comput. Geotechnics 2003 30* 30 (5), 579–597.

Kamalzadeh, A., and Pender, M. J. (2023). Dilatancy effects on surface foundations on dry sand. *Int. J. geomechanics* 23 (3), 1.1–1.13. doi:10.1061/IJGNAI.GMENG-7826

Kong, L., Ji, L., and Cao, J. (2013). Deformation mesomechanism of sands with different grain gradations under different stress paths. *Chin. J. Rock Mech. Eng.* 11, 2334–2341. (in Chinese). doi:10.1061/IJGNAI.GMENG-7826

Li, X., Sun, J., Ren, H., Lu, T., and Ren, Y. (2022). *The effect of particle size distribution and shape on the microscopic behaviors of loess via DEM*. Berlin, Germany: Springer.

Li, Y. Effects of particle shape and size distribution on the shear strength behavior of composite soils. *Bull. Eng. Geol. Environ.*, 2013, 72(3-4): 371–381.doi:10.1007/s10064-013-0482-7

Li, Y., Fang, Y., and Yang, Z. (2023). Two criteria for effective improvement depth of sand foundation under dynamic compaction using discrete element method. *Comput. Part. Mech.* 10 (3), 397–404. doi:10.1007/s40571-022-00506-5

Liu, F., Fu, J., Wang, J., Gao, Z., Li, H., and Li, J. (2022). Effect of the particle size ratio on macro- and mesoscopic shear characteristics of the geogrid-reinforced rubber and sand mixture interface. *Geotext. geomembranes* 50 (4), 779–793. doi:10.1016/j.geotexmem.2022.04.002

Li, Y., Fang, Y., and Yang, Z. (2015). Constitutive modeling for granular materials considering grading effect. *Chin. J. Getechnical Eng.* 37, 299–305. (in Chinese). doi:10.11779/CJGE201502013

Mollamahmutolu, M., and Avci, E. (2020). Effects of particle gradation, relative density and curing on the strength of silicate grouted sand. *Geotechnical Geol. Eng.* 38 (6). doi:10.1007/s10706-020-01463-7

Omar, T., and Sadrekarimi, A. (2014). Specimen size effects on behavior of loose sand in triaxial compression tests. *Can. Geotechnical J.* 52 (6), 1–15. doi:10.1139/cgj-2014-0234

Park, S. S., and Jeong, S. W. (2015). Effect of specimen size on undrained and drained shear strength of sand. *Mar. Georesources Geotechnol.* 28 (3), 353–358. doi:10.7843/kgs.2012.28.3.15

Tai, P., Wu, F., Chen, R., Zhu, J., Wang, X., and Zhang, M. (2023). Effect of herbaceous plants on the response of loose silty sand slope under rainfall. *Bull. Eng. Geol. Environ.* 82 (1), 42.1–42.10. doi:10.1007/s10064-023-03066

Sato, T., Saito, H., Tagashira, H., Hayashida, Y., Masutani, M., and Kohgo, Y. (2022). On seismic behavior of unsaturated fill dam models. *Paddy Water Environ.* 20 (3), 355–368. doi:10.1007/s10333-022-00897-4

Sezer, A. (2013). Simple models for the estimation of shearing resistance angle of uniform sands. *Neural Comput. Appl.* 22 (1), 111–123. doi:10.1007/s00521-011-0668-5

Vangla, P., and Latha, G. M. (2015). Influence of particle size on the friction and interfacial shear strength of sands of similar morphology. *Int. J. Geosynth. Ground Eng.* 1 (1), 1–12. doi:10.1007/s40891-014-0008-9

Wang, Z., Wang, P., Yin, Z., and Wang, R. (2022). Micromechanical investigation of the particle size effect on the shear strength of uncrushable granular materials. *Acta Geotech.* 17 (10), 4277–4296. doi:10.1007/s11440-022-01501-z

Xie, X., Ye, B., Zhao, T., Feng, X., and Zhang, F. (2023). DEM investigation into the effects of liquefaction history-induced anisotropy on sand behaviors. *Int. J. geomechanics* 23 (3), 1.1–1.18. doi:10.1061/IJGNAI.GMENG-7492

Zhao, H., Zhang, J., Liang, S., Lu, L., Zhang, L., and Zhang, Y. (2023). Evaluation of surrounding rock quality of tunnels using a combined method of weighted norms based grey relational analysis and fuzzy mathematics theory. *Geotechnical Geol. Eng.* 41 (1), 311–318. doi:10.1007/s10706-022-02281-9

frontiers | Frontiers in Materials

TYPE Original Research
PUBLISHED 11 July 2023
DOI 10.3389/fmats.2023.1201752

OPEN ACCESS

EDITED BY
Xianze Cui,
China Three Gorges University, China

REVIEWED BY
Han Zhiming,
Shijiazhuang Tiedao University, China
Hongliang Tu,
Chinese Academy of Sciences (CAS), China

*CORRESPONDENCE
Lei Dong,
donglei0401@hotmail.com

RECEIVED 07 April 2023
ACCEPTED 16 June 2023
PUBLISHED 11 July 2023

CITATION
Dong L, Yao A, Zhou D and Zhang P (2023), Characterizing the bending behavior of underground utility tunnel roofs in a fabricated composite shell system. *Front. Mater.* 10:1201752. doi: 10.3389/fmats.2023.1201752

Characterizing the bending behavior of underground utility tunnel roofs in a fabricated composite shell system

Lei Dong[1,2]*, Aijun Yao[1], Daxing Zhou[2,3] and Pengfei Zhang[2,3]

[1]Beijing University of Technology, Beijing, China, [2]China Railway Construction Group Co., LTD., Beijing, China, [3]CRCC Construction Industrialization Engineering Laboratory, Beijing, China

The traditional underground utility tunnel system is characterized by a lengthy construction period, material waste, and poor engineering quality. This study proposes the prefabricated composite shell system underground utility tunnel as a new type of prefabricated underground utility tunnel system. This system uses 20 mm thick high-performance cement-based materials as permanent templates, with steel reinforcement skeletons placed in the cavity between the two side molds, and concrete can be poured after on-site hoisting and positioning to form an integrated tunnel. This study first systematically introduces the system design method of the prefabricated composite shell system underground utility tunnel and clarifies its component and connection structures. Then, bending tests are conducted on the composite shell tunnel top plate specimens, and a cast-in-place top plate specimen is selected as a control group. A suitable bearing capacity calculation formula for composite shell top plates is derived and proposed based on test phenomena and results analysis. The results showed that the prefabricated outer template and internal cast-in-place concrete of the composite shell top plate specimen have good collaborative performance. Its bearing capacity, stiffness, and failure phenomena are consistent with those of cast-in-place components, as are its mechanical properties. In addition, the proposed bearing capacity calculation formula for a composite shell top plates is highly accurate and can guide the design of such components.

KEYWORDS

utility tunnels in composite shell system, high-performance cement-based material, bending test, theoretical calculation, fabricated composite shell system

1 Introduction

Since 2015, China has witnessed explosive growth in the mileage of constructed utility tunnels. Tunnels are the lifeline of cities (Valdenebro and Gimena, 2018; CANTO-PERELLO and CURIEL-ESPARZA, 2001; O'ROURKE et al., 2001; DARLI et al., 2021), and the stress on an underground structure is more complex than that on an above-ground structure (Bai et al., 2019; Luo et al., 2020; Bai et al., 2021a), so its safety is essential. From the perspective of the construction mode, the integral cast-in-place mode is applied to most of the tunnels. The integral cast-in-place mode provides good waterproof performance but has a longer construction duration, a greater environmental impact, and requires more field workers. Thus, it is an inevitable trend to adopt the fabricated construction method.

The composite slab-type concrete structure has been extensively studied and applied in constructing above-ground buildings (Gu et al., 2020; Bai et al., 2021b; Jiang et al., 2021;

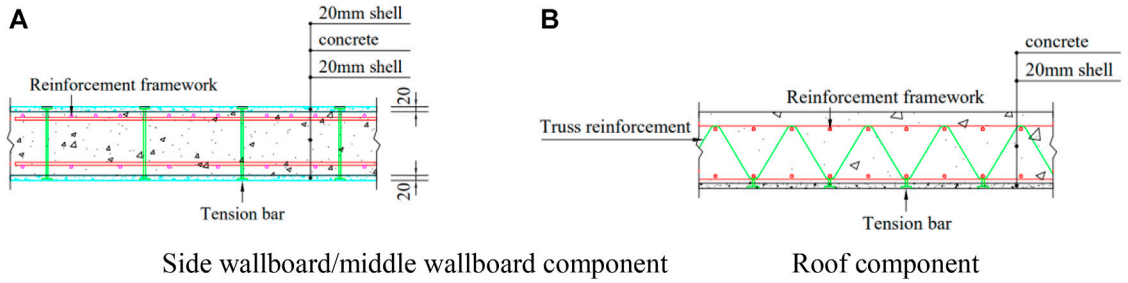

FIGURE 1
Structure of composite shell utility tunnel components. **(A)** Side wallboard/middle wallboard component, **(B)** Roof component.

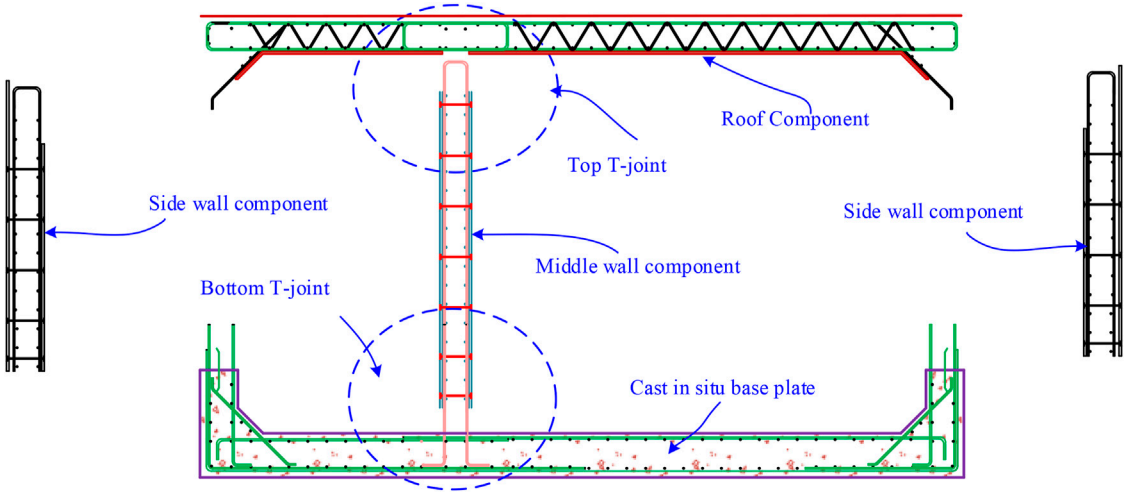

FIGURE 2
Schematic diagram for composite shell utility tunnels.

Zhou et al., 2021; Bai et al., 2023). As a structural member, it consists of the precast concrete arranged on both sides as the formwork connected through truss bars. In the construction process, concrete is poured into the cavity to form the integral structure.

Some scholars have studied composite slab-type underground utility tunnels. Yanmin Yang (YANG et al., 2020) conducted static loading tests on a fabricated composite tunnel and analyzed the phenomenon of its failure, bearing capacity and load-strain curve, and load-displacement curve of each measuring point on the axillary angle under the influence of simulated overburden load. They indicated that the axillary angle exhibits no obvious cracks under the normal service condition, which suffers significant deformation and presents good mechanical performance only under ultimate load. Weichen Xue (XUE et al., 2018) et al. Investigated the seismic performance outside the composite shear wall plane, and their results showed that the ultimate bearing capacity outside the composite shear wall plane is 10.7% lower than that of the cast-in-place shear wall. However, there are still some limitations in applying this technology to underground engineering, which are primarily illustrated by the following points:

(1) It is not easy to detect the molding quality of post-cast concrete. The prefabricated slab for existing underground fabricated composite concrete utility tunnels is generally made of ordinary concrete with a minimum thickness of 50 mm. In addition, there are steel bars within the post-cast concrete, making it difficult to detect the molding quality directly.
(2) The joint connection is poor. The utility tunnel is an out-of-plane stress component. The prefabricated component is thicker, the connecting steel bars are located in the cavity inside the prefabricated slab, and the ultimate bearing capacity outside the plane is lower than that of the cast-in-place structure.

The application of high-performance cement-based materials in construction engineering has become more mature (Roy et al., 1972; Wang et al., 2012; Zheng et al., 2015; Chong et al., 2016; De et al., 2016; Zheng et al., 2016). The prefabricated slab made of ordinary concrete is replaced with formwork made of high-

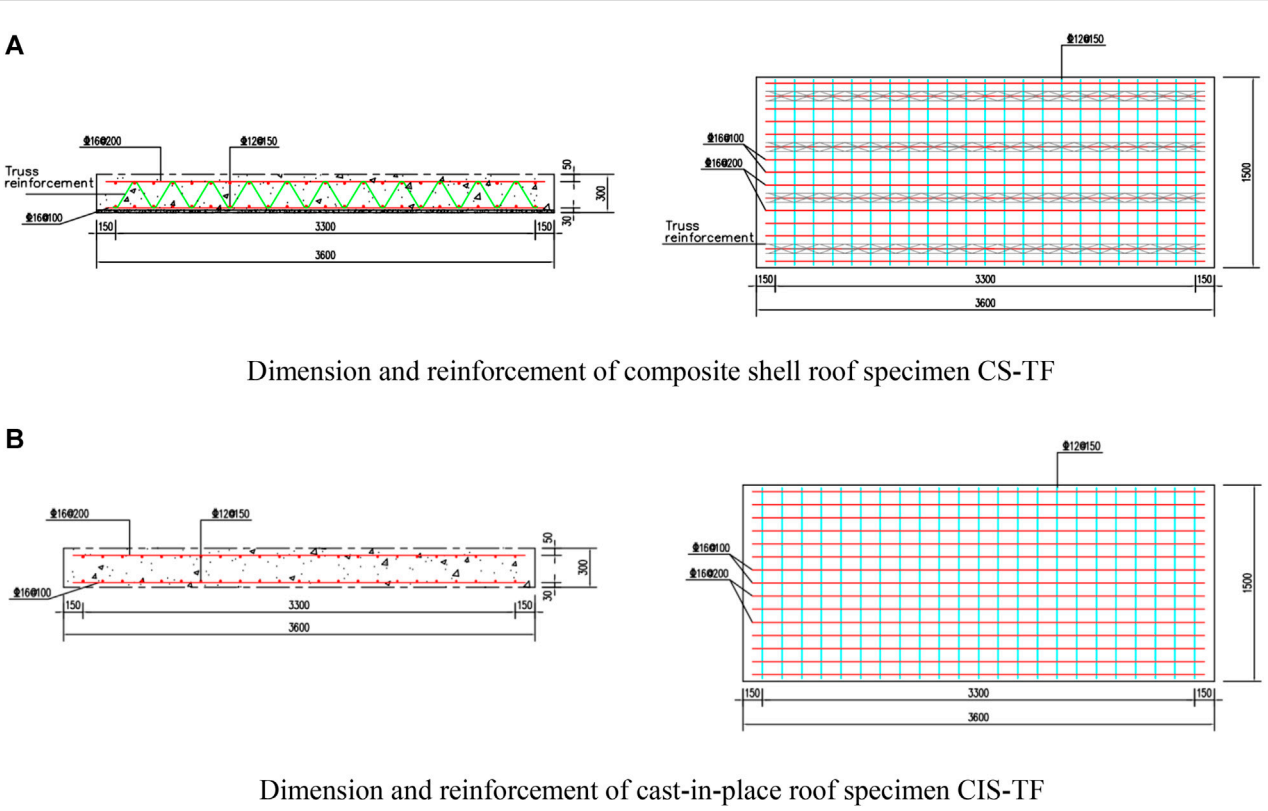

FIGURE 3
Geometric dimension and reinforcement of specimens. **(A)** Dimension and reinforcement of composite shell roof specimen CS-TF, **(B)** Dimension and reinforcement of cast-in-place roof specimen CIS-TF.

TABLE 1 Mix proportion of materials.

Name	Sulphoaluminate cement P·0 42.5	Quartz sand	Water	Admixture	Steel fiber	Polypropylene fiber
Weight (kg)	500.00	500.00	125.00	10.48	35.00	1.00

TABLE 2 Size and quantity of test specimens.

Cube test specimen 100 × 100 × 100	Prism test specimen 100 × 100 × 300	Slab-shaped test specimen 20 × 60 × 320	Cement mortar test specimen 40 × 40 × 160
6	8	9	6

performance material to reduce the thickness of the prefabricated component, thereby assisting in settling the problems mentioned above. Based on this concept, a new technical system of underground fabricated concrete utility tunnels is proposed—underground utility tunnels of prefabricated composite shell system (after this referred to as composite shell utility tunnels). High-strength materials can provide the following advantages:

1) The out-of-plane mechanical performance is better. The loaded and connecting steel bars are all located in the cavity between the formwork shells, and the steel bars at the joints are connected by a lapping connection. The connection method is consistent with the cast-in-place structure, and the distance between the two rows of connecting steel bars is significant, resulting in improved out-of-plane mechanical performance.
2) Transportation and installation costs are low. The weight of composite shell utility tunnels is about 40% lower than that of composite slab concrete pipe gallery, the transportation efficiency is high, and the mechanical requirements for on-site installation are less, with a broader application scenario.
3) Because the formwork shell is thin, thermal infrared technology can be employed to determine the quality of post-pouring concrete molding.

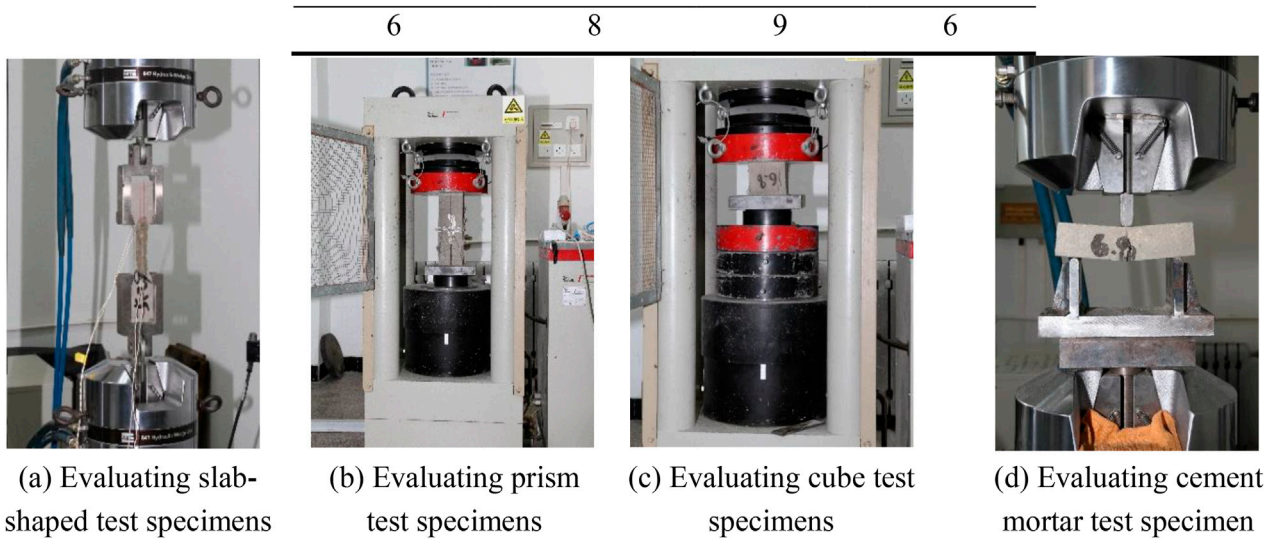

FIGURE 4
Fabrication and Evaluating test specimens. **(A)** Evaluating slab-shaped test specimens, **(B)** Evaluating prism test specimens, **(C)** Evaluating cube test specimens, **(D)** Evaluating cement mortar test specimen.

This study addresses the design structure of the system first, determines the component structure, joint construction, the ratio of formwork shell materials, and others of the composite shell utility tunnels, and tests the fundamental mechanical properties of formwork shell materials. Then, an experimental investigation is conducted on the composite shell roof specimens to analyze the primary performance indices and failure forms of cast-in-place and composite shell specimens. On the other hand, the test phenomena and results are utilized to derive the calculation formula for the bearing capacity of the composite shell roof specimens, providing a reference for the system's application.

2 System introduction

2.1 Component structure introduction

Depending on the structure, the composite shell utility tunnel components are divided into formwork shells, steel bar trusses, connectors, and post-cast concrete. The formwork shell is made of high-performance inorganic material, with a thickness of 20 mm, the steel bar truss is placed on the outside of the prefabricated formwork shell, and the connectors are attached to the steel reinforcement cage and poured into the formwork shell to secure the steel bar truss and the formwork shell, as depicted in Figure 1.

The composite shell utility tunnel components were prefabricated at the factory before being installed on-site and pouring concrete. The transient operating condition involves stripping, transporting, hoisting, concrete pouring, and others. Comprehensively considering the load to be borne by the formwork shell under various working conditions, the spacing between the opposite-pull type's connectors was 400 mm, the thickness of the formwork shell was 20 mm, and its flexural strength was no less than 12 MPa.

2.2 Joint construction of composite shell utility tunnels

The composite shell utility tunnels are divided into side wallboard, middle wallboard, and roof components based on the component types. Figure 2 depicts how the double-warehouse utility tunnels are subdivided into their component parts. The joint position between the side wallboard of the composite shell and the lower cast-in-place part was set at 500 mm above the top surface of the baseboard, and axillary angles were placed at the four corners of the utility tunnels. During the field operation, concrete was first poured into the bottom plate on-site, and once it reached a certain strength, the concrete on the contact surface was chiseled to create a rough surface. The composite shell's side wallboards and interior wallboards were placed and secured, followed by the installation of the composite shell's roof. After the composite shell components were assembled in place, concrete was poured into the cavity to form the integral structure.

Since the steel bars in the composite shell components were located in the cavity between formwork shells, the composite shell components, cast-in-place baseboard, and composite shell components can be connected utilizing steel bar splicing, which was consistent with the steel bar connection mode of cast-in-place structure.

3 Experimental study

3.1 Test overview

3.1.1 Specimen design

The geometric dimensions and reinforcement of two roof specimens of composite shell utility tunnels are illustrated in Figure 3. The length × width for both specimens CS-TF and

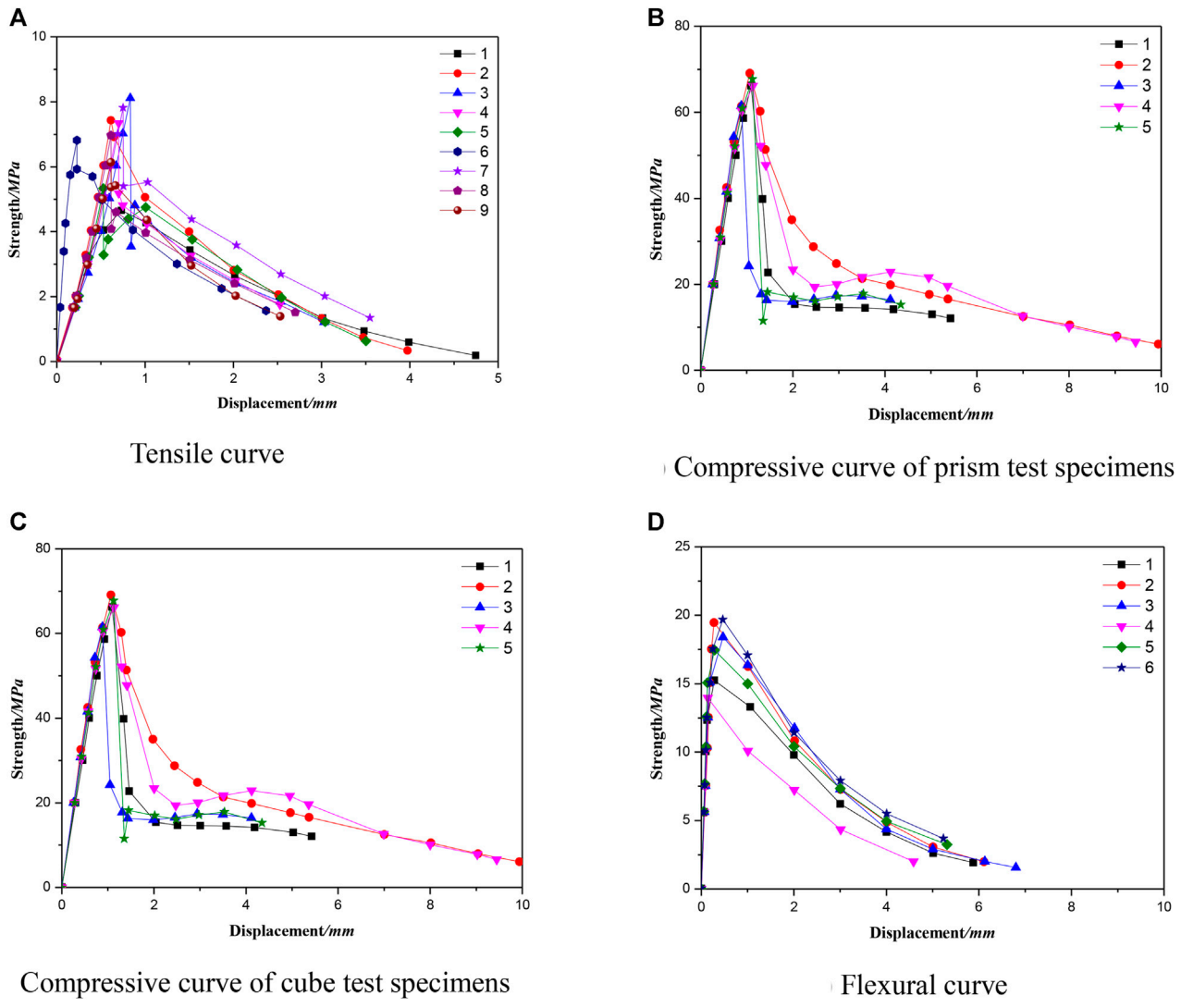

FIGURE 5
Loading curves. **(A)** Tensile curve, **(B)** Compressive curve of prism test specimens, **(C)** Compressive curve of cube test specimens, **(D)** Flexural curve.

CIS-TF were 3,600 × 1,500 mm^2, and the thickness of the cast-in-place specimen CIS-TF was 300 mm. The thickness of the formwork shell at the bottom of the composite shell specimen CS-TF was 20 mm, while the thickness of the cast-in-place concrete part was 280 mm. The upper longitudinal steel bars in the two specimens were C16@200, the lower longitudinal steel bars were C16@100, and the upper and lower horizontal steel bars were C12@150. The positioning of the middle and upper reinforcing and lower reinforcing meshes of the composite shell specimen CS-TF was achieved by the assembled four truss steel bars (Figure 3), whereas that of CIS-TF was accomplished by reinforced pony stools.

3.1.2 Design of mixture proportion of formwork shell materials and performance evaluation

Tests were conducted on the configuration and performance of formwork shell material to ensure the required mechanical properties of the above materials. Table 1 lists the mixture proportion of formwork shell materials. A total of 29 test specimens were created, whereas Table 2 exhibits their sizes and quantity. Cube specimens were employed to measure the cubic compressive strength, while cement mortar test specimens were conducted to compute the flexural strength. In addition, prism test specimens were performed to determine the elastic modulus, Poisson's ratio, compressive strength, and peak strain of prisms, whereas slab-shaped test specimens were utilized to calculate the tensile strength and peak tensile strain. Figure 4 illustrates the fabrication and test of various specimens. Before the test, resistance strain gauges were placed on the surface of each test specimen to obtain the elastic modulus, Poisson's ratio, and the equivalent values of peak tensile strain and compressive strain.

Figure 5 displays the loading curve obtained by the stroke of the testing machine, and Table 3 shows the detailed data indices for elastic modulus and Poisson's ratio measured with a resistance strain gauge. The peak tensile strain and the peak compressive strain obtained utilizing the resistance strain gauge were 150–300 με and 2,500–3,500 με, respectively.

TABLE 3 Strength, elastic modulus and Poisson's ratio.

	Tensile strength (MPa)	Compressive strength of prism (MPa)	Cube strength (MPa)	Flexural strength (MPa)	Elastic modulus (MPa)	Poisson's ratio
Test 1	4.78	66.24	75.88	15.54	34,985	0.212
Test 2	7.43	70.39	79.39	19.57	34,549	0.177
Test 3	8.15	61.53	77.71	18.46	34,450	0.195
Test 4	7.34	66.24	81.07	13.96	—	—
Test 5	5.33	67.94	80.37	17.51	—	—
Test 6	6.87	—	74.36	19.72	—	—
Test 7	7.82	—	—	—	—	—
Test 8	6.97	—	—	—	—	—

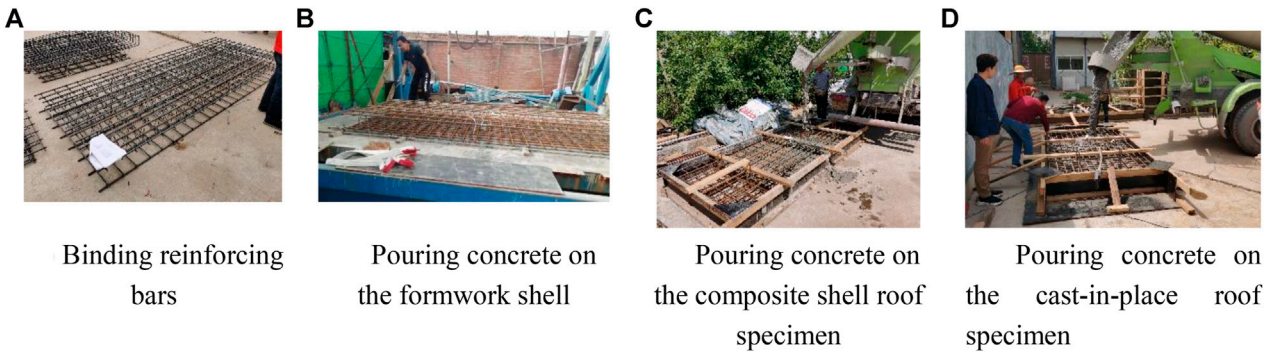

FIGURE 6
Fabricating process of roof specimen. **(A)** Binding reinforcing bars, **(B)** Pouring concrete on the formwork shell, **(C)** Pouring concrete on the composite shell roof specimen, **(D)** Pouring concrete on the cast-in-place roof specimen.

TABLE 4 Strength of concrete and mortar.

Test number	Concrete strength	Shell strength
	f_{c1} (MPa)	f_{c2} (MPa)
CS-TF	35.3	66.4
CIS-TF	42.4	—

TABLE 5 Mechanical properties of reinforcement.

Rebar model	f_y	f_u	Elongation after fracture
	(MPa)	(MPa)	(%)
C12	452	604	18
C16	424	598	19

3.1.3 Specimen fabrication

During the composite shell roof specimen CS-TF fabrication, the reinforcing mesh sheets on both sides were bound first. The reinforcing mesh sheets were then secured by truss bars to form a steel skeleton, as shown in Figure 6A. The steel skeleton was placed horizontally on the formwork table, supported on the bottom form by the truss bars, and 20 mm of inorganic high-performance material was poured to successfully fabricate the formwork shell, as illustrated in Figure 6B. When the formwork shell reached a specific strength, it was demolded, transported to a predetermined location, and concrete was poured, as revealed in Figures 6C, D.

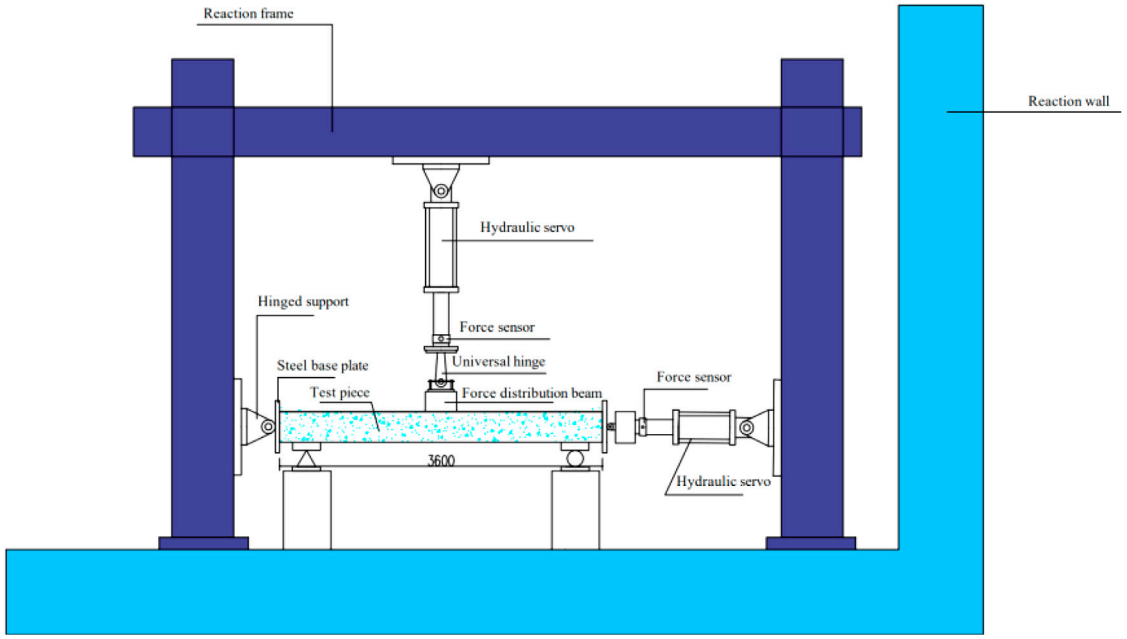

FIGURE 7
Loading device.

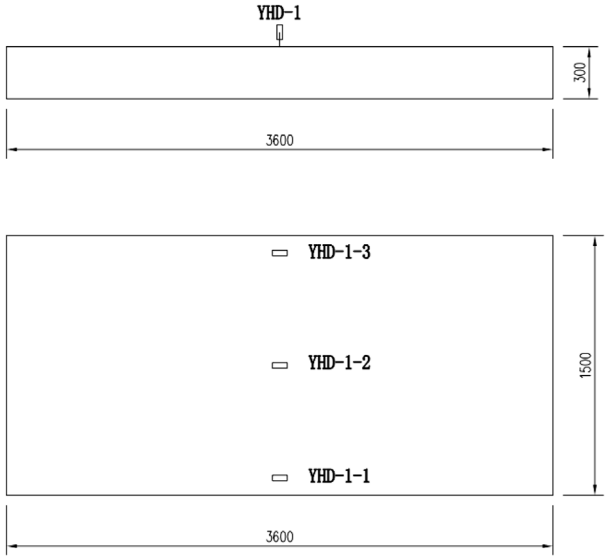

FIGURE 8
Layout of displacement meters.

3.1.4 Material strength

The design strength of the post-pour part of concrete on CS-TF and CIS-TF was C40. Standard mortar test specimens were reserved when the formwork shell was fabricated, and standard cube test specimens were reserved when concrete was poured. The test and wall specimens were cured under identical conditions. As shown in Table 4, on the day of the test, the average compressive strength f_{c1} of concrete prism and the average compressive strength f_{c2} of formwork shell mortar were determined. Table 5 displays the measured yield strength f_y, ultimate strength f_u, and elongation after fracture for steel bars.

3.1.5 Loading scheme and loading system

Midas software was employed to calculate the underground utility tunnel model with a 2.5 m burial depth to obtain the pressure of underground soil on each part of the utility tunnels under static conditions. Based on the calculation results, the axial pressure on the underground utility tunnel's roof was 100 kN. During loading, the specimen was placed horizontally on the supporting point, and the hydraulic jacks arranged horizontally exerted axial force by the steel distributive beam. Vertically arranged hydraulic jacks applied a linear load to the specimens' midspan by a steel distributive beam. In addition, force sensors were attached to the hydraulic jacks to obtain real-time load data.

Hierarchical monotone loading was used as the loading mode. First, loading up to 100 kN was performed using 20 kN as a level, followed by 40 kN as a level. The load holding time should not be between 5 and 10 min after completing the loading at each level. When it was determined that the load did not change greatly (the specimens yielded), but the displacement varied significantly during loading, the displacement was controlled, and loading was applied at a level of 10 mm. When the specimen's load-bearing capacity was reduced to 85% of its peak load, it was considered to have failed, and the loading was stopped. Figure 7 depicts the loading device and loading system.

3.1.6 Measurement scheme

A displacement meter was placed at the specimen's midspan to measure its loading point's displacement during loading, as illustrated in Figure 8. Reinforcement strain gauges were installed on the tension and compression sides of the specimen's midspan to

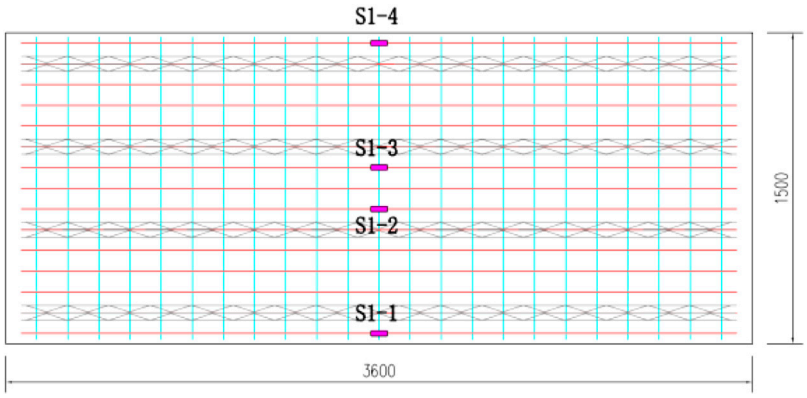

FIGURE 9
Layout of reinforcement strain gauges.

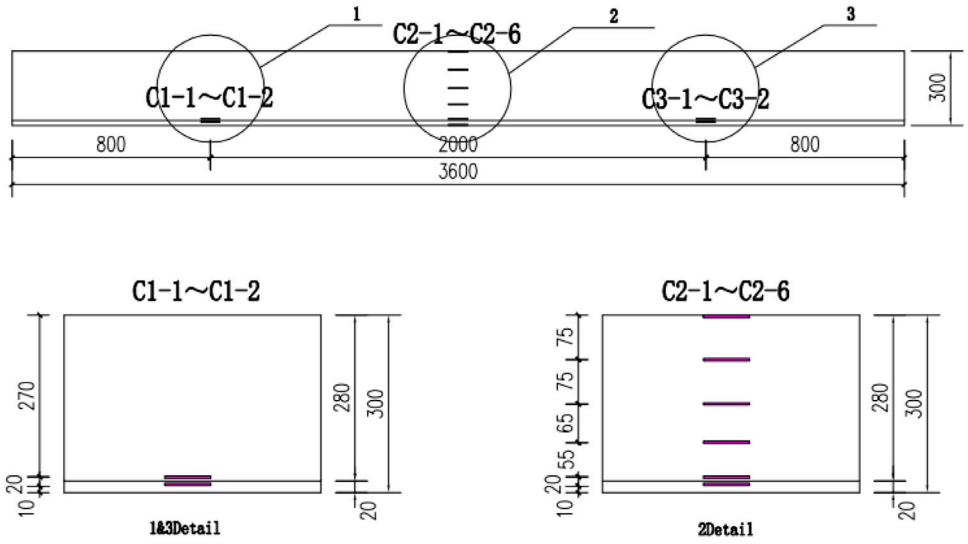

FIGURE 10
Layout of concrete strain gauges.

determine the variation laws on a strain of steel bars during loading, as demonstrated in Figure 9. Concrete strain gauges were located along the thickness direction of the roof specimen at the midspan of it and 1,000 mm away from the midspan on both sides to measure the variation laws on concrete strain at different heights during loading, as shown in Figure 10.

3.2 Testing phenomena and failure modes

3.2.1 Specimen CS-TF

(1) Specimen cracking: When the load at the loading point reached 143.73 kN (Δ = 3.18 mm), the first crack appeared below the loading point, and simultaneously the formwork shell and concrete cracked. The crack width was approximately 0.05 mm, and the length was about 100 mm.

(2) Cracking of the formwork shell-concrete joint surface: as the load rose, the width of the first crack gradually increased and extended upward, generating several new cracks. The cracks also passed through the joint surface, with the formwork and concrete cracking simultaneously, and the specimens exhibited good integrity. When the load reached 360.59 kN (Δ = 11.14 mm), cracks appeared within 300 mm of the loading point on the formwork shell-concrete joint surface. In this case, the maximum width of the cracks was 0.25 mm, the maximum length was approximately 180 mm, and the steel fibers at the cracking part on the formwork shell remained connected.

With the load increasing, existing cracks continued to develop and propagate, generating several new cracks. An obvious inflection point was observed on the load-displacement curve at the loading point, and then the loading was controlled by displacement.

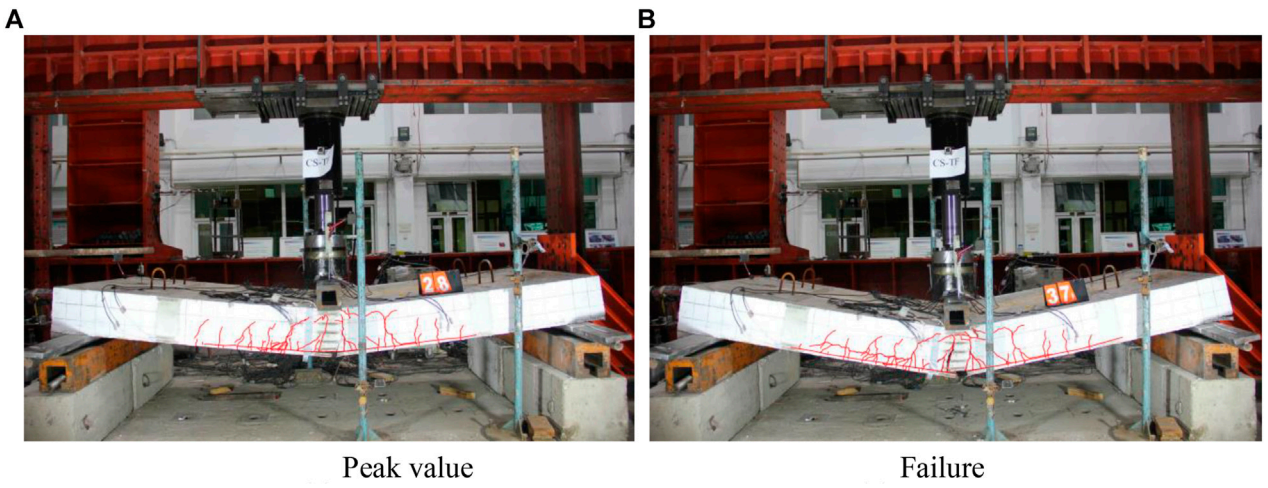

FIGURE 11
Evaluating phenomena of specimen CS-TF. **(A)** Peak value, **(B)** Failure.

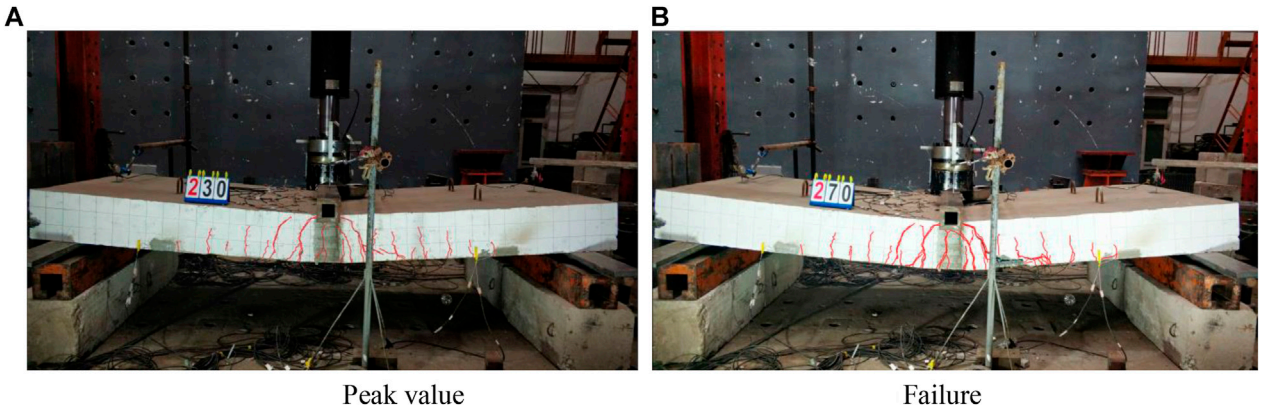

FIGURE 12
Evaluating phenomena of specimen CIS-TF. **(A)** Peak value, **(B)** Failure.

(3) Reaching the peak load: When the displacement at the loading point reached 142.79 mm, the specimen reached its peak load of 560.12 kN, and the corresponding specimen damage characteristics are shown in Figure 11A. In this case, the maximum crack width on the specimen was 8 mm, and the crack below the loading point extended to 250 mm in length. The formwork shell was disconnected below the loading point, and the steel fiber was no longer connected. Cracks appeared on the formwork shell-concrete joint surface within 1,800 mm below the loading point, and the concrete on the compression side was crushed.

(4) Completing loading: No new cracks were generated after reaching the peak load. The load decreased slowly as the control displacement increased, and the width of the existing crack continued to grow. When the displacement at the loading point achieved 248.00 mm, the load was reduced to 467.75 kN; cracks formed on the formwork shell-concrete joint surface within 2,000 mm below the loading point; and concrete crushing on the compression side was aggravated, the specimen failed severely, and the loading terminated. The corresponding specimen failure characteristics are shown in Figure 11B.

3.2.2 Specimen CIS-TF

(1) Specimen cracking: When the load reached 141.3 kN (Δ = 3.01 mm), the first crack appeared below the loading point, with a width of about 0.05 mm and a length of approximately 50 mm.
As the load increased, several new cracks appeared, and the first crack continued to extend. An obvious inflection point was observed on the load-displacement curve of the loading point, and the loading was subsequently controlled by displacement.

(2) Reaching the peak load: When the displacement at the loading point reached 107.05 mm, the specimen reached its peak load of 554.01 kN, and the corresponding specimen damage characteristics are shown in Figure 12A. In this case, the

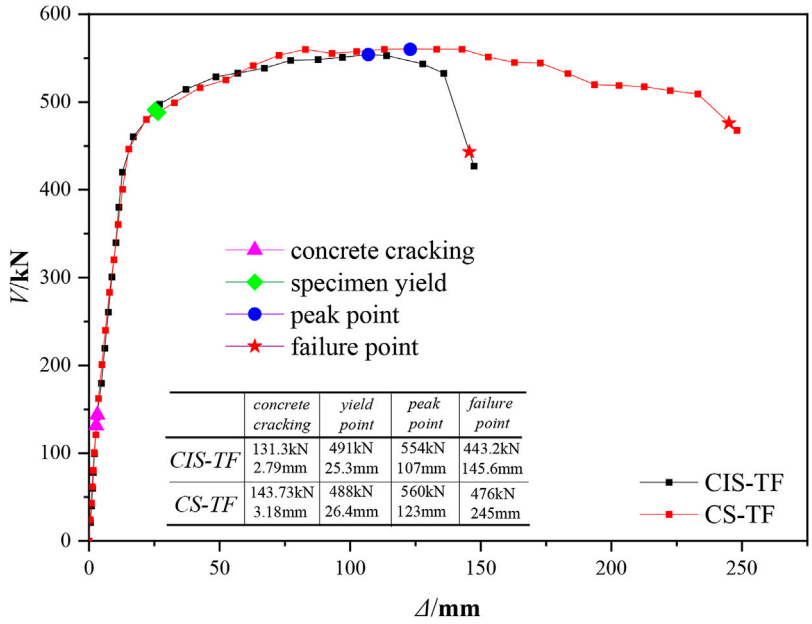

FIGURE 13
Load-displacement curve.

TABLE 6 Characteristics and ductility coefficients for each specimen's yield, peak, and failure points.

No.	Yield point		Peak point		Failure point	μ
	V_y	Δ_y	V_m	Δ_m	Δ_u/mm	
	(kN)	(mm)	(kN)	(mm)	(kN)	
CS-TF	488	26.4	560	123.0	245.2	9.29
CIS-TF	491	25.3	554	107.0	132.3	5.23

maximum width of the cracks was approximately 10 mm, the crack length below the loading point was 260 mm, and the concrete on the compression side was crushed.

(3) Completing loading: No additional cracks were produced after reaching the peak load. With the increase in displacement at the loading point, the load slowly decreased, existing cracks continued to develop, and the concrete in the compression zone was more severely crushed. When the displacement at the loading point achieved 147.41 mm, the load decreased to 427.08 kN, the specimen suffered a more severe failure, and the loading was terminated. The corresponding specimen failure characteristics are shown in Figure 12B.

3.3 Test results and analysis

3.3.1 Load-displacement skeleton curve

Figure 13 exhibits the load-midspan displacement (V-Δ) skeleton curve for the loading point of each specimen. It indicates that:

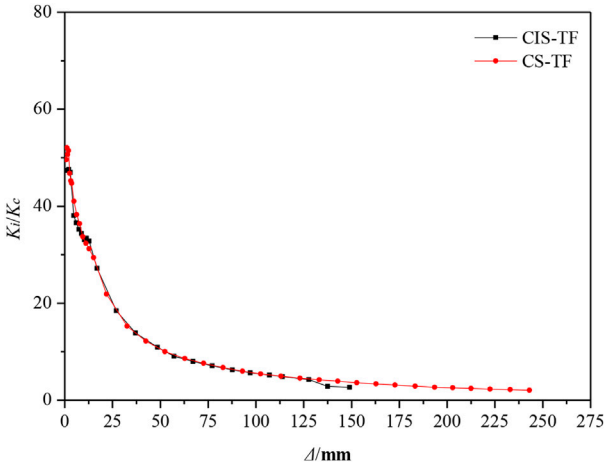

FIGURE 14
Secant stiffness degradation curve for roof component.

(1) The Load-displacement curve of the two specimens essentially coincided and presented the same variation trend. The formwork shell was located on the tensile side, not affecting the specimens' load-displacement characteristics.

(2) Both specimens were in an elastic state during the initial loading, and the load increased significantly while the displacement rose less. Cracks were then observed on the specimens, and the slope of the skeleton curves gradually decreased. As the loading progressed, an obvious inflection point appeared in the curves, and the specimens yielded.

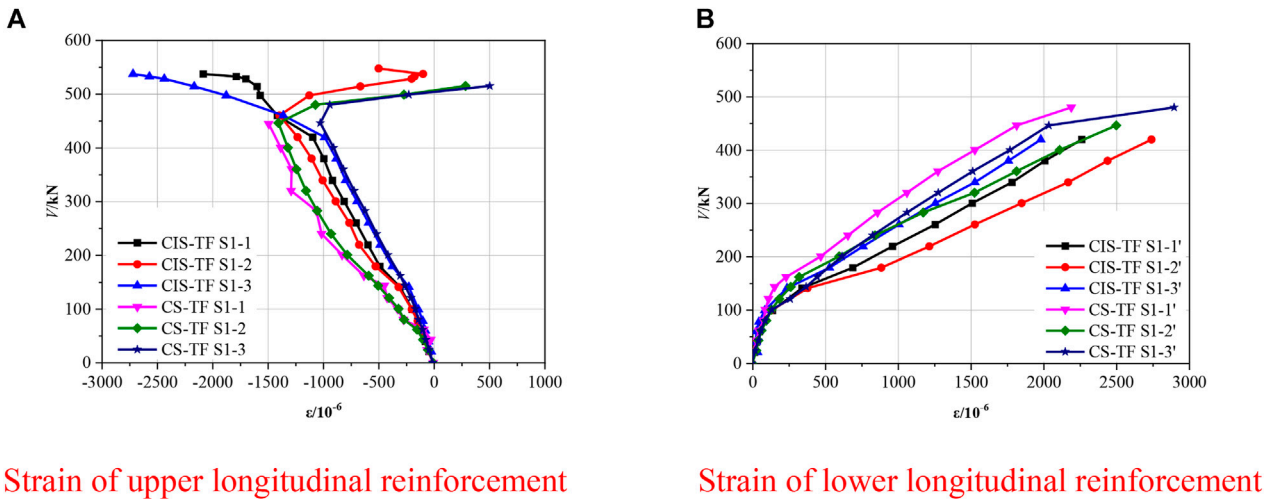

FIGURE 15
Strain curve for steel bars. **(A)** Strain of upper longitudinal reinforcement, **(B)** Strain of lower longitudinal reinforcement.

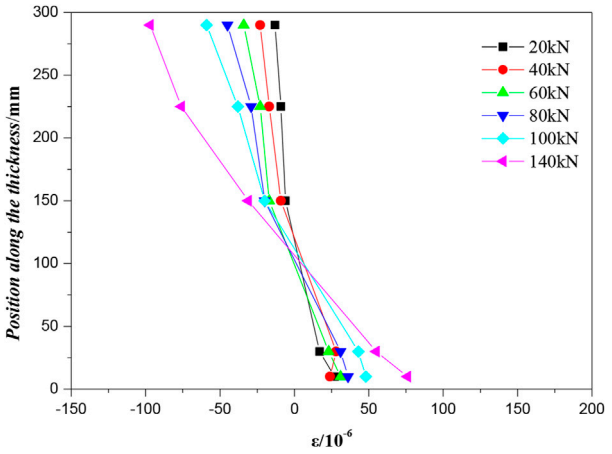

FIGURE 16
Strain curves for concrete at different positions.

After that, the specimen's load increased slowly, and its displacement grew significantly. After reaching the peak load, there were almost no new cracks on the tensile side at the specimen's midspan, the concrete on the compression side was crushed, and the load decreased slowly as the displacement improved. Finally, the load dropped to less than 85% of the peak load, and the loading terminated.

3.3.2 Characteristic values of load and displacement

Table 7 lists the characteristic values for the critical state points of the two specimens, wherein the yield point was determined by the energy method, and the limit point referred to the corresponding state point when the load on the specimen's skeleton curve decreased to 85% of the peak load. The following can be observed from Table 6:

(1) Both specimens' displacement ductility coefficients were greater than 5, indicating that both specimens had good deformability. The displacement ductility coefficient of composite shell specimen CS-TF was larger than that of cast-in-place specimen CIS-TF.
(2) The characteristic values for the yield point and peak point of the composite roof shell specimen CS-TF were comparable to those of the cast-in-place specimen CIS-TF, and their peak load differed by only 1%. The formwork shell was installed on the tensile side, which did not affect the specimens' bearing capacity.

3.3.3 Stiffness degradation

Figure 14 reveals the stiffness degradation curve of each specimen. It indicates that:

(1) The stiffness degradation law of composite shell specimens differed from that of cast-in-place specimens. When the cast-in-place specimen CIS-TF reached the yield state, the stiffness decreased relatively slowly, and a "small plateau" appeared in the stiffness degradation curve, and the stiffness decreased more rapidly after the yield point. During the loading process, the composite shell specimen CS-TF stiffness decreased slowly with the increased applied load/displacement, with no "plateau" appearing.
(2) The initial stiffness of composite shell specimens CS-TF is slightly larger than that of cast-in-place specimens CIS-TF, indicating that the formwork shell and concrete are integral at the initial loading stage, and the formwork shell made of high-performance materials on the tension side can improve the specimens' resistance to deformation during the normal use stage.
(3) Multiple cracks appeared on the tensile side of the concrete near the yield points of the two specimens at their midspan loading points. The formwork shell in the composite shell specimen CS-TF was ruptured in tension, and a slip appeared on the formwork shell-concrete's joint surface in the concrete's crack development area. The formwork

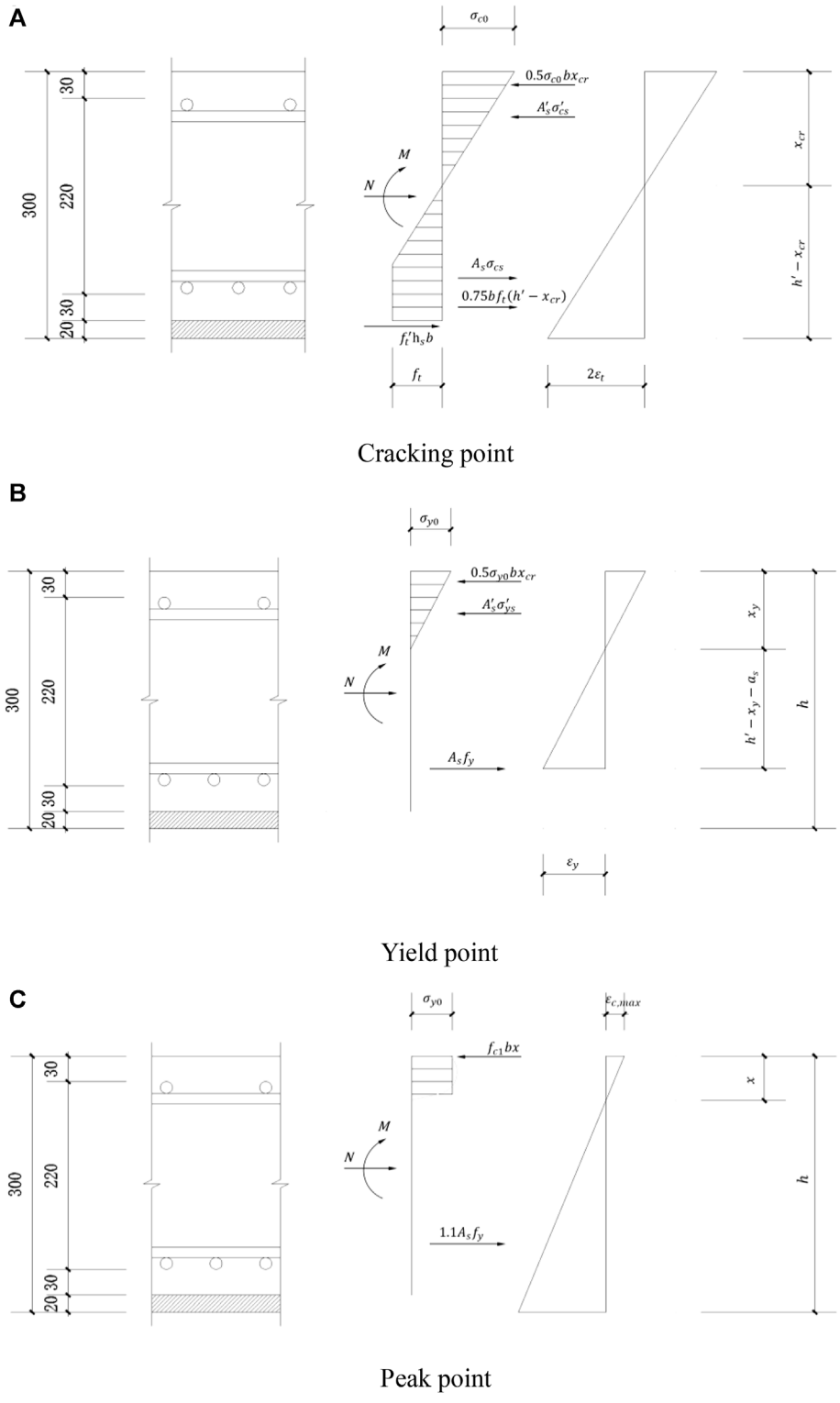

FIGURE 17
Calculation diagram for bearing capacity at different state points. **(A)** Cracking point, **(B)** Yield point, **(C)** Peak point.

shell's contribution to the specimen's stiffness faded away. After the yield point, the two specimens' stiffness values were identical.

3.3.4 Reinforcement strain

Steel bar strain gauges were placed at the midspan of the specimens with the strain-load curve indicated in Figure 15,

TABLE 7 Comparison between specimens' experimental and calculated bearing capacity values at various state points.

	Cracking point	Yield point	Peak point
Experimental value (kN)	144	488	560
Calculated value (kN)	134	430	490
Error (%)	6.5%	11.9%	12.5%

where the strain trends of steel bars in both specimens were identical. The initial loading state for the lower steel bars (S1-1′-S1-3′) was linear. Near the specimens' crack points, the steel bars' strain and load exhibited a nonlinear behavior; near the specimens' yield points, the steel bars' strain had reached yield strain, and with the load continuously increasing, the strain value increased significantly. In the initial loading state, the upper steel bars (S1-1-S1-3) were in compression, but with the increase of the load, the concrete on the tensile side cracked, cracks continued to develop and extend, and the compression zone kept decreasing. After the specimens yielded, the upper steel bars began changing from the compression to the tension state.

3.3.5 Concrete strain

Concrete strain gauges were installed at the midspan of the specimens along the thickness direction. Figure 16 depicts the variation of strain values at various positions of specimens before cracking. It demonstrates that the presence of the formwork shell had no effect on the strain distribution and that the specimens conformed to the plane-section assumption before cracking.

4 Formulas for calculating bearing capacity

The test phenomena and results showed that the first crack on the specimen occurred below the loading point, and the formwork shell and concrete cracked simultaneously during the normal section cracking mode, while the joint surface of the formwork shell-concrete did not crack. Based on this phenomenon, the formwork shell and concrete can be investigated as a unit when the force analysis is performed on the specimen's cracking point. Since the concrete stress was small in the compression zone, the compressive stress on the concrete was regarded as the linear distribution mode.

For ordinary concrete, it is believed that cracking occurred when the tensile strain on concrete reached two times the peak axial tensile strain ε_{t0}[21]. Based on the literature [22], the concrete used for specimen fabrication in this study has an elastic modulus E_1 of 31,500 MPa, the tensile strength f_t of 2.2 MPa, and the peak tensile strain ε_{t0} of 100×10^{-6}. According to the fundemental properties of the formwork shell material measured by tests, the elastic modulus E_2 was 34,500 MPa, the tensile strength $f_t^{'}$ was 6.7 MPa, and the peak tensile strain $\varepsilon_{t0}^{'}$was 200×10^{-6}. Based on force equilibrium and bending moment equilibrium on the section, the formula for calculating the bearing capacity of the cracking point is as follows:

$$0.5\sigma_{c0}bx_{cr} + A_s^{'}\sigma_{cs}^{'} = N + 0.75bf_t\left(h' - x_{cr}\right) + A_s\sigma_{cs} + f_t^{'}\mathrm{h}_s b \quad (1)$$

$$\frac{V_{cr}L}{4} + N\left(\frac{h}{2} - h_s\right) + A_s\sigma_{cs}a_s + \frac{7bf_t\left(h' - x_{cr}\right)^2}{24} = A_s^{'}\sigma_{cs}^{'}\left(h' - a_s^{'}\right) + \frac{b\sigma_{c0}x_{cr}\left(h' - \frac{x_{cr}}{3}\right)}{2} \quad (2)$$

In calculating the yield point's bearing capacity, the tensile strength of the concrete and formwork shell was disregarded, and the compressive stress of concrete in the compression zone was used as the mode of linear distribution. The state point of the yield of lower steel bars was determined to be the yield point of specimens, and the yield strain ε_y for steel bars was taken as 2000×10^{-6}. The following formula can calculate the bearing capacity of the yield point:

$$0.5\sigma_{y0}bx_y + A_s^{'}\sigma_{ys}^{'} = N + A_s f_y \quad (3)$$

$$\frac{V_y L}{4} + N\left(\frac{h}{2} - h_s - a_s\right) = A_s^{'}\sigma_{ys}^{'}\left(h' - a_s - a_s^{'}\right) + 0.5b\sigma_{y0}x_y\left(h' - a_s - \frac{x_y}{3}\right) \quad (4)$$

In calculating the peak point's bearing capacity, the tensile strength of the concrete and formwork shell was ignored, and the compressive stress on concrete in the compression zone was considered the uniformly distributed load mode. Based on the previous analysis, at the peak point, the upper steel bars changed from the compressive state to the tensile state, and the stress value was lower; therefore, the acting force on the upper steel bars was not accounted for in the equilibrium formula. The lower steel bars experienced greater deformation and entered the reinforcing stage, so the stress at the peak point was assumed to be 1.1 times the yield stress f_y. The formula for calculating the bearing capacity of the peak point is as follows:

$$f_{c1}bx = 1.1A_s f_y + N \quad (5)$$

$$\frac{VL}{4} + N\left(\frac{h}{2} - h_s - a_s\right) = f_{c1}bx\left(h' - \frac{x}{2} - a_s\right) \quad (6)$$

where f_t is tensile strength of concrete; $f_t^{'}$ is the tensile strength of the formwork shell; f_{c1} is the compressive strength of concrete; h' is the result of subtracting the thickness h_s of formwork shell on the tensile side from the section thickness h; b is section width; σ_{c0} and σ_y are maximum compressive stress of the concrete in the compression zone of the cracking point and yield point; x_{cr}, x_y and x are the height of the compression zone of the cracking point, yield point, and peak point; A_s and $A_s^{'}$ are sectional areas of longitudinal steel bars in tension and compression zones; σ_{cs} and $\sigma_{cs}^{'}$ are stress of longitudinal steel bars in the tension and compression zones of the cracking point; $\sigma_{ys}^{'}$ is stress of longitudinal steel bars in the compression zone of the yield point; V_{cr}, V_y, and V are concentrated force at the midspan of the cracking point, yield point, and peak point; L is span; N is axial compression; a_s *and* $a_s^{'}$ are the distance from the acting point of the resultant force on longitudinal steel bars in the tension and compression zones to the edge of the tension and compression zones of concrete; ε_{t0} is the peak axial tensile strain of concrete.

Figure 17 depicts the detailed calculation of various load points, with the calculation results illustrated in Table 7. The calculated bearing capacity of the cracking, yield, and peak points was 134, 430, and 490 kN, respectively, with errors of 6.5%, 11.9%, and 12.5%, respectively, compared with the test values. The calculated values were all lower than the test values. The proposed formula can be employed to accurately determine the bearing capacity of composite shell roof specimens in different states. It has certain safety redundancy, providing a reference for performance design in different operating conditions.

5 Conclusion

Due to the use of high-performance cement-based materials in the prefabricated parts, a new fabricated underground concrete utility tunnel technology system is introduced—underground utility tunnels in a fabricated composite shell system. In addition, the system's component structure and connection structure are proposed, and the properties of high-performance cement-based materials are tested. Based on the proposed structure, two roof specimens for utility tunnels are designed and fabricated, and an experimental study is conducted. The key findings are as follows:

(1) The failure processes and modes of composite shell specimen CS-TF and cast-in-place specimen CIS-TF were identical: lower steel bars suffered tensile yield, upper steel bars gradually transformed from compression to tension, and concrete on the compression side was crushed.
(2) The bearing capacity and stiffness of composite shell specimen CS-TF and cast-in-place specimen CIS-TF were the same, and the ductility of composite shell specimen CS-TF was significantly superior to that of cast-in-place specimen CIS-TF. The composite shell roof specimen achieved the same mechanical performance index as the cast-in-place structure. The existence of the formwork shell had no adverse effect on the mechanical properties of the integral structure.
(3) Based on the testing phenomena and data analysis results, formulas for calculating the bearing capacity of composite shell roof at the cracking point, yield point, and peak point were proposed, with an error of no more than 12.5%, which was in good agreement with the experiments.

Data availability statement

The original contributions presented in the study are included in the article/Supplementary Material, further inquiries can be directed to the corresponding author.

Author contributions

1) LD, responsible for the overall experiment and the preparation of the paper, as well as the main derivation of the formula. 2) AY, the corresponding author of the paper, undertakes the funding, design, writing and checking of the subject. 3) DZ, the person in charge of the on-site test of the thesis. 4) PZ is responsible for data processing. All authors contributed to the article and approved the submitted version.

Funding

The research reported in this article is sponsored by the China Railway Construction Scientific Research Program (Grant No. 2019-A01) and Research and Development Project of the Ministry of Housing and Urban-Rural Development (Grant No. 2021-K-047).

Conflict of interest

Authors LD, DX, and PZ were employed by China Railway Construction Group Co., LTD.

The remaining author declares that the research was conducted in the absence of any commercial or financial relationships that could be construed as a potential conflict of interest.

Publisher's note

All claims expressed in this article are solely those of the authors and do not necessarily represent those of their affiliated organizations, or those of the publisher, the editors and the reviewers. Any product that may be evaluated in this article, or claim that may be made by its manufacturer, is not guaranteed or endorsed by the publisher.

References

Bai, B., Fan, B., Nie, Q., and Jia, X. (2023). A high-strength red mud–fly ash geopolymer and the implications of curing temperature. *Powder Technol.* 416, 118242. doi:10.1016/j.powtec.2023.118242

Bai, B., Nie, Q., Zhang, Y., Wang, X., and Hu, W. (2021b). Cotransport of heavy metals and SiO2 particles at different temperatures by seepage. *J. Hydrology* 597, 125771. doi:10.1016/j.jhydrol.2020.125771

Bai, B., Yang, G., Tao, L., and Yang, G. (2019). A thermodynamic constitutive model with temperature effect based on particle rearrangement for geomaterials. *Mech. Mater.* 139, 103180. doi:10.1016/j.mechmat.2019.103180

Bai, B., Zhou, R., Cai, G., Hu, W., and Yang, G. (2021a). Coupled thermo-hydro-mechanical mechanism in view of the soil particle rearrangement of granular thermodynamics. *Comput. Geotechnics* 137 (8), 104272. doi:10.1016/j.compgeo.2021.104272

Canto-Perello, J., and Curiel-Esparza, J. (2001). Human factors engineering in utility tunnel design. *Tunn. Undergr. Space Technol.* 16 (3), 211–215. doi:10.1016/s0886-7798(01)00041-4

Chong, X., Xie, L., Ye, Xi, Jiang, Q., and Wang, D. (2016). Experimental study and numerical model calibration of full-scale superimposed reinforced concrete walls with I-shaped cross sections. *Adv. Struct. Eng.* 19 (12), 1902–1916. doi:10.1177/1369433216649392

Darli, C. M., Aiping, T., Delong, H., and Jiqiang, Z. (2021). Large scale shaking table model test and analysis on seismic response of utility tunnel in non-homogeneous soil. *Earthq. Eng. Eng. Vib.* 20 (2), 505–515. doi:10.1007/s11803-021-2035-6

De, A., Morgante, A. N., and Zimmie, T. F. (2016). Numerical and physical modeling of geofoam barriers as protection against effects of surface blast on underground tunnels. *Geotext. Geomembranes* 44 (1), 1–12. doi:10.1016/j.geotexmem.2015.06.008

Gu, Q., Ge, D., Yang, K., Tian, S., Wen, S., Tan, Y., et al. (2020). Seismic behavior of precast double-face superposed shear walls with horizontal joints and lap spliced vertical reinforcement. *Struct. Concr.* 21 (5), 1973–1988. doi:10.1002/suco.201900019

Jiang, Q., Shen, J., Chong, X., Chen, M., Wang, H., Feng, Y., et al. (2021). Experimental and numerical studies on the seismic performance of superimposed reinforced concrete shear walls with insulation. *Eng. Struct.* 240, 112372. doi:10.1016/j.engstruct.2021.112372

Luo, Y., Alaghbandrad, A., Genger, T. K., and Hammad, A. (2020). History and recent development of multi-purpose utility tunnels. *Tunn. Undergr. Space Technol.* 103, 103511. doi:10.1016/j.tust.2020.103511

O 'Rourke, T. D., Stewart, H. E., and Jeon, S. S. (2001). Geotechnical aspects of lifeline engineering. *Geotech. Eng.* 149 (1), 13–26. doi:10.1680/geng.149.1.13.39308

Roy, D. M., Gouda, G. R., and Bobrowsky, A. (1972). Very high strength cement pastes prepared by hot pressing and other high pressure techniques. *Cem. Concr. Res.* 2 (3), 349–366. doi:10.1016/0008-8846(72)90075-0

Valdenebro, J. V., and Gimena, Q. F. N. (2018). Urban utility tunnels as a long-term solution for the sustainable revitalization of historic centres: The case study of pamplona-Spain. *Tunn. Undergr. Space Technol.* 81, 228–236. doi:10.1016/j.tust.2018.07.024

Wang, C., Yang, C., Liu, F., Wan, C., and Pu, X. (2012). Preparation of ultra-high performance concrete with common technology and materials. *Cem. Concr. Compos.* 34 (4), 538–544. doi:10.1016/j.cemconcomp.2011.11.005

Xue, W., Li, Y., and Cai, L. (2018). In-plane and out-of-plain mechanical behavior of double faced superpdsed concrete shear walls. *Eng. Mech.* 35 (05), 47–53+142. doi:10.6052/j.issn.1000-4750.2017.07.ST11

Yang, Y., Xu, R., and Zhang, Z. (2020). Experimental study on the mechanical properties of axillary angle of aassembly superimposed pipe gallery and the overall failure pattern. *North. Archit.* 5 (02), 2096–2118.

Zheng, W., Lu, X., and Wang, Y. (2016). Flexural behaviour of concrete composite slabs with precast ribbed reactive powder concrete bottom panels. *J. Comput. Theor. Nanosci.* 13 (3), 1831–1839. doi:10.1166/jctn.2016.5120

Zheng, W., Lu, X., and Wang, Y. (2015). Flexural behaviour of precast, prestressed ribbed RPC bottom panels(Article). *Open Civ. Eng. J.* 9 (1), 98–106. doi:10.2174/1874149501509010535

Zhou, Q., He, H. G., Liu, S. F., Wang, P., Zhou, Y., Zhou, J., et al. (2021). Evaluation of blast-resistant ability of shallow-buried reinforced concrete urban utility tunnel. *Eng. Fail Anal.* 119, 105003. doi:10.1016/j.engfailanal.2020.105003

frontiers | Frontiers in Materials

TYPE Original Research
PUBLISHED 31 July 2023
DOI 10.3389/fmats.2023.1234145

OPEN ACCESS

EDITED BY
Bing Bai,
Beijing Jiaotong University, China

REVIEWED BY
Nan Zhou,
China University of Mining and Technology, China
Shan Gao,
Harbin Institute of Technology, China

*CORRESPONDENCE
Ke Yang,
yksp2003@163.com

RECEIVED 27 June 2023
ACCEPTED 14 July 2023
PUBLISHED 31 July 2023

CITATION
Li C, Chen D and Yang K (2023), Filling parameters and process optimization of mining–filling synergistic coal-based solid waste paste in Renjiazhuang mine. *Front. Mater.* 10:1234145.
doi: 10.3389/fmats.2023.1234145

Filling parameters and process optimization of mining–filling synergistic coal-based solid waste paste in Renjiazhuang mine

Chao Li[1,2], Denghong Chen[1,2] and Ke Yang[2]*

[1]School of Mining Engineering, Anhui University of Science and Technology, Huainan, China, [2]Energy Research Institute of Hefei Comprehensive National Science Center (Anhui Energy Laboratory), Hefei, China

In this paper, the authors address the issue of large solid waste output and surface subsidence in the western coal base. They focus on the 110904 filling working face of Renjiazhuang Mine and employ a combination of theoretical analysis, numerical simulation, and field practice to analyze the limit caving step and cycle pressure step of the working face. The authors propose a mining-filling coordination scheme called "three mining and one charging". Through numerical simulation, they demonstrate that this scheme ensures the time-space continuity of the mining-filling cycle and is theoretically feasible. Additionally, the authors conduct nine groups of orthogonal simulation tests to identify the main factors affecting the filling effect. They conclude that the filling rate is the primary controlling factor, and there is a positive correlation between the filling rate and 1-day strength. The authors implement hanging pipe filling in the return air roadway of the 110904 working face, achieving a filling material 1-day strength of 2 MPa and a filling ratio of 80%. The mining-filling synergy scheme proves effective and feasible. However, the issue of pipe plugging during the filling process requires further optimization of the particle gradation in the subsequent filling material ratio scheme. Overall, the proposed mining-filling collaborative process serves as a theoretical reference for similar filling faces.

KEYWORDS

mining–filling synergy, numerical simulation, orthogonal test, caving step distance, theoretical calculation

1 Introduction

In recent years, the rapid growth of the coal–electricity–chemical industry has resulted in significant economic progress. However, this growth has also led to the accumulation of large quantities of coal-based solid waste, such as gasification slag, gangue, fly ash, and slag, which pose challenges for major coal production areas. The disposal of these waste materials has caused land degradation and environmental deterioration, hindering the balanced development of coal resource extraction and environmental protection in mining areas (Zhang et al., 2021; Li et al., 2022). This situation contradicts the principles of ecological civilization, which emphasizes the harmonious coexistence between humans and nature, as well as sustainable development. Filling mining technology offers significant technical advantages in preventing and controlling rock instability, reducing solid waste emissions, and improving coal recovery rates. As a result, filling mining plays a crucial role in achieving green mining practices.

At present, many deep mines are actively exploring new paths that can not only protect the surface environment and buildings but also achieve safe and efficient mining. The "mining filling" integrated technology is an effective method to solve the aforementioned problems (Tu et al., 2021). The coordinated layout of underground coal mining and filling space in deep mining and filling integrated mines can fully leverage the technical advantages of the two types of mining processes and simultaneously meet the engineering needs of rock migration control, rock burst prevention and control, roadway surrounding rock control, water resource protection, and coal seam pressure relief and permeability enhancement (Zhang et al., 2019). At present, many domestic experts and scholars have conducted extensive research on the optimization layout of underground coal mining and filling space. For example, Zhang Qiang et al. studied the solid intelligent filling mining method in coal mines, providing the concept, characteristics, and difficulties of the solid intelligent filling mining method. Combining mining geological conditions, static size parameters of filling equipment mechanisms, and dynamic trajectory parameters during operation, a typical interference state judgment and coordination equation for the mechanism during the filling process was constructed, forming a mechanism for regulating the interference state of the filling equipment mechanism (Zhang et al., 2022); Wu Yabin et al. used numerical simulation methods to analyze the impact of overlying rock movement and surface deformation under three different mining and filling sequences in mines. The results showed that as the mining depth increased, the difference in surface deformation caused by the mining and filling sequence decreased (Wu et al., 2020). Based on theoretical analysis and practical experience, Sun Kai et al. derived formulas for calculating the key parameters of mining and filling process coordination, such as the number of separated tunnels between two alleys, the number of simultaneously filled tunnels in one group, and the number of circulating mining and filling tunnel groups. From this, they proposed a design method for coordinating and optimizing the mining and filling process of longwall tunnels by tunnel cementation filling (Sun et al., 2019); Ma Liqiang et al. proposed the "parallel mining and filling" and "continuous mining and filling" filling and water conservation coal mining methods (Ma et al., 2017). During the mining process, all the mining branches within the entire mining block are first divided into multiple mining stages. Once all the mining branches within one stage are mined and filled, the next stage of mining and filling of the mining branches is carried out until all the mining branches are mined and filled, ultimately achieving complete replacement of the filling body and coal; Lu Bin et al. proposed the short-wall gangue cementation filling technology and studied the material ratio, support tunnel parameters, evolution of surrounding rock stress field, and surface deformation laws (Lu et al., 2017); Ma Liqiang and Li Yongliang proposed the wall-type continuous mining and water filling coal mining method. First, the entire mining block was designed with a longwall system for coal transportation, material transportation, and ventilation systems. Afterward, the mining roadway (wide roadway) within the block was divided into several mining stages, during which skip mining was carried out on the mining roadway. A filling slurry underground mixing and ground mixing conveying system suitable for different coal seam dip angles was proposed, as well as corresponding working face compaction filling methods, forming a complete set of continuous mining and filling cementitious filling coal mining technology (Ma Li et al., 2019; Li et al., 2022); Wang Feifei and Ji Yu established an AHP-Fuzzy evaluation model for the safety status of mining areas and a safety analysis model of "mining area → overlying rock and surface." They used the elastic foundation beam theory to establish a differential equation for the deflection of the roof, clarifying the relationship between the elastic foundation coefficient of the filling body and the direct elastic modulus of the top and the subsidence of the roof (Jiang et al., 2018; Ji et al., 2023). Tang Weijun, Chang Qingliang, and Sun Xiaoguang used theoretical analysis, numerical simulation, and on-site measurement methods to study the "activation" mechanism of the overlying rock, the law of roof movement, and the factors affecting the stability of the overlying rock when filling and recovering coal pillars. They also predicted the range of damage and water inrush of the bottom plate during paste filling mining, revealing the mechanical mechanism of controlling the bottom plate damage during paste filling mining. The numerical simulation software FLAC was used. We studied the surface subsidence and distribution of elastic–plastic zones on the roof and floor after mining the lower layer of coal with different filling body strengths and analyzed the rock pressure and roof stability of the working face during filling mining (Sun et al., 2007; Chang et al., 2016; Tang et al., 2017). Zhou et al. analyzed the effects of raw material mix ratio, pore size, porosity, and surface structure on the performance of the filling body by a single-factor test. The influence of the mine water environment was simulated, the immersion and dry–wet cycle tests were carried out on the field filling materials, and corrosion was carried out with different durations. Then, the influence of mine water corrosion on the mechanical properties of filling materials was studied by the uniaxial compression test. In order to improve the shear and tensile properties of the filling material, three different lengths of glass fiber were added to the filling material. It is concluded that the average peak strength of the cement-based backfill material increases with the increase in the length of the glass fiber. (Zhou et al., 2021a; Zhou et al., 2021b; Zhou et al., 2022). A green thixotropic cement filling material containing molybdenum tailings was prepared by Gao et al. A thixotropic coefficient method based on the correlation between shear stress and time was proposed to evaluate the thixotropy of the paste. The rheological properties, hydrophilicity, segregation rate, and compressive strength of the oxyphilic paste filling material were studied by the orthogonal test. (Gao et al., 2023). Chen et al. designed experiments based on the response surface method to explore the effects of gasification slag, cement, and water on the performance of paste filling materials (Chen et al., 2022). Based on the response surface method test design and data analysis, Sun Guoqing et al. simulated the roof subsidence law of the paste filling face under different filling body stiffnesses, top coal stiffnesses, support stiffnesses, and filling body strengths by using the finite difference software UDEC and analyzed the influence of single-factor and multi-factor interactions on the roof stability of the paste filling face and its reasons (Sun et al., 2016). Li et al. explored the impact of backfill mining on rock burst prevention and control and used a comprehensive research method of theoretical analysis, numerical simulation, and on-site monitoring to study the influence of controlling backfill rate on the stress of backfill

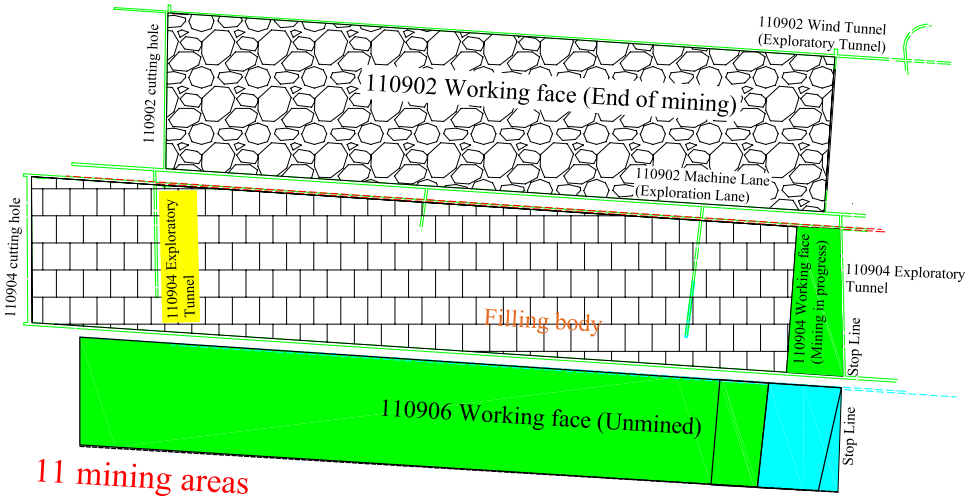

FIGURE 1
110904 working face position diagram.

working faces and the evolution of overlying rock spatial structure (Li et al., 2023). In order to reasonably and accurately determine the strength required for filling materials to fill the goaf, Han et al. proposed on-site measurement based on sensors and conducted on-site measurements in Jinchuan Mine. Formulas based on the thick plate theory were derived to verify the measurement results (Han et al., 2022). Ma et al. studied the mechanical properties of coal gangue gypsum filling materials through indoor experiments and analyzed the critical conditions for bending and fracture of the coal seam roof. The discrete element numerical simulation software was used to study the process of roof fracturing, and a reasonable filling ratio of 95% was determined to ensure the stability of the roof. At the same time, the movement of overlying strata and the law of rock pressure reduction were studied through numerical simulation and on-site measurements (Ma et al., 2022).

The abovementioned scholars have conducted a detailed analysis on the migration law, fracture characteristics, and deformation mechanism of the goaf roof in the filling working face. However, there is relatively little research on the spatiotemporal continuity of mining and filling replacement in the "mining filling coordination" operation of the working face. This article takes the 110904 working face of Renjiazhuang Mine as the background. Combined with theoretical analysis, the research methods of numerical simulation and on-site experiments have deeply analyzed the reasonable filling step distance that meets the mining and filling needs of the working face, as well as the main control factors that affect the filling effect. Good experimental results have been achieved on site, and the research results are helpful for promoting the efficient coordination and cooperation of underground coal mining and filling systems, guiding the planning and layout of underground mining and filling space, and dynamic adjustment. Realizing the integrated, safe, efficient, and green mining of "mining selection filling" in deep mines is of positive significance and can provide theoretical and technical support for the formulation of mining filling coordination plans for the same type of working face.

2 110904 working face project overview

Renjiazhuang Coal Mine employs a mixed development mode, utilizing inclined shafts and vertical shafts. The initial design of the mine divides it into five mining areas: 11, 12, 13, 21, and 23. The mining process starts with the central 11 and 21 mining areas, followed by the connection of the northern 12 mining area and the southern 13 and 23 mining areas. Finally, the mining areas in the west wing of the anticline are extracted. The mine commenced operations in 2008, with the current focus on the 11 mining area, while the 12 mining area remains the continuous mining area. As depicted in Figure 1, mining operations of the 110904 working face in the 9th coal seam of the 11 mining area are being conducted at Renjiazhuang Coal Mine. The 110904 working face is situated adjacent to the already completed 110902 working face on the left and the 110906 working face, which is scheduled for mining by the end of 2023, on the right.

The 9th coal seam of Renjiazhuang Mine is 4 m thick, mainly comprising dark coal. It is semi-dark, powdery, and occasionally lumpy and has a uniform structure and weak asphalt luster. The thickness of the coal seam is generally stable. There is a phenomenon of local thinning and thickening. The coal seam contains gangue, and the coal seam structure is more complicated. The uniaxial compressive strength of the coal seam is 1.83 MPa. After more than 0.05 m of the 9th coal seam is removed from the gangue, the average coal thickness is 3.59 m, and the overall thickness of the coal seam is stable. The 110904 working face is located in the east gate of Renjiazhuang Coal Mine Industrial Square, which is approximately 580.9 m eastward along the 120.5° direction, approximately 264.5 m east–west width, and approximately 1,452 m southward along the 207.5° direction. The ground elevation is + 1,324 m to + 1,328 m. The strike length of the working face is 1,435 m, the dip length is 265 m, and the average dip angle of the coal seam is 14°. The average thickness of the coal seam is 4.2 m, the bulk density is 1.46 t/m^3, and the mining method is longwall mining. With reference to the

10.3389/fmats.2023.1234145

Rock layer number	Thickness / m	Rock Formation Lithology	Legend	Unit weight / kN·m^{-3}	Elastic modulus / GPa	Lithological characteristics	Name of top and bottom plates
14	2.2	Fine sandstone		24.79	2.3	The top and bottom plates are black, fine, horizontal bedding, containing pyrite. According to the 208 borehole data, the thickness of mudstone is 6.73 m, becoming 9.35 m in the west and 8.05 m in the south.	Main roof
13	14.42	Medium grained sandstone		16	3.25		
12	3.33	Mudstone		25.5	3.05		
11	0.88	Siltstone		24.89	9.87		
10	2.81	Fine sandstone		24.70	2.3	Grayish black, brittle, containing pyrite, calcite, and lower marl. According to the drilling hole 208, the limestone is 1.85 m thick, and gradually thins to 1.0 m from the drilling hole 208 to the south and west.	Immediate roof
9	1.32	Sandy sandstone		25.1	5.42		
8	1.46	Siltstone		24.89	9.87		
7	1.87	Medium grained sandstone		16	3.25		
6	3.9	Fine sandstone		24.79	2.3	Black, mainly composed of dark coal, semi dark, powdery, occasionally blocky, uniform structure, weak asphalt luster, with an average thickness of 4.34 m for nine coal seams in machine tunnels,	Nine coal
5	5.9	Medium grained sandstone		15.89	3.23		
4	2.40	Siltstone		24.8	9.95		
3	8.04	Mudstone		25.5	3.05		
2	1.32	Limestone		24	5.53		
1	4.0	Nine coal		14.5	2.8	Siltstone with direct bottom in nine Coal Mine is grayish black, with layered structure, argillaceous cementation and poor sorting performance.	Immediate floor
0	4.46	Siltstone		24.89	9.87		

FIGURE 2
Coal seam borehole histogram and lithology characteristics.

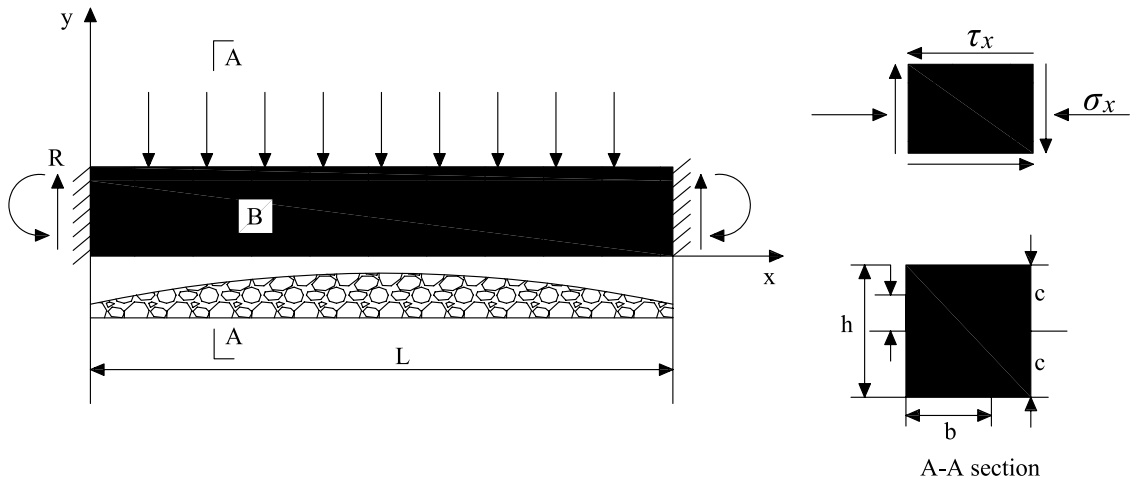

FIGURE 3
Mechanical analysis diagram of the beam model.

208 boreholes in the 110901 working face of the adjacent working face of the 110904 working face with the 11th mining area and the 9th coal seam, combined with the on-site technical data of the 110904 working face in Renjiazhuang, the comprehensive histogram of the 110904 working face rock stratum, rock stratum characteristics, and roof and floor conditions are shown in Figure 2.

3 Mining filling step calculation analysis

Based on the theory of beam structure in the mechanics of materials, combined with the comprehensive histogram of the 110904 working face and the characteristic table of rock strata, the theoretical analysis and calculation of the limit caving step distance are carried out. The stress state of the main roof of the working face is assumed to be the fixed beam breaking model, and the stress analysis diagram of the model is shown in Figure 3.

The normal stress of any point in the clamped beam is as follows:

$$\sigma = \frac{My}{J_z}. \tag{1}$$

In Formula 1, M represents the section bending moment in kN·m, y represents the distance to the central axis in meters, and J_z represents the central axis section distance. The section distance of the beam is denoted as follows:

$$J_z = \frac{h^3}{12}. \tag{2}$$

The stress at each position in the structure is as follows:

$$\sigma = \frac{12My}{h^3}, \tag{3}$$

$$\tau_{xy} = \frac{3}{2}Q_z\left(\frac{h^2 - 4y^2}{h^3}\right). \tag{4}$$

In Formula 3 and Formula 4, σ is the normal stress, MPa; h is the thickness, m; τ_{xy} is the shear stress, MPa; and Q_z is the shear force, kN.

According to the mechanical characteristics of the fixed beam model, the maximum bending moment and tensile stress are as follows:

$$M_{Max} = -\frac{qL^2}{12}, \tag{5}$$

$$\sigma_{Max} = -\frac{qL^2}{2h^2}. \tag{6}$$

According to the model structure, when the external force reaches the tensile strength of the rock mass, the rock layer begins to break and collapse. Based on this, the following conclusions are drawn:

$$R_T = -\frac{qL^2}{2h^2}, \tag{7}$$

$$l_c = h\sqrt{\frac{2R_T}{q}}. \tag{8}$$

In Formula 7 and Formula 8, h is the layer thickness, m; R_T is the tensile strength, MPa; and q is the uniform load.

It can be seen from Eq. 8 that the initial fracture step of the main roof is related to the tensile strength of the rock stratum, the thickness of the rock stratum, and the load above it. The determination of the load above the main roof is an important part of the initial breaking step. It is generally believed that the load above the overlying rock of the working face is evenly distributed in the original state (Li et al., 2022; Wang et al., 2022; Song et al., 2023). In addition, combined with the "key layer theory" proposed by academician Qian Minggao, it is believed that two discriminant conditions of the key layer are obtained from the characteristics of the key layer.

The first condition is that if the control range of the first stratum reaches the second stratum, the second stratum is the key stratum of the next stratum, which must satisfy the principle of Formula 8.

$$(q_{n+1})_1 < (q_n)_1. \tag{9}$$

In Formula 9, $(q_{n+1})_1$ is the load of the No. 1 layer of rock, kN, when the No. n + 1 layer acts on the 1 layer; $(q_n)_1$ is the load of the No. 1 layer of rock, kN, when the No. n layer acts on the 1 layer.

The second condition, according to Formula 9, to determine the hard rock layer is that the lower fracture distance must be less than the upper fracture distance.

$$l_j < l_{j+1}. \tag{10}$$

In Formula 10, l_j is the breaking distance of layer j.

According to the theory of key strata, it is assumed that n and m are two strata (n > m). If $L_n > L_m > L_l$, the n layer is the main key layer, and the m and l layers are the sub-key layers. If the j layer does not satisfy Formula 10, the discrimination is continued after recalculation.

According to the current classical surrounding rock control theory, the load on the rock stratum is calculated. According to the principle of composite beam, the load of overlying strata can be calculated by the following formulas:

$$q_n = \gamma_n h_n, \tag{11}$$

$$(q_m)_n = \frac{E_n h_n^3 (\gamma_n h_n + \gamma_{n+1} h_{n+1} + \ldots + \gamma_m h_m)}{E_n h_n^3 + E_{n+1} h_{n+1}^3 + \ldots + E_m h_m^3}. \tag{12}$$

In Formula 12, q_n is the load of the n_{th} layer. q_{mn} is the load on the n_{th} layer when the m_{th} layer acts on the n_{th} layer, where m > n. γ is the volume force, h is the thickness, and E is the elastic modulus.

Through the analysis of the characteristic parameters of the rock strata in Figure 2, the key strata of each rock stratum are distinguished. According to the detection data of the coal mine technology department and the fully mechanized mining team, the basic roof of the target working face in this paper is mudstone. The following calculation can be obtained.

The load of the first layer itself is q_1 = 31.68 kPa, and the effect of the second layer of rock on the first layer is $(q_2)_1$ = 1.88 kPa, $(q_2)_1 < q_1$, indicating that the second layer of rock has no effect on the first layer of rock; then, the second layer of mudstone is the first key layer. The load of the second layer (mudstone) is q_2 = 205.02 kPa, the effect of the third and fourth layers on the second layer is $(q_3)_2$ = 243.4 kPa and $(q_4)_2$ = 238.0 kPa, $(q_4)_2 < (q_3)_2$, indicating that the fourth layer has no effect on the second layer, and the fourth layer is the second key layer. Based on the aforestated calculation, the influence of the third layer on the load of the second rock layer should be considered. The load on the main roof is 0.25 MPa. Combining it with Formula 8, the initial ultimate fracture step of the main roof of the 110904 face is calculated to be 26.32 m.

The periodic weighting step of the basic roof is often determined by the cantilever fracture of the basic roof, according to the mechanics of materials, $\sigma = \frac{My}{J}$. Here, the maximum bending moment is $M_{Max} = \frac{qL^2}{2}$ (L is the ultimate span of the cantilever beam), Y is $\frac{h}{2}$ (h is the thickness of the rock layer), σ is the ultimate

tensile strength R_T, $L = h\sqrt{\frac{R_T}{3q}}$, and it is compared with the ultimate span of the main roof, $L_b = h\sqrt{\frac{2R_T}{q}}$. The periodic weighting step is equivalent to 1/2.45 of L_b, and after calculation, the periodic caving step of the main roof of the 110904 working face is 10.74 m. According to the operation rules, the cutting depth of each knife in the 110904 working face is 0.865 m. Four knives of coal are cut in one shift, 12 knives of coal can be cut in the periodic caving step, and three shifts of work can be taken. The mining and filling coordination scheme of three-mining and one-filling can be adopted, that is, filling once every three shifts of coal mining is completed (Cui et al., 2021; Wang et al., 2021; Jin et al., 2022; Xu et al., 2023; Zhang et al., 2023).

If the mining and filling step distance is greater than the periodic caving step distance, the filling space will have difficulty in meeting the requirements of the established filling ratio, thus affecting the space–time continuity of the mining and filling cycle. It is difficult to describe the law of roof migration after filling by theoretical calculation, and it cannot be simply considered that the periodic caving step obtained by theoretical calculation is the maximum filling step. Therefore, on the basis of theoretical calculation, it is very important to further study the law of roof migration in filling the working face and optimize the mining–filling synergistic process parameters through numerical simulation.

4 Numerical simulation mining–filling collaborative scheme

Based on the previous calculation, the reasonable mining–filling synergy step is analyzed using 3DEC numerical simulation (Cao et al., 2023). The 3DEC software includes a range of constitutive models, with the Mohr–Coulomb failure model being the most suitable for analyzing the linear failure surface of shear failure in rock mechanics. The transformation formula is as follows:

$$f_s = \sigma_1 - \left[\sigma_3 \frac{1 + sin\,\varphi}{1 - sin\,\varphi} + 2c\sqrt{\frac{1 + sin\,\varphi}{1 - sin\,\varphi}}\right]. \tag{13}$$

In Formula 13, σ_1 is the maximum principal stress, MPa; σ_3 is the minimum principal stress, MPa; φ is the angle of internal friction, °; and c is the force of cohesion, MPa.

If $f_s < 0$, shear yielding occurs.

In order to prevent the Mohr–Coulomb model from losing its meaning, this is simplified by assuming that the yield surface is extended to the $\sigma_3 = \sigma^t$ region. The minimum principal stress is not greater than the tensile strength. If $\sigma_3 > \sigma^t$, tensile yielding begins to occur. σ^t cannot exceed σ_3, and the maximum value σt max is determined by the following formula:

$$\sigma^t_{Max} = \frac{c}{tan\,\varphi}. \tag{14}$$

In the Mohr–Coulomb model, the post-peak characteristics of the material must be considered, that is, the response of the material after the initial damage. This chapter uses the Mohr–Coulomb model to simulate the dilatancy effect. In addition, the elastic material in this simulation is assumed to be isotropic. Its K and G can best describe the basic characteristics of the material, so regarding these material properties, the transformation formula is as follows:

$$K = \frac{E}{3(1 - 2\nu)}, \tag{15}$$

$$G = \frac{E}{2(1 + \nu)}, \tag{16}$$

where G is the shear modulus, GPa; E is the elastic modulus, GPa; and ν is the Poisson ratio.

The 3DEC built-in joint constitutive model mainly includes two types, as detailed in Table 1. The contact Coulomb slip model is the most frequently used engineering model.

In summary, this paper selects the Mohr–Coulomb failure criterion as the constitutive of the numerical model, and the joint constitutive selects the surface contact Coulomb slip model.

4.1 Numerical simulation scheme and result analysis

For the simulation of the 110904 working face all caving mining, from the model along the working face to 30 m excavation, in order to explore the goaf roof caving step distance, the excavation distance was set to 10 m, 12 m, 14 m, and 16 m, and the roof subsidence was set as shown in Figure 4. It can be seen from the diagram that when the excavation is 10 m, the roof only sinks in the middle, the maximum subsidence is not more than 25 cm, and the overall structure is stable. When the excavation is 12 m, the roof subsidence exceeds 3 m, which is in a complete failure state. When the excavation is 16 m, the roof collapses completely, indicating that the final roof failure range is stable at about 10 m, which is in line with the calculation result of the periodic weighting step. Therefore, taking “three-mining and one-filling” as the filling step is in line with the actual on-site working conditions.

The buried depth of the coal seam, the filling ratio, and the strength of the filling body are the three important factors affecting roof subsidence in the filling mining process. The buried depth of the coal seam cannot be changed, but in engineering practice, the filling effect can be better by changing the filling ratio and the strength of the filling body. According to the operation procedure of ”three-mining and one-filling,” in order to make the filling body effectively support the roof, the filling body must be consolidated to a certain strength during the three coal mining shifts. Therefore, the age of the strength of the filling body studied is 1 day, that is, 1-day strength. It is proposed to analyze the results of roof displacement change in goaf under different filling ratios and 1d strength by numerical simulation and obtain the 1d strength and filling ratio parameters that can effectively control roof subsidence, thus obtaining the parallel optimization scheme of paste filling mining–filling in the 110904 working face. It is beneficial to the collaborative control of coal-based solid waste paste filling. The roof caving morphology and migration deformation law are simulated when the 1d strength of the filling body is in the range of 1.5 MPa, 2 MPa, and 2.5 MPa and the filling ratio is 60%, 70%, and 80%, respectively. The three levels of the two aforementioned factors are orthogonal to each other to simulate nine sets of working conditions. As shown in Figure 5, the maximum roof subsidence on the filling side (D1), the maximum roof subsidence on the unfilled side (D2), the maximum lateral deformation of the filling body (D3), and the maximum contact stress between the roof and the filling body (S1) were collected to

TABLE 1 3DEC software joint constitutive model.

Model	Representation materials	Application example
Surface contact Coulomb slip model	Joints, faults, and planes in rock mass	General rock mechanics problems
Continuous yielding	Rock mass joints showing progressive damage and hysteresis characteristics	It has significant hysteresis cyclic loading and reverse loading; dynamic analysis

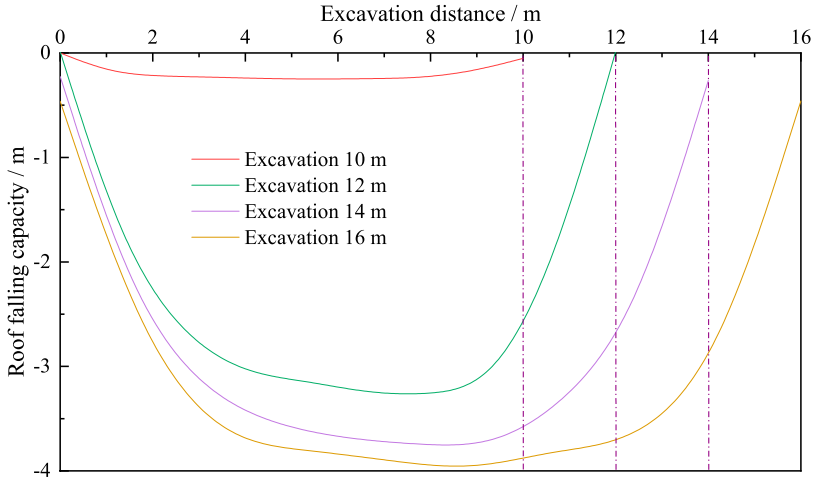

FIGURE 4
Roof subsidence at different excavation distances.

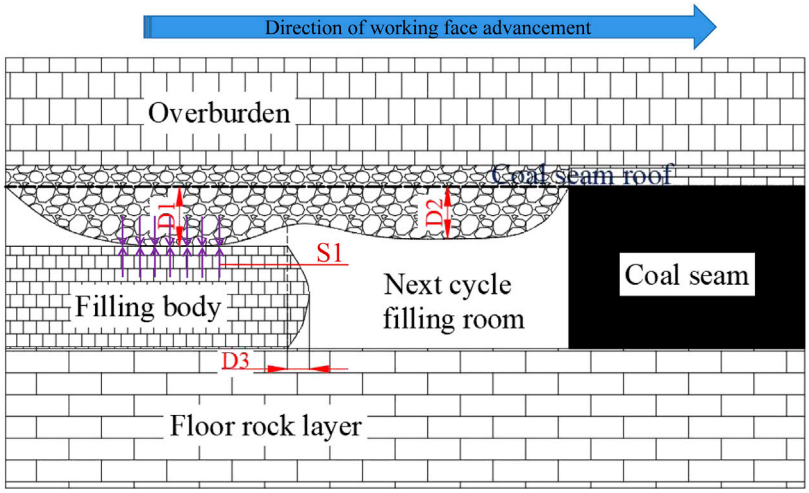

FIGURE 5
Working face mining–filling collaborative layout diagram.

comprehensively characterize the filling effect of the goaf. During the analysis, the slice position is located at 5 m along the coal seam.

As depicted in Figure 6A, both D1 and D2 decrease as the strength and filling ratio increase. The average values of D1 at a filling ratio of 60% and 80% are 2.41 m and 1.2 m, respectively, representing a decrease of 46.9%. Similarly, the average values of D2 at a filling ratio of 60% and 80% are 1.42 m and 0.66 m, respectively, with a decrease of 53.5%. It is worth noting that the decrease in D1 is slightly smaller than that of D2, suggesting that the filling body has a better control effect on the unfilled side roof

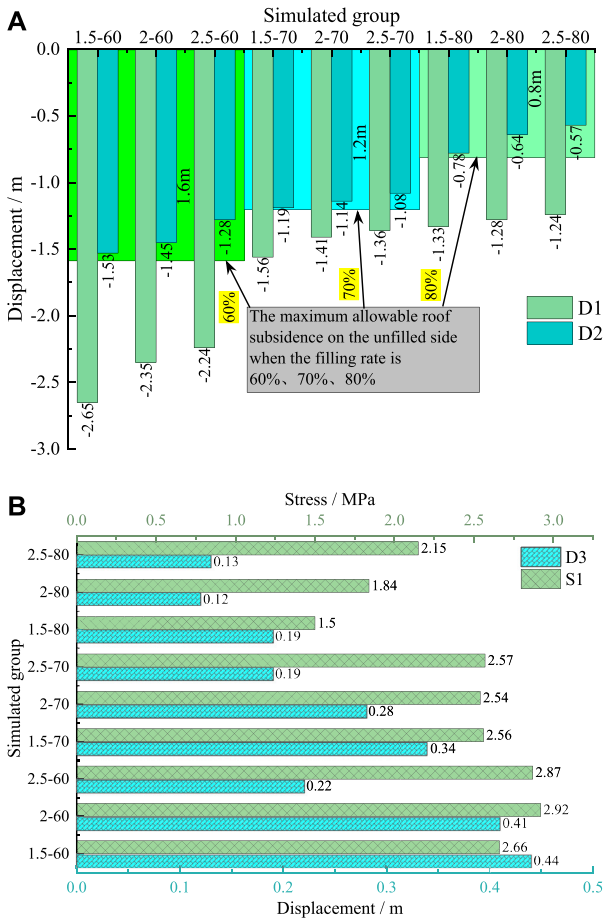

FIGURE 6
(A) Statistical results for D1 and D2. **(B)** Statistical results for D3 and S1.

compared to the filling side roof. The roof control effects of filling materials with different 1d strengths vary when the filling ratio is 60%, 70%, and 80%. However, the maximum value of D2 does not exceed 1.6 m, 1.2 m, and 0.8 m, respectively. This ensures that there is enough space for the next mining and filling cycle. Once the filling body is placed underground, it gets squeezed by the roof of the goaf. If the pressure exerted on the filling body exceeds its peak strength, the filling body will yield and deform to the side in order to release the stress. Figure 6B the average values of D3 at a filling ratio of 60% and 80% are 0.36 m and 0.15 m, respectively, representing a decrease of 58.3%. When the filling body is in contact with the roof strata, the vertical stress on the filling body increases due to the self-weight load and impact. The average values of S1 at a filling ratio of 60% and 80% are 2.82 MPa and 1.83 MPa, respectively, indicating a decrease of 35.1%.

The nonlinear surface fitting of the extracted data is shown in Figure 7. As shown in Figure 7A D1 decreases with the increase in filling ratio and filling body strength; that is, it decreases sharply and then decreases. In this process, the influence of filling ratio change on D1 is significantly stronger than that of strength change. As shown in Figure 7B D2 decreases with the increase in filling ratio and filling strength, and the change process tends to be linear. D2 is more sensitive to the change in filling ratio than the change in strength. As shown in Figure 7C D3 decreases with the increase in filling ratio and filling strength. In this process, the influence of the two factors on D3 tends to be consistent. As shown in Figure 7D S1 decreases with the increase in filling ratio and filling strength. In this process, the strength change has a weak influence on S1 when the filling ratio is at a high level. When the filling ratio is at a low level, the change of S1 is dominated by the filling ratio. In summary, the four indexes of the filling effect decrease with the decrease in filling ratio and filling strength, but the filling ratio is the main controlling factor affecting the overall filling effect.

The extremum difference analysis of the test results (Li et al., 2021; Xia et al., 2022; Cao et al., 2023) is carried out. The mean values of the four indicators at the three strength levels change with the filling ratio, as shown in Figure 8. From the kinetic energy formula $Q = \frac{1}{2}mv^2$, it can be seen that the kinetic energy converted from the gravitational potential energy during the roof sinking process is related to the sinking speed, and the speed depends on the vertical resultant force F_T during the roof sinking process, including gravity, the viscosity of the overlying strata to the roof, and the friction force during the sinking process. In the falling motion, $v = \sqrt{2gh}$, according to Newton's second law $F = ma$, $v = \sqrt{2h\frac{F_T}{m}}$, F_T changes with height and can be expressed as $F_T = f(h)$. It is assumed that the height difference between the roof and the filling body is h_0, that is, the kinetic energy of the roof when it sinks to the surface of the filling body. With the increase of the filling ratio, the height difference between the roof and the surface of the filling body can be reduced, thus reducing the kinetic energy $Q = h_0\int_0^{h_0} f(h)dh$ of the roof when it sinks to the surface of the filling body, which leads to a negative correlation between S1 and the filling ratio. S1 shows a decreasing trend of convex curve, which decreases first and then decreases sharply. When the filling ratio increases from 60% to 70%, S1 decreases by 8.9%. When the filling ratio increases from 70% to 80%, S1 decreases by 28.5%, and the difference is more than three times. In the case of a high filling ratio, further increasing the filling ratio can still weaken the impact of the roof on the filling body, while S1 and D3 decrease with the increase of the filling ratio. The greater the roof pressure on the filling body, the greater the lateral deformation of the filling body. There is a certain correlation between the two, and the trend of D3 decreasing with the increase in filling ratio tends to be linear; D1 shows a decreasing trend of concave curve, which decreases sharply and then slows down. When the filling ratio increases from 60% to 70%, D1 decreases by 40.2%. When the filling ratio increases from 70% to 80%, D1 decreases by 11.1%. The difference is more than 3 times, indicating that increasing the filling ratio can significantly control the roof subsidence under the condition of low filling ratio. When the filling ratio exceeds 70%, the control effect of increasing the filling ratio on the roof will be greatly weakened. When the filling ratio increases from 60% to 70%, D2 decreases by 19.7%. When the filling ratio increases from 70% to 80%, D2 decreases by 42.1%, and the difference is more than 2 times, indicating that when the filling ratio exceeds 70%, further increasing the filling ratio can still play a good control role in the roof subsidence of the unfilled side goaf.

The mean values of the four indexes at the three filling ratio levels change with the 1d strength, as shown in Figure 9. As the strength increases, both D1 and D2 show a downward trend,

10.3389/fmats.2023.1234145

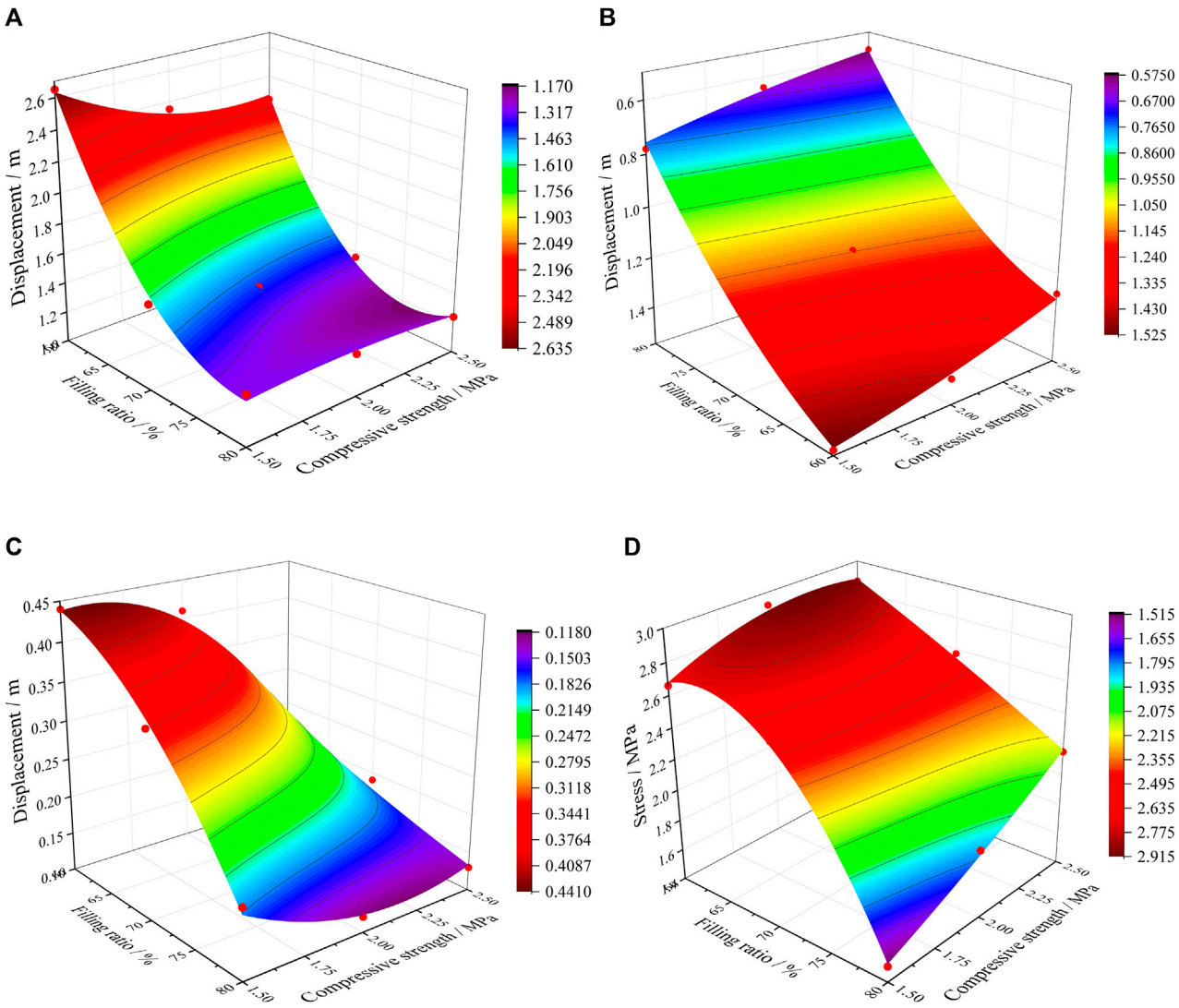

FIGURE 7
(A) The interaction of filling ratio and 1-day strength on D1. **(B)** The interaction of filling ratio and 1-day strength on D2. **(C)** The interaction of filling ratio and 1-day strength on D3. **(D)** The interaction of filling ratio and 1-day strength on S1.

D1 shows a concave curve downward trend, and D2 shows a linear downward trend. When the 1d strength of the filling body increases from 1.5 MPa to 2 MPa, D1 decreases by 9.2%, and when the 1d strength of the filling body increases from 2 MPa to 2.5 MPa, D1 decreases by 4.2%. Because the roof of the goaf is an integral rock system, the high-strength filling material not only resists the deformation of the roof on the filling side but also controls the subsidence of the roof on the unfilled side so that the subsidence is within a reasonable range and does not affect the normal operation of the next mining and filling cycle. D3 changes most significantly with the increase in 1d strength. The higher the strength of the filling body, the less prone it is to yield deformation, so the two are negatively correlated. The 1d strength increased from 1.5 MPa to 2.5 MPa, and D3 decreased by 43.8%. S1 changes little with the increase of strength. This is because the size of S1 depends on the distance between the roof and the filling body, that is, the filling ratio, so the change of the strength of the filling body will not have a great impact on S1. Based on the abovestated analysis, in order to achieve a good filling effect, it is required that the roof subsidence, the deformation of the filling body, and the contact stress between the filling body and the roof tend to the minimum value on the filling side and the unfilled side. Through the influence of different filling ratios and different filling body strengths on the filling effect, it can be seen that improving the strength and filling ratio of the filling body can achieve a better filling effect.

In this study, a comparative analysis was conducted on the numerical simulation results of the filling body strength of 2.5 MPa and filling ratio of 80% (group A) and the strength of 1.5 MPa and filling ratio of 60% (group B). Figures 10C, D illustrates the results. The model slice reveals that the maximum roof subsidence on the filling side is 2.47 m for group A and 1.41 m for group B. On the unfilled side, the maximum roof subsidence is 1.53 m for group A

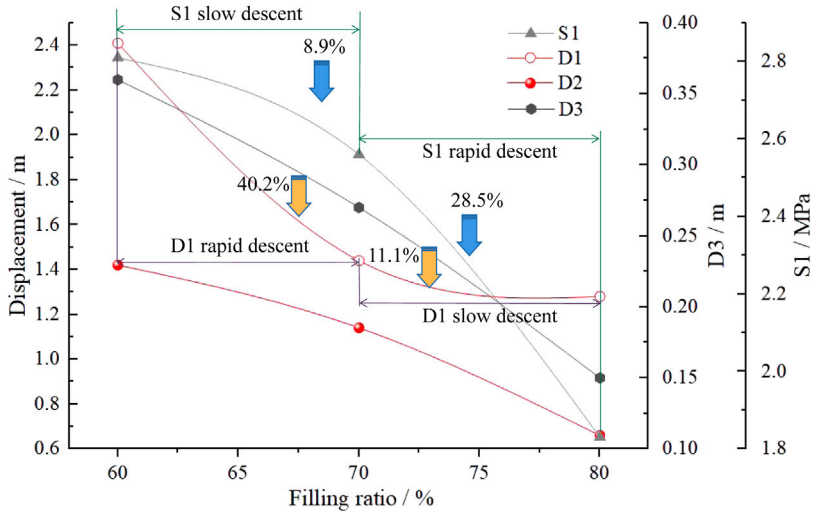

FIGURE 8
Sensitivity analysis of simulation results to filling rate change.

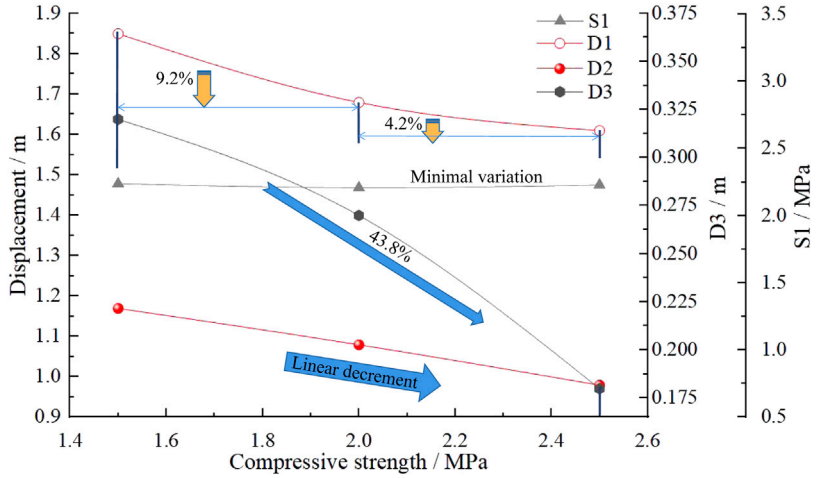

FIGURE 9
Sensitivity analysis of simulation results to 1-day strength change.

and 0.57 m for group B. Additionally, the lateral deformation of the filling body is 0.44 m for group A and 0.13 m for group B. As shown in Figures 10A, B, the bending and caving morphology of the roof in the goaf of group B is more pronounced compared to group A. As shown in Figures 10E, F, when comparing the horizontal and vertical displacement nephograms, it is evident that the displacement influence area caused by roof caving in group B is significantly larger than that in group A. As shown in Figures 10G, H, when comparing the longitudinal stress cloud diagram, it can be observed that the maximum contact stress between the roof and the filling body is 2.66 MPa in group A and 2.15 MPa in group B. Furthermore, the stress concentration area resulting from roof subsidence is much larger in group B compared to group A. In conclusion, group A demonstrates better control over goaf roof subsidence, which is crucial in preventing surface subsidence and creating a larger filling space to accommodate more coal-based solid waste. This finding holds practical significance.

5 Field engineering practice

5.1 Goaf filling scheme

Based on theoretical calculations and numerical simulation results, it has been observed that the immediate roof of the

10.3389/fmats.2023.1234145

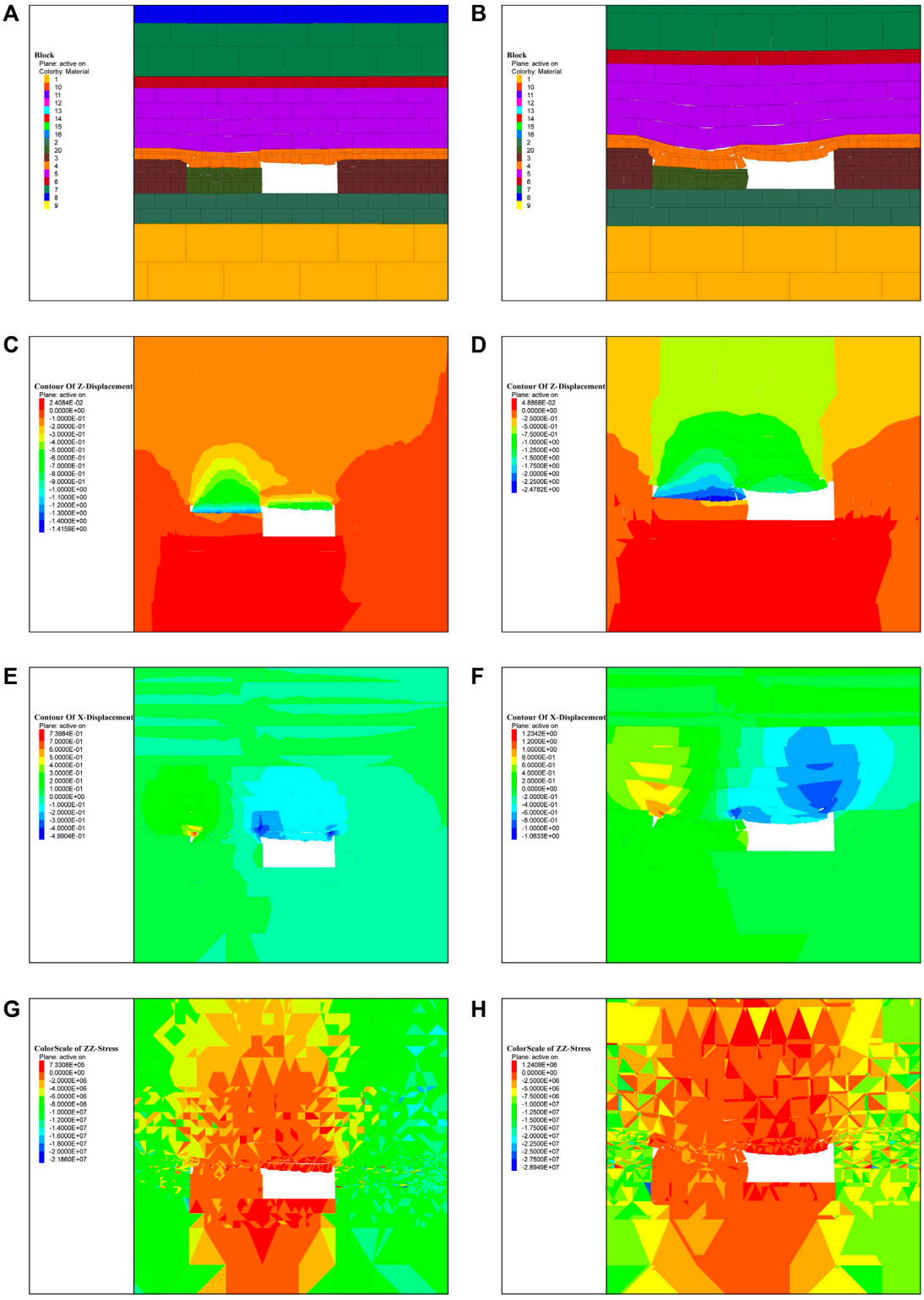

FIGURE 10
Comparative analysis of the filling effect.

working face initially breaks on the side of the goaf and then breaks again above the solid coal. The periodic weighting step distance of 10.74 m provides ample space for the disposal of solid waste. The 110904 working face of Renjiazhuang Coal Mine is characterized by a nearly horizontal coal seam with a small dip angle. Considering the actual working conditions of

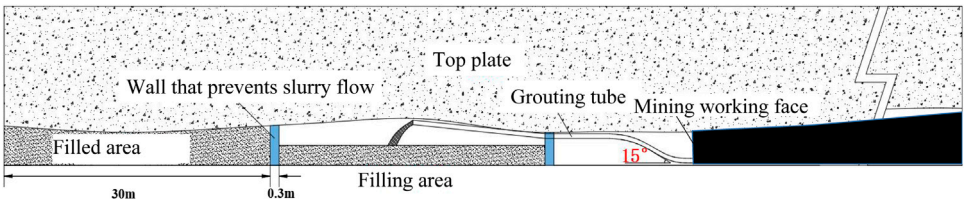

FIGURE 11
Pipe grouting filling roadway layout profile.

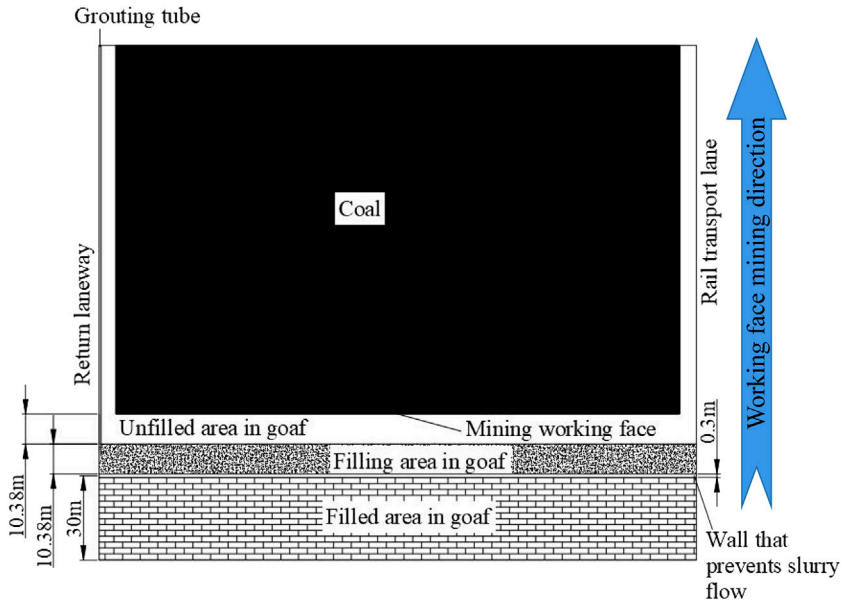

FIGURE 12
Pipe grouting filling roadway layout plan.

Renjiazhuang Coal Mine, a mining–filling coordination scheme is proposed, which involves a filling body strength of 2.5 MPa and a filling ratio of 80%, combined with three-mining and one-filling. To prevent the filling slurry from returning to the working face and affecting the normal mining operation, a grouting wall is set up after every three mining and filling cycles in the working face. Above the grouting wall, there are installation holes for grouting pipes. The angle between the grouting pipeline and the roadway direction behind the grouting wall is designed to be 15°, taking into account the grouting pump capacity and the resistance loss along the pipeline. Figure 11 and Figure 12 show the plane and profile of the grouting wall.

According to the ratio scheme of filling material with 1d strength of 2.5 MPa, the dry material loading is prepared, which is put down to the + 1,000 m yard through the auxiliary inclined shaft, transported to the 110904 air roadway mouth by electric locomotive, and transported to the underground temporary storage bin by the 110904 tractor. The volume of the storage bin is not less than 30 m^3, and the filling raw materials are transported to the filling working face. The filling material transportation system is shown in Figure 13.

The arrangement of the underground filling system is shown in Figure 14. In the experiment, the HBMG30/21-110 s mine filling pump of Feiyi Company was used, with a power of 110 kW, a maximum conveying pressure of 21 MPa, and a maximum conveying capacity of 30 m^3/h. The mixer is HBMG3021.11, the maximum aggregate size is 40 mm, and the volume is 0.7 m^3. The filling raw materials are manually loaded onto the screw feeder, and the screw feeder is transported to the mixer. The filling materials are added with water in the mixer to prepare the slurry and finally filled to the goaf through the mine concrete pump.

The layout of the underground filling pipeline system is illustrated in Figures 15A, B. The outlet of the mine concrete pump is connected to the φ125 filling special seamless elbow pipe, while the remaining sections are connected to the φ125 filling special seamless straight pipe. The total length of the underground φ125 filling pipeline is 174 m, and the total length of the φ108 seamless steel pipe is 54 m. The two filling pipelines are

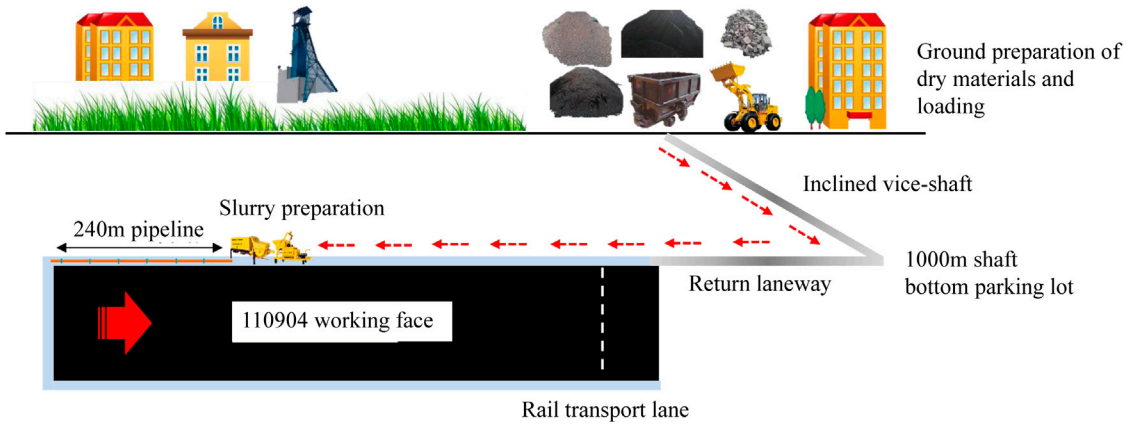

FIGURE 13
Underground transportation of filling materials.

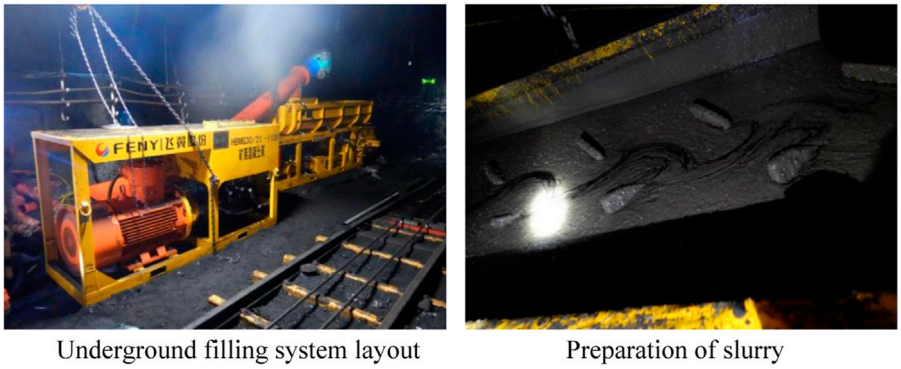

FIGURE 14
Underground filling system layout.

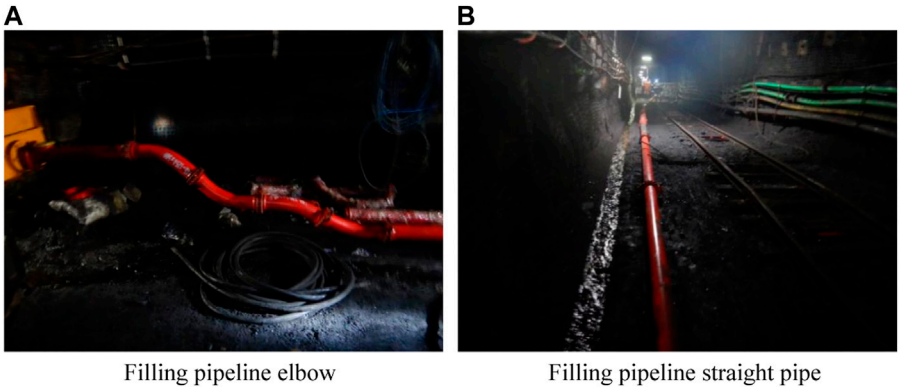

FIGURE 15
Underground filling pipeline system.

connected using a self-made variable diameter. To ensure complete filling of the slurry, the outlet of the filling pipeline is positioned 3 m behind the goaf.

Before grouting filling, the grouting pressure is first adjusted to 6 MPa, and after the pressure is stabilized, the water is pumped for 15 min to moisten the pipe. Then, the cement slurry is pumped for

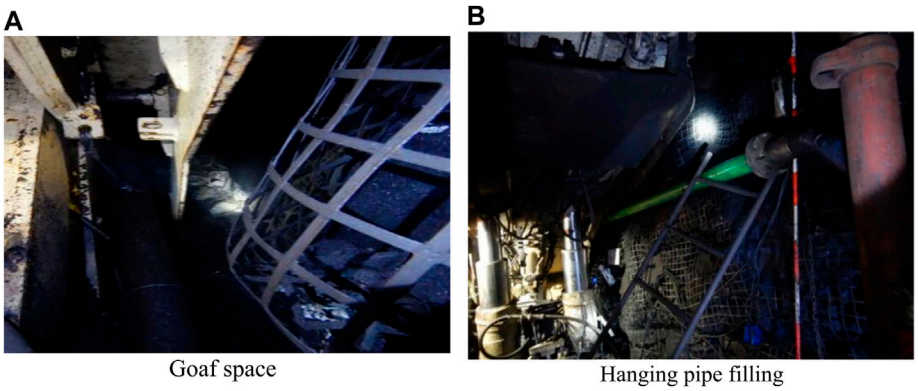

FIGURE 16
Managed filling of the underground roadway.

10 min to seal, and finally, the grouting material is stirred and pumped.

5.2 Experimental effect of goaf filling

In the return airway of the 110904 working face of Renjiazhuang Coal Mine, a two-cycle roadway hanging pipe filling test was carried out, and a good filling effect was achieved in combination with the three-mining and one-filling mining and filling coordination scheme. With the advancement of the working face, the roof subsidence of the roadway behind the goaf was controlled, and the filling space required for the next mining and filling cycle of 80% filling ratio was also guaranteed, absorbing the expected target solid waste. The three-mining and one-filling scheme combined with the hanging pipe filling method can be widely used in the working face.

As depicted in Figures 16A, B, hanging pipe filling is a filling method where the filling pipeline is suspended on the side guard plate of the support, and the pipeline outlet extends into the goaf. The total amount of solid waste disposed by the two-cycle hanging pipe filling method is 67 m^3, with each cycle taking approximately 1.5 h. The shorter filling time helps minimize the disruption caused by the filling work on the normal mining of the working face, while also allowing for sufficient consolidation time for the filling material. In the initial stage of the first cycle of pumping slurry, the underground pumping time-varying diameter pipeline gets blocked due to the mixing of block coal gangue with dry material. However, during the second circulation grouting, the slurry is transported smoothly in the pipeline, gradually filling the space behind the support. Just before the filling process is completed, it is observed that the hose at the end of the pipeline is blocked, and upon cleaning the blocked pipeline, a significant amount of gangue is found.

The ratio of slurry is a crucial factor that determines the filling effect. The change in the stress state of the filling body under load is closely linked to the rearrangement of particles in coal-based solid waste and the transformation between different material phases. The deposition coefficient of the filling slurry increases as the temperature rises during transportation in the pipeline, especially at high flow velocities, and eventually stabilizes (Bai et al., 2017; Bai et al., 2021). To ensure the strength of the filling material, it is important to adjust the ratio scheme during the later stage of preparing the filling material. Additionally, it is necessary to consider the impact of particle gradation on fluidity and the chemical reaction between raw materials on the performance of the filling material. By focusing on these factors, it is possible to prepare a filling material that has both high strength and good fluidity. This will effectively address the issue of filling and plugging on site and enhance the overall quality of the filling operation.

6 Conclusion

Based on the field engineering background of the 110904 working face in Renjiazhuang Mine, this paper aims to determine the limit caving step distance and periodic caving step distance of the goaf roof in the working face through theoretical analysis and calculation. Additionally, the influence of the filling ratio and 1d strength of the filling body on the filling effect is analyzed using numerical simulation. Furthermore, a hanging pipe filling test was conducted in the 110904 working face, leading to the following conclusions:

1) The key strata in the goaf roof are the second and fourth layers. The main roof has a limit caving step distance of 26.32 m and a periodic caving step distance of 10.74 m. The mining–filling coordination scheme is initially defined as “three-mining and one-filling,” which satisfies the engineering technical requirements. The increase in filling ratio and 1d strength of the filling body can result in roof subsidence on the filling side, roof subsidence on the unfilled side, lateral deformation of the filling body, and contact stress between the roof and filling body, all showing a downward trend. The filling ratio is positively correlated with the 1d strength of the filling body and the overall filling effect. The impact of changing the filling ratio on the filling effect is greater than that of changing the 1d strength of the filling body. The best filling effect is achieved when the filling ratio is 80% and the early compressive strength of the filling body is 2.5 MPa.
2) The mining and filling distance of three-mining and one-filling can ensure that each mining and filling cycle has enough space to meet the filling ratio.

3) The roadway's hanging pipe filling effect is excellent, and the roof subsidence of the goaf is effectively controlled after filling. The filling space in the goaf can meet the expected consumption of solid waste. It is important to ensure that there are no large blocks in the filling slurry, as this can easily cause pipe plugging. Furthermore, when determining the later filling material ratio, it is crucial to fully consider the influence of particle size distribution on fluidity.

Data availability statement

The datasets presented in this study can be found in online repositories. The names of the repository/repositories and accession number(s) can be found in the article/Supplementary material.

Author contributions

CL contributed to the conception of the study. DC and KY helped perform the analysis with constructive discussions. CL performed the data analyses and wrote the article. DC and KY performed the analysis with constructive discussions. All authors contributed to the articleand approved the submitted version.

Funding

This work was supported by the National Key Research and Development Program of China (2019YFC1904300), the Institute of Energy, Hefei Comprehensive National Science Center, under Grant No. 21kzs217, and the National Natural Science Foundation of China (Grant No. 51974008).

Conflict of interest

The authors declare that the research was conducted in the absence of any commercial or financial relationships that could be construed as a potential conflict of interest.

Publisher's note

All claims expressed in this article are solely those of the authors and do not necessarily represent those of their affiliated organizations, or those of the publisher, the editors, and the reviewers. Any product that may be evaluated in this article, or claim that may be made by its manufacturer, is not guaranteed or endorsed by the publisher.

References

Bai, B., Long, F., Rao, D., and Xu, T. (2017). The effect of temperature on the seepage transport of suspended particles in a porous medium. *Hydrol. Process.* 31 (2), 382–393. doi:10.1002/hyp.11034

Bai, B., Zhou, R., Cai, G., Hu, W., and Yang, G. (2021). Coupled thermo-hydro-mechanical mechanism in view of the soil particle rearrangement of granular thermodynamics. *Comput. Geotechnics* 137 (8), 104272. doi:10.1016/j.compgeo.2021.104272

Cao, J., Zhu, J., and Gao, Z. (2023). Mix design and performance study of EPS lightweight concrete based on orthogonal test. *Silic. Bull.* 42 (04), 1270–1281. doi:10.16552/j.cnki.issn1001-1625.20230228.00

Chang, Q., Tang, W., and Li, X. (2016). Study on failure law and field measurement of paste filling fully mechanized mining floor. *J. Min. Saf. Eng.* 33 (01), 96–101. doi:10.13545/j.cnki.jmse.2016.01.015

Chen, D., Li, C., and Zhang, Z. (2022). Study on performance optimization of gasification slag-based paste filling material in Ningdong mining area. *Coalf. Geol. Explor.* 50 (12), 41–50. doi:10.12363/issn.1001-1986.22.05.0385

Cui, D., Zhu, C., Li, Q., and Wu, H. (2021). Analysis of main key strata fracture and fracture span difference based on microseismic and electromagnetic radiation coupling. *J. Min. Saf. Eng.* 8 (06), 1152–1157. doi:10.13545/j.cnki.jmse.2020.0275

Gao, S., Li, W., Yuan, K. J., and Rong, C. (2023). Properties and application of thixotropic cement paste b-ackfill with molybdenum tailings. *J. Clean. Prod.* 391, 136169. doi:10.1016/j.jclepro.2023.136169

Han, B., Ji, K., Wang, J., Wang, S., Zhang, P., and Hu, Y. (2022). Determination of the required strength of artificial roof for the underhand cut-and-fill mine using field measurements and theoretical analysis. *Sustainability* 15, 189. doi:10.3390/su15010189

Ji, Y., Li, H., and Song, G. (2023). Stability analysis of surrounding rock and optimization of mining and filling process in partial filling mining face. *J. Henan Polytech. Univ.* doi:10.16186/j.cnki.1673-9787.2022010024

Jiang, F., Zhou, H., Sheng, J., Shuai, J., Sun, D., Hu, Y., et al. (2018). Analysis and evaluation of surface deformation characteristics under full filling mining. *J. Rock Mech. Eng.* 37 (10), 2344–2358. doi:10.13722/j.cnki.jrme.2018.0396

Jin, F., Xu, J., Liu, Y., Ma, X., Wang, X., Wang, Y., et al. (2022). Monitoring of key strata movement and 5-stage law of rock movement-Taking Hongqinghe Coal Mine as an example. *Coal J.* 47 (02), 611–622. doi:10.13225/j.cnki.jccs.xr21.1888

Li, H., Ji, Y., and Song, G. (2022c). Stability analysis of end face roof based on elastic foundation beam theory. *Sci. Technol. Eng.* 22 (30), 13234–13241.

Li, J., Li, S., Ren, W., Liu, H., Liu, S., and Yan, K. (2023). Seismic reduction mechanism and engineering application of paste backfilling mining in deep rock burst mines. *Sustainability* 15, 4336. doi:10.3390/su15054336

Li, M., Zhang, J., Huang, P., Wang, J., and Wang, Y. (2022a). Study on the control factors and influencing laws of roof subsidence in deep gangue filling stope. *J. Min. Saf. Eng.* 39 (02), 227–238. doi:10.13545/j.cnki.jmse.2021.0066

Li, Y., Lu, B., Yang, R., Lin, H., and Xu, B. (2022b). Wang Shushuai, Liu Chenhui. Continuous mining and filling cemented filling mining technology and typical engineering cases. *Coal J.* 47 (03), 1055–1071. doi:10.13225/j.cnki.jccs.2021.1612

Li, Y., Ren, Y., Wang, N., Jin, X., Ou, X., Luo, J., et al. (2021). Identification of genes involved in Fe-S cluster biosynthesis of nitrogenase in *Paenibacillus polymyxa* WLY78. *J. Coal* 46 (12), 3771–3780. doi:10.3390/ijms22073771

Lu, B., Zhang, X., Li, F., Zhang, B., and Pang, Z. (2017). Short-wall gangue cemented filling mining technology and application. *Coal J.* 42 (S1), 7–15. doi:10.13225/j.cnki.jccs.2016.1416

Ma Li, Q., Xu, Y., Zhang, D., Lai, X., Huang, K., and Du, H. (2019). Characteristics of aquiclude and surface deformation under the condition of wall continuous mining and water-preserved coal mining. *J. Min. Saf. Eng.* 36 (01), 30–36. doi:10.13545/j.cnki.jmse.2019.01.005

Ma, L., Zhang, D., Wang, S., Xie, Y., and Yu, Y. (2017). Mining and filling parallel type water-preserved coal mining method. *Coal J.* 43 (01), 62–69. doi:10.13225/j.cnki.jccs.2017.0809

Ma, Q., Zhang, Y., Zheng, Y., Li, Z., Song, G., and Hu, L. (2022). Overlying strata movement and mine-pressure weakening law of high-efficiency longwall paste backfilling of thick coal. *Sustainability* 14, 15356. doi:10.3390/su142215356

Song, G., Wei, Z., Yang, S., Wang, Z., and Kong, D. (2023). An Dong. Roof fall mechanism and similar simulation test based on Timoshenko beam theory. *J. Min. Saf. Eng.* 40 (02), 304–312. doi:10.13545/j.cnki.jmse.2021.0680

Sun, G., N, J., Du, M., Yan, R., and Zhang, Z. (2016). Multi-factor analysis of roof subsidence of paste filling surface based on response surface method. *J. Shandong Univ. Sci. a-nd Technol. Nat. Sci. Ed.* 41 (05), 51–59. doi:10.16452/j.cnki.sdkjzk.2022.05.006

Sun, K., Cao, X., Wu, Z., and Song, W. (2019). Longwall roadway-by-lane cemented filling mining and filling process coordination optimization design metho. *Min. Res. Dev.* 39 (06), 11–16. doi:10.13827/j.cnki.kyyk.2019.06.003

Sun, X., Zhou, H., and Wang, G. (2007). Numerical simulation study on strata control of solid waste paste filling. *J. Min. Saf. Eng.* 2007 (01), 117–121.

Tang, W., Sun, X., Wang, H., Shi, X., Li, X., and Li, Y. (2017). Study on the stability effect of strip coal pillar overburden in paste filling mining. *Coal Sci. Technol.* 45 (09), 109–115. doi:10.13199/j.cnki.cst.2017.09.018

Tu, S., Hao, D., Miao, K., Liu, X., and Li, W. (2021). Collaborative mining of complex system in deep mining-dressing-filling integrated mine. *J. China Univ. Min. Technol.* 50 (03), 431–441. doi:10.13247/j.cnki.jcumt.001276

Wang, G., Zhu, S., Jiang, F., Zhang, X., Liu, J., Wang, X., et al. (2021). Mechanism of coal pillar-key stratum structure instability type mine earthquake in fully mechanized caving face of inclined thick coal seam. *Coal J.* 47 (06), 2289–2299. doi:10.13225/j.cnki.jccs.2021.1316

Wang, T., Kang, Z., Fu, Q., Shi, Z., Chen, X., Wang, Y., et al. (2022). Ferroptosis plays an important role in promoting ionizing radiation-induced intestinal injuries. *Min. Saf. Environ. Prot.* 49 (06), 7–13. doi:10.1016/j.bbrc.2022.01.068

Wu, Y., Zhang, Z., and Li, Z. (2020). Porous-coated metaphyseal sleeves and MBT implant for severe bone loss in revision total knee arthroplasty: A mean 2.4-year follow-up. *Mine Res. Dev.* 40 (07), 12–17. doi:10.1186/s42836-020-00031-x

Xia, D., Li, X., and Hu, J. (2022). Experimental study on performance optimization of pervious recycled concrete based on orthogonal test. *Silic. Notif.* 41 (08), 2748–2758. doi:10.16552/j.cnki.issn1001-1625.2022.08.018

Xu, L., Zhang, K., Liu, X., Chen, B., Fan, T., and Gui, S. (2023). Deformation characteristics of key strata and control effect of surface subsidence in separation grouting mining. *J. Coal* 48 (02), 931–942. doi:10.13225/j.cnki.jccs.XH22.169

Zhang, J., Ju, Y., Zhang, Q., Ju, F., Xiao, X., Zhang, W., et al. (2019). Low damage mining system and method for mine ecological environment. *J. Min. Strata Control Eng.* 1 (02), 56–68. doi:10.13532/j.jmsce.cn10-1638/td.2019.02.005

Zhang, J., Tu, S., Cao, Y., Tan, Y., Xin, H., and Pang, J. (2021). Event-triggered model predictive control of positive systems with random actuator saturation. *J. China Univ. Min. Technol.* 50 (03), 417–437. doi:10.1007/s11071-021-06636-4

Zhang, Q., Wang, Y., Zhang, J., Zuo, X., Yang, J., Zhang, H., et al. (2022) Research on solid intelligent filling mining method in coal mine. *Coal J.* 47 (07), 2546–2556. doi:10.13225/j.cnki.jccs.2021.0982

Zhang, Q., Zou, J., Wu, K., Jiao, Y., Wang, C., and Yan, X. (2023). Study on the characteristics of mine earthquake induced by the fracture of overlying key strata in deep coal mining. *Rock Mech. Eng.* 42 (05), 1150–1161. doi:10.13722/j.cnki.jrme.2022.0612

Zhou, N., Dong, C., Zhang, J., Meng, G., and Cheng, Q. (2021a). Influences of mine water on the properties of construction and demolition waste-based cemented paste backfill. *Constr. Build. Mater.* 313, 125492. doi:10.1016/j.conbuildmat.2021.125492

Zhou, N., Du, E., Zhang, J., Zhu, C., and Zhou, H. (2021b). Mechanical properties improvement of Sand-Based cemented backfill body by adding glass fibers of different lengths and ratios. *Constr. Build. Mater.* 280, 122408. doi:10.1016/j.conbuildmat.2021.122408

Zhou, N., Xu, J., Zhang, J., Yan, H., Zhu, C., and Li, M. (2022). An experimental study of the permeability of sand-based cemented backfill under the influence of multi-factor interaction. *Environ. Earth Sci.* 81 (01), 320. doi:10.1007/s12665-022-10441-6

frontiers | Frontiers in Materials

TYPE Original Research
PUBLISHED 01 August 2023
DOI 10.3389/fmats.2023.1235690

OPEN ACCESS

EDITED BY
Xianze Cui,
China Three Gorges University, China

REVIEWED BY
Junxue Ma,
Ministry of Emergency Management, China
Yu Wang,
University of Science and Technology Beijing, China

*CORRESPONDENCE
Song Chen,
chennsongg@163.com

RECEIVED 06 June 2023
ACCEPTED 21 July 2023
PUBLISHED 01 August 2023

CITATION
Yang Z, Nie B, Xie Y, Li H, Chen S, Zhang Q, Tian Q, Lin S and Yuan Y (2023), Calculation method for holding prestress of corroded prestressed anchor cable in long-term operation slope.
Front. Mater. 10:1235690.
doi: 10.3389/fmats.2023.1235690

Calculation method for holding prestress of corroded prestressed anchor cable in long-term operation slope

Zhao Yang[1], Biao Nie[1], Yining Xie[2,3], Hongwen Li[1], Song Chen[4,5]*, Qingqing Zhang[1], Qingyan Tian[1], Sen Lin[1] and Ying Yuan[5]

[1]Guangdong Hualu Transport Technology Co., Ltd., Guangzhou, China, [2]Guangdong Provincial Freeway Co., Ltd., Guangdong, China, [3]Guangdong Provincial Freeway Co., Ltd., Jingzhubei Branch Guangdong, Shijiazhuang, China, [4]Hebei Key Laboratory of Optoelectronic Information and Geo-detection Technology, Hebei GEO University, Shijiazhuang, China, [5]College of Urban Geology and Engineering, Hebei GEO University, Shijiazhuang, China

Due to the rich water in the weathered layer of the free section, the prestressed anchor cable of the long-term operating slope is severely corroded and its mechanical properties are deteriorated, affecting the stability of the slope. Based on a certain number of long-term operation highway anchor cable excavation tests, the author found that the free section of the anchor cable orifice was seriously corroded. Currently, there is very little research on the relationship between the holding capacity of anchor cables and the degree of corrosion of the free section of the cable, and the research is mainly focused on the life of the anchor section. Therefore, the constitutive relationship of the cable body is established on the basis of corrosion force coupled statistical damage mechanics, and the relationship between the degree of corrosion of the cable body and the holding prestress of the operating slope anchor cables is derived using the load transfer method. The rationality of prestressed anchor cables on highway slopes during the operation period was verified by actual measurement. This study has positive significance for long-term stability analysis of slopes.

KEYWORDS

slope reinforcement, corrosion force interaction, statistical damage mechanics, load transfer method, anchor cable holding prestress

1 Introduction

Tension type prestressed anchor cables are widely used in transportation, land and resources, railways, industrial and civil buildings, water conservancy and hydropower projects, and other industries. The prestressed anchor cable is bonded to the grouting body through the steel strand to form an anchor solid, and a certain length of unbonded free section is set to apply prestress, thereby playing an active role in reinforcing the slope (Shi et al., 2019; Lin et al., 2020; Wang L. Q. et al., 2023).

For engineering slopes that have been reinforced with prestressed anchor cables for a long time, the prestress held by the landslide will decrease over time as the operation time increases after the anchor cable reinforcement is completed. The current research mainly focuses on the stress relaxation effect of the cable body caused by the creep of the rock mass in the anchoring section of the prestressed anchor cable (Jiang et al., 2014; Chen G. et al., 2018). However, for the prestressed anchor cable in hard rock areas, the creep effect of the

rock mass in the anchoring section is weak, and this factor is not the main reason for the anchor cable to hold the prestress (stress relaxation) (Fan et al., 2015).

The authors conducted anchor opening testing, prestressed anchor cable holding capacity testing, and anchor cable full length excavation tests on multiple operating highways and cutting slope points in Guangdong, China. The main types of slope strata are carbonaceous mudstone, quartz sandstone, granite, and fused tuff. In some slope points, even if the anchor section is located in moderately weathered hard rock stratum, the prestress held by the anchor cable still suffers from a loss of 30%–50%. The impact of construction quality factors is not considered for the time being, and the steel strands at the anchor head section often suffer from severe corrosion when the loss ratio is large. Many scholars have done some valuable engineering research on the corrosion of anchor cables during the operation period. He et al. (2010) studied the stress distribution characteristics of the anchor section of the anchor cable based on summarizing the corrosion damage laws of steel strands. Zheng et al. (2010) studied the variation of physical and mechanical parameters of the reinforcement under the influence of corrosion. Deng et al. (2014) focused on the impact of cable rust expansion on anchor solids in the anchoring section, and proposed a prediction model for anchor cable life. Jiang et al. (2014) and Fu et al. (2021) considered the damage and failure of the anchor section caused by the corrosion and expansion of rock bolts in the process of studying the long-term reliability of slopes. Li and Liu (2016) studied the effect of cable corrosion on the performance of the anchoring interface. However, during the anchor opening inspection and the full length excavation test, the author found that the corrosion of the shallow free section of the anchor cable is the most serious, and the corrosion of the anchor section is relatively rare. Rust in the free section reduces the force transmission performance of the anchor cable, and it is unable to transmit the anchoring force to the orifice reaction structure (lattice beam), which is intuitively manifested as a reduction in the holding prestress of the anchor cable. In practical engineering, the mechanical properties of rock masses can decrease due to precipitation cycles, temperature, and alternating disturbances (Li and Chen, 2022; Wang et al., 2022; Wang Y. et al., 2023). If the anchor cable does not have sufficient prestress, it is difficult to prevent cracks in the rock mass due to weathering and deformation, and the passive support force of the prestressed anchor cable is usually considered as a safety reserve in engineering. Therefore, the proportion of holding prestress has received great attention in practical engineering. At present, some scholars and experts have established models for the overall pull-out resistance of anchor cables (including passive support force) and the reduction of anchor cable prestress caused by soft rock creep (Shi et al., 2019; Yang et al., 2022). However, there are relatively few mechanical model studies on the reduction of prestress caused by reinforcement corrosion in hard rock formations. In order to effectively prevent disasters caused by slope instability and collapse, and guide corresponding engineering construction, it is necessary to explore the mechanical mechanisms of relevant aspects and establish corresponding mechanical models.

In order to explore the mechanism by which corrosion in the free section affects the holding prestress of anchor cables, a mechanical model for calculating the holding prestress of anchor cables under corrosion conditions of hard rock and non soft rock slopes is established. Based on statistical damage mechanics, a new tensile constitutive model of steel strands considering the interaction of corrosion and force is derived, and the constitutive model and load transfer method are applied to the mechanical analysis of the corroded free section of anchor cables. In the analysis of the application of the model to field tests, it was found that the calculated results were relatively close to the measured values, verifying the rationality of the model.

2 Rust force statistical damage constitutive equation

To simplify the analysis, the following assumptions are made.

(1) Only consider uniform corrosion of steel strands;
(2) The shear stress in the anchoring section of the anchor cable is uniformly distributed on the surface of the steel strand;
(3) This model only considers the effect of anchor cable corrosion on maintaining pre-stress of the anchor cable, without considering the interaction with other factors. It is applicable to the corrosion of steel strands in the free section of the anchor cable in hard rock slopes.

After a series of chemical and electrochemical actions, steel strands can form rust. Rust has poor mechanical properties, is relatively loose, and basically has no bearing capacity. It is assumed that the actual bearing capacity cross-sectional area of the steel strand decreases, causing damage.

$$\eta = \frac{g^o - g}{g^o} \tag{1}$$

Where, η is the corrosion rate, which is a dimensionless percentage, g^o is the weight of the steel strand before corrosion, and g is the weight of the steel strand after corrosion.

The research by Luo and Li (2008) shows that the physical and mechanical properties of unbonded steel strands affected by normal corrosion have decreased to varying degrees, as shown in Table 1 below.

From Table 1, it can be seen that under normal uniform corrosion, the physical and mechanical parameters of the steel strand are negatively correlated with the corrosion rate, which is caused by damage caused by corrosion. The actual engineering design is often conservative and generally does not place the steel strand in a relatively plastic tensile state, but rather requires a certain safety reserve. In order to reflect the impact of the combined action of corrosion and force, damage factors can be introduced. Therefore, the damage discussed in this article refers to the process that under the combined action of corrosion and force, the internal micro elements of the steel strand cable or tendon become unable to withstand stress, and the effective cross-sectional area decreases.

The damage of solid materials is usually defined by the following formula (Liu et al., 2018):

$$D = \frac{A_D}{A_{total}} \tag{2}$$

10.3389/fmats.2023.1235690

TABLE 1 Change trend of physical and mechanical parameters of unbonded free section steel strands with different corrosion rates.

Operating mode	Test number	Rust rate/%	Nominal ultimate strength/MPa	Nominal yield strength/MPa	Nominal elastic modulus/GPa	Elongation %
Normal uniform corrosion	1	0	1956.83	1,663.94	209.1	5.35
	2	0	1955.45	1,663.25	211.9	5.33
	3	0	1956.92	1,664.15	217.3	5.36
	4	0.52	1923.56	1,659.12	212.8	4.21
	5	0.51	1926.54	1,658.57	213.6	4.32
	6	0.52	1920.98	1,658.85	212	4.39
	7	0.97	1900.23	1,656.24	212.7	3.87
	8	0.99	1892.33	1,652.35	213.6	3.84
	9	1.01	1905.36	1,655.36	212.1	3.86
	10	1.49	1859.74	1,649.79	212.4	3.62
	11	1.52	1855.67	1,649.45	211.9	3.46
	12	1.53	1856.89	1,647.52	212.4	3.56
	13	2.03	1836.04	1,643.24	212	3.11
	14	2.03	1837.85	1,644.54	211.9	3.09
	15	2.06	1836.52	1,640.21	211.9	3.24
	16	2.61	1786.21	1,637.94	211.3	2.75
	17	2.63	1798.56	1,638.54	211.3	3.33
	18	2.65	1798.56	1,637.01	211	2.56
	19	3.81	1748.2	1,617.72	209	2.16
	20	3.82	1748.2	1,616.54	208.1	1.5
	21	3.84	1748.2	1,618.74	209	2.26
	22	5.01	1721.62	1,606.27	205.6	1.69
	23	5.01	1721.62	1,605.01	205.9	1.51
	24	5.03	1719.51	1,605.86	205.5	1.76
	25	6.35	1,676.26	1,570.53	200.2	1.2
	26	6.37	1,674.32	1,573.2	200.1	1
	27	6.37	1,674.3	1,571.35	200.9	1.13
	28	6.97	1,510.79		197.2	0.83
	29	7.27	1,496.4		196.5	0.42
	30	7.33	1,490.74		195.2	0.52
	31	8.03	1,342.68		191.2	0.45
	32	8.1	1,336.21		190.3	0.57
	33	8.16	1,335.54		189.9	0.38
	34	8.97	1,237.41		181.3	0.16
	35	9.01	1,239.98		183.1	0.12
	36	9.03	1,238.69		183.6	0.09
	37	9.81	1,231.25		176.1	0
	38	9.9	1,230.36		176.6	0

(Continued on following page)

TABLE 1 (*Continued*) Change trend of physical and mechanical parameters of unbonded free section steel strands with different corrosion rates.

Operating mode	Test number	Rust rate/%	Nominal ultimate strength/MPa	Nominal yield strength/MPa	Nominal elastic modulus/GPa	Elongation %
	39	9.92	1,230.36		176.1	0
	40	10.29	1,226.1		173.2	0
	41	10.42	1,223.02		172.9	0
	42	10.45	1,221.75		171.7	0

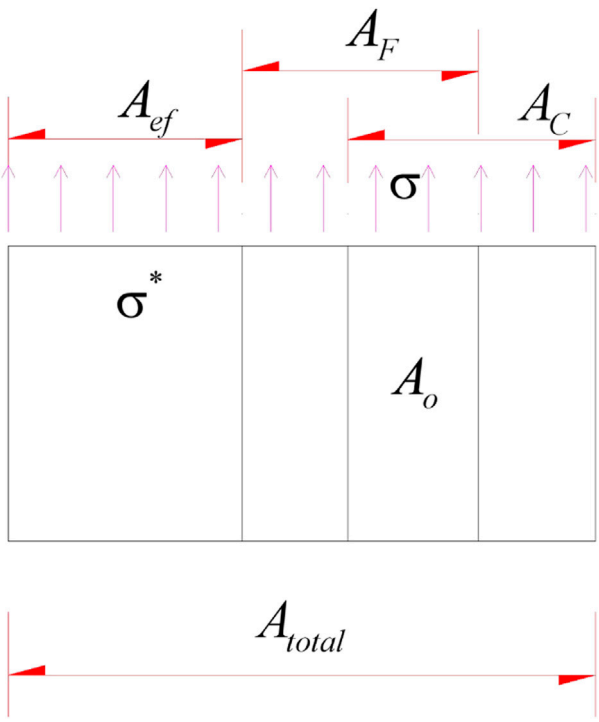

FIGURE 1
Damage distribution mode of steel strand during tension.

Where, D is the damage factor, it is a dimensionless parameter, A_D is the cross-sectional area of the loss, and A_{total}, is the total cross-sectional area of the material.

Under corrosion conditions, the unbonded free section steel strand is damaged by the combined action of external force and corrosion, as shown in Figure 1.

The steel strand is subjected to tensile load, and the total tensile stress and total area borne by the cross section micro element are σ and A_{total}, the undamaged part bears effective shear stress σ^* and cross-sectional area carrying effective stress A_{ef}, and the areas of corrosion, pullout load, and common damage are A_C, A_F and A_o.

At a certain corrosion rate, the corrosion damage area is A_C, so the damage expression caused by corrosion is (Liu et al., 2018):

$$D_c = \frac{A_C}{A_{total}} \tag{3}$$

After corrosion, the damage area caused by tensile load is A_F, and the damage area caused by both corrosion and tensile load is A_F. Therefore, the damage expression caused by pure tensile load is:

$$D_F = \frac{A_F - A_o}{A_{total} - A_C} \tag{4}$$

The total damage caused by corrosion and load is defined as the cumulative damage caused by both minus the common damage caused by their intersection, and the expression is:

$$D = \frac{A_F + A_C - A_o}{A_{total}} \tag{5}$$

The expression of the total damage factor obtained is:

$$D = D_C + D_F - D_C D_F \tag{6}$$

From a mesoscopic perspective, material damage leads to loss of cross-sectional area, resulting in a reduction in macroscopic mechanical properties, which is essentially caused by the destruction of material microelements. Therefore, the damage factor can also be defined by counting the number of micro element failures, as shown in the following equation.

$$D = \frac{n}{N} \tag{7}$$

Where, n is the number of damaged micro elements, and N is the total number of micro elements of the steel strand.

Taking the corrosion rate as the strength index, it is assumed that the microcracks and microelements of the steel strand under the influence of corrosion follow the Weibull probability distribution (Chen S. et al., 2018). The expression of the probability distribution density function of the Weibull distribution is:

$$\Phi(\eta) = \frac{b}{a}\left(\frac{\eta}{a}\right)^{b-1} \exp\left[-\left(\frac{\eta}{a}\right)^{b}\right] \tag{8}$$

Where, a and b are model parameters of Weibull distribution, reflecting the brittleness and morphology of the model curve.

As the corrosion rate changes, the number of micro cracks and micro elements in the steel strand that are damaged is:

$$n = \int_0^{\eta} N\Phi(\eta)d\eta = N\left(1 - \exp\left[-\left(\frac{\eta}{a}\right)^{b}\right]\right) \tag{9}$$

Therefore, the expression of the damage factor caused by pure corrosion is:

$$D_C = 1 - \exp\left[-\left(\frac{\eta}{a}\right)^{b}\right] \tag{10}$$

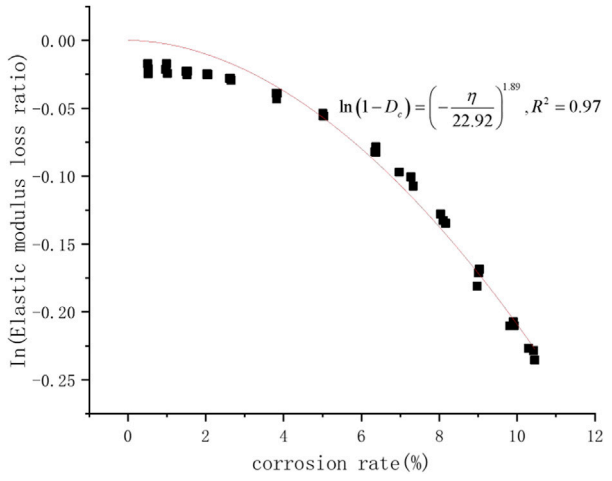

FIGURE 2
Evolution law of the damage along with the corrosion rate.

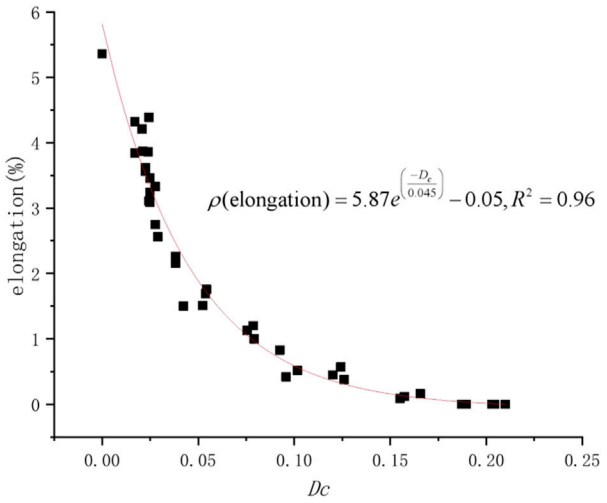

FIGURE 4
Ultimate strength of steel strands under different degrees of corrosion damage.

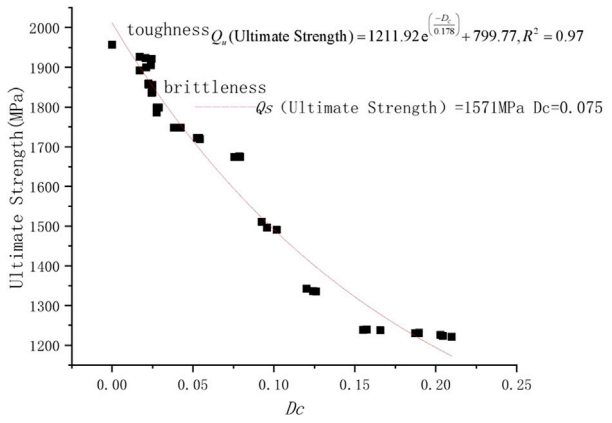

FIGURE 3
Ultimate strength of steel strands under different degrees of corrosion damage.

Macroscopically, damage can be characterized as a loss of modulus, so the formula can also be written as:

$$D_C = \frac{E_{r\eta}}{E_{\eta=0}} = 1 - \exp\left[-\left(\frac{\eta}{a}\right)^b\right] \tag{11}$$

Where, E_r is the elastic modulus after corrosion damage, and $E_{\eta=0}$ is the elastic modulus when the corrosion rate is equal to 0.

Based on the data in Table 1, a scatter plot (see Figure 2) of the corrosion rate damage evolution law can be drawn to verify the rationality of the formula.

It can be seen from Figure 2 that this figure can better describe the evolution of steel strands with corrosion rate, which indicates that the law of micro element failure of steel strand section under corrosion obeys Weibull probability distribution.

With the evolution of corrosion damage, the rule between the tensile ultimate strength of steel strands and corrosion damage can be obtained through nonlinear regression analysis (see Figure 3).

It can be seen from Figure 3 that the ultimate strength of corroded steel strands decreases exponentially with the evolution of corrosion damage factors. When the corrosion damage of the steel strand reaches a certain degree, the ultimate strength value tends to converge and tend to be gentle. This is because as the degree of corrosion increases, the initial damage increases under load, and the internal micro cracks and pores become larger, making it more prone to low stress instability and expansion. Under normal corrosion conditions, the ultimate strength approaches or even equals the yield strength. Under local corrosion damage conditions, the yield strength of steel strands also decreases with the ultimate strength.

As can be seen from Figure 4, as the corrosion damage evolves, the elongation of the steel strand decreases exponentially, and the brittleness of the material increases as the corrosion damage evolves.

Load action is also an important factor that affects the mechanical properties of steel strands in corroded environments. It is assumed that under tensile load, with strain as the strength index, the strength of the microelement obeys a uniform distribution, as shown in the following equation.

$$\Phi(\varepsilon) = \frac{1}{a_F} \tag{12}$$

a_F is a model parameter that reflects the uniformity of the distribution of microelements under tensile load.

Eq. 13 considers the location parameter c_F, which can reflect the condition that the elastic modulus of the tensile elastic section of the steel strand is not damaged due to force. As the strain increases, the number of microelements that fail is:

$$n = \int_{c_F}^{\varepsilon} N\Phi(\varepsilon)d\varepsilon = N\frac{\varepsilon - c_F}{a_F} \tag{13}$$

Where, c_F is the strain threshold for force induced damage. Combining Eqs. 13 and Eqs 6, 7 obtain Eq. 14:

$$D = \begin{cases} 1 - \exp\left[\left(-\frac{\eta}{a}\right)^b\right], \varepsilon \le c_F \\ 1 - \exp\left[\left(-\frac{\eta}{a}\right)^b\right]\left(1 - \frac{\varepsilon - c_F}{a_F}\right), \varepsilon > c_F \end{cases} \tag{14}$$

Based on the assumption of strain equivalence, the Constitutive equation acting on the damaged material is equivalent to the effect produced by the effective force on the nondestructive material, the expression is as follows (Chen G. et al., 2018):

$$\sigma = E_{\eta=0}(1 - D)\varepsilon \tag{15}$$

Combining Eqs. 14, 15, the stress-strain relationship (constitutive model) of the steel strand can be obtained as follows:

$$\sigma = \begin{cases} E_{\eta=0} \exp\left[\left(-\frac{\eta}{a}\right)^b\right]\varepsilon, \varepsilon \le c_F \\ E_{\eta=0} \exp\left[\left(-\frac{\eta}{a}\right)^b\right]\left(1 - \frac{\varepsilon - c_F}{a_F}\right)\varepsilon, \varepsilon > c_F \end{cases} \tag{16}$$

Select tensile test data of steel strands with normal corrosion rates of 0%, 2.63%, 6.35%, 8.97%, and 10.42% to verify the rationality of Formula (16). See Figure 2; Figure 5 for relevant model parameters and curves.

It can be seen from Figure 5 that the derived model agrees well with the experimental data. The model can better reflect the constitutive relationship of steel strands under the combined action of corrosion and force damage. In practical engineering, the unbonded free section of steel strands is prone to corrosion and corrosion during highway slope operation, resulting in loss of cross-sectional area, resulting in a decrease in the holding prestress of the anchor cable, and affecting the long-term stability of the slope.

3 Calculation method of anchor cable holding prestress based on damage statistical theory and load transfer method

The tendons of anchor bolts and anchor cables are usually in an elastic state under working conditions. The elastic situation in the constitutive model derived in this paper can be used in the load transfer analysis of corroded prestressed anchor bolts (cables). On the anchored micro segment, assuming that the interfacial shear stress on the micro segment is uniformly distributed, it can be obtained based on the force balance of the micro segment (Li and Stillborg, 1999):

$$dp(x) + \pi d\tau dx = 0 \tag{17}$$

Where, d is the diameter of the anchor rod; $P(x)$ The axial force at a certain rod length, and τ is the shear stress between the reinforcement and the anchor body.

The magnitude of the axial force is related to the strain of the steel strand, as shown in the formula.

$$P(x) = E_{cable}\pi d^2\frac{\varepsilon(x)}{4} \tag{18}$$

Where, E_{cable} is the elastic modulus of the steel strand, which is related to factors such as corrosion rate is $\varepsilon(x)$ the strain value along the length of the anchor cable.

In the free section of the anchor cable, $\tau = 0$, it can be seen by substituting Formula (17) that the axial force of the anchor cable in the free section is:

$$P(l_f) = E_{cable}\pi d^2\frac{\varepsilon(x = l_f)}{4} \tag{19}$$

Where, l_f is the length of the free section.

It is assumed that the deformation of the steel strands of the anchor cable is coordinated, there is $\varepsilon(x = l_f) = \varepsilon(x = 0)$ at the boundary between the free section and the anchor section, and the strains at both ends are equal. Under the same strain, after corrosion damage to the unbonded free section steel strand, the elastic modulus E_{cable} decreases under the combined action of force and corrosion, which is reflected in a decrease in the anchor head holding capacity on the macro level.

The shear stress and shear displacement of the anchoring section of the anchor cable follow the following constitutive relationship:

$$\tau = Ku \tag{20}$$

Where, K is the interfacial shear stiffness, and if the anchor cable at the anchor section is not corroded, this value is not affected. Parameter u is the shear displacement between the cable body and the grouting body.

From the geometric equation of the steel strand, it can be obtained that:

$$\varepsilon = \frac{du}{dx} \tag{21}$$

From Eqs. 18–21, it can be obtained that:

$$\frac{d^2u}{dx^2} = -\frac{4}{E_{cable}d}Ku \tag{22}$$

Since the elastic modulus of the anchor cable does not decrease due to corrosion during the pre tensioning and post tensioning periods, taking E_{cable} = 215GPa, the general solution expression can be obtained by solving the differential equation as follows:

$$u = C1e^{\left(x\sqrt{\frac{4K}{E_{cable}d}}\right)} + C2e^{\left(-x\sqrt{\frac{4K}{E_{cable}d}}\right)} \tag{23}$$

Where, $C1, C2$ are undetermined coefficients.

The expression for the axial force distribution of the anchoring section along the rod length can be obtained from the above various methods as follows:

$$\begin{aligned} P(x) &= \frac{E_{cable}\pi d^2}{4}\left[C1\sqrt{\frac{4K}{E_{cable}d}}e^{\left(x\sqrt{\frac{4K}{E_{cable}d}}\right)} - C2\sqrt{\frac{4K}{E_{cable}d}}e^{\left(-x\sqrt{\frac{4K}{E_{cable}d}}\right)}\right] \\ &= M\left[C1Ne^{(xN)} - C2Ne^{(-xN)}\right] \end{aligned} \tag{24}$$

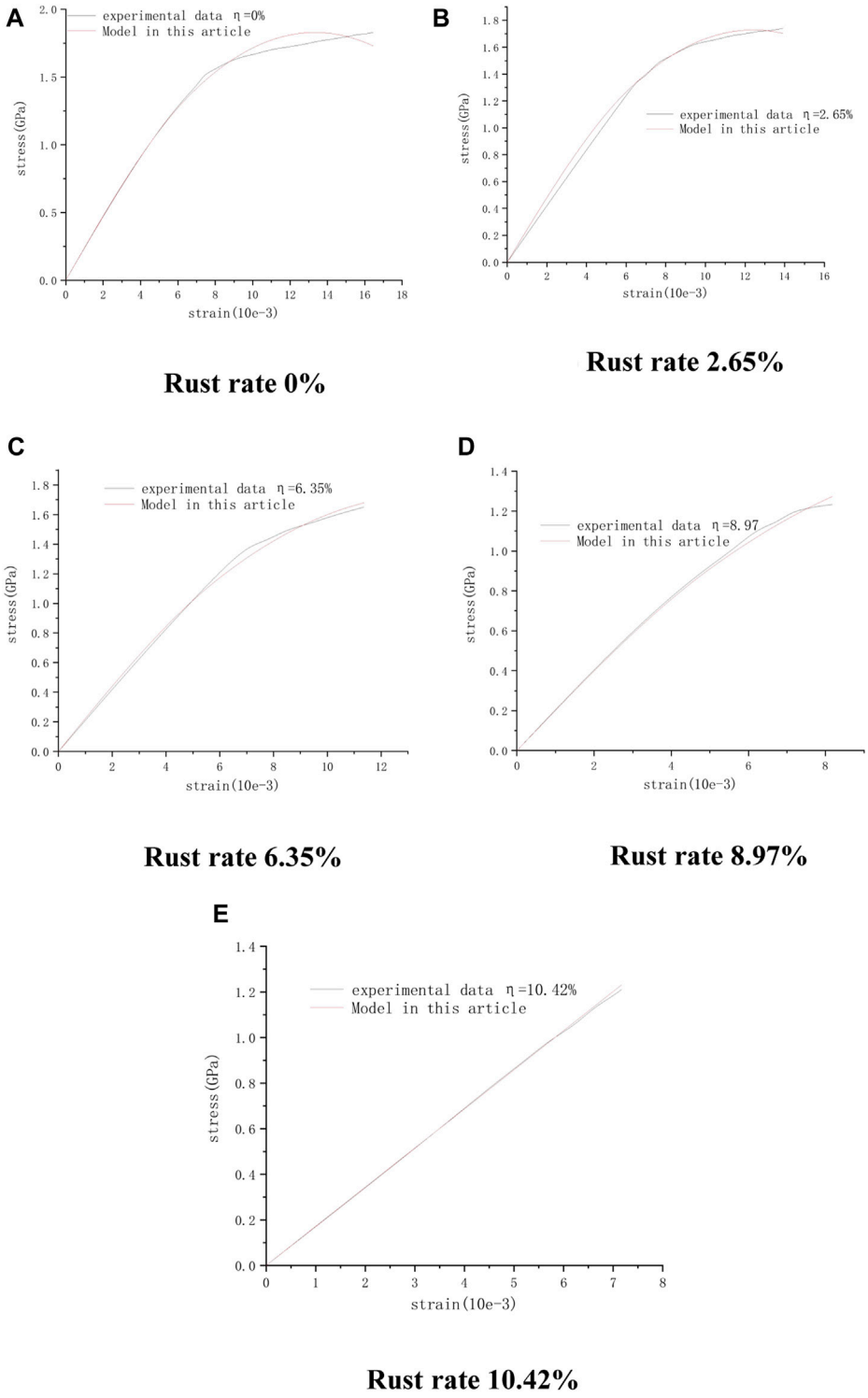

FIGURE 5
Comparison of model and test data.

After tensioning the anchor cable, there is a boundary condition of $P(x = 0) = P_{\text{Pretensioning}}$ at the junction of the free section and the anchor section, and there is a boundary condition of $P(x = l_r) = 0$ at the end of the anchor section. Therefore, the specific solution expression of the above equation is:

$$P(x) = \frac{P}{(1 - e^{2l_r N})} e^{xN} - \frac{Pe^{2l_r N}}{(1 - e^{2l_r N})} e^{-xN} \tag{25}$$

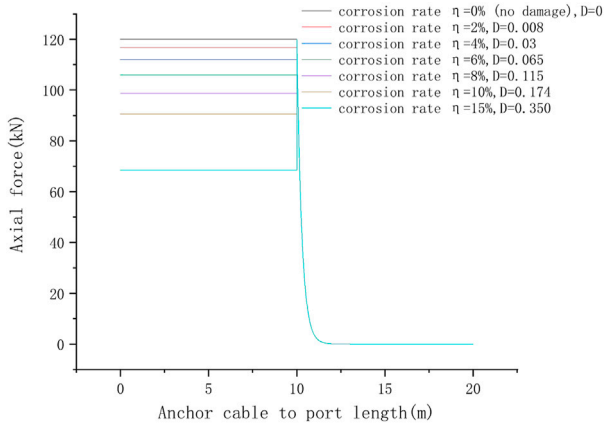

FIGURE 6
Distribution curve of axial stress of corroded/non corroded anchor cables along the length of the rod in the free section.

Considering the stress transfer characteristics of the free section of the anchor cable, the expression for the axial force distribution along the length of the anchor cable is shown in the following equation.

$$\begin{cases} P = P(x=0), \text{Free rusting section} \\ P(x) = \dfrac{P}{\left(1-e^{2l_rN}\right)}e^{xN} - \dfrac{Pe^{2l_rN}}{\left(1-e^{2l_rN}\right)}e^{-xN}, 0 < x \le l_r, \text{Anchoring section} \end{cases} \tag{26}$$

If the free section of the anchor cable is corroded during highway operation, the formula can be rewritten as follows:

$$\begin{cases} P(x=0) = P(1-D), \text{Free rusting section} \\ P(x) = \dfrac{P}{\left(1-e^{2l_rN}\right)}e^{xN} - \dfrac{Pe^{2l_rN}}{\left(1-e^{2l_rN}\right)}e^{-xN}, 0 < x \le l_r, \text{Anchoring section} \end{cases} \tag{27}$$

In addition to the decrease in the elastic modulus, the relative increase in the nominal diameter of the corroded reinforcement in the free section under the same strain also affects the force transmission performance of the anchor cable. The expression for the nominal diameter of the steel strand under corrosion is:

$$d_m = \sqrt{(n-1)\eta + 1d} \tag{28}$$

Where, n is the volume expansion rate of the corroded steel bar, and research shows that this value is usually 2–4. η is the reinforcement corrosion rate, calculated based on the weight loss of the reinforcement section. The expression can be seen from the previous formula, where n = 3 is taken (Xu et al., 2015).

Combining Eq. 28, Eq. 19, Eq. 27 can be rewritten as:

$$\begin{cases} P(x=0) = P(1-D)\dfrac{d}{d_m}, \text{Free rusting section} \\ P(x) = \dfrac{P}{\left(1-e^{2l_rN}\right)}e^{xN} - \dfrac{Pe^{2l_rN}}{\left(1-e^{2l_rN}\right)}e^{-xN}, 0 < x \le l_r, \text{Anchoring section} \end{cases} \tag{29}$$

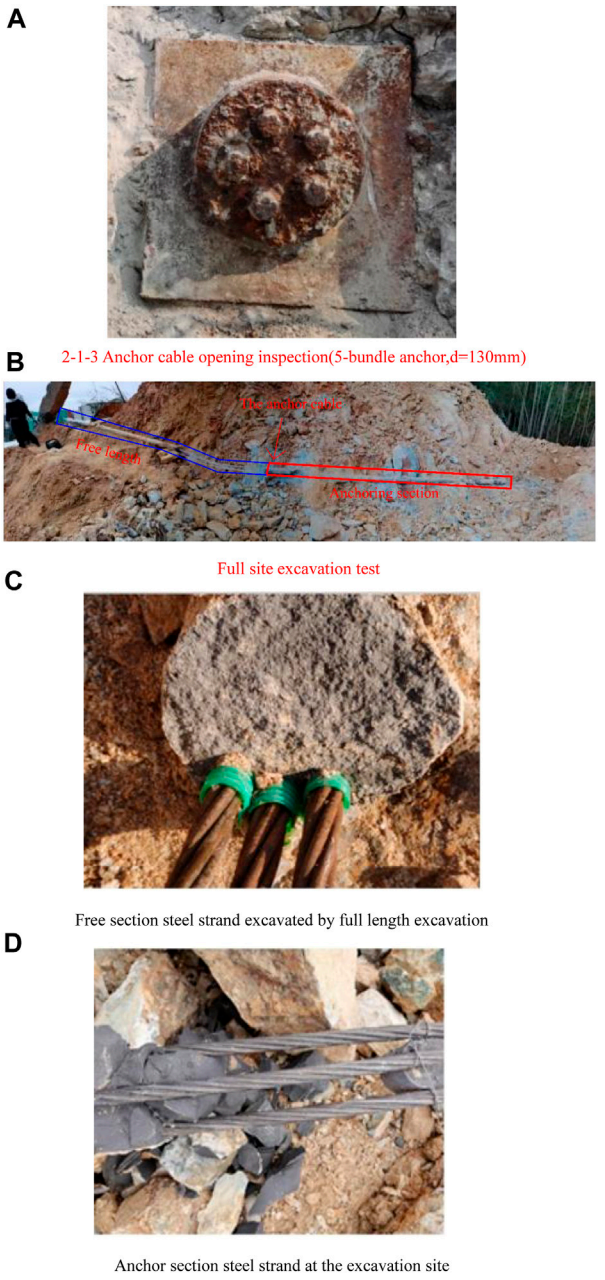

FIGURE 7
Photos of on-site inspection and excavation.

The combination of Eq. 29 and Eq. 14 can determine the distribution of axial stress in the corroded free section of the anchor cable along the length of the rod. The calculation results are shown in Figure 6.

As can be seen from Figure 5, there is a negative correlation between the corrosion rate of steel strands in the free section and the magnitude of the axial force in the free section. This is because under the influence of corrosion, the free segment steel strand is damaged, and a portion of the load-bearing microelement is damaged. On the macro level, it is reflected in the decrease in the elastic modulus of the steel strand, so that the axial force of the free segment is less than that of the non-corroded anchor segment under the same strain. The

TABLE 2 Test results of holding prestress of no. 2–one to three anchor cable.

Anchor rope number	Design anchoring force (kN)	Current holding force (kN)	Percentage of prestress held (%)	Loss of prestress ratio (%)
2-1–3	470	282	60	40

anchor cable provides tensile force by anchoring into the stratum with good engineering geological conditions, and acts on the potential sliding mass at the orifice to strengthen the engineering slope. Therefore, corrosion of the free section of the anchor cable means that the axial force at the orifice decreases, and the reinforcement effect of the anchor cable becomes poor, affecting the overall stability of the engineering slope.

4 Engineering verification and case analysis

During the operation period, the entire Shanwei Longgang section of the expressway - Shenhai Expressway needs to be reconstructed and expanded. In order to provide design basis for the designers of the reconstruction and expansion project, the author conducted anchor opening inspection, anchor cable holding force test, and full-length excavation test for No. 2-one to three anchor cables at the edge of the secondary slope that will be expanded and excavated on a fully to moderately weathered fused tuff slope (see Figure 7).

From Figure 7, it can be seen that the shallow free section of the anchor head (0~2 m along the depth of the anchor cable axis) has a relatively serious degree of corrosion. This is because the free section of the anchor cable is located in a soil like weathered layer, and is affected by environmental factors such as groundwater, surface water infiltration, and oxygen. In addition, the long grouting length of the free section makes it difficult to ensure that it is as dense as the anchor section, resulting in sufficient contact between the free section steel strand and water and air, resulting in corrosion.

During the construction period, the prestressed anchor cable is tensioned, and its prestress is provided by the frictional resistance between the anchor body and the stratum, and transmitted to the slope reaction structure (lattice beam) through the steel strand, which plays a role in strengthening the engineering slope. Fused tuff is hard rock, and relevant data shows that the rock is dense and hard (Bao, 1985), with a uniaxial saturated compressive strength of 68.8–241.4 MPa. The survey data of this section of expressway shows that the uniaxial saturated compressive strength of Ignimbrite is 76.9 MPa. The classification standard of engineering rock hardness is specified in the Standard for Classification of Engineering Rock Masses (Ministry of Water Resources of the Ministry of Water Resources of the People's Republic of China, 2014). The rocks on the slope of this study are typical hard rocks. When the anchor section is located in moderately weathered rock stratum, there is basically no rheological effect, which can provide a large anchoring force. However, after a certain service life, the free section anchor cable body is corroded, the force transmission performance is reduced, and the holding prestress of the anchor cable is reduced. In Guangdong region, four to six bundles of anchor cables are commonly used in highway slope engineering. In order to increase the active support force of soft rock highway slopes, 6 strands of anchor cables are usually used. For hard rock highway slopes, the tensioning pre-stress of four to five anchor cables can meet the design requirements, so more economical anchor cable specifications and sizes were selected in the design. Generally speaking, the diameter of four to five anchor cables is 130 mm, and the diameter of 6 anchor cables is 150 mm.

The authors determined that the corrosion rate of the free section steel strand was 13% by cutting the anchor cable at a distance of 0~2 m, cleaning and chemical composition analysis. The holding prestress test results of this anchor cable are shown in Table 2 below. In Table 2, the percentage of retained prestress refers to the percentage of retained prestress and design prestress value of the current anchor cable, while the prestress loss rate refers to the percentage of lost prestress and design prestress value of the anchor cable.

Considering the actual testing results, the corrosion of steel strands is mainly concentrated in the shallow free section of the orifice, so during the transfer of anchoring force to the ground, a sudden drop occurs near the free section of the orifice corrosion. Eq. 29 can be adjusted as follows:

$$\begin{cases} P = P(x=0)(1-D)\dfrac{d}{d_m} = P(x=0)\exp\left[-\left(\dfrac{\eta}{a}\right)^b\right]\dfrac{d}{d_m}, \text{Free rusting section} \\ P = P(x=0), \text{Free non corroded section} \\ P(x) = \dfrac{P}{\left(1-e^{2l_r N}\right)}e^{xN} - \dfrac{Pe^{2l_r N}}{\left(1-e^{2l_r N}\right)}e^{-xN}, 0 < x \le l_r \text{Anchoring section} \end{cases} \tag{30}$$

In order to verify the validity of the established model, the corrosion rate of the free section steel strand is 13% and substituted into the first formula in Eq. 30 Referring to relevant data, it is taken that $n = 3$ (Xu et al., 2015), and the steel strand is in the elastic state. From Table 3, a = 2, b = 3, and c = 4, it is calculated that the holding force of the anchor cable is 300.8 kN, the holding prestress ratio is 64%, and the loss prestress ratio is 36%. The calculated result of the derived expression is relatively close to the measured value, and the calculated result of holding prestress is

TABLE 3 Model parameters.

Corrosion rate/%	a/%	b	c_F	a_F
0	22.97	1.89	5.97	20.7
2.63	22.97	1.89	6.02	18.8
6.35	22.97	1.89	5.48	22.5
8.97	22.97	1.89	4.9	22.0
10.42	22.97	1.89	-	-

slightly greater than the measured value by 4%, which indicates that the derived expression has certain rationality. The reason for the slightly larger calculation result is that the calculation method in this article does not consider the loss of holding prestress caused by other factors (such as prestress loss caused by clamping pieces, prestress loss caused by sequential tensioning, *etc.*).

5 Conclusion

(1) Based on statistical damage mechanics, a tensile constitutive model of steel strand under the combined action of corrosion and force is established, and the validity of the model is verified. The model can accurately analyze the prestress loss of prestressed anchor cable in hard rock slope due to corrosion of free section.
(2) When corrosion occurs in the free section of the anchor cable, which leads to a decrease in the modulus and physical and mechanical parameters of the reinforcement, weakening the force transmission performance, and preventing the effective transmission of anchoring force to the reaction structure (grid beam) on the surface slope.
(3) Through the actual measurement of the highway reconstruction and expansion project, the results show that the predicted prestress bearing force of the calculation model is close to the actual data, which proves the validity and rationality of the calculation model. The overall stability evaluation of engineering slopes and landslides after treatment has important positive significance.

Data availability statement

The original contributions presented in the study are included in the article/Supplementary Material, further inquiries can be directed to the corresponding author.

Author contributions

Conceptualization: ZY; methodology: ZY and SC; software: BN and YX; validation: HL; Data curation: HL and QZ; writing—original draft preparation, ZY and SL; writing—review and editing: YY and QT. All authors contributed to the article and approved the submitted version.

Funding

This research was funded by Science and Technology Project of Hebei Education Department (QN2023060), and National Pre-research Funds of Hebei GEO University in 2023 (KY202305) and Funding for the Science and Technology Innovation Team Project of Hebei GEO University (KJCXTD-2021-08).

Conflict of interest

Authors ZY, BN, HL, QZ, QT, and SL were employed by Guangdong Huadu Transport Technology Co., Ltd. Author YX was employed by Guangdong Provincial Freeway Co., Ltd.

The remaining authors declare that the research was conducted in the absence of any commercial or financial relationships that could be construed as a potential conflict of interest.

Publisher's note

All claims expressed in this article are solely those of the authors and do not necessarily represent those of their affiliated organizations, or those of the publisher, the editors and the reviewers. Any product that may be evaluated in this article, or claim that may be made by its manufacturer, is not guaranteed or endorsed by the publisher.

References

Bao, Y. N. (1985). Structural characteristics and genetic significance of fused tuff with different occurrences in Zhejiang. *Zhejiang Land Resour.* (1), 15–24.

Chen, G., Chen, T., Chen, Y., Huang, R., and Liu, M. (2018a). A new method of predicting the prestress variations in anchored cables with excavation unloading destruction. *Eng. Geol.* 241, 109–120. doi:10.1016/j.enggeo.2018.05.015

Chen, S., Qiao, C., Ye, Q., and Khan, M. (2018b). Comparative study on three-dimensional statistical damage constitutive modified model of rock based on power function and Weibull distribution. *Environ. earth Sci.* 77 (3), 108. doi:10.1007/s12665-018-7297-6

Deng, D. P., Li, L., Zhao, L. H., and Liu, J. H. (2014). Prediction of the service life of prestressed anchor rods (cables) based on rust expansion cracking. *J. Geotechnical Eng.* 36 (8), 1464–1472. doi:10.11779/CJGE201408012

Fan, Q., Zhu, H., and Gen, J. (2015). Monitoring result analyses of high slope of five-step ship lock in the Three Gorges Project. *J. Rock Mech. Geotechnical Eng.* 7 (2), 199–206. doi:10.1016/j.jrmge.2015.02.007

Fu, G., Deo, R., Ji, J., and Kodikara, J. (2021). Failure assessment of reinforced rock slopes subjected to bolt corrosion considering correlated multiple failure modes. *Comput. Geotechnics* 132, 104029. doi:10.1016/j.compgeo.2021.104029

He, S. M., Wang, Q. C., and Luo, Y. (2010). The effect of steel strand corrosion on the load transfer characteristics of prestressed anchor cables. *J. Sichuan Univ. Eng. Sci. Ed.* 42 (1), 1–4. doi:10.15961/j.jsuese.2010.01.022

Jiang, S. H., Li, D. Q., Zhang, L. M., and Zhou, C. B. (2014). Time-dependent system reliability of anchored rock slopes considering rock bolt corrosion effect. *Eng. Geol.* 175, 1–8. doi:10.1016/j.enggeo.2014.03.011

Li, C., and Stillborg, B. (1999). Analytical models for rock bolts. *Int. J. Rock Mech. Min. Sci.* 36 (8), 1013–1029. doi:10.1016/S1365-1609(99)00064-7

Li, F. M., and Liu, Z. G. (2016). The effect of cable corrosion on the anchoring performance of anchor cable structures. *Chin. J. Highw. Eng.* 29 (2), 23–31. doi:10.19721/j.cnki.1001-7372.2016.02.004

Li, W., and Chen, W. H. (2022). Linear crack initiation analysis on rock surface under the combined action of sub-elevated temperature stress and fracture air-vapor pressure. *Theortical Appl. Fract. Mech.* 122, 103582. doi:10.1016/j.tafmec.2022.103582

Lin, C., Li, T., Zhao, L., Zhang, Z., Niu, Z., Liu, X., et al. (2020). Reinforcement effects and safety monitoring index for high steep slopes: A case study in China. *Eng. Geol.* 279, 105861. doi:10.1016/j.enggeo.2020.105861

Liu, X. S., Tan, Y. L., Ning, J. G., Lu, Y. W., Gu, Q. H., and Lu, Y. (2018). Mechanical properties and damage constitutive model of coal in coal-rock combined body. *Int. J. Rock Mech. Min. Sci.* 110, 140–150. doi:10.1016/j.ijrmms.2018.07.020

Luo, X. Y., and Li, Z. (2008). Study on the mechanical properties of unbonded prestressed steel strands after corrosion. *J. Railw.* 142 (02), 108–112. doi:10.3321/j.issn:1001-8360.2008.02.021

Ministry of Water Resources of the Ministry of Water Resources of the People's Republic of China (2014). *GB/T 50218-2014, standard for engineering rock mass classification. Ministry of housing and urban rural development of the Ministry of*

housing and urban-rural development. China: General Administration of Quality Supervision, Inspection and Quarantine of the China.

Shi, K., Wu, X., Liu, Z., and Dai, S. (2019). Coupled calculation model for anchoring force loss in a slope reinforced by a frame beam and anchor cables. *Eng. Geol.* 260 (3), 105245. doi:10.1016/j.enggeo.2019.105245

Wang, L. Q., Xiao, T., Liu, S. L., Zhang, W. G., Yang, B. B., and Chen, L. C. (2023a). Quantification of model uncertainty and variability for landslide displacement prediction based on Monte Carlo simulation. *Gondwana Res.*, doi:10.1016/j.gr.2023.03.006

Wang, Y., Cao, Z., Li, P., and Yi, X. (2023b). On the fracture and energy characteristics of granite containing circular cavity under variable frequency-amplitude fatigue loads. *Theor. Appl. Fract. Mech.* 125, 103872. doi:10.1016/j.tafmec.2023.103872

Wang, Y., Song, Z. Y., Mao, T. Q., and Zhu, C. (2022). Macro–meso fracture and instability behaviors of hollow-cylinder granite containing fissures subjected to freeze–thaw–fatigue loads. *Rock Mech. Rock Eng.* 55, 4051–4071. doi:10.1007/s00603-022-02860-5

Xu, G., Bao, H., Wang, Q., and Xu, L. L. (2015). Study on the volume expansion rate of steel corrosion in concrete structures. *J. Huazhong Univ. Sci. Technol. Nat. Sci. Ed.* 43 (9), 105–109. doi:10.13245/j.hust.150920

Yang, Z., Chen, S., Sun, J. L., Zheng, Y. B., Li, L. F., and Yuan, Y. (2022). Bar load-displacement curve model based on statistical damage mechanics. *Front. Earth Sci.* 10. doi:10.3389/feart.2022.1001777

Zheng, J., Zeng, H. H., and Zhu, B. Z. (2010). Experimental study on the influence of corrosion on the mechanical properties of anchor cable. *J. rock Mech. Eng.* 29 (12), 2469–2474.

frontiers | Frontiers in Materials

TYPE Original Research
PUBLISHED 04 August 2023
DOI 10.3389/fmats.2023.1242764

OPEN ACCESS

EDITED BY
Xianze Cui,
China Three Gorges University, China

REVIEWED BY
Zhiheng Zhao,
Petrochina Southwest Oil and Gas Field Company, China
Yanzhi Hu,
Chinese Academy of Sciences (CAS), China

*CORRESPONDENCE
Yu Wang,
wyzhou@ustb.edu.cn

RECEIVED 19 June 2023
ACCEPTED 20 July 2023
PUBLISHED 04 August 2023

CITATION
Zhang Y, Wu J, Tang P and Wang Y (2023), Three-dimensional laser scanning and numerical investigation on the influence of freeze-thaw and hang-wall mining on the instability of an open-pit slope. *Front. Mater.* 10:1242764. doi: 10.3389/fmats.2023.1242764

Three-dimensional laser scanning and numerical investigation on the influence of freeze-thaw and hang-wall mining on the instability of an open-pit slope

Yanfei Zhang[1], Jihuan Wu[1], Pufeng Tang[2] and Yu Wang[2]*

[1]Shenyang Center of Geological Survey, China Geological Survey, Shenyang, China, [2]Department of Civil Engineering, School of Civil and Resource Engineering, University of Science and Technology Beijing, Beijing, China

The instability of the open-pit slope and associated disasters of complex orebodies such as hanging-wall mining are the key problems to be solved urgently in the development of western resources. In this work, taking the hanging-wall mining in the open-pit mine of Hejing iron mine, for example, the disaster mechanism influenced by the coupling freeze-thaw and hanging-wall mining is systematically studied by 3D laser scanning and numerical simulation. Firstly, the rock mass structure information such as dip, dip angle, spacing, and equivalent trace length characteristics was obtained using 3D intelligent recognition technology. Then, numerical simulation is employed to reveal the influence of freeze-thaw and excavation sequences on the overall stability of the open-pit slope. The stress, displacement, plasticity zone, and maximum shear strain patterns are revealed in detail. The results show that the excavation engineering will lead to frequent increase and unloading of the internal stress of the rock mass, and the gradual increase of the goaf area will cause great damage to the rock mass. The slope failure mode is strongly impacted by freeze-thaw weathering and orebody excavation.

KEYWORDS

freeze-thaw weathering, 3D laser scanning, hang-wall mining, intelligent recognition, stability predication

1 Introduction

The exploration of mineral resources is advancing into cold regions currently. In the high cold and high-altitude regions, the rock mass is encountered with repeated freeze-thaw weathering, especially for the rock joints where frost-heaving forces increase aperture and length (Forte et al., 2021; Song et al., 2021; Wang et al., 2022; Fakhri et al., 2023; Xu et al., 2023). The communication of the rock joints would lead to the instability of the rock mass (Ghobadi and Babazadeh, 2015; Bai et al., 2019; Bai et al., 2021). In addition, strong excavation disturbance during orebody recovery also leads to damage accumulation (Shang, 2022; Wang et al., 2023a); damage and failure of the rock mass is accelerated for the rock subjected to the coupling freeze-thaw and disturbance conditions. As a result, it is important to investigate the structural deterioration mechanism for the rock mass in cold regions in order to ensure long-term stability during the rock mass construction.

In mining, underground engineering and related geotechnical engineering and the collection and identification of the rock mass structural plane information in cold regions are very important for the rock mass stability analysis. At present, many scholars have put forward a variety of methods for collecting the rock mass structural plane information, which is summarized as follows: fine line method, window method, drilling method, digital photogrammetry, GPS-RTK technology, 3D laser scanning, etc. (Battulwar et al., 2019; Huang et al., 2023). Among them, 3D laser scanning has a wide measurement range and can obtain large-scale structural plane information, and point cloud data information which has strong optimizability can be processed by multiple methods, and has high practicability to a certain extent. For example, Kocak et al. (1999) first surveyed the seafloor with 3D laser scanning technology. Slob et al. (2005) proposed a method of triangular mesh reconstruction of point cloud data and combined it with the fuzzy K-means method to group the rock mass structural planes. Tuckey and Stead (2016) proposed a new method to improve the efficiency and accuracy of three-dimensional laser scanning to map discontinuity persistence and intact rock bridges in rock slopes; the method was validated from several slope cases. Ge et al. (2012) thoroughly studied and optimized the method of 3D laser scanning technology measurement to obtain the appearance of a structural plane. Fekete and Diederichs (2010, 2013). employed 3D laser scanning technology to map rock joints for stability analysis of tunnels in blocky rock masses. In addition, the geotechnical and operational applications for 3-dimensional laser scanning were also extended to the drill holes. Maerz et al. (2013) proposed a simple method for the extraction of the rock joints from the Terrestrial LIDAR Data; the accuracy of the method was proved afterward. Gigli and Casagli (2011) proposed a semi-automatic extraction method to obtain the rock mass structure plane from high-resolution LIDAR point clouds. Lato and Vöge (2012) used cluster analysis techniques on the vector data from the rock mass to investigate joint information. Menegoni et al. (2019) used a remotely piloted aircraft system (RPAS) and digital photogrammetry to obtain the point cloud of an outcrop rock mass; they found that the 3D texturized digital outcrop model was effective to represent the discontinuity data. Battulwar et al. (2021) summarized the state-of-the-art of automated extraction of the rock mass discontinuity characteristics using 3D surface models; the strengths and drawbacks of each method of extracting rock joints were discussed. Zhang et al. (2018) presented a methodology for the automated extraction of rock discontinuities from a point cloud and the resulting 3D digital model of the rock mass. A sensitivity analysis was conducted to reveal the influencing factors of the extraction results. The rock mass structural plane information recognition and acquisition at the present stage have limitations; they are mainly restricted by technology and sampling equipment, cost, and complex terrain factors, such as difficulty in achieving more accurate information acquisition and characteristic point recognition. There is a deviation from the actual situation; it is necessary to further perfect and improve access to information technology and method to improve the accuracy of the rock mass structural plane information collection.

Slope stability is a key problem that cannot be ignored in mining engineering. Currently, quantification and qualitative analysis of slope stability have been realized (Wang et al., 2023a; Wang et al., 2023b; Chen et al., 2023). The qualitative analysis method can only have a preliminary estimate of the stability of the rock slope but cannot accurately analyze the stability of the slope. The numerical analysis method is widely used in slope stability analysis by applying advanced computer simulation technology to predict slope displacement trends. Some scholars have realized the influence analysis of rainfall, earthquake, blasting, and other factors on slope stability (Bai et al., 2021; Wang et al., 2022). For hanging-wall mining in an open-pit mine, the stability of an open-pit slope geometry but also the excavation disturbance and other engineering disturbance factors have been investigated. Liu and Zeng (2020) made a detailed summary of the mining methods of hanging-wall ore. Du (2013) used FLAC 3D numerical simulation software to analyze the distribution law of slope stress when mining the lower side of the joint filling mining method. However, at present, there are many kinds of methods to study the stability of rock mass in cold regions, but each has some shortcomings. The stability analysis of rock slopes in the Alpine region needs to consider a variety of factors. In addition to the engineering condition, the rock mass structural plane, freeze-thaw weathering, and other factors should also be considered. At the same time, there are few studies on special projects such as hanging wall mining in the Alpine region.

In this work, the influencing factors of freeze-thaw and excavation disturbance were considered to reveal the instability mechanism of an open-pit slope in Hejing County, Xinjiang province. Firstly, 3D laser scanning technology was used to extract the rock mass structural plane and get the geometric information, including orientation, spacing, and consistency. Secondly, numerical simulators were employed to establish the geometrical model, and the generalized Hoek-Brown criterion and Bardon-Bandis criterion were introduced to represent the stress condition during freeze-thaw treatment and excavation. The patterns of stress, displacement, shear strain, and plasticity zone that were influenced by the freeze-thaw weathering and excavation disturbance were discussed.

2 Research methods

2.1 Engineering background

At present, the open-pit and hanging-wall mining schemes are adopted in the Hejing Iron Mine. The height of the open pit step is 12 m, the height of the section step is 24 or 36 m, and the peel elevation is 3464 ~ 3596 m. At present, the level of the open-pit mining has reached 3390 m level, and the open-pit step above the level of 3,476 m has been completed. The final limit of the open-pit mining is an oval stope, with a length of 593 m from east to west and a width of 385 m from north to south. The highest mining elevation of the limit is 3,680 m, the elevation of the sealing ring is 3,428 m, and the mining height is approximately 290 m. Currently, the remaining open-pit limit mining volume is 3.78 million t. According to the mine production plan, the open-pit mine can continue to produce for 4 years, and the production scale is between 580,000 and 1.4 million t/a. The mining scope of this design is the hang-wall ore body between 3,380 and 3,536 m

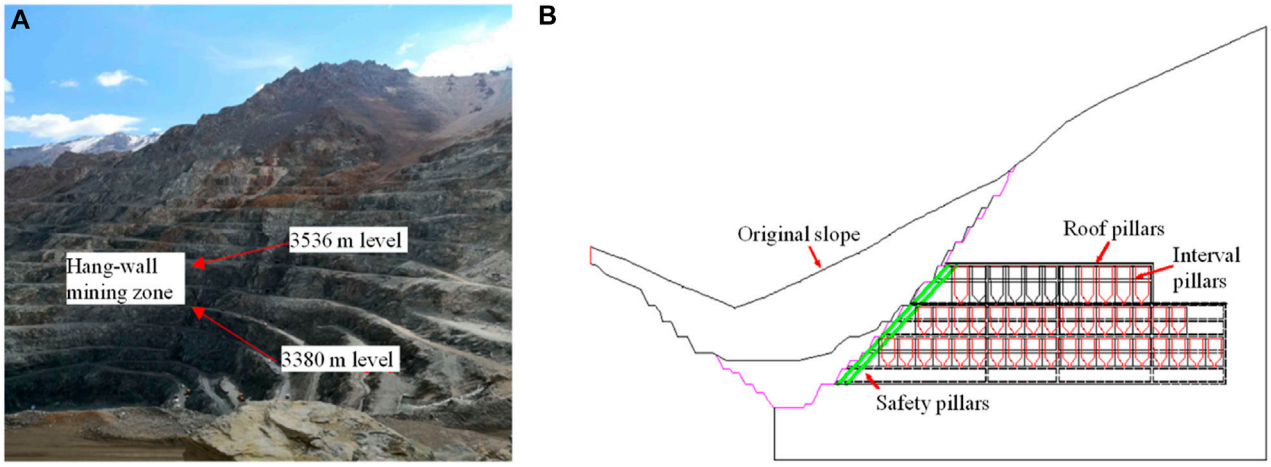

FIGURE 1
The hang-wall mining of the Beizhan iron mine. **(A)** The full view of the open pit slope; **(B)** The hang-wall mining method.

TABLE 1 Main parameters of Polaris LR 3D laser scanner.

Parameter	Index
Maximum distance (m)	2000
Minimum distance (m)	1.5
Scan the field Angle (°)	360 × 120
Ranging principle	Pulse
Laser head rotation mechanism	Swing-in-mirror
Operating temperature (°C)	−20~50
Maximum point speed (n/s)	500,000
Wavelength (nm)	1,550
Beam diameter	36 mm @ 100 m; 20 mm @ 50 m

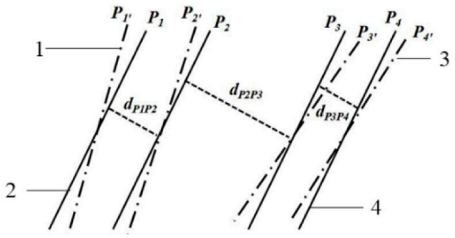

1- The first group of the structural plane's natural state;
2- The first set of the structural plane's ideals;
3- The second group of the structural plane's natural state;
4- The second set of the structural plane's ideals.

FIGURE 2
Schematic diagram of transformation and spacing calculation of the same group of structural planes.

at the east of the open pit. Figure 1 shows the current mining status of the open-pit mine and the actual scope of hanging-wall mining.

2.2 Structural plane extraction algorithm

In this paper, the Optech Polaris LR 3D laser scanner was used to scan the open-pit slope of an iron mine. The main technical parameters are shown in Table 1. The collected information is the point cloud data of the eastern rock slope, which contains 581,623 points in total. The scanning range is 3636.6565 m^2, and the maximum size of the scanning area is 30.3549 m × 149.1210 m × 26.0951 m. Massive point cloud data of rock outcrops are obtained, which mainly contain three-dimensional coordinates and gray-level information of each point in the point cloud. The spatial geometric coordinates are mainly used to extract the rock mass structural plane information, and the gray level information can be used to verify the scanning results.

Before extracting structural plane information, point cloud data should be preprocessed. Firstly, the 3D image difference method is used to grid the point cloud data to improve the calculation speed. Then, the same structural plane of the point cloud data can be recognized by discriminating whether the plane normal vector fitted by the adjacent lattice is the same or not based on the eigenvector. Then, the traversal method is used to detect the flatness of the point cloud data. Finally, the optimal threshold is selected to improve the recognition effect of the structural plane and obtain accurate structural plane information.

The least square method is used for linear fitting to obtain the occurrence information of the structural plane, assuming that the coordinates of each point on the plane are (x_1,y_1,z_1), (x_2,y_2,z_2),. . ., (x_n,y_n,z_n). Then the matrix form is shown in Eq. 1:

$$\begin{bmatrix} x_1 & y_1 & 1 \\ x_2 & y_2 & 1 \\ \vdots & \vdots & \vdots \\ x_n & y_n & 1 \end{bmatrix} \begin{bmatrix} a \\ b \\ c \end{bmatrix} = \begin{bmatrix} z_1 \\ z_2 \\ \vdots \\ z_n \end{bmatrix} \tag{1}$$

order

$$A = \begin{bmatrix} a \\ b \\ c \end{bmatrix} \tag{2}$$

TABLE 2 Parameter values of each part of the rock mass.

Terrane	Unit weight (kg/m^3)	Elasticity modulus (GPa)	Poisson's ratio	Generalized Hawker Brown parameter			
				σ_c (MPa)	*GSI*	m_i	*D*
Overburden strata	2,590	22.5	0.22	67.53	76	20	1
Ore body	2,480	34.2	0.16	96.80	76	25	1
Wall rock	2,560	29.2	0.23	86.73	76	22	1
Underlying strata	2,680	25.6	0.17	82.78	76	22	1
Surface level	2,390	12.3	0.22	58.65	76	15	1

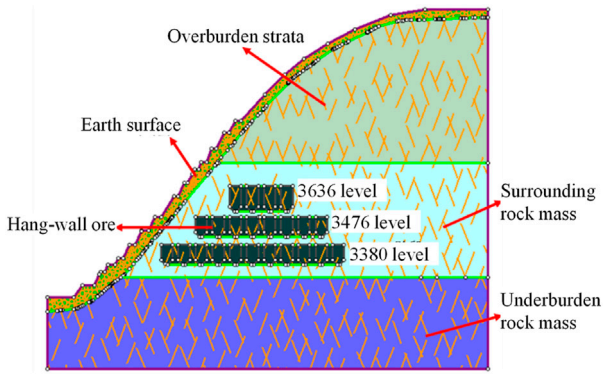

FIGURE 3
The calculation model of hanging-wall mining in an open-pit mine.

$$x = \begin{bmatrix} x_1 & y_1 & 1 \\ x_2 & y_2 & 1 \\ \vdots & \vdots & \vdots \\ x_n & y_n & 1 \end{bmatrix} \tag{3}$$

$$z = \begin{bmatrix} z_1 \\ z_2 \\ \vdots \\ z_n \end{bmatrix} \tag{4}$$

Vector A is obtained by fitting, and $\varphi(A) = \|Ax - z\|$ is minimized, that is, the plane equation of the structural plane is obtained by fitting.

Assume that the normal vector of the rock mass structural plane is (a, b, c), where c > 0 (only a well-exposed surface can be scanned). According to the formula, the inclination α and inclination β of the rock mass structural plane in the geodetic coordinate system can be obtained, as shown in Eq. 5:

$$\left.\begin{array}{l} \beta = arccos(c) \\ if\ a \geq 0, b \geq 0, \alpha = arcsin(a/\sin\beta) \\ if\ a < 0, b > 0, \alpha = 360 - arcsin(-a/\sin\beta) \\ if\ a < 0, b < 0, \alpha = 180 - arcsin(a/\sin\beta) \\ if\ a > 0, b < 0, \alpha = 180 + arcsin(-a/\sin\beta) \end{array}\right\} \tag{5}$$

In view of the grouping of structural planes, the K-means clustering analysis method is used to identify three groups of steep dip joints. For the plane, it can be regarded as a deterministic structural plane, and the corresponding geometric parameters of the plane can be determined mainly through manual identification or field investigation. Secondly, the sample is preset as the initial cluster center, and the value of the cluster center is calculated after the sample is classified into the cluster center. After repeated calculations, all the sample points are classified into the cluster center. Finally, the value of the cyclic sample points classified to the cluster center does not change. Combined with the site geological survey information, the average occurrence of the three groups of structural planes is

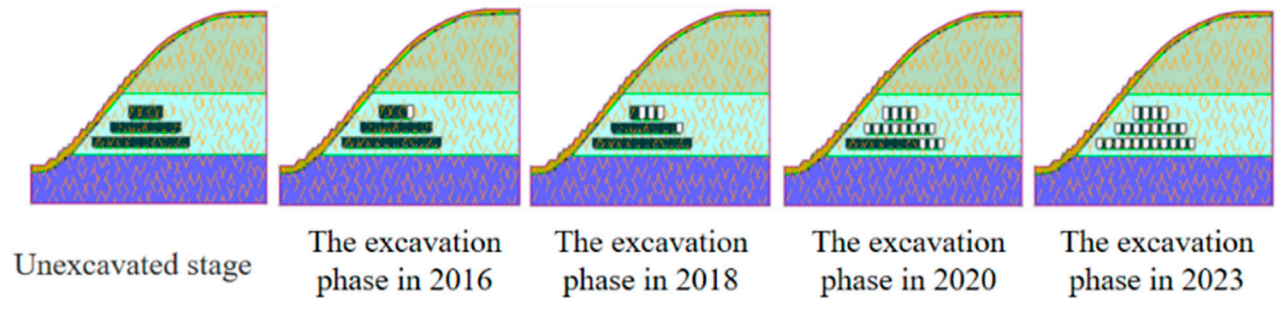

FIGURE 4
Schematic diagram of hanging wall mine excavation model at different stages.

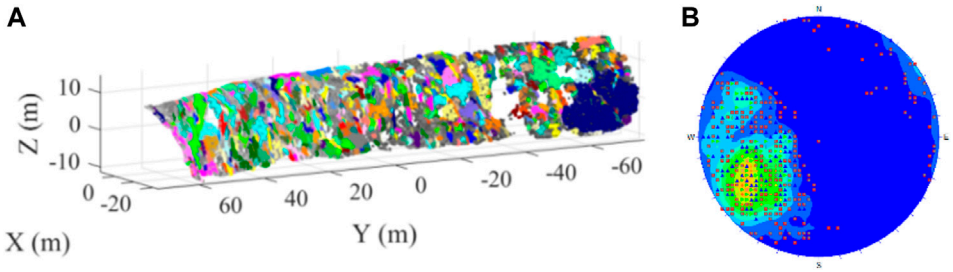

FIGURE 5
The identified rock mass structural plane. **(A)** Structural plane distribution characteristics; **(B)** The result of the equatorial projection.

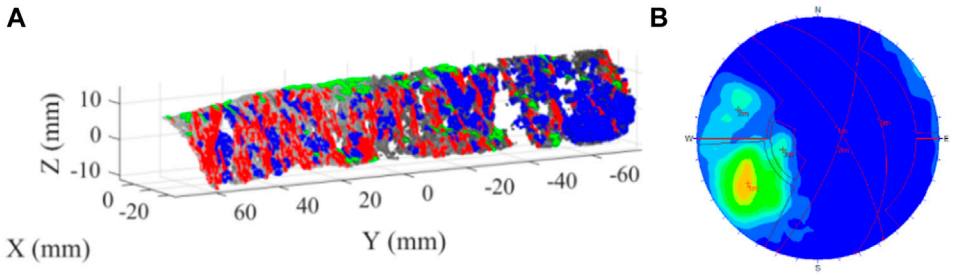

FIGURE 6
Distribution of classified rock mass structural planes. **(A)** Occurrence and distribution characteristics; **(B)** The result of the equatorial projection.

TABLE 3 Mathematical statistics of structural planes of different types of rock masses.

Parameter	Distribution type	Statistical parameter		Group
Dip (°)	Probabilistic experience	Average	237.000	Rock structure: Group 1
Dip angle (°)	Probabilistic experience	Average	69.000	
Distance (m)	Negative exponential distribution	Average	0.223	
Equivalent trace length (m)	Negative exponential distribution	Average	0.688	
Dip (°)	Probabilistic experience	Average	290.000	Rock structure: Group 2
Dip angle (°)	Probabilistic experience	Average	69.000	
Distance (m)	Negative exponential distribution	Average	0.699	
Equivalent trace length (m)	Negative exponential distribution	Average	1.140	
Dip (°)	Probabilistic experience	Average	251.000	Rock structure: Group 3
Dip angle (°)	Probabilistic experience	Average	33.000	
Distance (m)	Negative exponential distribution	Average	0.481	
Equivalent trace length (m)	Negative exponential distribution	Average	0.784	

calculated by the coordinate information of each point and the classification situation.

According to the spacing between structural planes, the same set of structural planes is first transformed into ideal structural planes, as shown in Figure 2. The normal vectors of the two planes before and after the transformation are consistent with the average normal vector.

The distance between adjacent structural planes can be calculated by combining the formula in Eq. 6 with the vertical distance between two parallel planes.

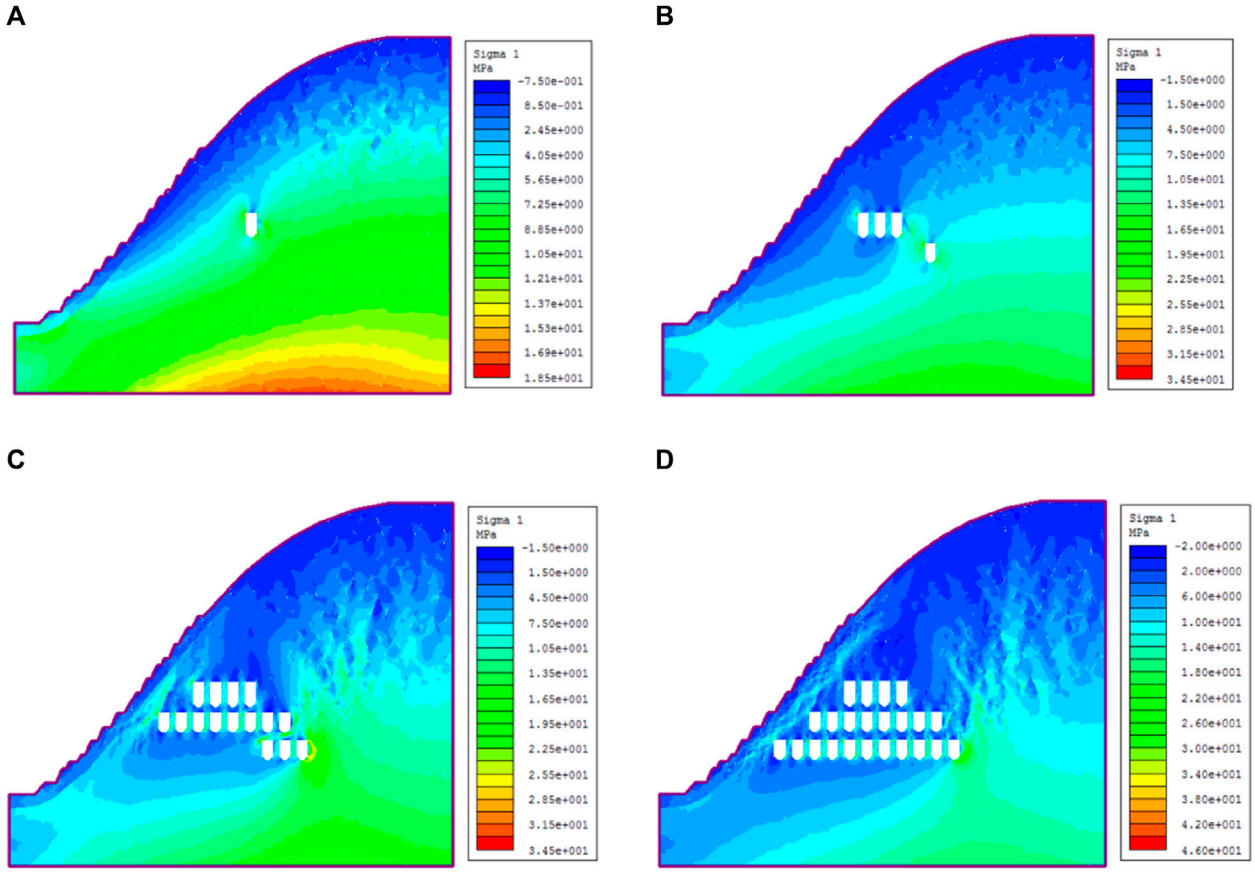

FIGURE 7
The maximum principal stress nephogram of models at different excavation stages. **(A)** The excavation stage in 2016. **(B)** The excavation stage in 2018. **(C)** The excavation stage in 2020. **(D)** The excavation stage in 2023.

$$P_1\colon Ax + By + Cz + D_1 = 0$$
$$P_2\colon Ax + By + Cz + D_2 = 0 \tag{6}$$
$$d_{p_1p_2} = \frac{|D_1 - D_2|}{\sqrt{A^2 + B^2 + C^2}}$$

Where: $\boldsymbol{P_1}$ and $\boldsymbol{P_2}$ are equations of planes 1 and 2, respectively; $\boldsymbol{d_{p1p2}}$ is the vertical distance of ***P1*** and ***P2***.

According to the equivalent trace length of the structural plane, each point of the structural plane is projected to the xoy plane according to the coordinate system; the area of the projection area **S**xoy is obtained, and the area $\boldsymbol{S}$ of the structural plane is obtained according to the projection relation:

$$S = S_{xoy} \Big/ \cos\gamma \tag{7}$$

In order to simplify the calculation, the equivalent circle with an equal area was used to represent the structural plane, and the radius of the equivalent circle $\boldsymbol{r}$ is shown in Eq. 8:

$$S = \pi r^2 \tag{8}$$

The equivalent trace length information of the structural plane is represented by the equivalent circle radius.

For roughness, the fractal dimension D is obtained by using the overlying box method based on the fractal theory. For the rock mass structural plane, taking the 3D geometric model as an example, it is assumed that the side length of the square box is δ, the total number of boxes is $N(\delta)$, and the box covers the profile line. The existence relationship is shown in Eq. 9:

$$N(\delta) \sim \delta^{-D} \tag{9}$$

Where, the fractal dimension D is obtained by fitting Eq. 10:

$$D = \lim_{\delta \longrightarrow 0} \frac{lg\,N(\delta)}{-lg(\delta)} \tag{10}$$

2.3 The establishment of the numerical calculation model

At present, the generalized Hoek-Brown criterion is widely used in the study of slope stability. This criterion introduces disturbance factors D based on the original formula, and

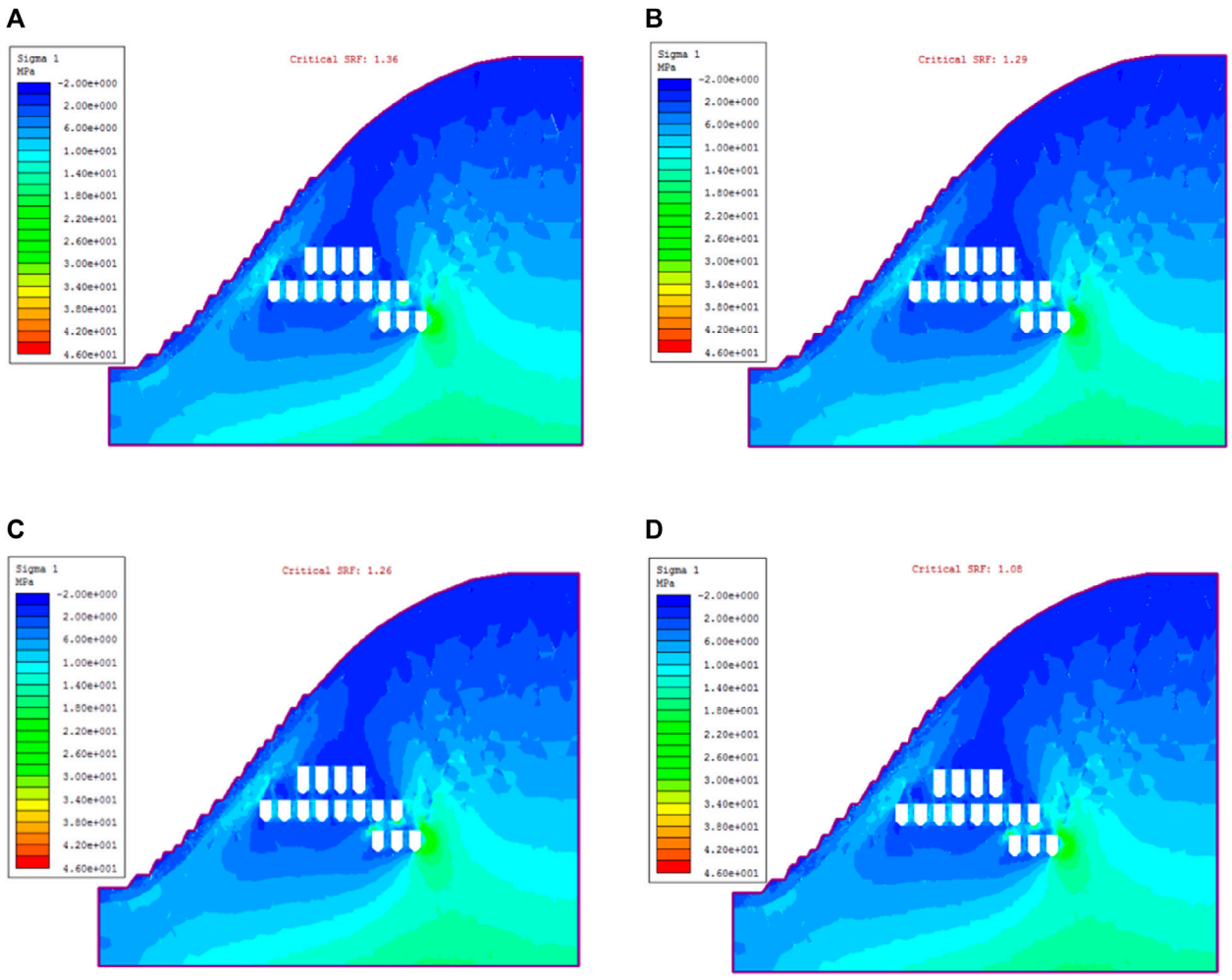

FIGURE 8
Maximum principal stress contour of the model under different freeze-thaw cycles. **(A)** Freeze-thawing 0 cycle. **(B)** Freeze-thawing 30 cycles. **(C)** Freeze-thawing 50 cycles. **(D)** Freeze-thawing 100 cycles.

comprehensively considers the characteristics of the structural plane so as to calculate the rock mass quality more accurately based on the geological strength index (*GSI*). The formula is shown in Eq. 11:

$$\left.\begin{aligned} \sigma_1 &= \sigma_3 + \sigma_c\left(m_b\frac{\sigma_3}{\sigma_c} + s\right)^a \\ m_b &= exp\left(\frac{GSI-100}{28-14D}\right)m_i \\ s &= exp\left(\frac{GSI-100}{9-3D}\right) \\ a &= \frac{1}{2} + \frac{1}{6}\left[exp\left(-\frac{GSI}{15}\right) - exp\left(-\frac{20}{3}\right)\right] \end{aligned}\right\} \tag{11}$$

Where m_i is the empirical parameter of the intact rock; D is the rock mass disturbance coefficient; GSI is the geological strength parameter of the rock mass; The value m_b, s, a is calculated after the assignment, which symbolizes the quality characteristics of the rock mass.

According to the laboratory rock mechanics test data and the Hoek-Brown parameter value method above, and comprehensively considering the mining environment and geological conditions, the final parameter values of each part of the rock mass are shown in Table 2.

Barton proposed the nonlinear JRC-JCS empirical formula, which can be widely used to calculate the shear strength of structural surfaces with rough surfaces and no filling[10]. The formula is shown in Eq. 12:

$$\tau = \sigma_n tan\left[\varphi_b + JRC\ lg\left(\frac{JCS}{\sigma_n}\right)\right] \tag{12}$$

Where τ is the shear strength of the joint; σ_n is the joint normal stress acting on the rock mass structural plane; φ_b is the basic friction angle of the rock joint plane; JRC is the joint roughness coefficient; JCS is the joint compression strength.

The value JRC can be used to quantitatively analyze the roughness of rock joint surface and the value can be taken according to the typical joint roughness map[11].

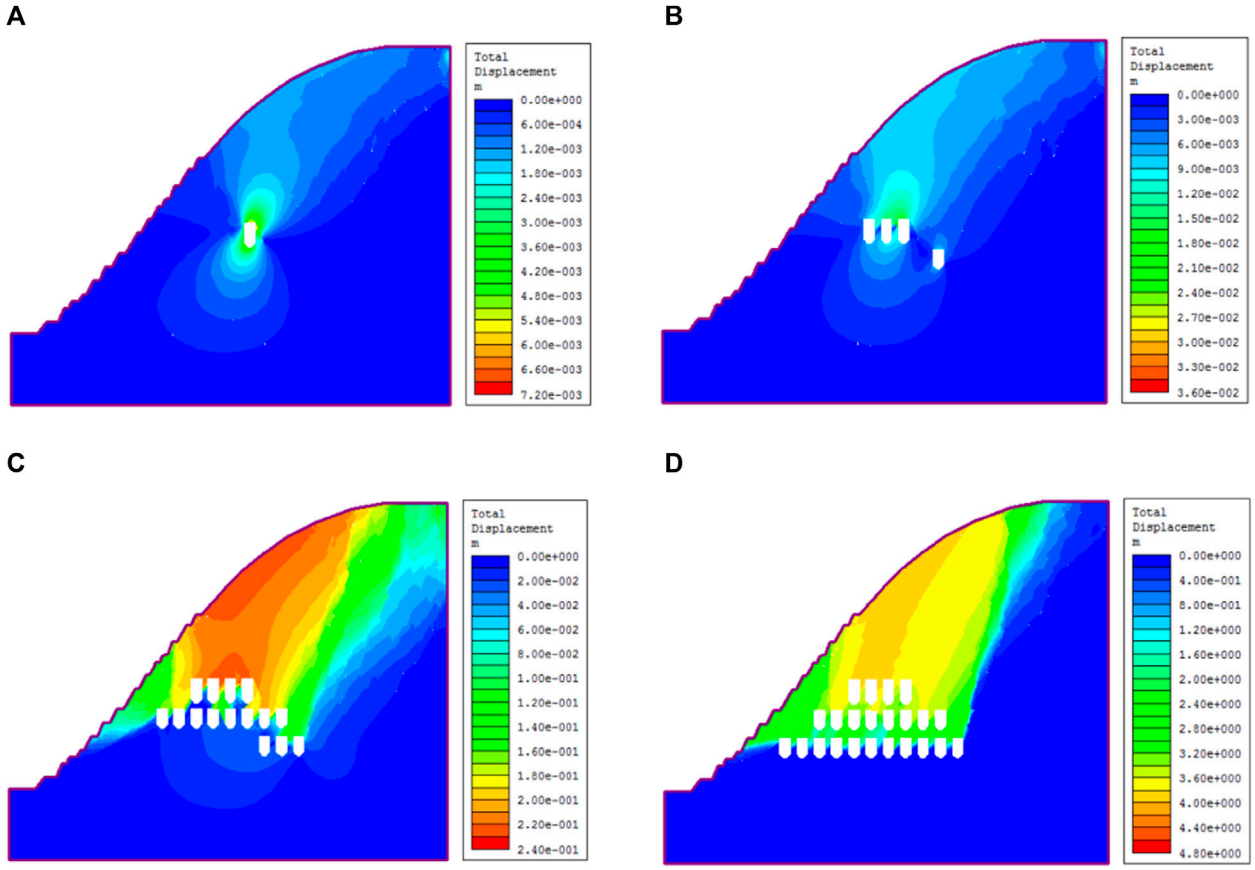

FIGURE 9
Total displacement contour for the slope at different excavation stages. **(A)** The excavation stage in 2016. **(B)** The excavation stage in 2018. **(C)** The excavation stage in 2020. **(D)** The excavation stage in 2023.

The value *JCS* reflects the compressive strength of joints, which is judged according to whether the rock mass is weathered. When the weathering degree of the rock mass is serious, the compressive strength value range is approximately 25% of the uniaxial compressive strength.

The basic friction angle of the rock joint surface φ_b can usually be measured by the shear strength measuring instrument, and the value range of the basic internal friction angle of weathered rock surface is usually between 25° and 35°, which the internal friction angle can be obtained according to the existing literature[12].

Based on the original outer boundary and excavation area boundary of the Hejing iron mine in Xinjiang, the model boundary, excavation area, and other elements of the model were automatically generated by importing the DXF file from AutoCAD by modifying lines and changing layer names. According to the above data of the laboratory rock test, three-dimensional laser scanning intelligent identification, and site survey report, combined with the actual situation of the site, the rock mass in different areas and the material in different areas are respectively assigned values. The finite element mesh with a three-node triangle as the basic element is automatically generated to limit the hinge supports in the X direction on both sides of the model, and the hinge supports the *X* and *Y* directions at the bottom of the model, thereby removing the slope restrictions. The final model is shown in Figure 3.

It can be seen from the engineering background that the scheme of open-pit mining and hanging-wall mining is adopted at the same time, and hanging-wall mining is a backoff mining along the strike from the west to the east. In view of the representative stages in the overall hanging-wall mining project, the correlation analysis is carried out, and the variation range of the stages is considered. The horizontal mining progress is taken as the division node, and the comparative analysis is made on the 16-year excavation stage, 18-year excavation stage, 20-year excavation stage, and 23-year excavation stage. Figure 4 shows the schematic diagram of the hanging-wall mine excavation model in different stages.

3 Intelligent recognition and extraction of rock joints

Based on the point cloud data of the rock slope, the method of point cloud information extraction and intelligent identification of the rock mass structural plane is used to obtain the distribution law of the occurrence, spacing, and trace length of the rock mass structural plane by using mathematical statistics theory. The intelligent identification of the rock mass structural plane and its distribution are shown in Figures 5, 6, and the parameters are shown in Table 3.

Combined with the occurrence information of the structural plane, according to the probability distribution model of the geometric parameters of the rock mass structural plane, the statistical characteristic parameters can be calculated accordingly. The volume density of the rock mass

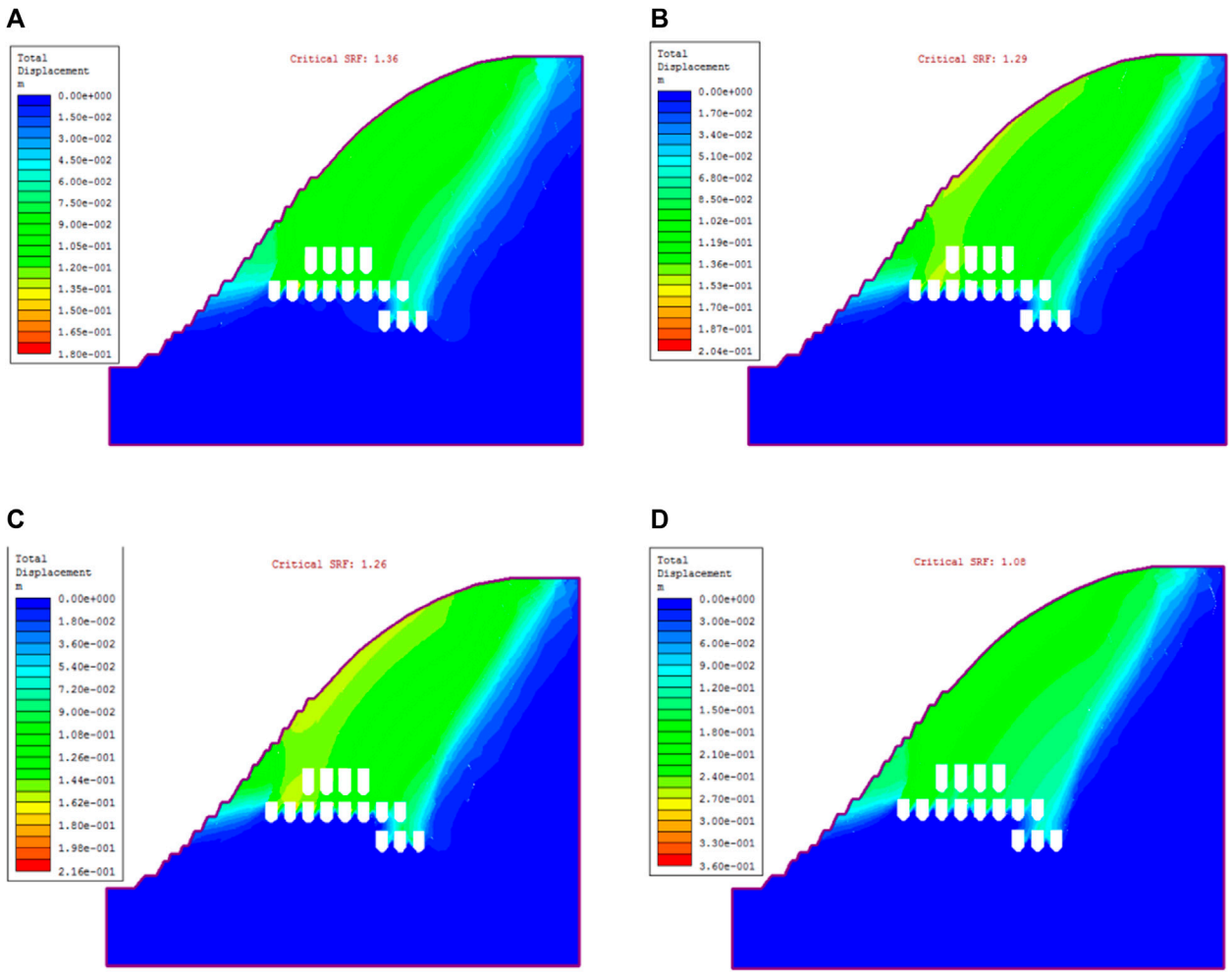

FIGURE 10
Total displacement contour of the model under different freeze-thaw cycles. **(A)** Freeze-thawing 0 cycles. **(B)** Freeze-thawing 30 cycles. **(C)** Freeze-thawing 50 cycles. **(D)** Freeze-thawing 100 cycles.

structural plane can be obtained by the distance information of the rock mass structural plane measured on-site. Finally, it was determined that the average occurrence of the three groups of the rock mass structural planes at different stations of the open-pit slope were 237° < 69°, 290° < 70°, and 252° < 34°; the average spacing was 0.223, 0.699, and 0.481; and the equivalent trace length was 0.688, 1.140, and 0.784, respectively. The roughness (fractal dimension) was 2.857, 2.862, and 2.847; and the joint number per unit area was 0.111, 0.034, and 0.020, respectively.

4 Numerical analysis of slope instability

4.1 Stress pattern impacted by freeze-thaw and excavation

It is very important to analyze the change in the slope model at different excavation periods for the overall mining layout and disaster prediction. According to the current excavation state of the hanging-wall mine, the rock stability analysis considering freeze-thaw factors is carried out by virtue of the deterioration characteristics and failure evolution process of freeze-thaw rock.

In view of the characteristics of maximum principal stress, as shown in Figures 7, 8, overall, the excavation results in the redistribution of *in-situ* stress of rock mass engineering. The unloading effect results in the expose of ore room at the bottom of top area. Large stress change occurs at the pillar and mine roof after the mining activities. Under the condition of freeze-thaw, these areas have little correlation with the number of freeze-thaw. Under the same excavation condition, the variation of slope stress with different numbers of freeze-thaw is very small, and the maximum principal stress is still concentrated around the ore house and pillar area. Freeze-thaw has no obvious influence on the distribution of rock mass stress.

4.2 Displacement pattern impacted by freeze-thaw and excavation

On displacement characteristics, as shown in Figures 9, 10, overall, with excavation area increases, the total displacement change area

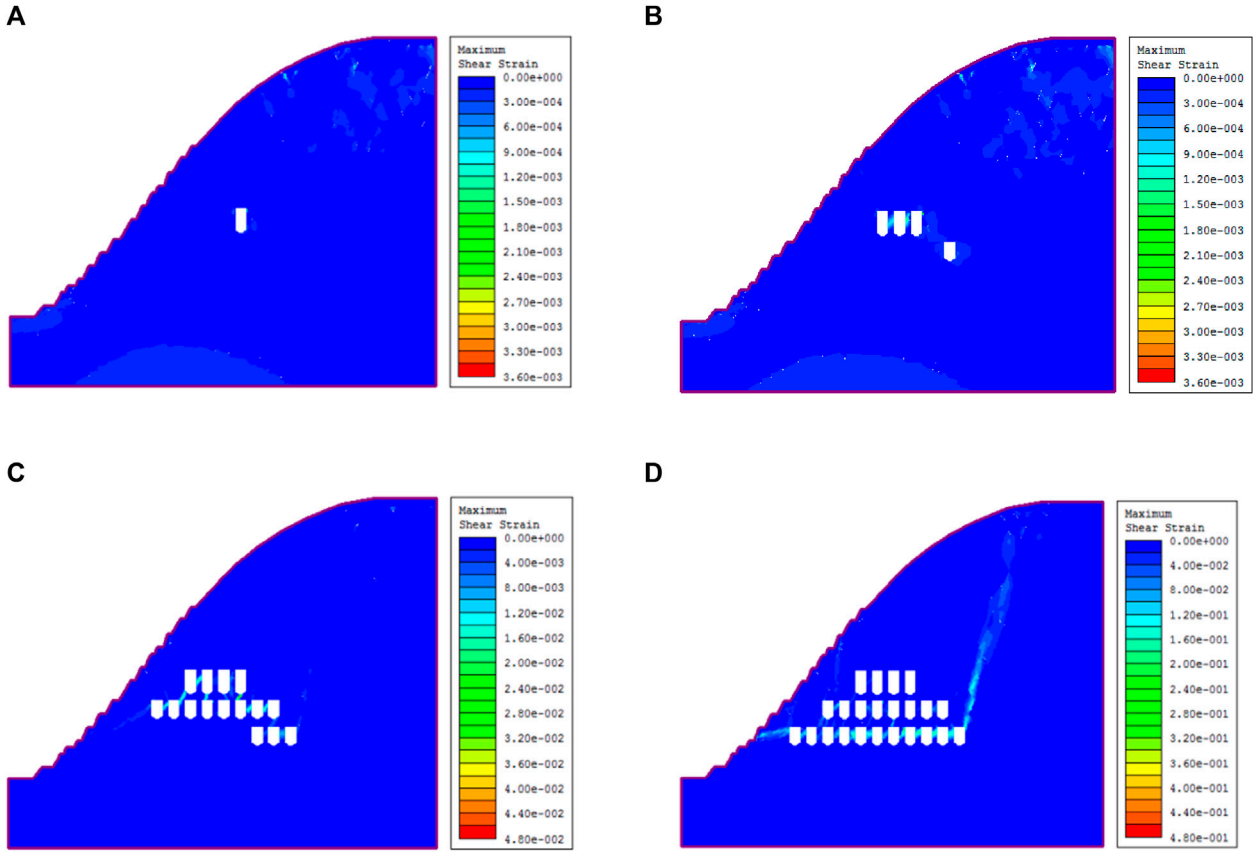

FIGURE 11
Maximum shear strain nephogram of models at different excavation stages. **(A)** The excavation stage in 2016. **(B)** The excavation stage in 2018. **(C)** The excavation stage in 2020. **(D)** The excavation stage in 2023.

gradually expanded, increasing the largest displacement; displacement of the overall trend is consistent with the stress changes, showing that stress changes are the root cause of the engineering rock mass deformation and failure. Stress change trends decided to cause rock mass deformation and failure patterns Treatment measures should be taken at the excavation stage when displacement changes greatly. In the case of freeze-thaw, the trend in the total displacement increases with the increase in the number of freeze-thaw, and the maximum displacement area expands with the increase in the number of freeze-thaw and gradually shifts to the interior of the slope. The displacements after 30 times of freezing and thawing and 50 times of freezing and thawing are almost the same, which are 204 and 216 mm, respectively. This also indicates that a small increase in the freezing and thawing has a small impact on rock mass failure and slope stability. After 100 times of freezing and thawing, the total displacements of rock mass increase sharply to 360 mm. It indicates that the slope has great displacement changes and the accumulation of freeze-thaw damage has caused the rock mass instability and failure.

4.3 Maximum shear strain pattern impacted by freeze-thaw and excavation

In view of the characteristics of shear strain, as shown in Figures 11, 12, overall, with the deepening of the excavation process and change in regional shear extension, shear strain continues to increase. In addition to this, the chamber surrounding the rock and joint junction appears to have a larger shear strain; the shear strain area in different levels and the relative position of two ore rooms also caused shear failure to happen The shear strain is larger than that of the same horizontal chamber. It is worth noting that a large shear strain occurred along the diagonal direction in the rightmost chamber at the 3,380 m mining stage, which was due to the increase in the horizontal mining stage and the continuous expansion of joints in coalescing, forming a large shear strain area. Prevention and control should be focused on the above areas. In the case of freeze-thaw, the increase in freeze-thaw times does not change the shear strain of rock mass. Maximum shear strain concentration on reservation pillar areas, and with the increasing number of freezing and thawing, while the maximum shear strain did not change, but increased shear strain zone area, slope site in a small amount of shear deformation; the reason of this phenomenon is the slope degradation caused by the freeze-thaw action. As the freeze-thaw action increases gradually, the freeze-thaw damage extends to the rock mass. As a result, the joints and fractures are damaged, the overall shear strain increases greatly, and the rock mass will fail along the new shear plane, which is consistent with the change in displacement.

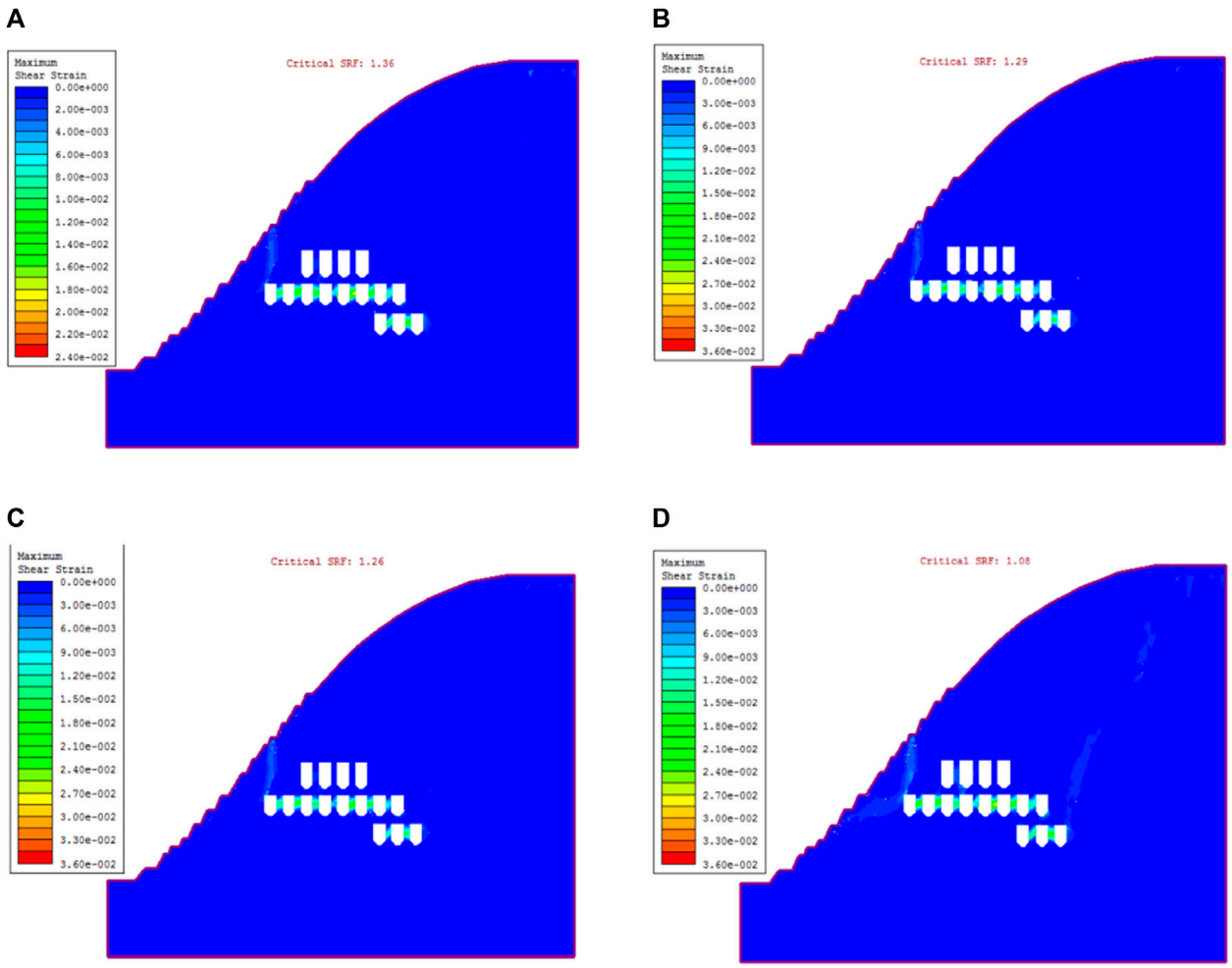

FIGURE 12
Shear strain nephogram of the model under different freeze-thaw times. **(A)** Freeze-thawing 0 cycle. **(B)** Freeze-thawing 30 cycles. **(C)** Freeze-thawing 50 cycles. **(D)** Freeze-thawing 100 cycles.

For the yield rock unit and joint unit characteristics, as shown in Figures 13, 14, rock mass begins to yield and is mainly concentrated at the top of the slope rock mass, with the increase in the excavation stage. The yield unit and joint increases; along the ore mining area, the yield unit with plenty of expansion joints occur and gradually increases, resulting in damage to the slope stability. In the last stage, the yield unit observation shows that the tensile failure is mainly concentrated in the bottom of the roof, while the shear failure is mainly concentrated in the retaining pillar area. Under freeze-thaw conditions, both the yield joints and yield rock units continue to expand with an increase in the number of freeze-thaw cycles. They gradually extend from the original area up to the lower part, and the main concentration area is still in the shallow part of the rock slope, indicating that the damage and deterioration of rock mass caused by freeze-thaw is mainly concentrated in the surface of the slope. The yield joint and element of the slope reach the maximum after 100 freezing and thawing cycles, and the yield element and joint of the slope are connected with the excavation area. The freeze-thawing damage is from the surface to the inside, which aggravates the deformation and failure of the excavation area, and the rock mass is unstable.

According to the characteristics of slope instability, as shown in Figures 15, 16, with the gradual increase in the excavation area and the continuous expansion of the mining level stage, the slope failure performance is different. The rock mass deformation in the excavation stage of 2016 and the excavation stage of 18 years is mainly realized as a small amount of damage on the surface of the rock mass, and the overall displacement of rock mass is not obvious. With the continuous development of the project, different horizontal stages are put into mining one after another, and the tendency of rock mass deformation becomes obvious. During the 20-year excavation stage, a small amount of slippage occurs in the rock mass slope, and the slope is affected by gravity and stress redistribution after excavation, resulting in great failure and deformation. In the excavation stage of 23 years, the rock mass has been damaged more obviously, and a large area of goaf has appeared in the rock mass. At the same time, the stress redistribution phenomenon occurs frequently after excavation, which makes it difficult for the rock mass to withstand the deformation and failure caused by stress changes. In the case of freeze-thaw, the deformation of rock mass is greatly affected by the freeze-thaw cycle. With the increase in freeze-thaw times, the failure modes of

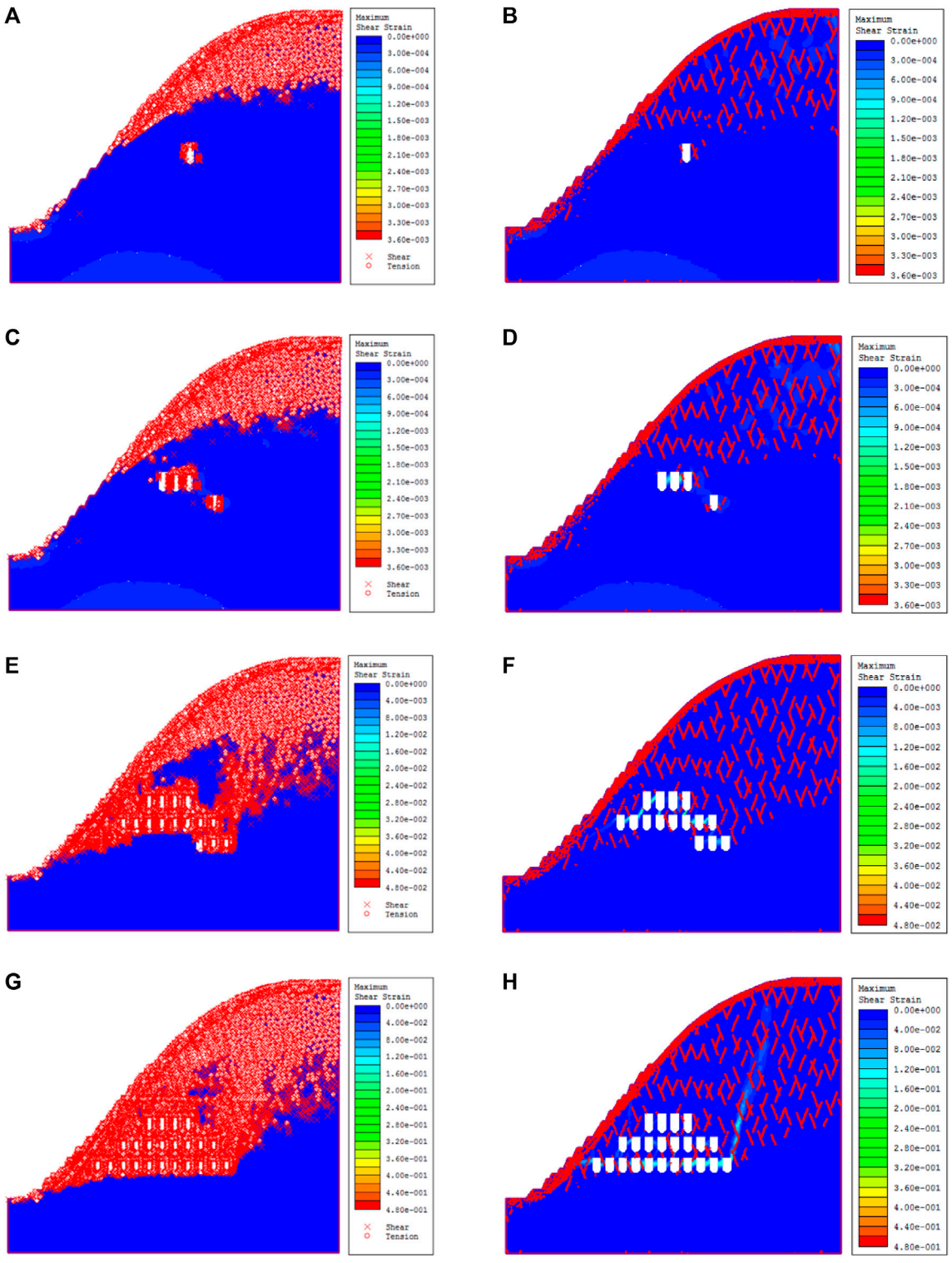

FIGURE 13
Yield element and joint cloud map of models at different excavation stages. **(A)** Concurrence of yield unit during excavation in 2016. **(B)** Yield joint cloud map during excavation in 2016. **(C)** Cloud image of yield unit during excavation in 2018. **(D)** Yield joint cloud map during excavation in 2018. **(E)** Cloud image of yield unit during excavation in 2020. **(F)** Yield joint cloud map during excavation in 2020. **(G)** Cloud image of yield unit during excavation in 2023. **(H)** Yield joint cloud map during excavation in 2023.

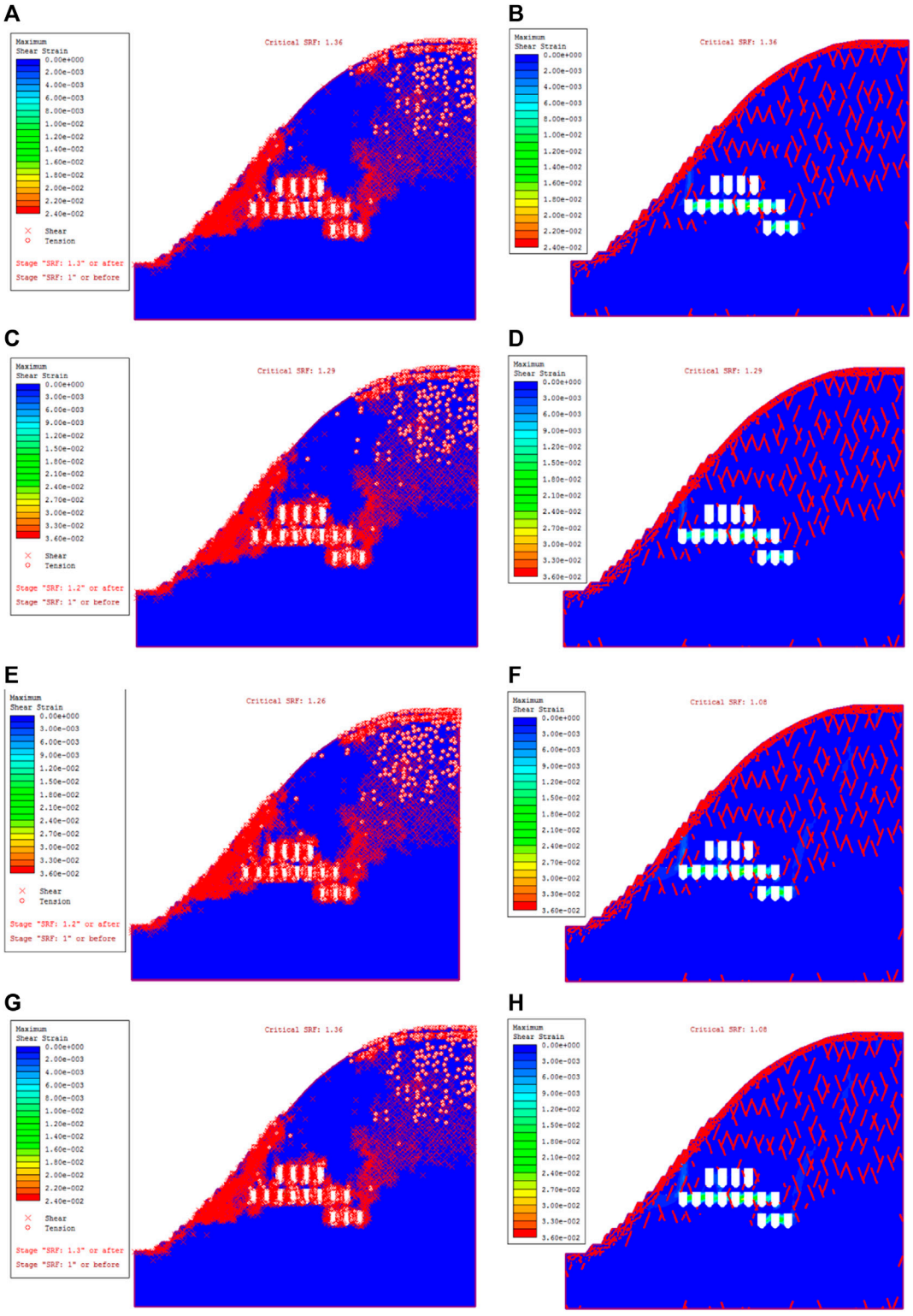

FIGURE 14
The yield rock unit and joint unit of the slope model were subjected to different freeze-thaw cycles. **(A)** Yield rock unit of 0 freeze-thaw cycle. **(B)** Yield joint of 0 freeze-thaw cycle. **(C)** Yield rock unit of 30 freeze-thaw cycles. **(D)** Yield joint of 30 freeze-thaw cycles. **(E)** Yield rock unit of 50 freeze-thaw cycles. **(F)** Yield joint of 50 freeze-thaw cycles. **(G)** Yield rock unit of 100 freeze-thaw cycles. **(H)** Yield joint of 100 freeze-thaw cycles.

10.3389/fmats.2023.1242764

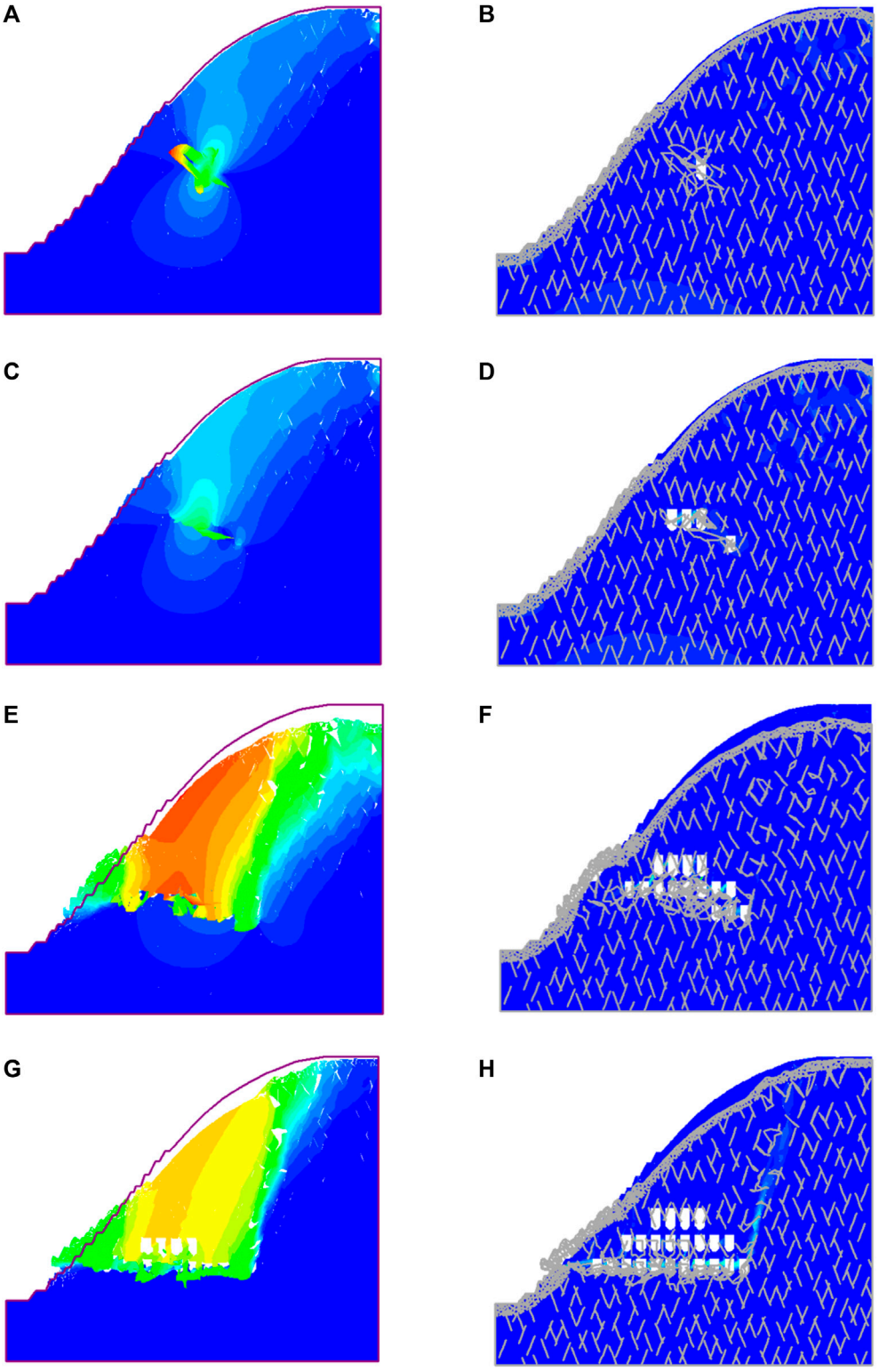

FIGURE 15
Deformation cloud map of the model at different excavation stages. **(A)** Deformation contour during excavation in 2016. **(B)** Deformation contour during excavation in 2016. **(C)** Deformation cloud map during excavation in 2018. **(D)** Deformation contour during excavation in 2018. **(E)** Deformation contour during excavation in 2020. **(F)** Deformation contour during excavation in 2020. **(G)** Deformation contour during excavation in 2023. **(H)** Deformation contour during excavation in 2023.

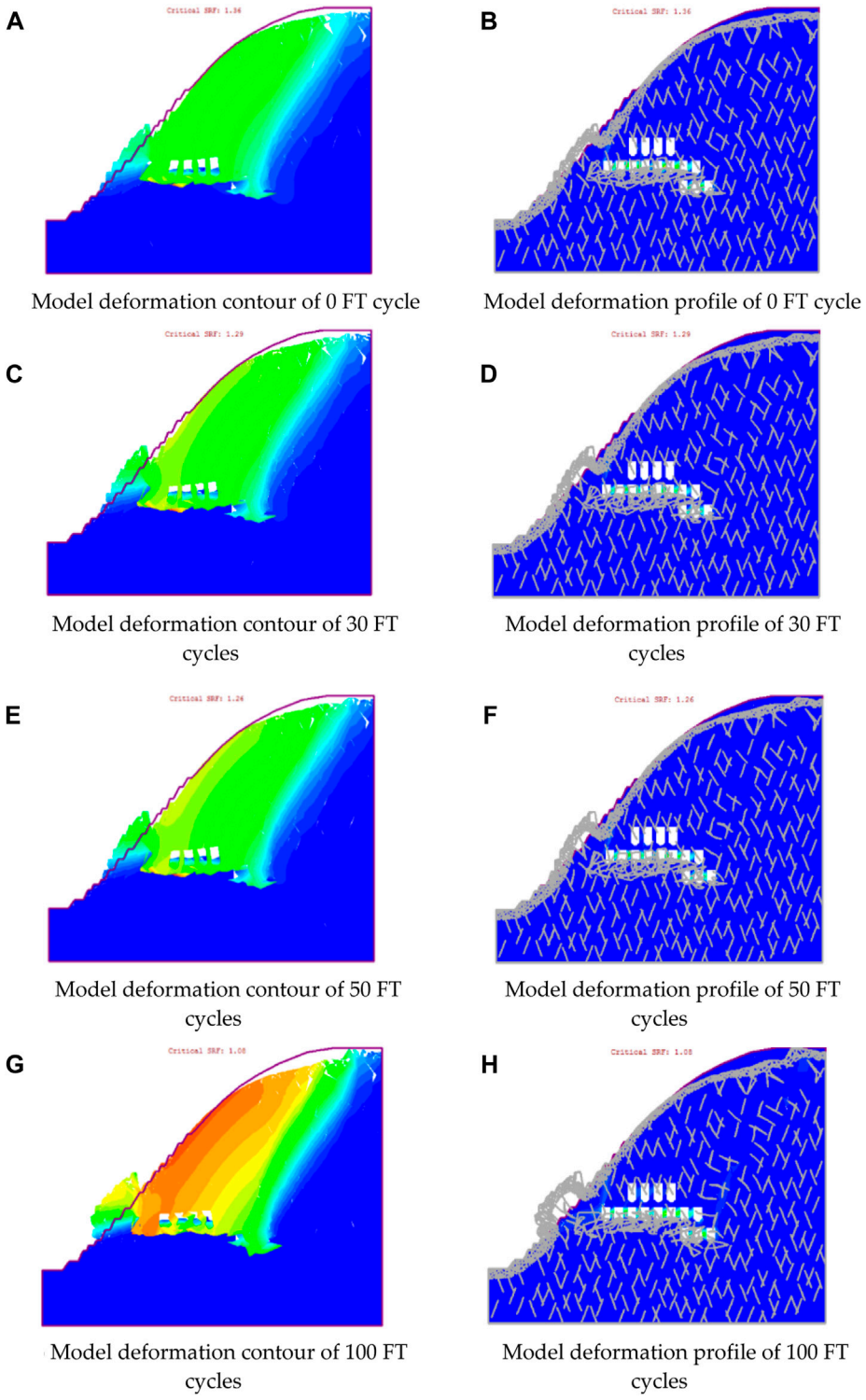

FIGURE 16
Cloud map of rock mass deformation under different freeze-thaw times. **(A)** Model deformation contour of 0 FT cycle. **(B)** Model deformation profile of 0 FT cycle. **(C)** Model deformation contour of 30 FT cycles. **(D)** Model deformation profile of 30 FT cycles. **(E)** Model deformation contour of 50 FT cycles. **(F)** Model deformation profile of 50 FT cycles. **(G)** Model deformation contour of 100 FT cycles. **(H)** Model deformation profile of 100 FT cycles.

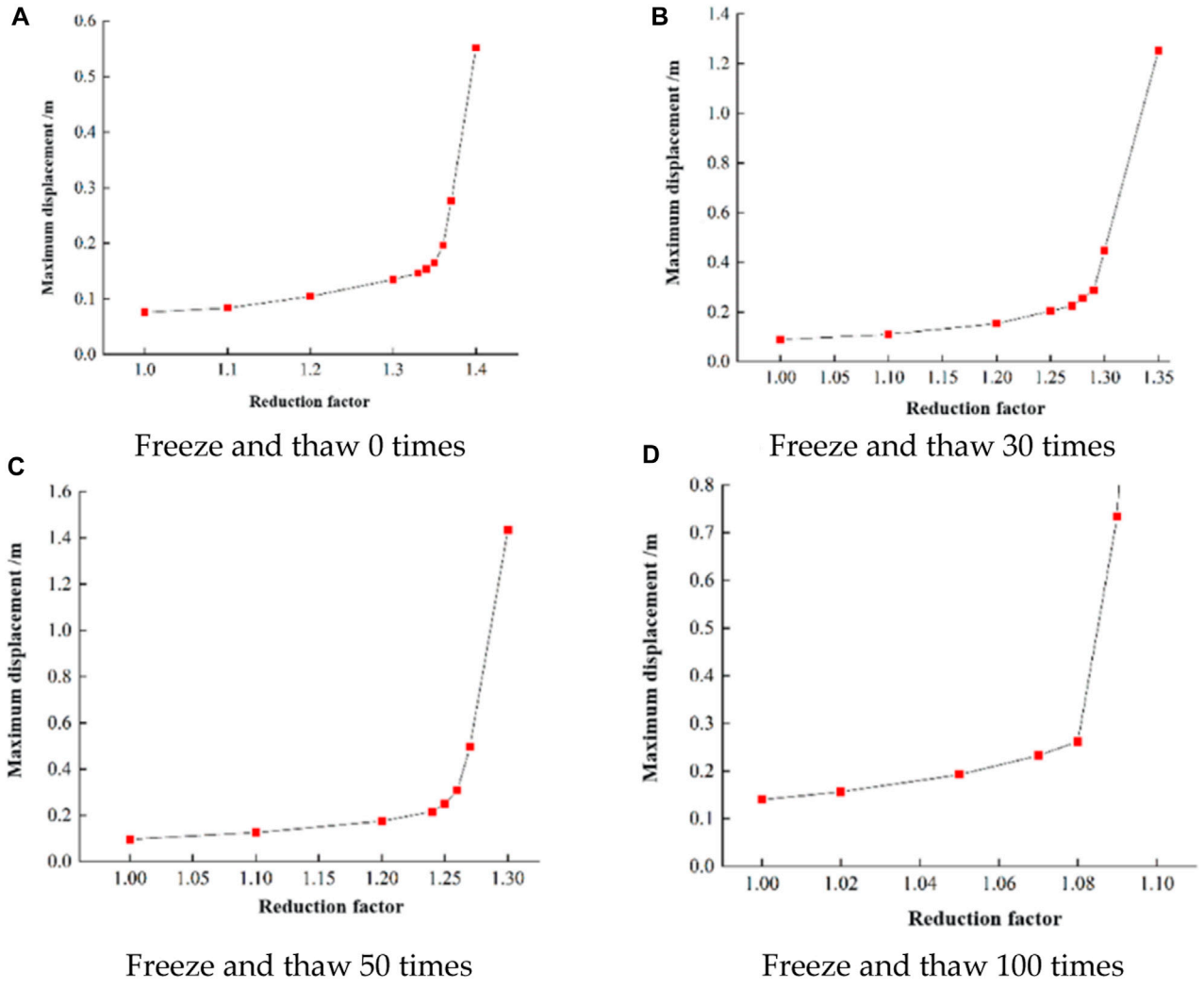

FIGURE 17
The relationship between stability coefficient and maximum displacement under different freeze-thaw cycles. **(A)** Freeze and thaw 0 times. **(B)** Freeze and thaw 30 times. **(C)** Freeze and thaw 50 times. **(D)** Freeze and thaw 100 times.

rock mass are different. The deformation of unfrozen and thawed rock mass is small, mainly manifesting as a small deformation at the slope. With the increasing number of freeze-thawing times, the slope deformation becomes larger and larger, and the deformation framework becomes more complex. The slope has been unstable after 100 freeze-thawing times.

According to different excavation stages of hang-wall for mine stress, displacement, shear strain, and the yield unit and joint changes, the trend of the overall destruction of rock mass at a glance, excavation will cause internal thickening of unloading rock mass effect occurred frequently, the mined-out area gradually expanded, will result in rock mass deformation and destruction shall be to stress, displacement, shear strain in the process of the excavation area, great changes have taken place in various parameters, such as Monitoring and prevention in advance. In the case of freeze-thaw, the deformation and failure of rock mass are significantly affected by freeze-thaw, and the internal pores and cracks will gradually be connected, the stable performance of rock mass is influenced obviously. The model with the maximum number of freeze-thaw under the same excavation condition has the largest deformation, which is consistent with the changing trend of volume strain in the previous rock test.

Finally, through the numerical model, the strength reduction method is used to calculate the safety factor of the slope model under different freeze-thaw times, and the slope stability is quantitatively analyzed. The relationship between the model strength reduction coefficient and maximum displacement under different freeze-thaw cycles is shown in Figure 17. Finally, the safety and stability coefficients of rock mass under 0, 30, 50, and 100 freeze-thaw times are 1.36, 1.29, 1.26, and 1.08, respectively. The safety factor can reflect the stability of the slope, and the above changes indicate that the stability of the slope rock mass decreases with the increase in freeze-thaw times.

5 Conclusion

In this work, based on the eastern hanging-wall orebody of the Hejing iron mine in Xinjiang, a systematic study was conducted on the distribution of rock mass structural plane information and the

slope stability analysis under the disturbance of freeze-thaw rock mass excavation by adopting the comprehensive methods of field investigation and numerical simulation. The main conclusions are as follows:

(1) 3D laser scanning is adopted to obtain the point cloud data of the open-pit slope. By getting the point cloud data grid, intelligent identification of the rock mass structure plane information was investigated to propose the image segmentation algorithm The K-means clustering analysis method was used to divide the structural plane information, and the spacing and equivalent trace lengths of the structural plane were obtained. The average attitude of the three groups of structural planes was determined to be 237° < 69°, 290° < 70°, and 252° < 34°; the average spacing was 0.223, 0.699, and 0.481; and the equivalent trace length was 0.688, 1.140, and 0.784, respectively. The number of joints per unit area of the rock mass structural plane is 0.111, 0.034, and 0.020, respectively.

(2) A numerical model considering the joint distribution is established for the eastern hang-wall orebody of the open-pit slope. The generalized Hoek-Brown criterion equation and Barton-Bandis criterion equation are used to calculate the shear strength of the rock block and joint plane, respectively, and the impact of hanging-wall mining engineering on the disaster of the rock mass structural plane is analyzed. The simulation results show that the gradual increase in the goaf area will destroy the stability of the rock mass; the roof area of the mine and the preserved pillar area have frequent load increasing and unloading behaviors, and the stress change area has large displacement and deformation.

(3) The strength reduction method is used to calculate the safety factor of rock mass at the current excavation stage, and the deformation development caused by 0, 30, 50, and 100 freeze-thawing cycles on the rock mass excavation project is analyzed. The results show that the rock mass displacement, strain, and plasticity zone all increase after freeze-thaw weathering. The slope stability coefficient decreases sharply under high freeze-thaw cycles; in addition, excavation of orebody causes stress and strain concentration which accelerates rock deformation.

Data availability statement

The original contributions presented in the study are included in the article/supplementary material, further inquiries can be directed to the corresponding author.

Author contributions

YW supervised the study, acquired the funding, and administered the project. YZ conducted the laser scanning and analyzed the data. JW conducted the experiments. PT visualized the study, curated the data, and provided the resources. All authors contributed to the article and approved the submitted version.

Funding

This research was funded by the Shenyang Science and Technology Talent Project (RC220450), the Geological Survey Project of CGS (DD20230437), and the National Natural Science Foundation of China (52174069).

Conflict of interest

The authors declare that the research was conducted in the absence of any commercial or financial relationships that could be construed as a potential conflict of interest.

Publisher's note

References

Bai, B., Nie, Q., Zhang, Y., Wang, X., and Hu, W. (2021a). Cotransport of heavy metals and SiO2 particles at different temperatures by seepage. *J. Hydrology* 597, 125771. doi:10.1016/j.jhydrol.2020.125771

Bai, B., Rao, D., Chang, T., and Guo, Z. (2019). A nonlinear attachment-detachment model with adsorption hysteresis for suspension-colloidal transport in porous media. *J. Hydrology* 578, 124080. doi:10.1016/j.jhydrol.2019.124080

Bai, B., Zhou, R., Cai, G., Hu, W., and Yang, G. (2021b). Coupled thermo-hydro-mechanical mechanism in view of the soil particle rearrangement of granular thermodynamics. *Comput. Geotechnics* 137, 104272. doi:10.1016/j.compgeo.2021.104272

Battulwar, R., Zare-Naghadehi, M., Emami, E., and Sattarvand, J. (2021). A state-of-the-art review of automated extraction of rock mass discontinuity characteristics using three-dimensional surface models. *J. Rock Mech. Geotechnical Eng.* 13 (4), 920–936. doi:10.1016/j.jrmge.2021.01.008

Chen, L., Zhao, X., Liu, J., Ma, H., Wang, C., Zhang, H., et al. (2023). Progress on rock mechanics research of Beishan granite for geological disposal of high-level radioactive waste in China. *Rock Mech. Bull.* 2 (3), 100046. doi:10.1016/j.rockmb.2023.100046

Du, J. C. (2013). Study on surrounding rock stability of Hanging wall Mine under high and steep slope based on FLAC3D. *Technol. Innov. Appl.* (12), 2-3.

Fakhri, D., Mahmoodzadeh, A., Mohammed, A. H., Khodayari, A., Ibrahim, H. H., Rashidi, S., et al. (2023). Forecasting failure load of Sandstone under different Freezing-Thawing cycles using Gaussian process regression method and grey wolf optimization algorithm. *Theor. Appl. Fract. Mech.* 125, 103876. doi:10.1016/j.tafmec.2023.103876

Fekete, S., and Diederichs, M. (2013). Integration of three-dimensional laser scanning with discontinuum modelling for stability analysis of tunnels in blocky rockmasses. *Int. J. Rock Mech. Min. Sci.* 57, 11–23. doi:10.1016/j.ijrmms.2012.08.003

Fekete, S., Diederichs, M., and Lato, M. (2010). Geotechnical and operational applications for 3-dimensional laser scanning in drill and blast tunnels. *Tunn. Undergr. space Technol.* 25 (5), 614–628. doi:10.1016/j.tust.2010.04.008

Forte, G., Verrucci, L., Di Giulio, A., De Falco, M., Tommasi, P., Lanzo, G., et al. (2021). Analysis of major rock slides that occurred during the 2016–2017 Central Italy seismic sequence. *Eng. Geol.* 290, 106194. doi:10.1016/j.enggeo.2021.106194

Ge, Y. F., Tang, H. M., Huang, L., Wang, L. Q., Sun, M. J., and Fan, Y. J. (2012). A new representation method for three-dimensional joint roughness coefficient of rock mass discontinuities. *Chin. J. Rock Mech. Eng.* 31 (12), 2508–2517.

Ghobadi, M. H., and Babazadeh, R. (2015). Experimental studies on the effects of cyclic freezing–thawing, salt crystallization, and thermal shock on the physical and mechanical characteristics of selected sandstones. *Rock Mech. Rock Eng.* 48, 1001–1016. doi:10.1007/s00603-014-0609-6

Gigli, G., and Casagli, N. (2011). Semi-automatic extraction of rock mass structural data from high resolution LIDAR point clouds. *Int. J. rock Mech. Min. Sci.* 48 (2), 187–198. doi:10.1016/j.ijrmms.2010.11.009

Huang, F., Teng, Z., Guo, Z., Catani, F., and Huang, J. (2023). Uncertainties of landslide susceptibility prediction: Influences of different spatial resolutions, machine learning models and proportions of training and testing dataset. *Rock Mech. Bull.* 2 (1), 100028. doi:10.1016/j.rockmb.2023.100028

Kocak, D. M., Caimi, F. M., Das, P. S., and Karson, J. A. (1999). "A 3-D laser line scanner for outcrop scale studies of seafloor features," in Proccedings of the Oceans' 99. MTS/IEEE. Riding the Crest into the 21st Century. Conference and Exhibition. Conference Proceedings (IEEE Cat. No. 99CH37008), Seattle, WA, USA, Septembe 1999 (IEEE), 1105–1114.

Lato, M. J., and Vöge, M. (2012). Automated mapping of rock discontinuities in 3D lidar and photogrammetry models. *Int. J. rock Mech. Min. Sci.* 54, 150–158. doi:10.1016/j.ijrmms.2012.06.003

Liu, F. Q., and Zeng, W. Z. (2020). Mining methods and stability measures of the mining of the lower hanging side of high and steep slope. *World Nonfer. Metals* (02), 46–47.

Maerz, N. H., Youssef, A. M., Otoo, J. N., Kassebaum, T. J., and Duan, Y. E. (2013). A simple method for measuring discontinuity orientations from terrestrial LIDAR data. *Environ. Eng. Geoscience* 19 (2), 185–194. doi:10.2113/gseegeosci.19.2.185

Menegoni, N., Giordan, D., Perotti, C., and Tannant, D. D. (2019). Detection and geometric characterization of rock mass discontinuities using a 3D high-resolution digital outcrop model generated from RPAS imagery – ormea rock slope, Italy. *Italy. Eng. Geol.* 252, 145–163. doi:10.1016/j.enggeo.2019.02.028

Shang, J. (2022). Stress path constraints on veined rock deformation. *Rock Mech. Bull.* 1 (1), 100001–100112. doi:10.1016/j.rockmb.2022.100001

Slob, S., van Knapen, B., Hack, R., Turner, K., and Kemeny, J. (2005). Method for automated discontinuity analysis of rock slopes with three-dimensional laser scanning. *Transp. Res. Rec.* 1913 (1), 187–194. doi:10.1177/0361198105191300118

Song, Y., Tan, H., Yang, H., Chen, S., Che, Y., and Chen, J. (2021). Fracture evolution and failure characteristics of sandstone under freeze-thaw cycling by computed tomography. *Eng. Geol.* 294, 106370. doi:10.1016/j.enggeo.2021.106370

Tuckey, Z., and Stead, D. (2016). Improvements to field and remote sensing methods for mapping discontinuity persistence and intact rock bridges in rock slopes. *Eng. Geol.* 208, 136–153. doi:10.1016/j.enggeo.2016.05.001

Wang, Y., Yan, M. Q., and Song, W. B. (2023a). The effect of cyclic stress amplitude on macro-meso failure of rock under triaxial confining pressure unloading. *Fatigue & Fract. Eng. Mater. Struct.* 45 (10), 2212–2228. doi:10.1111/ffe.13993

Wang, Y., Cao, Z., Li, P., and Yi, X. (2023b). On the fracture and energy characteristics of granite containing circular cavity under variable frequency-amplitude fatigue loads. *Theor. Appl. Fract. Mech.* 125, 103872. doi:10.1016/j.tafmec.2023.103872

Wang, Y., Song, Z. Y., Mao, T. Q., and Zhu, C. (2022). Macro–Meso fracture and instability behaviors of hollow-cylinder granite containing fissures subjected to freeze–thaw–fatigue loads. *Rock Mech. Rock Eng.* 55, 4051–4071. doi:10.1007/s00603-022-02860-5

Xu, Y., Fu, Y., Yang, Y., Yao, W., Xia, K., and Peng, J. (2023). Dynamic compression properties of a saturated white sandstone under ambient sub-zero temperatures. *Acta Geotech.* 18, 4245–4260. doi:10.1007/s11440-023-01836-1

Zhang, P., Du, K., Tannant, D. D., Zhu, H., and Zheng, W. (2018). Automated method for extracting and analysing the rock discontinuities from point clouds based on digital surface model of rock mass. *Eng. Geol.* 239, 109–118. doi:10.1016/j.enggeo.2018.03.020

frontiers | Frontiers in Materials

TYPE Original Research
PUBLISHED 07 August 2023
DOI 10.3389/fmats.2023.1237190

OPEN ACCESS

EDITED BY
Xianze Cui,
China Three Gorges University, China

REVIEWED BY
Bo Yang,
Henan University of Technology, China
Ni Zhang,
Xi'an Jiaotong University, China

*CORRESPONDENCE
Zhang Ming,
zhangming@zua.edu.cn

RECEIVED 09 June 2023
ACCEPTED 11 July 2023
PUBLISHED 07 August 2023

CITATION
Feng T, Huiqiang Z, Fengbo D, Shaoqiang C, Feng L and Ming Z (2023), Experimental study on the bearing property of the composite foundation with stiffened deep cement mixing pile based on the PHC pile.
Front. Mater. 10:1237190.
doi: 10.3389/fmats.2023.1237190

Experimental study on the bearing property of the composite foundation with stiffened deep cement mixing pile based on the PHC pile

Tao Feng[1], Zhu Huiqiang[2], Dong Fengbo[1], Chai Shaoqiang[1], Liu Feng[1] and Zhang Ming[3]*

[1]Project Department, The Seventh Engineering Co., Ltd. of CFHEC, Zhengzhou, China, [2]Survey Department, Zhongyun International Engineering Co., Ltd., Zhengzhou, China, [3]School of Civil Engineering and Architecture, Zhengzhou University of Aeronautics, Zhengzhou, China

Inserting a prestressed high-intensity concrete pipe pile into a cement–soil mixing pile can form a new composite pile named the composite foundation with stiffened deep cement mixing (SDCM) pile. The Huanghuai alluvial stratum in China is selected to carry out the *in situ* test for the SDCM pile, and the bearing capacity of the SDCM pile is tested by the slow-speed maintenance load method. The results show that for an SDCM pile with dense silt and fine sand as the bearing layer, the characteristic value of bearing capacity can reach 2,300 kN, which means an SDCM pile with a length of 8.0 m meets the load requirement of a general high-rise building. Further analysis shows that the SDCM pile saves more than 40% of the cost compared with the traditional CFG pile and has better quality control advantages at the same time. This research can provide basic data and design references for similar site foundation projects.

KEYWORDS

prestressed high-intensity concrete pipe pile, composite foundation with stiffened deep cement mixing pile, characteristic value of bearing capacity, construction cost, *in situ* test

1 Introduction

The composite foundation with stiffened deep cement mixing (SDCM) pile, as a new type of pile composed of a prestressed high-intensity concrete pipe (PHC) pile and a cement–soil mixing pile, bears most of the vertical load through the PHC pile with higher strength and rigidity and avoids cement–soil mixing pile loss of bearing capacity due to insufficient strength of the pile body, leading to premature bearing capacity loss. At the same time, the shear strength of the surrounding soil of the PHC pile can be increased by solidification of the cement–soil mixing pile so that the strength of the PHC pile can be fully exerted. The combination of the two pile types can maximize strengths and avoid weaknesses. Using the SDCM pile can obtain a higher bearing capacity with a cheaper construction cost (Bai et al., 2021; Zhu, 2021; Bai et al., 2023). Under the condition of vertical load, the axial force of the inner core at the same cross-section is much greater than that of the cement–soil mixing pile, and the PHC pile is the main undertaker of the vertical load. The SDCM pile was first proposed in Japan (Lu, 2016) and introduced in China in 1988 (Ding et al., 2005).

Jamsawang et al. (2010), Wonglert et al. (2018), and Phutthananon et al. (2018) performed field tests for the SDCM pile, finding that the bearing capacity of the SDCM pile will increase with the increment of the pile diameter and pile length under the same working condition. Among the influencing factors of pile bearing capacity, pile length is the most significant one. Voottipruex et al. (2010) studied the bearing mechanism of SDCM piles in the form of numerical simulation based on a field full-scale test. The research results also showed that increasing the "core length ratio" of SDCM piles can effectively improve their ultimate bearing capacity. Wonglert and Jongpradist (2015) and Voottipruex et al. (2011) also used numerical simulation to study the effect of stiffness of the PHC pile on the bearing capacity of the SDCM pile, pointing out that the stiffness will have a more significant impact on the vertical bearing capacity only when the PHC pile length is large enough.

In China, Gao et al. (2012), Yang (2019), Wang (2020) studied the load transfer characteristics of the SDCM pile through an *in situ* pile test and non-destructive inspection, finding that the influence range of the SDCM pile on the soil around the pile is larger, which is more conducive to the exertion of the bearing capacity of the soil around the pile, providing the technical applicability and economic feasibility of the SDCM pile in the southern region in China. Wang et al. (2013) and Wang et al. (2014) conducted a comprehensive study on the bearing property of the SDCM pile using numerical simulation on the basis of an *in situ* test. The research results show that the ring-layer structure of the SDCM pile can prevent the soft soil around the pile from being crushed under a large load and, at the same time, ensure that the upper load can be transmitted to the deeper soil. Compared with the cement–soil mixing pile, the "effective pile length" of the SDCM increases. Wang et al. (2018) and Cheng (2021) used laboratory tests and the theoretical analysis method to study the mechanical characteristics of the SDCM pile and obtain the influence law of pile body parameter on the bearing characteristics of the composite pile. Several scholars only carried out laboratory tests or numerical simulations. Ye et al. (2014) and Peng et al. (2007) used the finite-element analysis software to obtain the vertical bearing characteristics of the SDCM pile, including the axial force distribution characteristics of the SDCM pile, the load sharing ratio of the pile skin and the pile end, and the influence of stiffness on the load transfer of the SDCM pile.

Most of the abovementioned studies are aimed at a single layer of soil and mainly based on laboratory tests and numerical simulations. In actual engineering, the SDCM pile will pass through various soil layers, and the same soil layer is also of certain inhomogeneity. In addition, most of the research is conducted in the southern region of China, so it is necessary to carry out experimental research on the bearing characteristics of the SDCM pile on the hard soil layer in the northern region of China.

2 Characteristics of the test site

The research site is located in Zhoukou city, shown in Figure 1. The topography and geomorphology unit of the site is relatively simple, and the geomorphology unit is the alluvial plain of the Huanghuai River. The original terrain of the site is basically flat. The main strata in the field are covered by Quaternary soil layers. According to the drilling description, *in situ* test, and geotechnical test result, the foundation soil within the exploration depth of 50 m is divided into nine layers. The lithological characteristics of each layer are described from top to bottom as follows:

① Layer of mixed backfill: Mainly composed of construction waste, mixed with bricks, concrete blocks, and building foundations. This layer is not uniform, so it is not suitable for direct use.
② Layer of silt: Brownish yellow, wet, and slightly dense and contains snail shell fragments, with rapid shake response, matte response, low dry strength, low toughness, and moderate compressibility.
③ Layer of silty clay: Brownish yellow to brownish gray and soft plastic, with no shaking reaction, slightly glossy reaction, dry strength, medium toughness, and high compressibility.
④ Layer of silt: Grayish brown to brownish gray, mainly composed of quartz, feldspar, mica flakes, etc., saturated, and medium to dense, with average particle gradation, containing a small amount of snail shavings, etc., and partially mixed with fine sand and silt.
⑤ Layer of fine sand: Brownish yellow, saturated, and dense, with low compressibility, containing mineral components such as quartz, feldspar, and mica, with general particle gradation, iron oxides, a small amount of ginger stone, snail debris, etc., and a partially silty thin layer and medium and coarse sand.
⑥ Layer of silty clay: Taupe, yellowish brown, and plastic, with no shaking response, medium dry strength, and medium toughness, and yellowish gray, wet, and dense, with sandy silt and a large number of yellow–brown stripes, rust spots, and blue–gray stripes, occasionally containing snail shells, ginger stones, and calcareous nodules.
⑦ Layer of silty clay with silty soil: Yellowish brown and plastic to hard plastic, with medium dry strength, medium toughness, and bluish-gray stripes, more locally available, containing a large number of yellow–brown rust spots and occasionally calcareous nodules with a particle size of about 2 cm, with partially silty soil.
⑧ Layer of silty clay: Yellowish brown, plastic to hard plastic, with medium dry strength and medium toughness, containing a large number of yellow–brown rust spots and occasionally calcareous nodules with a particle size of about 2 cm, partially silty, wet, and dense.
⑨ Layer of silty clay with silty soil: Yellow to yellowish brown and plastic to hard plastic, with high dry strength and medium toughness, containing a lot of yellow–brown rust spots and occasional calcareous concretions with a particle size of about 2 cm.

The detailed distribution of each soil layer can be seen in Table 1, and the typical engineering geological profile of the site is shown in Figure 2.

3 Test method

3.1 Pile foundation parameters

The SDCM pile based on the PHC pile selected in this test is shown in Figure 3. The inner core PHC pile is PHC-400AB95, the

FIGURE 1
Location of the test.

TABLE 1 List of soil layer properties of the project site.

No. of layers	Thickness (m)	Cone tip resistance q_c (MPa)	SPT *N*	PHC pile			
				q_s (kPa)	Skin resistance adjustment coefficient ξ_{si}	q_p (*kPa*)	End resistance adjustment coefficient ξp
①	0.4~2.4	—	—	—	—	—	—
②	1.7~5.1	1.45	3.7	—	—	—	—
③	3.2~6.3	0.60	4.2	21	1.6	—	—
④	1.4~3.6	9.7	35.0	35	1.8	2,000	1.6
⑤	8.1~11.2	16.5	45.1	40	2.0	2,500	1.8
⑥	3.9~8.1	—	14.6	—	—	—	—
⑦	0.8~12.5	—	18.3	—	—	—	—
⑧	2.8~8.2	—	19.2	—	—	—	—
⑨	-	—	22.2	—	—	—	—

outer core is the Φ700 mixing pile, the effective pile length is 8.0 m, the bearing layer at the pile end is layer ⑤, the pile enters into the bearing layer at about 4.0 m, and the constructional requirement of the characteristic value of bearing capacity for one single pile is more than 1,300 kN.

3.2 Experimental design

Three groups of test piles are designed for this test in total, and the absolute elevation of the top of the test piles is 39.45 m. Since the characteristic value of the bearing capacity of a single pile is not less than 1,300 kN, the maximum loading capacity of the test pile is 2,600 kN. The test started on 25 June 2020 and ended on 10 August 2020, using static pressure equipment. The equipment parameters and main control indicators used in the site are shown in Table 2. Because the construction quality cannot be guaranteed due to the small construction torque of the mixing piles in the sand layer, the three-axis mixing is changed into single-axis mixing for the construction technology of the cement–soil mixing pile. The background grouting pump is between the high-pressure rotary grouting pile and the low-pressure ordinary mixing pile. The pile part is stirred evenly, and the amount of cement is in an appropriate amount in accordance with the research requirement.

Partial construction photos of the site are shown in Figure 4.

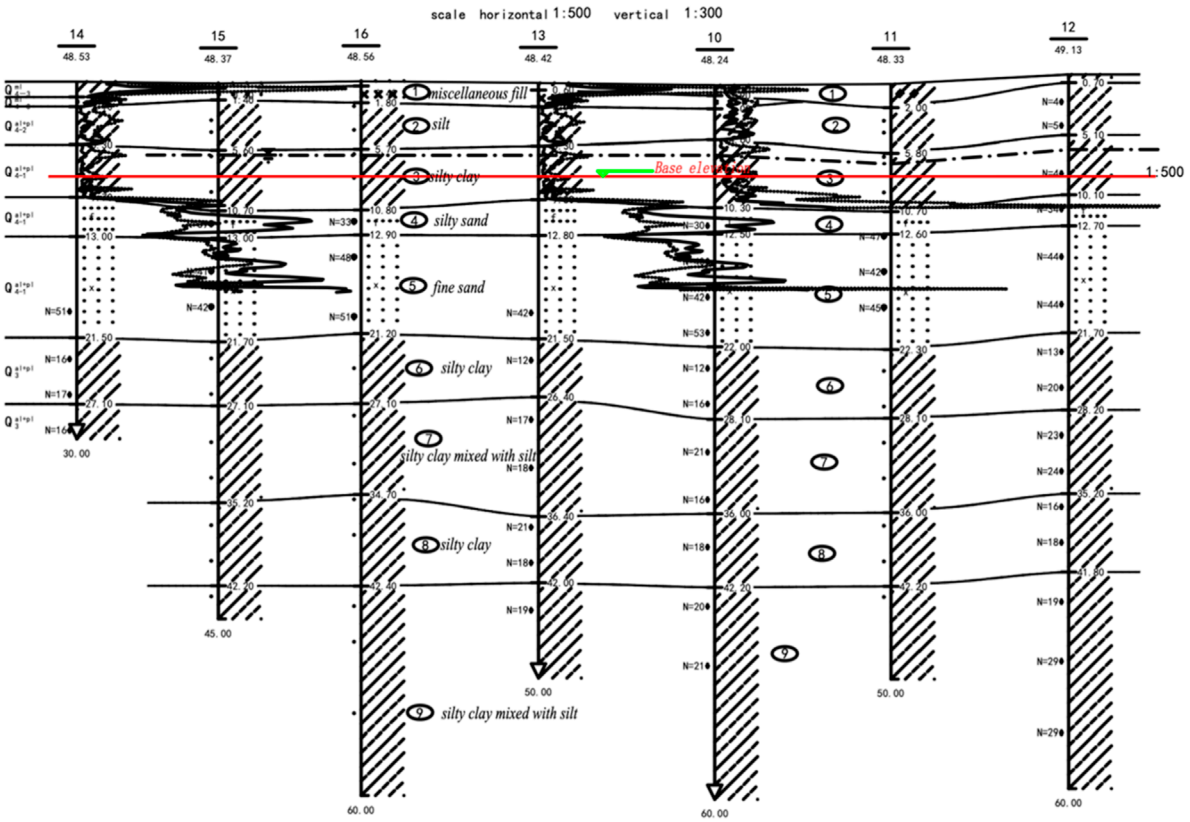

FIGURE 2
Typical engineering geological profile.

4 Test results

4.1 Basis for determining the characteristic value of bearing capacity

According to the "Technical Specifications for Building Foundation Pile Testing" (JGJ 106-2014), the vertical ultimate bearing capacity Q_u of a single pile can be comprehensively analyzed and determined according to the following methods.

(1) According to the characteristics of the changing of settlement with load, for the steep drop-type Q_s curve, the load value corresponding to the starting point of the obvious steep drop should be taken.
(2) According to the characteristics of the settlement over time, the load value of the previous level at which the tail of the s-lgt curve appears to bend downward should be taken.
(3) When under the action of a certain level of load, the settlement of the pile is greater than twice that under the action of the previous level of load and the relative stability standard has not been reached after 24 h, the value of the previous level of load is taken.
(4) For the slowly changing Q_s curve, it is better to take the load value corresponding to the total settlement of 40 mm from the pile top. When the pile diameter is more than 800 mm, the total settlement should be 0.05 D (pile diameter). When the pile length is greater than 40 m, the elastic compression of the pile body should be considered.
(5) When the vertical compressive bearing capacity of the pile is determined not to reach the limit according to the abovementioned four items, the maximum test load value should be taken as the vertical compressive ultimate bearing capacity of the pile.

Finally, the characteristic value R_d of the vertical bearing capacity of a single pile under the same conditions of the research should be weighted by 50% of the statistical value of the ultimate compressive capacity of the single pile.

4.2 Vertical static load test result of a single pile

The test results of the three groups of test piles are shown in Tables 3–5. The test adopts equal loading step by step, the step-by-step load is 1/10 of the design's ultimate bearing capacity, the first step takes twice the step-by-step load, and the maximum load is 2600 kN, classified as 0, 520, 780, 1,040, 1,300, 1,560, 1,820, 2,080, 2,340, and 2,600 kPa. Unloading is carried out in stages, the amount

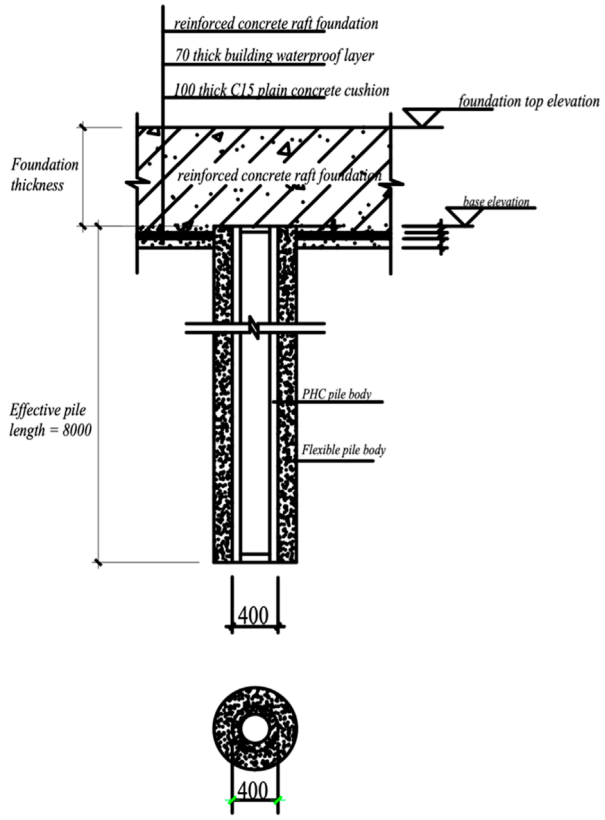

FIGURE 3
Schematic diagram of the SDCM pile.

of unloading at each stage is twice the load of the stage during loading, and the amount is equal step by step. They are 2,080, 1,560, 1,040, 520, and 0 kN, respectively.

According to the "Technical Specifications for Building Foundation Pile Monitoring," the test load has reached the maximum load required by the design, and the settlement of the pile top has reached the relatively stable level, so the test is terminated. The load-settlement (Q_s) curve of the test pile is shown in Figure 5. It can be seen that the vertical load of the pile, 2,600 kPa, has not reached the ultimate bearing capacity. Therefore, the vertical compressive ultimate bearing capacity of the pile should be the maximum test load value. It is concluded in Table 6.

5 Discussion

5.1 Comparison of the test result and the code method result

When the pile skin failure surface of the SDCM pile is located at the interface between the inner and outer cores, the characteristic value of the ultimate bearing capacity of the foundation pile is calculated according to the "Technical Regulations for Stiffened Composite Pile" (JGJT327-2014) as follows:

$$R_a = u^c q_{sa}^c l^c + q_{pa}^c A_p c = 0.5 \times 3.14 \times 0.07 \times 2000 \times 9.0 + 2500 \times 0.196,$$
$$= 2460\,\text{kN}$$

u^c—Perimeter of the PHC pile of the SDCM pile (mm)

l^c—The thickness of soil layer of the length of the composite section of the SDCM pile (m)

A_P^c—The cross − sectional area of the PHC pile in the SDCM pile (m^2)

q_{sa}^c—Skin resistance of the PHC pile in the SDCM pile (kPa)

q_{pa}^c—End resistance of the PHC pile in the SDCM pile (kPa)

When the pile skin failure surface of the SDCM pile is located at the interface between the outer core and the soil around the pile, the ultimate bearing capacity of the foundation pile is calculated according to "Technical Regulations for Stiffened Composite Pile" for the SDCM pile as follows:

$$R_a = u\sum \xi_{si} q_{sia} l_i + \alpha \xi_p q_{pa} A_p = 0.7 \times 3.14 \times (35 \times 9.0 \times 1.8) + 0.8$$
$$\times 1.8 \times 2500 \times 3.14 \times 0.7 \times 0.7/4 = 2628\,\text{kN}$$

ξ_{si}—Adjustment coefficient of lateral resistance of the i − th soil layer of the outer core of the composite section of the SDCM pile

ξ_p—Adjustment coefficient of end resistance of the i − th soil layer of the outer core of the composite section of the SDCM pile

q_{sia}—The lateral resistance characteristic value of the i − th soil layer of the outer core of the composite section of the SDCM pile (kPa)

l_i— Thickness of the i − th soil layer in the composite section of th eSDCM pile (m)

TABLE 2 Construction equipment parameter list.

Pile type	Device parameters	Construction main control indicators
Static pile driver, ZYG680-type	Static pile driver, ZYG680	The pressure pile pressure should not be less than 3,000 kN, the pressure pile is repressed three times under the maximum pile pressure force, the cumulative settlement of the three repressed piles should not be greater than 30 mm, and the effective pile length is not less than 8.0 m
Φ700 cement–soil mixing pile	Single-shaft double-tube mixing pile driver, DZSJ28-type	The cement uses class P.O32.5 cement, the amount of cement added is not less than 200 kg per meter, the water–cement ratio of the cement slurry is 1:1, and the cement mixing time is not less than 2–3 min

10.3389/fmats.2023.1237190

TABLE 3 Test results of the No. 1 pile.

No.	Load (kN)	Duration (min)		Settlement (mm)	
		Current	Total	Current	Total
0	0	0	0	0	0
1	520	120	120	0.45	0.45
2	780	120	240	0.68	1.13
3	1,040	120	360	0.62	1.75
4	1,300	120	480	0.86	2.61
5	1,560	120	600	0.9	3.51
6	1,820	120	720	1.1	4.61
7	2,080	120	840	1.09	5.7
8	2,340	120	960	1.46	7.16
9	2,600	120	1,080	1.8	8.96
10	2,080	60	1,140	−0.31	8.65
11	1,560	60	1,200	−0.46	8.19
12	1,040	60	1,260	−0.87	7.32
13	520	60	1,320	−1.19	6.13
14	0	180	1,500	−2.22	3.91

TABLE 4 Test results of the No. 3 pile.

No.	Load (kN)	Duration (min)		Settlement (mm)	
		Current	Total	Current	Total
0	0	0	0	0	0
1	520	120	120	0.3	0.3
2	780	120	240	0.25	0.55
3	1,040	120	360	0.43	0.98
4	1,300	120	480	0.68	1.66
5	1,560	150	630	1.13	2.79
6	1,820	120	750	1.86	4.65
7	2,080	150	900	2.79	7.44
8	2,340	120	1,020	4.74	12.18
9	2,600	150	1,170	6.99	19.17
10	2,080	60	1,230	−0.25	18.92
11	1,560	60	1,290	−0.97	17.95
12	1,040	60	1,350	−1.03	16.92
13	520	60	1,410	−1.22	15.7
14	0	180	1,590	−2.18	13.52

α—Reduction factor of bearing capacity of natural foundation soil at the pile end of the SDCM pile

q_{pa}—End resistance of the SDCM pile (kPa)

A_p—The cross − sectional area of the SDCM pile (m^2)

TABLE 5 Test results of the No. 8 pile.

No.	Load (kN)	Duration (min)		Settlement (mm)	
		Current	Total	Current	Total
0	0	0	0	0	0
1	520	120	120	1.12	1.12
2	780	120	240	1.21	2.33
3	1,040	120	360	1.49	3.82
4	1,300	120	480	1.74	5.56
5	1,560	120	600	1.98	7.54
6	1,820	120	720	1.8	9.34
7	2,080	120	840	1.67	11.01
8	2,340	120	960	1.77	12.78
9	2,600	150	1,110	2.44	15.22
10	2,080	60	1,170	−0.15	15.07
11	1,560	60	1,230	−0.26	14.81
12	1,040	60	1,290	−0.48	14.33
13	520	60	1,350	−0.7	13.63
14	0	180	1,530	−1.36	12.27

We take the smaller value of the abovementioned two; that is, the characteristic value of the bearing capacity of the test pile calculated by the code method is 2,460 kN, which is greater than 2,300 kN. This test also directly verified that the piles do not fail when the characteristic value is 2,300 kN, which indirectly explained the rationality of 2,460 kN. For the sake of safety in actual engineering, the characteristic value of the bearing capacity of the SDCM pile foundation pile can be taken as 2,300 kN.

5.2 Economic comparison

Compared with the traditional CFG pile, the SDCM pile is used. Combined with the actual project on which this test is based, the base pressure of the SDCM pile is 490 kPa/m^2, and the basement area is temporarily 1,200 m^2. The upper load is 588,000 kN, the characteristic bearing capacity value of a single pile is 2,300 kN, and the actual pile layout is 588,000/2,300 = 256. The actual number of piles should be more than 256 according to the floor area and pile spacing, the pile spacing is 2.1 m by 2.1 m, the single pile treatment area is 4.41 m^2, and the foundation bottom area is 1,200 m^2, 1,200/4.41 = 272. The length of the strength composite pile is 9 m, totally 2,448 m, and the comprehensive price per meter is 560 yuan (including all material costs, labor and machinery costs, empty pile fees, electricity costs, value-added tax, pile inspection fees, and pile head cutting costs). The final cost of the SDCM pile is 560 by 2,448, that is, 1.3708 million Yuan.

If CFG piles were used, the base area is 1,200 m^2, the pile spacing is 1.2 by 1.2 = 1.44 m^2, 1,200/1.44 = 833 (roots), the single pile length is 19 + 0.5 = 19.5 m, the total pile length is 19.5 by 833 = 16,243 m, the unit price is 139 Yuan/m (including C25 concrete, labor, machinery,

FIGURE 4
Construction photos of the *in situ* test.

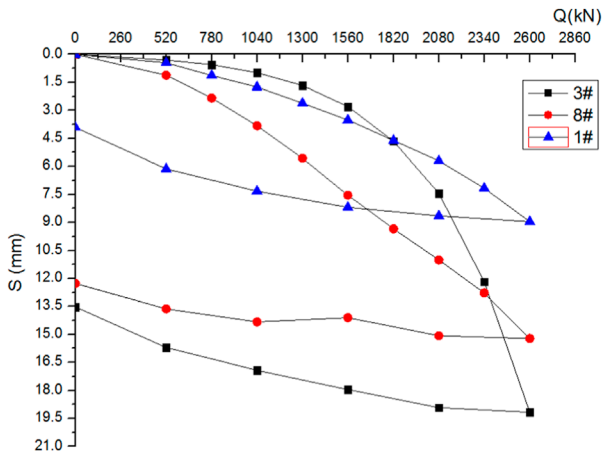

FIGURE 5
Q_s curves of test piles 1#, 3#, and 8#.

TABLE 6 Statistical table of vertical compressive static load test.

No.	Time (days)	Max. load (kN)	Max. settlement (mm)	Rebound amount (mm)	Rebound rate (%)	Characteristic value of bearing capacity (kN)
1#	21	2,600	8.96	5.05	56.36	≥1,300
3#	21		19.17	5.65	29.47	
8#	21		15.22	2.95	19.38	

electricity, value-added tax, pile inspection fee, and pile head cutting costs), the construction cost is 16,243 by 139 = 2.2577 million Yuan, and cancel cushion is 1,200 by 0.2 = 240 cubic meters (sand and gravel), 350 Yuan/m^3, which is 84,000 Yuan in total. The final cost of CFG piles is 2.2577 + 8.4 = 2.3417 million Yuan.

In summary, the core composite pile is 1.378 million Yuan, the CFG pile is 2.3417 million Yuan, and the pile foundation can save 960,000 Yuan in cost; that is, the SDCM pile saves 41% of cost.

In addition, for CFG piles, because the upper part of the pile length is in the fine sand layer and the lower part is in the clay layer during construction, the quality of the pile body is not easy to control, and the pile may have shrinkage and mud inclusions. Since the pile distance is only 1.2 m, it is necessary to take jump driving, it is difficult to remove the soil at the pile position for the second time, and the pile position is not easy to control. During the construction of the CFG pile, a large amount of sediment is displaced, limited by the control of dust, and it is difficult to transport outside, which affects the construction period, especially in the rainy season, and construction in the foundation pit, as the supply of concrete is not timely. Due to air pollution, the mixing station cannot guarantee the continuous supply of concrete, resulting in repeated stoppage of drilling, broken piles, and waste of concrete. We can easily control the quality using the SDCM pile, and the quality of the finished PHC pipe piles is guaranteed. The construction period is short, no soil is unearthed, and it is not restricted by the environment. After the strength of composite piles is processed, the length of the piles can be guaranteed to enter the fine sand layer.

6 Conclusion

Taking the silt and sandy soil of Huanghuai alluvial strata as the research background, this study carried out an *in situ* test on the SDCM pile based on the PHC pile, and the results are as follows:

(1) The SDCM pile based on the PHC pile with a length of 8.0 m can provide the characteristic value of bearing capacity of 2,300 kN, which can meet the vertical load requirements of general high-rise buildings.
(2) The SDCM pile has high promotion value in similar sites. The construction quality of the outer core has a significant effect on the bearing capacity of the SDCM pile. The construction quality should be strictly controlled.
(3) Compared with the CFG pile, the SDCM pile has the advantages of high strength, guaranteed construction quality, large bearing capacity, and good economy.

Data availability statement

The original contributions presented in the study are included in the article/Supplementary Material, further inquiries can be directed to the corresponding author.

Author contributions

ZM contributed to the conception of the study; TF, ZH, and DF performed the experiment; and CS and LF contributed significantly to analysis and manuscript preparation. All authors contributed to the article and approved the submitted version.

Funding

The authors are grateful for the financial support from the Henan Province Science and Technology Research Project (No. 222102320137), Henan Province Housing and Urban–Rural Construction Science and Technology Project (No. HNJS-2020-k25), and Post-doctoral Research Project (2022M721046).

Conflict of interest

Authors TF, DF, CS, and LF were employed by The Seventh Engineering Co., Ltd., of CFHEC; ZH was employed by the Zhongyun International Engineering Co., Ltd.

The remaining author declares that the research was conducted in the absence of any commercial or financial relationships that could be construed as a potential conflict of interest.

Publisher's note

All claims expressed in this article are solely those of the authors and do not necessarily represent those of their affiliated organizations, or those of the publisher, the editors, and the reviewers. Any product that may be evaluated in this article, or claim that may be made by its manufacturer, is not guaranteed or endorsed by the publisher.

References

Bai, B., Fan, B., Nie, Q., and Jia, X. (2023). A high-strength red mud–fly ash geopolymer and the implications of curing temperature. *Powder Technol.* 416, 118242. doi:10.1016/j.powtec.2023.118242

Bai, B., Zhou, R., Cai, G., Hu, W., and Yang, G. (2021). Coupled thermo-hydro-mechanical mechanism in view of the soil particle rearrangement of granular thermodynamics. *Comput. Geotechnics* 137 (8), 104272. doi:10.1016/j.compgeo.2021.104272

Cheng, J. (2021). *Research on the effect of compaction and expansion of cement-soil strength composite piles[D]*. Taiyuan: North University of China.

Ding, Y., Li, J., and Hui, L. (2005). Development status of stiff mixing pile[J]. *Low. Temp. Archit.* (6), 100–101.

Gao, X. N., Liu, S. Y., and Dong, P. (2012). "Application of concrete-cored DCM pile in soft ground treatment of highway bridgehead[C]". In Proceeding of the Fourth International Conference on Grouting and Deep Mixing, New Orleans.

Jamsawang, P., Bergado, D. T., and Voottipruex, P. (2010). Field behaviour of stiffened deep cement mixing piles. *Proc. ICE-Ground Improv.* 164 (1), 33–49. doi:10.1680/grim.900027

Lu, J. (2016). *Analysis of bearing capacity of stiff composite pile [D]*. Hefei: Hefei University of Technology.

Peng, B., Xinliang, J., and Guilin, S. (2007). Static and dynamic analysis of bearing performance of stiffened mixing pile composite foundation[J]. *Rock Soil Mech.* 1, 63–68+82. doi:10.16285/j.rsm.2007.01.012

Phutthananon, C., Jongpradist, P., Yensri, P., and Jamsawang, P. (2018). Dependence of ultimate bearing capacity and failure behavior of T-shaped deep cement mixing piles on enlarged cap shape and pile strength. *Comput. Geotechnics* 97, 27–41. doi:10.1016/j.compgeo.2017.12.013

Voottipruex, P., Bergado, D. T., Suksawat, T., Jamsawang, P., and Cheang, W. (2011). Behavior and simulation of deep cement mixing (DCM) and stiffened deep cement mixing (SDCM) piles under full scale loading. *Soils Found.* 51 (2), 307–320. doi:10.3208/sandf.51.307

Voottipruex, P., Taweephong, S., Bergado, D. T., and Jamsawang, P. (2010). Numerical simulations and parametric study of SDCM and DCM piles under full scale axial and lateral loads. *Comput. Geotechnics* 38 (3), 318–329. doi:10.1016/j.compgeo.2010.11.006

Wang, A. H., Zhang, D. W., and Deng, Y. G. (2018). A simplified approach for axial response of single precast concrete piles in cement-treated soil. *Int. J. Civ. Eng.* 16 (10), 1491–1501. doi:10.1007/s40999-018-0341-9

Wang, C., Xu, Y., and Dong, P. (2014). Working characteristics of concrete-cored deep cement mixing piles under embankments. *J. Zhejiang Univ. Sci. A* 15 (6), 419–431. doi:10.1631/jzus.a1400009

Wang, C., Xu, Y., and Pang, J. (2013). Field test research on concrete core cement-soil mixing pile composite foundation under embankment load[J]. *Chin. J. Geotech. Eng.* 35 (5), 974–979.

Wang, M. (2020). *Experimental research on vertical bearing capacity of cement-soil composite pipe pile based on B0TDR distributed optical fiber sensing technology [D]*. Taiyuan: North University of China.

Wonglert, A., and Jongpradist, P. (2015). Impact of reinforced core on performance and failure behavior of stiffened deep cement mixing piles. *Comput. Geotechnics* 69, 93–104. doi:10.1016/j.compgeo.2015.05.003

Wonglert, A., Jongpradist, P., Jamsawang, P., and Larsson, S. (2018). Bearing capacity and failure behaviors of floating stiffened deep cement mixing columns under axial load. *Soils Found.* 58 (2), 446–461. doi:10.1016/j.sandf.2018.02.012

Yang, Y. (2019). *Research on bearing characteristics of composite piles based on stiff bodies in typical strata in guangxi[D]*. Guizhou: Guangxi University.

Ye, G., Cai, Y., and Deng, Y. (2014). "Numerical analysis of stress and deformation characteristics of cored cement-soil piles[C]", In Proceedings of the 13th National Academic Discussion Conference on Foundation Treatment. Xi'an, 3–8.

Zhu, Z. (2021). *Research on the working characteristics of composite foundation with stiff composite pile [D]*. Yangzhou: Yangzhou university.

frontiers | Frontiers in Materials

TYPE Original Research
PUBLISHED 15 September 2023
DOI 10.3389/fmats.2023.1270865

OPEN ACCESS

EDITED BY
Bing Bai,
Beijing Jiaotong University, China

REVIEWED BY
Chen Peipei,
Beijing University of Civil Engineering and Architecture, China
Yang Gaosheng,
Shanxi Agricultural University, China

*CORRESPONDENCE
Huawei Tong,
faiychen@gzhu.edu.cn

RECEIVED 01 August 2023
ACCEPTED 05 September 2023
PUBLISHED 15 September 2023

CITATION
Chen J, Yuan J, Tong H, Fang Y and Gu R (2023), Mechanism study on the soil mechanical behavior of the mixed soil based on energy multi-scale method. *Front. Mater.* 10:1270865. doi: 10.3389/fmats.2023.1270865

Mechanism study on the soil mechanical behavior of the mixed soil based on energy multi-scale method

Jian Chen[1,2], Jie Yuan[1], Huawei Tong[1]*, Yingguang Fang[3] and Renguo Gu[3]

[1]School of Civil Engineering, Guangzhou University, Guangzhou, China, [2]School of Railway Engineering, Guangzhou Railway Polytechnic, Guangzhou, China, [3]South China University of Technology, Guangzhou, China

The presence of mixed soil is widespread in nature, rendering it susceptible to geological hazards such as landslides, liquefaction, and debris flows. This soil type displays pronounced structural anisotropy due to its diverse mineral composition and the broad range of particle sizes it encompasses across multiple geometric scales. However, there exists an array of conflicting research outcomes concerning the impact of particle composition, size, and content on the mechanical properties of mixed soil. This study delves into the mechanical behavior of mixed soil across varying particle contents and sizes using direct shear testing. Subsequently, the distinctive mechanical responses are dissected by scrutinizing the interplay of particle contact interfaces. Concurrently, the underlying mechanism behind this behavior is explored by examining particle surface adsorption energy through a multi-energy scale approach. In conclusion, the following findings are established: 1) The influence of fine particle content (FC) on mixed soil strength varies according to distinct filling conditions; 2) The contribution to mixed soil strength differs among particles with distinct mineral components; 3) Sand particle size within mixed soil holds no sway over its strength under equivalent mass conditions; 4) The particle surface energy equation derived from the multi-energy scale technique comprehensively elucidates the interplay between particle composition, content, and mechanical behavior in mixed soil.

KEYWORDS

mixed soil, energy multi-scale method, direct shear test, mechanical behavior, contact interface, microstructure, adsorbed water, microscopic forces

1 Introduction

Mixed soil, found extensively in natural contexts such as weathered mountain slopes, alluvial deposits, sea-land interactions, and tailings, holds significant relevance for both human life and engineering endeavors. Within mixed soil, the presence of fine particles interspersed among coarser particles, with distinct geometric scales and mineral compositions, results in complex particle-to-particle contact interfaces. This intricate arrangement contributes to the conspicuous anisotropy characterizing the soil's structure. Disturbingly, the collapse of mixed soil readily triggers substantial deformations and gives rise to geological hazards, including landslides, liquefaction, and mudslides, as illustrated in Figure 1. Notably, research underscores the substantial mechanical divergence between mixed soil and pure sand or clay (Yamamuro and Lade,

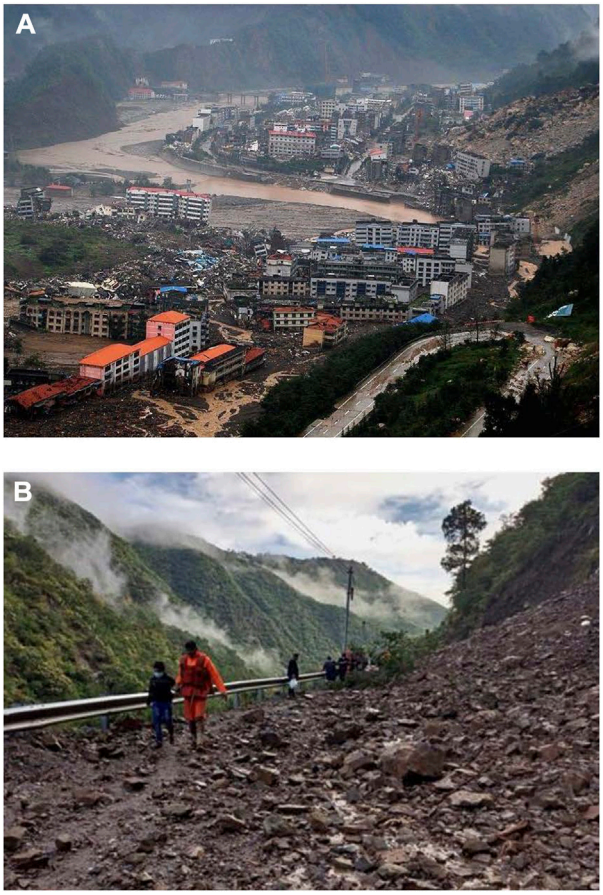

FIGURE 1
Instances of geological hazards in mixed soil. **(A)** Landslides and mudslides post Wenchuan earthquake; **(B)** Landslides induced by rainstorms in East Akhand, India.

1998; Bobei and Lo, 2009; Ke and Chen, 2019; Wei and Yang, 2019; Porcino and Diano, 2020; Bai et al., 2021). To elucidate these differential behaviors, scholars have extensively investigated factors encompassing fine particle content (FC), particle physical attributes, and internal soil structure.

Foremost among these factors, the influence of FC on mixed soil properties garnered early attention. Troncoso and Verdugo (1985) executed cyclic shear tests on tailings with varying mass proportions of silt, showcasing decreased cyclic shear strength with rising silt content. However, Amini and Qi (2000) demonstrated enhanced cyclic resistance in fine-grained sandy soil as FC increased, based on triaxial experiments. Conversely, Polito and Martin (2001) reported an initial decrease followed by an increase in liquefaction resistance with fine-grained sandy soil's FC. Examining the anisotropic effect of sand-silt mixtures, Bahadori and Ghalandarzadeh et al. (2008) identified a trend of decreasing and then increasing anisotropy with silt content. Carraro and Prezzi. (2009) noted variations in critical state friction angle and peak stress of sandy soil due to FC changes, differing based on the properties of the fines. Krim and Arab. (2017) linked reduced liquefaction resistance to increased clay content. Porcino and Diano et al. (2020) established that, upon reaching a threshold fines content at constant porosity, a more contractive behavior emerged, with heightened strain softening as fines content increased. Monkul and Kendir. (2021) documented two tendencies: cyclic resistance ratio (CRR) initially increased and then decreased for small FC values (approximately 5%–10%) within the studied range (FC ≤ 35%); CRR consistently diminished for FC values up to 35%. Li and Liu, (2022) findings exhibited linear growth in cohesion, uniformity coefficient, and curvature coefficient with increasing FC, while friction angle declined. Zuo and Gu. (2023) found that a non-linear decrease in small-strain shear modulus accompanied FC increase to 30%, reaching nearly 50% of clean sand's modulus at maximum FC.

Beyond geometric size, the plasticity of fine particles holds significant sway over mixed soil strength (Lee and Seed, 1967). Carraro and Prezzi. (2009) highlighted elevated critical state friction angle and peak stress as silt content increased within mixed sand, with opposing trends observed for clay. Park and Kim (2013) demonstrated decreased dynamic strength in sand-clay mixtures of differing densities with higher clay plasticity indices. Monkul and Yamamuro (2011), as well as Monkul and Etminan. (2017), underscored the influence of fine particle shape on sandy soil liquefaction. Krim and Arab, (2017) associated both particle shape and FC with mixed soil liquefaction resistance. Zhu and Zhang, (2020) noted that larger particles generated occlusal structures, enhancing friction, while identical-sized sand particles were more prone to sliding. Monkul and Kendir et al. (2021) delineated coarse-fine contacts' impact on overall stress-strain behavior, with fines creating substructures between coarser grains. Chang and Yin et al. (2010) conceived soil as a particle aggregate, where all-direction particle contact dictated stress-strain correlation. Gong and Nie, (2019) quantified different contact types' contributions to residual shear strength, including coordination number and normal contact force. Phan and Bui, (2021) attributed mixed soil shear resistance to particle contact type and proportion, emphasizing fine powder's role in altering sand properties. Allahyari and Maleki (2022) affirmed relative density and confining pressure's substantial impact on maximum shear modulus.

In the domain of FC, fine particles within the 0%–8% range were found to stabilize anisotropic structures and enhance stiffness anisotropy (Gao and Wang, 2015). Sabbar and Chegenizadeh (2017) posited that fine particles create a structure that narrows inter-particle pores, subsequently altering soil liquefaction resistance. Zhu and Zhang (2020) observed larger particles forming occlusal structures, providing greater friction, while particles of uniform size were more susceptible to sliding. Monkul and Kendir et al. (2021) highlighted the role of coarse-fine contacts in shaping soil's stress-strain behavior. Chang and Yin, (2010) regarded soil as an aggregate, where particle contacts in all directions dictated stress-strain relationships. Gong and Nie, (2019) established varying contributions of contact types to residual shear strength, encompassing coordination number and normal contact force. Phan and Bui, (2021) attributed mixed soil shear resistance to particle contact type and proportion, emphasizing fine powder's role in altering sand properties. Allahyari and Maleki (2022) affirmed relative density and confining pressure's substantial impact on maximum shear modulus.

Mixed soil, being a confluence of varying particle sizes and mineral compositions, exhibits mechanical behavior significantly influenced by particle geometry, mineral composition, and content.

TABLE 1 The basic information of the experimental materials.

Object	Average diameter (mm)	Specific gravity	Plastic limit	Liquid limit	Plasticity index	Minerals
Bentonite	0.015	2.53	48%	213.50%	165.5	Quartz 0.8%, cristobalite 0.39%, Montmorillonite 91.7%, clinoptilolite 1.7%, Sodalite 2.0%
Quartz sand	0.5,0.7,0.9,1.5	2.63	--	-	--	--

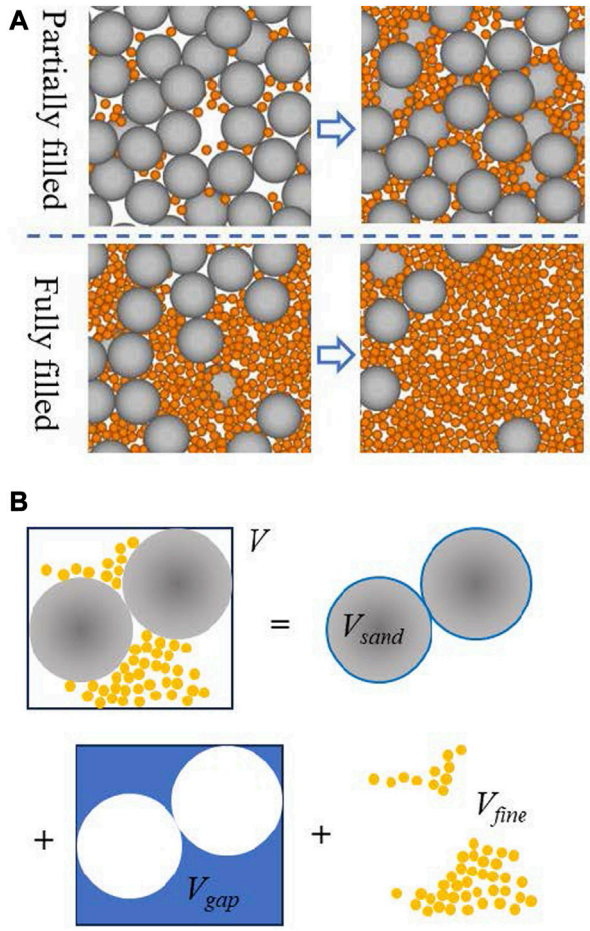

FIGURE 2
Schematic diagram of sample preparation method. **(A)** Schematic representation of fabric cases; **(B)** Schematic diagram of sample method.

FIGURE 3
Test on the mechanical behavior of mixed soil. **(A)** Sample of mixed soil; **(B)** Experimental instrument.

Prior research has provided insight into certain aspects of this behavior via internal structure analysis. However, the precise mechanisms remain unclear, resulting in conflicting findings across mixed soil studies. Given these challenges, this paper endeavors to dissect the mechanical behavior of diverse mixed soil samples via experimentation. The ensuing analysis encompasses FC, particle composition, and size, scrutinizing their contribution to microstructural deformation and particle interface properties. Subsequently, utilizing an energy scale approach, the paper delves into the mechanism behind this behavior at the micro-level, particularly focusing on particle surface energy and contact interfaces. This comprehensive approach aims to draw valuable conclusions from the investigation.

2 Experimental investigation of mechanical behavior in mixed soil

2.1 Test configuration

In this experimental study, we systematically investigate how various factors, including particle size, mineral composition, and particle content, influence the mechanical behavior of mixed soil.

TABLE 2 Sample preparation plan and experimental plan.

No.	M_{sand}(g)	V_{sand} (cm^3)	$M_{wet\ fines}$(g)	$V_{wet\ fines}$ (cm^3)	CF (%)	Vertical load	d_{sand}
ZJ-03V	91.90	34.55	12.79	7.63	0.13	100kPa, 150kPa, 200kPa, 250kPa	0.5 mm, 0.7 mm, 0.9 mm, 1.5 mm.
ZJ-04V	91.90	34.55	17.05	10.18	0.17		
ZJ-05V	91.90	34.55	21.31	12.72	0.21		
ZJ-06V	91.90	34.55	25.58	15.26	0.25		
ZJ-07V	91.90	34.55	29.84	17.81	0.30		
ZJ-08V	91.90	34.55	34.10	20.35	0.34		
ZJ-1M	91.90	34.55	40.95	24.44	0.41		
ZJ-09M	82.71	31.09	48.42	28.90	0.48		
ZJ-08M	73.52	27.64	54.21	32.35	0.54		
ZJ-07M	64.33	24.18	59.99	35.81	0.60		
ZJ-06M	55.14	20.73	65.78	39.26	0.65		
ZJ-03M	27.57	10.36	83.15	49.63	0.83		

Our experimental setup involves quartz sand as the coarse-grained component and wet bentonite powder as the fine-grained component. The quartz sand was screened using sieves with pore sizes of 0.4 mm–0.6 mm, 0.6 mm–0.8 mm, 0.8 mm–1.0 mm, and 1.0 mm–2.0 mm, respectively. So, the average diameters of the quartz sand particles are 0.5 mm, 0.7 mm, 0.9 mm, and 1.5 mm. Since bentonite is purchased commercially, its mineral composition was tested to ensure that the clay mineral content meets the requirements. Detailed information about these materials is provided in Table 1.

Figure 2A illustrates the two predominant states that can be observed in mixed soil samples: one in which there are sufficient fine particles to completely fill the gaps between coarse particles, resulting in minimal contact between the coarse grains, and another where there are enough coarse grains, causing the fine grains to partially fill the gaps. These states play a crucial role in determining the mechanical behavior of the soil (Yin and Zhao, 2014; De Frias Lopez and Silfwerbrand et al., 2016).

To investigate the mechanical behavior of mixed soil under different conditions as shown in Figure 2A, we prepare samples by carefully controlling the content of fine and sand particles. The sample preparation process is outlined in Figure 2B. Each sample is prepared within a ring knife with a diameter of 6.18 cm and a height of 2 cm, as depicted in Figure 3. The volume of the ring knife is denoted as V.

The sample preparation process proceeds as follows:

1. Calculate the mass (M_{0sand}) and volume (V_{0sand}) of the sand in the ring knife based on the natural bulk density of the sand.
2. Determine the gap volume (V_{gap}) between the sand particles.
3. Gradually fill the gaps by controlling the volume of fine particles (V_{fine}), such as V_{fine} = 0.3Vgap, V_{fine} = 0.4V_{gap}, V_{fine} = 0.5V_{gap}, and so on, until the gaps are fully filled.
4. Gradually reduce the sand content in the mixed soil by controlling the quality of sand particles (M_{sand} = 0.9M_{0sand}, M_{sand} = 0.8M_{0sand}, M_{sand} = 0.7M_{0sand}, and so on), while the remaining volume is filled with fines.

The sample preparation plan for mixed soil with varying particle sizes and fine content is detailed in Table 2. This article focuses on the contact interface between particles in mixed soil. Compared to the mass fraction, the volume fraction can better represent the number of contact surfaces between sand particles and fine particles. So, the fine particle content (FC) in this study is expressed as a volume ratio (V_{fine}/V).

Considering the inherent water content of soil in its natural state, and the characteristics of the particle surface of bentonite are gradually displayed after absorbing water, so the fine particles in this article are bentonite with a certain water content. The research focus of this article is on the effects of content, particle size, and mineral composition on the contact interface between particles. Therefore, there is not much discussion on the water content of fine particles. However, considering the feasibility of sample preparation and the role of fine particle surface, this experiment chooses a water content of 50% for fine particles. Bentonite is prone to swelling and agglomeration after absorbing water, which can affect sample preparation. To eliminate these effects, this experiment adopts the unsaturated sample preparation method. Firstly, add 47% water to the dry bentonite and stir evenly. Then, seal and let the bentonite fully absorb water and expand. Then, use a 1–2 mm sieve to screen out small moist particles and test the water content. Based on the water content tested, spray a certain amount of water to reach 50% of the water content, and let it sit overnight.

Subsequently blending the prepared fines uniformly with sand according to predetermined proportions. Subsequently, the mixture is compacted within a ring knife using a consistent striking method, ensuring uniform energy application for each strike. An illustration of the prepared sample is presented in Figure 3A. Following the preparation of samples, they are carefully enclosed with plastic wrap alongside the ring knife. These wrapped samples are then placed within a controlled environment with constant temperature and humidity conditions, allowing them to stand undisturbed for a duration of 24 h. This resting period facilitates the establishment of a stable soil state within the samples.

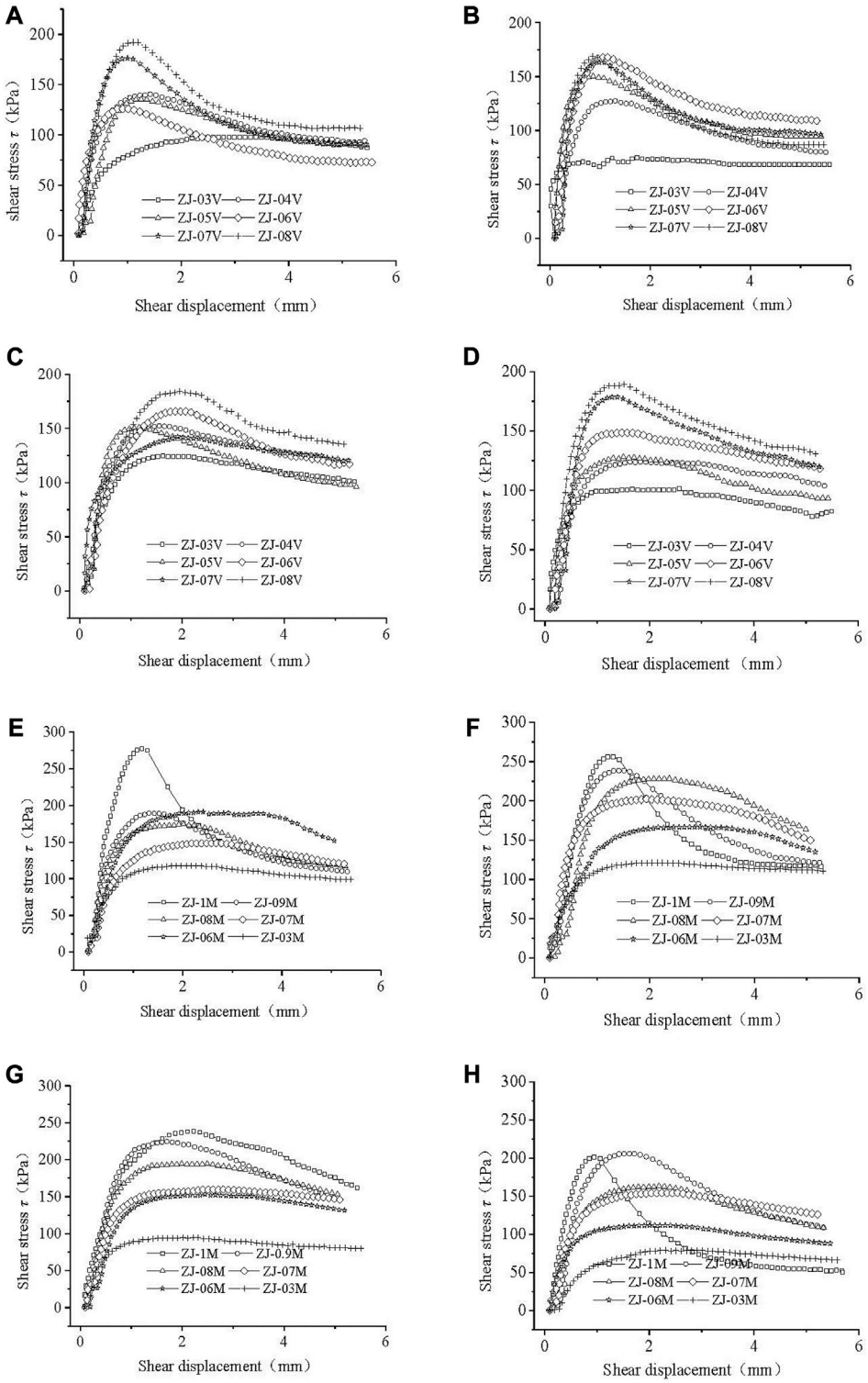

FIGURE 4
Relationships between shear stress and shear displacement of mixed soil samples (p = 150 kPa). **(A)** D_{sand} = 0.5 mm; **(B)** D_{sand} = 0.7 mm; **(C)** D_{sand} = 0.9 mm; **(D)** D_{sand} = 1.5 mm; **(E)** D_{sand} = 0.5 mm; **(F)** D_{sand} = 0.7 mm; **(G)** D_{sand} = 0.9 mm; **(H)** D_{sand} = 1.5 mm.

Subsequent to the resting period, the samples undergo direct shear testing in accordance with the specifications outlined in Table 2. The experimental apparatus employed for the direct shear tests is the strain-controlled direct shear instrument, as depicted in Figure 3B. Throughout the direct shear experiments, the vertical load is consistently controlled at values of p = 100kPa, p = 150kPa, p = 200kPa, and p = 250kPa, while the shear rate remains maintained at 0.8 mm/s. It is essential to highlight that both

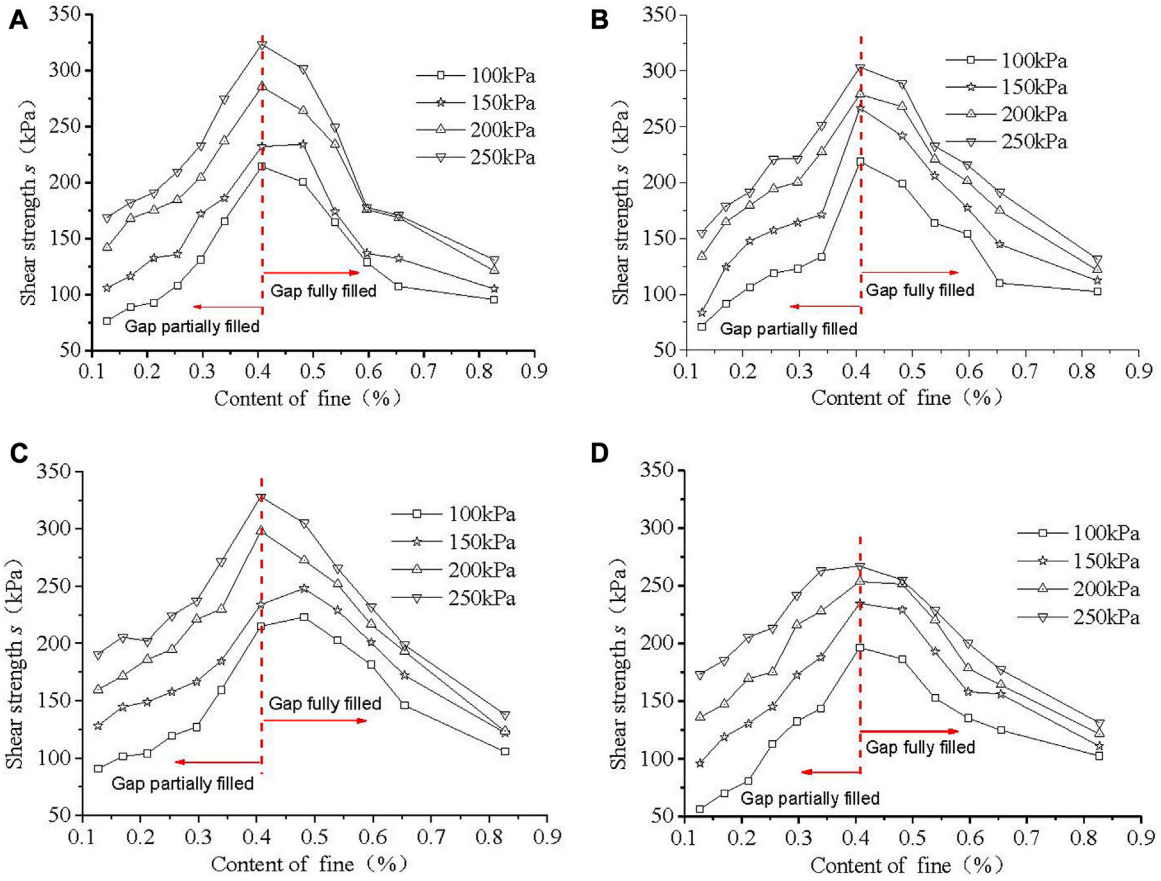

FIGURE 5
Shear strength of the sample with different FC. **(A)** D_{sand} = 0.5 mm; **(B)** D_{sand} = 0.7 mm; **(C)** D_{sand} = 0.9 mm; **(D)** D_{sand} = 1.5 mm.

the sample preparation and the execution of the direct shear tests are carried out meticulously in adherence to relevant standards (ASTM: D420 – D5876/D5876m), ensuring the accuracy and reliability of the results obtained.

2.2 Test results

(1) Relationship between shear stress and shear displacement

The interplay between shear stress and shear displacement provides insights into various soil properties during the shearing process. Due to the extensive range of experimental groups, only samples subjected to a vertical pressure of p = 150 kPa are illustrated in Figure 4. From Figure 4, it can be seen that most specimens exhibit strain softening phenomenon during the shear process. The shear stress-shear displacement curves for these samples highlight a general trend of initial increase followed by decrease, with the rate of decrease gradually diminishing until the curve levels off.

Shear strength, a vital parameter, is characterized by peak shear stress as well as strength indices such as cohesive force (c) and friction angle (φ). Figure 5 presents the peak shear strength of samples with varying sand particle sizes and FC, obtained from the experiment.

Additionally, the shear strength indices, including cohesive force and friction angle, are depicted in Figure 6.

Figure 5 reveals a distinct pattern in the shear strength of soil mixtures concerning FC. An increase and subsequent decrease in shear strength is observed with varying FC values. Specifically, when the gaps between sand grains are partially filled, shear strength increases progressively with rising FC. However, after complete filling of these gaps, shear strength decreases as FC continues to increase. Furthermore, it is notable that under identical conditions, greater vertical pressures correspond to higher shear strengths in the soil.

2.3 Result analysis

The mechanical behavior of soil is intricately tied to the fundamental properties of particles and the resultant soil structure. For instance, the honeycomb structure formed by clay particles translates to elevated porosity and reduced engineering bearing capacity, while the densely packed arrangement of gravel and fine clay particles offers greater bearing capacity. In the context of mixed soil, the interplay between fine and coarse particles adheres to specific rules, yielding a diversity of structural configurations. The transmission of forces and coordination of deformations among soil

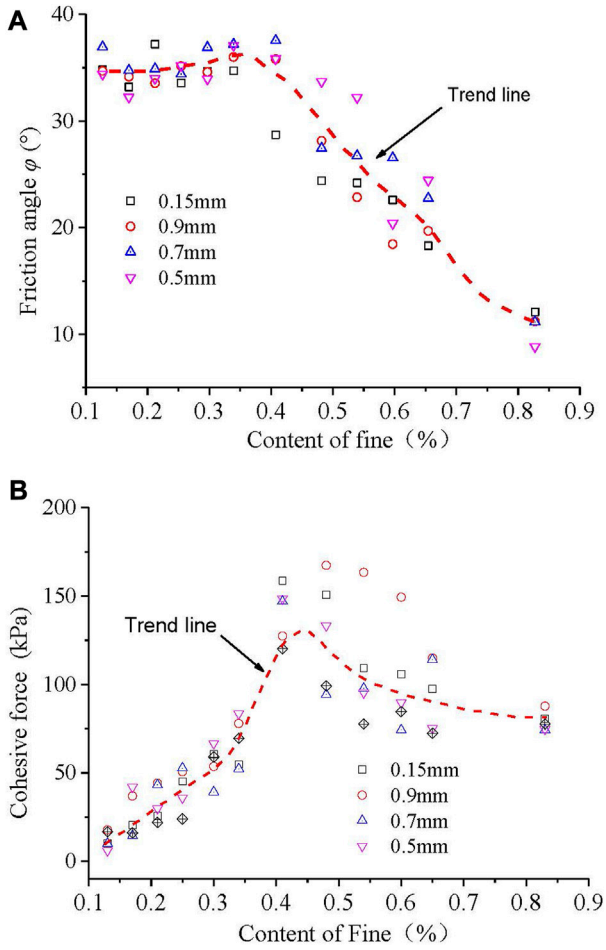

FIGURE 6
The cohesive force and friction angle of the sample with different sand diameters and FC. **(A)** Variation of friction angle of mixed soil; **(B)** Variation of the cohesive force of mixed soil.

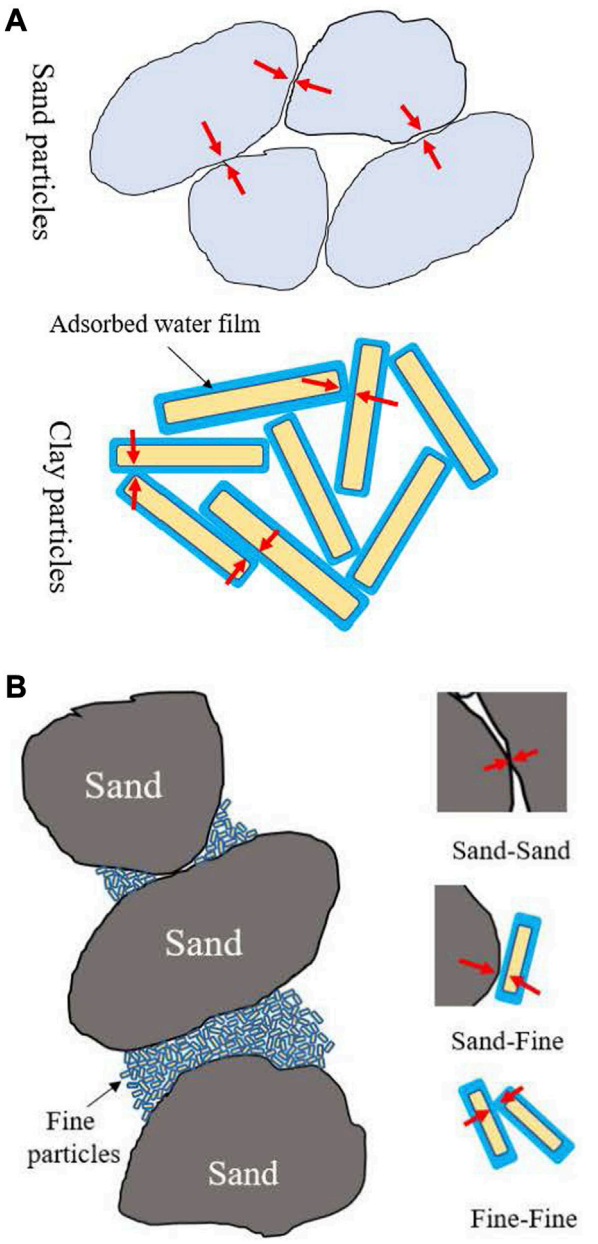

FIGURE 7
Contact interface of particles in mixed soil. **(A)** Surface and contact surface of different particles; **(B)** Mixed soil of clay fines with sands.

particles occur via contact interfaces. Concurrently, particle surface properties significantly influence soil structure formation. For instance, fine clay particles exhibit relatively thick water absorption films on their surfaces, facilitating the development of a honeycomb structure. In contrast, the electric double layer on sand and gravel particles' surfaces is notably thin, promoting denser structures.

Consequently, the outcomes of our conducted tests can be elucidated through the lens of particle contact interfaces within the microstructure of mixed soil. In the case of pure sand, the particle contact involves rigid interactions, leading to pronounced friction effects when particles undergo relative movement, as illustrated in Figure 7A. Conversely, pure clay particles possess thicker adsorbed water films on their surfaces, primarily resulting in soft particle contacts and generating cohesion effects during relative particle movement.

Mixed soil, comprised of larger sand particles and smaller clay particles, engenders intricate contact scenarios. Here, particle contacts are diverse, encompassing hard contacts between sand particles, soft contacts among fine particles, and hybrid contacts between sand and fine particles, as depicted in Figure 7B. This complex interplay contributes to the mixed soil's mechanical behavior.

In conclusion, the diverse mechanical behavior exhibited by mixed soil samples in our study is inherently tied to the intricate contact interfaces formed between particles within the microstructure. The interplay between hard, soft, and mixed contacts contributes to the complex behavior observed during shear testing.

(1) Shear Stress-Shear Displacement Relationship

In our experiment, the particles established a relatively stable structure due to the 24-h resting period post-compaction. During the initial stages of shear, when the displacement is minimal, particle

contacts undergo elastic deformation. Consequently, resistance between particles gradually escalates within the elastic range. With continued shear displacement, select sand contact points and fine particle surfaces begin exhibiting plastic deformation while preserving the initial contact structure. This phase is marked by increasing bearing capacity of contact surfaces.

As shear displacement further increases, the stable particle structure collapses, leading to disruption of force transfer platforms and heightened motion freedom for sand particles. This instability markedly reduces the bearing capacity. Consequently, the shear stress-shear displacement curve transitions from an increasing phase to a decreasing one. Subsequent to extensive particle displacement, the reduced motion space culminates in the formation of a new contact structure among particles. This fragile contact arrangement provides limited bearing capacity, leading to the plateau observed in the curve.

Furthermore, vertical pressure influences the contact structure within the mixed soil during shear. Greater vertical loads enhance soil compaction, thereby amplifying the contact area and strength between particles. This effect is evidenced by the overall increase in shear strength with heightened vertical pressure.

(2) Influence of Mineral Composition

The shearing process highlights distinct stress and deformation behaviors between sand and fine clay particles. Fine clay particles, possessing an extensive specific surface area and considerable negative surface charges, tend to develop thicker adsorbed water films. Consequently, contact between clay fines predominantly involves interactions between these water films, showcasing a pronounced cohesive effect. On the other hand, sand particles exhibit a smaller specific surface area, lower surface charge density, and minimal impact of adsorbed water films relative to their volume. Consequently, particle contacts within sand primarily entail direct interactions between quartz crystals, leading to pronounced frictional effects.

Throughout shear, relative displacement between fine clay particles results in cohesive force at contact surfaces. Meanwhile, rotational or translational displacement of sand particles triggers friction force among sand particles and cohesion force at the fine-sand interface. This combination of cohesive and frictional forces at contact interfaces contributes to the macroscopic cohesive and frictional bearing capacities of mixed soil. Notably, the cohesive bearing capacity increases with rising FC (Figure 6).

(3) Influence of Content

Content, whether fines or sands, significantly influences mixed soil shear strength. When gaps between sand particles are partially filled, contacts primarily involve hard interactions, leading to larger friction angles (Figure 6A). Gradual increments in fines content introduce new contacts between fine-fine and fine-sand particles, contributing to increased cohesive force. Consequently, shear strength experiences a gradual rise within a FC range of 0.13–0.41 (Figure 5).

Upon complete gap filling, contact between sand particles diminishes with decreasing sand content and increasing FC. This leads to decreasing friction angles. Surprisingly, cohesion force does not continue increasing with higher fines content; instead, it decreases. High sand content and saturated fines reduce sand movement freedom, invoking internal crystal cohesion. Subsequently, cohesion within mixed soil relies on fines-fines, fine-sand, and internal crystal cohesion of sand, resulting in high cohesion. As fines content rises, cohesion diminishes due to reduced fine-sand cohesion and internal crystal cohesion. Hence, shear strength decreases as FC increases (Figure 5).

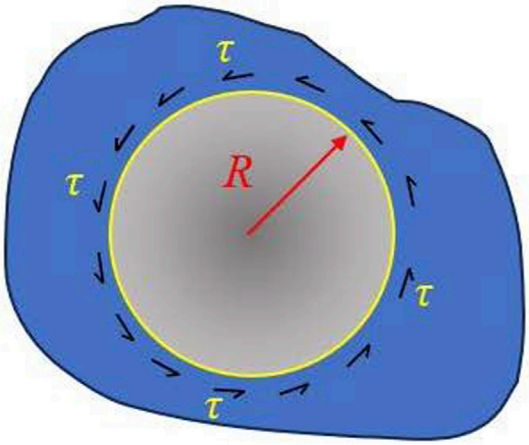

FIGURE 8
Schematic diagram of the rotational moment resistance of sand particles.

(4) Influence of Sand Particle Size

The experiment underscores the pivotal role of sand particle size. Sand particles mainly undergo rotational displacement during shear. Cohesive force exerted by fines generates shear stress on contact surfaces between sand and fines, restraining sand rotation and contributing to shear load capacity (Figure 8).

Assuming spherical particles with their centers as rotation centers, the anti-rotation moment exerted by fines on a single sand particle can be expressed as:

$$M = R \cdot S \cdot \tau \tag{1}$$

Where, R represents the particle radius, and S is the particle's surface area. For all particles, the collective anti-rotation moment of the particles becomes:

$$\sum M = \sum R \cdot S \cdot \tau = n \cdot \bar{R} \cdot S \cdot \tau \tag{2}$$

In the latter formula, $\bar{R}$ represents the average particle radius, n is the particle count which can be deduced from the total sand mass and the individual sand mass. This allows us to rewrite the formula as:

$$\sum M = \sum R \cdot S \cdot \tau = n \cdot \bar{R} \cdot S \cdot \tau = \frac{m}{\frac{4}{3}\pi \bar{R}^3 \rho} \cdot \bar{R} \cdot 4\pi \bar{R}^2 \cdot \tau = \frac{m\tau}{3\rho} \tag{3}$$

Within formula (3), m denotes the sand mass, and ρ signifies the sand density. The derivation of this equation underscores that, as

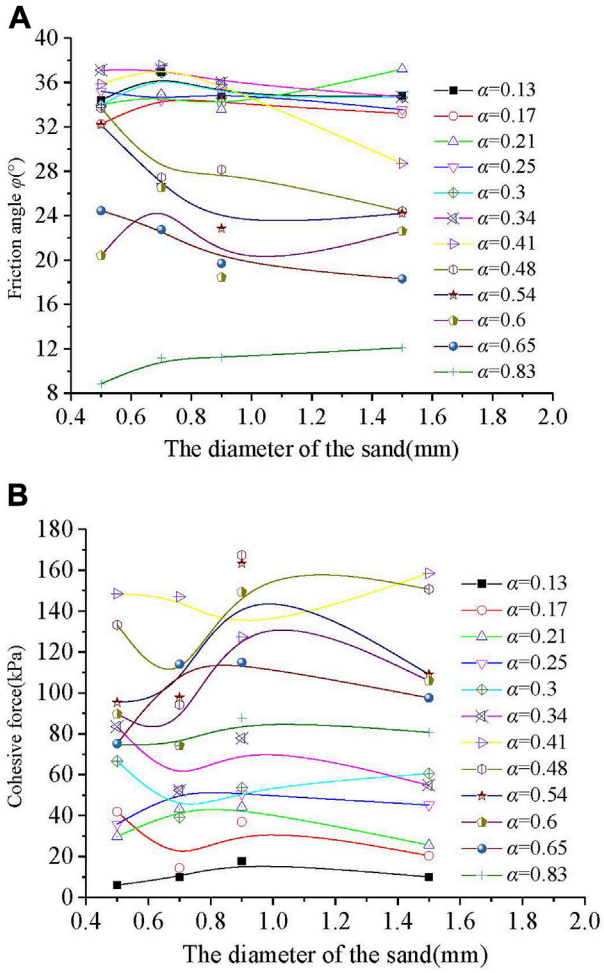

FIGURE 9
Influence of sand particle size on friction angle and cohesive force of mixed soil. **(A)** Particle size-friction angle; **(B)** Particle size-cohesive force.

long as the total sand mass in the mixed soil remains constant, sand particle size does not influence the mixed soil's shear strength.

In our experiment, Figure 9 illustrates the relationship between the shear strength indices of samples and the diameters of sand particles. The graph showcases varied trends, including decreasing strength indices with larger particle sizes, increasing indices, and inconsistent trends. Eq. 5 would suggest a linear relationship, but several factors could contribute to the observed deviation. Since the calculation formula simplifies particle shapes to standard spheres, real-world particle encapsulation by fines might not be guaranteed. This could potentially explain the lack of a consistent pattern in the curves within Figure 9.

3 Discussion on mechanism of mixed soil mechanics using multi-scale method

The previous analysis has demonstrated that factors such as particle composition, particle content, and other variables influence the mechanical properties of mixed soil through the contact interfaces between particles. However, a more detailed mechanism requires further exploration. In the realm of metals and nanomaterials, changes in particle size can alter surface properties, subsequently impacting the state of particle contact interfaces. The particles in mixed soil encompass a range of sizes, spanning multiple scales. As particle size diminishes, specific surface area and the ratio of fractured crystal bonds increase. Consequently, surface charges and adsorption energy on particle surfaces rise, resulting in more pronounced adsorbed water films. This phenomenon, in turn, affects the contact surfaces between particles. Simultaneously, the diverse mineral composition of particles in mixed soil contributes to distinct characteristics. Under the same particle size, clay particles exhibit considerably higher surface charge than non-clay particles, and the relative thickness of adsorbed water on clay particle surfaces exceeds that of non-clay particles. Consequently, contact interfaces between clay particles largely involve water film interactions, while contact interfaces between sand particles primarily constitute mineral crystal interactions. Evidently, the properties of particle surfaces and interfaces within mixed soil correlate with the relative thickness of adsorbed water films on particle surfaces. Moreover, this thickness is directly associated with the particle surface's adsorption capacity.

Chen and Tong, (2023) explored how clay particles possess heightened electric field forces, whereas sand particles exhibit stronger van der Waals forces. Leveraging these insights within an energy multi-scale framework (Chen and Tong, 2023), the current study adopts van der Waals and electric field forces to represent particle friction and adsorption energies, respectively. This is encapsulated in the following equations:

$$F = \alpha(F_e + F_w)_B + \beta(F_e + F_w)_S \tag{4}$$

Here, F denotes particle microforces, Fe signifies Coulomb force, Fw represents van der Waals force, B designates bentonite (fines), and S stands for sand. Concretely:

$$F_e = \frac{1}{4\pi\varepsilon_0}\frac{q_1 q_2}{r^2}; G = \rho g V = \rho g \pi d^3/6; F_w = \frac{Ad}{24H^2} \tag{5}$$

Within the above equation, represents vacuum permittivity, q1 and q2 denote particle charge, r signifies particle center distance, ρ indicates particle density, d represents particle diameter, A corresponds to the Hamaker constant, and H stands for particle net distance. Specific parameter values can be extracted from pertinent literature (Chen and Tong, 2023), with microforces calculated for all samples. The computed outcomes, alongside shear strength derived from testing, are visually depicted in Figure 10.

Figure 10 unmistakably illustrates the consistent relationship between particle force F and fines content, mirroring the effect of fines content on mixed soil shear strength. This congruence substantiates the employment of particle microforces as a plausible explanation for the mechanical behavior of mixed soils.

4 Conclusion

In this paper, the analysis of the mechanical behavior of mixed soil is conducted through direct shear experiments. The initial explanation of the mixed soil's mechanical behavior is provided

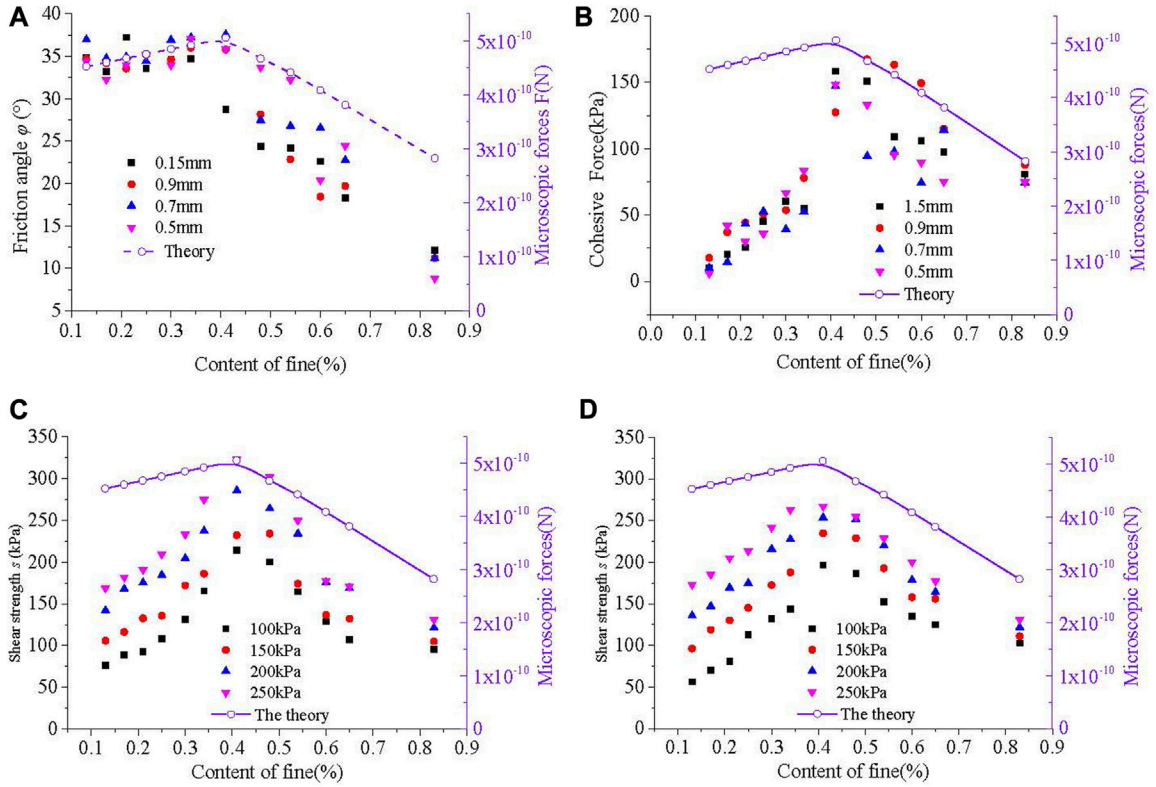

FIGURE 10
Variation of microscopic forces and shear strength with fines content. **(A)** The microscopic forces *F*-friction angle φ; **(B)** The microscopic forces *F*-cohesive force *c*; **(C)** The microscopic forces *F* -shear strength *s* (*d* = 0.5 mm); **(D)** The microscopic forces *F* -shear strength *s* (*d* = 1.5 mm).

by considering the contact surfaces between particles. Subsequently, the discussion delves into the mechanics through the lens of microscopic adsorption energy of particles. This comprehensive research leads to the formulation of four primary conclusions:

(1) Effect of Fine Particle Content: The strength of mixed soil is influenced differently by the content of fine particles under various filling states. When the gap between particles is partially filled, increasing the fine particle content enhances the strength of the mixed soil. However, when the gap is completely filled by fines, an increase in fine particle content leads to a gradual decrease in the strength of the mixed soil.

(2) Role of Particle Composition: Different types of particles contribute distinctively to the strength of the mixed soil. Larger sand particles predominantly contribute to frictional effects, where the friction angle gradually diminishes as sand content decreases. Clay fines primarily contribute to cohesive effects, while also restraining sand displacement, thereby enhancing the friction angle and cohesive force of the mixed soil.

(3) Impact of Particle Size: Particle size of sand particles, when holding mass constant, does not directly impact the strength of mixed soil. The anti-rotation moment of sand particles under shear load is influenced by factors such as particle surface area, size, cohesive contribution from fines, and particle count. This combined influence indicates that the shear strength of mixed soil does not exhibit a direct correlation with particle size.

(4) Microscopic Analysis: Microscopic considerations, specifically surface energy and interface contact of particles, effectively elucidate the mechanism behind the mechanical behavior of mixed soil. When the gap is partially filled, the cumulative microscopic force of particles increases with higher fine particle content. Conversely, under fully filled conditions, the cumulative microscopic force decreases with elevated fine particle content. This trend in the cumulative microscopic force curve of mixed soils aptly describes and predicts the relationships between shear strength and fine content, internal friction angle and fine content, and cohesion and fine content.

In essence, this study provides a nuanced understanding of how different factors at various scales contribute to the complex mechanical behavior of mixed soil. The combination of experimental investigation, theoretical analysis, and microscopic insights contributes to a comprehensive explanation of the observed behaviors.

Data availability statement

The original contributions presented in the study are included in the article/Supplementary Material, further inquiries can be directed to the corresponding author.

Author contributions

JC: Funding acquisition, Writing–original draft, Writing–review and editing, Methodology. JY: Data curation, Funding acquisition, Writing–review and editing. HT: Methodology, Supervision, Writing–review and editing. YF: Methodology, Supervision, Writing–review and editing. RG: Formal Analysis, Resources, Writing–review and editing.

Funding

The authors declare financial support was received for the research, authorship, and/or publication of this article. This research is supported by the Guangdong Basic and Applied Basic Research Foundation (Nos. 2022A1515110793 and 2023A1515030051).

Conflict of interest

The authors declare that the research was conducted in the absence of any commercial or financial relationships that could be construed as a potential conflict of interest.

Publisher's note

All claims expressed in this article are solely those of the authors and do not necessarily represent those of their affiliated organizations, or those of the publisher, the editors and the reviewers. Any product that may be evaluated in this article, or claim that may be made by its manufacturer, is not guaranteed or endorsed by the publisher.

References

Allahyari, N., and Maleki, M. (2022). Investigation into small-strain shear modulus of sand-gravel mixtures in different moisture conditions and its correlation with static stiffness modulus. *Int. J. geotechnical Eng.* 16 (8), 962–973. doi:10.1080/19386362.2022.2033482

Amini, F., and Qi, G. Z. (2000). Liquefaction testing of stratified silty sands. *J. Geotechnical Geoenvironmental Eng.* 126 (3), 208–217. doi:10.1061/(asce)1090-0241(2000)126:3(208)

Bahadori, H., Ghalandarzadeh, A., and Towhata, I. (2008). Effect of non plastic silt on the anisotropic behavior of sand. *Soil Found.* 48 (4), 531–545. doi:10.3208/sandf.48.531

Bai, Bing, Zhou, Rui, Cai, Guoqing, Hu, Wei, and Yang, Guangchang (2021). Coupled thermo-hydro-mechanical mechanism in view of the soil particle rearrangement of granular thermodynamics. *Comput. Geotechnics* 137 (8), 104272. doi:10.1016/j.compgeo.2021.104272

Bobei, D. C., Lo, S. R., Wanatowski, D., Gnanendran, C. T., and Rahman, M. M. (2009). Modified state parameter for characterizing static liquefaction of sand with fines. *Can. Geotechnical J.* 46 (3), 281–295. doi:10.1139/t08-122

Carraro, J., Prezzi, M., and Salgado, R. (2009). Shear strength and stiffness of sands containing plastic or nonplastic fines. *J. Geotechnical Geoenvironmental Eng.* 135 (9), 1167–1178. doi:10.1061/(asce)1090-0241(2009)135:9(1167)

Chang, C. S., Yin, Z. Y., and Hicher, P. Y. (2010). Micromechanical analysis for interparticle and assembly instability of sand. *J. Eng. Mech.* 137 (3), 155–168. doi:10.1061/(asce)em.1943-7889.0000204

Chen, J., Tong, H., Yuan, J., Fang, Y., and Huang, X. (2023). Energy multi-scale method to analyze the scale effect of soil particles. *Front. Mater.* 10. doi:10.3389/fmats.2023.1137758

De Frias Lopez, R., Silfwerbrand, J., Jelagin, D., and Birgisson, B. (2016). Force transmission and soil fabric of binary granular mixtures. *Géotechnique* 66 (7), 578–583. doi:10.1680/jgeot.14.p.199

Gao, Y., Wang, Y. H., and Su, J. C. (2015). Experimental characterization of the influence of fines on the stiffness of sand with inherent fabric anisotropy. *Soils Found.* 55 (5), 1148–1157. doi:10.1016/j.sandf.2015.09.015

Gong, J., Nie, Z., Zhu, Y., Liang, Z., and Wang, X. (2019). Exploring the effects of particle shape and content of fines on the shear behavior of sand-fines mixtures via the DEM. *Comput. Geotechnics* 106, 161–176. doi:10.1016/j.compgeo.2018.10.021

Karakan, E. (2023). Flow index-liquid limit relationship by fall-cone tests in clay-sand mixtures. *Eng. Sci. Technol. Int. J.* 41, 101405. doi:10.1016/j.jestch.2023.101405

Ke, X., Chen, J., and Shan, Y. (2019). A new failure criterion for determining the cyclic resistance of low-plasticity fine-grained tailings. *Eng. Geol.* 261, 105273. doi:10.1016/j.enggeo.2019.105273

Krim, A., Arab, A., Chemam, M., Brahim, A., Sadek, M., and Shahrour, I. (2017). Experimental study on the liquefaction resistance of sand–clay mixtures: effect of clay content and grading characteristics. *Mar. Georesources Geotechnol.* 37, 129–141. doi:10.1080/1064119x.2017.1407974

Lee, K. L., and Seed, H. B. (1967). Cyclic stress conditions causing liquefaction of sand. *ASCE Soil Mech. Found. Div. J.* 93 (1), 47–70. doi:10.1061/jsfeaq.0000945

Li, X., Liu, J., and Nan, J. (2022). Prediction of dynamic pore water pressure for calcareous sand mixed with fine-grained soil under cyclic loading. *Soil Dyn. Earthq. Eng.* 157, 107276. doi:10.1016/j.soildyn.2022.107276

Monkul, M. M., Etminan, E., and Şenol, A. (2017). Coupled influence of content, gradation and shape characteristics of silts on static liquefaction of loose silty sands. *Soil Dyn. Earthq. Eng.* 101, 12–26. doi:10.1016/j.soildyn.2017.06.023

Monkul, M. M., Kendir, S. B., and Tütüncü, Y. E. (2021). Combined effect of fines content and uniformity coefficient on cyclic liquefaction resistance of silty sands. *Soil Dyn. Earthq. Eng.* 151, 106999. doi:10.1016/j.soildyn.2021.106999

Monkul, M. M., and Ozden, G. (2007). Compressional behavior of clayey sand and transition fines content. *Eng. Geol.* 89 (3-4), 195–205. doi:10.1016/j.enggeo.2006.10.001

Monkul, M. M., and Yamamuro, J. A. (2011). Influence of silt size and content on liquefaction behavior of sands. *Can. Geotechnical J.* 48 (6), 931–942. doi:10.1139/t11-001

Park, S., and Kim, Y. (2013). Liquefaction resistance of sands containing plastic fines with different plasticity. *J. Geotechnical Geoenvironmental Eng.* 5 (139), 825–830. doi:10.1061/(asce)gt.1943-5606.0000806

Phan, Q. T., Bui, H. H., Nguyen, G. D., and Bouazza, A. (2021). Effect of particle rolling resistance on drained and undrained behaviour of silty sand. *Acta Geotech.* 16 (16), 2657–2682. doi:10.1007/s11440-020-01128-y

Polito, C. P., and Martin, J. R. (2001). Effects of nonplastic fines on the liquefaction resistance of sands. *J. Geotechnical Geoenvironmental Eng.* 5 (127), 408–415. doi:10.1061/(asce)1090-0241(2001)127:5(408)

Porcino, D. D., Diano, V., Triantafyllidis, T., and Wichtmann, T. (2020). Predicting undrained static response of sand with non-plastic fines in terms of equivalent granular state parameter. *Acta Geotech.* 2020 (15), 867–882. doi:10.1007/s11440-019-00770-5

Sabbar, A. S., Chegenizadeh, A., and Nikraz, H. (2017). Static liquefaction of very loose sand-slag-bentonite mixtures. *Soils Found. -Tokyo-* 57 (3), 341–356. doi:10.1016/j.sandf.2017.05.003

Shan, Y., and Ke, X. (2021). Reexamination of collapse failure of fine-grained soils and characteristics of related soil indexes. *Environ. Earth Sci.* 80 (11), 402. doi:10.1007/s12665-021-09678-4

Troncoso, J. H., and Verdugo, R. (1985). Silt content and dynamic behavior of tailing sands. *Proc. Icsmfe.*

Wei, X., and Yang, J. (2019). Characterizing the effects of fines on the liquefaction resistance of silty sands. *Soils Found. -Tokyo* 59 (6), 1800–1812. doi:10.1016/j.sandf.2019.08.010

Yamamuro, J. A., and Lade, P. V. (1998). Steady-state concepts and static liquefaction of silty sands. *J. Geotechnical Geoenvironmental Eng.* 124 (9), 868–877. doi:10.1061/(asce)1090-0241(1998)124:9(868)

Yao, Y., Li, J., Ni, J., Liang, C., and Zhang, A. (2022). Effects of gravel content and shape on shear behaviour of soil-rock mixture: experiment and DEM modelling. *Comput. Geotechnics* 141, 104476. doi:10.1016/j.compgeo.2021.104476

Yin, Z., Zhao, J., and Hicher, P. Y. (2014). A micromechanics-based model for sand-silt mixtures. *Int. J. Solids Struct.* 51, 1350–1363. doi:10.1016/j.ijsolstr.2013.12.027

Zhu, Z., Zhang, F., Dupla, J. C., Canou, J., and Foerster, E. (2020). Investigation on the undrained shear strength of loose sand with added materials at various mean diameter ratios. *Soil Dyn. Earthq. Eng.* 137, 106276. doi:10.1016/j.soildyn.2020.106276

Zuo, K., Gu, X., Hu, C., Hu, J., and Gao, G. (2023). Shear stiffness of sand-fines binary mixtures: effects of sand gradation and fines content. *Constr. Build. Mater.* 383, 131364. doi:10.1016/j.conbuildmat.2023.131364

frontiers | Frontiers in Materials

TYPE Original Research
PUBLISHED 02 October 2023
DOI 10.3389/fmats.2023.1284068

OPEN ACCESS

EDITED BY
Bing Bai,
Beijing Jiaotong University, China

REVIEWED BY
Xirong Niu,
Shanxi University, China
Lin Li,
Chang'an University, China

*CORRESPONDENCE
Jian Huang,
huangjian@bucea.edu.cn

RECEIVED 27 August 2023
ACCEPTED 07 September 2023
PUBLISHED 02 October 2023

CITATION
Huang J, Lu X and Hu H (2023), Creep subsidence prediction algorithm considering the effect of stress history for subgrades.
Front. Mater. 10:1284068.
doi: 10.3389/fmats.2023.1284068

Creep subsidence prediction algorithm considering the effect of stress history for subgrades

Jian Huang[1]*, Xusheng Lu[1] and Hexiang Hu[2]

[1]School of Civil and Transportation Engineering, Beijing University of Civil Engineering and Architecture, Beijing, China, [2]China Construction First Group Corporation Limited, Beijing, China

In this study, the power function model was modified to explain the creep strain of coarse-grain and fine-grain soils in a uniform manner. And then, two creep subsidence prediction algorithms considering stress history and without considering stress history were proposed based on the modified power function model and Bjerrum's reclassification of consolidation. The two proposed algorithms were in comparison with two widely used subsidence prediction algorithms in practical engineering based on field subsidence observation data from the subgrade of Haolebaoji-Ji'an Railway. According to the comparison results, the prediction algorithm considering stress history provides a more precise and reliable prediction over two conventional algorithms with a limited amount of available observation data. However, the prediction algorithm without considering stress history have poor prediction results.

KEYWORDS

subgrade, consolidation, stress history, creep subsidence, prediction algorithm

1 Introduction

The filler of subgrade is generally earth-rock mixtures, which are composed of fine-grain soil such as clay and coarse-grain soil such as gravel. Thus, the creep properties of coarse grain and fine grain soils decide jointly the subsidence of subgrade. The consolidation lines of fine-grain soil are often drawn on the semi-logarithmic coordinate in soil mechanics because the creep part of the curves is almost straight (Bai et al., 2019; Bai et al., 2021; Wang et al., 2022). A large number of experimental results have shown that the consolidation lines of coarse grain soil are perhaps not suitable for drawing on the semi-logarithmic coordinate, but it can be well described by the power function model (Kuwano and Jardine, 2002; Cheng and Ding, 2007; Sun et al., 2016; Huang et al., 2023). However, when the power function model is used to explain the consolidation lines of fine-grain soil, the long-term trend of creep deformation is not satisfactory (Briaud and Garland, 1985; Briaud and Gibbens, 1999; Bi et al., 2019). Therefore, if the power function model is used to explain the creep strain of fine-grain and coarse-grain soils in a uniform manner, it needs to be modified.

It has been debated for decades whether creep is generated in the process of primary consolidation. There are two opposing views. According to Hypothesis A, creep is generated only in the process of secondary consolidation, while creep is generated both in the process of primary consolidation and secondary consolidation according to Hypothesis B. Proponents of both views have proposed theoretical explanations. For example, scholars holding the view of Hypothesis A believe that creep is a consecutive process of decreasing volume with time under constant effective stress (Mesri and Choi, 1985; Mesri, 2009; Feng, 2010), whereas scholars supporting Hypothesis B argue that creep is an intrinsic property of granular

materials, including soils, and occurs at any stage of consolidation (Bjerrum, 1967; Stolle et al., 1999; Yin, 1999; Karim et al., 2010; Yao et al., 2013). However, Degago et al. (2011) demonstrate that Hypothesis B is more consistent with the experimental law after analyzing data from numerous sets of consolidation tests and field experiments.

In this paper, the power function model is modified and the reasonableness of the modified power function model (called MPF model below) is verified by indoor experiment data of silty clay and earth-rock mixtures. Based on the MPF model and Bjerrum's reclassification of consolidation, two one-dimensional creep deformation formulas were proposed. Two simplified algorithms to predict creep subsidence were developed on the basis of these two formulas, which are the prediction algorithm considering the stress history and the prediction algorithm without considering the stress history. Finally, the feasibility of the two prediction algorithms was confirmed by using the field monitoring data of creep subsidence from three sections of the subgrade of the Haolebaoji-Ji'an Railway. Meanwhile, the reliability and accuracy of the two prediction algorithms were verified by comparing the prediction results with two widely used subsidence prediction algorithms in practical engineering.

2 Theoretical basis

2.1 The MPF model

Numerous consolidation tests have shown that the compression curves are not unique but are essentially parallel to each other in a cluster of curves (Crawford, 1964; Yao et al., 2013). Bjerrum (1967) confirmed this law and referred to these parallel lines as 'time lines'. Assuming there exists an instant normal compression line (INCL) with a creep time of zero, Yao et al. (2013) established the UH model considering the time effect. INCL is used as a reference line to reflect the stress history, which is plotted as a solid blue line in Figure 1. The points on INCL indicate that the soil element is normally consolidated soil without any creep. Since there is a limit to creep, there is also a limit to the creep deformation in Figure 1 (Yao and Fang, 2019). The limit of creep deformation under different loads is named Stable Normal Compression Line (SNCL), which is plotted as a blue dotted line in Figure 1.

From Hypothesis B of creep, it is clear that the consolidation deformation of soil elements is practically caused by the mixture of an increase in effective stress and an increase in time. A new definition of instant compression and delayed compression was established by Bjerrum to clarify the deformation due to multiple factors. Point A to point A′ in Figure 1 is represented as instant compression. In this compression process, we assume that the pore water pressure dissipates instantaneously and the skeleton composed of soil particles bears all loads instantaneously. Point A′ to point B′ in Figure 1 is represented as delayed compression, in which the soil skeleton is assumed to creep only with time. The deformation in these two compression processes is referred to as instant deformation and delayed deformation, respectively.

The power function model is often used to calculate the creep strain of fine-grain soils such as clay and silty fine sand (Briaud and Garland, 1985; Briaud and Gibbens, 1999; Bi et al., 2019). The commonly used formula of the power function model is (1)

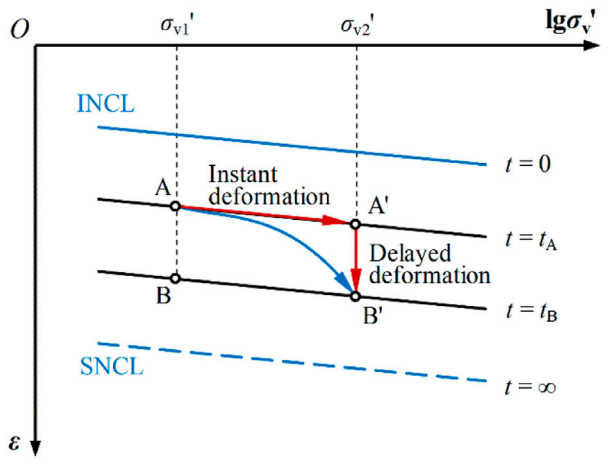

FIGURE 1
Schematic diagram of timelines and deformation.

$$\frac{\varepsilon_t}{\varepsilon_1} = \left(\frac{t}{t_1}\right)^n \tag{1}$$

where t is the time that creep lasts; t_1 is the unit reference time, generally expressed as 1s, 1min, or 1d; ε_t and ε_1 are creep strain at time t and t_1, respectively; n is the creep index.

According to Bjerrum's division of the consolidation process, the delayed deformation includes the creep deformation in the primary consolidation process. As the focus is on creep, Eq. 1 is used to describe the delayed deformation without considering consolidation. Equation 1 indicates that in the bi-logarithmic coordinate, the deformation versus time is linear with a slope of n. However, as time t grows, creep deformation will keep growing until infinity. The true creep deformation law is that the creep rate decreases to zero as time t increases. The mathematical description is that the deformation-time curve will eventually be parallel to the time axis. Therefore, the MPF model can be expressed as:

$$\frac{\varepsilon_{t\infty} - \varepsilon_t}{\varepsilon_{t\infty}} = \left(\frac{t}{t_0} + 1\right)^{-n} \tag{2}$$

where ε_t is creep strain; $\varepsilon_{t\infty}$ is creep strain when creep time is infinite; t_0 is the unit time used to unify the dimension of Eq. 1 and its value is one for the same dimension as creep time t; n is creep index dependent on the physical properties of soil.

By transforming Eq. 2, the expression of creep deformation ε_t can be obtained as:

$$\varepsilon_t = \varepsilon_{t\infty}\left[1 - \left(\frac{t}{t_0} + 1\right)^{-n}\right] \tag{3}$$

According to Eq. 3, ε_t is zero when t is zero and ε_t increases to $\varepsilon_{t\infty}$ when t is infinite. That is, the creep strain increases non-linearly with creep time t to the limit $\varepsilon_{t\infty}$. When $\varepsilon_{t\infty}$ is constant, creep index n controls the rate of creep deformation. Figure 2. Shows a diagram of the creep curves based on Eqs 1, 3. As can be seen from Figure 2, the MPF model is more consistent with the creep law of soil.

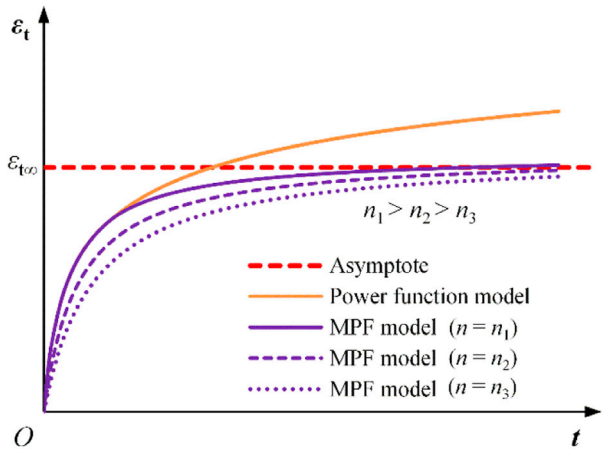

FIGURE 2
Schematic diagram for power function model and MPF model.

The value of strain measured by the dial indicator in the consolidation test is total strain. The creep deformation ε_t in Eq. 3 is only the delayed deformation. So, the formula of total strain ε is

$$\varepsilon = \varepsilon_t + \varepsilon_{ep} \tag{4}$$

where ε_{ep} is the strain without creep, which is equivalent to instant deformation.

Similarly, the difference between the limit of total deformation ε_{∞} and the limit of creep deformation $\varepsilon_{t\infty}$ is ε_{ep}. Thus, the expression of ε_{∞} is given as

$$\varepsilon_{\infty} = \varepsilon_{t\infty} + \varepsilon_{ep} \tag{5}$$

where ε_{∞} is the limit of total strain when t is infinite.

Combining Eqs 3–5 yields:

$$\varepsilon = \varepsilon_{\infty} - (\varepsilon_{\infty} - \varepsilon_{ep})\left(\frac{t}{t_0} + 1\right)^{-n} \tag{6}$$

According to Eq. 6, ε is ε_{ep} when $t = 0$, i.e., total strain is instant deformation at the beginning. When t is infinite, ε increases to ε_{∞}, i.e., the total strain increases non-linearly with time to a stable value ε_{∞}.

2.2 The verification of the MPF model

Equation 6 yields

$$\varepsilon_{\infty} - \varepsilon = (\varepsilon_{\infty} - \varepsilon_{ep})\left(\frac{t}{t_0} + 1\right)^{-n} \tag{7}$$

Equation 7 yields

$$lg\left(\frac{\varepsilon_{\infty} - \varepsilon}{\varepsilon_{\infty}}\right) = lg\left(\frac{\varepsilon_{\infty} - \varepsilon_{ep}}{\varepsilon_{\infty}}\right) - nlg\left(\frac{t}{t_0} + 1\right) \tag{8}$$

Equation 8 indicates that in bi-logarithmic coordinates, deformation versus time is also linear with a slope of -n. For clays, ε_{ep} is the strain corresponding to the point where the primary and secondary consolidation divides. The strain ε_{ep} can be determined by the ε-lg$t$ curve obtained through consolidation tests. For earth-rock mixtures, there is no generally accepted standard for dividing instant deformation and delayed deformation. At present, the deformation value of 1 h under the last load is often used as the demarcation between instant and creep deformation of earth-rock mixtures (Cheng and Ding, 2007; Sun et al., 2016; Huang et al., 2023). If test data at 1 h is not available, the first measured deformation value after 1 h is used as an approximation of ε_{ep}. Currently, there are two methods for identifying the value of ε_{∞}: (i) The same soil is prepared into soil elements with different over-consolidated ratios and subjected to one-dimensional compression creep tests and one-dimensional expansion creep tests, respectively. The location of SNCL is then determined according to the relationship between the creep deformation and the over-consolidated ratio. In turn, the ε_{∞} under the corresponding load can be determined (Yao et al., 2013; Yao and Fang, 2019). (ii) The ε_{∞} is one of the parameters to be solved, which will be determined by optimization calculation. The first method to determine ε_{∞} is more complicated because it requires multiple creep tests. Therefore, the second one is selected.

Huang et al. (2023) used silty clay and Zhang et al. (2021) used three kinds of earth-rock mixtures to carry out consolidation tests. These experimental data were re-plotted under semi-logarithmic coordinates, as detailed in Figure 3.

According to Figure 3A, the secondary consolidation part of clay's experimental data under different stress levels is linear and with essentially the same slope. According to Figures 3B–D, the creep part of the experimental data of three kinds of earth-rock mixtures is essentially nonlinear, but the trends of deformation are broadly similar. Due to the lack of deformation data between 0 and 8 h in Zhang et al. (2021), the deformation corresponding to the 8th hour, which is also the first deformation data in Fig. 10, is used as the demarcation between instant and creep deformation. Through these test data, the parameters ε_{ep}, ε_{∞}, and n in Eq. 8 are determined, as shown in Table 1 and Table 2. Combined with the parameters in the two tables, these experimental data were sorted based on Eq. 8 and then replotted in bi-logarithmic coordinates, as shown in Figure 4.

According to Figure 4, these rearranged experimental data for different soil samples at various stress levels are almost straight with essentially the same slope. This shows that Eq. 8 derived on the basis of the MPF model is consistent with the creep characteristics of granular materials. Therefore, the MPF model is suitable for creep calculations of subgrade soils.

2.3 Creep deformation formulas

2.3.1 Creep deformation formula without considering stress history

When the state point lies on the reference line INCL, as in point A in Figure 5, the soil element is in a normal consolidated state. There has been no creep of any time in history. ε_{λ} and ε denote the instant and total strain of normal consolidated soil elements under an effective stress σ_{v1}', respectively. At this point, the instant deformation ε_{ep} of the normal consolidated soil element is ε_{λ}. Based on the MPF model and Bjerrum's reclassification, the creep strain ε_t of a normal consolidated soil element from point A after time t is obtained from Eq. 6 as:

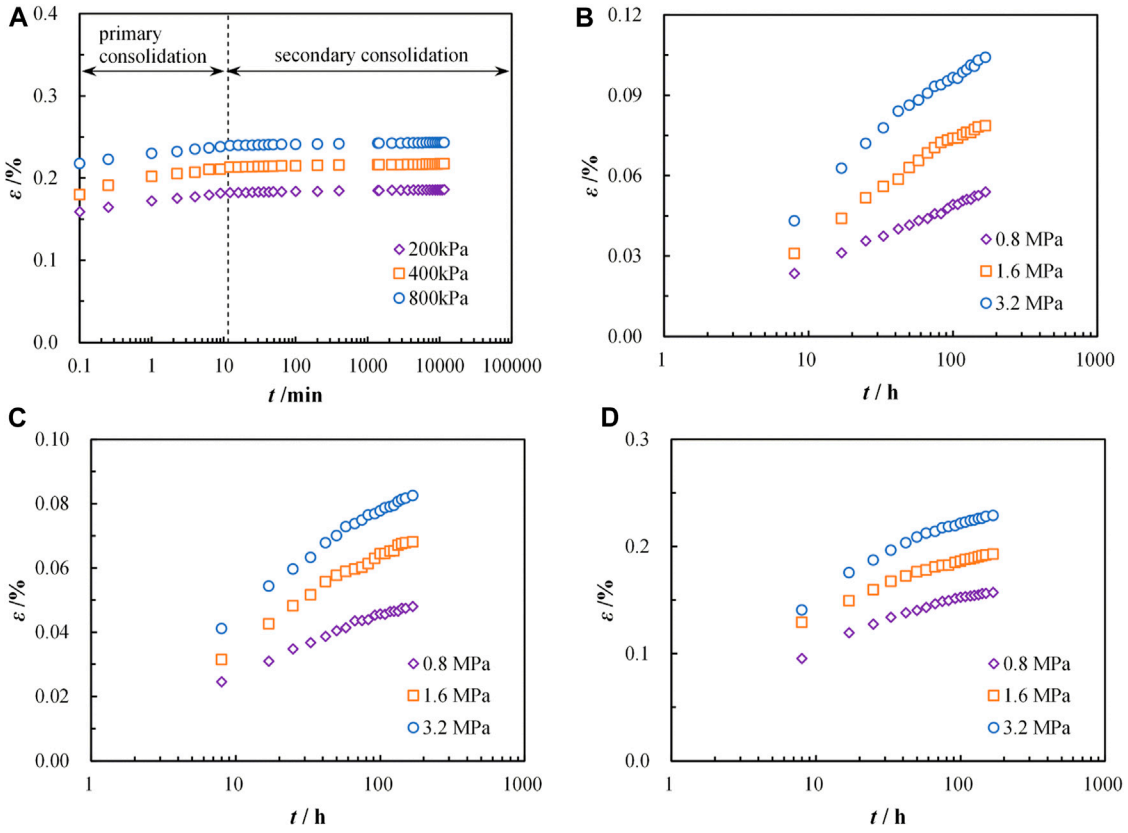

FIGURE 3
The experimental data of different soils replotted in the ε-lg$t$ coordinate: **(A)** clay; **(B)** earth-rock mixture of sample 1; **(C)** earth-rock mixture of sample 2; **(D)** earth-rock mixture of sample 3.

TABLE 1 Creep formula parameters of different soil elements.

Load (kPa)	Parameters		
	ε_{ep}	ε_{∞}	ε_{ep}
200	0.176	0.196	0.041
400	0.207	0.228	0.043
800	0.234	0.254	0.043

$$\varepsilon_t = \varepsilon - \varepsilon_\lambda = (\varepsilon_\infty - \varepsilon_\lambda) - (\varepsilon_\infty - \varepsilon_\lambda)\left(\frac{t}{t_0} + 1\right)^{-n} \quad (9)$$

According to Eq. 9, ε_t is zero when t is zero, and ε_t is (ε_∞-ε_λ) when t is infinite. That is, creep strain ε_t increases non-linearly with time to the maximum deformation (ε_∞-ε_λ).

2.3.2 Creep deformation formula considering stress history

When the state point B lies below the INCL, as shown in Figure 6, the soil element is in an over-consolidated state. The load is unloaded from σ_{v2}' to σ_{v1}' and then held constant; C_c and C_s are the slopes of INCL and reload lines, respectively. ε_{ep} is the instant strain corresponding to point B. t_a is the equivalent creep time of the current state point with respect to the INCL. For state point B, t_a is the equivalent creep time between point A and point B.

From the analysis of Figure 6, it can be seen that starting creep from the current state point B after time t, the corresponding creep strain ε_t is:

$$\varepsilon_t = \varepsilon - \varepsilon_{ep} = (\varepsilon_\infty - \varepsilon_{ep}) - (\varepsilon_\infty - \varepsilon_\lambda)\left(\frac{t + t_a}{t_0} + 1\right)^{-n} \quad (10)$$

where t_a is the equivalent creep time of the current state point relative to the reference line INCL.

When the normal consolidated soil element experiences the creep of time t_a from point A to point B, the strain of point B can be obtained from Eq. 6:

$$\varepsilon_{ep} = \varepsilon_\infty - (\varepsilon_\infty - \varepsilon_\lambda)\left(\frac{t + t_a}{t_0} + 1\right)^{-n} \quad (11)$$

From Eq. 11, the expression of t_a can be obtained as:

$$t_a = t_0\left(\frac{\varepsilon_\infty - \varepsilon_{ep}}{\varepsilon_\infty - \varepsilon_\lambda}\right)^{-\frac{1}{n}} - t_0 \quad (12)$$

Substituting Eq. 12 into Eq. 10 yields:

10.3389/fmats.2023.1284068

TABLE 2 Creep formula parameters of different soil elements.

Load (MPa)	Parameters of sample 1			Parameters of sample 2			Parameters of sample 3		
	ε_{ep}	ε_{∞}	n	ε_{ep}	ε_{∞}	n	ε_{ep}	ε_{∞}	n
0.8	0.023	0.365	0.033	0.025	0.110	0.125	0.095	0.199	0.299
1.6	0.031	0.481	0.036	0.031	0.147	0.130	0.120	0.239	0.311
3.2	0.043	0.560	0.041	0.041	0.169	0.133	0.144	0.278	0.325

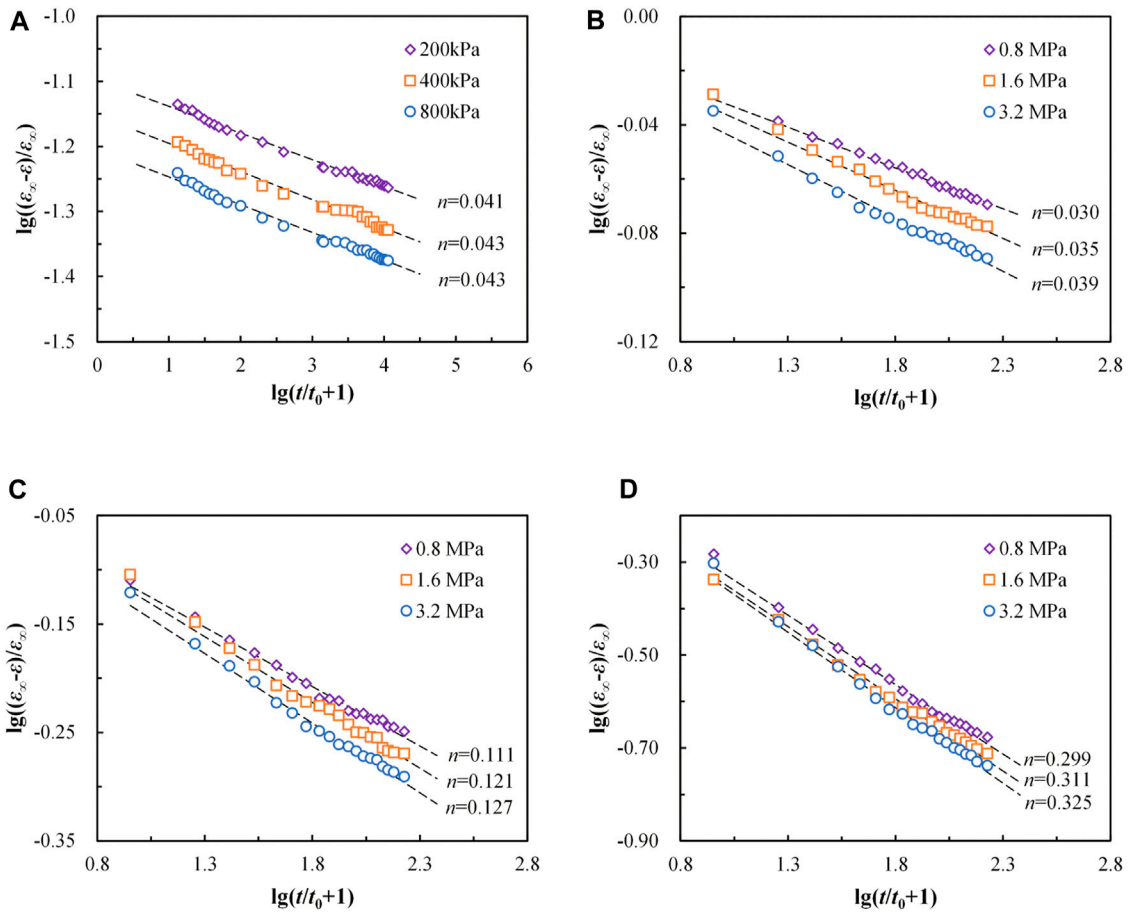

FIGURE 4
The experimental data of different soils replotted in the lg $((\varepsilon_{\infty}-\varepsilon)/\varepsilon_{\infty})$-lg (t/t_0+1) coordinate: **(A)** clay; **(B)** earth-rock mixture of sample 1; **(C)** earth-rock mixture of sample 2; **(D)** earth-rock mixture of sample 3.

$$\varepsilon_t = (\varepsilon_{\infty} - \varepsilon_{ep}) - (\varepsilon_{\infty} - \varepsilon_{\lambda})\left[\frac{t}{t_0} + \left(\frac{\varepsilon_{\infty} - \varepsilon_{ep}}{\varepsilon_{\infty} - \varepsilon_{\lambda}}\right)^{-\frac{1}{n}}\right]^{-n} \quad (13)$$

From Eq. 13, ε_t is zero when t is zero, and ε_t is $(\varepsilon_{\infty}$-$\varepsilon_{ep})$ when t is infinite. That is, creep deformation ε_t increases non-linearly with time to the maximum deformation $(\varepsilon_{\infty}$-$\varepsilon_{ep})$ in an over-consolidated state. It should be noted that after the same creep time t, the creep deformation ε_t between Figure 5 and Figure 6 are different. For the same soil, the void ratio in the over-consolidated state is smaller than that in the normal consolidated state. The creep rate of over-consolidated soil is smaller than that of normal consolidated soil under the same load σ_{v1}'. Therefore, the ε_t of the over-consolidated soil element in Figure 6 is smaller than that of the normal consolidated soil element in Figure 5, after experiencing the same creep time t.

The parameters ε_{λ}, ε_{ep}, ε_{∞}, n in Eq. 9 and Eq. (13) can be ascertained by one-dimensional creep tests (Bi et al., 2019; Huang et al., 2023). The creep strain ε_t of normal consolidated soil element and over-consolidated soil element is therefore only time-dependent. Let $\alpha = \varepsilon_{\infty}$-$\varepsilon_{ep}$, $\beta = \varepsilon_{\infty}$-$\varepsilon_{\lambda}$, then Eq. 9 and Eq. (13) are simplified as follows:

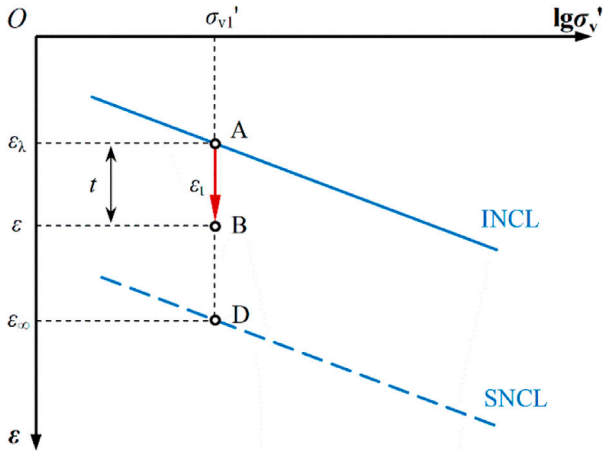

FIGURE 5
Schematic diagram for the creep of normally consolidated soil.

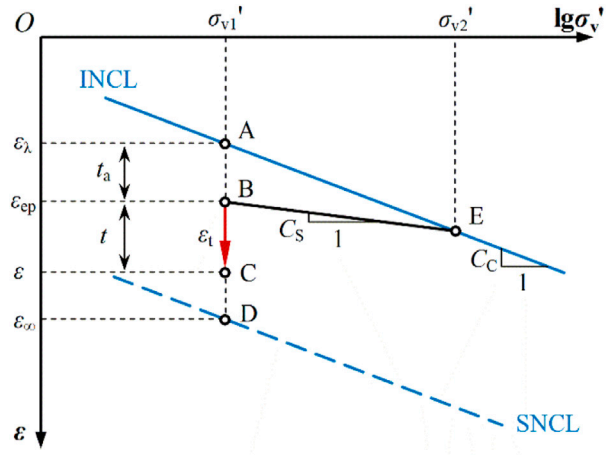

FIGURE 6
Schematic diagram for the creep of over-consolidated soil.

$$\varepsilon_t = \alpha - \alpha\left(\frac{t}{t_0}+1\right)^{-n} \tag{14}$$

$$\varepsilon_t = \beta - \alpha\left(\frac{t}{t_0}+\left(\frac{\beta}{\alpha}\right)^{-\frac{1}{n}}\right)^{-n} \tag{15}$$

where α and β denote the maximum creep deformation of the over-consolidated and normal consolidated soil element, respectively, under the effective stress σ_{v1}', and $\beta \geq \alpha > 0$.

3 Creep subsidence prediction algorithm for subgrades

3.1 The formula of the simplified algorithm

Referring to the idea of calculating the final subsidence by the layer-wise method, it is assumed that creep subsidence of each soil layer only occurs in the vertical direction and there is no lateral deformation. Based on the layer-wise method, the creep subsidence of the ith layer can be calculated as follows:

$$s_i = \varepsilon_{ti} H_i \tag{16}$$

where ε_{ti} and H_i are the creep deformation and thickness of the ith layer.

Assuming that all the soil layers of the subgrade are regarded as normal consolidated soils, substituting Eq. 14 into Eq. 16 yields:

$$s_i = H_i\left[\alpha_i - \alpha_i\left(\frac{t}{t_0}+1\right)^{-n_i}\right] \tag{17}$$

If each soil layer's parameters are known, creep subsidence of subgrade at different times can be calculated. After creep time t, the creep subsidence is:

$$s = \sum_{i=1}^{k} s_i = \sum_{i=1}^{k} H_i\left[\alpha_i - \alpha_i\left(\frac{t}{t_0}+1\right)^{-n_i}\right] \tag{18}$$

where k is the layer number for subgrades.

As can be seen from Eq. 18, to calculate creep subsidence using the layer-wise method, it is necessary to know the parameters of all soil layers. These parameters are difficult to obtain accurately because of the complexity of the construction environment and the tight construction schedule. Therefore, for subgrades that lack soil parameters and have limited on-site subsidence monitoring data, the layer-wise method described above needs to be simplified when predicting creep subsidence. Treating subgrade and original foundation as a whole, a simplified algorithm without considering stress history is proposed with reference to Eq. 14. Since the subgrade soil is regarded as normally consolidated soil, the prediction algorithm is called the NC algorithm below. The formula of the NC algorithm can be expressed as:

$$\frac{s}{s_0} = \alpha - \alpha\left(\frac{t}{t_0}+1\right)^{-n} \tag{19}$$

where s is creep subsidence; s_0 is the unit subsidence used to unify the dimension, which has the same dimension as s and the value of one; n is the subsidence index; α is the ultimate creep subsidence in the normally consolidated state; t_0 is a specific time, which serves to balance dimension, and its value is one.

If the subgrade soil is regarded as over-consolidated soil, the simplified prediction algorithm is called the OC algorithm below. Similarly, with reference to Eq. 15, the formula of OC algorithm can be expressed as:

$$\frac{s}{s_0} = \beta - \alpha\left(\frac{t}{t_0}+\left(\frac{\beta}{\alpha}\right)^{-\frac{1}{n}}\right)^{-n} \tag{20}$$

where the parameters n, α, and t_0 have the same meaning as in Eq. 19; β is the final creep subsidence in an over-consolidated state.

3.2 Method of determining parameters

The parameters α, β, and n of the two simplified algorithms can be determined by parameter optimization based on

TABLE 3 Algorithm parameters determined based on 256d subsidence monitoring data at section DK 1806 + 800.

Algorithm	Fitting parameters	*DC*		Final subsidence (mm)
		Fitting	Prediction	
Hyperbola algorithm	$\alpha = 7.560$, $\beta = 0.042$	0.993	0.642	24.1
Richards algorithm	$s_\infty = 18.680$, $\alpha = 1.002$, $\beta = 0.005$, $n = -0.279$	0.996	0.398	18.7
NC algorithm	$\alpha = 0.661$, $n = -0.563$	0.992	0.525	1579.5
OC algorithm	$\alpha = 156.076$, $\beta = 46.867$, $n = 0.267$	0.993	0.899	46.8

TABLE 4 Algorithm parameters determined based on 256d subsidence monitoring data at section DK 1806 + 925.

Algorithm	Fitting parameters	*DC*		Final subsidence (mm)
		Fitting	*Prediction*	
Hyperbola algorithm	$\alpha = 7.188$, $\beta = 0.061$	0.993	0.052	16.4
Richards algorithm	$s_\infty = 15.238$, $\alpha = 1.005$, $\beta = 0.004$, $n = -0.567$	0.999	0.607	15.2
NC algorithm	$\alpha = 0.915$, $n = -0.474$	0.997	0.124	639.5
OC algorithm	$\alpha = 82.764$, $\beta = 49.010$, $n = 0.139$	0.996	0.957	49.0

monitoring data. The specific steps are as follows: (i) An objective function f is determined by the minimum residual sum of squares between subsidence monitoring data and subsidence calculation value at the corresponding monitoring time. The expression of the objective function is given by Eq. 21. (ii) After setting the parameter value scope for α, β, and n, the optimal parameters are obtained by using optimization algorithms such as genetic algorithm.

$$f = min\sum_{i=1}^{p}(s_i - \hat{s}_i)^2 \tag{21}$$

where p is the times of on-site subsidence observation; s_i is the subsidence value of the ith field observation; $\hat{s}_i$ is the subsidence calculation value based on prediction algorithms corresponding to the monitoring time.

4 Case studies and comparisons

4.1 Introduction of comparison algorithm

To validate the accuracy of the proposed algorithms, two prediction algorithms usually applied in real engineering were chosen for comparison in predicting creep subsidence. The subsidence value versus time of the Hyperbola algorithm is a simplified hyperbolic relationship (Prakash et al., 1987). The formula of the Hyperbola algorithm is expressed as:

$$s = s_0 + \frac{t - t_0}{\alpha + \beta(t - t_0)} \tag{22}$$

where, t_0 and s_0 are the monitoring time and subsidence of the initial reference point, and the values of them are generally zero; α and β are parameters to be solved.

The Richards algorithm belongs to the growth curve model (Huang et al., 2018). The subsidence value predicted by the Richards algorithm increases non-linearly with time t until it tends to be stable. The expression of the Richards algorithm is as:

$$s = s_\infty\left(1 - \alpha e^{-\beta t}\right)^{\frac{1}{(1-n)}} \tag{23}$$

There are various indicators for evaluating the prediction results. After comprehensive consideration, the coefficient of determination DC was selected (Mei et al., 2018). The value range of DC is (-∞, 1]. The closer the DC value is to one, the better the fitting result is. It can be expressed as:

$$DC = 1 - \frac{\sum_{i=1}^{n}(s_i - \hat{s}_i)^2}{\sum_{i=1}^{n}(s_i - \bar{s})^2} \tag{24}$$

where, s_i and $\hat{s}_i$ have the same meaning as in Eq. 21; $\bar{s}$ is the average value of all the subsidence monitoring data used for fitting.

4.2 Subsidence prediction of Haolebaoji-Ji'an

Haolebaoji-Ji'an Railway is a heavy haul railway that connects Haolebaoji in Inner Mongolia with Ji'an in Jiangxi Province, and it is one of the strategic transportation corridors for China's "north-south coal transport". The foundation soils of a test section in Xinyu City, Jiangxi Province of the Haolebaoji-Ji'an Railway are mainly silty clay and fully weathered soft phyllite. The subgrade heights of three sections DK 1806 + 800, DK 1806 + 925, and DK 1807 + 250 are 11.12 m, 14.28 m, and 12.7 m, respectively, which are all filled with fully weathered soft phyllite. The subsidence observation is carried out by single-point settlement gauges. The subsidence monitoring of the three sections began on 11 September 2017 after the completion of filling and ceased on 24 February 2019, that is, the whole monitoring time was 528 days (Luo et al., 2020). The on-site subsidence observation data of the first 256 days were used to

TABLE 5 Algorithm parameters determined based on 256d subsidence monitoring data at section DK 1807 + 250.

Algorithm	Fitting parameters	*DC*		Final subsidence (mm)
		Fitting	*Prediction*	
Hyperbola algorithm	α = 6.778, β = 0.073	0.993	0.052	13.8
Richards algorithm	s_∞ = 11.773, α = 1.011, β = 0.006, n = −0.601	0.999	0.607	11.8
NC algorithm	α = 1.107, n = −0.423	0.997	0.124	383.1
OC algorithm	α = 57.695, β = 36.654, n = 0.137	0.996	0.957	36.6

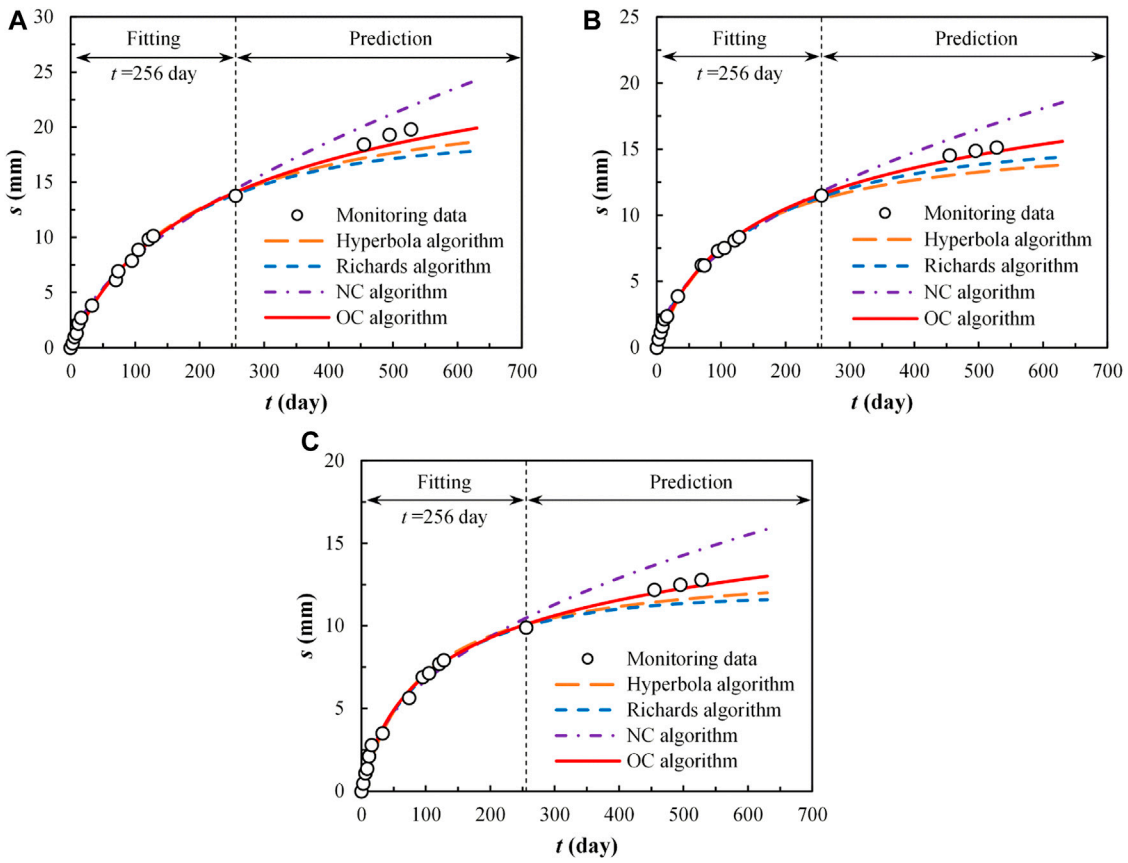

FIGURE 7
Prediction curves for different sections: **(A)** for section DK 1806 + 800; **(B)** for section DK 1806 + 925; **(C)** for section DK 1807 + 250.

ascertain the computation parameters of these algorithms, and then, the determined parameters were used to plot the prediction curves. Finally, the prediction results during 256–528d of each algorithm were compared. The parameters are shown in Tables 3–5 respectively. Figures 7A–C show the prediction curves for each algorithm based on the parameters in Tables 3–5.

According to Figure 7, all the curves fit the monitoring data from days 1–256 well. Combining the values of *DC* for the prediction stages of each algorithm in Table 3 ~ 5, the OC algorithm has the best prediction results when predicting the subsidence from days 256–528.

4.3 Analysis and discussion

The prediction results of the Hyperbola algorithm and the Richards algorithm are almost smaller than the subsidence monitoring data from days 256–528. This is similar to the subsidence prediction results of other foundations (Yao et al., 2020). The prediction results of the NC algorithm are obviously larger than the actual subsidence because it regards subgrade soil as normally consolidated soil. In fact, each soil layer must be compacted in the process of subgrade filling, even utilizing dynamic compaction. In this compaction process, part of the

subgrade soil has become over-consolidated soil. In addition, subsidence monitoring is generally carried out sometime after the completion of filling. During this time, the subgrade soil has experienced a period of creep. After creep deformation, the void ratio of subgrade soil is smaller, which is equivalent to increasing the over-consolidated ratio. Therefore, the effect of stress history should be considered in subsidence predictions. The OC algorithm regards the subgrade soil as over-consolidated soil and already takes into account the effect of stress history. This is also the reason the OC algorithm has the best prediction results among these four algorithms.

5 Conclusion

Based on the MPF model, this study derives two creep deformation formulas in normal consolidation and over-consolidated state. On this basis, two creep subsidence prediction algorithms are proposed, which consider stress history and do not consider stress history, respectively. The main conclusions can be drawn:

(1) The MPF model is capable of describing the creep properties in one dimension of both fine-grain soil and coarse-grained soil in a uniform manner. At the same time, it also meets the request that the creep deformation grows non-linearly with time to stability. The consolidation test can determine all the parameters of the MPF model.
(2) Based on the MPF model and Bjerrum's reclassification, and using the INCL in the UH model as the reference line, the MPF model is developed into two creep strain formulas under normal consolidation and over-consolidation conditions. Both formulas satisfy that the creep deformation increases non-linearly from zero to a certain maximum deformation value with time.
(3) Referring to the idea of the layer-wise method, two creep subsidence prediction algorithms considering stress history and without considering stress history are proposed. The parameters of the two prediction algorithms can be obtained through on-site subsidence observation data.
(4) By comparing the fitting results and prediction results with two widely used subsidence prediction algorithms in practical engineering, the proposed prediction algorithm considering stress history has the best prediction results for the subgrade of Haolebaoji-Ji'an Railway because it treats the subgrade soil as over-consolidated soil and already takes into account the effect of stress history.
(5) The prediction algorithm considering stress history provides an efficient tool for calculating creep subsidence of subgrades. However, the applicability of the prediction algorithm for special soils such as expansive soil, wet-collapsible loess, and frozen soil needs further research. In addition, rainfall-induced wetting deformation can also affect the settlement of subgrades. In this case, the applicability of the proposed algorithm also needs to be further researched.

Data availability statement

The raw data supporting the conclusion of this article will be made available by the authors, without undue reservation.

Author contributions

JH: Funding acquisition, Writing–original draft, Writing–review and editing. XL: Writing–original draft, Writing–review and editing. HH: Data curation, Formal Analysis, Writing–review and editing.

Funding

The author(s) declare financial support was received for the research, authorship, and/or publication of this article. This work was supported by the Beijing Postdoctoral Research Foundation of China (Grant No. 2021-zz-106) and the Pyramid Talent Training Project of the Beijing University of Civil Engineering and Architecture (Grant No. JDYC20220813).

Conflict of interest

Author HH was employed by the Company China Construction First Group Corporation Limited.

The remaining authors declare that the research was conducted in the absence of any commercial or financial relationships that could be construed as a potential conflict of interest.

Publisher's note

References

Bai, B., Cai, G., Hu, W., Yang, G., and Zhou, R. (2021). Coupled thermo-hydro-mechanical mechanism in view of the soil particle rearrangement of granular thermodynamics. *Comput. Geotechnics* 137 (8), 104272. doi:10.1016/j.compgeo.2021.104272

Bai, B., Li, T., Yang, G. C., and Yang, G. S. (2019). A thermodynamic constitutive model with temperature effect based on particle rearrangement for geomaterials. *Mech. Mater.* 139, 103180. doi:10.1016/j.mechmat.2019.103180

Bi, G., Briaud, J. L., Kharenaghi, M. M., and Sanchez, M. (2019). Power law model to predict creep movement and creep failure. *J. Geotechnical Geoenvironmental Eng.* 145 (9), 04019044. doi:10.1061/(asce)gt.1943-5606.0002081

Bjerrum, L. (1967). Engineering geology of Norwegian normally-consolidated marine clays as related to settlements of buildings. *Géotechnique* 17 (2), 83–118. doi:10.1680/geot.1967.17.2.83

Briaud, J. L., and Garland, E. (1985). Loading rate method for pile response in clay. *J. Geotechnical Eng.* 111 (3), 319–335. doi:10.1061/(ASCE)0733-9410(1985)111:3(319)

Briaud, J. L., and Gibbens, R. (1999). Behavior of five large spread footings in sand. *J. Geotechnical Geoenvironmental Eng.* 125 (9), 787–796. doi:10.1061/(ASCE)1090-0241(1999)125:9(787)

Cheng, Z. L., and Ding, H. S. (2007). Experimental study on engineering characteristics of rockfill materials. *Yangtze River* 120 (7), 110–114. doi:10.16232/j.cnki.1001-4179.2022.07.035

Crawford, C. B. (1964). Interpretation of the consolidation test. *J. Soil Mech. Found. Div.* 90 (SM5), 87–102. doi:10.1061/JSFEAQ.0000664

Degago, S. A., Grimstad, G., Jostad, H. P., Nordal, S., and Olsson, M. (2011). Use and misuse of the isotache concept with respect to creep hypotheses A and B. *Géotechnique* 61 (10), 897–908. doi:10.1680/geot.9.P.112

Feng, T. W. (2010). Some observations on the oedometric consolidation strain rate behaviors of saturated clay. *J. Geoengin.* 5 (1), 1–7. doi:10.6310/JOG.2010.5(1).1

Huang, C. F., Li, J. Y., Li, Q., Wu, S. C., and Xu, X. L. (2018). Application of the Richards model for settlement prediction based on a bidirectional difference-weighted least-squares method. *Arabian J. Sci. Eng.* 43 (10), 5057–5065. doi:10.1007/s13369-017-2909-0

Huang, J., Lu, X. S., Peng, R., Qi, J. L., and Yao, Y. P. (2023). A simplified algorithm for predicting creep settlement of high fills based on modified power law model. *Transp. Geotech.*, 101078. doi:10.1016/j.trgeo.2023.101078

Karim, M. R., Gnanendran, C. T., Lo, S. C., and Mak, J. (2010). Predicting the long-term performance of a wide embankment on soft soil using an elastic-viscoplastic model. *Can. Geotechnical J.* 47 (2), 244–257. doi:10.1139/T09-087

Kuwano, R., and Jardine, R. J. (2002). On measuring creep behaviour in granular materials through triaxial testing. *Can. Geotechnical J.* 39 (5), 1061–1074. doi:10.1139/t02-059

Luo, Q., Cheng, M., Wang, T. Fei., and Zhu, J. J. (2020). Three-parameter power function model for prediction of post-construction settlement of medium compressive soil foundation. *J. Beijing Jiaot. Univ.* 44 (3), 93–100. doi:10.11860/j.jssn.1673-0291.20190078

Mei, S. A., Chen, S. S., Zhong, Q. M., and Yan, Z. K. (2018). Parametric model for breaching analysis of earth-rock dam. *Adv. Eng. Sci.* 50 (02), 60–66. doi:10.15961/j.jsuese.201700828

Mesri, G., and Choi, Y. K. (1985). Settlement analysis of embankments on soft clays. *J. Geotechnical Eng.* 111 (4), 441–464. doi:10.1061/(ASCE)0733-9410(1985)111:4(441)

Mesri, G. (2009). Effects of friction and thickness on long-term consolidation behavior of Osaka Bay clays. *Soils Found.* 49 (5), 823–824. doi:10.3208/sandf.49.823

Prakash, K., Murthy, N. S., and Sridharan, A. (1987). Rectangular hyperbola method of consolidation analysis. *Géotechnique* 37 (3), 355–368. doi:10.1680/geot.1987.37.3.355

Stolle, D., Vermeer, P. A., and Bonnier, P. G. (1999). A consolidation model for a creeping clay. *Can. Geotechnical J.* 36 (4), 754–759. doi:10.1139/t99-034

Sun, G., Zhang, Y. Q., Li, H. F., Nie, K., Qi, J., Deng, C., et al. (2016). The research of rockfill creep model and parameters. *J. China Inst. Water Resour. Hydropower Res.* 14 (2), 115–117. doi:10.13244/j.cnki.jiwhr.2016.02.006

Wang, H., Li, L., Li, J. P., and Sun, D. A. (2022). Drained expansion responses of a cylindrical cavity under biaxial *in situ* stresses: numerical investigation with implementation of anisotropic S-CLAY1 model. *Can. Geotechnical J.* 60 (2), 198–212. doi:10.1139/cgj-2022-0278

Yao, Y. P., and Fang, Y. F. (2019). Negative creep of soils. *Can. Geotechnical J.* 57 (1), 1–16. doi:10.1139/cgj-2018-0624

Yao, Y. P., Huang, J., Wang, N., Luo, T., and Han, L. (2020). Prediction method of creep settlement considering abrupt factors. *Transp. Geotech.* 22, 100304. doi:10.1016/j.trgeo.2019.100304

Yao, Y. P., Kong, L. M., and Hu, J. (2013). An elastic-viscous-plastic model for over-consolidated clays. *Sci. China-Technological Sci.* 56, 441–457. doi:10.1007/s11431-012-5108-y

Yin, J. H. (1999). Non-linear creep of soils in oedometer tests. *Géotechnique* 49 (5), 699–707. doi:10.1680/geot.1999.49.5.699

Zhang, Y. Y., Deng, G., Wen, Y. F., Wang, J. P., Wan, Q. W., and Wang, X. H. (2021). Experimental study on consolidation-rheology characteristics of soil-aggregate mixture materials. *J. Hydroelectr. Eng.* 40 (2), 187–194. doi:10.11660/slfdxb.20210219

frontiers | Frontiers in Materials

TYPE Original Research
PUBLISHED 19 October 2023
DOI 10.3389/fmats.2023.1276785

OPEN ACCESS

EDITED BY
Xianze Cui,
China Three Gorges University, China

REVIEWED BY
Ming Zhang,
Henan Institute of Engineering, China
Guangchang Yang,
University of Science and Technology Beijing, China

*CORRESPONDENCE
Xiaoyang Li,
2021930676@stu.haut.edu.cn

RECEIVED 13 August 2023
ACCEPTED 09 October 2023
PUBLISHED 19 October 2023

CITATION
Zhao C, Li L, Li X, Chen W and Li Y (2023), Multi-scale analysis of the synergistic strengthening effect of silane coupling agent on PVA and cement interface. *Front. Mater.* 10:1276785. doi: 10.3389/fmats.2023.1276785

Multi-scale analysis of the synergistic strengthening effect of silane coupling agent on PVA and cement interface

Chen Zhao[1], Lijuan Li[2], Xiaoyang Li[2]*, Wuxin Chen[2] and Yongquan Li[2]

[1]Henan Vocational College of Water Conservancy and Environment, Zhengzhou, China, [2]Henan University of Technology, College Civil Engineering, Zhengzhou, China

Conventional polyvinyl alcohol (PVA) cementitious composites are susceptible to macroscopic cracking when subjected to reduced compressive strength, diminished toughness, tensile impact and other external loads. In order to address these issues, this study investigates the mechanism of the modifier's influence by modifying PVA fibers with a silane coupling agent (KH560) through experimental studies and molecular dynamics simulations for multiscale computational analyses. Macro test results showed that the mechanical properties of PVA fiber concrete were significantly improved after silane coupling agent modified PVA fiber. The microscopic test results showed that the SCA-modified polymer film acted as a bridging ligament in the interfacial transition zone, effectively prevented crack extension, and enhanced the interfacial adhesion between the organic components of the PVA fibers and the cement matrix. Nanoscale molecular dynamics simulations showed that the hydrated calcium silicate exhibited a stable skeletal structure, while the introduction of SCA expanded the hydrogen bonding interactions at the interface, thus enhancing its stability.

KEYWORDS

fiber-cement composites, silane coupling agent, mechanical properties, molecular dynamics, impact mechanism

1 Introduction

Concrete is a crucial construction material in modern engineering, offering a range of advantages including high mechanical strength, good durability, low raw material cost, and easy availability. Cement-based composite materials have emerged as an advancement over traditional cement-based materials. They find extensive application in foundational engineering projects such as buildings, roads, and bridges. However, as material science and construction technology progress, there is a growing demand for improved performance from building materials and structures. Cement-based composites, despite their strengths, suffer from drawbacks like low tensile strength and poor toughness. They tend to develop macroscopic cracks under loads such as tension, impact, and bending. These cracks continue to propagate, eventually leading to brittle fracture and significantly reducing the service life of the composite (Sagar and PrasadKumar, 2012; Mayercsik et al., 2015). Extensive research has demonstrated that the incorporation of fibers in cement-based composites can address these issues by bridging

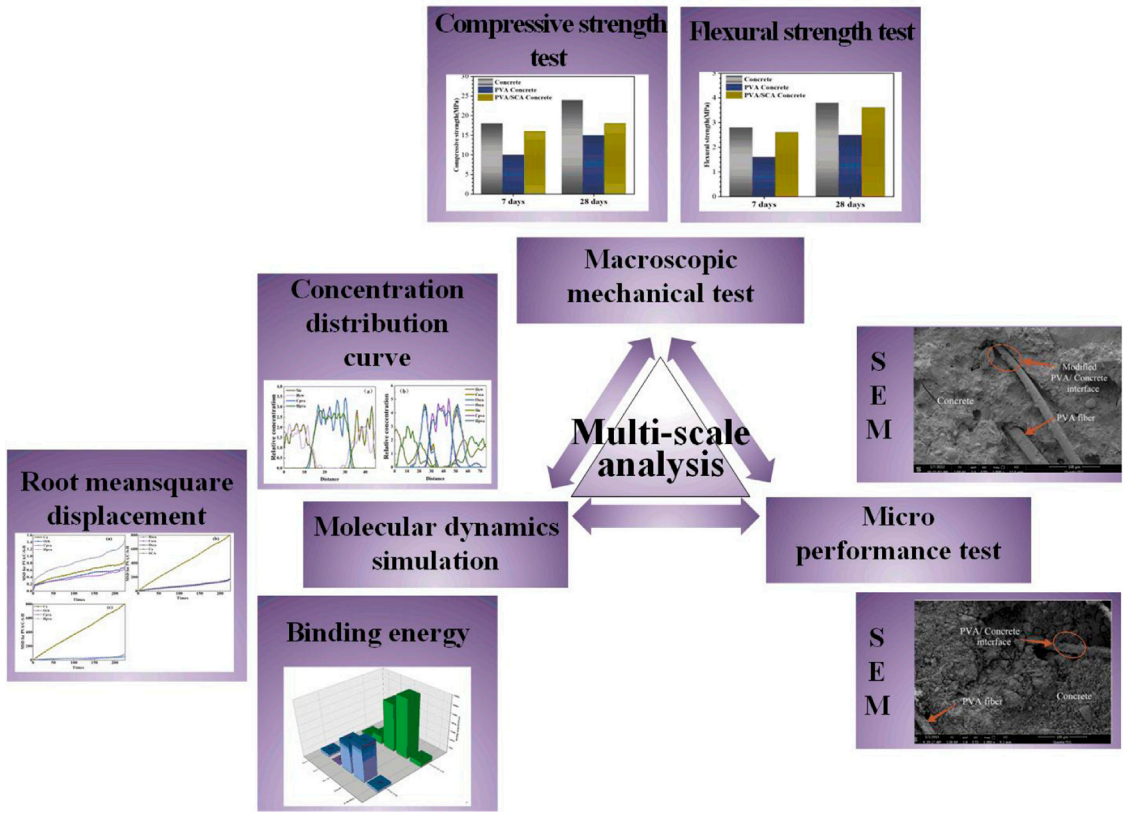

GRAPHICAL ABSTRACT

cracks and enhancing load transmission. This, in turn, significantly improves the mechanical properties, durability, and toughness of the composites (Dong and HuangShu, 2013; Yong and DajingChen, 2023). Currently, commonly used fibers in cement-based composites include polyvinyl alcohol fibers, polypropylene fibers, and steel fibers (Zhou et al., 2018; Zhuang et al., 2020; Mei-Ling et al., 2022; LamenJohn, 2023). Polyvinyl alcohol fiber (Said et al., 2021), also known as PVA (Wang and YangYin, 2021), is a novel synthetic fiber with a molecular formula of -[$CH_2CH(OH)$]n- (Guoliang et al., 2023). PVA possesses a unique molecular structure, rendering it a high-elasticity, high-modulus fiber and an environmentally friendly reinforcement material for cement. Its molecular structure facilitates better affinity and interfacial bonding with the cement matrix, thereby expanding the bond-forming surface (Yong and DajingChen, 2023). Moreover, PVA exhibits strong resistance to acids and alkalis, offers a wide range of applications, demonstrates good dispersion performance, and can establish a stable spatial network structure within the concrete system. Several studies have contributed to our understanding of PVA fiber reinforced concrete. Wang et al. (2018) conducted compression tests on PVA fiber rubber concrete and observed a significant reduction in the modulus of elasticity compared to conventional concrete due to the absence of coarse aggregates. Qiu and LimYang (2016) investigated the degradation of the PVA microfiber and the interface with the cement matrix under fatigue loads through single fiber fatigue pulling tests. The study shed light on the mechanisms involved in the degradation of the fiber-matrix interface microstructure. BaominYunqing (2021) examined the effects of partially hydrolyzed and fully hydrolyzed PVA on the physical and bonding properties of fresh and hardened cement mortar. The findings indicated that both partially hydrolyzed and fully hydrolyzed PVA can considerably enhance the bonding properties of cement mortar. In summary, research on polyvinyl alcohol fiber reinforced concrete has yielded significant advancements in building materials and structures (Lisheng and YaxingShunlei, 2022; Wenping et al., 2022).

However, it is important to note that the addition of PVA to concrete can lead to a slight reduction in compressive strength. Therefore, an alternative approach to address this issue is the utilization of modifiers. The modification of concrete through the use of silane coupling agents has gained significant development. Due to the impact of their unique molecular structure on the performance of cement-based materials, researchers have explored the application of silane coupling agents in cement-based materials. In cement paste, the hydroxyl group (-OH) present on the surface of cement particles and their hydration products can undergo condensation with the silicon hydroxyl group (≡Si-OH) in the hydrolyzate of the silane coupling agent, resulting in the formation of a covalent bond (Liu et al., 2020). Franceschini et al. (2007) conducted an analysis that confirmed the chemical bonding between the silane hydroxyl groups in the hydrolyzed product of the silane coupling agent and the surface of

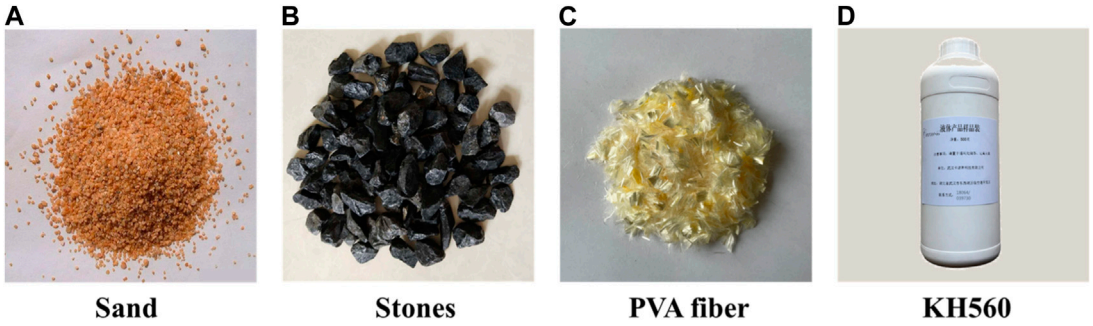

FIGURE 1
Main materials for the experiment. **(A)** Sand **(B)** Stones **(C)** PVA fiber **(D)** KH560.

TABLE 1 Physical and mechanical properties of cement.

Specific surface area/$m^2 \cdot kg^{-1}$	Standard consistency/%	Coagulation time/min		Stability	Flexural strength/MPa		Compressive strength/MPa	
		Initial setting time	Final setting time		3 d	28 d	3 d	28 d
370	27	150	205	√	4.8	8.0	29.2	48.5

TABLE 2 Physical and mechanical properties of PVA fiber.

Density/kg/m^3	Diameter/ *μm*	Elastic Modulus/GPa	Length/ mm	Tensile strength/MPa	Break elongation/%	Poisson ratio
1.3	15	39	6	1704	12	0.3

TABLE 3 Technical indexes of silane coupling agent-KH560.

Type	Density/kg/m^3	Chromatographic purity/%	Boiling point/°C	Refractive index/ND25	Flash point/°C
KH560	950	97.5	290	1.426	110

the C-S-H gel. This indicates that the silane coupling agent can serve as a connector between the organic polymer and the hydration product. Similarly, Minet et al. (2006) utilized this technique to demonstrate that the silane coupling agent can establish a connection with the C-S-H crystal without damaging the inorganic framework of the C-S-H gel. In another study by Dong and HuangShu (2013) a silane coupling agent was applied to the surface of rubber particles, which were then incorporated into concrete. Through the bridging effect of the silane coupling agent between the rubber particles and the cement matrix, the interface bond strength between the cement matrix and rubber was enhanced. As a result, the mechanical properties of the composite concrete, including improvements of 10%–20%, were observed. These findings highlight the potential of using silane coupling agents as a means to improve the performance of cement-based materials. By establishing stronger interface bonds, these agents offer a promising approach to enhance the mechanical properties of composite concrete while minimizing the reduction in compressive strength. Further research in this area is warranted to explore the full potential and optimize the application of silane coupling agents in cement-based materials.

2 Methodology

2.1 Main materials

The raw materials used in this experiment are PVA fiber, stone, sand, cement, and KH-560 coupling agent, whose main materials are shown in Figure 1.

The sand and stone used in this experiment are mainly provided by the laboratory of Henan University of Technology, in which the fineness modulus of sand is 2.5 and the particle grading of stone is 5–25 mm; the cement is provided by Zoomlion Cement Xingtai Co., Ltd. and P-O42.5 ordinary silicate cement is selected, and the main chemical compositions are shown in Table 1; the PVA fibers are provided by Changzhou

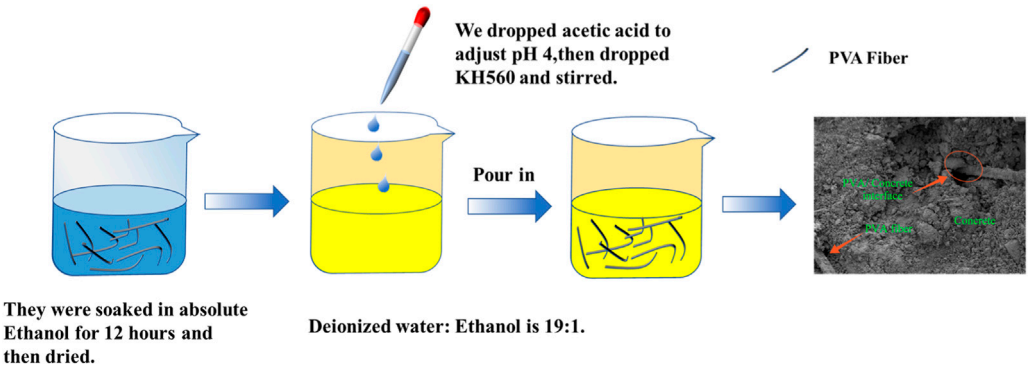

FIGURE 2
PVA fiber treatment process.

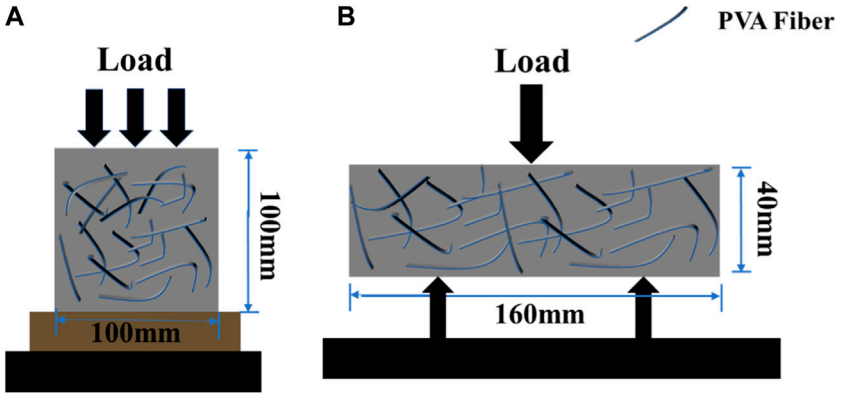

FIGURE 3
The schematic illustration of **(A)** pressure and **(B)** flexural test of samples.

Tianyi Engineering Fibers Co., Ltd. and the physical properties are shown in Table 2; KH-560 coupling agent is provided by Jinan Xingfeilong Chemical Co., Ltd., the physical properties are shown in Table 3; fine aggregate is made of river sand with fineness modulus of 2.5, apparent density of 2,650 kg/m^3, bulk density of 1,850 kg/m^3; coarse aggregate is continuously graded (5–25 mm) gravel with bulk density of 1,550 kg/m^3, apparent density of 2,703 kg/m^3.

2.2 Treatment method and mechanism

As shown in Figure 2, the PVA fibers were soaked in anhydrous ethanol for 12 h to remove residues, washed, and dried to constant weight. The deionized water and ethanol solution was stirred well in a volume ratio of 95:5, and acetic acid was added slowly to bring the pH of the solution to about 4.0, and a certain mass of SCA was added after this. The coupling agent prepared as described above was then slowly poured into a container containing the PVA fibers and stirred for 5 min in order to make a homogeneous mixture. It was left at 20°C for 6 h, filtered and then cooled to room temperature, then dried at 40°C to constant weight and set aside.

In this paper, the coupling agent KH560 is used as a modifier for PVA fibers. KH560 ($C_9H_{20}O_5Si$) has a reactive epoxy group in its molecular structure, which allows it to react with various compounds containing reactive epoxy groups by addition or hydrogen bonding, and to bond firmly with organic polymers (Li et al., 2016a). Notably, KH560 is hydrolyzable in a mixture of ethanol and water. The hydrolysis process is mainly due to the fact that the methoxy (-OCH_3) in SCA is a hydrolyzable group, which hydrolyzes in water to form Si-OH hydroxyl groups and -OH bonds. In addition, if the dosage is high, a -OH bond self-condensation reaction may occur, and the Si-O-Si bond formed can react with inorganic materials containing hydroxyl groups (Bingxiang et al., 2022a). Many -OH bonds are present on the surface of PVA fibers treated with coupling agent KH560, and -OH bonds and $Ca(OH)_2$ products are present in the cement hydration products. This makes it easy to form chemical bond connections at the interface between organic materials and cement hydration products. In other words, the Si-OH groups in the coupling agent KH560 and the -OH groups in the hydration products can be condensed and merged to form Si-O-Ca bonds, which can increase the van der Waals interaction force at the interface, and the hydrogen bonding

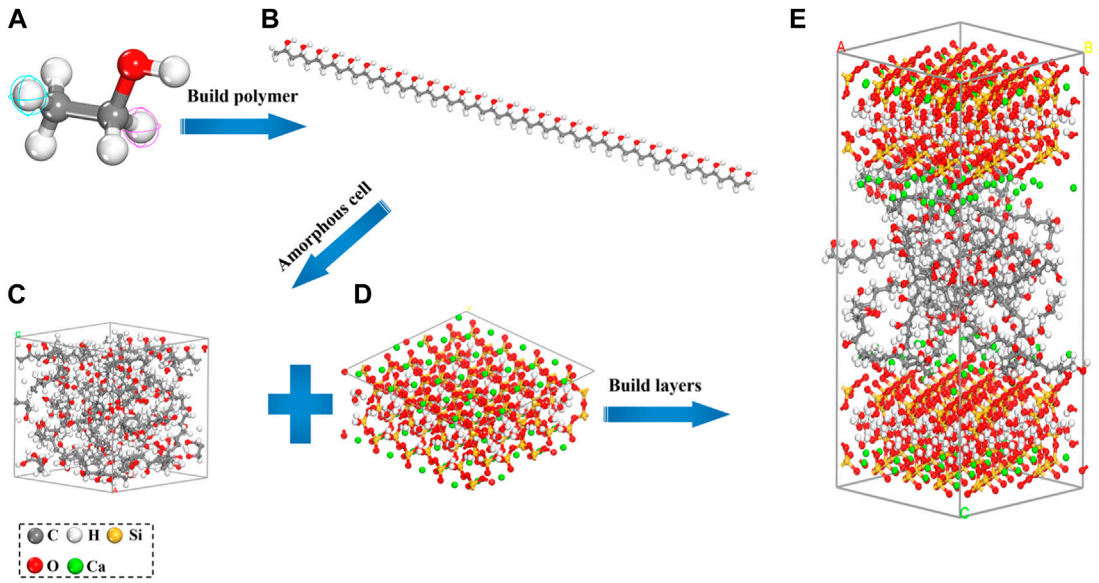

FIGURE 4
PVA/C-S-H Model building process.

between the hydroxyl groups can further improve the interfacial adhesion.

2.3 Test method

2.3.1 Mechanical properties

In order to understand the effect of SCA on the mechanical properties of PVA fibre concrete, mechanical tests were carried out on composite concrete samples that reached the curing target period (7–28 days). In this study, the relevant mechanical property tests were conducted in accordance with the standard "Test Methods for Physical and Mechanical Properties of Concrete" (GB/T50008-2019). As shown in Figures 3A, B, the size of the specimen block used for the cube compressive strength test was 100 mm × 100 mm × 100 mm, and the size of the bending strength specimen was 40 mm × 40 mm × 160 mm. In addition, the Y250 digital electric stress type straight shear and DKZ-5000 electric bending tester were used for the compressive strength and bending strength tests, respectively.

2.3.2 SEM microscopic experiments

Firstly, the specimens cured to the specified age were cut into 10 mm × 10 mm × 10 mm cubes, polished with 2000 grit sandpaper and the hydration reaction was terminated by immersion in anhydrous ethanol. Then, they were placed in a vacuum drying oven at 40°C for 24 h and the samples were filtered by blowing air, and finally the composite interfaces were fixed on a sample stage for vacuum gold plating. Then, Quanta FEG series scanning electron microscope equipment was used to observe the microscopic morphology of the interface with the cement matrix before and after SCA-modified PVA fibers. The schematic diagrams of the compressive (a) and flexural (b) tests of the samples are shown in Figure 3.

3 Molecular dynamics simulation

3.1 Model building

In order to further investigate the mechanism of synergistic enhancement of PVA fibre composite cementitious by SCA coupling agent on molecular scale, molecular dynamics simulation of composite cementitious is required. In this paper, molecular dynamics simulations of the interfacial model of PVA cementitious with and without SCA modification were carried out on the nanoscale, respectively, by using Materials Studio (MS) software (Feng et al., 2021; Feng and QinZhao, 2023). MS software can build a set of effective models and algorithms at the atomic level, and apply the classical mechanics method to study the laws of motion of microscopic molecules in order to obtain the basic laws and macroscopic properties of the system. And on this basis, macro and microscopic tests are combined to complete further research on new composite materials (Yang and Cao, 2021).

The performance of concrete is primarily influenced by the hydration products of cement, with the key component being calcium silicate hydrate gel (C-S-H). The C-S-H gel, which is an incomplete crystal, has been extensively studied regarding its structure and dynamics (Tu et al., 2022). Among various models, the Tobermorite molecular structure has proven successful in characterizing the properties of C-S-H during its evolution. Therefore, this study adopts the Tobermorite model as the basis for this investigation (BowersKirkpatrick, 2009; Churakov, 2009). Initially, the Tobermorite crystal is cut, expanded, and combined into a plane along the crystal plane (0 0 1) with parameters U = 22.00 Å and V = 22.00 Å. This plane is then used to construct gel pores, serving as the cement-based model. The chosen PVA type in this study has a density of 1.0 kg/m^3. The amorphous unit of the PVA polymer chain consists of three PVA polymer chains, with

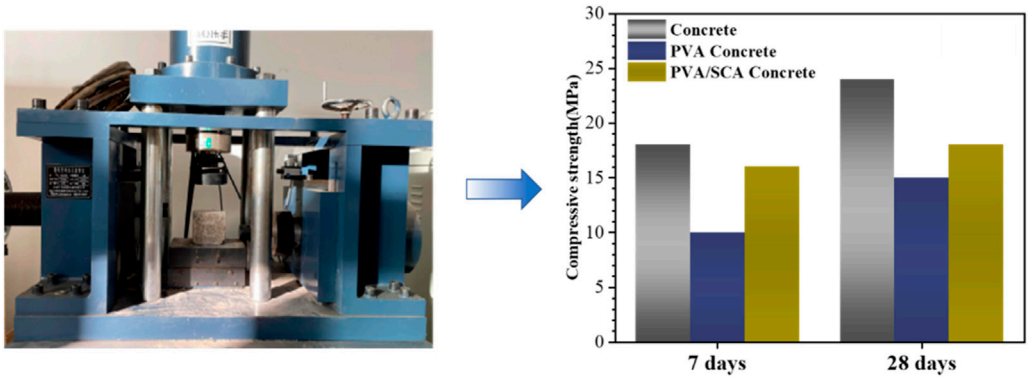

FIGURE 5
Compressive strength test results of mechanical properties.

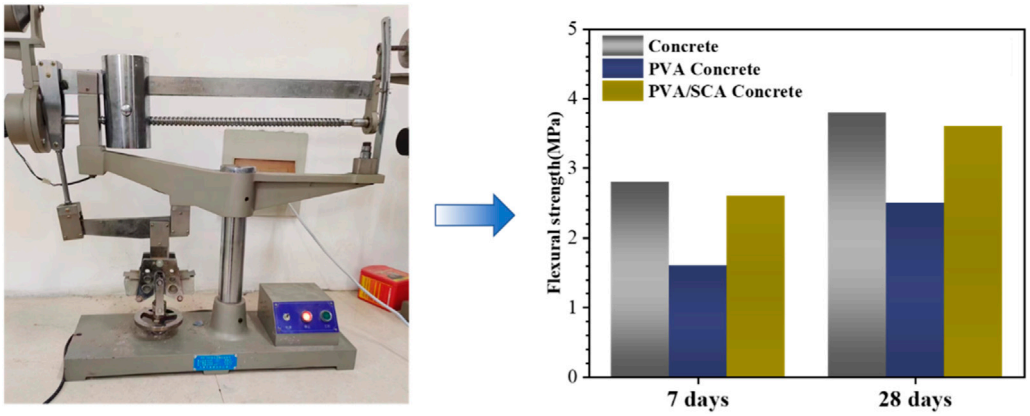

FIGURE 6
Flexural strength test results of mechanical properties.

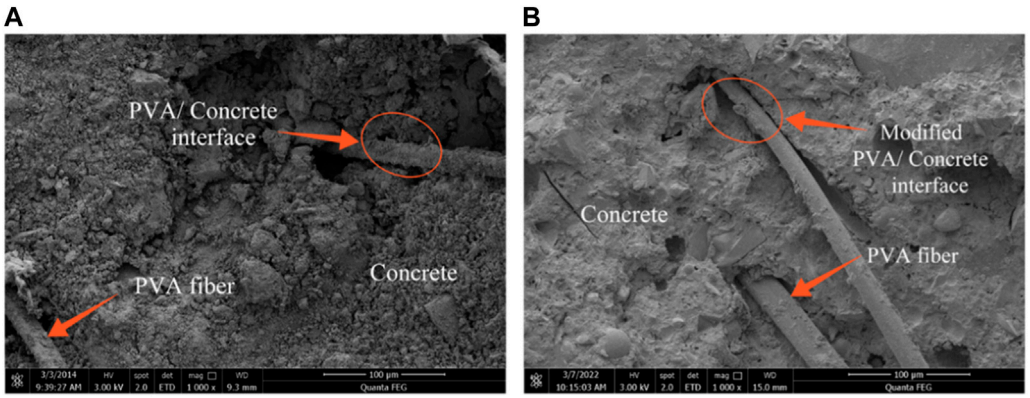

FIGURE 7
The SEM photos of the interface between PVA/cement paste before and after modification. **(A)** KH560 unmodified PVA fiber PVC/grout interface. **(B)** KH560 modified PVA fiber PVC/grout interface.

each chain comprising 30 PVA monomers. The amorphous unit has dimensions of a = 20.20 Å, b = 20.20 Å, c = 20.87 Å, and α = β = γ = 90°. KH560, an amorphous battery composed of 10 molecules with a density of 1.047 kg/m^3, has dimensions of a = 22.00 Å, b = 22.00 Å, c = 6.33 Å, and α = β = γ = 90°. Using the Build Layer module, the PVA/C-S-H model (a = 21.40 Å, b = 21.40 Å, c =

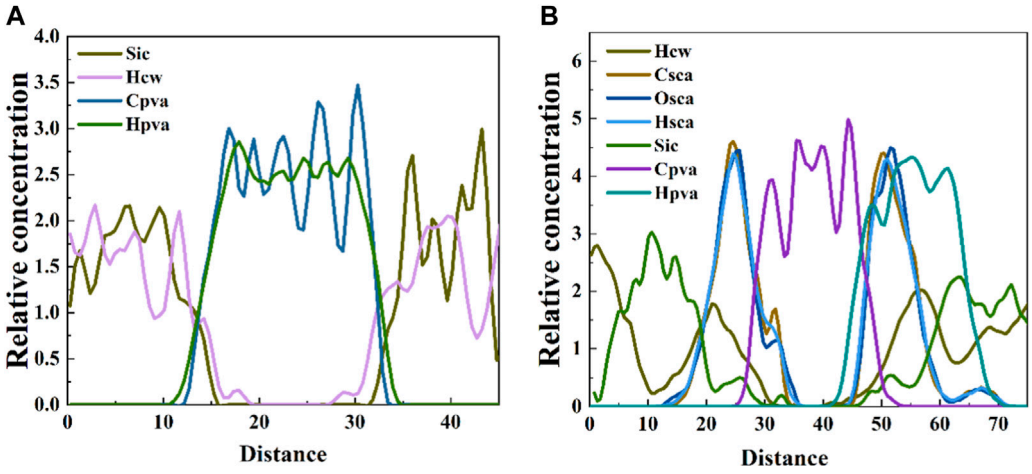

FIGURE8
Relative concentration distribution of **(A)** PVA/CSH; and **(B)** PVA/SCA/CSH along the Z-direction of the system. Si and Hcw, silicic and hydrogen atom where subscript wrepresents water molecule; Cpva and Hpva, carbon and hydrogen atom in PVA molecule respectively; and Csca, Osca, and Hsca = carbon, oxygen, and hydrogen atoms in SCA molecule, respectively.

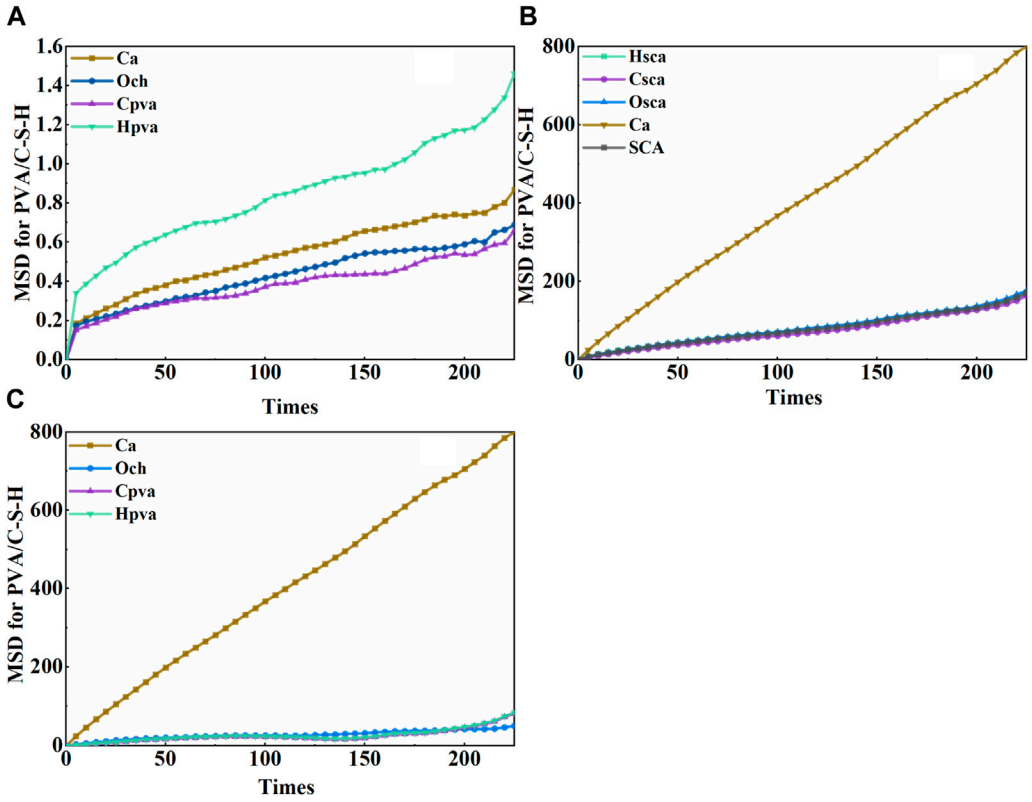

FIGURE9
MSD evolution of Ca, O, C, and H atoms from **(A)** PVA–C-S-H; **(B)** PVA–SCA–C-S-H; and **(C)** PVA–SCA–C-S-H system at 1,000 ps.

46.61 Å) and the PVA/SCA/C-S-H model (a = 21.80 Å, b = 21.80 Å, c = 77.68 Å) were constructed. It should be noted that in these models, the PVA and SCA components do not have fixed surfaces. This is because they can be energetically optimized to assume more suitable positions. Figure 4 (referenced below) provides a visual representation of the construction process for the PVA/C-S-H model (Note: Figure 4 is not provided in the text. Please refer to the original source for the specific figure).

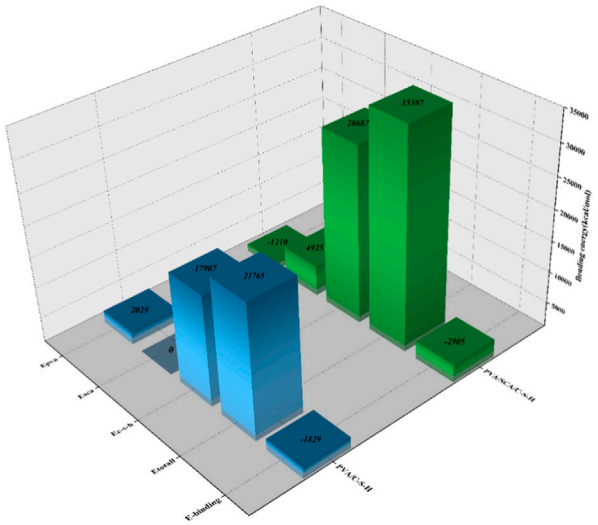

FIGURE 10
Interaction of PVA/C-S-H, and PVA/SCA/C-S-H interfaces.

3.2 Force field selection and simulation process

In this study, Materials Studio 2020 software was employed for simulating and analyzing all models. The selection of a suitable force field is crucial in molecular dynamics simulations, as it directly impacts the accuracy of the calculation results. After consulting relevant research findings, the Compass (Condensed-phase Optimized Molecular Potential for Atomistic Simulation Studies) force field was chosen for this investigation (Al-Ostaz et al., 2010; Feng et al., 2023). The Compass force field provides a reasonable model for describing organic and inorganic systems, and it has been extensively validated by concrete research scholars, demonstrating high compatibility with cement-based materials and reducing potential errors in the test data. To ensure the convergence of the models and eliminate any unreasonable structural components introduced during the model construction process, the geometry of the two interface models was initially optimized (Bai et al., 2023). Subsequently, an isothermal and isobaric (NPT) equilibrium run was conducted using a time step of 300 ps and 1 fs, with the simulation temperature set to 300 K. The system temperature and pressure were controlled using the Andersen and Berendsen methods, respectively. To strike a balance between simulation accuracy and duration, a dynamic simulation was performed under the NVT ensemble (Bingxiang et al., 2022b). This simulation utilized a time step of 1 fs and a total simulation time of 1 ns, resulting in the generation of the final simulation file. By following these procedures, the study aimed to obtain reliable simulation results while considering the trade-off between accuracy and computational efficiency.

4 Results and discussion

4.1 Mechanical properties analysis

Figure 5 shows the test results of compressive properties of PVA concrete with and without added silane coupling agent at 7 and 28 days of curing, while the results of mechanical properties of plain concrete were used as a control group. The test results show that the compressive and flexural strengths of the concrete were increased to

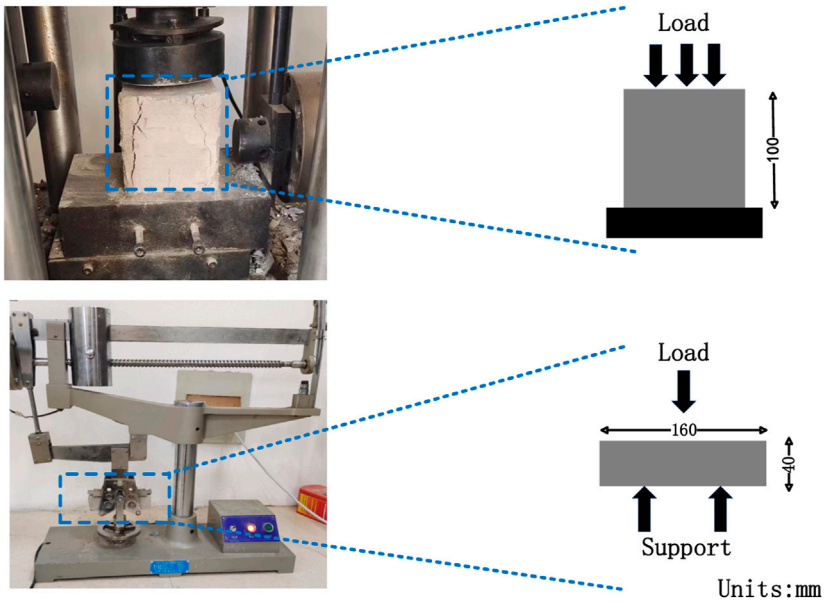

FIGURE11
Failure mechanism diagram of different macroscopic test blocks.

different degrees after incorporation of SCA. Compared with the results of the blank control group, the compressive strength of concrete increased by 0.70 and 0.37 times at 7 and 28 days, respectively, after the incorporation of PVA fibers, which is due to the fact that the incorporation of PVA fibers caused changes in the internal structure of the self-compacting concrete body, which led to an increase in the number of interfaces between the self-compacting concrete and the cementitious matrix, and an increase in the number of internal weak surfaces in the body, which in turn lowered the compressive strength of the PVA concrete. In addition, the compressive strength of PVA/SCA concrete was increased more significantly, by 1.58 and 0.62 times at 7 and 28 days, respectively. It can be seen that PVA fibers modified by SCA can effectively improve the compressive properties of PVA concrete, and the improvement effect is more and more obvious with the increase of curing time.

Figure 6 shows the test results of the flexural strength of the three types of concrete at curing times of 7 and 28 days. The flexural strength of PVA concrete at 7 and 28 days increased by 0.72 and 0.35 times, respectively, and the compressive strength of PVA/SCA concrete increased by 1.68 and 1.01 times, respectively, compared to the control. The results showed that the flexural properties of PVA concrete with SCA were significantly improved compared to PVA concrete without modifier. It is proved that PVA fibers can reduce the brittle damage of concrete and improve its toughness. In addition, the bridging effect of SCA can improve the weak interfacial transition zone between the polymer and the cement matrix and improve the mechanical properties of the composite concrete. This hypothesis will be verified by SEM and molecular dynamics simulations in the following sections.

4.2 Analysis of SEM results

As shown in Figures 7A, B, the smooth traces left by the shedding of PVA fibers and the presence of a large gap at the interface between the cementitious and PVA fibers can be seen, indicating that the unmodified PVA fibers are not tightly bonded to the cementitious, which may lead to cracking of the composite concrete when it is subjected to external loading, and thus indirectly lead to the degradation of its mechanical properties. It is worth noting that the treated PVA fibers were embedded in the concrete without obvious interfacial gaps. This is due to the coupling effect between SCA and the interfacial materials after the PVA fibers are treated with SCA, and this interaction optimizes the hydrophilic fibers of PVA so that they can be more easily bonded with the gel material, thus leading to a significant improvement in their adhesion to the cement matrix. It can be seen that the SCA-modified polymer membrane can act as a bridging ligament at the interface, inhibit the extension of cracks, enhance the interfacial bond between the PVA fiber organic material and the gel material, and play an important role in improving the mechanical properties of PVA composite concrete.

4.3 Molecular dynamics simulation

4.3.1 Concentration distribution curve

Concentration distribution curves are used to reflect the spatial location of key molecules in the interfacial model and to characterize the molecular state, which is able to reflect the local structure of the modifier and the cement material (Li et al., 2016b; Quan et al., 2021). Due to the limitations of the modeling direction and cycle boundaries, it is necessary to define the bottom of the model as the starting point (0 distance) and analyze the distribution of the concentration function only in the Z direction. In the calculation process, the region along the Z-direction of the model is divided into several cells, the relevant atoms are counted, and the relative concentration can be expressed by Eq. 1:

$$\text{Relative}\,[\Theta]_{\text{slab}} = \frac{[\Theta]_{\text{slab}}}{[\Theta]_{\text{bulk}}} \tag{1}$$

$$Where\ [\Theta]_{slab} = (no.atoms\ in\ slab)/(volume\ of\ slab)$$

$$[\Theta]_{bulk} = (total\ no.atoms\ in\ system)/(volume\ of\ system)$$

Figure 8 represents the atomic concentration distribution function of major elements along the Z direction before and after coupling agent addition. As can be seen from the figure, the atomic concentration distribution is nearly symmetric and perpendicular to the nanopore substrate. Within the C-S-H region, Si and Hcw show multiple strong peaks, which indicates that the nanopore has a high affinity for water molecules in a layered structure. In Figure 9A, the atomic concentrations of Sic, Cpva, and Hpva in the 11–16 and 30–33 Å regions show linear fluctuations, suggesting that the number of molecules in this range is low and that nanogaps and simulated boundary effects may exist. In Figure 9B, it is noteworthy that Cpva and Hpva show peaks on both sides of the nanopore and the atomic density distribution within the SCA system in the 20–30 and 45–60 Å regions appears to be disordered, which suggests that there is an interaction between the PVA and coupling agent atoms and that the two have a good coordination ratio. In other words, the incorporation of SCA makes it possible to have a favorable arrangement and bonding between the atoms at the interface between PVA and cement, which greatly improves the interfacial bond strength between the composites.

4.3.2 Root mean square displacement

The root mean square displacement (MSD) serves as a significant parameter for evaluating the kinematic properties of atoms. It is calculated as the average of the squared particle displacements. The slope of the MSD curve determines the molecular diffusion coefficient, which increases with the curve's steepness. It is, therefore, a valuable tool for assessing atomic motion (XuWang, 2018; Feng et al., 2022). The root mean square displacement and time-dependent function can not only provide a visualization of the stability of the interface between PVA and cement, but also allow for characterization of kinetic behaviour prior to and post SCA treatment. To determine the root mean square displacement of the model, initially, we measure the deviation of the atoms from their starting positions over time as a quantifiable displacement. This approach enables us to compare the atomic variances and intermolecular forces in diverse systems (Liu et al., 2021),. The formula used for calculation is listed below.

$$\text{MSD}\,(\text{t}) = \{|r_i\,(t) - r_i\,(0)|^2 \tag{2}$$

$ri\,(t)$ is the position vector of particle I at time t, $ri\,(0)$ is the position vector of particle I at the initial time, represents the average of all atoms in the group. The larger MSD value at time t indicates that the

atom diffuses rapidly and moves farther away from its original position.

Figure 9 shows the MSD values of atoms in PVA-C-S-H and PVA/SCA/C-S-H and PVA/SCA/C-S-H, respectively, for discussing the effect of coupling agent on the dynamic properties of PVA fiber concrete. It can be found that the MSD values of H atoms in PVA-C-S-H are higher than the other atoms, on the contrary, the MSD values of Ca and Ocsh atoms in C-S-H are smaller, which indicates that the reactive H atoms at the interface are unstable and have a high degree of activity, whereas the hydrated calcium silicate is more stable after the chemical reaction occurs, and it also indicates that it has a stable skeleton structure. In addition, the MSD values of Figure 9B are all lower than that of Figure 9A, especially the Hpva curve has the largest decrease in MSD value, which is due to the fact that the incorporation of SCA not only reduces the free stretching motions of the Hpva, Ca, and Ocsh atoms at the interface but also increases the hydrogen bonding interactions on the interfaces (Hsca- Hw, Hpva- Ow, and Hsca-Hpva), thus improves the stability of the interface. It is noteworthy that the MSD values of the major atoms decreased before and after SCA addition, but their order did not change. This indicates that the introduction of the coupling agent does not affect the stability of the two systems, but only plays an inhibitory role to enhance the bonding of the PVA-cementitious interface.

4.3.3 Binding energy

In Materials Studio 2020, the binding energy is used to evaluate the interaction strength between different components in the interface model, which represents the energy difference between the total energy of the system and the separation energy of the two parts. It is not only an important parameter reflecting the interfacial interaction, but also a key indicator to measure the adsorption strength during the adsorption process (Caihua et al., 2021; Yong et al., 2021). PVA/CSH binding energy can be calculated by formula (3), and PVA/SCA/CSH formula (4).

$$E_{binding} = E_{PVA} + E_{CSH} - E_{PVA/CSH} \quad (3)$$

$$E_{binding} = E_{PVA} + E_{SBL} + E_{CSH} - E_{PVA/SBL/CSH} \quad (4)$$

The results of the analysis can be used to assess the stability, strength and kinetic properties of the main atoms of the interfacial model under the conditions of the presence or absence of coupling agent. If the result of the binding energy calculation is positive, the two systems are attracted to each other; if the result of the binding energy is negative, these two systems maintain each other; the larger the absolute value of the binding energy, the stronger the interaction between the two systems and the more stable the system is. From Figure 10, it can be seen that the introduction of coupling agent makes the binding energies of both SCA and C-S-H significantly improved, which is due to the hydrophobicity of PVA molecules, and the chemical bond formed between the H atoms of SCA and the H atoms of the PVA fibers by the addition of SCA can improve this hydrophobicity. At the same time, it is considered that the interaction energy is provided by non-bonding interactions, which mainly consist of van der Waals and electrostatic interaction forces between atoms. The absolute value of the energy of the binding energy is significantly larger after the modification of SCA than before the modification, which mainly relies on the hydrogen bonding formed by the H and O atoms of the coupling agent with the water molecules in the PVA and the hydrated calcium silicate, as well as the ionic bonding with Ca, which is important for the enhancement of the PVA cementitious interface.

4.4 Microstructure mechanical property relationships

In Figure 11, it is shown that when composite concrete is subjected to compression, shear, or bending forces, there is a chemical bond formed between the mortar and the aggregate, as well as between the mortar and the coarse aggregate. Additionally, PVA fibers exhibit good tensile properties, and their addition significantly enhances the shear and flexural properties of the test blocks (Bai et al., 2019). However, it is observed that as the amount of PVA fiber increases, the mechanical properties of PVA concrete start to decrease or even deform due to the relatively weak adhesion between PVA and mortar. In order to address this issue, KH560 is introduced as a reinforcing agent to enhance the interfacial bonding between PVA and cement. The addition of KH560 ultimately improves the mechanical properties of PVA concrete specimens and ensures the specimens remain in good compactness.

5 Conclusion

In this study, the synergistic strengthening effect of coupling agent-modified PVA fibers on cementitious interfaces at different scales was investigated by combining macroscopic tests, molecular dynamics simulation and analysis. First, at the macro-scale, the effects of different SCA (KH560) contents on the mechanical properties of modified PVA composite concrete were investigated and compared by macroscopic mechanical property tests. At the micro-scale, the effect of SCA on the microstructure of the PVA cementitious interface was observed and analyzed by scanning electron microscopy. On the nanoscale, the molecular dynamics simulation and analysis of the two interfacial models with and without SCA were carried out respectively, and the synergistic reinforcement of the interface was investigated by analyzing the concentration of the main atoms, the root-mean-square displacements and the binding energy. Based on the above comprehensive analysis and study, the following conclusions were drawn:

(1) Macro-mechanical test results show that the addition of SCA can improve the mechanical properties of PVA composite concrete, and PVA fibers can reduce the brittle damage of concrete and improve its toughness.
(2) SEM observation shows that there are obvious cracks at the interface between PVA and cementitious before modification, while the cracks between the two phases are not obvious after modification, but are filled instead, which effectively modifies the interfacial defects between PVA and cementitious, and strengthens the interfacial bonding ability between PVA fiber organic materials and cementitious materials.

(3) In the modeling and analysis of molecular dynamics, we found that the hydrated calcium silicate has a stable skeleton structure, and the addition of SCA increases the hydrogen bonding interactions at the interface, making the PVA-cement interface more compact and stable.

Data availability statement

The raw data supporting the conclusion of this article will be made available by the authors, without undue reservation.

Author contributions

CZ: Writing–original draft. LL: Writing–review and editing. XL: Writing–original draft, Writing–review and editing. WC: Writing–review and editing. YL: Writing–review and editing.

Funding

The author(s) declare financial support was received for the research, authorship, and/or publication of this article. This research was funded by the 2023 Henan Province Science and Technology Research Project (232102320173, 232102111126). This research was funded by the 2021 Henan Higher Education Teaching Reform Research and Practice Project (2021SJGLX670). This research was funded by the Project type: 2022 Special project of Science and Technology Development Center of Ministry of Education (Grant No. ZJXF2022254).

Conflict of interest

The authors declare that the research was conducted in the absence of any commercial or financial relationships that could be construed as a potential conflict of interest.

Publisher's note

References

Al-Ostaz, A., Wu, W., Cheng, A. H. D., and Song, C. (2010). A molecular dynamics and microporomechanics study on the mechanical properties of major constituents of hydrated cement. *Compos. PART B-ENGINEERING* 41 (7), 543–549. doi:10.1016/j.compositesb.2010.06.005

Bai, B., Bai, F., Nie, Q., et al. (2023). A high-strength red mud-fly ash geopolymer and the implications of curing temperature. *Powder Technol.*, 416. doi:10.1016/J.POWTEC.2023.118242

Bai, B., Rao, D., Chang, T., and Guo, Z. (2019). A nonlinear attachment-detachment model with adsorption hysteresis for suspension-colloidal transport in porous media. *J. Hydrology* 578, 124080. doi:10.1016/j.jhydrol.2019.124080

BaominYunqing, W. X. (2021). Effect of degree of hydrolysis of polyvinyl alcohol on adhesive properties of cement mortar. *J. Test. Eval.* 49 (4), 20190036. doi:10.1520/jte20190036

Bingxiang, Y., Weijie, C., Jin, Z., Liu, F., Guo, Y., et al. (2022a). Addition of alkaline solutions and fibers for the reinforcement of kaolinite-containing granite residual soil. *Appl. Clay Sci.* 228, 106644. doi:10.1016/j.clay.2022.106644

Bingxiang, Y., Weijie, C., Zihao, L., Zhao, J., Luo, Q., Chen, W., et al. (2022b). Sustainability of the polymer SH reinforced recycled granite residual soil: properties, physicochemical mechanism, and applications. *J. Soils Sediments* 23 (1), 246–262. doi:10.1007/s11368-022-03294-w

BowersKirkpatrick, G. M. R. J. (2009). Natural Abundance^{43}Ca NMR spectroscopy of tobermorite and jennite: model compounds for C-S-H. *J. Am. Ceram. Soc.* 92 (2), 545–548. doi:10.1111/j.1551-2916.2008.02906.x

Caihua, Y., Kui, H., Qilin, Y., Wang, D., Zhang, W., Chen, G., et al. (2021). Analysis of the storage stability property of carbon nanotube/recycled polyethylene-modified asphalt using molecular dynamics simulations. *Polymers* 13 (10), 1658. doi:10.3390/polym13101658

Churakov, S. V. (2009). Structure of the interlayer in normal 11 A tobermorite from an *ab initio* study. *Eur. J. MINERALOGY* 21 (1), 261–271. doi:10.1127/0935-1221/2009/0021-1865

Dong, Q., and HuangShu, B. X. (2013). Rubber modified concrete improved by chemically active coating and silane coupling agent. *Constr. Build. Mater.* 48, 116–123. doi:10.1016/j.conbuildmat.2013.06.072

Feng, Y., Li, Y., Zhao, C., Dajing, Q., Chao, W., and PeiYan, W. (2022). Nano-CaCO3 enhances PVA fiber-matrix interfacial properties: an experimental and molecular dynamics study. *Mol. Simul.* 48 (15), 1378–1392. doi:10.1080/08927022.2022.2094373

Feng, Y., Qin, D., Li, L., Li, Y., Wang, C., and Wang, P. (2021). EVA enhances the interfacial strength of EPS concrete: a molecular dynamics study. *J. Exp. Nanosci.* 16 (1), 382–396. doi:10.1080/17458080.2021.2003338

Feng, Y., and QinZhao, D. C. (2023). The synergistic strengthening effect of silane coupling agent on the interface between PVA/EPS and cement: experiment and molecular simulation. *Compos. INTERFACES* 30 (1), 21–41. doi:10.1080/09276440.2022.2109788

Feng, Y., Wang, W., Wang, S., Niu, Z., and Li, L. (2023). Multi-scale analysis of mechanical properties of KH-560 coupling agent modified PVA fiber-rubber concrete. *Compos. INTERFACES* 30 (9), 983–1010. doi:10.1080/09276440.2023.2179267

Franceschini, A., AbramsonMancini, S. V., Bresson, B., Chassenieux, C., and Lequeux, N. (2007). New covalent bonded polymer-calcium silicate hydrate composites. *J. Mater. Chem. An Interdiscip. J. Deal. Synthesis* 17 (9), 913–922. doi:10.1039/b613077a

Guoliang, Y., Zhiwen, D., Jingjiu, B., et al. (2023). Experimental study on the dynamic splitting tensile properties of polyvinyl-alcohol-fiber-reinforced cementitious composites. *Constr. Build. Mater.*, 383. doi:10.1016/J.CONBUILDMAT.2023.131233

LamenJohn, S. F. (2023). Long-term loss of tension stiffening of concrete containing recycled aggregate and steel fibres. *Structures* 54, 1312–1319. doi:10.1016/j.istruc.2023.05.145

Li, G., Wang, Z., Leung, C. K. Y., Tang, S., Pan, J., Huang, W., et al. (2016a). Properties of rubberized concrete modified by using silane coupling agent and carboxylated SBR. *J. Clean. Prod.* 112, 797–807. doi:10.1016/j.jclepro.2015.06.099

Li, G., Wang, Z., Leung, C. K. Y., Tang, S., Pan, J., Huang, W., et al. (2016b). Properties of rubberized concrete modified by using silane coupling agent and carboxylated SBR. *J. Clean. Prod.* 112, 797–807. doi:10.1016/j.jclepro.2015.06.099

Lisheng, L., and YaxingShunlei, X. H. (2022). Bending and crack evolution behaviors of cemented soil reinforced with surface modified PVA fiber. *Materials* 15 (14), 4799. doi:10.3390/ma15144799

Liu, Q., Wu, J., Xie, L., et al. (2021). Micro-scale investigation of aging gradient within bitumen film around air-binder interface. *Fuel*, 286. doi:10.1016/j.fuel.2020.119404

Liu, T., Wei, H., Zhou, A., et al. (2020). Multiscale investigation on tensile properties of ultra-high performance concrete with silane coupling agent modified steel fibers. *Cem. Concr. Compos.*, 111. doi:10.1016/j.cemconcomp.2020.103638

Mayercsik, N. P., Shaeffer, M., Graham-Brady, L., and Kurtis, K. E. (2015). Analysis of Portland cement mortar under impact: a combined material characterization, micromechanics modeling, and dynamic testing approach. *Cem. Concr. Res.* 73, 190–206. doi:10.1016/j.cemconres.2015.01.021

Mei-Ling, Z., Chuanzhi, S., Li, G., Qiao, Y., Chen, J., Zhang, W., et al. (2022). Investigation on drift ratio limits of PVA fiber reinforced concrete columns under different performance levels based on the Kunnath damage model. *Case Stud. Constr. Mater.* 17, e01403. doi:10.1016/j.cscm.2022.e01403

Minet, J., Abramson, S., Bresson, B., Franceschini, A., Van Damme, H., and Lequeux, N. (2006). Organic calcium silicate hydrate hybrids:a new approach to cement based nanocomposites. *J. Mater. Chem. An Interdiscip. J. Deal. Synthesis* 16 (14), 1379. doi:10.1039/b515947d

Qiu, J., and LimYang, X.-N. E.-H. (2016). Fatigue-induced deterioration of the interface between micro-polyvinyl alcohol (PVA) fiber and cement matrix. *Cem. Concr. Res.* 90, 127–136. doi:10.1016/j.cemconres.2016.08.021

Quan, L., Gongying, D., Zeyu, Z., Fu, C., and Oeser, M. (2021). Investigation on bitumen-epoxy interface in cold mixed epoxy bitumen using experimental observation and molecular dynamics simulation. *Constr. Build. Mater.* 303, 124490. doi:10.1016/j.conbuildmat.2021.124490

Sagar, R. V., and PrasadKumar, B. K. R. S. S. (2012). An experimental study on cracking evolution in concrete and cement mortar by the b -value analysis of acoustic emission technique. *Cem. Concr. Res.* 42 (8), 1094–1104. doi:10.1016/j.cemconres.2012.05.003

Said, M., Montaser, W., Elgammal, A. S., Zahir, A. H., and Shaaban, I. G. (2021). Shear strength of reinforced mortar beams containing polyvinyl alcohol fibre (PVA). *Int. J. Civ. Eng.* 19 (10), 1155–1178. doi:10.1007/s40999-021-00628-6

Tu, Y. M., Shi, P., Liu, D. Y., Wen, R., Yu, Q., Sas, G., et al. (2022). Mechanical properties of calcium silicate hydrate under uniaxial and biaxial strain conditions: a molecular dynamics study. *Phys. Chem. Chem. Phys.* 24 (2), 1156–1166. doi:10.1039/d1cp04474e

Wang, F., and YangYin, Y. S. (2021). Thermal and moisture performance parameters of high toughness engineered cementitious Composite(ECC) with PVA fibers. *J. Build. Eng.* 43, 102905. doi:10.1016/j.jobe.2021.102905

Wang, J., Dai, Q., Si, R., and Guo, S. (2018). Investigation of properties and performances of Polyvinyl Alcohol (PVA) fiber-reinforced rubber concrete. *Constr. Build. Mater.* 193, 631–642. doi:10.1016/j.conbuildmat.2018.11.002

Wenping, D., Caiqian, Y., Hans, D. B., Wang, C., and Pan, Y. (2022). Investigation of the flexural behavior of reinforced concrete beams strengthened with a composite reinforcement layer: polyvinyl alcohol fiber-reinforced ferrocement cementitious composite and steel wire mesh. *Struct. Concr.* 24 (1), 1612–1626. doi:10.1002/suco.202100894

XuWang, G. H. (2018). Diffusion and interaction mechanism of rejuvenating agent with virgin and recycled asphalt binder: a molecular dynamics study. *Mol. Simul.* 44 (17), 1433–1443. doi:10.1080/08927022.2018.1515483

Yang, Y., and Cao, J. (2021). Interfacial heat transfer behavior of graphene-based filler and calcium-silicate-hydrate in cement composites. *Int. J. HEAT MASS Transf.*, 176. doi:10.1016/J.IJHEATMASSTRANSFER.2021.121165

Yong, F., Caihua, Y., Kui, H., Yujing, C., Yu, L., and Taoli, Z. (2021). A study of the microscopic interaction mechanism of styrene-butadiene-styrene modified asphalt based on density functional theory. *Mol. Simul.* 49, 1203–1214. doi:10.1080/08927022.2021.1876874

Yong, F., and DajingChen, Q. Z. (2023). The synergistic strengthening effect of silane coupling agent on the interface between PVA/EPS and cement: experiment and molecular simulation. *Compos. Interfaces* 30 (1), 21–41. doi:10.1080/09276440.2022.2109788

Zhou, C., Shi, S. Q., Chen, Z., Cai, L., and Smith, L. (2018). Comparative environmental life cycle assessment of fiber reinforced cement panel between kenaf and glass fibers. *J. Clean. Prod.* 200, 196–204. doi:10.1016/j.jclepro.2018.07.200

Zhuang, L., Robert, W., Fen, D., et al. (2020). Measurement of stress-time avalanches inside polypropylene fiber reinforced concrete beams during flexure. *Constr. Build. Mater.* doi:10.1016/J.CONBUILDMAT.2020.121428

frontiers | Frontiers in Materials

TYPE Original Research
PUBLISHED 03 November 2023
DOI 10.3389/fmats.2023.1284722

OPEN ACCESS

EDITED BY
Bing Bai,
Beijing Jiaotong University, China

REVIEWED BY
Pan Liu,
Guangzhou Maritime College, China
Ming Zhang,
Zhengzhou University of Aeronautics, China

*CORRESPONDENCE
Xue qiang Yang,
xqyfls@126.com

RECEIVED 29 August 2023
ACCEPTED 04 October 2023
PUBLISHED 03 November 2023

CITATION
Deng X, Zhu Z, Lin Xy and Yang Xq (2023), Effect of matrix suction on the shear strength characteristics of reinforced granite residual soil.
Front. Mater. 10:1284722.
doi: 10.3389/fmats.2023.1284722

Effect of matrix suction on the shear strength characteristics of reinforced granite residual soil

Xiangwen Deng, Zhengyu Zhu, Xi yang Lin and Xue qiang Yang*

School of Civil and Transportation Engineering, Guangdong University of Technology, Guangzhou, China

Introduction: The soil in geogrid-reinforced structures is typically unsaturated, with the shear strength provided by both the matrix suction and the reinforced body. Traditional structural designs for saturated soils only consider the shear strength provided by the reinforced body, neglecting the part provided by matrix suction. As a result, the design for reinforced structures is biased toward conservatism.

Method: The study examined the matrix suction-provided shear strength in reinforced soils through strain-controlled triaxial and soil-water characteristic curve (SWCC) pressure plate instrumentation. The feasibility of the Schrefler and Khalili unsaturated soil shear strength formulas for predicting shear strength based on matrix suction forces was verified.

Results: The study revealed that the cohesion of saturated reinforced soil exhibits a significant decrease in contrast with unsaturated reinforced soil, with matrix suction serving as a crucial consideration for reinforced structure design.

Discussion: The experimental results confirm the suitability of applying the quasi-cohesion increment theory to reinforced clays. The Khalili formula can be utilized to predict the quasi cohesion of unsaturated reinforced soils with greater accuracy under diverse dry density conditions. The results obtained using post-shear moisture content were closer to the measured values than those using initial moisture content.

KEYWORDS

reinforced soil, granite residual soil, matrix suction, shear strength, soil-water characteristic curve

1 Introduction

Granite residual soil is widely distributed in the southeast coastal area of China and is a common filling material in this area for engineering construction, and geogrid reinforced soil technology is often used to improve the overall stability of granite residual soil slopes and embankments. Based on the theory of apparent cohesion, it is well known that the reinforced geogrid mainly improves the shear strength of the soil by increasing the cohesion of the soil (Wang et al., 2021); however, the superficial layer of the filled slope is usually in the unsaturated state, and the literature (Gao et al., 2018) points out that the apparent cohesion of unsaturated granite residual soil mainly includes two parts, matrix suction and soil cohesion itself, so ignoring the influence of matrix suction on the shear strength of reinforced granite residual soil will lead to excessively cautious designs (Chehade et al., 2020).

Researchers around the world have investigated the effects of factors such as the size and shape of the reinforcing material, particle size, and loading rate on the

frictional characteristics of the interface between soil and reinforcement. They conducted these investigations using standard direct shear and pullout tests (Infante et al., 2016; Mohammadehsan and Mohammadreza, 2017; Abdi et al., 2019; Kouchaksaraei and Khalkhali, 2020; Wei-xiang et al., 2023). To investigate the stress state of reinforced soil in actual conditions, scholars both domestically and internationally have employed triaxial tests to analyze the strength and deformative properties of reinforced soil. The shear strength characteristics of reinforced soils were investigated through triaxial tests by Vidal et al. (Vidal, 1969; Lei, 2000; Zhang et al., 2023); the results of the tests revealed that the reinforcement primarily improves soil shear strength by increasing the cohesive force. Furthermore, the shear strength also varies non-linearly with an increase in the number of reinforced layers. The study by Chen et al. (Chen et al., 2014; He et al., 2019; He et al., 2021) investigated the impact of perimeter pressure, the number of reinforcement layers, and the method of reinforcement placement on the shear strength of reinforced soils using triaxial tests.

In practice, matrix suction also significantly influences the shear strength of unsaturated soils. Zhong et al. (Zhong et al., 2015) and Luo et al. (Luo and Fu, 2019) conducted triaxial testing analyses of unsaturated soil to examine the impact of matrix suction on the shear strength of unsaturated soil. The experimental results revealed that the cohesion is significantly affected by matrix suction, exhibiting a linear growth relationship. However, the effective internal friction angle is minimally influenced by matrix suction. Zhao et al. (Zhao et al., 2021) investigated the connection between soil samples' strength properties, water retention capacities, and pore sizes during cyclic direct shear testing under both wet and dry conditions. The results indicated that the decline in water retention capacities and variation in strength parameters of soil samples were primarily due to changes in pore properties. Huang et al. (Huang et al., 2022) obtained soil-water characteristic curves (SWCCs)for typical granite residual soils in Huangpu, Guangzhou, using the filter paper test method. The results indicate that the matrix suction in strongly weathered granite residual soil zones in a higher saturation state experiences smaller changes as the saturation is increased further, and maintains higher residual matrix suction than that in fully weathered granite residual soil zones. At the same time, it is suggested by much of the literature that alterations in matrix suction also impact the strength of reinforced soils. Ghazavi et al. (Bergado et al., 1993; Mahmoud and Omid, 2021) conducted a study on the impact of moisture content on peak pullout force through pullout tests. The findings indicate that there was a substantial reduction in the peak pullout force as the moisture content escalated. Zhou (Zhou and Xu, 2013) carried out consolidated undrained triaxial tests to investigate the differences in the strength characteristics of reinforced expansive soils in their saturated and unsaturated states. The results indicate that, for the same type of reinforcement, the cohesive force of the unsaturated specimen was significantly greater than that of the saturated specimen. Zhao (Zhao and Lin, 2019) derived the analytical solution for the reinforcement length needed to sustain slope stability under a linear suction distribution using the horizontal split method. The results showed that an increase in matrix suction leads to a significant decrease in the reinforcement length. At present, scholars worldwide have proposed unsaturated soil shear strength equations based on Bishop's unsaturated shear strength equation. For instance, Cai (Guoqing et al., 2022) investigated the impact of pore ratio on the SWCC; they also introduced a novel formula to estimate the shear strength of unsaturated soils with different pore ratios and a wide range of variations in matrix suction. (Pham, 2022) proposed a shear strength equation reflecting the non-linear effects of saturation and matrix suction on the shear strength of unsaturated soils, through considering the micromechanical equilibrium conditions of the interaction among the solid, liquid, and air phases in soil. Bai (Bai et al., 2021) established a generalized principle for effective stress that can be applied to coupled processes involving heat, water, and force in both saturated and unsaturated soils, in which the approach is rooted in particle thermodynamics.

This paper is based on the municipal engineering project of the Flavor and Fragrance Industrial Park in Youxi County, Fujian Province, China, and the shear strengths and SWCC of the typical granite residual soil from Youxi were tested by using a strain-controlled triaxial instrument and SWC-150 SWCC pressure plate meter, respectively, to study the effect of matrix suctions and reinforcements on the shear strength of granite residual soil in saturated and unsaturated states, which provided certain theoretical basis and reasonable strength parameter references for actual reinforced soil structure design and construction.

2 Experiment

2.1 Reinforced geogrid and reinforced soil samples

The soil samples for testing were taken from the municipal project in Youxi County. The granite residual soil is a sandy silt with a mixture of light red and grayish-white color, slightly wet, and in a plastic to hard plastic state. The basic physical parameters of the soil measured by the indoor geotechnical tests are shown in Table 1, the particle gradation curve is shown in Figure 1A, and the static compaction curve is shown in Figure 1B.

The optimum moisture content and maximum dry density of the soil samples were measured by static compaction tests. As shown in Figure 1B, the optimum moisture content of the soil was 18.7%, and the corresponding maximum dry density was 1.73 g/cm^3.

The dimensions and strength parameters of the bidirectional glass fiber geogrid used in the test are shown in Table 2, the schematic picture of the geogrid is shown in Figure 2A, and the one-layer reinforced geogrid placed in the soil sample is shown in Figure 2B.

2.2 Test apparatus

The conventional triaxial strain-controlled apparatus TSZ30-2.0 and volumetric pressure controller SVPC-200–3, which maintains the accuracy and stability of the pressure during the loading process, were both used together during the sample consolidation and drainage shearing process. The other accessory parts, including rubber molds, film-covering cylinders, scales, and so on, support the triaxial testing. The SWCC were measured using a SWC-150 SWCC pressure plate meter. The main instruments used in this paper are shown in Figure 3; the triaxial instrument is shown

TABLE 1 Basic physical parameters of granite residual soil in Youxi, Fujian.

Natural moisture content (%)	Natural dry density (g/cm^3)	Natural gravity (KN/m3)	Saturated gravity (KN/m^3)	Plastic limit (%)	Liquid limit (%)	Plastic index
22.1	1.64	18.4	19.0	31.9	45.6	13.7

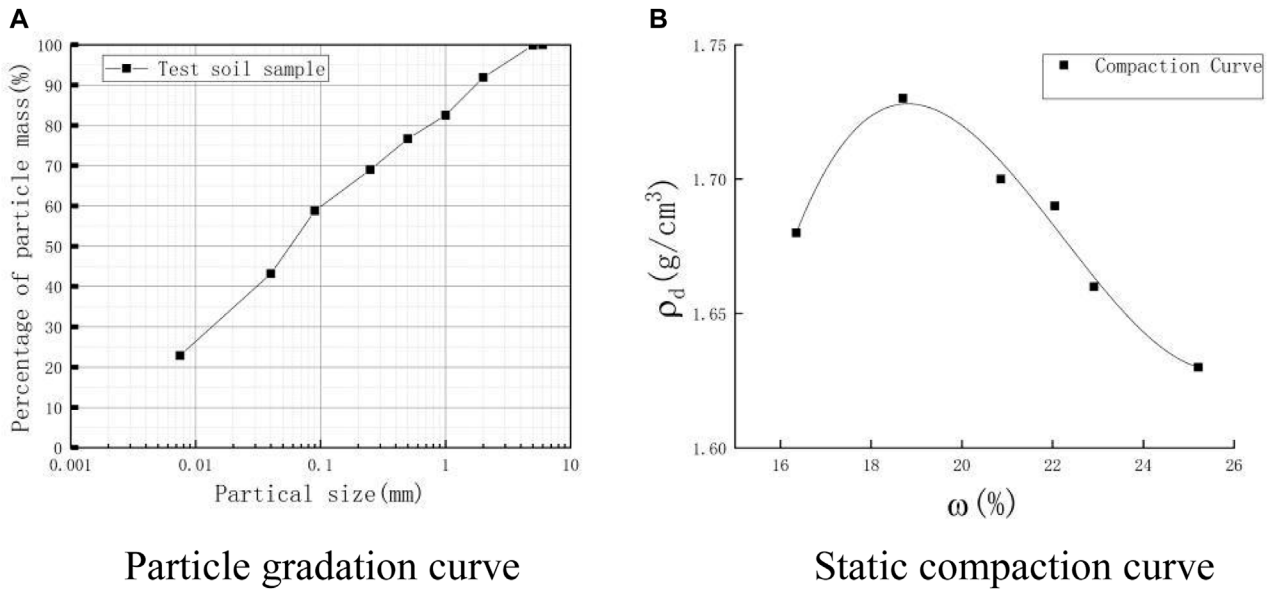

FIGURE 1
Particle gradation curve and compaction curve of soil. **(A)** Particle gradation curve **(B)** Static compaction curve.

TABLE 2 Physical parameters of the geogrid.

Name of reinforcing material	Reinforced geogrid	Mesh size (mm)	Tensile strength of glass fiber	
Bi-directional geogrid	Glass fiber	12.7 × 12.7	Lateral (kN/m)	Longitudinal (kN/m)
			50	50

in Figure 3A and the SWCC pressure plate meter is shown in Figure 3B.

2.3 Laboratory testing procedure

2.3.1 Triaxial consolidation and drainage shear tests

Approximately 2 kg of the residual soil was taken and then dried, crushed, and sieved through a 2 mm aperture step by step to remove the coarse particles. Finally, water was added to the remolded soil powder to reach an 18.7% moisture content and then the soil was sealed in a container for 24 h to make the moisture distribution in the soil uniform.The soil specimens with fixed dry densities and moisture content were made using the two layers static compacting soil method. After the first soil layer was compacted, the top surface of the soil layer was shaved using a scraper, and then the second layer of soil mass of the same weight was added to ensure the upper and lower layers were compacted to same compaction as far as possible. For saturated reinforced soil specimens and saturated soil specimens, the two types of specimens were saturated using the pumping saturation method; unsaturated reinforced soil specimens were kept at a moisture content of 18.7%.

The specimen dimensions for this test were d = 39.1 mm in diameter and h = 80 mm in height. The triaxial consolidation and drainage shear test methodology is outlined in Table 3, wherein the unsaturated specimen displayed a water content of 18.7%.

2.3.2 SWCC pressure plate meter test

In this paper, the SWC-150 SWCC pressure plate meter was used to determine the volumetric moisture contents of the residual soil under different matrix suction levels to obtain the SWCC. The soil dry density of the test was set at 1.64 g/cm^3, and the test apparatus measures matrix suction within a range of 0 to 500 kPa. The soil specimen size was d = 60 mm in diameter and h = 20 mm in thickness. The testing was divided into two stages; the saturated soil specimen was put into the device for the dehydration

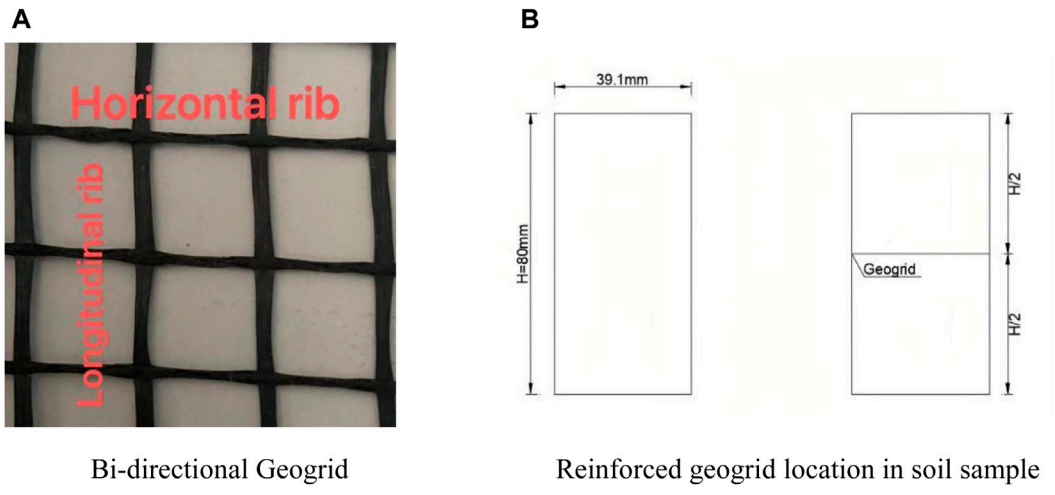

FIGURE 2
Diagrams of the geogrid and reinforced geogrid location. **(A)** Bi-directional geogrid **(B)** Reinforced geogrid location in soil sample.

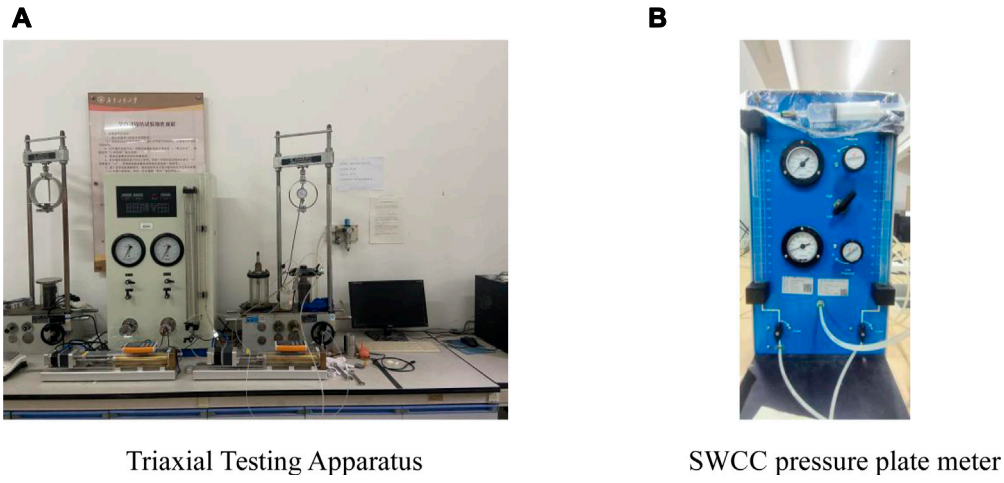

FIGURE 3
Testing instruments. **(A)** Triaxial testing apparatus **(B)** SWCC pressure plate meter.

process firstly, and after the dehydration stage, then, water was added and absorbed until water was continued until the soil specimen became saturated again. According to the volume moisture contents and corresponding matrix suction levels obtained from the testing, SWCC could be plotted for the granite residual soil.

3 Test results

3.1 Triaxial consolidation and drainage shearing tests

3.1.1 Saturated granite residual soil tests

By rearranging the triaxial consolidation and drainage shearing test data, the stress–strain relationship curves of the saturated soil samples under different dry densities and confining pressure levels are shown in Figure 4. It can be seen that the soil stress–strain relationship curves basically show a strain hardening tendency during the shearing process in saturated states for samples with a dry density of 1.56 g/cm^3, whereas there was a slight strain softening tendencyfor samples with dry densities of 1.73 g/cm^3 and 1.64 g/cm^3.

Figure 4 shows that the peak deviatoric stresses of soil specimens decrease as the dry density decreases, in which interlock friction between soil particles is lowered for the lower dry densities when shearing.

3.1.2 Geogrid reinforced granite residual soil tests in saturated states

The stress–strain relationship curves of the one-layer geogrid reinforced soil samples in the consolidation shearing drainage tests

TABLE 3 Triaxial consolidation and drainage shearing test scheme.

Saturated state and number of reinforced layers		ρ_d = 1.73 g/cm^3	ρ_d = 1.64 g/cm^3	ρ_d = 1.56 g/cm^3
Saturation state with confining pressures/kPa	Soil samples	σ_3 = 100	σ_3 = 100	σ_3 = 100
		σ_3 = 200	σ_3 = 200	σ_3 = 200
		σ_3 = 300	σ_3 = 300	σ_3 = 300
		σ_3 = 400	σ_3 = 400	σ_3 = 400
	One-layer reinforced soil samples	σ_3 = 100	σ_3 = 100	σ_3 = 100
		σ_3 = 200	σ_3 = 200	σ_3 = 200
		σ_3 = 300	σ_3 = 300	σ_3 = 300
		σ_3 = 400	σ_3 = 400	σ_3 = 400
Unsaturated state with confining pressure/kPa	One-layer reinforced soil samples	σ_3 = 100	σ_3 = 100	σ_3 = 100
		σ_3 = 200	σ_3 = 200	σ_3 = 200
		σ_3 = 300	σ_3 = 300	σ_3 = 300
		σ_3 = 400	σ_3 = 400	σ_3 = 400

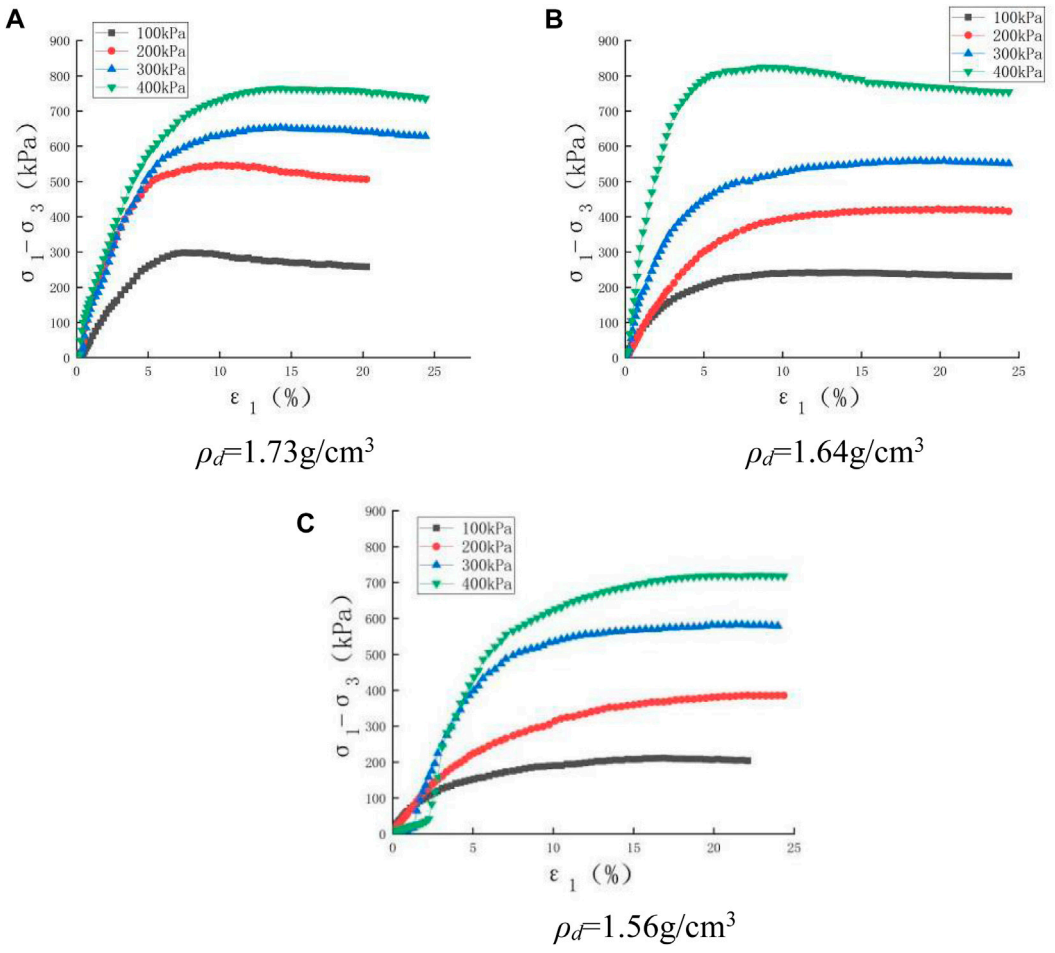

FIGURE 4
Stress–strain relationship curves of saturated soil samples with different dry densities. **(A)** ρ_d = 1.73 g/cm^3 **(B)** ρ_d = 1.64 g/cm^3 **(C)** ρ_d = 1.56 g/cm^3.

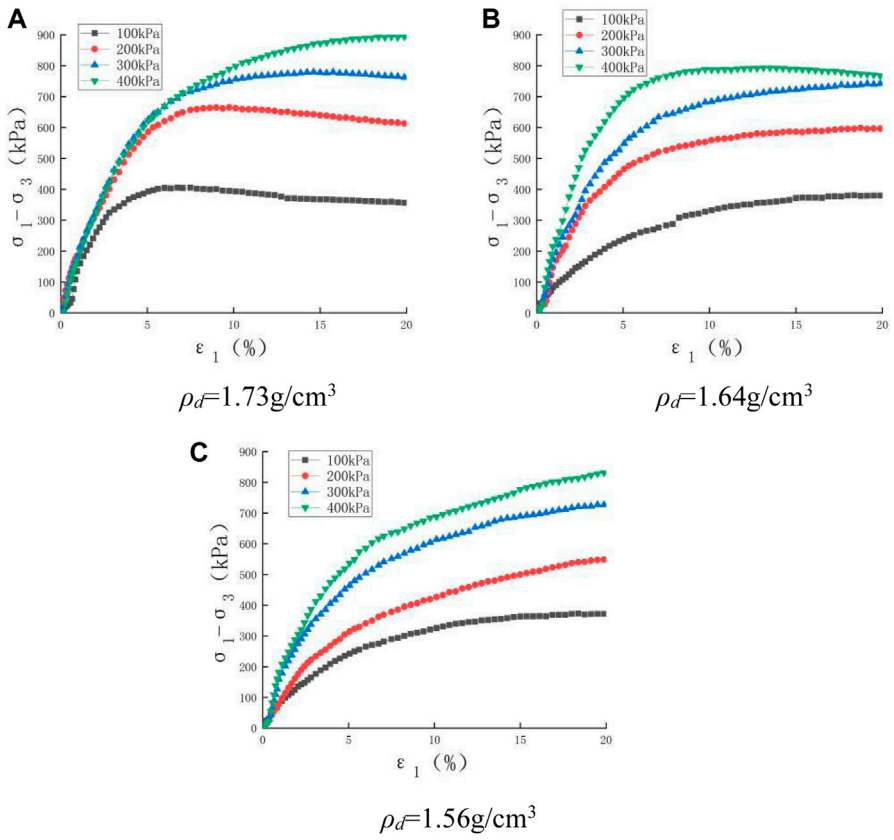

FIGURE 5
Stress–strain relationship curves of one-layer reinforced saturated samples under consolidation drainage shear tests. **(A)** ρ_d = 1.73 g/cm^3 **(B)** ρ_d = 1.64 g/cm^3 **(C)** ρ_d = 1.56 g/cm^3.

are shown in Figure 5. These basically show the trend of strain hardening, besides seldom slight strain softening curves for soil samples with a dry density of 1.73 g/cm^3 under lower confining pressure levels. The peak deviatoric stresses become larger as the confining pressure and dry density were increased individually, which indicates that the peak deviatoric stresses of the reinforced specimen gradually became larger by comparing with the testing peak deviatoric stresses of unreinforced saturated soil samples as shown in Figure 4.

For one-layer geogrid reinforced soil samples in saturated states and under lower confining pressure levels such as σ_3 = 100 kPa, relative horizontal displacement between the geogrid and the soil was produced obviously because of the relatively smaller frictional coefficient on the geogrid–soil interface and bigger geogrid tensile strength; this induced bulking deformation at the geogrid–soil interface location, and further soil lateral deformations along soil sample height were uneven, as shown in Figure 6A. Under higher confining pressure levels such as σ_3 = 400 kPa, the relative horizontal displacement between the geogrid and the soil was still bigger, but soil lateral deformations along soil sample height were relatively even because of the higher confining pressure preventing them, as shown in Figure 6C. For the intermediate confining pressure levels such as σ_3 = 200 kPa, the deformation shape of the geogrid reinforced soil samples were similar to the transition between that of Figures 6A,C.

3.1.3 Geogrid reinforced granite residual soil tests in unsaturated states

The one-layer geogrid reinforced specimens with three dry densities and the same moisture content of 18.7% in unsaturated states were tested in consolidation and drainage shear test, and the corresponding stress–strain curves obtained from these tests are shown in Figure 7.

From Figure 7, it can be seen that the soil particle pore space in the soil samples decreases when there is an increase in dry density, the peak deviatoric stresses of the geogrid reinforced soil increases; compared with the deviatoric stresses obtained from triaxial consolidation and the drainage shearing tests of saturated geogrid reinforced soil, the peak deviatoric stresses of unsaturated reinforced soil increased significantly due to the contribution of matrix suction.

3.1.4 Shear strength parameters

Based on the data from triaxial consolidation and drainage shearing tests, Table 4 summarizes the corresponding shear strength parameters.

From Table 4, it can be seen that the cohesion of the geogrid reinforced soil has a significant increase compared with that of unreinforced soil in the saturated shearing state, whereas variation in the internal friction angle was small relatively. The test results verify the correctness of the quasi-cohesion theory stated below, which is not only applicable to reinforced

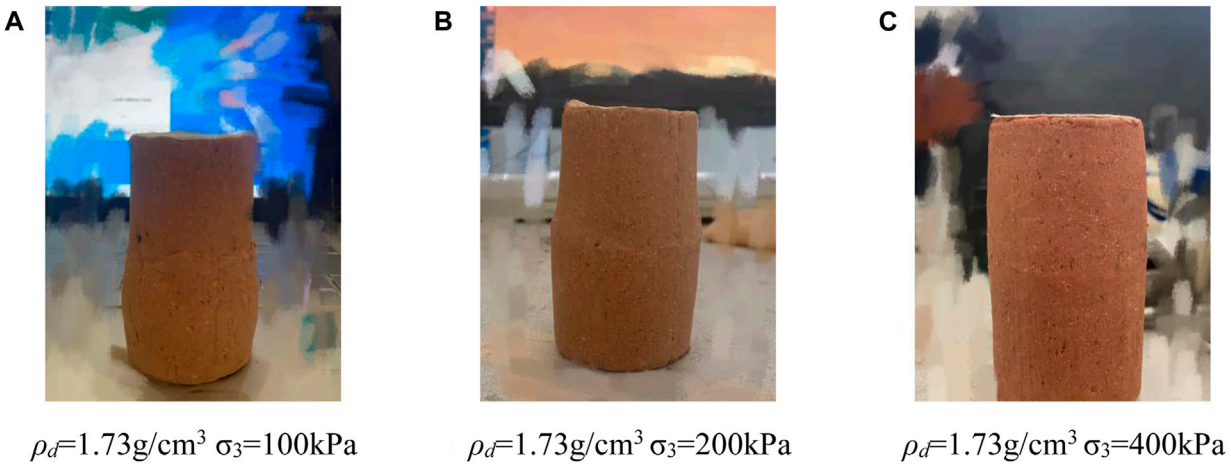

FIGURE 6
One-layer geogrid reinforced saturated sample failure status after testing. **(A)** ρ_d = 1.73 g/cm^3 σ_3 = 100 kPa **(B)** ρ_d = 1.73 g/cm^3 σ_3 = 200 kPa **(C)** ρ_d = 1.73 g/cm^3 σ_3 = 400 kPa.

sandy soil but also applicable to reinforced clay. The unsaturated geogrid reinforced soil has a significant increase in cohesion compared with that of saturated geogrid reinforced soil, which indicates that the cohesion provided by matrix suction is an important contribution that cannot be neglected totally in the design, construction, and maintenance of reinforced soil structures, and consideration of the cohesion contributed by soil matrix suctionis beneficial for reinforced soil structures in reducing the construction and maintenance expense.

3.2 SWCC test

For the remodeled soil samples with a dry density of 1.64 g/cm^3, the SWCC between soil volume moisture contents and matrix suctions are plotted in Figure 8 using the pressure plate meter testing results.

From Figure 8, it can be seen that the SWCC in the dehydration stage differed greatly from curve in the hygroscopy stage, and there was an obvious hysteresis phenomenon between the two curves. In the process of dehydration, the volumetric moisture content gradually decreases as the matrix suction increases; whereas in the process of hygroscopy, the matrix suction gradually decreases as the volumetric moisture content in the soil increases, and the rate of change in SWCC during the hygroscopic process also transitioned from slow to fast. The appearance of the hysteresis loop reflects the unique pore size distributing pattern in the soil mass, indicating the existence of medium to large pores in dimension and uneven pore size distribution inside the soil body; the more medium to large size pores existing inside the soil body, the more water is retained in the medium to large size pores due to the bottleneck effect in the dehydration stage, which eventually leads to the increase in the hysteresis area between the dehydration curve and hygroscopy curve of the granite residual soil obtained from Youxi county.

On the other hand, the soil skeleton is deformed with the changes in volumetric moisture content in the dehydration and hygroscopy stages. In the first dehydration stage, the soil sample has a slight decrease in pore volume induced by the increase in matrix suction due to the decrease in moisture content in the soil, and resulted in a slight decrease in the saturated volumetric water content of the soil sample was observed following the wetting stage.

4 Strength characteristics of geogrid reinforced soil in unsaturated states

4.1 Unsaturated soil shearing strength formula

Among the many shear strength formulas for unsaturated soils, Bishop's effective stress strength formula is currently the most famous. Bishop (Bishop and Blight, 1963; Xie, 2015) proposed a shear strength formula for unsaturated soils, combined with experimental studies, as expressed in Equation 1:

$$\tau = c' + \left[(\sigma - ua) + \chi(ua - uw)\right]\tan\phi' \quad (1)$$

where $(\sigma - u_a)$ denotes the net normal pressure, $(ua - u_w)$ denotes the matrix suction, c' denotes the effective cohesion, and ϕ' denotes the effective internal friction angle. χ is a parameter relating to the soil saturation and its value varies in the range of 0–1.0, which is a function of the soil saturation, soil type, and loading pressure. Since the equation is similar in form to the effective stress equation for saturated soils and relatively simple in expression, it is widely used in the study of shearing strength of unsaturated soils.

Equation 1 is further written in the form of Eq. 2:

$$\tau = c' + (\sigma - ua)\tan\phi' + \chi(ua - uw)\tan\phi' \quad (2)$$

Equation 3 can be obtained from Eq. 2 as follows:

$$c = c' + \Delta c_s = c' + \chi(ua - uw)\tan\phi' \quad (3)$$

where c is the apparent cohesion of unsaturated soil. Since the matrix suction is associated with the soil moisture content and $\triangle c_s$ is the quasi-cohesion increment induced by the matrix suction, scholars

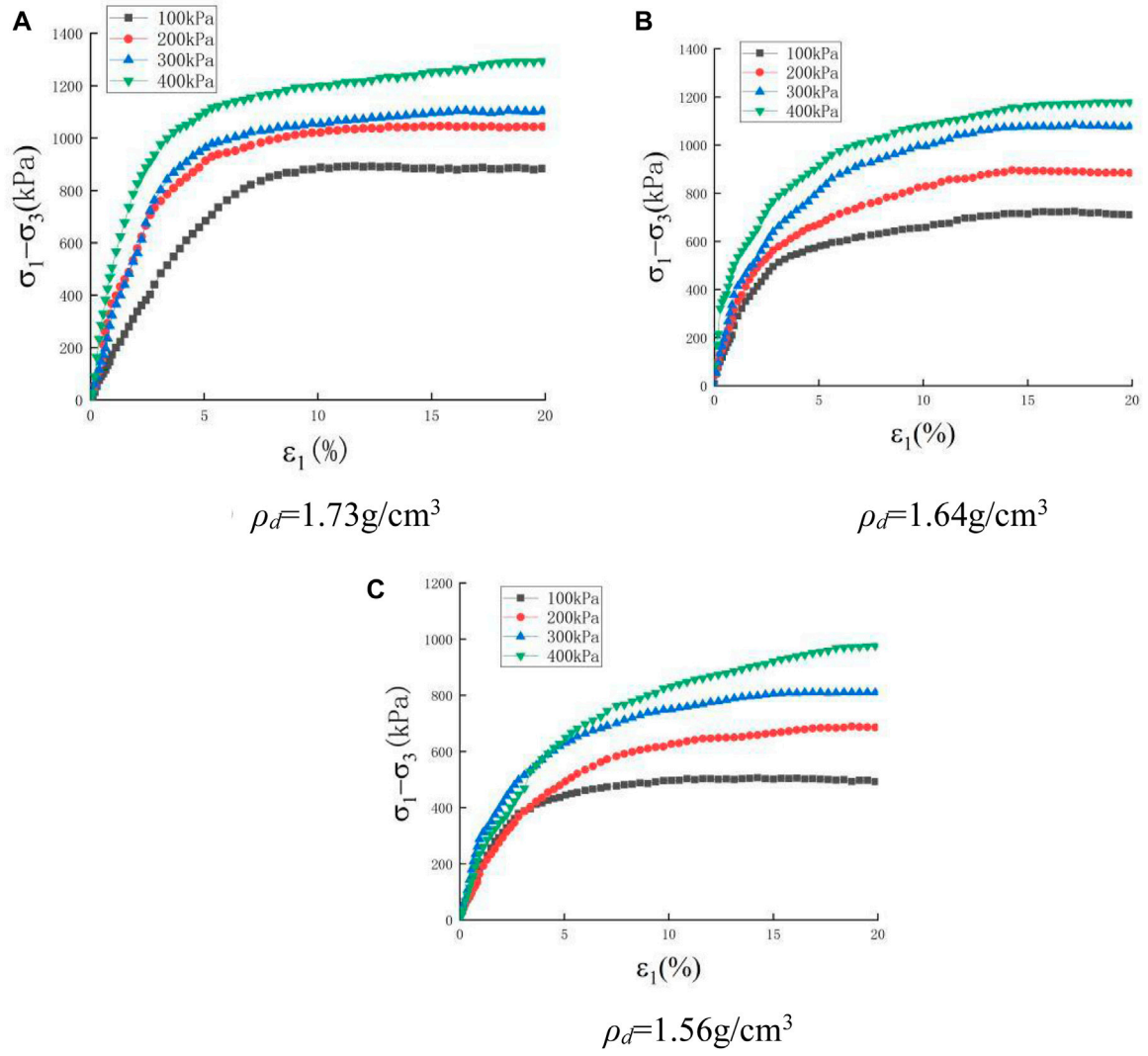

FIGURE 7
Stress–strain curves of one-layer geogrid reinforced unsaturated samples under consolidation drainage shearing tests. **(A)** ρ_d = 1.73 g/cm^3 **(B)** ρ_d = 1.64 g/cm^3 **(C)** ρ_d = 1.56 g/cm^3.

TABLE 4 Shearing strength parameters under triaxial consolidation drainage.

Dry density/(g/cm^3)	1.73	1.64	1.56
Saturated unreinforced soil	c' = 37.57 kPa	c' = 24.10 kPa	c' = 12.14 kPa
	ϕ' = 24.7°	ϕ' = 24.1°	ϕ' = 22.3°
Saturated geogrid reinforced soil	c = 74.74 kPa	c = 68.36 kPa	c = 59.63 kPa
	ϕ' = 26.4°	ϕ' = 28.2°	ϕ' = 25.5°
Unsaturated geogrid reinforced soil	c = 243.37 kPa	c = 189.96 kPa	c = 148.37 kPa
	ϕ' = 27.7°	ϕ' = 27.8°	ϕ' = 27.3°

established the parameter χ as a function of volume water content or saturation based on the SWCC to avoid the complicating experimental measurements.

Schrefler (Schrefler, 1984) proposed soil saturation replacing χ to derive Eq. 4 for the shearing strength of unsaturated soils:

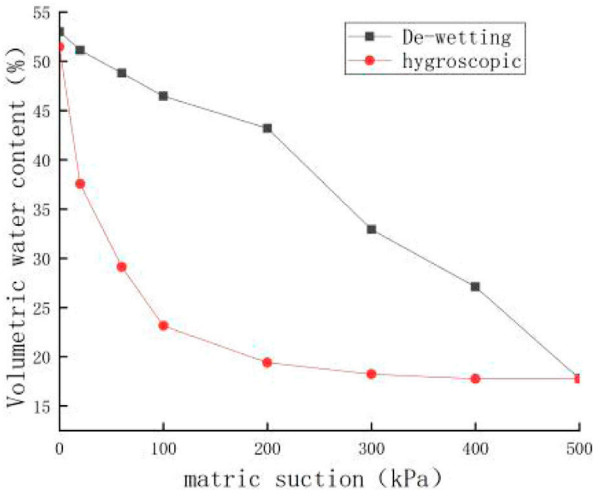

FIGURE 8
SWCC of remodeled granite residual soil.

$$\tau_f = c' + (ua - uw)Sr\tan\phi' + (\sigma - ua)\tan\phi' \quad (4)$$

Khalili et al. (Khalili and Khabbaz, 1998) introduced an air-entry suction value of unsaturated soil through extensive experimental studies and proposed the unsaturated soil shearing strength Eq. 5 as follows:

$$\tau_f = c' + (ua - uw)\left[\frac{ua - uw}{(ua - uw)b}\right]^{-0.55}\tan\phi' + (\sigma - ua)\tan\phi' \quad (5)$$

where $(ua - uw)b$ is the air-entry suction of unsaturated soil; this replaces the Eq. 3 parameter χ as the form $[(ua - uw)/(ua - uw)b]^{-0.55}$ to improve Bishop's formula shearing strength prediction ability for the unsaturated soil.

4.2 Quasi-cohesion increment calculation

The current research focuses on the reinforcement strengthening mechanism in reinforced soil as well as the corresponding equivalent quasi-cohesion increment calculating method. The quasi-cohesion increment calculation considers the internal friction angle of reinforced soil being basically equal to that of unreinforced soil, reinforcement simply increases the cohesion of the soil mass.

The quasi-cohesion increment calculation of reinforced soil could be explained further by using Mohr–Coulomb failure criterion as Eq. 6 expressing:

$$\sigma_{1f} = \sigma_3\tan^2\left(45° + \frac{\phi'}{2}\right) + 2\left(c' + \Delta c_r\right)\tan\left(45° + \frac{\phi'}{2}\right) \quad (6)$$

where σ_{1f} represents the major principal stress, kPa, at the shearing failure state of the reinforced soil; σ_3 represents the minor principal stress, kPa; c' represents soil effective cohesion, kPa; ϕ' represents angle of effective internal friction, °; and Δc_r is the quasi-cohesion increment contributed by the geogrid reinforcing function, kPa.

Comparing Eq. 6 with the limit equilibrium condition of unreinforced soil, the quasi-cohesion increment Δc_r contributed by the geogrid reinforced function in the reinforced soil can be calculated.

Through the triaxial compression tests of reinforced soil, the action of the reinforced geogrid in the soil can be regarded as an additional equivalent minor stress increment acting on the soil mass, thus the Δc_r formula (7) is proposed as follows:

$$\Delta c_r = \frac{\Delta\sigma_3\tan\left(45° + \frac{\phi'}{2}\right)}{2} \quad (7)$$

where $\Delta\sigma 3$ is the equivalent minor principal stress increment, generated by the reinforced geogrid restriction, and the increment cannot be measured directly and can be predicted theoretically. Eqs. 8 and 9 can be obtained from Figure 9 as follows:

$$\sigma_{1f} = \sigma_{3f}k_p + 2c'\left(k_p\right)^{1/2} \quad (8)$$

$$\sigma_1 = \sigma_3 k_p + 2c'\left(k_p\right)^{1/2} \quad (9)$$

Subtracting Eq. 8 from Eq. 9, then Eq. 10 is obtained:

$$k_p = \frac{\sigma_{1f} - \sigma_1}{\sigma_{3f} - \sigma_3} = \frac{\Delta\sigma_1}{\Delta\sigma_3} \quad (10)$$

Substituting Eq. 10 into Eq. 9, then Eq. 11 is obtained:

$$\Delta\sigma_3 = \sigma_3\left[\frac{\Delta\sigma_1}{\sigma_1 - 2c'\left(k_p\right)^{1/2}}\right] \quad (11)$$

Substituting Eq. 11 into Eq. 7, the quasi-cohesion increment of reinforced soil can be deduced as Eq. 12:

$$\Delta c_r = \frac{\sigma_3\sqrt{k_p}}{2}\left(\frac{\Delta\sigma_1}{\sigma_1 - 2c'\sqrt{k_p}}\right) \quad (12)$$

The quasi-cohesion increments of reinforced soil are calculated from Eq. 12, and are further compared with the measuring cohesion increments, as shown in Table 5.

As shown in Table 5, the increase in quasi-cohesion increments calculated by Eq. 12 is smaller than the measured value, which is because Eq. 12 calculates the quasi-cohesion increments only by the peak stress difference and the effective cohesion and effective angle of internal friction of the unreinforced soil, and does not sufficiently consider the influence of the reinforcing material, the size of the reinforcing material, and the number of reinforcing layers, which results in the calculated value usually being smaller than the measured value. The quasi-cohesion increments calculated based on the theory of quasi-cohesion for the reinforcing body shows a slight discrepancy from the measured value obtained from testing. However, the difference is relatively small and can be utilized as the safety consideration for reinforced soil structures.

4.3 Calculation of the shearing strength of unsaturated reinforced soil

It is usually difficult to measure the volumetric moisture content of the specimen during the shearing process; thus, this limits the study of shearing strength characteristics of the

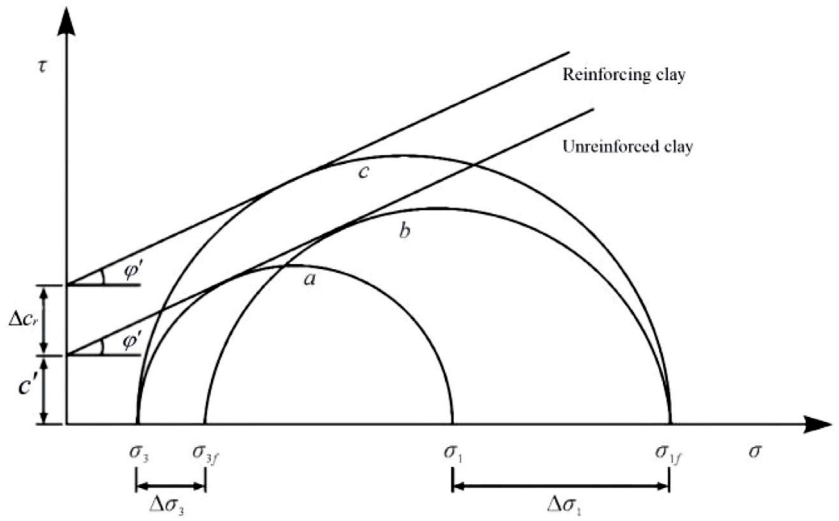

FIGURE 9
Stress analyses of reinforced and unreinforced clay samples.

TABLE 5 Calculating and measuring increments of quasi-cohesion of saturated reinforced clay.

Dry density/ (g/cm^3)	Confining pressure/kPa	Peak deviatoric stress of reinforced soil/kPa	Peak deviatoric stress of unreinforced soil/kPa	Peak deviatoric stress difference/kPa	Quasi-cohesion increment Δc_r/kPa	Measuring quasi-cohesion increment/kPa
1.73	100	392.8	284.2	108.6	31.40	37.14
	200	662.1	545.9	116.2		
	300	756.4	627.0	129.4		
	400	798.4	724.8	73.6		
1.64	100	332.4	239.2	93.2	41.28	44.26
	200	559.3	394.5	164.8		
	300	683.4	526.1	157.3		
	400	787.2	699.8	87.4		
1.56	100	325.8	180.1	145.7	39.62	47.49
	200	426.1	313.6	112.5		
	300	613.8	501.7	112.1		
	400	688.0	585.5	102.5		

unsaturated soil to some extent, because the volumetric moisture content of the specimen at shearing failure is easily measured, usually to be used to evaluate shear strength of unsaturated soil, as pointed out in the literature (Zhao, 2022). It can be also assumed approximately that the volume change of the specimen during shear is small, and the volumetric moisture content during shear is close to the initial volumetric moisture content. Based on the moisture absorbing curve in Figure 8, the shearing strengths of unsaturated reinforced soil are calculated in this section using the shearing failure volumetric water content and initial volumetric water content separately, and the calculating shear strengths using the two volumetric water contents are compared and commented upon further.

The volume moisture contents of unsaturated reinforced granite residual soil on shearing failure for the triaxial CD tests were measured, and corresponding matrix suctions are shown in Table 6. As can be seen from Table 6, there is a slight increase in the moisture content of the specimens after shearing compared with the initial moisture content of 18.7%.

1) Schrefler's formula for shear strength of unsaturated reinforced soil

TABLE 6 Water contents of specimens after shearing and the corresponding matrix suctions.

Dry density/(g/cm³)	Confining pressure/kPa	Volume moisture content after shearing/%	Saturation/%	Matrix suction/kPa
1.73	100	19.9	42.2	251.75
	200	21.1	44.7	208.70
	300	20.8	44.1	218.71
	400	21.7	46.0	189.69
1.64	100	20.0	37.8	245.74
	200	22.0	41.5	180.68
	300	18.9	35.7	295.29
	400	19.6	37.0	263.76
1.56	100	20.7	35.0	222.22
	200	19.8	33.2	255.75
	300	20.3	34.1	236.23
	400	21.4	35.9	198.69

The saturation in Table 6 can be substituted into Eq. 3 to calculate the quasi-cohesion increment of unsaturated reinforced granite residual soil, and the calculated results are summarized in Figure 10. The calculated results have obvious differences with the experimental measured values, which are due to the fact that the shear strength formula proposed by Schrefler only considers the linear effect of saturation on shear strength, thus Schrefler's formula cannot better reflect the effect of matrix suction on the shearing strength of unsaturated soil correctly.

2) Khalili unsaturated soil shear strength formula

From the literature (Zhang, 2018) and the testing results in this paper, it is known that the air-entry matrix suction of granite residual soil is about 10 kPa, thus $(ua - uw)b$ = 10kPa is used for calculation so that the apparent cohesion of unsaturated reinforced granite residual soil can be calculated by substituting the air-entry matrix suction 10 kPa into Equation 5, and the calculating results are summarized in Figure 10.

At the same time, the cohesion of unsaturated reinforced granite residual soil was also calculated using the initial volume moisture content 18.7% of the specimen, and corresponding matrix suction of granite residual soil according to initial volume moisture content 18.7% was read as 279.27 kPa from the moisture absorbing curve in Figure 8, and the apparent cohesion of the unsaturated reinforced granite residual soil was calculated according to Eq. 13. The calculated results were also shown in Figure 10:

$$c = c' + \Delta c_r + \Delta c_s = c' + \frac{\sigma_3\sqrt{k_p}}{2}\left(\frac{\Delta\sigma_1}{\sigma_1 - 2c'\sqrt{k_p}}\right) + \chi\,(u_a - u_w)\tan\phi' \tag{13}$$

where Δc_s is the apparent cohesion increment induced by matrix suction, being different from quasi-cohesion increment Δc_r contributed by the geogrid restriction.

As shown in Figure 10, relatively to the Schrefler unsaturated soil shear strength formula, the Khalili unsaturated soil shear strength formula can predict the cohesion of unsaturated reinforced soil more accurately, in which the cohesion includes three parts, i.e., effective cohesion c' contributed by the soil mass itself, apparent cohesion increment Δc_s produced by matrix suction, and quasi-cohesion increment Δc_r contributed by reinforced effecting of geogrid. Comparing the cohesion calculated using the shearing failure volume moisture content with cohesion calculated based on initial volume moisture content, the cohesion calculated using the shearing failure volume moisture content is closer to the measured cohesion of the unsaturated reinforced soil. The calculating cohesion errors using the Khalili method were 2.28% for the dry density 1.64 g/cm³ sample and 6.36% for the dry density 1.56 g/cm³ sample, and calculating cohesion for the dry density 1.73 g/cm³ sample can also reflects the measured value to some extent, but the error is large.

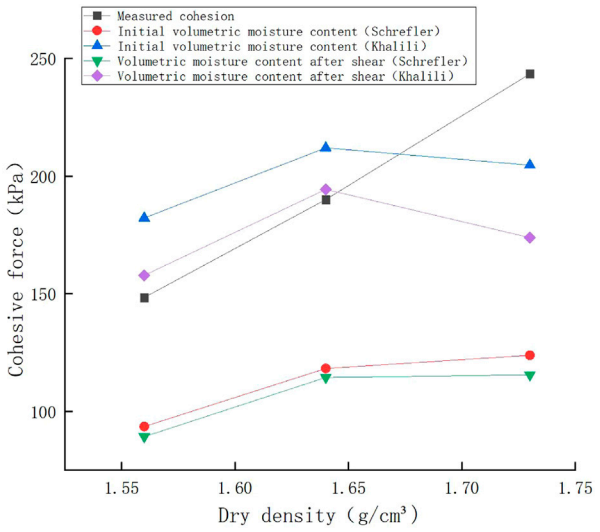

FIGURE 10
Calculated and measured cohesions of unsaturated reinforced granite residual soil.

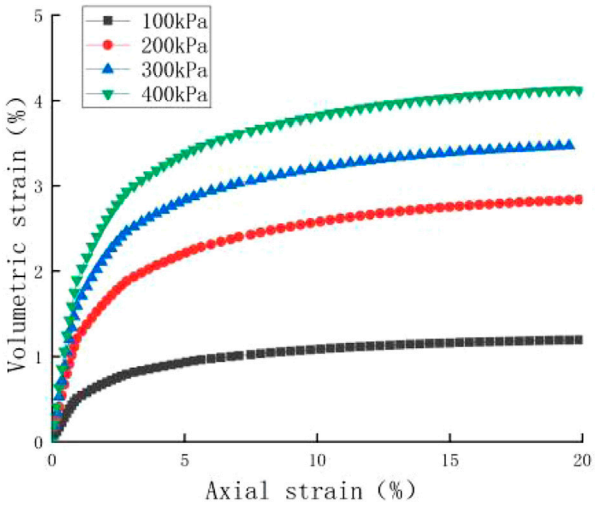

FIGURE 11
Volume strain and axial strain curves for unsaturated reinforced soil with ρ_d = 1.64 g/cm^3.

When the initial volume moisture content was considered, the errors using the Khalili method were significantly larger for the dry density 1.64 g/cm^3 and 1.56 g/cm^3 samples than those calculated using the shearing failure volume moisture content, but the error for the dry density 1.73 g/cm^3 sample was relatively smaller.

Combining SWCC under a specific dry density condition with the Khalili formula may predict the cohesion of unsaturated reinforced soil approaching the specific dry density for unsaturated soil. Thus, formula (13) provides theoretical and experimental evidence to support the practical design, construction, and maintenance of reinforced soil structures.

It is also important to add in that both unsaturated soil and unsaturated reinforced soil tests always keep the back pressure at zero during testing, as the water content in soil samples do not have enough time to change during the triaxial shear process, and the volume change of unsaturated reinforced soil is caused mainly due to gas seepage; thus, soil volume at the moment of shearing failure is expressed in Eq. 14:

$$v = \left(1 - \varepsilon_{vf}\right)v_0, \varepsilon_{vf} = \varepsilon_{1f} + 2\varepsilon_{3f} \tag{14}$$

In order to verify the volume change mainly induced by gas seepage, a smaller back pressure of 20 kPa was applied for the soil specimen triaxial consolidation and drainage shear test in unsaturated states. During the shear test, any gas or water discharged from the specimen was measured. To minimize the impact of back pressure on the results, a lower back pressure 20 kPa was used. Using the dry density 1.64 g/cm^3 specimens for the tests, Figure 11 displays the volume strain curves acquired through the triaxial consolidation and drainage shear tests.

The volumetric water contents calculated from Eq. 14 at the moment of shearing failure approached the measured values listed in Table 6, which indicates that the volume change was mainly due to dissipated gas.

5 Conclusion

1) Unsaturated reinforced soil has a significantly greater cohesion than saturated reinforced soil due to matrix suction. Experimental and theoretical results indicate that matrix suction contributes more to the total cohesion.
2) The water-added remodeling process of granite residual soil exhibited similarities to the hygroscopic stage. As a result, utilizing the hygroscopic stage's soil-water characteristic curve allows for more accurate prediction of the apparent cohesion increment of unsaturated soil.
3) Quasi-cohesion increment calculating using formula (12) for the geogrid reinforced saturated soil was verified to be correct compared with the experimental results; Khalili's modified formula accurately predicts the quasi-cohesive strength of unsaturated reinforced soils based on the effective cohesion, matrix suction, and reinforcement, as demonstrated.
4) By verifying theoretical results to the results of triaxial tests with three dry density specimens in unsaturated states, it is pointed that the Khalili unsaturated soil shear strength formula predicts the shear strength of soil using shearing failure volumetric water content slightly better than that calculated using the initial volumetric water content, by using reasonable SWCC.

Data availability statement

The raw data supporting the conclusion of this article will be made available by the authors, without undue reservation.

Author contributions

XD: Writing–original draft. ZZ: Writing–original draft. XL: Writing–original draft. XY: Writing–review and editing.

Funding

The author(s) declare financial support was received for the research, authorship, and/or publication of this article. National Natural Science Foundation of China (51978177).

Conflict of interest

The authors declare that the research was conducted in the absence of any commercial or financial relationships that could be construed as a potential conflict of interest.

Publisher's note

References

Abdi, M. R., Zandieh, A. R., Mirzaeifar, H., and Arjomand, M. A. (2019). Influence of geogrid type and coarse grain size on pull out behaviour of clays reinforced with geogrids embedded in thin granular layers. *Eur. J. Environ. Civ. Eng.* 25 (12), 2161–2180. doi:10.1080/19648189.2019.1619627

Bai, B., Zhou, R., Cai, G., Hu, W., and Yang, G. (2021). Coupled thermo-hydro-mechanical mechanism in view of the soil particle rearrangement of granular thermodynamics. *Comput. Geotechnics* 137 (8), 104272. doi:10.1016/j.compgeo.2021.104272

Bergado, T. D., Shivashankar, R., Alfaro, C. M., Chai, J. C., and Balasubramaniam, A. S. (1993). Interaction behaviour of steel grid reinforcements in a clayey sand. *Géotechnique* 43 (4), 589–603. doi:10.1680/geot.1993.43.4.589

Bishop, A. W., and Blight, G. E. (1963). Some aspects of effective stress in saturated and partly saturated soils. *Géotechnique* 13 (3), 177–197. doi:10.1680/geot.1963.13.3.177

Chehade, A. H., Dias, D., Sadek, M., Jenck, O., and Hage Chehade, F. (2020). Upper bound seismic limit analysis of geosynthetic-reinforced unsaturated soil walls. *Geotext. Geomembranes* 48 (4), 419–430. doi:10.1016/j.geotexmem.2020.02.001

Gao, Y., Chang, L. I. U., Tian, W., and Zhao, Y. (2018). Experimental study on the relationship between saturation and shear strength of silty clay. *Pearl River* 39 (02), 1–4.

Guoqing, C., Yi, L., Jian, L., Yang, R., and Zhao, C. (2022). Water retention curve with different void ratios over a wide suction range and its application to shear strength. *Int. J. Geomechanics* 22 (8). doi:10.1061/(asce)gm.1943-5622.0002484

He, Y., Liao, H., and Dong, Q. (2021). Experimental study on strength characteristics of geogrid -reinforced loess. *Chin. J. Geotechnical Eng.* 43 (S1), 181–185. doi:10.11779/CJGE2021S1033

He, Z. J., SiGa, A., and Zou, J. F. (2019). Research for reinforced fine-grained sand based on large-scale triaxial tests. *J. Railw. Sci. Eng.* 16 (10), 2451–2458. doi:10.19713/j.cnki.43-1423/u.2019.10.010

Huang, J., Fan, P., and Shan, Y. (2022). Study on unsaturated characteristics of granite residual soil and its slope stability. *Build. Struct.* 52 (24), 138–143. doi:10.19701/j.jzjg.ZJ220082

Infante, U. J. D., Martinez, A. M. G., Arrua, A. P., and Eberhardt, M. (2016). Shear strength behavior of different geosynthetic reinforced soil structure from direct shear test. *Int. J. Geosynth. Ground Eng.* 2 (2), 17. doi:10.1007/s40891-016-0058-2

Khalili, N., and Khabbaz, M. H. (1998). A unique relationship for χ for the determination of the shear strength of unsaturated soils. *Geotechnique* 48 (5), 681–687. doi:10.1680/geot.1998.48.5.681

Kouchaksaraei, K. M., and Khalkhali, B. A. (2020). The effect of geocell dimensions and layout on the strength properties of reinforced soil. *SN Appl. Sci.* 2 (10), 1701. doi:10.1007/s42452-020-03480-w

Lei, S. Y. (2000). Study on reinforced loess by triaxial tests. *J. Xi'an Highw. Univ.* (02), 1–5. doi:10.3321/j.issn:1671-8879.2000.02.001

Luo, X., and Fu, M. (2019). Experimental study of strength characteristics of unsaturated granite residual soil in collapsing erosion area. *Water Power* 45 (01), 107–111. doi:10.3969/j.issn.0559-9342.2019.01.027

Mahmoud, G., and Omid, B. (2021). Analytical solution for calculation of pull out force-deformation of geosynthetics reinforcing unsaturated soils. *Geotext. Geomembranes*. doi:10.1016/j.geotexmem.2021.12.005

Mohammadehsan, Z., and Mohammadreza, Z. (2017). Study on the impact of strain rate and loading speed on geogrid-reinforced soil. *J. Sustain. Dev.* 10 (2), 238. doi:10.5539/jsd.v10n2p238

Pham, A. T. (2022). Micromechanical-Based Shear strength equation considering the stress-state effect for unsaturated soils. *Int. J. Geomechanics* 22 (9). doi:10.1061/(ASCE)GM.1943-5622.0002495

Schrefler, B. A. (1984). *The finite element method in soil consolidation:with applications to surface sidence*. Swansea: University College of Swansea.

Vidal, H. (1969). *The principle of reinforced earth*. Washington, D.C.: Highway Research Record.

Wang, Z., Chang, L. I., and Xiao, L. (2021). Triaxial test study on reinforcement effect of reinforced cohesive soil. *J. Chongqing Jiaot. Univ. Nat. Sci.* 40 (07), 99–106. doi:10.3969/j.issn.1674-0696.2021.07.15

Wei-xiang, Z., Meng-jie, Y., and Fei-yu, L. (2023). Investigation on the cyclic shear response of stereoscopic geogrid-reinforced coarse-grained soil interface. *Transp. Geotech.*, 38. doi:10.1016/j.trgeo.2022.100905

Chen, X., Zhang, J., and Li, Z. (2014). Shear behaviour of a geogrid-reinforced coarse-grained soil based on large-scale triaxial tests. *Geotext. Geomembranes* 42 (4), 312–328. doi:10.1016/j.geotexmem.2014.05.004

Xie, D. (2015). *Soil mechanics for unsaturated soils*. Beijing: Higher Education Press.

Zhang, He, and YaLong, L. I. (2023). Study of mechanical properties of reinforced red sandstone. *J. Liaoning Tech. Univ. Sci.* 42 (02), 143–151. doi:10.11956/j.issn.1008-0562.2023.02.003

Zhang, S. (2018). *The safety of the unsaturated soil slope stability analysis under different moisture content*. Shijiazhuang, China: Shijiazhuang Tiedao University.

Zhao, B., and Lin, Y. (2019). Stability analysis of the reinforced soil retaining wall against unsaturated soils. *Railw. Eng.* 59 (10), 100–103. doi:10.3969/j.issn.1003-1995.2019.10.24

Zhao, J., Xu, Z., and Chai, J. (2021). Experimental investigation in strength and water retention behaviors of remolded loess under drying-wetting cycle. *Water Resour. Power* 39 (09), 169–172+139.

Zhao, L. (2022). *Research on physical and mechanical properties of unsaturated soil for Lanzhou-Cooperative high-speed railway line*. Xi'an, China: Chang'an University.

Zhong, Z., Liu, Y., Liu, X., Li, X. y., and Wang, S. (2015). Influence of moisture content on shearing strength of unsaturated undisturbed quaternary system middle pleistocene. *J. Central South Univ.* 22 (7), 2776–2782. doi:10.1007/s11771-015-2808-z

Zhou, J., and Xu, H. (2013). Triaxial tests of expansive soil reinforced with basalt fiber geogrid. *J. Nanjing Univ. Technol. Nat. Sci. Ed.* 35 (05), 105–109. doi:10.3969/j.issn.1671-7627.2013.05.020

Frontiers in Materials

Investigates the discovery and design of materials for future application

A multidisciplinary journal that explores the breadth of materials science, engineering and mechanics - from carbon-based materials to smart materials.

Discover the latest Research Topics

See more →

Frontiers

Avenue du Tribunal-Fédéral 34
1005 Lausanne, Switzerland
frontiersin.org

Contact us

+41 (0)21 510 17 00
frontiersin.org/about/contact